THE UNIVERSITY
of EDINBURGH

This thesis has been submitted in fulfilment of the requirements for a postgraduate degree (e.g. PhD, MPhil, DClinPsychol) at the University of Edinburgh. Please note the following terms and conditions of use:

This work is protected by copyright and other intellectual property rights, which are retained by the thesis author, unless otherwise stated.
A copy can be downloaded for personal non-commercial research or study, without prior permission or charge.
This thesis cannot be reproduced or quoted extensively from without first obtaining permission in writing from the author.
The content must not be changed in any way or sold commercially in any format or medium without the formal permission of the author.
When referring to this work, full bibliographic details including the author, title, awarding institution and date of the thesis must be given.

3D Visualisation of Melts at the Conditions of Earth's Deep Interior

Madeleine TL Berg

Thesis submitted for the degree of Doctor of Philosophy

School of Geosciences

The University of Edinburgh

2015

Abstract

Constraining the behaviour of small fractions of partial melt in a solid silicate matrix has been the focus of numerous experimental petrology studies over several decades, and is an important factor in constraining upper mantle rheology, melt extraction at mid-ocean ridges and mechanisms of core formation in the early solar system. Deformation of partially molten rock has been observed to change melt geometry, and may enhance permeability and interconnectivity of melt otherwise trapped in a solid silicate matrix, although it is uncertain how applicable results of high strain-rate laboratory experiments are to the real Earth. The addition of deformation precludes attainment of textural equilibrium, complicating textural analysis, which has previously relied on extrapolation of 3D textures from quenched and polished 2D sections for hydrostatically annealed samples. X-ray computed tomography gives the potential to visualise sample textures directly in three dimensions, and is becoming popular as a complementary technique for textural analysis in petrologic studies. The aim of this project has been to develop techniques to improve visualisation of small fractions of partial melt within a solid silicate matrix using X-ray CT, to examine textures of various partially molten systems at high PT in hydrostatic, and dynamically deforming systems.

Experiments carried out in the FeS-melt, solid olivine system have examined the potential for deformation-enhanced percolation of core forming melts before the onset of silicate melting. Access to the newly designed rotational Paris-Edinburgh Cell (roPEC/rotoPEC) equipment has allowed us to carry out controlled, torsional deformation experiments under PT conditions applicable to planetary interiors. Experiments conducted at lower strain-rates over longer duration than in previously published studies show that deformation enhances connectivity at low melt fractions, at strain-rates down to $10^{-6}s^{-1}$. This is in contrast to earlier work suggesting melt textures are unaffected at strain-rates below $10^{-5}s^{-1}$. Quenched melt networks have been fully characterised in 3D using multi-scale CT, with voxel sizes down to 70nm for small sample sub-volumes. Results suggest segregation of metallic melt below the silicate solidus could be an efficient process, and should be taken into account in geochemical models of planetary evolution.

Experiments on basaltic melt in a solid silicate matrix were conducted in application to upper mantle melting. A heavy element, hafnium, was added to the basaltic glass starting composition to enhance contrast between the basalt and olivine phases during CT scans. In-house micro-CT equipment was used to visualise post-quench run products of hydrostatic and deformation experiments. The doping technique was successful for long-duration, high temperature hydrostatic experiments. Some issues with undissolved / re-precipitated HfO¬2 crystals complicated tomographic imaging of partial melt textures in a number of experiments, particularly those carried out on the rotoPEC equipment, limiting comparison between samples. The doping technique requires further adjustment, but is shown to be a viable way to improve visibility of basaltic melt without significantly affecting melt texture.

The X-ray transparent design and fully rotating top and bottom anvils of the rotoPEC allow X-ray tomography to be carried out in-situ while experiments are in progress, enabling collection of 4D datasets. During this project, the rotoPEC equipment was incorporated into two different synchrotron beamlines, to carry out time-resolved studies of textural development within samples of varying composition. The migration of gold melt along fractures with a BN matrix was imaged using 2D radiography, in combination with repeated 3D tomography to fully characterise the 3D fracture geometry. This allowed melt migration velocity to be estimated directly from in-situ observations. These techniques could be developed further to constrain melt migration processes quantitatively for a number of geological systems in the near future.

Lay Summary

A rock is a mixture of minerals of different compositions and therefore different melting points. As a rock heats up, materials melt at different temperatures, meaning the initial molten rock will exist as small fractions of liquid in a mainly solid matrix (a partial melt). We are interested in the behaviour of this liquid: Is it able to move around in the solid matrix, or is it trapped in isolated pockets and cannot move? The way melt behaves at depth might be an important factor in controlling the mechanics of plate tectonics, as well as having a potentially important role to play in the way planets grew and evolved in the early solar system, to produce a metallic core and rocky outer mantle. By investigating the behaviour of liquids of different compositions under high pressure and temperature conditions in the lab, we are able to investigate partial melt in different geological systems in the real Earth and other Earth-like planets.

We create synthetic powdered mixtures of olivine crystals (the most common mineral in the deep Earth) and another material of lower melting temperature (basalt glass or iron metal), which acts as the melt phase. We can use specialised pressure vessels to put small volumes of this material under high pressure-temperature (P-T) conditions similar to those found at depths of hundreds of kilometres in the Earth's interior, where the 'melt phase' is liquid. We also have access to equipment that can physically twist samples while they are at high P-T, applying a force to deform the sample, i.e. change its shape.

After the experiment, the sample is quenched to freeze in resulting textures, and examined both visually and in terms of chemical composition to infer processes occurring during the experiment. Traditionally this analysis has been carried out using powerful electron microscopes on 2D slices of the sample. However, when looking at complicated experimental results, it is advantageous to see the geometry of melt within the sample in 3D. A main aim of this project has been to use computed tomography (CT), an X-ray imaging technique, to produce detailed 3D images of the inside of experimental samples. We have also worked on ways to observe melt movement and textural changes in real time during high P-T experiments. By using a powerful synchrotron X-ray source and specially designed high P-T press, which allows X-rays to pass through the central sample capsule even at high P-T, we have been able to track the movement of melt through fractures in a solid material and observe changes in 3D geometry during an experiment, essentially creating a 4D dataset.

This research shows the potential of using 3D and 4D visualisation techniques to understand more about experiments conducted in the laboratory, which can be used (with caution) to learn about the deepest, most inaccessible parts of our planet.

Author's Declaration

I declare that this thesis has been composed solely by myself and that it has not been submitted, either in whole or in part, in any previous application for a degree. Except where otherwise acknowledged, the work presented is entirely my own.

Madeleine Berg

2015

Acknowledgments

This project would never have made it to this stage without the help of a long list of people. This includes academic support from university colleagues, but also emotional and moral support from friends and family.

Firstly I would like to thank my supervisors Geoff Bromiley and Ian Butler, who have always been available for guidance when I needed it, and have given excellent feedback on my work, at whatever stage of completion! Other members of staff have also been a source of invaluable advice, equipment, and inspiration: Godfrey Fitton, particular thanks for giving me a piece of mid-ocean ridge! Florian Fusseis for help with CT processing and tipping me off about interesting conferences. John Craven for letting me use so much equipment and giving me much needed advice so often. Nicola Cayzer for fantastic support on the SEM, particularly when it came to EBSD work. Nic Odling for loaning me his watchmaker's lathe, showing me how to make capsules with it, and always being around for mineral-based problems. Mike Hall, who let me loose in his thin-section lab so often, and was always very patient with my unusual polishing/grinding problems. My PhD had an additional emphasis on science outreach through the Principal's Career Development Scholarship, which allowed me to take more time to expand my experience in this field. I would like to thank Colin Graham (also an excellent advisor), Catherine Morgan and Brian Cameron for letting me take part in many fun and varied activities, which I have enjoyed immensely over my time in Edinburgh. I would also like to thank John Dixon, for inviting me to join a fantastic geo-archaeological expedition to Keros, Greece (with Mark Beaumont, Tim Kinnaird) - a fascinating distraction to my PhD project. I am honoured to have worked with him until his final days (and to take on the responsibility of the JEDI golf estate!).

The work carried out in this project was highly collaborative between Universities, both in the UK and abroad. Without access to external facilities and laboratories, the majority of work carried out here would not have been possible. Thanks to Simon Redfern for the loan of his lab space for roPEC experiments in Cambridge. Kate Dobson at Manchester University / DIAMOND for supporting us through beamtime applications and invaluable help at DIAMOND. Also Rob Bradley and James Carr from Manchester University for CT support and flow simulations. Elisabetta Mariani and Daniel Tatham at Liverpool University were kind enough to carry out EBSD scans and assist with analysis of resulting data. Finally Yann le Godec, Julien Phillippe from UPMC, University of Paris, who not only allowed us to use their new rotoPEC equipment, but also came along to each week of beamtime, and let me use their laboratory in Paris for 2 weeks. It is fair to say that half of the work in this thesis would not exist without them, and the help of others at UPMC. Three long, demanding weeks of synchrotron beamtime were carried out for this project, greatly supported by our collaborating team of scientists (Yann, Julien and Frederic from UPMC, Kate Dobson from Manchester) as well as the hard work of the beamline scientists: Rob Atwood at DIAMOND, Mohamed Mezouar at ESRF. Additional assistance was given by a number of post-docs, beamline scientists and researchers at both synchrotrons,

who helped to install equipment and fix problems efficiently at any time of the day and night.

Thanks to PhD students in the school of Geosciences for making three years of toil not only bearable, but also enjoyable: Alice, Tannaz, Jen B, Matt H, Gus, and Axel, Romesh, Kit Rachel, Robyn, Sophie, Jamie, Claire, Nick, Rory, Matt C, Mark B, Andrew T, Ed, Emma, J-P. Special mention to Johannes for providing the Latex thesis template and helping me work out how to use it. I'd never have compiled the beast without you, literally!

Thanks to flatmates old and new: Helen, Payam, Dave, Andy, Emilia, Ryan, Finn (little goat), Robyn, Calum, Cailean. Living with you all has been brilliant. Thanks to other good friends for putting up with grumbling and providing much needed support: Vijay, Rachel Ed and Alfie (team CDWM 2012-2013), Erika and James (thanks for moving back!), Jakob (for teaching me about trees when I was fed up with rocks) Fiona, Nikki, Andy, Marcus (honorary flatmates). Thanks to Caro, Tom M, Matt, Jamie, Rowland (also Nicole, Tom W and Ire) for all the music therapy.

Finally, I would never have got to this point without the support of my brilliant family: Pa-Patrick, Regine and Clara Bergs. Grandma Jean, who gave me financial support when I was writing up with no funding and some excellent games of scrabble to keep my brain lubricated. Thanks to Fred (bro-face) for putting up with my misery at times of desperation, and excellent answers to bizarre engineering-related questions. And of course Vivi-Mum for proof-reading, feeding, motivational chats and just generally being there.

You are all excellent.

Thank you

Contents

Abstract i

Lay Summary i

Author's Declaration ii

Acknowledgments iii

Table of Contents v

List of Figures xii

List of Tables xviii

List of Abbreviations xxi

1 Introduction 1

1.1 Introduction . . . 2

1.1.1 Outline of research . . . 3

1.2 Background . . . 4

1.2.1 Principles of partial melt and deformation . . . 5

Melt geometry and permeability in a hydrostatic system . . . 6

Ductile deformation of crystalline solids at high P-T . . . 10

Deformation of partially molten solids . . . 16

1.2.2 Principles of X-ray tomography . . . 21

The need for 3D visualisation in experimental petrology . . . 21

Principles of X-ray interaction with matter . . . 22

The X-ray Computed Tomography (XCT) system . . . 23

Reconstruction . . . 28

Resolution limitations and nano-CT . . . 30

Contrast limitations . . . 33

Noise and artefacts . . . 35

Application of CT in visualisation of geological melts . . . 37

Development of in-situ tomographic techniques in the geosciences . . . 38
1.3 Geological context . . . 40
1.3.1 Core formation in planets and planetesimals . . . 40
Constraints on core formation processes . . . 41
The magma ocean model . . . 45
Deformation aided percolation model . . . 46
Summary of open questions . . . 48
1.4 Basaltic melt . . . 49
1.4.1 Where do we find melt in the upper mantle? . . . 49
The LVZ . . . 49
Mid-ocean ridges: melt extraction . . . 53
Mid-ocean ridges: melt focusing . . . 56
Experimental constraints on basaltic melt geometry . . . 59
The influence of deformation on basaltic melt geometry . . . 60
Deformation of large melt fractions . . . 61
Extrapolation from experiments to the Earth . . . 62
3D visualisation of basaltic melts . . . 63
Summary of open questions . . . 69

2 Methods **71**
2.1 Introduction . . . 72
2.2 Experimental methods . . . 72
2.2.1 Experimental equipment . . . 72
Static . . . 72
Deformation equipment . . . 73
roPEC . . . 73
rotoPEC . . . 76
Calibration . . . 76
2.2.2 Materials, Conditions . . . 80
Starting materials . . . 80
Synthetic Olivine Synthesis . . . 81
Grain Sizes . . . 83
2.2.3 Conditions . . . 83
Temperature and pressure . . . 83
Experimental duration . . . 84
Deformation rates . . . 87
2.3 Tomography . . . 89
2.3.1 In-house CT . . . 89
2.3.2 Manchester micro- and nano-CT . . . 90
Xradia Versa . . . 90
Xradia Ultra nanoXCT . . . 91
2.3.3 Synchrotron X-rays . . . 92
2.3.4 Estimating spatial resolution . . . 94

2.3.5 Image Processing . . . 95
Noise filters and artefact removal . . . 95
Segmentation . . . 98
Ground-truthing with BSE imaging . . . 101
Visualisation . . . 102
Quantitative analysis . . . 102
Melt network topology . . . 103
2.4 Other Analysis . . . 108
2.4.1 Diffraction patterns for in-situ temperature and pressure calibration . . . 108
2.4.2 SEM . . . 111
2.4.3 EPMA . . . 114
2.4.4 EBSD . . . 116
Sample preparation . . . 116
Output data . . . 116

3 3D visualisation of core-forming melts 121
3.1 Introduction . . . 122
3.1.1 Previous experiments . . . 122
3.1.2 Deformation-enhanced permeability of metallic melts . . . 123
3.1.3 The importance of 3D visualisation . . . 123
3.1.4 Aims . . . 124
3.2 Methods . . . 125
3.2.1 Experiments . . . 125
3.2.2 Analysis . . . 126
X-ray CT . . . 126
3D Image processing . . . 128
SEM . . . 128
EPMA . . . 129
EBSD . . . 129
3.3 Results . . . 129
3.3.1 2D textures . . . 129
3.3.2 Quantitative 2D analysis . . . 135
Plucking analysis of deformed samples . . . 136
2D particle analysis . . . 138
Auto-correlation function analysis of fabric strength . . . 141
Summary of 2D textural observations . . . 144
3.3.3 micro-CT . . . 145
3D melt distribution . . . 145
3D melt alignment and orientation . . . 150
Limitations of micro-CT analysis . . . 153
3.3.4 nano-CT . . . 155
Qualitative observations . . . 157
Particle shape analysis . . . 160

Skeletonisation to characterise melt connectivity 168
Qualitative modelling of fluid flow within a deformation melt network 175
3.3.5 Summary of results from 3D analysis 177
3.3.6 Structural analysis 178
EBSD maps and CPO development 178
Kink bands / twinning 186
Conclusions of EBSD analysis 188
3.3.7 EPMA 189
3.4 Applications to core formation in the early solar system 193
3.4.1 Comparsion to previous laboratory results 193
3.4.2 Extrapolation techniques 194
3.4.3 Prediction of permeability and timescales of core formation . 199
3.4.4 Could core formation be completed without the need to invoke a magma ocean? 202
3.5 Conclusions 204

4 Visualisation of basaltic melt networks in an olivine matrix 207
4.1 Introduction 208
4.1.1 Background 208
4.1.2 Previous 3D visualisation of basaltic melts 209
4.1.3 Aims 209
4.2 Preliminary method development 210
4.2.1 Hf-Doping 210
Preliminary results 213
4.3 Methods 217
4.3.1 Experimental methods 217
4.3.2 Analytical techniques 217
4.4 Results 222
4.4.1 2D analysis of undeformed samples 222
Textural changes with anneal time 222
Volume series VS1-4: Textures at varying melt fractions . . . 226
4.4.2 2D analysis of deformed samples 230
Pdef3 234
4.4.3 Tomographic visibility 237
Comparison of undeformed basalt across volumes 244
Comparison of basalt with changing anneal time 247
Comparison of deformed vs. undeformed basalt 247
4.4.4 Comparison of olivine structures using EBSD 251
'Undeformed' samples 251
Deformed samples 260
4.5 Discussion and conclusions 268
4.5.1 is Hf-doping a useful technique for visualisation of melts in three dimensions? 268

4.5.2 Application of results to real Earth systems 269
4.6 Conclusions 270

5 In-situ melt migration **271**
5.1 Introduction 272
5.1.1 Previous *in-situ* investigations of partial melt geometries . . . 273
5.1.2 Geological applications 273
5.1.3 Outline of aims 276
5.2 Methods 277
5.2.1 Capsule designs 277
5.2.2 Composition of starting mixtures 279
5.2.3 Synchrotron beamlines, rotoPEC installation and tomographic set-up 279
Diamond I12 280
ESRF ID27 285
5.3 Results 287
5.3.1 Diamond I12 - Investigating grain-scale melt migration 287
Quality of tomographic scans 287
Textural changes with annealing and deformation 289
Quantitative analysis of particle shape 294
Quantitative analysis of fabric development 300
SEM analysis and groundtruthing 305
Discussion 308
Successes and limitations 309
5.3.2 ESRF 1 - basaltic melt migration along cracks 309
Experimental summary 309
OlBa2 experimental summary and data collection 310
In-situ tomographic scans 312
Further constraints from post-quench analysis 315
Discussion/Textural interpretation 318
Limitations 318
5.3.3 ESRF Phase 2 - Gold melt movement along fractures 319
Experimental adaptations 319
AuBN1: Experimental outcomes and data collection 320
Characteristics of observed melt movement and changes in geometry 325
Calculating melt migration velocity 334
Explaining characteristics of gold melt migration 340
5.3.4 Comparison between *in-situ* experiments in different partial melt systems 346
5.4 Conclusions 347

6 Synthesis and conclusions **349**
6.1 Introduction . . . 350
6.2 Summary of results . . . 350
6.2.1 Chapter 3 . . . 350
6.2.2 Chapter 4 . . . 351
6.2.3 Chapter 5 . . . 353
6.3 Comparison of different partial melt systems . . . 354
6.3.1 FeS vs basaltic partial melts . . . 354
Static textures . . . 354
Dynamic textures at low melt fractions . . . 355
Olivine structure . . . 357
6.3.2 Comparison of off-line experiments to *in-situ* observations . . . 359
The importance of hydrofracture in different partial melt systems 360
6.3.3 Are processes comparable? . . . 361
6.4 Evaluation . . . 361
6.4.1 Computed tomography . . . 362
Development of in-house techniques . . . 362
Methods to improve visualisation . . . 362
CT vs. other visualisation techniques . . . 363
6.4.2 Experimental Equipment . . . 366
Piston cylinder for static experiments . . . 366
roPEC and rotoPEC equipment in relation to partial melting experiments . . . 366
6.5 Future Work . . . 368
6.5.1 Core Formation . . . 368
6.5.2 Basalt . . . 368
6.5.3 In-situ . . . 369

References

Appendices

A Appendix A
A.1 Appendix A1 . . .
A.1.1 EBSD Noise reduction and processing . . .
A.1.2 Resolution calculations of *in-house* CT scans . . .
A.2 Appendix A2 . . .
A.2.1 FeS Olivine deformation experiments on roPEC: Experimental Logs . . .
A.2.2 FeS Olivine deformation experiments on roPEC: Experimental Logs . . .
A.3 Appendix A3 . . .
A.3.1 Paris-Basalt Deformation Samples (Pdef Series): Experimental Logs . . .

A.4 Appendix A4 . . . . .
A.4.1 In-situ experiments: Experimental Logs . . . . .
ESRF Phase I . . . . .
ESRF Phase II . . . . .

B Appendix B

B.1 B1 - Movie data to accompany chapter 5 . . . . .
B.1.1 Movie2 . . . . .
normalised . . . . .
subtractframe1 . . . . .
B.1.2 Movie5 . . . . .
normalised . . . . .
p1to130-p0 . . . . .
p20to130-p20 . . . . .

List of Figures

1.1 The dihedral angle and melt geometry 7
1.2 Types of Ductile Deformation 11
1.3 Olivine Slip Systems 14
1.3 Slip systems in olivine crystals: A. Schematic diagrams demonstrating the most common slip systems affecting olivine undergoing dislocation creep at high temperatures and pressures (Adapted and expanded from Deer et al., 1992), showing the initial crystal prior to slip, with crystal faces labelled, and the orientation of A-slip, B-slip and C-slip with respect to crystallographic axes. NB An idealised crystal shape has been used to demonstrate the systems, however the shape is known to change with temperature and pressure and therefore is not a necessary part of the crystal geometry. B. An example of the changes observed in slip systems of olivine with changes in (i) strain-rate, (ii) confining pressure (Raleigh, 1968), and (iii) water content (Jung and Karato, 2001). The number of slip systems far exceeds the initial A-B-C systems discovered, and complexity appears to increase with each study conducted. 15
1.4 The effect of melt on CPO 19
1.5 Serial Sectioning technique 21
1.6 Cone beam laboratory CT 24
1.7 Synchrotron X-ray source 26
1.8 X-ray spectra from different sources 27
1.9 CT reconstruction example 29
1.10 Schematic illustration of geometric blurring 31
1.11 The nano-CT system 31
1.12 CT resolution capabilities 32
1.13 Forsterite and Pyrite Attenuation coefficient 34
1.14 Example of previous 3D tomography 37
1.15 PREM model of Earth density 44
1.16 Effect of deformation on FeS melt 47
1.17 Model of asthenospheric partial melting 51
1.18 Map of Mantle Anisotropy 52
1.19 Melt under mid-ocean ridges - Geophysics 55

1.20 Deformation melt focussing . . . 58
1.21 Deformation melt focussing . . . 64
1.22 Deformation melt focussing . . . 66
1.23 Doping to improve X-ray contrast . . . 68

2.1 Piston Cylinder Apparatus . . . 74
2.2 roPEC equipment . . . 75
2.3 rotoPEC equipment . . . 77
2.4 Thermocouple Gasket Design . . . 78
2.5 Calibration Curve . . . 79
2.6 Fe-S phase diagram . . . 81
2.7 FeS and Basalt starting grain size . . . 84
2.8 Dihedral Angle Changes with Experimental Duration . . . 86
2.9 Strain rate calculation . . . 88
2.10 Xradia Versa Tomography . . . 91
2.11 Xradia Versa Tomography . . . 93
2.12 Image Processing: Flow chart . . . 96
2.13 Noise Filters examples . . . 99
2.14 Examples of segmentation methods . . . 105
2.15 Example segmentation process . . . 106
2.16 The skeletonisation process . . . 107
2.17 Diffraction set-up at ID27 . . . 109
2.18 Diffraction pattern examples . . . 112
2.19 Sample Sections used during BSE imaging . . . 113
2.20 EPMA analysis example . . . 115
2.21 EBSD Maps . . . 119
2.22 EBSD Plots . . . 120

3.1 Stress vs strain-rate graph . . . 126
3.2 Textural observations in undeformed sample FeOlPC8 . . . 130
3.3 Textural changes with varying strain-rate . . . 132
3.4 Textural features of sample FeOl1 . . . 133
3.5 Textural features of early generation samples . . . 134
3.6 Results of plucking analysis . . . 137
3.7 2D particle analysis . . . 140
3.8 ACF analysis processing example . . . 142
3.9 ACF analysis results . . . 143
3.10 micro-CT sample reconstructions . . . 147
3.11 quantitative melt distribution . . . 148
3.12 Volume distribution in shells . . . 149
3.13 Quant 3D sample fabric analysis I . . . 151
3.14 Quant 3D sample fabric analysis II . . . 152
3.15 Blob3D melt orientation analysis . . . 154
3.16 Example of segmentation from CT slice . . . 156
3.17 3D reconstructions at increasing magnification . . . 158

3.18 Nano-CT reconstructions of melt geometry . . . 159
3.19 3D nano-tomographic reconstruction of a deformation melt network . 160
3.20 Fragmentation Index for connectivity . . . 164
3.21 Nano-scan particle shape analysis . . . 165
3.22 Nano-scan particle shape analysis 2 . . . 166
3.23 Nano-scan particle shape analysis graph . . . 167
3.24 Skeletonisation results . . . 171
3.25 Skeleton connectivity comparison graph . . . 172
3.26 Skeleton connectivity graphs 2: Evaluation . . . 173
3.27 Skeletonisation 3: branch thickness and length . . . 174
3.28 Modelling flow along a deformation melt network . . . 176
3.29 EBSD map of undeformed sample . . . 179
3.30 EBSD map of FeOl1 . . . 182
3.31 EBSD map of FeOl4 . . . 183
3.32 EBSD map of FeOl4 . . . 184
3.33 Pole Figure Comparisons . . . 185
3.34 Kinking in deformed olivine grains . . . 187
3.35 EPMA analysis - sample edge . . . 191
3.36 EPMA analysis - other features . . . 192
3.37 Extrapolation to Core Formation scenarios: Walte model . . . 197
3.38 Permeability and Timescales of Core Formation . . . 201

4.1 Olivine basalt attenuation differences . . . 212
4.2 Dual Capsule Design . . . 212
4.3 Doped basaltic melt - high T run . . . 213
4.4 Preliminary Shadowgrams . . . 214
4.5 Hf basalt starting mix . . . 214
4.6 48 hour run - dihedral angle analysis . . . 216
4.7 OlBaPCTS1 . . . 223
4.8 OlBaPCTS3 BSE imaging . . . 224
4.9 OlBaPCTS3 melt distribution . . . 225
4.10 OlBaPCVS3 BSE imaging . . . 227
4.11 OlBaPCVS1 BSE imaging . . . 228
4.12 OlBaPCVS4 BSE imaging . . . 229
4.13 Other deformation experiments BSE images . . . 231
4.14 full capsule BSE sections . . . 232
4.15 Pdef1 BSE images . . . 233
4.16 Pdef2 BSE images . . . 234
4.17 Pdef3 BSE images . . . 236
4.18 BSE vs. CT slice comparisons A . . . 238
4.19 BSE vs. CT slice comparisons B . . . 239
4.20 TS1 high magnification segmentation . . . 240
4.21 3D melt geometry of sample OlBaVS1 . . . 241
4.22 3D melt geometry of sample OlBaVS4 . . . 242

4.23 3D melt geometry of sample OlBaVS3 243
4.24 3D melt geometry in samples of differing volumes 245
4.25 Connectivity of melt with changing basaltic volume 246
4.26 3D melt geometry with changing high P-T anneal time 248
4.27 3D melt geometry of deformed samples Pdef1-3 249
4.28 3D melt geometry and connectivity with different thresholding techniques 252
4.29 EBSD analysis summary of sample OlBaPCTS1 254
4.30 EBSD analysis summary of sample OlBaPCTS3 257
4.31 EBSD analysis summary of sample OlBaPCVS4 259
4.32 EBSD analysis summary of sample Pdef1 263
4.33 EBSD analysis summary of sample OlBaPCVS4 264
4.34 EBSD analysis summary of sample OlBaPCVS4 265
4.35 EBSD analysis summary of sample OlBaPCVS4 266
4.36 Grain and sub-grain development within deformed samples 267

5.1 mm-scale melt movement observed during preliminary work 274
5.2 Capsule designs for *in-situ* melt migration 278
5.3 Experimental set up at I12 281
5.4 Diamond scan quality comparisons 288
5.5 DLS3 Time-series: tomographic reconstructions 290
5.6 DLS4 Time-series: tomographic reconstructions 291
5.7 DLS5 Time-series: tomographic reconstructions 292
5.8 DLS6 Time-series: tomographic reconstructions 293
5.9 DLS3 particle analysis 296
5.10 DLS4 particle analysis 297
5.11 DLS5 particle analysis 298
5.12 DLS6 particle analysis 299
5.13 Quant3D fabric analysis: DLS3 301
5.14 Quant3D fabric analysis: DLS4 302
5.15 Quant3D fabric analysis: DLS5 303
5.16 Quant3D fabric analysis: DLS6 304
5.17 SEM imaging of sample DLS5 306
5.18 SEM imaging of sample DLS6 307
5.19 Diffraction patterns of OlBa2 311
5.20 Tomographic reconstructions of sample OlBa2, from ESRF ID27 . . . 313
5.21 Post-quench *in-house* CT reconstructions of sample OlBa2 316
5.22 BSE images of ESRF sample OlBa2 317
5.23 AuBN1 Experimental variation in power and Au d-spacing 322
5.24 AuBN1 diffraction patterns showing melting of Au 323
5.25 Orthoslices of tomographic scans from experiment AuBN1 327
5.26 AuBN1 stills of initial sample movement 328
5.27 3D reconstructions of melt geometry throughout experiment AuBN1: greyscale values preserved 329

5.28 Projections showing melt movement in movie 2 330
5.29 3D reconstructions of melt geometry throughout experiment AuBN1: base 331
5.30 screenshots showing radiography of melt movement M1 332
5.31 screenshots showing radiography of melt movement M2 and M3 . . . 333
5.32 Processing and results of 2D melt migration tracking 336
5.33 Matching radiography to 3D reconstructions: M1 338
5.34 Matching radiography to 3D reconstructions: M2 339
5.35 Overpressure vs. melt velocity with varying fracture aperture 341
5.36 Fracture processes in polycrystalline material 345

6.1 Comparison of partial melt textures 356
6.2 Comparison of partial melt textures 358
6.3 Improvement of CT scan quality 365
6.4 Potential capsule design for deformation experiments 370

A.1 Spot size vs energy . . . . . .

List of Tables

3.1 Sample Run Conditions and Scans 127
3.2 Material compositions 190
3.3 Permeability Parameters 200

4.1 Hf-doping test conditions 211
4.2 Experimental Summary 218
4.3 CT scan summary 220
4.4 Reconstruction conditions 221

5.1 DLS sample summary 283
5.2 DLS scan summary 284
5.3 A summary of samples produced in two phases of work carried out at ID27, ESRF, Grenoble. A large number of samples failed to reach melting temperatures before blow-outs occurred. Starred experiments indicate successful melting of sample material. These are the samples used for further analysis. P,T in Phase I are estimates from previous calibration. Phase II P,T are taken from direct estimates based on *in-situ* gold and MgO diffraction patterns. 286
5.4 AuBN1 Imaging Conditions 324
5.5 Melt velocity calculations 337
5.6 Liquid phase mechanical properties 346

A.1 Resolution calculations . . . . .
A.2 Deformation sample FeOl1: Experimental log . . . . .
A.3 Experimental log: Sample FeOl1 continued . . . . .
A.4 Sample FeOl2: Experimental log . . . . .
A.5 Experimental log: FeOl3 . . . . .
A.6 Experimental log: sample FeOl4 . . . . .
A.7 Example of error propagation, EPMA analysis . . . . .
A.8 Experimental log: Sample Pdef1 . . . . .
A.9 Experimental log: Sample Pdef2 . . . . .
A.10 Experimental log: Sample Pdef3 . . . . .
A.11 Experimental log: Sample Pdef3 - continued . . . . .
A.12 Experimental log: Sample OlBa2 . . . . .

A.13 Experimental log: Sample AuBN1 . . . . . .
A.14 Experimental log: AuBN1 . . . . . .

List of Abbreviations

BSE	Backscatter Electron (imaging)
EBSD	Electron Backscatter Diffraction
EDS	Energy Dispersive X-ray Spectroscopy
EPMA	Electron Probe Microanalysis
High P-T	High Pressure and Temperature
MORB	Mid-Ocean Ridge Basalt
SEM	Scanning Electron Microscope
XCT	X-ray Computed Tomography

CHAPTER 1

Introduction

1.1 The PhD project in context of igneous petrology and experimental development

"without truly knowing what they see, they think they know those regions of the earth which never can be seen; and they judge of the great operations of the mineral kingdom, from having kindled a fire, and looked into the bottom of a little crucible."
James Hutton's opinion on early experimentalists, from his *Theory of the Earth* 1795

At the turn of the 19th Century, James Hall and his contemporaries first began experiments to melt whinstone (basalt or dolerite) to attempt to prove its igneous origin (Young, 2003). By cooling the liquid slowly, Hall was able to produce a crystalline texture reminiscent of basaltic rock. This refuted the popular theory at the time that basalt was precipitated from aqueous fluids, although even Hall's friend and colleague James Hutton, a great supporter of the igneous origin theory, was critical of his experimental techniques (see above). It took a number of years of further experiments, along with collection of field evidence and mineralogical observation, to finally confirm the igneous origin of basalt (Young, 2003). Since then, conducting melting experiments on geological specimens in the laboratory has played a hugely important role in constraining models of igneous processes.

The partial melting of multi-phase geological materials and the extraction of melts from a solid matrix is an important process in many geological systems. Separation of liquid metal from solid silicate was key to the formation of terrestrial bodies in the early solar system (Wood et al., 2006), and partial melting and melt release from solid silicate has remained a major part of the magmatic and volcanic processes which have constantly reformed the Earth throughout geological time (McKenzie, 1989). Laboratory experiments conducted at high P-T (pressure and temperature) are still one of the only methods available to empirically investigate these processes occurring at great depths within the Earth (Kohlstedt and Holtzman, 2009).

Hutton's words of caution do still ring true in modern petrology, however. The nature of laboratory experiments - their timescale, dependence on small volumes, fine grain sizes and simplified compositions, mean that processes occurring during experiments are often difficult to extrapolate directly to Earth systems. Analytical techniques have also limited the ability to fully characterise experimental samples; until recently, textural analysis has been limited to imaging of polished slices of quenched run products (Hustoft and Kohlstedt, 2006; VonBargen and Waff, 1986). Particularly for investigation of partial melt processes, the inference of 3D melt

geometry and connectivity from 2D sections has led to conflicting results and a lack of agreement within the experimental community, particularly in the investigation of characteristics of very small melt fractions (Kohlstedt and Holtzman, 2009). In addition, the reliance on interpretation from quench products mean that dynamic processes in a continuously changing system must be inferred from a single resultant texture. An analogy could be trying to interpret the plot of a film solely from its final still image.

In the last decade, the growing availability of X-ray Computed Tomography (XCT) and synchrotron sources for use in the geosciences have allowed experimental petrologists to begin to directly visualise run products in three dimensions (Watson and Roberts, 2011; Zhu et al., 2011), and to carry out *in-situ* experiments to gain multiple, time resolved datasets from individual runs (Wang, Lesher, et al., 2011). The use of CT for investigation of partial melt systems is still limited - work is still in the developmental stage and only very few studies have been published to date. The technically demanding nature of this work, and its reliance on new technology at the limit of its current capabilities, means the majority of work published describes method development in the form of feasibility studies. The work produced in this thesis represents experimental work conducted in the context of this new emphasis on 3D visualisation of experimental products and *in-situ* observations.

1.1.1 Outline of research

In this thesis I present work carried out to investigate the potential for, and evaluate limitations of 3D visualisation of partial melts from experiments conducted at high P-T in the laboratory. Access to unique experimental equipment and advanced 3D imaging technology has allowed us to examine the distribution and textures of partial melts within Earth materials at simultaneous high P-T, under hydrostatic or dynamically deforming conditions. The work has been carried out in conjunction with continued development of the University of Edinburgh *in-house* XCT system, and in addition has used some of the most advanced XCT technologies currently available in geoscience research (Maire and Withers, 2014). Work has focused on the application of melt migration processes to the following two contrasting geological systems:

1. Mobility of core-forming melts during planetary formation, and the potential for deformation-enhanced core-mantle segregation.

2. Basaltic melts in the uper mantle, their geometry, mobility and extraction from beneath spreading ridges.

Significant aspects of the work are developmental in nature - a broad investigation into the potential scope of future projects and current limitations of 3D visualisation and *in-situ* techniques. Other aspects of the work, in particular regarding application to models of deformation-enhanced percolative core formation in planets and planetesimals, may already make a significant impact on theories within the igneous petrology community. This shows how the development of 3D visualisation techniques may bring about significant advances in theories of partial melt and melt migration system, if the rapid development in technology continues at its present pace. It is worth realising that the development of new 3D visualisation techniques are not only likely to reinforce and confirm old theories, but may also lead to new discoveries and potentially a number of initial theories being completely rewritten over the course of the next few decades.

1.2 Background information and theoretical principles

From planetary formation to present day volcanism, the melting of rocks is a key process in a wide range of systems on Earth and on extra-terrestrial bodies. Despite this, we still know a limited amount about the initiation of melting in rocks. Advances in experimental equipment and techniques over the last decade have allowed researchers to more accurately reproduce melting under deep Earth conditions in the laboratory (Miller et al., 2014), but there are still gaps in knowledge regarding the mobility of very small fractions of partial melt in rocks at high temperature and pressure conditions (Garapic et al., 2013; Kohlstedt and Holtzman, 2009). Concurrently, improvements in geophysical surveying indicate that this knowledge may be key to understanding the fundamental processes of plate tectonics, and therefore the ongoing evolution of our planet (Forsyth et al., 1998; Karato, 2014).

The following review sections aim to provide background knowledge on the basic principles governing partial melt systems at high pressure and temperature (High P-T), and aims to place the work into the context of existing literature and the numerous open questions that remain in the study of partially molten systems. I will cover theoretical background regarding the movement of partial melt in solid rock, both at hydrostatic high temperature and pressure, and in dynamic deforming systems. This includes principles of ductile deformation of minerals, the effects of partial melt on

deformation mechanisms, and methods that have been used to extrapolate to 3D melt geometries from classic 2D sample analysis. I will detail the principles of X-ray tomography, a technique used extensively in this work, its use in the geosciences, and the techniques developed to analyse partially molten systems *in-situ* at high pressures and temperatures.

The final two sections will focus on the two specific geological applications of planetary core formation and upper mantle melting, with emphasis on constraints made by previous studies, and particular gaps in knowledge that require further research.

1.2.1 Principles of partial melt and deformation

The following general questions regarding processes in a partially molten rock are applicable to a number of geological systems and have been the focus of a great deal of experimental research:

1. At what fraction of melting does the melt become interconnected and mobile? What factors, in the melt and solid, affect this fraction?

2. How are small melt fractions distributed in the host rock (i.e. what is the geometry of the melt phase within the host rock?) and how does this change with increasing melt fraction?

3. How permeable is the system, and what factors affect this permeability?

4. What are the driving forces that cause melt to migrate from its original host rock?

5. What is the velocity of melt permeating through a crystalline solid?

Further questions examine the addition of non-hydrostatic stresses to a system:

1. How do different degrees of partial melting affect the rheology of the host rock, in response to deformation?

2. Conversely, what effect does deformation have on geometry and permeability of melt, particularly at low melt fractions?

This section will examine methods for investigating these systems, and constraints on processes from a combination of experimental and numerical studies.

Melt geometry and permeability in a hydrostatic system

Initial studies of partial melt textures focused on the simplest system of melt within a polycrystalline solid heated under hydrostatic confining pressure, allowing the partial melt system to develop an equilibrated texture (Jurewicz and Jurewicz, 1986; VonBargen and Waff, 1986). In such a system, the distribution of melt is controlled solely by interfacial tension between the liquid and crystal faces. Although this cannot be measured directly, it can be estimated from dihedral angles i.e. the angle between two solid crystal faces and a melt pocket, linked to interfacial tension by the equation (VonBargen and Waff, 1986)

$$\frac{\gamma_{ss}}{\gamma_{sl}} = 2\cos\left(\frac{2}{\theta}\right) \tag{1.1}$$

where γ_{ss} is solid-solid interfacial energy, γ_{sl} is solid-liquid interfacial energy and θ is the dihedral angle. The dihedral angle can, therefore, also be taken as a measure of interconnectivity and inference of 3D geometry when we are unable to image the 3D network directly (Figure 1.1).

Dihedral angles are usually determined by backscattered or secondary electron imaging of quenched, recovered experimental samples; at least 100 dihedral angles should be measured to give a statistically significant normal distribution (Ballhaus and Ellis, 1996), taking into account that 2D sections will often give an apparent angle if pockets are cut at an oblique angle (Jurewicz and Jurewicz, 1986). If the average dihedral angle is found to be less than 60°, the melt is thought to be interconnected and can be completely extracted from the system. A dihedral angle of 0° suggests all crystal faces should be wetted by liquid, while an angle of between 0 and 60° will have a geometry of interconnected tubules (Karato, 2008). If the angle is greater than 60°, a critical melt volume termed the 'percolation threshold' is required for an interconnected network to form, which increases with increasing dihedral angle. Therefore, for any system with dihedral angles above 60°, a 'pinch-off' fraction of the melt phase, which is slightly less than the percolation threshold, will remain stranded in the polycrystalline matrix.

The dihedral angle, and therefore melt connectivity, depends on the liquid and solid composition, as well as the P-T conditions of the system. Generally, the ability of a fluid to wet grain faces increases with increasing solubility of the solid in the liquid phase (Yoshino, Nishihara, et al., 2007). This means that surface tension appears to decrease as compositions of fluid and liquid phases converge. Effect of compositions

and conditions of phases on dihedral angles in various systems have been studied for several decades, and will be discussed specifically for each geological application (see sections 1.3.1 and 1.4).

Defining permeability by measurement of dihedral angles assumes an isotropic system of cubic crystals, therefore use of the method with anisotropic crystals (e.g. olivine) assumes that melt-silicate interaction is unaffected by differences in interfacial energy due to crystallographic orientation. This assumption is unlikely to be true in complex systems and is relatively untested, although experimental results using alternative measures suggest the angle is still a viable approximation of interconnectivity in the olivine system (Yoshino et al., 2004). To gain reliable data from dihedral angle measurement, it is important for a system to be in textural equilibrium, defined as a state in which pore shape is determined by interfacial energies of fluid and solid rather than changing shape due to crystal growth or deformation (VonBargen and Waff, 1986). This requires long periods (>48 hours) of annealing time in a hydrostatic system (Bagdassarov, Golabek, et al., 2009). The addition of dynamic deformation to a system precludes textural equilibrium and therefore makes the use of dihedral angles to infer 3D melt geometry obsolete for proposed deformation experiments. Alternative methods to assess permeability are required for these systems.

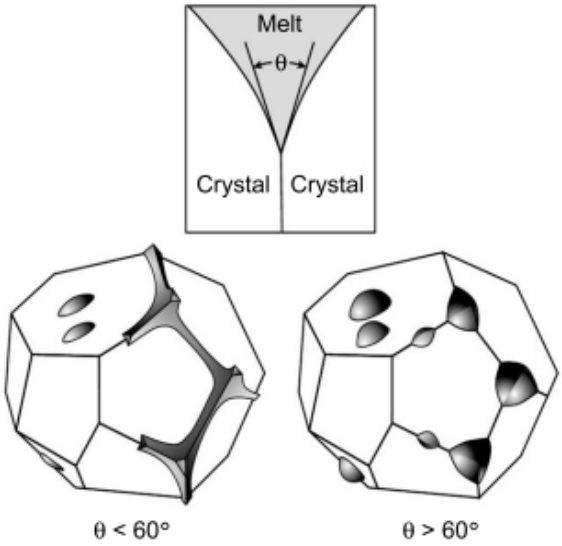

Figure 1.1: The Dihedral Angle as a measure of permeability. Top: illustration defining the dihedral angle; bottom left: an interconnected system at dihedral angle <60°; Bottom right: Isolated pockets in a system with dihedral angle >60° (Adapted from Karato, 2008)

As long as a melt network remains interconnected above its percolation threshold, melt is able to segregate from the solid matrix if there is a migration gradient to encourage movement. A melt migration gradient may be caused by differences in buoyancy between the liquid and solid leading to separation of melt and solid during compaction at high pressures (McKenzie, 1984), could be thermally driven, or caused by pressure differences created by differential stress or a change in melt fraction across a material (Kohlstedt and Holtzman, 2009).

The efficiency of melt movement is in part dictated by the geometry of the melt network, the melt fraction and grain size of the matrix. The permeability of the system, k, can be estimated quantitatively using the following empirical relationship (an adaptation of Darcy's law) (Hustoft and Kohlstedt, 2006; Turcotte and Schubert, 2002).

$$k = \frac{d^2 \phi^n}{C} \tag{1.2}$$

where d= grain size, ϕ = melt fraction, C = geometric factor, n = melt fraction exponent. The geometric factor and the melt fraction exponent values vary depending on the assumed geometry of the melt network. For example, a melt network consisting of interconnected tubules will give a geometric factor of $C = 72\pi$, and a melt fraction exponent of $n = 2$, whilst a series of parallel sheets of melt would use $n = 3$ and $C = 12$ (Gueguen and Dienes, 1989). The geometric factor has traditionally been inferred by 2D textural observations including dihedral angle measurements (Faul et al., 1994). This extrapolation from 2D to 3D systems brings with it an inherent uncertainty, resulting in disputes as to the exact 3D geometry of partial melts and subsequent estimates of permeability and value of percolation thresholds (e.g. Wark et al., 2003).

Another method of determining permeability is to perform *in-situ* electrical conductivity measurements of samples while they are partially molten (Yoshino et al., 2004). These experiments can be conducted in adapted piston-cylinder apparatus or using gas-pressure vessels. Liquid has a higher electrical conductivity than solid; therefore, an interconnected network will produce a sudden increase of conductivity through the sample, in comparison to one where melt is trapped in isolated pockets (Watson and Roberts, 2011). However, results from conductivity experiments are regularly criticised as unreliable due to the complexity of experiments (Roberts et al., 2007). Importantly, the technique may not be accurate enough to reliably determine percolation thresholds at small melt fractions (Watson and Roberts, 2011), and does

not give further constraints on partial melt geometry.

Ductile deformation of crystalline solids at high P-T

Before examining the effects of deformation on partial melt systems, I will briefly outline theories of ductile deformation of crystalline material at high P-T. Solid and partially molten materials can undergo ductile deformation in two distinct ways (Figure 1.2):

- **Diffusion creep** whereby the movement of defects / vacancies in a material, combined with an opposing flux of atoms, leads to a change in shape. This type of deformation is very sensitive to differences in grain size, and less sensitive to the applied stress. Such diffusion occurring by mass transport through the interior of grains is known as Nabarro-Herring creep (Herring, 1950; Nabarro, 1948). In a multi-granular material however, the application of stress will lead to a heterogeneous stress field as stress will concentrate in areas of weakness i.e. the highest stress will be at grain boundaries, causing sliding along these weak points on application of stress and a concentration of vacancies in this area (Nabarro, 1948). This type of creep is known as Coble creep (Coble, 1963), which takes into account the effect of weaker paths of high diffusivity (e.g. grain boundaries).

- **Dislocation Creep** step-wise deformation occurs by a "collective motion of atoms as crystal dislocations" (Karato, 2008). This type of deformation is anisotropic at grain-scale, with a non-linear relationship between stress and strain. Dislocation creep will produce recognisable micro-structures such as new grain boundaries, and grain boundary migration. This type of deformation is more likely to create a crystallographic preferred orientation (CPO).

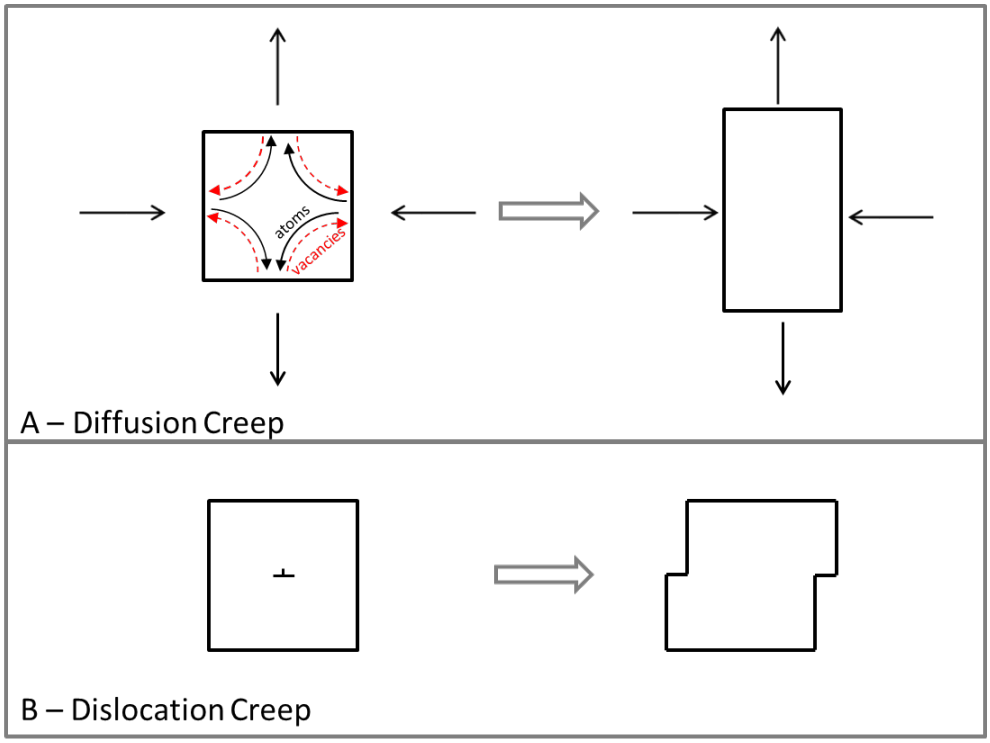

Figure 1.2: Schematic diagrams of the two principle modes of plastic deformation. A. Diffusion creep showing relocation of vacancies and atoms within the solid, B. Dislocation creep creating discrete stepped changes in shape, which will produce recognisable micro-structures (Adapted from Karato, 2008).

The type of deformation a solid material undergoes will depend on grain size of the material and strain-rate of the deformation taking place. Dislocation creep will occur if a sample is unable to respond to the differential stresses by the slower process of diffusion, and occurs at higher strain-rates and within larger grains. The most effective method of testing the mechanism of deformation is to measure both stress and strain within a sample and plot the relationship between both. However, this is not possible in deformation experiments carried out in this study. Other evidence for deformation by dislocation creep can be found by detailed examination of crystal grain microstructure, and the presence of a Crystallographic Preferred Orientation (CPO), which can be found using Electron Backscatter Diffraction (EBSD - see section 2.4.4).

Crystallographic Preferred Orientation (CPO) CPO can develop within crystals of non-cubic symmetry in response to deformation, either by physical rotation in response to external stresses, or by preferential orientation of crystal growth in a stress field. Crystals undergoing dislocation creep will tend to slip more easily along certain planes of weakness, and on that plane in a particular direction. Together, the plane of slip and direction of slip are known as a slip system. The CPO created by crystal rotation is thought to show the dominance of a particular crystal slip system in response to deformation. It is, therefore, possible to infer to some extent the deformation mechanisms occurring within experimental samples, by examining crystal preferred orientations of samples that have undergone deformation.

Olivine is the most abundant mineral within the mantle and is most often used as the crystal matrix in experiments to represent mantle material (as is the case in this study). A significant number of studies have investigated in detail the deformation mechanisms in olivine on the microscopic and macroscopic scale. The behaviour of olivine deformation over a large range of temperature and pressure conditions is, therefore, reasonably well constrained. Olivine has a number of slip systems - which dominates depends not only on the orientation of the crystal with respect to the deforming force, but also to environmental conditions such as the magnitude of the deforming stress, confining pressure, temperature, oxygen fugacity and crystal water content (Carter and Ave'Lallemant, 1970; Jung and Karato, 2001). The dominant slip system can be inferred from CPO measurements. Figure 1.3A shows in 3D the orientation of three major slip systems in olivine. Figure 1.3B shows pole figures of olivine at different conditions showing dominance of a number of different slip systems. 1.3C shows how these dominant systems are thought to vary with strain-rate (i.e. differential stress) and temperature, and with addition of water.

At conditions of 2GPa, 1400°C, relevant to our experiments, the dominant slip

system of olivine is A-slip. Therefore we should see evidence of this slip in the CPO observed in our experiments, if there are no other factors affecting the deformation of our olivine crystals and dislocation slip is the main mechanism of deformation.

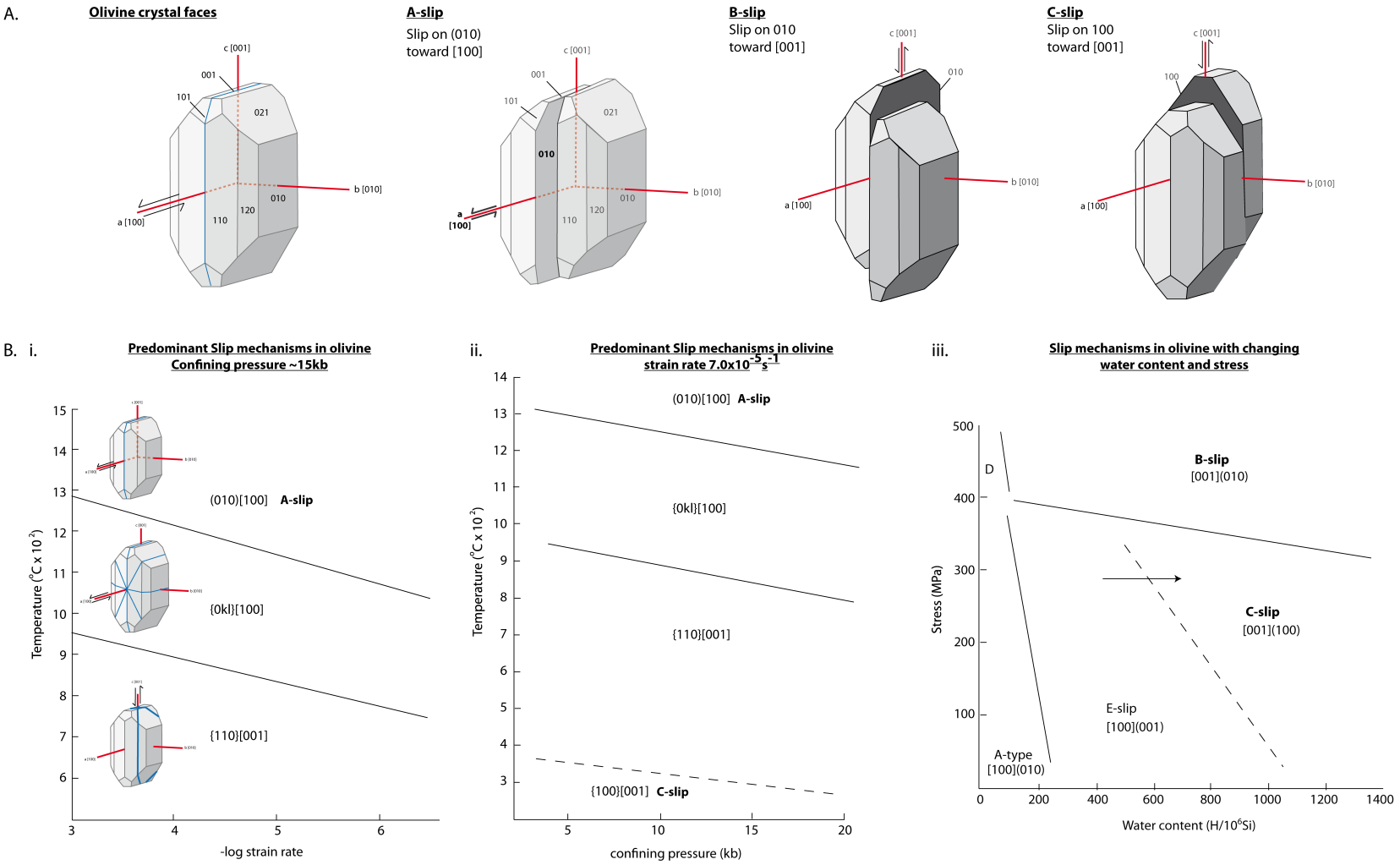

Figure 1.3:

Caption on next page

Figure 1.3 ***(preceding page)*****:** Slip systems in olivine crystals: A. Schematic diagrams demonstrating the most common slip systems affecting olivine undergoing dislocation creep at high temperatures and pressures (Adapted and expanded from Deer et al., 1992), showing the initial crystal prior to slip, with crystal faces labelled, and the orientation of A-slip, B-slip and C-slip with respect to crystallographic axes. NB An idealised crystal shape has been used to demonstrate the systems, however the shape is known to change with temperature and pressure and therefore is not a necessary part of the crystal geometry. B. An example of the changes observed in slip systems of olivine with changes in (i) strain-rate, (ii) confining pressure (Raleigh, 1968), and (iii) water content (Jung and Karato, 2001). The number of slip systems far exceeds the initial A-B-C systems discovered, and complexity appears to increase with each study conducted.

In contrast, diffusion creep has generally been thought not to lead to a crystal preferred orientation, as there is no mechanism to rotate material within the crystals with respect to the crystal lattice. In fact, LPO has been known to be destroyed by application of diffusion creep (Warren and Hirth, 2006). Until recently, the presence of CPO in a sample has been thought to imply deformation in the dislocation creep regime. However, recent studies suggest diffusion creep may be able to create its own weak CPO by chemical interaction of phase boundaries in multi-phase materials (Sundberg and Cooper, 2008), or by grain boundary sliding and alignment of crystal shape (Miyazaki et al., 2013). This discovery means it may be more difficult than previously considered to infer deformation mechanism from CPO alone. Other evidence, such as the stress-strain relationship and physical presence of dislocations must be used to confirm deformation is taking place by dislocation creep.

Deformation of partially molten solids

The simplest form of deformation of a porous (partially molten) rock is by hydrostatic compaction acting to compress the solid matrix, which can lead to melt segregation due to melt buoyancy. The influence of compaction is best measured by the compaction length, δ_c which is the characteristic length at which porosity changes during compaction (McKenzie, 1984), defined as

$$\delta_c = \sqrt{\frac{k\eta_{solid}}{\eta_{melt}}} \tag{1.3}$$

Where k is the permeability and $\eta_{(solid/melt)}$ is the viscosity of the solid / melt. As the viscosity term also takes into account bulk viscosity, and this tends to infinity as porosity approaches zero, it becomes harder to remove melt by compaction as porosity decreases (McKenzie, 1984). Higher permeability melts will have larger compaction lengths, as melt is able to flow more quickly to equalise internal pressure changes.

The response of a solid to non-hydrostatic deformation can be significantly altered by the addition of a partial melt. Conversely, the geometry and permeability of a partial melt system is shown to be significantly affected by non-hydrostatic stresses.

Effect of partial melt on host rock rheology.

Ductile deformation of a partial molten material can be seen theoretically as the deformation of a multi-phase solid, but with large differences in physical properties between the two phases (Karato, 2008). The addition of partial melt to a solid will significantly weaken a rock due to lubrication of grain boundaries. As melt fraction

increases, the rock will weaken until at a certain melt fraction, crystals will be fully suspended and bulk viscosity is controlled by melt viscosity. The melt fraction at which the strength of a partially molten rock decreases to almost that of the liquid is known as the Rheologically Critical Melt Fraction (Φ, RCMF) (Arzi, 1978). This threshold is thought to roughly correspond to the percolation threshold (Karato, 2008).

For a solid with a small amount of melt, creep strength can be expressed as

$$\sigma_s \approx \frac{\sigma}{1-\Phi} \tag{1.4}$$

Where σ_s is the strength of the solid, σ is the bulk strength and Φ is the porosity. This relationship has been supported by experiments on basaltic melt in an olivine matrix by Hirth and Kohlstedt (1996).

The effect of small partial melt fractions on deformation depends on the type of plastic deformation the material is undergoing. The degree of partial melt has a large impact on the strength (rheology) of a material if it is undergoing Coble creep, as partial melt leads to further weakening of grain boundaries, but it will have less impact if deforming by Nabarro-Herring or dislocation creep. It is, therefore, important to understand exactly how deformation occurs in the deep Earth in order to understand how melt will affect rock strength.

For a rock undergoing Coble creep deformation, melt geometry is an important factor in determining rock strength. A partial melt that wets grain boundaries will cause greater lubrication and therefore reduce rock strength more than a rock where melt is trapped in isolated pockets. In other words the $\Phi RCMF$ will be much lower for partial melt systems which exhibit low dihedral angles in texturally equilibrated systems (Renner, Evans, et al., 2000). Knowledge of the interconnectivity and geometry of melt networks in partially molten systems is, therefore, of critical importance if we are to understand the rheology and deformation mechanics in the upper mantle.

The presence of melt is also likely to change the response of the crystal matrix to deformation, and therefore any development of CPO. In their experiments of olivine deforming in the diffusion regime, Miyazaki et al. (2013) noted that the presence of a signficant melt fraction (30vol%) reduced the CPO in olivines significantly. This was thought to be due to the crystal axial ratio of olivines being significantly lower in olivines crystallising in the presence of melt – equigranular crystals have no elongate side to line up to a stress field in a certain orientation. Another reason for a change in CPO in the presence of melt may be strain partitioning, which is affected by melt connectivity. A study by Holtzman, Kohlstedt, et al. (2003) examined the change in

crystal preferred orientation of samples of olivine plus MORB, with comparison to samples in which a third phase (FeS melt, or chromite solid) was added to the system to significantly reduce permeability. Melt behaved differently in the two samples – in the highly permeable system, melt was distributed evenly in elongate pockets aligned at an angle to the shear plane. The less permeable system led to melt partitioning into anastomosing melt rich bands, surrounding melt rich lenses. CPOs of these two systems both differed significantly from those expected from dry olivine samples, and also showed very different patterns depending on melt permeability (Figure 1.4). CPO in the mobile melt networks was mostly attributed to the effect of melt preferred orientation (MPO) acting to randomise a- and c- axes while leaving slip plane b-axes at the same orientation (the MPO-CPO effect). The CPO in the lower permeability segregated melt lenses could be attributed to strain partitioning into melt depleted lenses leading to a change in the overall stress orientations producing CPO (Figure 1.4B.).

Melt connectivity may therefore affect CPO of olivines significantly, giving an indication of permeability within experimental samples. EBSD analysis can be used to investigate CPO in experimental samples and infer processes of strain partitioning, and their relation to melt connectivity.

Effect of deformation on partial melt geometry

In a review examining deformation of partially molten rocks, Kohlstedt and Holtzman (2009) describe three main ways in which ductile deformation has been observed to change the texture of a partially molten solid

1. **Melt alignment at the grain scale** Although diffusion of solids can also relieve stresses, grain boundary wetting is a faster process and is the dominant factor. In this way, deformation leads to grain boundary wetting, but only at a specific orientation to shear, creating a melt alignment (Wimert and Hier-Majumder, 2012). This is thought to occur due to local tensile stresses. For less mobile melts, this process could act to force melt into grain boundaries oriented at a certain angle to the stress field, leading to enhanced melt connectivity in that direction.

2. **Alignment into melt-rich bands** Localised migration of melt into anastomosing melt-rich bands is observed in a number of studies (King et al., 2010). Melt bands are generally developed at 20°, antithetic to shear. For melt bands to appear, the permeability needs to be low enough for internal pressure gradients to be formed before their removal by fluid flow (i.e. a short compaction length

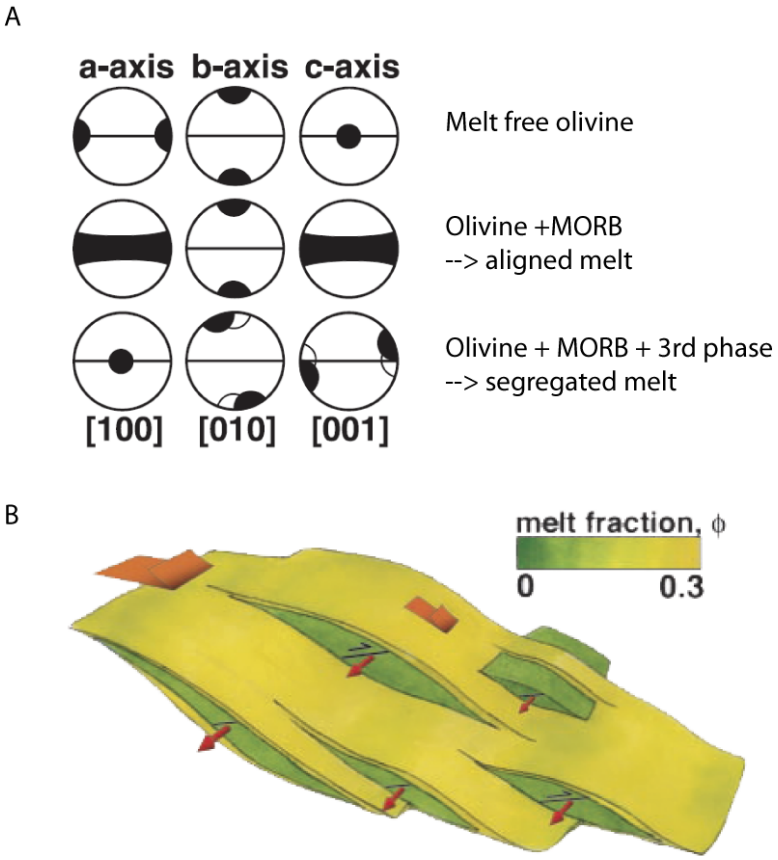

Figure 1.4: Images adapted from Holtzman, Kohlstedt, et al. (2003) showing their interpretation of the effect of partial melting on the CPO of olivine crystals. A. three pole figure sketches showing the average orientation of a, b and c axes in dry olivine (top), olivine with highly mobile MORB melt, in which melt has a distinct preferred orientation (middle), and olivine with a lower permeability melt (3rd phase of either iron rich liquid or solid chromite used to inhibit permeability of MORB) which has led to segregation of the material into melt-rich and melt-poor regions (bottom). In each case, shear direction is horizontal, top to the right. Change in CPO due to presence of 'aligned melt' is thought to be due to the MPO-CPO effect (see text) B. The reason for the change in CPO in the segregated melt example is given to be due to strain partitioning between melt rich bands (yellow) and melt-poor lenses. Strain is partitioned into melt-poor lenses, which, due to their orientation, and the faster movement between lenses, leads to a change in the orientation of the strain ellipse and overall deformation direction of olivine. This leads to the apparent a-c switch in orientation (vs. dry olivine), and back-rotation of the CPO in the b and c axes of olivines.

is required). The presence of melt bands is evidence for melt connectivity, as it implies that melt has been able to migrate locally and segregate in response to pressure gradients (Bruhn et al., 2000) (Figure 1.5).

3. **Large scale melt migration** A non-uniform stress in a sample can create a gradient causing sample-scale melt migration, for example in a 'toothpaste squeeze test', where stress on the base of a sample is greater than on the top in an attempt to push melt from one zone to another (Renner, Viskupic, et al., 2003). Pressure gradients within solid mantle could be a cause for melt segregation and migration on large scales (Takei and Holtzman, 2009).

Importantly for this research, experimental work performed at a range of strain-rates indicates that differential stress can significantly enhance melt interconnectivity (Bruhn et al., 2000) and generally leads to a smaller pinch-off melt fraction remaining in a system after melt migration (Groebner and Kohstedt, 2006). This effect will be examined more closely in the Geological Context section, in application to each system of interest.

1.2.2 Principles of X-ray tomography

The need for 3D visualisation in experimental petrology

As discussed above, the extrapolation to 3D geometry from 2D textural data leads to a significant uncertainty in results of interconnectivity and permeability analysis. In particular, it is impossible to use the majority of extrapolation techniques for samples that have undergone deformation, due to the lack of textural equilibration. Being able to visualise the three-dimensional melt network directly bypasses these limitations. Numerous attempts have been made over the last two decades to visualise partial melt systems directly in 3D. Until recently, this has generally involved serial sectioning and compilation of 2D slices (e.g. Bruhn et al., 2000, figure 1.5), which is a laborious and fully destructive technique, and will often produce an image with an anisotropic resolution with respect to the three principal axes, meaning a certain amount of subjective interpolation is required to characterise the 3D geometry.

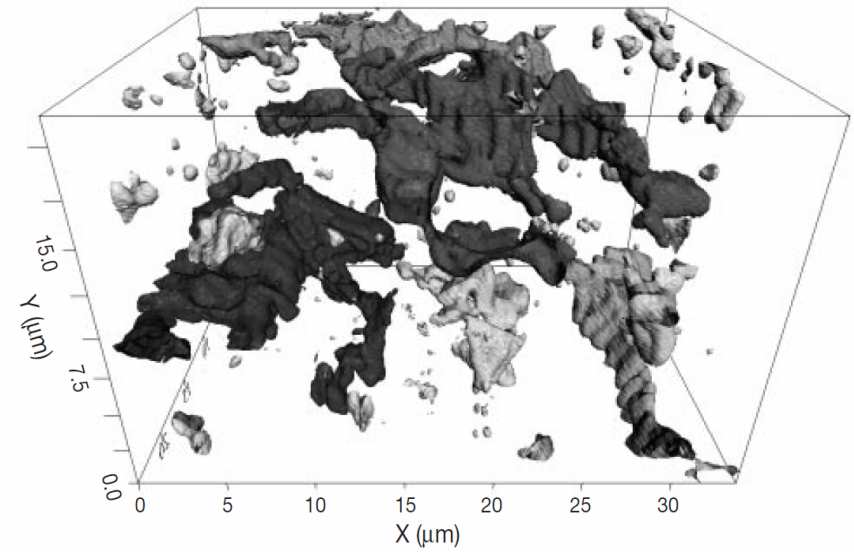

Figure 1.5: Three-dimensional reconstruction of an Fe-Ni-S melt from Bruhn et al. (2000) created by serial sectioning. It is made up of 40 SEM images such as image 2b, each separated by 0.6µm in the Z direction. Despite the high number of sections taken to make this image, serial sectioning still requires subjective judgment as to whether a melt pocket is connected in the Z-direction, especially where features are very fine.

X-ray computed tomography (CT) is a non-destructive technique which allows direct visualisation of sample interiors. The following section outlines the principles of the technique and equipment available, the continued development of its use in the geosciences, and evaluates limitations of the technique.

Principles of X-ray interaction with matter

X- and γ- ray beams lose energy as they pass through a sample due to interaction of photons with the sample material. The loss of intensity will vary depending on the composition and/or density of the material, and can be modelled by the Beer-Lambert law:

$$I = I_0 \exp(-\mu x) \tag{1.5}$$

where I_0 = integral current of incident photons, I= integral current transmitted by sample, μ = linear attenuation coefficient of the sample and x = sample width. This relationship is complicated if the beam passes through more than one material of different properties and the energy of incoming photons.

The energy of the incoming photon will affect the mechanism of interaction with the material: at moderate X-ray energies (100-200kV), a photon interacts by Compton scattering, transferring part of its energy to an electron in the atom, which is ejected. The extent of absorption and scattering is mostly dictated by the density of the material. At lower energies (50-100kV), a photon interacts with material via the photo-electric effect, transferring all its energy to an electron as it collides with an atom. In addition, coherent or Raleigh scattering may take place, where photons are scattered by particles smaller than their wavelength. These are affected more by the chemical composition of the absorber. Therefore, varying the energy of the incoming beam will affect whether the density, or composition of the sample has the greatest effect on beam attenuation. The linear attenuation coefficient (μ) incorporates these different scattering effects and can be calculated for materials of different characteristic properties.

The majority of laboratory X-ray sources will be polychromatic (i.e. of variable energy), and the majority of samples will be inhomogeneous. The Beer-Lambert law, for a polychromatic X-ray beam passing through an inhomogeneous sample becomes (Ketcham and Carlson, 2001)

$$I = I_0 exp\left[\sum(-\mu_i x_i)\right] \tag{1.6}$$

Differences in the physical properties of each part of the sample will therefore result in spatial variations in the energy of X-rays leaving the sample (i.e. variation in the attenuation of the X-rays). In essence, an X-ray image (shadowgram) captures a

'shadow' of the sample cross-section at a certain orientation. Each point on the image will represent the cumulative attenuation the X-rays experience travelling through the sample in a straight line between the X-ray source and the X-ray camera.

The X-ray Computed Tomography (XCT) system

Used as a diagnostic tool in medicine since the 1970s, on-going improvements in resolution and processing time have made X-ray tomography a viable analytical tool in materials science and geosciences (Duliu, 1999). The CT system operates by collecting a series of X-ray shadowgrams at multiple angles around an object of interest, which can be used to build up a 3D image of the object's interior.

An X-ray micro-CT scanner consists of an X-ray source, an X-ray detector, and a central rotating sample stage (Figure 1.6). The scanned sample must be rotated with respect to the source-detector system, to enable images to be taken at 180-360° around the sample. While medical tomography usually requires the source-detector system to be rotated around the patient, custom-built CT scanners for use in the geosciences, like that available to our research, usually have a fixed source-detector system and a sample which can be rotated within the X-ray beam (Pavlinsky, 2008). By taking many projections of changing sample orientation during a 180-360° rotation of a sample, sufficient data are collected to reconstruct a full 3D image of the sample interior.

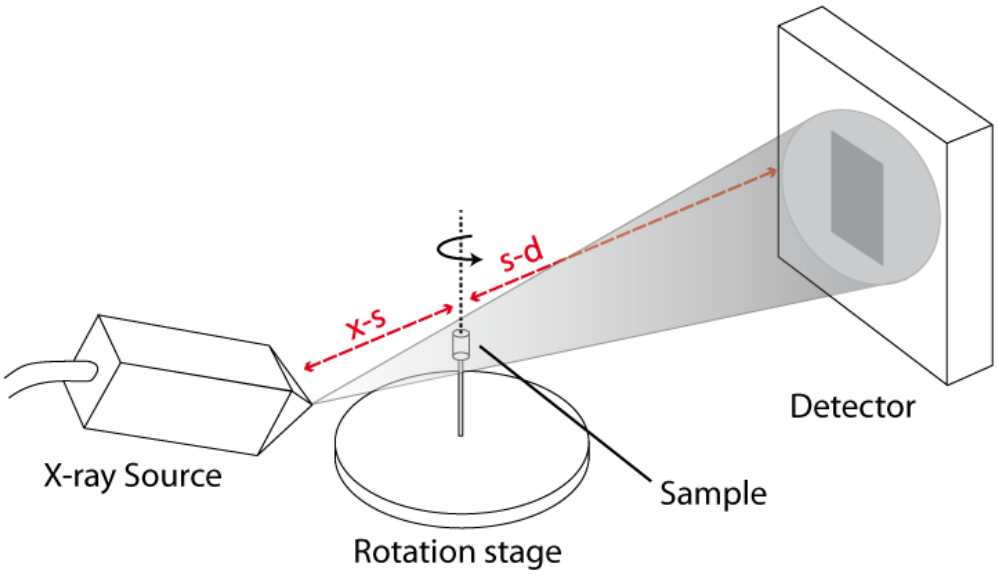

Figure 1.6: The standard set up for a laboratory CT system, including the X-ray source, fully rotating sample stage and detector. The sample stage can be moved relative to the source-detector system to change the source-sample (x-s) and sample-detector (s-d) distances. A shorter x-s distance will generally increase resolution due to the magnification effect of the cone beam.

X-ray sources The X-ray source for laboratory CT equipment produces X-rays by interaction of electrons from a filament which are accelerated across a potential difference to collide with an anode target (usually tungsten, W). The resulting deceleration leads to photon emission to conserve energy, in a process known as *Bremsstrahlung*. Photons are scattered in all directions, leading to the emission of an expanding cone beam of X-rays from the source exit hole. The beam produced from a laboratory X-ray source is polychromatic (exhibiting a range of energies) and of a relatively low intensity (Figure 1.8 A).

An alternative source of X-rays is a synchrotron particle accelerator, which produces X-rays by magnetic deflection of high energy particles (Figure 1.7). The X-ray beams produced are very intense and penetrating in comparison to laboratory cone-beam sources, allowing the beam to be, for example, filtered to X-rays of a limited wavelength to produce a monochromatic beam without dropping the beam intensity to unusable values (Figure 1.8 B). In addition, the X-rays produced are parallel and collimated, simplifying reconstruction. This limits resolution to detector quality, as the magnification cannot be increased by moving the sample closer to the source as is possible with cone beam tomography (Ketcham, 2005a), although higher resolution nano-tomographic techniques have been developed using high resolution detectors and X-ray lenses to focus the beam to the nano-scale.

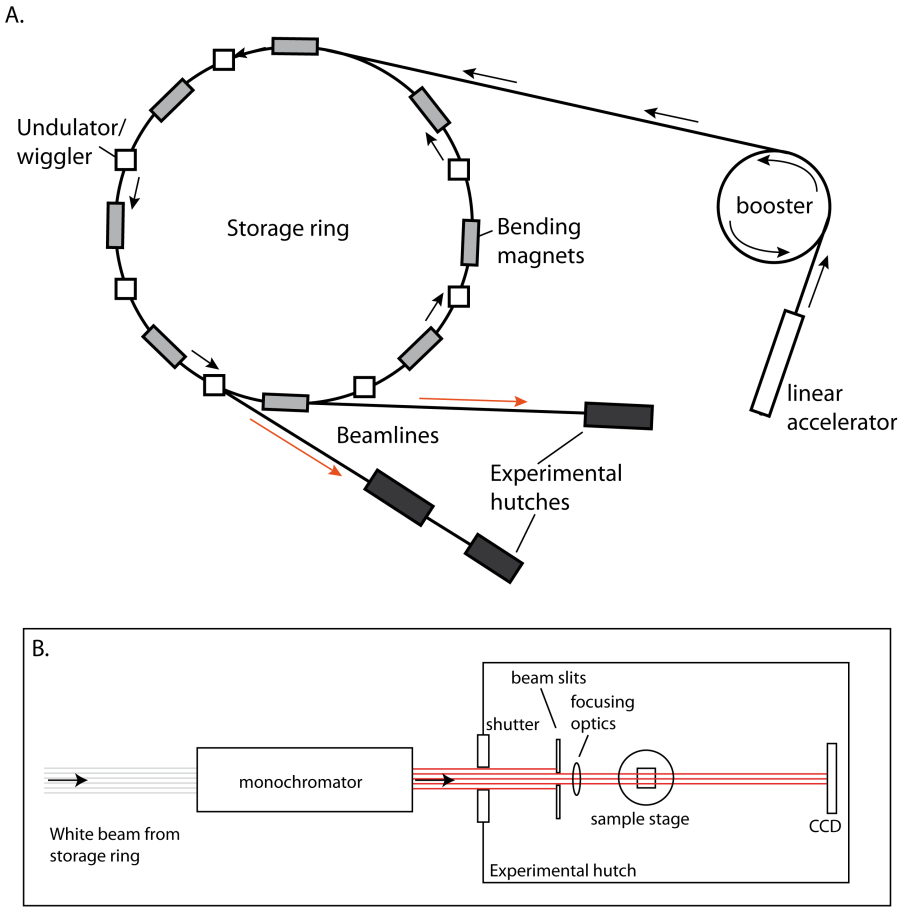

Figure 1.7: A. Plan-view of a synchrotron X-ray source: An electron gun emits electrons which are accelerated in a booster synchrotron to just below the speed of light. These electrons are released into a large 'storage ring', which is in fact a polygon of linear accelerators joined by magnets which bend the electron beam around the circuit. As they are deflected, the electrons decelerate, and the energy lost is emitted in the form of photons (*Bremsstrahlung*). X-rays are channelled along beam-lines at the vertices of the polygon (2 shown as an example in the diagram). Additional magnets known as 'wigglers' and 'undulators' are often placed between the main polygon vertices to further manipulate the beam and produce more X-ray sources. Not to scale: The storage ring of a synchrotron can vary in size - the ESRF synchrotron is the largest in Europe, with a storage ring circumference of 844m. B. A simplified schematic of a beamline (plan view) set up for X-ray tomographic imaging. The white beam initially passes through a monochromator, where a series of mirrors and filters can (if required) reduce the energy range of the X-rays emitted to a monochromatic range. The beam enters the hutch via shutters, operated from the control room. Beam slits can be used to reduce the field of view of the X-rays, and further optic lenses may be used to focus the beam if required. The sample stage is operated from the control room. The total beamline length varies depending on the requirements and set-up of the beamline. For example, at DIAMOND I12, the interior hutch is ~50m from the storage ring.

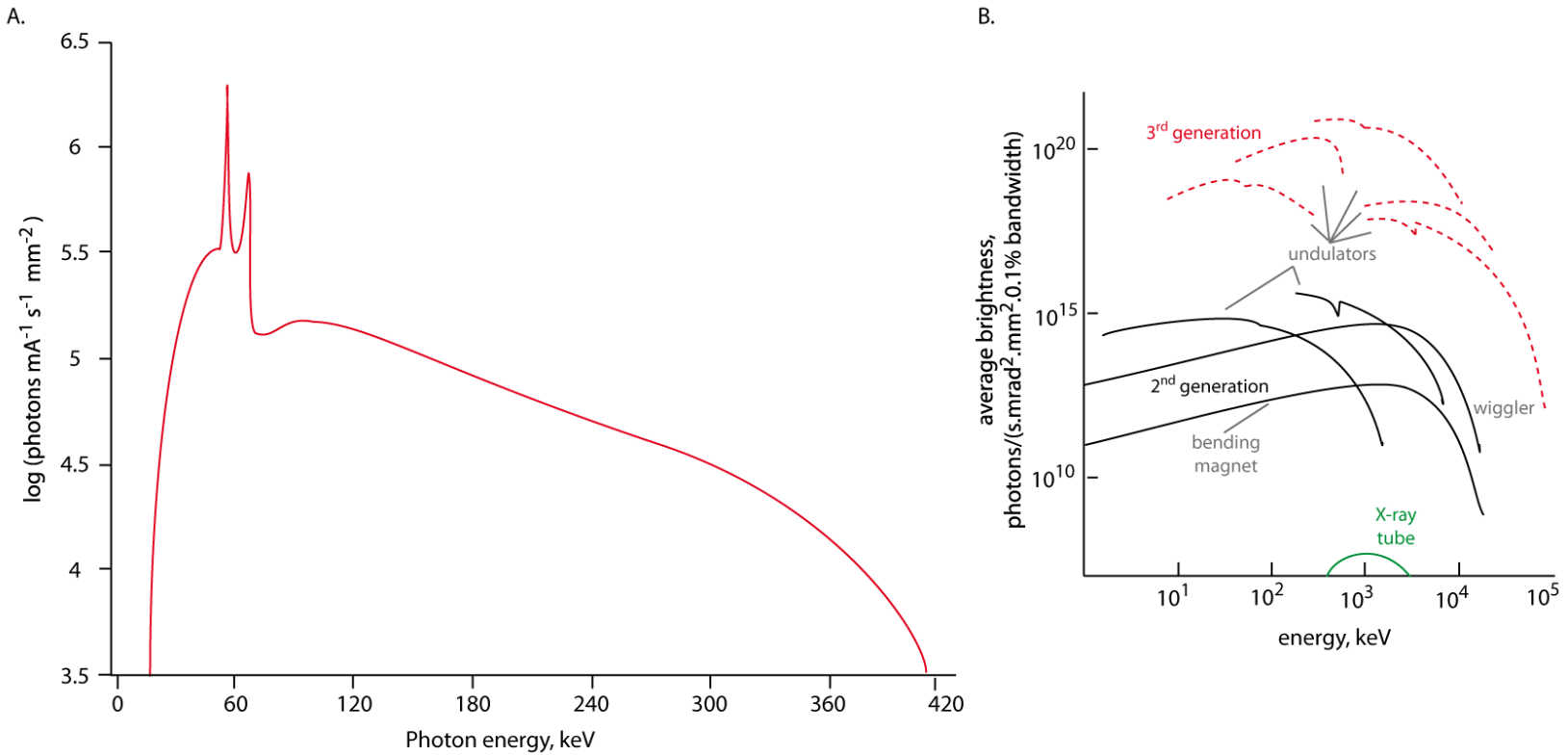

Figure 1.8: The X-ray energy spectra and intensities produced from various X-ray sources. A. An idealised spectrum from a 420kV laboratory X-ray source with a W target (http://www.ctlab.geo.utexas.edu/). The broad spectrum is produced by *Bremsstrahlung*, while the sharp peaks at ~58 and 68 keV represent the characteristic K-edge energies of the W target (Ketcham and Carlson, 2001). For laboratory CT, the energy stated is the mean energy of the polychromatic beam (here 114keV). B. Intensities and energy spectra of 2nd and 3rd generation X-ray sources, adapted from Fusseis et al. (2014) with the laboratory source (X-ray tube) intensities shown for comparison (green line). The energy and spectra depend on whether X-rays are produced by wigglers, undulators or bending magnets. Intensities are many orders of magnitude higher than those of laboratory sources, allowing more intensive filtering and monochromation without incurring too great a loss of energy.

The X-ray detector works by converting X-rays hitting the flat panel screen into electrical charges and from there into digital radiographs stored on a hard disk. Two types of detectors exist: Direct detectors, which convert X-ray photons directly into an electric charge, and indirect detectors (more common), which use intermediate scintillators, such as photodiodes or charge coupled devices (CCD) to convert incoming X-rays into visible light, which is then converted to an electric charge by a photodetector. Detectors are usually 2-d pixel arrays e.g. CCD cameras or flat panel detectors (Pavlinsky, 2008). The resolution of the detector is an important factor in determining overall image resolution, particularly in parallel beam CT where no magnification of the sample occurs by beam geometry.

Reconstruction

Figure 1.9 shows an example of the reconstruction process from 2D projections to tomographic slices. Several hundred projections are taken at regular intervals during a 360° rotation of the sample. These images are normalised to remove background texture created by, for example, CCD screen artefacts or fluctuations in the X-ray energy during the scan. Normalised images are collated using a computer algorithm to create an intermediate image known as a sinogram for each horizontal slice through the sample. A sinogram is made up of vertically stacked lines of greyscale variation. On a single sinogram, each horizontal line represents the attenuation of a particular slice through the sample, with each vertically stacked line representing the same slice at all orientations around 360°. The number of pixels in the X-direction of a sinogram represents the camera resolution, and in the Y direction is the number of projections taken during the rotation. Each sinogram, therefore, contains all the data needed to reconstruct one horizontal slice through the sample, and the number of sinograms produced is equal to the final number of slices reconstructed.

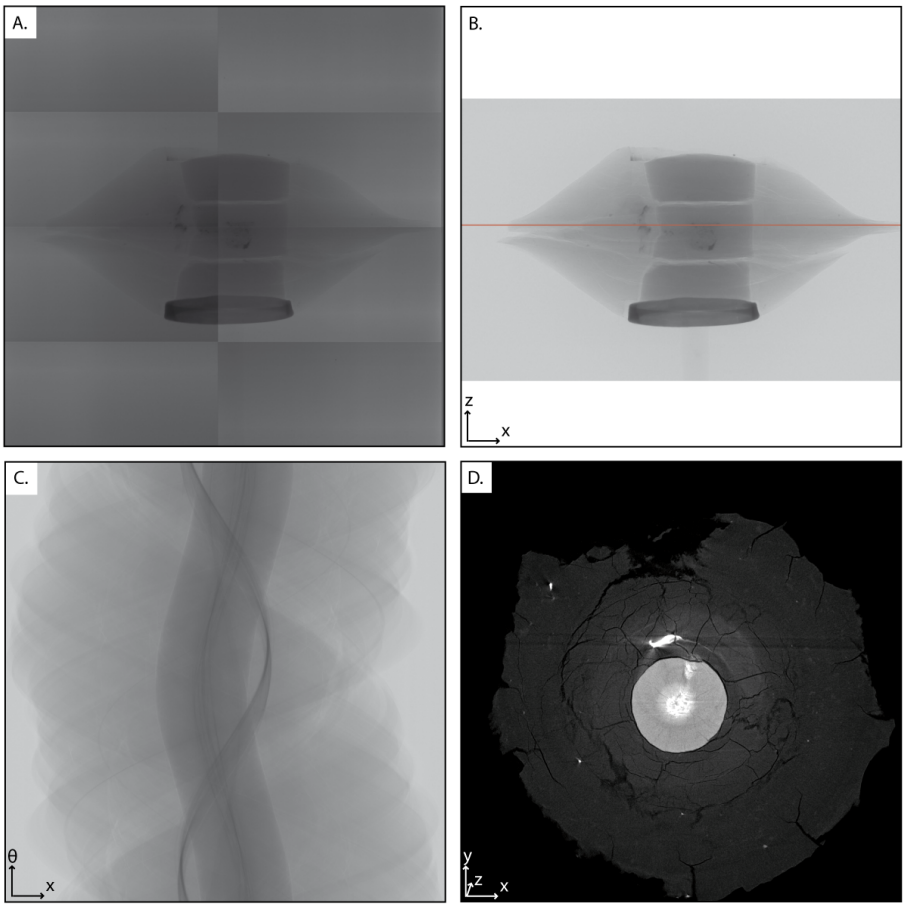

Figure 1.9: Example of the stages of reconstruction of a CT slice - experimental gasket from an experimental gasket produced in this project, scanned using the *in-house* CT system. A. Raw image from the CCD detector. A background texture is present, caused by the CCD detector being made up of a number of different panels of subtly different sensitivity. B. Normalised image removing background texture at a given angle θ. The red line indicates location of data for sinogram. C. Intermediate sinogram image for a given z position. Horizontal change is the attenuation change with x position. Vertical position shows changes of attenuation in the same z position during the rotation (i.e. changing θ). D. Resulting slice through the sample at given z position. In A-C, dark areas are the most highly attenuating. In the final slice D., the scale is inverted and pale areas are more attenuating.

By stretching these 1D line integrals across a 2D plane, and layering up each of these projections at the correct orientation, the attenuation in each 2D point will add up to recreate the features present within a sample. This method of reconstruction is known as filtered backprojection, and is the method applied by Octopus 8.7 CT software available with the *in-house* CT equipment (Dierick et al., 2004).

It is then possible to reconstruct the sample into prismatic volumetric pixels (voxels), each representing the attenuation coefficient of that volume within the sample (Pavlinsky, 2008). By assigning a grayscale to these coefficient values a map of the variation in attenuation through the sample can be produced. This allows construction from a stack of 2D slices through a sample into 3D models of its exterior and interior.

Resolution limitations and nano-CT

Resolution is a key limitation in the use of CT scans for reconstructing the interior of a complex object. Resolution quantifies the ability to resolve two lines of a certain thickness, sometimes measured in the number of lines per length that can still be visibly distinguished. In comparison, a pixel, or voxel, is the smallest unit that a digitial image is subdivided into. Spatial resolution should not be compared directly to voxel size (often quoted in micro-CT). The true resolution is usually lower than the pixel size, and is rarely higher. An important exception to this rule is the resolution of 2-dimensional fracture planes or sheet-like features, which can often be resolved even if their thickness is significantly lower than the voxel size. Even small changes in greyscale from partial volume effects across the fracture can create a resolvable feature due to the relatively large dimensions of the 2D plane (Hunt et al., 1988; Johns et al., 1993).

Blurring can be caused by increasing the focal spot size of the X-ray beam. As spot size increases, there are more possible paths between the source and detector through which X-rays pass, which can lead to blurring. Generally, lowering the beam current can increase resolution by decreasing spot size (Carlson et al., 2003), but this also reduces intensity, therefore a compromise is required to get the best focal size and intensity from an X-ray beam for the sample properties.

The cone beam geometry of a laboratory X-ray source can be used to magnify samples to a higher resolution simply by moving them closer to the X-ray source (Figure 1.6). However, increasing magnification will also increase the blurring effect of the X-ray source spot. The total resolution will be a combination of these factors and the resolution of the detector, as demonstrated in figure 1.10. A simple calculation

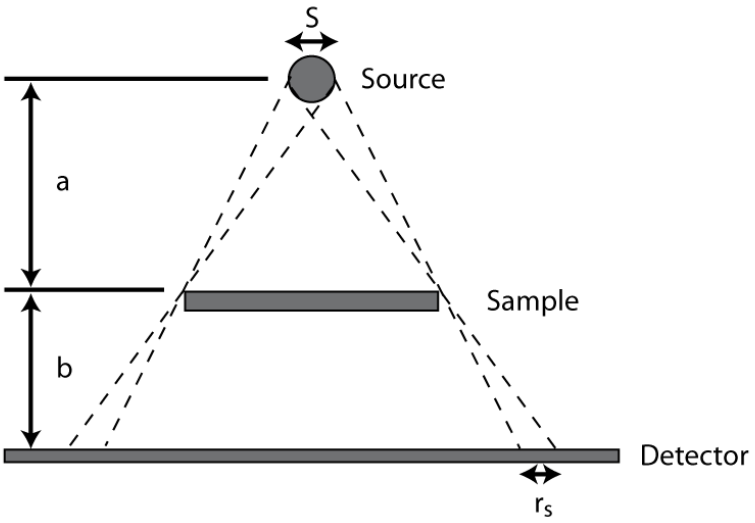

Figure 1.10: A schematic diagram from Feser et al. (2008) illustrating the concept of geometric blurring r_s, and how it is affected by spot size (S), and the ratio of distances between sample-source, a and sample-detector, b.

used to estimate spatial resolution for cone beam tomography is used in this thesis (Feser et al., 2008), and is described in methods section 2.3.4.

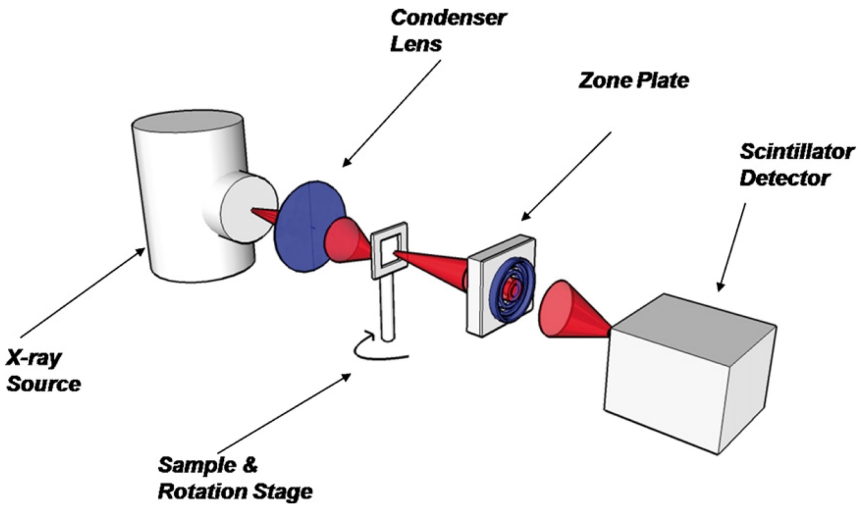

Figure 1.11: A schematic diagram from Shearing et al. (2010) showing additional optics used by the Xradia Ultra nano-CT system to focus the X-ray beam to a smaller area. A condenser lens before the sample focuses the beam to a point at the sample. Behind the sample a Fresnel zone plate refocuses the beam onto the high resolution scintillator/ X-ray detector.

In X-ray Nano-CT a very high magnification is achieved by reducing the sample size to less than 100µm, or at highest resolution to less than 15µm. An additional X-ray condenser is used to focus the X-rays onto the sample, and once the X-rays have passed through the sample, a Fresnel zone plate focuses the X-rays onto the detector (Figure 1.11), reducing blurring effects. In fact, it is the spacing of the slits in the Fresnel zone plate which finally limits the resolution in the current commercial nano-scan detectors (Shearing et al., 2010). Nano-CT technology has been developed for both synchrotron and laboratory cone beam sources. A graph showing the resolution capabilities of various instruments and synchrotron beamlines are shown in figure 1.12.

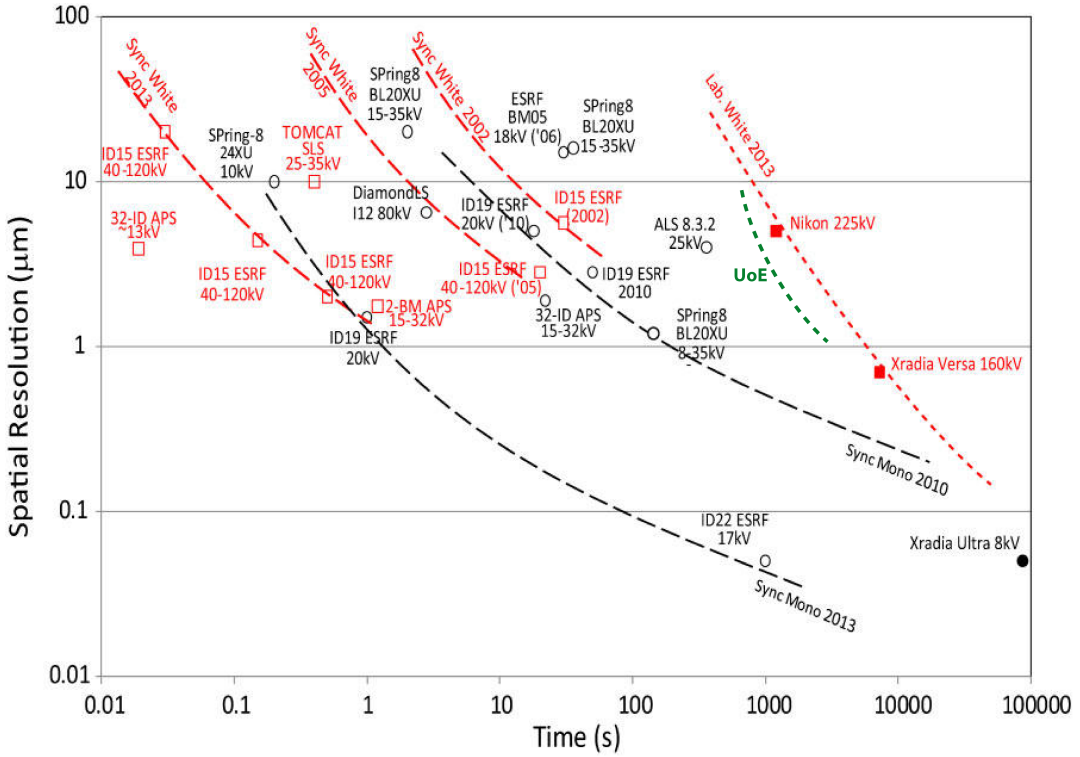

Figure 1.12: A graph of spatial resolution against time (s) required to complete a full tomographic scan, from Maire and Withers (2014). The resolution, where possible, is the true spatial resolution. In other cases an estimated resolution of twice the pixel size is used. Red data is white beam (full energy spectrum) while black data represents monochromatic beam. Sync = synchrotron source, Lab. = laboratory source. The University of Edinburgh CT system has been added to the diagram (green dashed line) and is comparable to the resolution and speed offered by commercial laboratory sources (Nikon and Xradia Versa).

Contrast limitations

The contrast between phases of interest in a sample is a key factor in ensuring good quality segmentation and 3D reconstruction of images. Contrast between phases is caused by differences in X-ray attenuation, i.e. interaction of X-rays with the material in question.

As previously described, changing the energy of an X-ray beam can change the mechanism of particle interaction of photons and therefore the level of attenuation with respect to either the density or chemical composition of a material (Pavlinsky, 2008). Therefore, by varying the energy of the X-ray beam, contrast between phases of interest can be increased or decreased depending on their density and compositional differences. The linear attenuation coefficient will change according to the physical properties of a material, and is calculated incorporating the effects of coherent, compton scattering and the photo-electric effect.

A plot of the linear attenuation coefficient vs. beam energy can be created for a material, and can be used to determine the optimum range of energies needed to scan a sample. An Excel spreadsheet tool, MuCalc, has been created by University of Texas CT group, using collated experimental attenuation data from XCOM the Photon Cross-Sections Database (Berger et al., 1998). This can be used as a preliminary tool to allow comparison of attenuation curves before scanning, in order to choose the best energy range for scans of different material types (Figure 1.13).

In some cases the contrast between phases is very low, and an alternative technique is required to separate the materials on CT scans. This is often the case in biological materials (soft tissue), but can also occur in geological materials. An important example is the low contrast between olivine and basaltic melt (see chapter 4). A technique known as Phase Contrast imaging (Gluckstad, 2000) has been developed to enable low-contrast phases to be distinguished. X-rays travelling through a material of interest will travel out of phase compared to those travelling within the material, creating interference patterns at phase edges, which are enhanced by the detector system, thereby highlighting phase edges. This effect requires large distances between the source, sample and detector, and is therefore mostly restricted to synchrotron beam tomography, although the technique has recently been developed for some laboratory instruments.

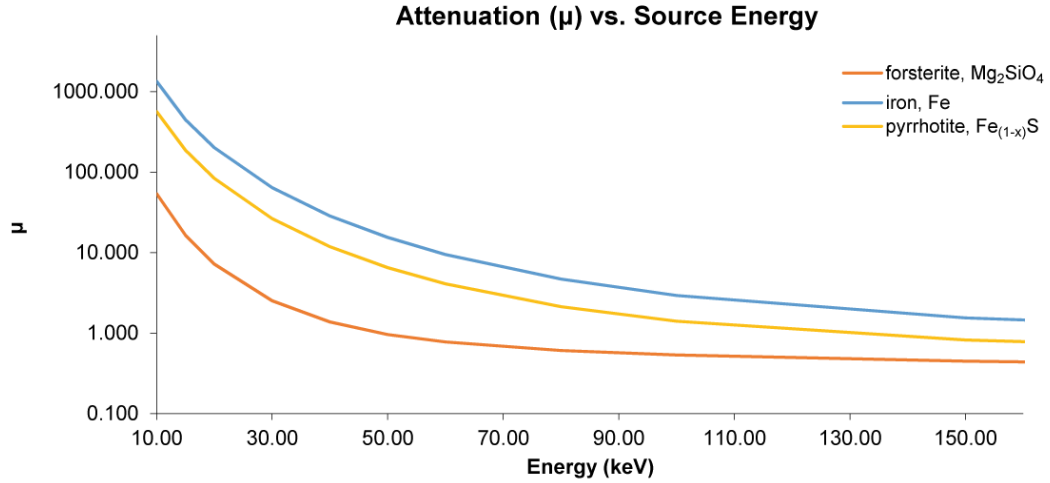

Figure 1.13: A graph showing attenuation (μ) vs. X-ray source energy, of forsterite, pyrrhotite and iron created by the excel tool MuCalc. The tool allows a comparison of attenuation contrast of numerous geological materials at varying X-ray energies. This preliminary analysis can be used to tune X-ray energies and enhance contrast between materials in an inhomogeneous sample. For example, the contrast between these two minerals is significantly higher at low energies, where the photoelectric effect dominates scattering.

Noise and artefacts

Certain aspects of the source-detector system, sample properties and the basic characteristics of X-rays can lead to background noise, and artefacts. Major artefacts can often be reduced if not removed entirely by post- or pre-reconstruction corrections, particularly if the noise is produced by a systematic, predictable flaw in the system (Sijbers and Postnov, 2004). Ketcham (2005a) give a clear description of common artefacts in a review paper . The main artefacts, their cause, and potential methods of removal are summarised below:

- **Misalignment** – Blurring can occur if the source, detector and rotation axis of sample are not lined up perfectly. Although this can be dealt with to a certain extent by post-processing, the best way to reduce misalignment artefacts is to align the system as accurately as possible.

- **Beam hardening** – In a polychromatic beam, low energy X-rays are absorbed more than those of high energy, which leads to an increase in the overall energy of the X-ray beam as it passes through the sample. The amount of beam hardening depends on the distance the beam has travelled within a sample, therefore shorter paths (e.g. through thin edges of a circular sample) will appear brighter than longer paths (e.g. through the thicker centre). Although beam hardening effects are relatively symmetric in an object with a circular cross-section or other regular shape, the effect of beam hardening can be more difficult to recognise in irregular objects. A simple way of reducing beam hardening effects is to use a high enough energy beam so that the beam hardening effect of low energy X-rays is negligible (e.g. synchrotron). However, this may cause problems if a low energy beam is required to differentiate between the materials in the sample (see above). Another option is to eliminate low energy X-rays from analysis by adding a physical filter consisting of a metal sheet in the system, allowing X-rays to pass through it either before or after entering the sample. This blocks low energy photons reaching the detector and therefore analyses only the narrower range of high-energy photons, which are unaffected by beam hardening. Materials used include copper, aluminium and brass of varying thickness. This reduces the overall intensity of the X-ray beam which can increase noise, although exposure time can be increased to compensate for the relative loss of signal. It is also possible to carry out a correction during reconstruction which shifts the greyscale of the sample edges down compared

to the sample interior, which works well in samples of a uniform shape (e.g. cylinders).

- **Ring Artefacts** Ring artefacts are caused by shifts in the output on the detector caused by changes in scanning conditions, such as beam strength and temperature, combined with differences in detector sensitivity on a 2D array. Fluctuations will affect these anomalous detectors differently, creating regular anomalous values that appear as light and dark rings in reconstructed slices (linear features in sinograms). Due to their regular shape, these rings are relatively easy to identify as artefacts and remove by e.g. Fourier transform filters either in the sinogram or reconstruction stage. However, care must be taken to avoid removing real linear / circular features within a sample with ring removal filters. Environmental factors such as temperature fluctuations can be reduced by carefully controlling the scanning environment.

- **Star/Streak artefacts** These occur if a very dense material is present. They appear as dark streaks connecting opposite corners of a dense object and can intensify ring artefacts. A relatively dense area within an otherwise less dense material can create 'starburst' features, where bright streaks radiate from the area out into the remaining sample. Increasing energy to improve the penetration of X-rays through dense samples can remove some of these effects.

- **Partial Volume Effects** The volume of a voxel is the smallest unit of information in a 3D scan. If a voxel spans, for example, a material boundary, and two or more materials are present within it, the voxel will give the average attenuation value of all the materials within that volume. This leads to blurring of sample edges, particularly if features are often smaller than the voxel size of a scan. This is called a *partial volume effect*, and can have a large effect on the accuracy of phase segmentation, as a significant amount of data within a scan could be assigned to an intermediate 'multi-phase' greyscale. Higher resolution scans will reduce partial volume effects, but they are otherwise impossible to remove by any filtering technique. Any image analysis carried out, particuarly quantitative analysis, must therefore take into account the presence of partial volumes.

In general, the addition of a physical filter is able to reduce many of the above artefacts in a laboratory system. The loss of intensity from its addition is usually compensated for by increasing exposure time, making scan speeds slower (see Figure 1.12). The addition of a physical filter also reduces the likelihood of clipping

as it reduces the total energy spectrum hitting the detector, reducing likelihood of overexposure and clipping of data. However, increasing the scan time can also increase artefacts caused by subtle movement of the sample, or fluctuations in beam intensity/spot drift. A compromise is always required between each factor to optimise scan conditions.

Application of CT in visualisation of geological melts

Over the last 5-10 years, X-ray tomography has been used in the analysis of partial melt networks for examining melting in the upper mantle as well as core formation processes (Watson and Roberts, 2011; Zhu et al., 2011), with promising results. The technique is still limited by the relatively low resolution achieved by CT scans (Figure 1.14), and the work is generally supported by detailed BSE imaging to groundtruth findings. The use of synchrotron X-ray sources and the development of nano-tomographic techniques and phase contrast imaging has improved the technique's potential over recent years.

Studies examining partial melt using tomography are described in detail in the Geological Context sections (1.3.1-1.4).

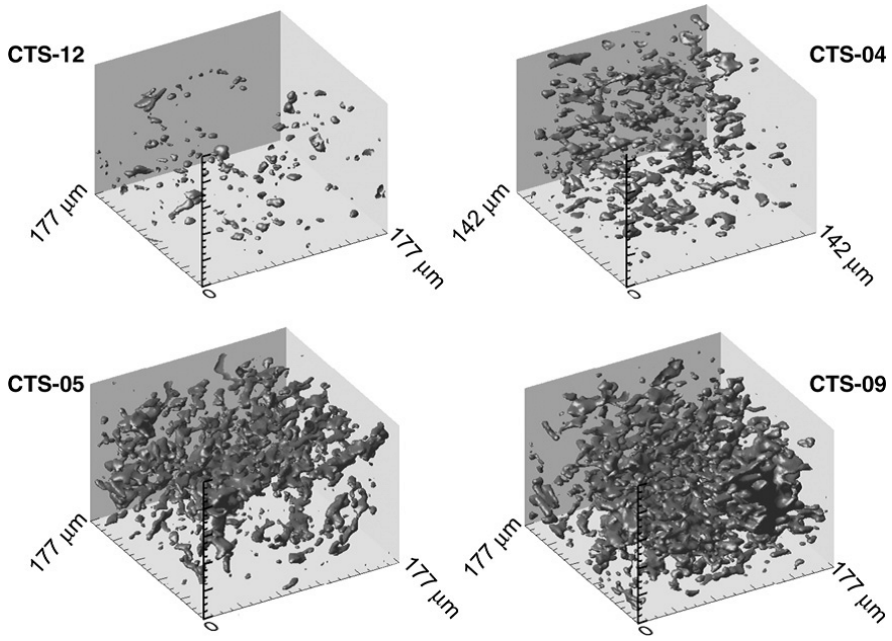

Figure 1.14: Three-dimensional reconstruction from X-ray Tomographic scans of an Fe-S melt network within a solid olivine matrix (here transparent), at various melt fractions, from Watson and Roberts (2011). The resolution is relatively poor (2µm voxel size), currently precluding visualisation of sub-micron melt networks, as seen in two-dimensional SEM images in our work.

Development of in-situ tomographic techniques in the geosciences

Since X-ray CT was applied to problems in the geosciences, researchers in the geo- and materials sciences have begun to develop methods to conduct *in-situ* experiments, allowing continuous, time-resolved observations within the same sample over the course of an experiment by simple 2D radiography, 3D CT scans, or by X-ray diffraction (see Methods 2.4). Although time-resolved studies are possible using laboratory X-ray sources, the scope for *in-situ* high P-T petrological experiments has increased significantly since synchrotron technology was developed and has become readily available to geosciences researchers. The high energy flux of synchrotron X-ray sources is generally required to allow X-rays to pass effectively through high P-T equipment, even if outer gaskets etc. are designed to be X-ray transparent, and the ability to fine-tune the X-ray energy spectrum allows for more effective imaging or quantitative use of the X-ray data (e.g. by diffraction).

The adaptation of high P-T presses in combination with diffraction technologies using synchrotron X-rays has allowed density and structural changes of crystalline materials to be measured up to the pressures and temperatures associated with the Earth's deep mantle and core, and more recently techniques have been developed to gain density measurements on non-crystalline materials (Hong et al., 2007). Ultra-high pressure experiments have been conducted using diamond anvil cell technologies (particularly effective as the cell itself is already X-ray transparent), while adaptation of high P-T presses such as the multi-anvil and Paris-Edinburgh cells have allowed larger volume experiments at pressures up to 7GPa and temperatures up to 2000K, for both radiographic imaging (Funakoshi and Nozawa, 2012) and diffraction studies (Mezouar, Faure, et al., 2002). Classic high pressure and temperature cells are generally designed with the sample geometry stabilised by a thick containment ring - design adaptations therefore generally require reducing the thickness of the containment ring and/or changing the material to be X-ray transparent, or creating an X-ray transparent window through to the sample centre e.g. using an Al-alloy ring on Drickamer devices instead of the thick W alloy ring used in the traditional apparatus; although this reduces the stability of the equipment, it still permits sample pressures of up to 8GPa (Wang, Uchida, et al., 2005). Multi-anvil devices can be oriented to allow X-rays to pass through gaps between metallic anvils (Chen et al., 2011). The Paris-Edinburgh large volume press, as used in this project, uses a toroidal anvil allowing high pressures to be attained with the gasket open at the centre between the anvils, meaning only the gasket immediately surrounding the sample has to be X-ray transparent (Mezouar, Le Bihan,

et al., 1999).

An example of an area of study that has advanced rapidly with the use of in-situ technology is that of melt viscosity / density measurements using the 'falling sphere' technique. This technique has been used since 1963 (Shaw, 1963) to measure characteristics of geological melts, and involves timing the fall of a sphere of material of known composition and density through a molten medium. Until recently, quenched and polished sections of the run products were used to measure the distance the sphere had fallen within a known time at high temperature, providing one data point per experimental sample (Mori et al., 2000). Conducting similar experiments on a synchrotron beamline, 2D radiography can be used effectively to image the sphere-drop experiment in real time to gain a full dataset showing onset of melting, not only giving the velocity of the falling sphere but also providing data on its acceleration and attainment of terminal velocity (Chen et al., 2011). Adaptation of high P-T multi-anvil presses to include an X-ray transparent window have allowed the falling-sphere technique to be used at a range of pressures up to ~9GPa (Funakoshi and Nozawa, 2012; Urakawa et al., 2001) and even higher pressures by using diamond anvil cells (Cook et al., 1993; Piermarini et al., 1978). Investigating changes in viscosity of geological liquids (including metallic and metal-sulphide melts) over a large range of pressure and temperature values proves invaluable to the majority of research investigating partial melt processes in the deep Earth, and the results of a number of these studies have been used in this thesis.

Other examples of the use of *in-situ* radiography to investigate melting processes include bubble growth experiments within lavas heated at 1 atm pressure (Bai et al., 2008). This study also used ex-situ 3D tomographic imaging to examine post-run products, thereby using a combination of 2D and 3D data to fully characterise experimental processes, and a 2-phase liquid immiscibility in the Fe-O-S system at high P-T. Here, observations of two separate melt phases at high P-T were confirmed by *in-situ* imaging (Tsuno et al., 2007) - this is difficult to conclude from quench products as the process of quenching itself can lead to exsolution and produce immiscibility textures.

In the field of materials sciences, a study examining migration of gallium melt into an aluminium polycrystalline material has been conducted using transmission radiography to gain a pseudo-three dimensional view of the melt moving along grain boundaries (Pereiro-Lopez et al., 2004). The effect of differential strain on melt propagation was examined, but the observations were limited to ambient pressure conditions.

3D visualisation of partial melt geometries at concurrent high P-T is an area that is currently the focus of continued development. This requires further adaptation of experimental equipment to allow the sample to rotate fully within its confining pressure frame (otherwise the bulky metal frame would block X-rays from passing through the capsule centre). A number of experimental presses have been adapted to allow this to take place, including an adaptation of the Drickamer apparatus (Wang, Uchida, et al., 2005), and the rotational Paris-Edinburgh cell used in this experiment (LeGodec et al., *in prep*), both of which use rotating anvils to rotate the sample within the confining frame. This allows full 3D scans to be carried out at concurrent high P-T, with the potential to deform samples using the two motors independently and investigate the effects of torsional deformation on sample texture. Previous *in-situ* work has been conducted using the Drickamer apparatus investigating the effects of deforming a multiphase Fe-Ni-S + olivine system to extreme values of torsional strain (Wang, Lesher, et al., 2011), although the temperatures at which this has been carried out (800K) mean both phases were solid during deformation. *In-situ* work carried out in this thesis is the first carried out using the novel rotoPEC design.

1.3 Application to geological systems

1.3.1 Core formation in planets and planetesimals

The standard model of accretion of terrestrial planets requires initial formation of planetesimals a few km in radius by coalescence from the solar nebula, a hot disk of dust and gas which surrounded the proto-sun (Wetherill, 1994). These planetesimals combined by a process of accretion to form small bodies up to the size of the moon. Around 100 'planetary embryos' are predicted to have aggregated through a series of large impacts to form the terrestrial planets of the inner solar system (Koeberl, 2006). Earth is believed to have started this phase of growth around 4.6 Ga, the bulk of accretion ending around 100 Ma after solar system formation with the moon-forming impact of a Mars-sized object with the proto-Earth (Canup, 2008; Wood et al., 2006). At some point during the formation of the terrestrial planets, this amalgamation of heterogeneous bodies of rock differentiated to form a layered planet, with a dense metallic core and silicate outer mantle. A significant amount of research has focussed on determining the timing and processes of mantle-core segregation in the Earth and other terrestrial bodies over the last three decades (Wood et al., 2006 and references within).

Constraints on core formation processes

Any viable theory for core formation must be physically possible within the timescales constrained by core chronometry and be able to reproduce the inferred geochemistry of the mantle and core of each planetary body (Jacobsen, 2004). Constraints on core formation therefore include geochemical and geophysical evidence of planetary interiors, as well as evidence of physical processes from laboratory experiments.

Geochemical constraints

Timescales of core formation are generally constrained by ^{182}Hf-^{182}W isotope systematics (Jacobsen, 2004; Kleine, Mezger, et al., 2004; Kleine, Munker, et al., 2002; Kleine, Touboul, et al., 2009). ^{182}W is relatively siderophile and partitioned preferentially into core forming melts, while its parent isotope ^{182}Hf is lithophile, partitioning into silicate portions of the Earth. The quantity of ^{182}W in the mantle can, therefore, be used as a measure of the amount of ^{182}Hf stranded in the mantle after core formation ceased. The relatively short lifetime of this isotope system makes it an excellent indicator for timing of core formation: ^{182}Hf decays to ^{182}W with a half-life of 9Myrs; therefore, the ratio of ^{182}W and ^{183}W in the Earth's mantle, compared with the Chondritic Uniform Reservoir (CHUR) compositions, might give an estimate of the maximum timespan of core formation.

Initial estimates using this core chronometry technique by Kleine, Munker, et al. (2002) gave a timescale constraint of 30Myr. However, estimates of timing vary from <30Myr to >100Myr depending on end member theories of core formation used during calculations (Rudge et al., 2010). Inferences of core formation change estimated timescales, making the processes of constraining core formation processes highly complex.

The same limitation applies to compositional constraints. The Earth's bulk composition is inferred to be similar to that found on meteorites known as chondrites, thought to represent the most primitive, undifferentiated meteorites and therefore closest in composition to the original solar nebula (Ringwood, 1979). This claim has been disputed, as the exact bulk composition of a planet is likely to depend on its distance from the sun (Jones and Drake, 1986). The only other direct constraints of deep Earth composition come from seismic interpretations of the interior of the Earth, which give estimates of bulk density and physical properties of each Earth layer (Anderson and Kovach, 1968; Dziewonski and Anderson, 1981). This information can only help to constrain bulk chemistry and cannot provide high resolution data required to deduce precise composition of the deep Earth. For example, the density values

of the inner core are slightly lower than expected for pure iron at high pressures, a deficit which is explained by the inferred presence of 5-10±5% of a lighter siderophile element such as sulphur, oxygen or silicon (Anderson and Isaak, 2002; Poirier, 1994; Shanker et al., 2004). Further constraints on core composition are generally inferred from differentiation processes, and should be used with caution when evaluating theories of core formation.

It is possible, however, to infer certain aspects of core formation processes from direct observations of crustal and upper mantle geochemistry (Jones and Drake, 1986). Comparison of the observed geochemistry to the chondritic bulk composition indicates that highly siderophile elements (HSEs) are severely depleted in the terrestrial mantle. This is expected, as they would be expected to partition preferentially into the core during segregation. However, the amount of highly siderophile elements left stranded in the mantle are higher than expected for a completely efficient core formation process (Drake and Righter, 2002 and references within). The excess siderophile elements in the mantle can be explained by the presence of around 1% of potentially core forming material in the mantle. Therefore, an inefficient core formation mechanism must either leave remnant core material stranded in the mantle (Jones and Drake, 1986), or a late addition of new bulk chondritic material was added to the Earth after Earth differentiation ceased (Chou, 1978; Holzheid et al., 2000). Any model of core formation must be able to explain this 'excess siderophile element problem'.

Experimental constraints

The core formation process must also be physically possible at relevant pressure and temperature conditions, in order to reproduce the geochemistry observed in the mantle. A major debate concerning core formation has been whether iron or iron alloy melts are able to form an interconnected network through a solid silicate matrix, or whether silicate melting is required to segregate core and mantle material effectively.

Over the last two decades, a large number of petrologic experiments have been conducted over various pressures, temperatures, compositions and timescales to determine permeability of metallic melts in silicate matrices analogous to core-forming processes in terrestrial bodies. The large majority of studies have focussed on dihedral angle measurements of SEM images to infer melt interconnectivity (Shannon and Agee, 1996, 1998; Terasaki, Kato, et al., 2001), with a number of additional studies based on electrical conductivity measurements (Yoshino et al., 2003, 2004). An olivine matrix is usually used as a simplified model for upper mantle silicate composition, although experimental work has also been carried out on other silicates, e.g. perovskite (Terasaki et al., 2007) as well as natural meteorite samples (Rushmer, Petford, et al.,

2005). Core melts are usually simulated using a pure iron or iron-nickel alloy, with the addition of varying amounts of a 'light element' such as silicon, oxygen or sulphur required to explain the core's density deficit (see above). Addition of volatiles such as sulphur and oxygen to a liquid tends to significantly decrease dihedral angle as viscosity of the liquid decreases, which is thought to be due to lighter elements being 'surface active', reducing surface energy by accumulating at the boundary between solid and liquid phases (Terasaki et al., 2005). Studies have generally found that dihedral angles decrease with increasing temperature (Terasaki, Kato, et al., 2001), decreasing pressure (Terasaki et al., 2008) and increasing sulphur content (Terasaki et al., 2005). However, the vast majority of studies suggest that, at conditions appropriate for core formation within the Earth, interconnected melt networks do not form. The large dihedral angles found, and therefore large pinch off fractions required, cannot be justified in terms of the quantities of siderophile elements observed in the mantle.

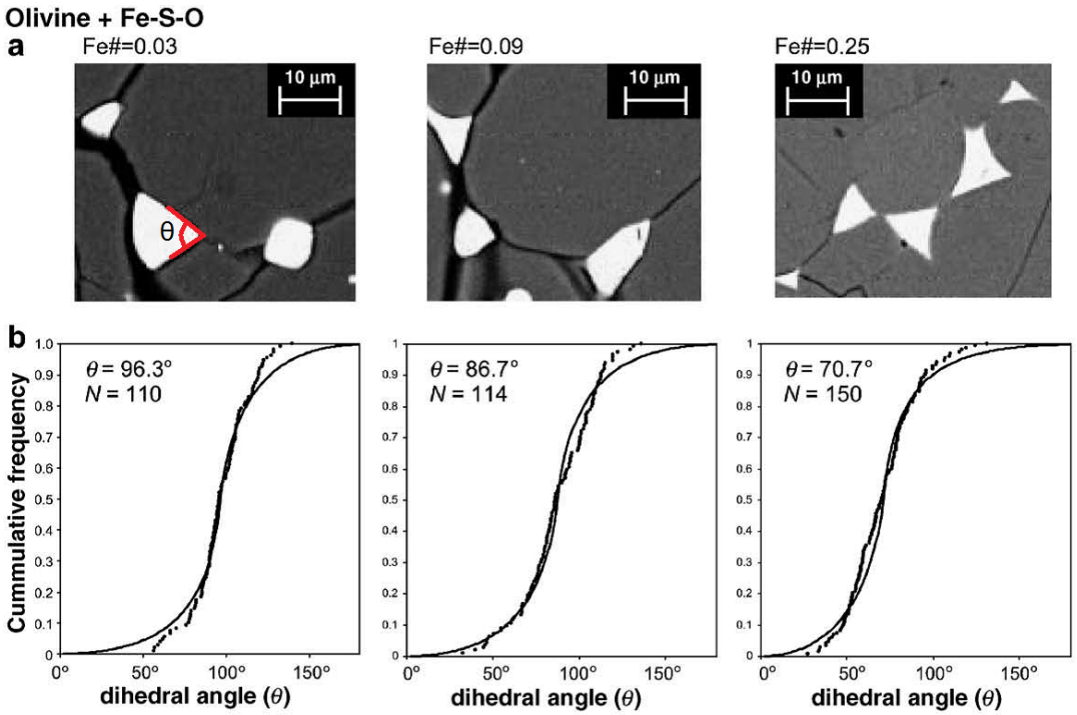

Figure 1.15: Work by Terasaki et al. (2007) showing dihedral angle analysis on Fe-O-S liquids in a solid silicate matrix at high pressure conditions remain stranded in a solid olivine matrix at high pressures in a hydrostatic system at very high pressure conditions. a) Backscatter electron images show Fe-O-S melt is trapped in isolated pockets at varying compositions of liquid. The dihedral angle is measured as the angle between two grain boundaries and the melt pocket, as labelled. B) Cumulative frequency curves of measured dihedral angles (along with solid theoretical curves for comparison). Average dihedral angles are significantly greater than 60° at each liquid composition, meaning a significant fraction of melt would be stranded, unless the system underwent significant silicate melting. This, and similar work led to the development of the magma ocean model of core formation.

The magma ocean model

On the basis of these experimental studies, the general consensus is that the silicate portion of the early Earth must have undergone a moderate amount of melting for the Earth to differentiate efficiently, giving rise to the 'deep magma ocean model' in which denser metal droplets drift to the bottom of a largely liquid silicate upper mantle. The dense metallic melt collects at the base of the silicate magma ocean until its mass is high enough to form a diapir, which sinks through the remaining solid lower mantle to the centre of the Earth, forming the core (Ringwood, 1979; Stevenson, 1981). This model implies chemical equilibration between the metallic and silicate material during mingling of liquid droplets and at the base of the magma ocean (Walter and Tronnes, 2004). Modelling and extrapolation of siderophile element partitioning during equilibration suggests P-T conditions required to form such a magma ocean are around 3500°C and 40GPa (Wood et al., 2006). This is roughly 400°C above the liquidus of silicates, although this temperature could be reduced to the liquidus value if oxygen fugacity increases during core formation (Wade and Wood, 2005). Both short-lived radiogenic isotopes and giant impacts during the proto-Earth's accretion are proposed to have provided enough energy to melt the Earth's silicate mantle partly or even entirely several times (Righter and Drake, 1996).

The presence of metallic cores in a large number of terrestrial bodies, ranging from the planets of the inner solar system to large asteroids, implies that differentiation of these bodies and the formation of metallic cores was a key process in the evolution of the solar system. As such, the magma ocean model has been used to explain the presence of cores in many other terrestrial bodies including Mars, the Moon and even Vesta (Taylor et al., 1993). Whilst temperatures during accretion may theoretically have risen high enough to induce extensive silicate melting on larger terrestrial planets, it is unclear whether or not localised impacts would lead to global magma ocean formation, and estimates of global magma ocean depths (P-T conditions) and overall lifetimes are highly variable (Rubie and Jacobson, 2015 and references within). A global magma ocean is more difficult to invoke for smaller bodies, due to the short timeframe of core formation of small bodies implied by $^{182}\mathrm{Hf}-^{182}\mathrm{W}$ isotope data and efficiency of heat-loss from smaller bodies (Kleine, Munker, et al., 2002; Kleine, Touboul, et al., 2009). The most likely heat sources for planetesimals and asteroids are short-lived isotopes such as ^{26}Al and ^{60}Fe (Bizzarro et al., 2005), localised heating from impacts (Rushmer, Petford, et al., 2005), and possibly heating by electrical conduction from solar winds (Walter and Tronnes, 2004). ^{26}Al heating is able to

provide heating to the silicate solidus within 2-3 Myr if the isotope is abundant, but McCoy et al. (2006) suggest that aluminium could be transported out of the mantle in the first partial melt, removing the heat source early on. The lack of consensus regarding heat sources for magma oceans on smaller planetary bodies has reopened the debate on early processes of metal-silicate segregation.

Additional doubt has been thrown on the magma ocean model by recent high resolution iron isotope measurements of sea-floor basalts (Craddock et al., 2013), which show no evidence of liquid fractionation at high P-T in a deep magma ocean (Halliday, 2013). In fact, a number of recent modelling papers favour models of disequilibrium to explain terrestrial compositions (Rudge et al., 2010), and the original idea that we may be able to infer core formation processes directly from equilibrium models is becoming less popular in the research community (Halliday, 2013).

Deformation aided percolation model

Initial experimental work focussed on constraining core-formation at high temperature, high pressure conditions in hydrostatic systems. However, continuous bombardment during on-going accretion and vigorous convection in bodies hot enough to melt their metallic component is likely to have resulted in a very dynamic, continually deforming environment in terrestrial bodies (Bruhn et al., 2000; Hustoft and Kohlstedt, 2006; Rushmer, Petford, et al., 2005). Recent work has considered how shear deformation during accretion could aid segregation of sulphur-rich metallic liquid from solid silicate melt (Bruhn et al., 2000). In the context of planetesimal and asteroid differentiation in particular, this work suggests that deformation may help to remove melt that would otherwise remain stranded in static systems (Bruhn et al., 2000; Groebner and Kohstedt, 2006; Hustoft and Kohlstedt, 2006; Rushmer, Petford, et al., 2005) and therefore could be a possible mechanism for core formation that does not require extensive silicate melting.

Initial work examining deformation induced melt segregation indicated that application of shear led to a clear change in melt textures from isolated round pockets to elongate structures aligned at an angle to direction of shear (Bruhn et al., 2000). Seen throughout deformed samples, this alignment suggested the metallic liquid created an interconnected network in the deforming system.

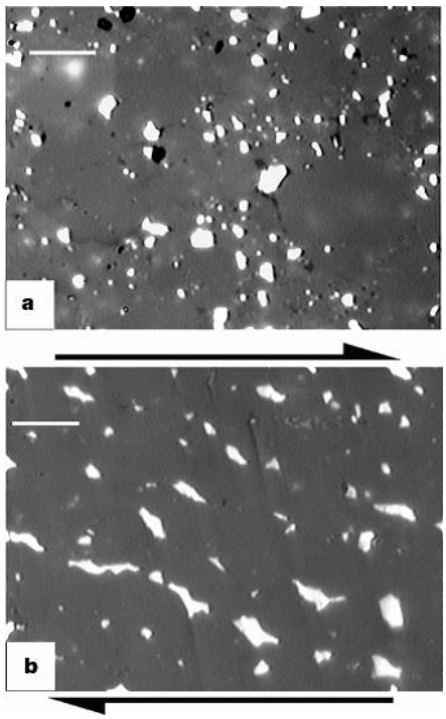

Figure 1.16: Reflected light images of olivine (grey) and Fe-Ni-S (white) sample sections from experiments by Bruhn et al. (2000) Scale bar is 10μm a) Undeformed sample indicates classic texture of isolated melt pockets (white) with high dihedral angles. b) Deformed sample has larger, more elongate melt pockets, aligned at an angle to shear deformation. The melt must be relatively mobile to be able to line up in response to the shear deformation. These experiments have been criticised in more recent publications for unrealistically high strain-rates and low pressures (Terasaki et al., 2005; Walte et al., 2011)

However, these early deformation experiments have been criticised for their large strain values, high melt fractions and low confining pressures (Wood et al., 2006). As such, the relevance of this mechanism in extrapolation to core formation in the terrestrial planets has been disputed.

In order for deformation to control melt geometry in a solid matrix, the effect of differential stress must overcome that of interfacial tension which, in the case of iron rich liquids, acts to keep melt isolated at grain boundary triple-junctions (Groebner and Kohstedt, 2006). The effect of interfacial tension is greater in pockets of smaller radii, therefore it will become larger as melt drains from the system during melt migration, and there must still remain a 'pinch off' fraction below which differential stress will not affect melt geometry.

This melt fraction has been observed to be much lower than in static systems in laboratory experiments (Groebner and Kohstedt, 2006; Walte et al., 2011). However, it is disputed whether it would be possible to observe this effect on a planetary scale applicable to core formation (Walte et al., 2011). As differential stress is affected by strain-rates, the stress affecting a system on a planetary scale, even in hot, vigorously deforming planetesimals, will be far lower than that in laboratory experiments. However, grain size, and therefore melt pocket volume, will also be several orders of magnitude larger, thereby reducing the effect of surface tension . The exact methods of extrapolation to planetary conditions are disputed among leading studies in this field (Groebner and Kohstedt, 2006; Walte et al., 2011), which highlights a clear need for further experiments to constrain melt behaviour, particularly at very low strain-rates.

Summary of open questions

For the last ~2 decades, the magma ocean model has been the accepted model of core formation (Wood et al., 2006), and many geochemical studies begin with the assumption that equilibration of metal and silicate liquids could allow us to infer directly from geochemical compositions the processes of core formation (Jones and Drake, 1986). However, these initial ideas relied heavily on experimental work in a hydrostatic high P-T system that showed metal melt to be immobile in a solid silicate matrix (Shannon and Agee, 1996). Deformation experiments have since shown this assumption to be potentially flawed (Bruhn et al., 2000), but experimental limitations have meant that their applicability to core forming conditions are still uncertain (Walte et al., 2011). There is a clear need for more experiments at small melt fractions to

constrain processes of deformation enhanced percolation over a larger range of strain-rates, strains and deformation mechanisms. 3D characterisation of run products is a vital part of this - permeability and interconnectivity of melts is inherently a 3D problem, which cannot be examined in detail using only 2D textural interpretation.

1.4 Basaltic melt in the upper mantle

Basaltic melt represents the initial partial melt phase of the solid mantle (Winter, 2001). Basaltic melt is found beneath young volcanic centres, mid-ocean spreading centres, and small melt fractions are also inferred by some to be present at depth within the upper mantle, invoked to explain specific seismic observations (Shankland, OConnell, et al., 1981). The importance of basaltic melt in studies of the Earth's interior means many studies have been conducted on the geochemistry, geophysics and physical properties of basaltic partial melts in a silicate system.

General questions investigated by this research include the following

- What causes the seismic and mechanical characteristics of the low-velocity zone (LVZ)? If partial melting is involved, to what extent and how exactly can it produce the seismic signatures observed?
- How is melt extracted rapidly and efficiently from the melt source, deep beneath mid-ocean ridges, to the Earth's surface, without significant re-equilibration with surrounding mantle?
- How is melt focussed from a broad >100km region of melting, to a narrow (<15km) zone of melt extraction at mid-ocean ridges on the Earth's surface?

This section of the literature review will attempt to summarise these three areas of interest, and highlight key gaps in knowledge.

1.4.1 Where do we find melt in the upper mantle?

The LVZ

The seismic low velocity zone (LVZ) was originally discovered by Gutenberg (Gutenberg, 1948, 1954) from observations of a distinct reduction in seismic wave amplitude at a depth of around 80-100km depth in the mantle. This zone, characterised by low seismic velocity, high seismic attenuation (loss of seismic amplitude) and

anomalously high conductivity (Shankland and Waff, 1977) indicates a mechanically weak layer (i.e. the presence of the asthenosphere). The distinction between weak and strong layers of the lithosphere and asthenosphere have since been shown to be key to the mechanism of plate tectonics. The ability of the asthenosphere to flow over geological time allows the transport of the overlying brittle plates. Understanding the reason for asthenospheric weakness is therefore essential to understanding fully the mechanism responsible for plate tectonics.

Although initially this 'weakness' was assumed to imply partial melting throughout the asthenosphere (Gutenberg, 1926; Shankland, OConnell, et al., 1981), later studies disputed this: Whether a small fraction of partial melt significantly influences seismic character and mechanical strength of the rock depends on its geometry – if it completely wets grain boundaries it has been shown to have a large effect on seismic characteristics and mechanical properties (Spetzler and Anderson, 1968), but if melt does not wet 2-grain boundaries, as suggested by some laboratory experiments (Kohlstedt, 1992), the effect of melt presence will be less significant (Karato, 2014). Studies of the melting regime and efficiency of melt extraction suggest that only very small melt fractions (<0.1%) are present away from mid-ocean spreading ridges (Plank and Langmuir, 1992) therefore it is uncertain whether these small quantitites of melt will affect geophysical properties of the mantle (Karato, 2014). In addition, it has been shown that the effect of changing temperature acting to reduce the strength of silicate material could create seismic effects such as a drop in seismic velocity and an increase in seismic attenuation below the silicate solidus (Jackson, 2007).

Evidence from seismology and geochemistry has been incorporated into a model to explain geochemical homogeneity of upper mantle (Karato, 2012), in which the geometry of small melt fractions plays an important role (Figure 1.17). More complex models of 3D melt geometry created by computer simulation have shown that seismic characteristics may be created by smaller melt fractions than originally predicted by 2D models (Wimert and Hier-Majumder, 2012). Further characterisation of 3D melt geometry, particularly at low melt fractions, is key to constraining this problem further.

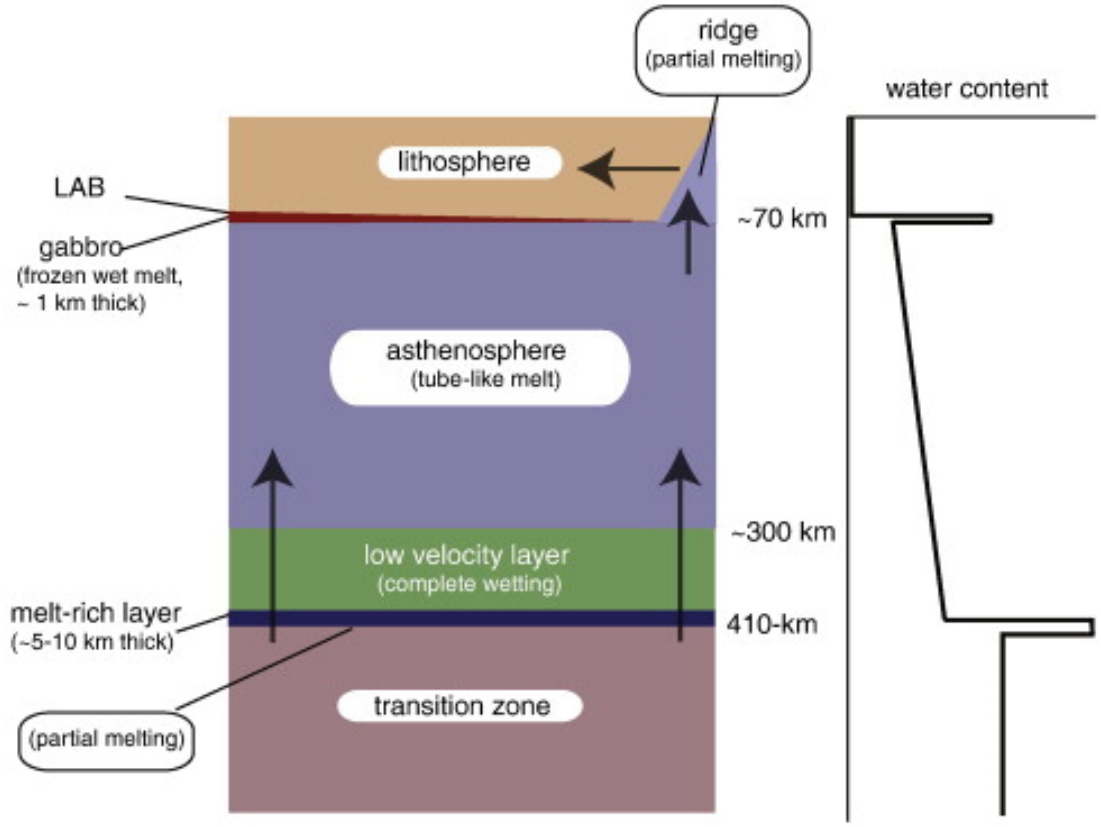

Figure 1.17: A model of asthenosphere partial melting and melt migration from Karato (2012) incorporating factors of water content and melt geometry. The best evidence for the presence of melt is found at a depth of 410km defined as a low velocity region known as the Ultra Low Velocity Zone (ULVZ). At pressures equivalent to this depth, melt has been shown to fully wet grain boundaries even at very small melt fractions (Yoshino, Nishihara, et al., 2007), and seismic character can be fully explained by a very small melt fraction (~0.1-1%). Karato (2012) suggests the majority of partial melting occurs at 410km depth, due to high mineral water content. Melt above this depth is buoyant and migrates up to the upper mantle asthenosphere, where melt is present in tubes with no wetted grain boundaries (Kohlstedt, 1992). At the very top of the asthenosphere, extensive melting, again in the presence of water, produces a region of gabbro (essentially frozen melt), which produces the sharp seismic boundary of the LVZ (Hirth and Kohlstedt, 1996).

Another seismic observation requiring explanation is the significant radial anisotropy observed in at least the top 220km of the mantle, decreasing rapidly with depth (Dziewonski and Anderson, 1981).

Anisotropy appears to be linked with age of the ocean floor (more pronounced and extends deeper in young ocean crust), which suggests there may be a link to ocean ridge processes (Beghein and Trampert, 2004). The fast direction is generally parallel to overall movement of material (Montagner and Tanimoto, 1991), as shown in figure 1.18.

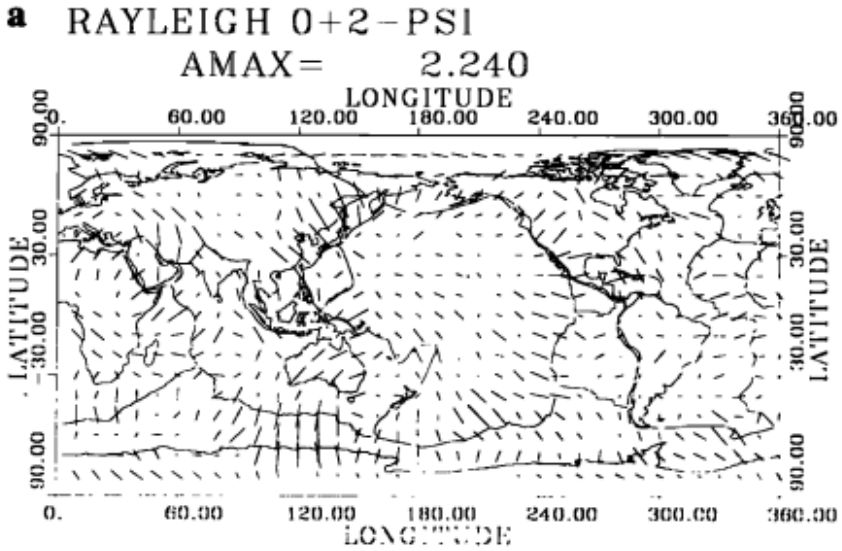

Figure 1.18: From Montagner and Tanimoto (1991) - map of anisotropy from tomography at 100s depth. Lines are normalised to maximum anisotropy (A_{max} =2.240). This shows how the direction of anisotropy tends to be parallel to the movement of material in the asthenosphere (similar to motion of tectonic plates). An exception to this is the presence of anisotropy normal to plate motion at certain subduction zones (Karato, 2012 and references within)

Anisotropy of the upper mantle has been explained by the presence of a lattice preferred orientation of olivine crystals in response to deformation from mantle flow, but the exact seismic characteristics (change in sign of P-wave anisotropy at 220km depth with negligible shear wave anisotropy) are incompatible with this simple model (Beghein and Trampert, 2004). A change of deformation mechanism at depth (Savage, 1999), or the addition of significant quantities of water to change olivine fabric (Jung and Karato, 2001), could explain the observed anisotropy. Partial melting could, however, also be responsible for the marked anisotropy. The alignment of melt itself may affect mantle seismic velocity (Hammond and Humphreys, 2000; Karato, 1998), although the effect is thought to be small in comparison to CPO of crystalline material (Savage, 1999). However, the presence of melt has a marked influence on olivine fabric (Holtzman, Kohlstedt, et al., 2003) and the influence of small melt fractions could help to explain upper mantle anisotropy. Investigating changes of melt geometry, and the influence of these changes on olivine CPO are therefore important factors to understand mantle anisotropy.

Mid-ocean ridges: melt extraction

Undisputed is the presence of partially molten mantle beneath mid-ocean spreading ridges. The production of magma under spreading ridges is the dominant source of magma production on Earth (Cheadle et al., 2004). However, the initial process of partial melting of the upper mantle, its separation from the host rock and subsequent migration to the surface is poorly understood, constrained by seemingly conflicting geophysical, geochemical and experimental observations (Faul, 2001). Increasingly complex theories of melt transport have been put forward in an attempt to reconcile these observations, but as yet no agreement has been reached (Kelemen, Hirth, et al., 1997 and references witin).

Geophysical data of the subsurface indicates mid-ocean ridges are underlain by extensive regions of melt, potentially hundreds of km wide, caused by decompression melting of rising mantle material. The presence of volatiles may also act to lower the solidus, allowing partial melting to occur deeper than it would for a ‘dry’ mantle (Faul, 2001; Hirth and Kohlstedt, 1996). This broad melting zone narrows in every case to a very narrow region of surface eruptions where new oceanic crust is created (Forsyth et al., 1998). Further constraints on the processes of melt extraction and focussing come from geochemical observations of mid ocean ridge basalts (MORB) and ophiolite assemblages (Kelemen, Shimizu, et al., 1995), as well as experiments to

examine physical characteristics of partial melts (e.g.Yoshino, Nishihara, et al., 2007).

Geophysical observations of e.g. seismic velocity, anisotropy and electrical conductivity give an indication of the structure of the subsurface beneath a spreading ridge, and the location and extent of melting. Several large-scale surveys have been carried out on fast-, slow- and ultra-slow-spreading ridges (Gregg et al., 2012 and references within). An example of data from the fast-spreading East Pacific Rise is shown in Figure 4 (Forsyth et al., 1998). Similar characteristics of subsurface structure are seen beneath other spreading ridges surveyed, although the scale of subsurface structures varies depending on mantle temperature and speed of spreading (Gregg et al., 2012). The roughly triangular shape of low seismic velocity and high attenuation found below the spreading ridge suggests the presence of significant partial melting. This supports theoretical models that melting is caused by decompression from mantle upwelling (Figure 4 A). Seismic velocities suggest melt fractions of 1-2% in the region of primary melting, which indicates efficient extraction and melt interconnectivity at low melt fractions (Zhu et al., 2011). Additional evidence of incipient melting, of very small melt fractions, at up to 150km depth also suggests the presence of volatiles is required at depth to lower the basaltic melting point (Langmuir and Forsyth, 2007).

Marked seismic anisotropy observed under spreading ridges (Forsyth et al., 1998) can be explained by alignment of melt pockets or alignment of crystal lattices, or a combination of the two. Data from the East Pacific Rise suggests the anisotropy in the region is mainly due to crystal lattice alignment, as the location of lowest seismic velocity does not correspond with the region of highest anisotropy, which would be expected if it was caused by melt pocket alignment (Faul, 2001).

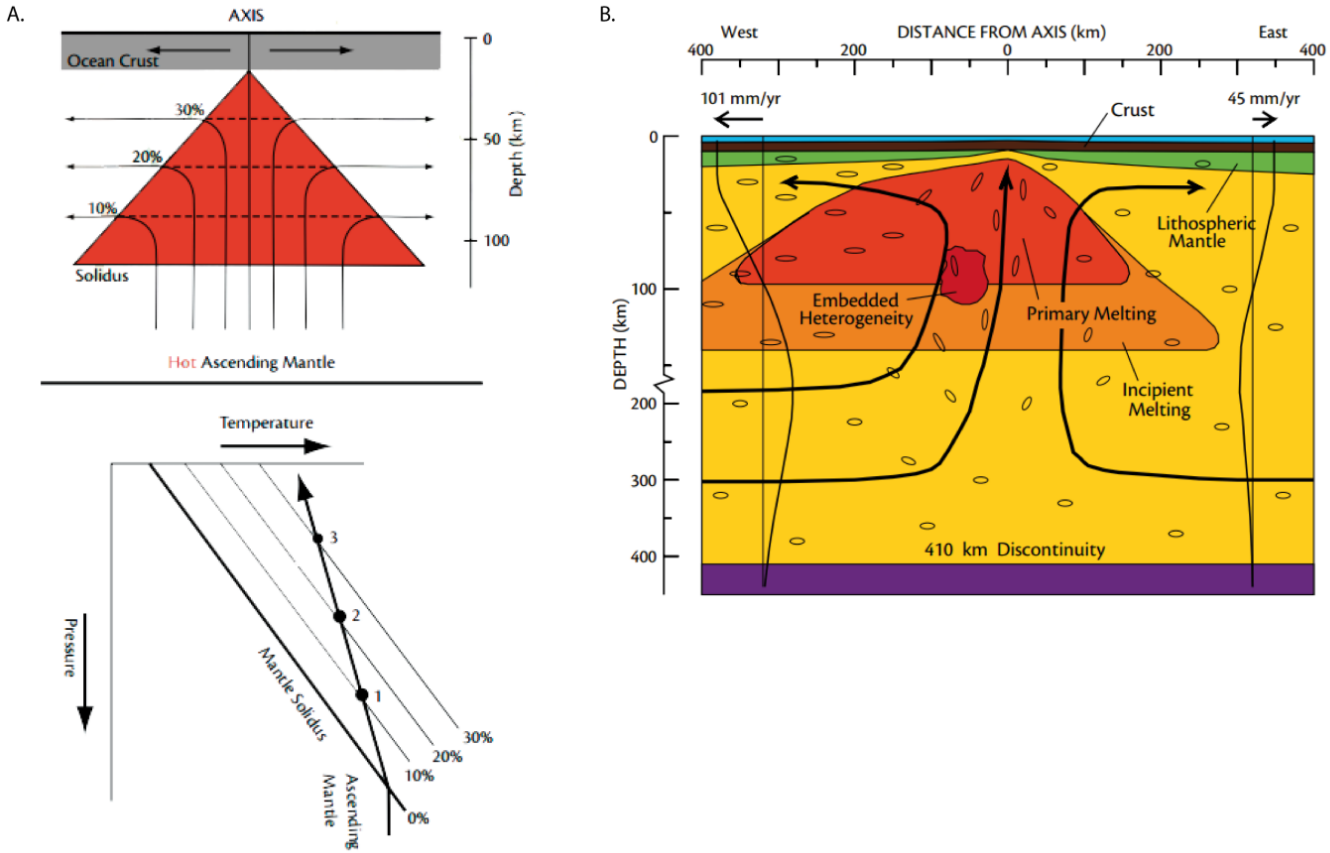

Figure 1.19: Figures from Langmuir and Forsyth (2007) showing the characteristics of partial melting below ocean spreading ridges. A. Theoretical model of mantle melting beneath a spreading ridge caused by upwelling of material melting by decompression as the geotherm crosses the mantle solidus. B. Schematic cross-section of the subsurface beneath the East Pacific Rise as observed by the MELT experiment (Forsyth et al., 1998). The asymmetric orange and red regions are suggested to be the main zones of melt production. Oval shapes indicate observed anisotropy caused by Lattice Preferred Orientation of solid and/or alignment of melt pockets (more flattened oval = more anisotropic). Similarities between theoretical models and observations are evident. The asymmetry of the East Pacific Rise may be caused by deep flow in the mantle coming mainly from the West, potentially fuelled by hotspots under e.g. Tahiti (Phipps Morgan et al., 1995)

The geochemical signatures of MORB magmas are strongly controlled by melt flow rates and partial melt fractions and can, therefore, be used to constrain mantle processes (Peate and Hawkesworth, 2005). Significant inferences can, for example, be made from ^{230}U-^{238}Th isotope systematics. Uranium and Thorium have similarly low bulk distribution coefficients, meaning they both partition preferentially into the first partial melt. However, there is a distinct excess of ^{230}Th with respect to ^{238}U, its parent nuclide. These signatures require very low fractions (<1 %) of partial melt. From petrology of Mid Ocean Ridge Basalts (MORB) and comparison to inferred host rock, however, it is thought that these liquids are formed from a 20% partial melt of peridotite (Langmuir, Klein, et al., 1993). MORB is shown not to be in equilibrium with shallow peridotite, and instead shows signatures of melting at a range of high pressures (Kelemen, Hirth, et al., 1997 and references within). This suggests melting initiates at depth and rapid transport moves melted material to the surface, without re-equilibration with shallower mantle.

The most popular current model for melt extraction is a "two-porosity" model (Lundstrom, 2003; Spiegelman and Elliott, 1993) which suggests transport occurs by a combination of permeable flow at grain scale feeding larger scale channels which allow rapid transport to the surface (Connolly and Podladchikov, 2007). These channels must be chemically isolated from the mantle peridotite, which can be explained if melt is transported through high-permeability dunite channels with >90% olivine (Kelemen, Shimizu, et al., 1995). These dunite channels are thought to be initially created by melt reacting with peridotite, dissolving peridotite and precipitating olivine – therefore melt is able to create its own high permeability olivine-rich pathways.

If melt is able to retain signatures of <1 % partial melting, this suggests very efficient melt migration taking place at the grain scale. The exact geometry and connectivity of basaltic melt at these very low melt fractions is still disputed - constraining this will help to confirm the processes suggested in these theories (see below).

Mid-ocean ridges: melt focusing

Several mechanisms have been proposed to focus flow from the broad >100km melting region to the central spreading ridge axis (<15km wide). Several review papers examine and evaluate theories of melt focussing and migration in detail (Gregg et al., 2012; Hebert and Montesi, 2010; Kelemen, Hirth, et al., 1997). There follows a brief summary of proposed theories:

1. **Focused upwelling of mantle material** Buoyancy of peridotite is increased as partial melting from decompression reduces density and chemically depletes the host rock. A mechanism of focussed mantle upwelling (essentially diapirism) could act to focus melt by movement of melt within the solid matrix (i.e. little grain-scale melt migration). This is disputed because of the low mantle viscosities required (Hirth and Kohlstedt, 1996), which are less than those estimated below mid-ocean ridges (Gregg et al., 2012).

2. **Flow along permeability channels** The most generally accepted model is that of flow along permeability barriers created by crystallisation (Katz et al., 2006; Kohlstedt and Holtzman, 2009). Partial melt rises through the asthenosphere and freezes against the relatively cool base of the lithosphere (similar to model of Karato (2012), Figure 1.17). Below this melt may flow along a high porosity pathway along the sloping thermal gradient towards the spreading ridge, potentially in an isolated dunite channel to account for MORB geochemistry (Kelemen, Shimizu, et al., 1995). The permeability barrier is thought to relate to the plagioclase crystallisation point, and this mechanism can explain to some extent the relation between ridge spreading rates, crustal thickness and extent of volcanism, although this mechanism alone cannot fully explain features of ultraslow spreading ridges (Hebert and Montesi, 2010).

3. **Deformation creating high permeability pathways** Spiegelman and McKenzie (1987) initially suggested melt pressure gradients caused by mantle flow may be enough to focus melt to a narrow zone, but further modelling showed that melt migration due to pressure gradients requires too high a viscosity compared to estimated viscosity of the mantle Morgan (1987). The effect of deformation to create anisotropic permeability by alignment of melt is a more likely mechanism. Deformation of basaltic melt in solid matrix is known to create melt-rich bands aligned at an angle to maximum stress, enhancing permeability parallel to these bands. Changing direction of mantle flow could act to focus melt migration towards the spreading ridge, as shown in figure 1.20 (Hirth and Kohlstedt, 1996; Kelemen and Dick, 1995; Spiegelman and McKenzie, 1987). This mechanism must be combined with focused flow e.g. through dunites or channel flow in fractures as grain-scale flow cannot be the only mechanism to transport magma beneath ocean ridges (Kelemen, Hirth, et al., 1997). It is acknowledged that the effect of deformation on melt migration has not been investigated in enough

detail, particularly at high pressures (due to equipment limitations) appropriate to movement of mantle material at depth (Gregg et al., 2012).

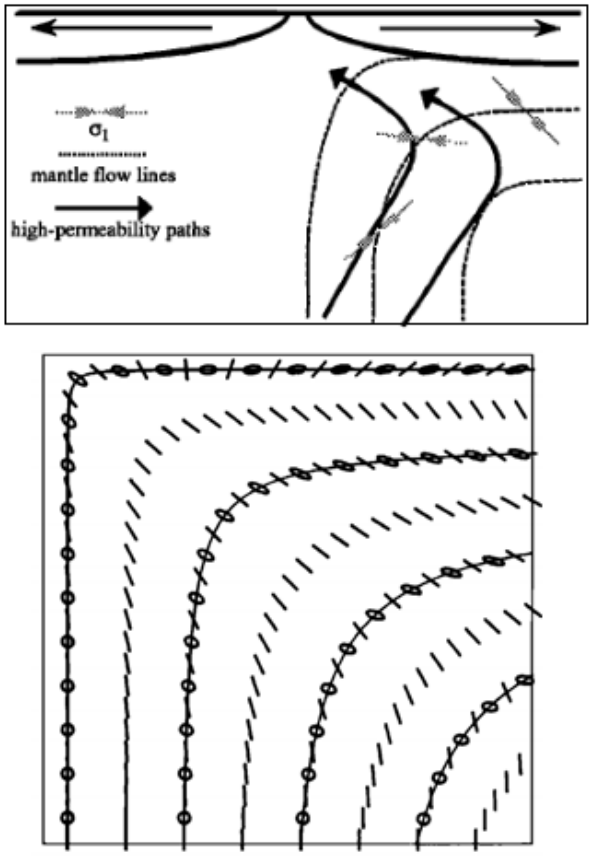

Figure 1.20: Diagram of melt focusing beneath a mid-ocean ridge from Daines and Kohlstedt (1997). The diagram shows the principal stress orientation, mantle flow lines and high permeability pathways that could develop from preferred orientation of melt. B. diagram from Morgan (1987) showing detailed analysis of mantle flow lines on one side of a theoretical spreading ridge (thick solid lines), resulting strain ellipses and predicted melt flow direction caused by a combination of buoyancy and permeability anisotropy (small line segments)

The key questions described above can be investigated further by constraining the geometry of MORB at a range of melt fractions, compositions, and P-T conditions is key to understanding the mechanical and seismic characteristics of the upper mantle and the processes of melt extraction at spreading ridges. In addition, the effect of deformation both on melt geometry and on silicate fabrics may be an important factor to consider. Laboratory experiments allow systematic testing of basaltic melt behaviour at varying conditions and compositions, with and without deformation. Numerous studies have been conducted on solid silicate – liquid MORB systems over the last decade to help to constrain these processes. Key observations are described below.

Experimental constraints on basaltic melt geometry

Geometry and interconnectivity of basaltic melt has been constrained to a certain extent from experimental work, although until very recently analysis has been limited to 2D interpretation of textures in order to infer 3D geometry (Faul et al., 1994). Experiments undertaken at pressures and temperatures applicable to upper mantle conditions (1-7GPa, 1473-1993K) suggest that basaltic melt forms will consistently create an interconnected network at very low melt fractions within tubules at grain triple junctions, with average dihedral angle values estimated at 25-50° for upper mantle conditions (Kohlstedt, 1993).

Examination of melt at very high resolution using transmission electron microscopy originally suggested dry basaltic melt does not wet 2-grain boundaries. Only at extreme compositions synthesised in laboratory experiments (e.g. very high Pb contents) could melts be shown to wet grain boundaries at upper mantle conditions (Riley and Kohlstedt, 1991). Yoshino, Nishihara, et al. (2007) observed a trend of reducing dihedral angle with increasing pressure, suggesting that melt will fully wet grain boundaries at depth in the mantle (13GPa), with a theoretically negligible pinch-off melt fraction. However, dihedral angle theory makes major assumptions regarding system equilibrium and crystal homogeneity giving only a first estimate of permeability and melt geometry.

In contrast, detailed studies of melt pocket geometry by Faul et al. (1994) suggested that at very low melt fractions (<1%), basaltic melt is present in flat disks of wetted 2-grain boundaries. These are the narrowest connection and therefore limit the total permeability of the network (Faul, 2001). As melt fraction increases to around 1% a threshold is reached and the disks become directly connected, leading to a sudden

increase in permeability. Therefore dry basaltic melts should remain trapped until around 1% porosity (Forsyth et al., 1998). These results appear to agree with S- and P-wave ratios from the East Pacific Rise (Yoshino, Nishihara, et al., 2007). Due to their differing properties travelling through solids and liquids, the ratios of S and P waves can give an indication of the shape of the melt network. Spheroids are believed to give a ratio of around 2.3, while a randomly orientated network of thin films gives a ratio of 3.9 (Forsyth et al., 1998). The observed ratio of 3.0 under the East Pacific Rise (Forsyth et al., 1998) suggests thin films are dominant.

The presence of a permeability threshold has been disputed (Wark et al., 2003; Yoshino, Laumonier, et al., 2010) due to the uncertain nature of interpreting 3D geometry from a 2D texture. Several studies indicate that a gradual increase in permeability with increasing melt porosity is more likely (Yoshino, Laumonier, et al., 2010), and can still explain geophysical and geochemical data. This has also been supported by more recent tomographic scans (Zhu et al., 2011) that indicate a texture of interconnected triple junctions persists to low melt fractions with no clear change in melt geometry. However, the lowest melt fraction imaged by this study is 0.02 and the tomographic imaging technique, with a resolution of 0.7μm, may not be able to image thin melt films at very small melt fractions (Garapic et al., 2013).

The most recent studies of melt geometry by serial sectioning (Garapic et al., 2013) suggest that basaltic melt does wet 2-grain boundaries even at <2vol% and 1 GPa, despite dihedral angle measurements of >0°. Wetted grain boundaries are thought to be part of the transient nature of grain growth and re-organisation of grain boundaries which takes place even in samples that have been hydrostatically annealed for >400h. Their presence is likely to affect permeability and mechanical characteristics of the partially molten rock. Continued conflicting results suggest that dihedral angle measurements may not be the best method to predict 3D melt geometry even in samples at textural equilibrium (Garapic et al., 2013).

The influence of deformation on basaltic melt geometry

As previously described in section 1.2.1, deformation will act on melt geometry on a grain-scale, aligning melt pockets on a localised scale to produce melt-rich banding, and on a larger macro scale inducing melt migration across pressure gradients (Kohlstedt and Holtzman, 2009).

Basaltic melt sitting at a triple junction will preferentially wet grain boundaries aligned at a certain angle (~30°) to the shear plane, thought to be due to the presence of

local tensile stresses leading to melt migration into the 2-grain boundary to relieve the differential stress (Daines and Kohlstedt, 1997; Hier-Majumder et al., 2004). Localised migration of melt into anastomosing melt-rich bands is observed in a number of studies (Holtzman, Groebner, et al., 2003; Holtzman and Kohlstedt, 2007; King et al., 2010). The formation of melt bands is only seen on a sample scale in melts where compaction length is less than sample scale and is therefore not usually observed in a system of highly permeable basaltic melt. This is because melt migrates too quickly to set up internal pressure gradients (Kohlstedt and Holtzman, 2009). An additional phase (e.g. chromite) is sometimes added in experiments to reduce permeability and thereby reduce compaction length (King et al., 2010). Melt bands in these reduced permeability samples are generally developed at ~20°, antithetic to shear. It is possible that melt-rich bands of basaltic melt would form on a larger scale within the Earth - this is discussed further in section 1.4.1. On a larger scale, highly mobile basaltic melt has been shown to be influenced by pressure gradients leading to melt migration on a sample scale (Kohlstedt and Holtzman, 2009; Renner, Viskupic, et al., 2003, and references within). Pressure gradients could be a cause for melt segregation and migration on large scales within the upper mantle (Takei and Holtzman, 2009).

Deformation of large melt fractions

Deformation of large melt fractions is relevant to the study of melt in magma chambers, during crystallisation of large scale magma oceans, within volcanically active moons, particularly Io, and at the core-mantle boundary of the Earth (Scott and Kohlstedt, 2006). At high melt fractions, melt will be interconnected, therefore the majority of studies have focussed on the effect of high melt % on rheology, and the majority focus on silicic melt within magma chambers. At melt fractions of >~40%, melt is thought to separate the majority of grains, allowing the partially molten solid to behave in a near Newtonian fashion, with the viscosity resembling that of the fluid phase. The suspended crystals will theoretically respond to deformation simply by aligning themselves to flow, although complications caused by shear flow of melt around crystals, variation of crystal shape, and potential contact between crystals may lead to behaviour such as stacking or tiling of the crystal population (Arbaret et al., 2007). At melt fractions of 30-40% the system will begin to exhibit non-Newtonian behaviour (Bagdassarov and Pinkerton, 2004), and micro-structure is likely to develop, e.g. strain localisation into narrow shear zones by localised alignment of elongate minerals, leading to the development of S-C patterns.

Reduction of melt fraction below this point can lead to a sudden reduction in viscosity by several orders of magnitude at the transition to the Rheologically Critical Melt Fraction (RCMF) (Arzi, 1978). At this point the characteristics of the grains, e.g. shape, play a more important role and a solid framework of crystals means that fracturing can develop during high strain-rate deformation (Arbaret et al., 2007). The RCMF of partially molten peridotite is predicted from theory to be around 19% (Riley and Kohlstedt, 1991), but this is calculated assuming isotropic wetting of grains boundaries, and experiments find the large drop in viscosity occurs at around 25-30vol% melt (Scott and Kohlstedt, 2006). The orientation of non-wetted grain boundaries is shown to be affected by shear direction, but on the scale of laboratory samples melt distribution remains homogeneous (Scott and Kohlstedt, 2006).

Extrapolation from experiments to the Earth

Experiments clearly show that deformation significantly changes textures of partial melt within a laboratory setting. These effects may combine to lead to focussing and melt extraction observed beneath mid-ocean ridges. However, it is important to evaluate the effects of scaling laboratory deformation experiments up to conditions observed in the Earth. As is the case with the olivine metallic melt system discussed in section 1.3.1, the main changes that occur with scaling up are a dramatic decrease in strain-rates (convection in the Earth's upper mantle is estimated at a strain-rate of ~$10^{-14}s^{-1}$) and a significant increase in grain size (up to ~50μm in laboratory experiments, to mm-cm scale on Earth), enhancing the role of surface tension at experimental conditions. Unlike metallic melt, basaltic melt is highly mobile even at conditions where surface tension plays a greater role, and stress at laboratory conditions always dominates to affect melt geometry. Calculations examining the ratio between surface energy, grain size and differential stress consistently suggest that melt will be affected by differential stress even at lower strain-rates observed in the mantle (Kohlstedt and Holtzman, 2009 and references within).

Aligned melt-rich bands created in the laboratory therefore have the potential to be created in the mantle. As described above, experiments have been designed to reduce mantle permeability in order to create melt-rich bands on the scale of laboratory samples (<2mm total length). Calculations of compaction length may be used to infer the potential scale of such bands in the Earth's upper mantle. High permeability MORB melts, with much larger compaction lengths, are expected to create similar bands but with a much larger spacing, estimated at ~10-1500m within the upper mantle (King

et al., 2010).

3D visualisation of basaltic melts

As shown by the review above, gaining an understanding of 3D geometry of basaltic melt is key to constraining melt permeability and characteristics of partially molten solids. However, a limited number of studies have examined melt geometry directly in three dimensions. The majority of early experiments have relied on dihedral angle analysis and 2D textural observations to predict 3D melt characteristics (e.g. Faul et al., 1994; Hustoft and Kohlstedt, 2006).

Very fine serial sectioning work by was carried out by Garapic et al. (2013) on small melt fractions of basalt melt in olivine (Figure 1.21), producing images of 300x230μm and a resolution of 0.026 μm/ pixel in X- and Y- orientations (in the plane of section). Using a lengthy polishing process, 24 sections were imaged across 38μm total depth to create a resolution of ~1.6μm in the Z-orientation, although the exact thickness of each section was variable. This technique allows very fine features to be resolved, but does add complication with a difference in resolution in different dimensions requiring significant interpolation, and only allows visualisation of a small sample thickness in the Z direction. The majority of 3D visualisation so far has been carried out on undeformed samples, although deformation studies have recognised the need to examine melt in 3 dimensions due to the dynamic nature of deformation experimental samples. By carrying out a serial sectioning technique, Holtzman and Kohlstedt (2007) managed to estimate 3D permeability of melt in deformed networks, but due to its time-consuming nature the technique was only conducted on one experimental sample and then extrapolated to further experiments.

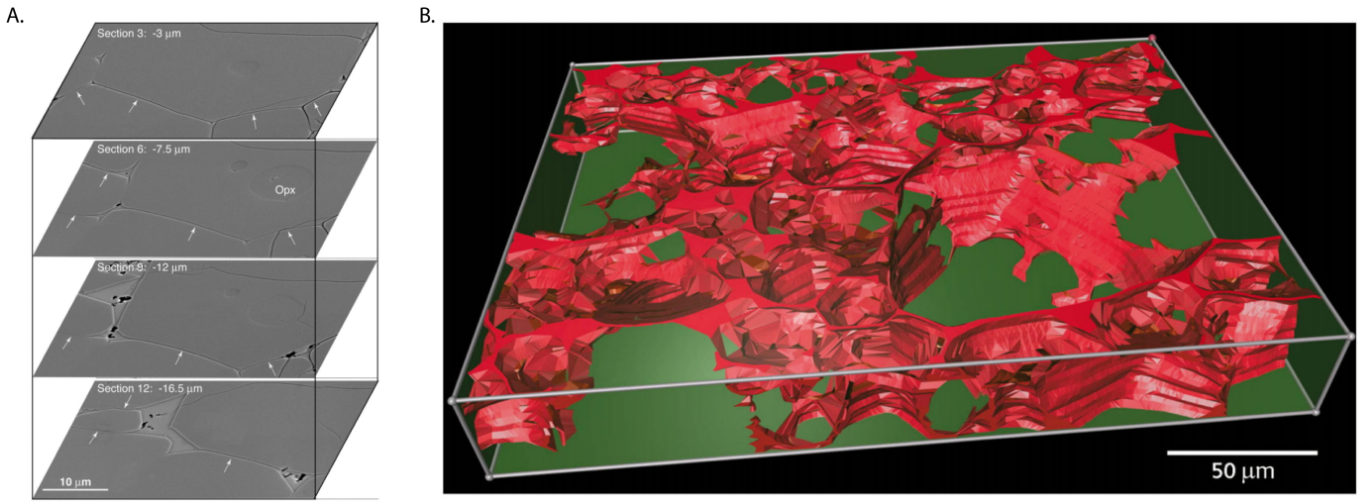

Figure 1.21: Example of 3D melt visualisation using a serial sectioning technique from Garapic et al. (2013). A. examples of four 2D sections through the sample showing high resolution SEM imaging in X and Y directions. These SEM sections are separated by 4.5µm but sections between these create a rough resolution of 1.6µm in the z direction for the 3D image. High resolution 2D sections allow fine melt sheets down to ~30nm to be visualised (white arrows). B. 3D reconstruction created by binarising 2D images and stacking images together (taking into account variable thickness of sections. The melt phase is shown in red. This technique only allows 3D visualisation across a small thickness of the sample, and the lower resolution in the Z direction is evident from the stepped nature of the reconstruction. However, the overall character of melt geometry is clearly represented, showing the presence of wetted 2-grain boundaries.

The use of computed tomography to examine olivine and basalt systems has been limited due to the low contrast between olivine and basalt compared to, for example, the Fe-melt solid olivine system (due to similarities in composition and density). This means that simple attenuation-based imaging of samples does not allow melt and olivine to be segmented effectively. This problem can be overcome by the use of phase contrast imaging. The technique uses edge effects between low-contrast phases to pick out phase boundaries, and is commonly used at synchrotron X-ray sources. Zhu et al. (2011) use this technique to characterise 3D basaltic melt network geometry and connectivity in textural equilibrium at varying melt fractions, although a voxel size of 0.7μm may still be too large to accurately resolve melt geometry at small melt fractions (Garapic et al., 2013).

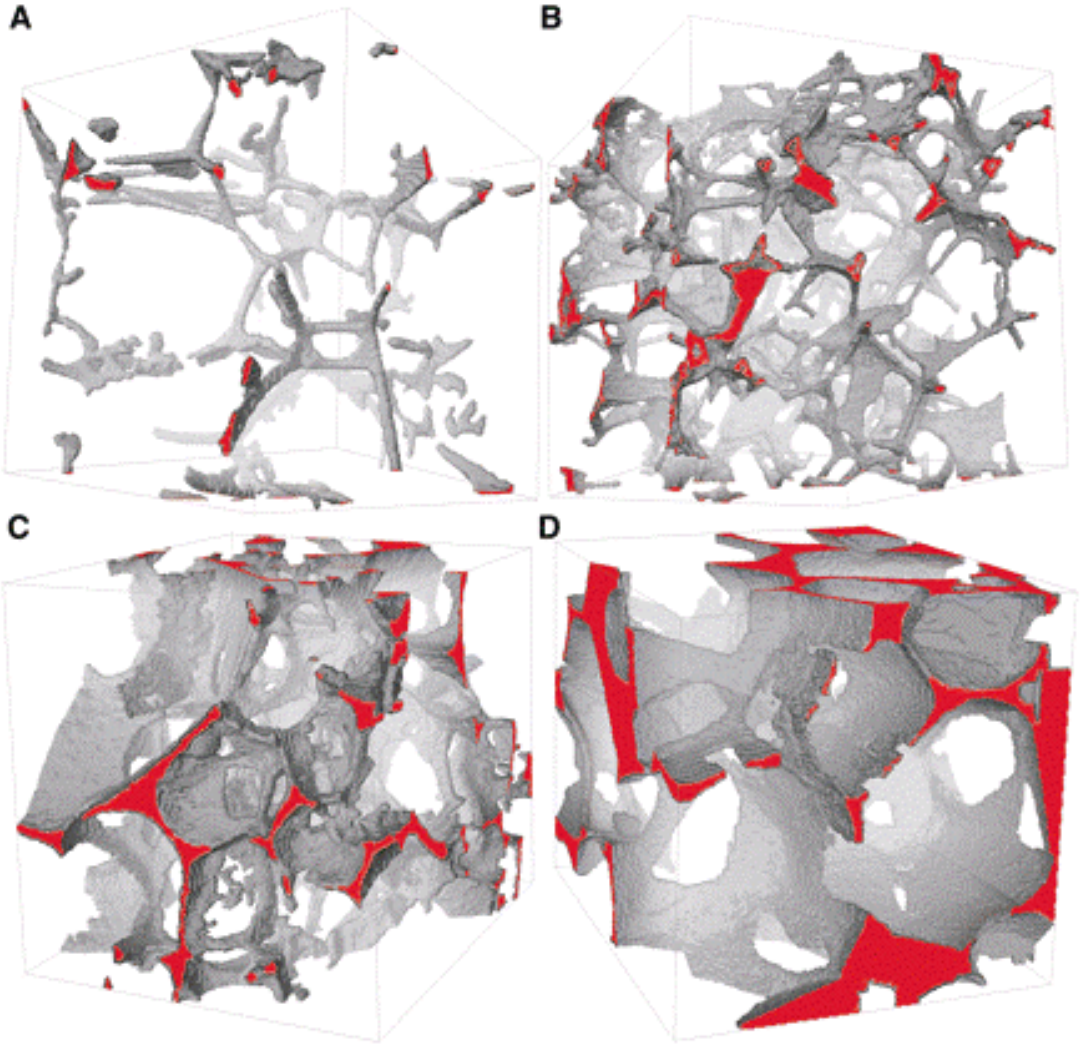

Figure 1.22: Tomographic scans of basaltic melt distribution in a solid olivine matrix from Zhu et al. (2011). Cube sides are each 140μm. Melt fractions: A) 0.02 B) 0.05 C) 0.10 D) 0.20. Red: interior of melt channels, grey: boundary between melt and olivine. Olivine crystals are not imaged. Resolution of image 0.7μm. Melt is connected along tubules at grain boundaries at all melt fractions. Only at high melt fractions are faces of olivines shown to be wetted significantly, creating interconnected sheets of melt. This observation is disputed by Garapic et al. (2013) due to the resolution limitation of the tomographic technique.

Phase contrast imaging is not always possible using small laboratory cone-beam tomographic equipment, as large distances are required between the X-ray source and sample, requiring a higher power X-ray source. In addition, it is not a technique that can be used for high P-T *in-situ* experiments as the gasket surrounding experimental samples is no longer transparent using phase contrast imaging and therefore interferes with reconstructions of the experimental sample.

Doping of basaltic liquids with heavy metals has been used to test connectivity of melts from 2D radiographs and in 3D tomographic scans. Early experiments examined diffusion of samarium 151 from a doped zone to a non-doped zone (Daines and Richter, 1988) using radiographs to track the more attenuating heavy element. Cs-doping of partially molten granite has been used in combination with tomographic element mapping (using an absorption edge technique) at Spring-8 synchrotron X-ray source, again to trace diffusion of Cs to test partial melt connectivity (Ikeda et al., 2004). In both cases, metals were chosen to be highly incompatible with the solid to ensure the metal highlights the melt phase. However, doping of basaltic liquid to improve contrast is a technique that has not been used previously for the purpose of tomographic imaging.

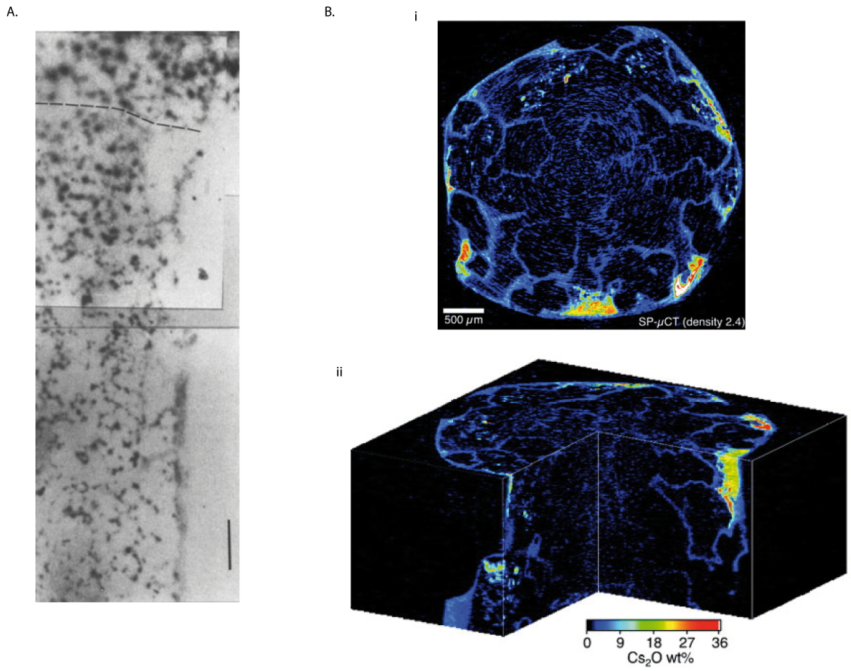

Figure 1.23: Previous studies using doping of partial melts to estimate connectivity of melt by tracing diffusion of doped element through melt networks. A. a radiograph from the study by Daines and Richter (1988) of samarium diffusing from non-doped portion of the sample (above the dashed black line) to the non-doped sample below. Samarium shows up as black specks, therefore showing significant diffusion has taken place and therefore that the melt is well connected throughout the sample. Scale bar bottom right is 250μm B. A more recent study involving Cs-doping of partial melts in granite (Ikeda et al., 2004). An absorption edge technique was used to map quantitatively the concentrations of Cs within the sample in three dimensions. i) shows an individual tomographic slice (spatial resolution ~20μm) ii) is a 3D orthogonal view produced from 300 stacked slices. Scale is the same in both images.

Summary of open questions

The above review shows the complexity of melt migration processes in the upper mantle and beneath spreading ridges in the deep Earth. A number of key debates surround the geometry and interconnectivity of basaltic melt at very small fractions of partial melt - does melt wet grain boundaries? If so, what effect does this have on melt migration velocities, seismic character of the upper mantle? What role does deformation play in altering melt geometry, and could it play a part in focussing melt at spreading ridges?

Concurrently, developments of methods to visualise basaltic melt in silicate systems using tomographic techniques are complicated by the low resolution contrast between phases - techniques such as phase contrast imaging can be used, although not for the majority of laboratory CT equipment. There is a need to develop new techniques for visualising basaltic melt in three dimensions. Doping of melts by heavy elements may be a simple way to allow basaltic melt to be visualised effectively in 3D using standard laboratory CT equipment. As yet, there has been no published study detailing 3D visualisation of basaltic melt experiments that have undergone deformation.

CHAPTER 2

Methods

2.1 Introduction

The following chapter details the methodological techniques used for experiments conducted over the course of this PhD project. As the specifics of techniques vary depending on the investigation of interest, the information given here is of a broad nature and applicable to multiple chapters - details of individual experiments are given in relevant chapters.

General aspects examined here will be as follows

1. Experimental equipment - its specifications and use
2. General techniques for creating starting mixtures for experiments, including choice of compositions.
3. Experimental conditions (pressure, temperature, timescales, deformation rates etc.)
4. Analytical techniques used to investigate run products including details of X-ray tomographic equipment available during this project.
5. Techniques and software used for characterisation of resultant melt geometry and interconnectivity in experimental samples.

2.2 Experimental methods

2.2.1 Experimental equipment

The piston cylinder

Hydrostatic experiments were all performed at the University of Edinburgh using an end-loaded piston-cylinder apparatus and high-temperature talc-pyrex-graphite assembly (Figure 2.1). The starting mix was loaded into 4mm o.d. graphite capsules which were inserted into alumina sleeves and then loaded into the sample assembly. Experiments were pressurised and then slowly heated (100°/min) to the final run temperature. Temperatures were measured using an R-type thermocouple adjacent to the capsule, and both temperature and pressure monitored throughout the experiment. Samples were quenched by switching off power to the heating circuit whilst maintaining run pressure (quench rates >100°/s).

Deformation equipment

Dynamic experiments were performed using two uniquely adapted Paris-Edinburgh Cells, designed to allow controlled, low strain-rate torsional deformation while at extreme temperature and pressure conditions. Each has been adapted to allow X-rays to penetrate the sample centre, to allow in-situ X-ray radiography, diffraction and tomography. The presses are relatively light-weight and can be assembled and dissembled with relative ease, facilitating transport and set-up in synchrotron hutches for *in-situ* work.

rotational Paris-Edinburgh Cell (roPEC)

rotational Paris-Edinburgh Cell experiments were performed at the Dept. Earth Sciences, University of Cambridge. This equipment is now housed at Maquarie University, Sydney, Australia. Figure 2.2 is a diagram of the roPEC equipment and gasket dimensions.

The sample is compressed between two opposing carbide anvils which have a toroidal anvil face to maximise sample dimensions, and high temperatures are attained by passing a current through the internal graphite furnace. Samples may be deformed by rotating the upper anvil with respect to the stationary lower anvil, which imparts a torque on the entire sample assembly.

Experimental capsules used were cylinders 1.5-2mm in length, 3mm in diameter (including outer capsule). Exact capsule design varied between experiments and are described in detail in further chapters. Capsules and alumina spacers were loaded into an outer gasket made of fired pyrophyllite or amorphous boron epoxy (later sample generation), with an internal graphite furnace. A Teflon ring was used to minimise gasket flow during compression (Bromiley et al., 2009).

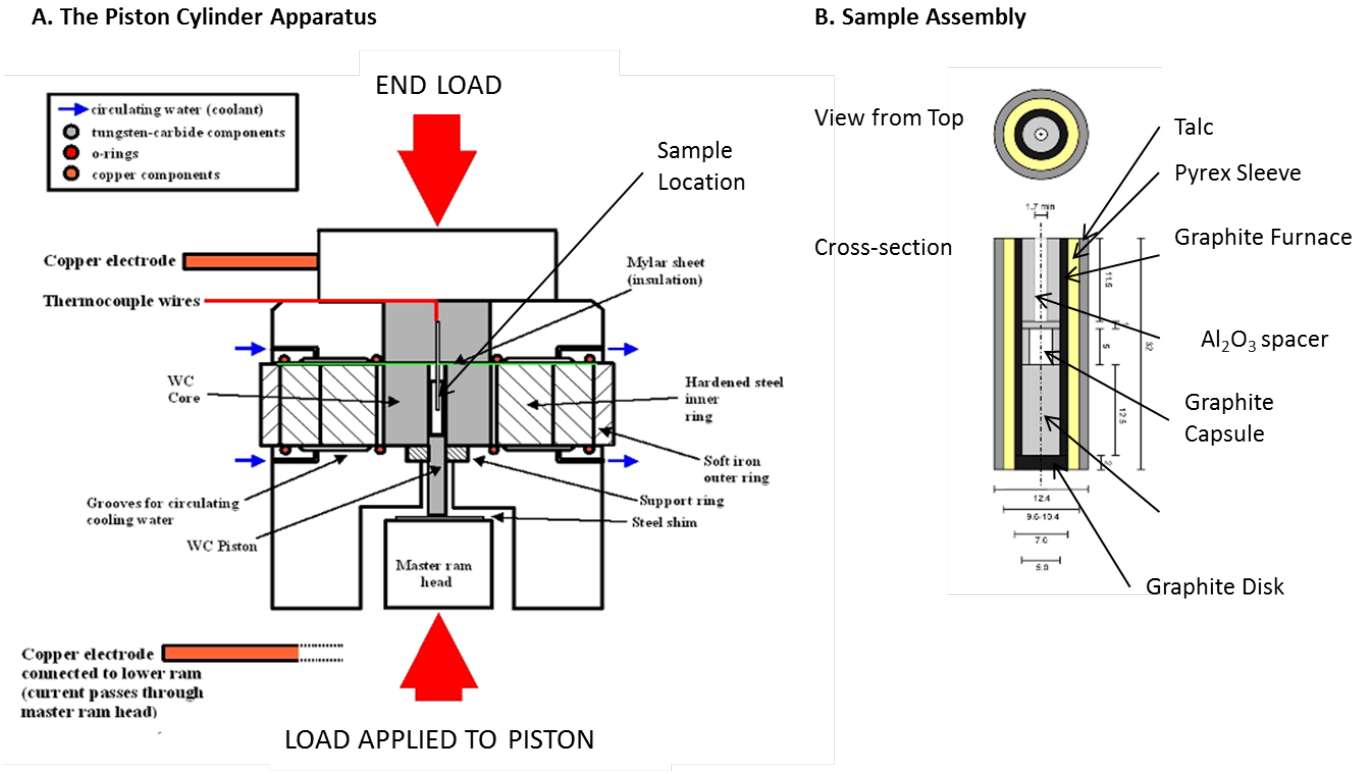

Figure 2.1: The piston cylinder apparatus and high temperature talc-pyrex-graphite assembly. The piston cylinder is a high P-T press designed to produce hydrostatic confining pressures for relatively large sample volumes (several mm^3). The sample is placed inside a soft pressure medium within the sample assembly (here talc and pyrex), inserted into a thick cylinder of metal, and a piston is advanced into the sample, pushing against the confining pressure frame (end load). The pressure medium surrounding the sample is relatively soft and deforms, theoretically applying an isotropic load to the sample. The sample is heated by passing current through the graphite furnace in the sample assembly (via the metallic press frame). A thermocouple is used to measure temperature directly at the sample location. Exact design of sample capsule has varied depending on the experiment carried out (more details in appropriate sections of thesis).

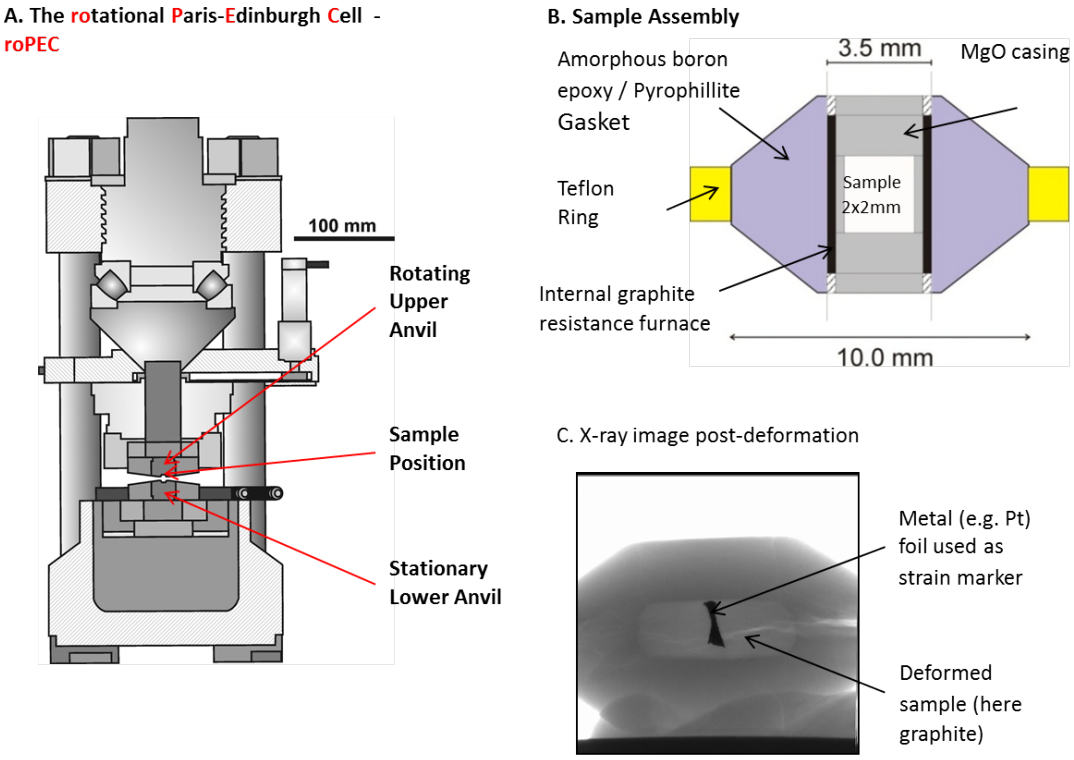

Figure 2.2: A. The rotational Paris-Edinburgh Cell apparatus with sample position shown. B. Sample Assembly as used in Fe-S + Olivine Experiments. C. An example X-ray shadowgram of a sample after deformation. A metal strain marker has been used here to show samples have undergone significant deformation.

rotational tomography Paris-Edinburgh Cell (rotoPEC)

An adaptation to the design of the roPEC, this device has been specifically designed to allow in-situ 3D tomographic imaging without the need of a separate rotational stage. The equipment is housed at Universite de Pierre et Marie Curie, Paris, France. Anvil shape and sample gasket design are the same as on the roPEC, but in this case both the top and bottom anvil are motorised and able to rotate independently of each other and of the press frame (Figure 2.3 A).

The rotoPEC is specifically designed to allow in-situ tomographic work to be carried out at a synchrotron by using the following design adaptations:

- Opposing anvils have been designed to leave the central sample and gasket open to allow X-rays to pass through the sample centre. The toroidal gasket shape ensures that confining pressure remains hydrostatic despite the edges being open to the air (Figure 2.3 B).
- The design is relatively compact and lightweight for a high-T-P press. The total weight of equipment is 200kg and can be taken apart into its component parts for ease of transport. This allows the equipment to be transported relatively easily and set up in synchrotron beamline hutches for in-situ experiments.
- The dual rotation of the upper and lower anvils allows full 360° rotation to take place internally, without the need for an additional rotating sample stage. This is very important as the rotation takes place without the solid metal frame coming between the sample and the X-ray beam. The two anvils can rotate independently, allowing rotation at different speeds or in opposing directions. This allows concurrent 360° rotation and torque deformation of the sample for in-situ deformation experiments.

The weight of the rotoPEC does limit the use of this equipment to engineering beamlines or high pressure beamlines which have large hutches and are able to incorporate bulky equipment, which means that the equipment cannot be used in all specialised X-ray microtomography beamlines.

Temperature and pressure calibration

Unlike the Piston Cylinder, neither roPEC nor rotoPEC equipment have a direct measure of temperature during off-line runs. Instead, pressure and temperature were calibrated during initial experiments at the European Synchrotron Radiation Facility

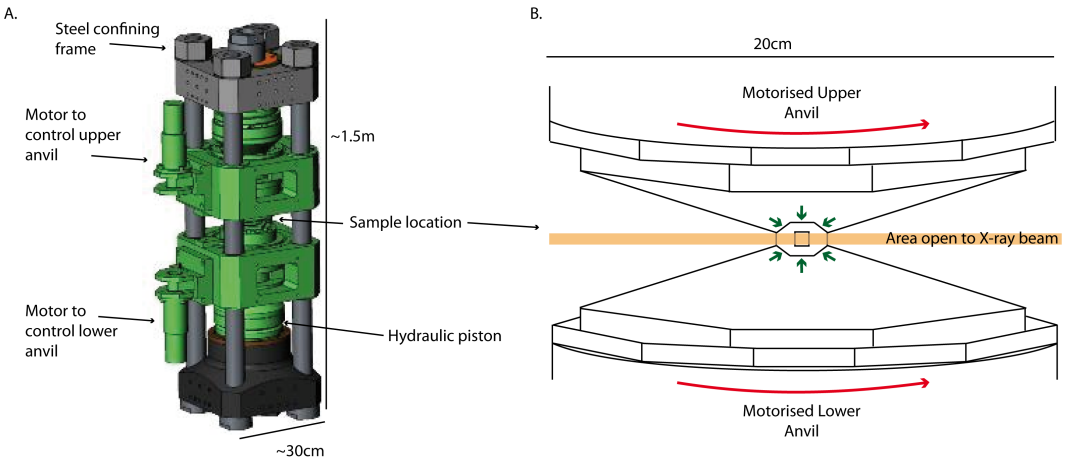

Figure 2.3: The rotoPEC equipment - a design adaptation of the original roPEC design to allow *in-situ* tomographic imaging by rotation of both upper and lower anvils within the confining frame (see text). A. The press itself, showing sample location, anvils and hydraulic press at base of press. B. A close-up of the anvils with the central gasket design (as in roPEC design), showing the volume of the gasket that is X-ray transparent, and the ability for the top and bottom motors to rotate separately, allowing deformation and in-situ tomography to take place simultaneously.

(ESRF) Grenoble, France, using *in-situ* X-ray diffraction of MgO outer capsules and internal platinum strain markers and calibrating with known patterns at varying temperatures and pressures (Bromiley et al., 2009). Experiments were also carried out using a thermocouple inserted into the capsule by drilling into the side of the gasket.

Figure 2.5 shows the temperature calibration curve used in initial off-line experiments while using the roPEC at University of Cambridge, and during synchrotron work at Diamond, Oxfordshire, where X-ray diffraction techniques were not initially available.

These calibrations have limitations, particularly as we were interested in reaching temperatures of 1400-1600°C, which are near the top of the curve where the linear relationship between power and temperature potentially begins to break down. The exact power required to reach a certain temperature depends on the exact gasket design and the thermal conductivity of the ceramic capsules and spacers used.

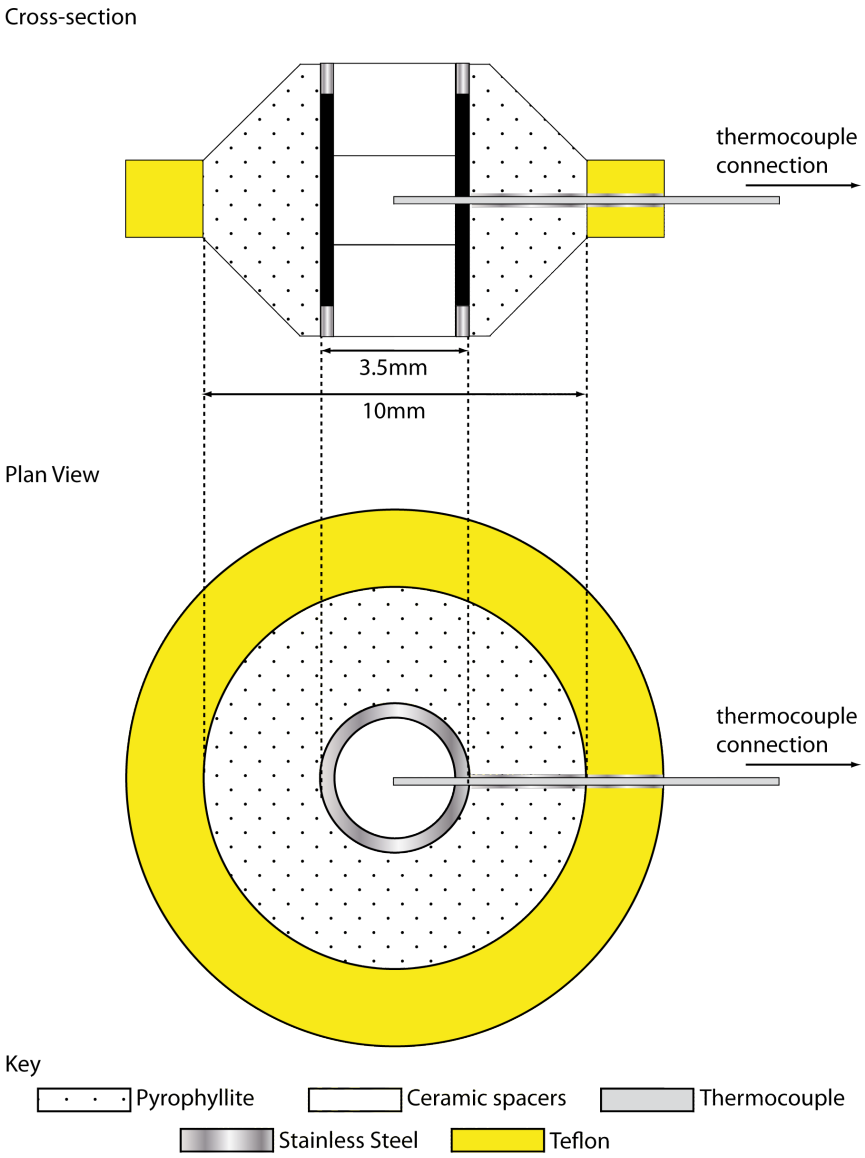

Figure 2.4: The gasket design used for thermocouple calibration experiments. A 0.8 mm hole must be drilled into the teflon ring, pyrophyllite gasket, and central furnace and capsule assembly (in this case no sample capsule is used, just a ceramic spacer). Pressure and power are applied to the gasket as it would be in normal experiments, and the temperature and power relationship is recorded. A calibration curve such as that shown in Figure 2.5 is produced. This technique cannot be used for every experiment, as drilling into the gasket side greatly increases the chances of an experimental blowout.

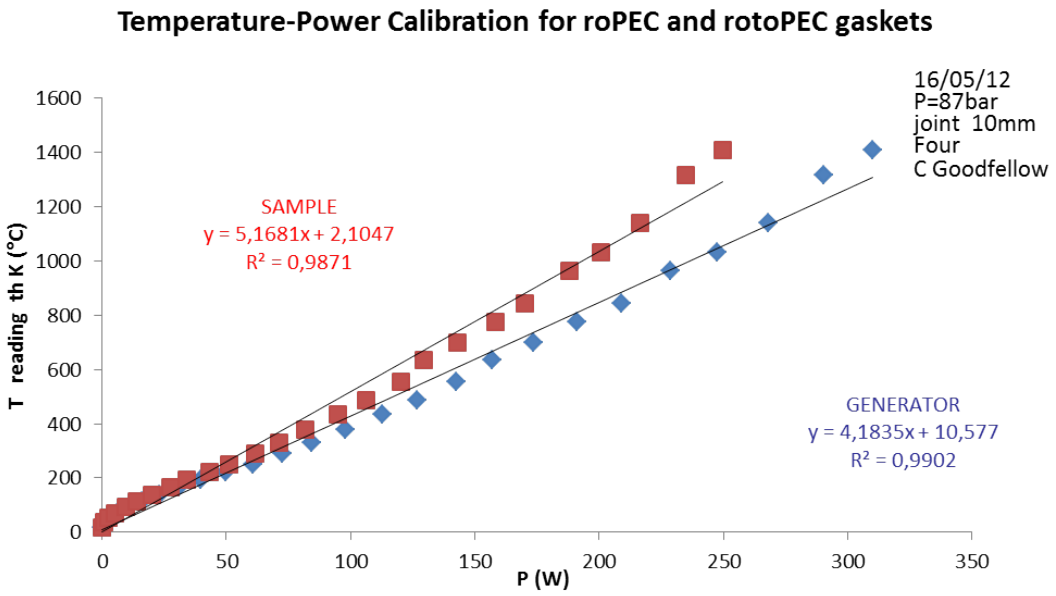

Figure 2.5: Calibration between power input and temperature reached at sample. The two curves show the power readings at the generator (blue), and reading across the anvils on the sample equipment (red). Note the way the roughly linear relationship between power and temperature begins to break down at higher temperatures (see text).

2.2.2 Starting materials and conditions

Choice of starting materials

Starting materials were chosen to

1. represent effectively the geological system studied
2. create a simple system to reduce the number of physical processes that need to be resolved to explain the textures
3. make the work easily comparable to previous studies

In some ways the first two points are mutually incompatible, given the enormous complexity of geological systems and interacting processes. However, the aim of this, and previous studies, is to examine one specific process in any given experiment, and this can only be done by greatly simplifying the system studied. Care must be taken when extrapolating these experimental results to the 'real world' and drawing larger conclusions (see further discussion in chapter 3, section 3.4.2).

The olivine used in these experiments are natural samples from two sources, both representing a typical mantle olivine composition. The first is a natural sample from Aheim, Norway (Fo_{95}), while further olivine for basaltic melt experiments was sourced from the type-locality of San-Carlos, Arizona ($Mg_{0.95}Fe_{0.05}SiO_4$). Single, inclusion free crystals were crushed and ground by hand using an agate pestle and mortar (see below)

For core formation systems, iron sulphide (FeS) was used as a proxy for core forming melts. Sulphur is a highly siderophile element and it is considered one of the potential 'light elements' that produces the density deficit in the Earth's outer core (see lit review discussion, (Ringwood, 1977). Previous studies have also used a combination of iron and sulphur (+-Nickel and Oxygen) for metal-silicate segregation experiments (Bruhn et al., 2000; Terasaki et al., 2005), making this composition easily comparable. Our early work was carried out using a composition of Fe_3S which is particularly interesting due to iron-FeS having variable melting temperatures (Figure 2.6, Berg, 2010).

Initial compositions for upper mantle melting experiments have been chosen to allow direct comparison to similar work (Zhu et al., 2011). Materials used were a synthetic combination of natural San Carlos olivine (see above) and natural basalt: a dredged sample of mid-Atlantic ridge N-MORB (major oxide compositions by weight:

50.76% SiO_2, 14.32% Al_2O_3, 10.74% FeO, 9.11% MgO, 11.77% CaO, 1.84% Na_2O, 1.108% TiO_2), which was kindly provided by Prof. Godfrey Fitton, University of Edinburgh.

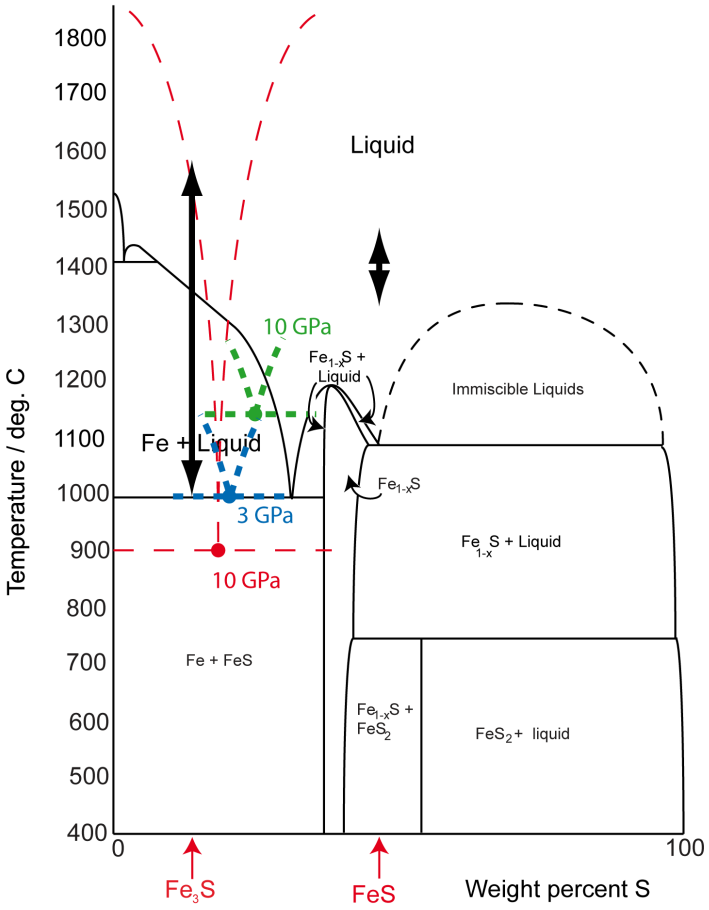

Figure 2.6: Fe-S phase diagram at ambient pressure, adapted from Rietmeijer et al. (2008). The phase diagram at higher pressures is disputed. The location of the eutectic as inferred by Usselman (1975) at 3GPa (blue) and 10GPa (red) and by Fei, Bertka, et al. (1997) at 10GPa (green), are included. At 2GPa, the liquidus temperature for Fe_3S is likely to be higher than at ambient temperature. Experiments carried out over the course of this project, at FeS compositions, are still likely to be in the pure liquid field even at 2GPa.

Synthetic Olivine Synthesis

For *in-situ* analysis of melt migration, we wanted to create a liquid volume gradient in order to encourage melt migration with a traceable melt front, through an olivine matrix. To do this we designed a capsule made from olivine, which could have a

central melt rich area. This involved pressing olivine powder and sintering the capsules in order to drill their centres. We decided to synthesise pure forsterite (Mg_2SiO_4) in order to simplify the sintering process (the addition of Fe requires a controlled oxygen fugacity at high temperature in order to avoid oxidation). Pure forsterite was created from a mixture of 43wt% SiO_2 and 57wt% MgO to make up the 2:1 molar ratio required. The mixture was ground in a pestle and mortar for >3 hours to homogenise, then pressed into 2x2mm cylindrical pellets using a pin-press and hydraulic ram. A small drop of PVA solution was mixed with the powder in order to improve cohesion. Capsules were sintered in air for >8 hours using a tube furnace. Resulting mineral content was analysed by *in-house* XRF. We found that capsules had to be re-ground, pressed and sintered for another 8 hours to produce a purity of >99% Fo. Impurities consisted of remnants of raw materials, MgO and SiO_2, and 0.1% enstatite, a common reaction product of these materials.

Ensuring Homogeneity of Starting Materials

Ensuring a well-mixed and even grain size in starting powders has been shown through early work to be a very important factor to ensure textures can be reliably interpreted. Preliminary experiments conducted as part of an earlier degree thesis investigating the core formation system (Berg, 2010) were conducted using coarser grained, poorly sorted starting mixtures. Large grains of FeS in the starting mixture led to the presence of large melt pockets in both static and deformed samples, which meant measuring melt redistribution in a sample due to interconnectivity was much harder to interpret. In addition, the large melt pockets led to hydrofracturing of crystals situated close to larger melt pockets. Later starting mixtures were created to be more homogeneous in size, reducing the complexity of the ongoing processes in the sample. This was carried out by simply grinding for a longer time range.

Basaltic starting mixtures were ground using a mechanical milling process to ensure a very small and even grain size. Final average grain size was <2μm (Figure 2.7). The same process was not carried out for the olivine grains, as resolution limitation in 3D scans means very fine grain size leads to unresolvable features within tomographic reconstructions.

For basaltic melt + olivine crystal experiments, olivine crystals were filtered to ensure a starting mixture of more even grain size, using a wet filtering technique. The sample was ground in ethanol and flushed through clean woven nylon mesh fabric strips of 65μm and 35μm spacing respectively. This process was repeated several times during grinding. The filtered grains were examined using a petrographic microscope to ensure a homogeneous grain size (Figure 2.7C).

2.2.3 Experimental conditions

Temperature and pressure conditions

For each experiment, pressure and temperature conditions were chosen to

1. be relevant to the Earth systems of interest

2. be comparable to the conditions chosen for previous studies

3. allow the melt phase to be fully molten, while the polycrystalline phase does not reach its solidus

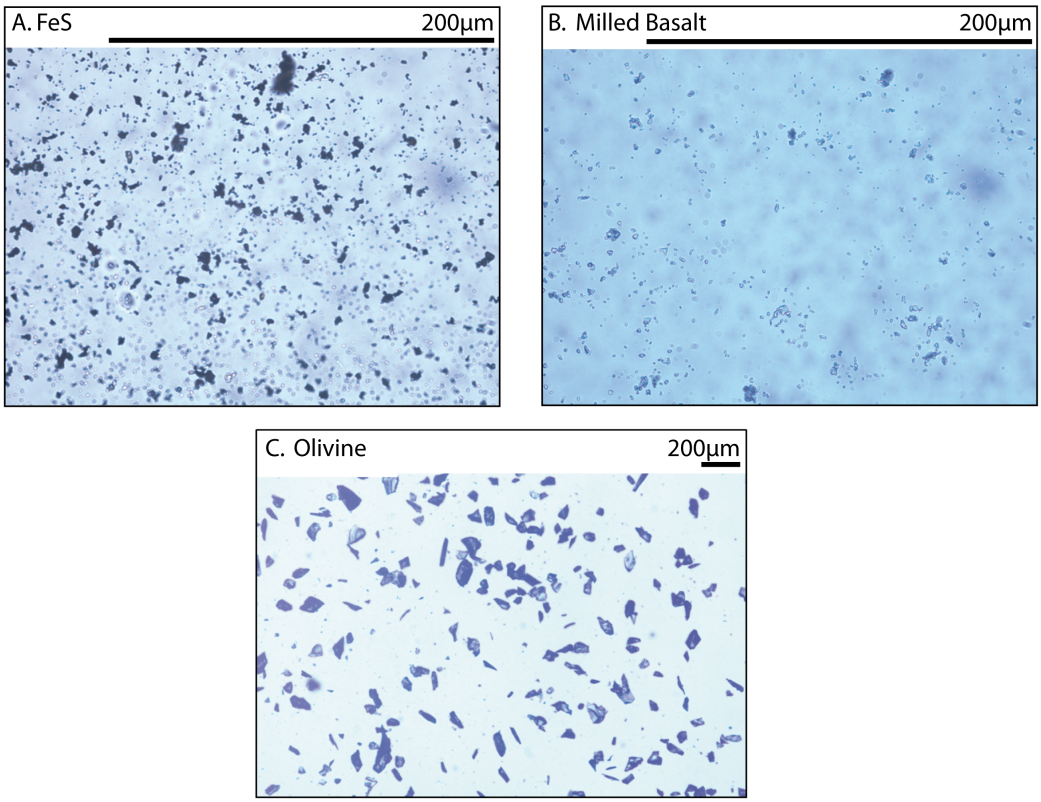

Figure 2.7: Petrographic Microscope image in plane polarised light, showing starting mix grain sizes. A. FeS ground by hand to an average grain size ~5µm B. basaltic glass mechanically milled to <2µm diameter and C. Olivine ground by hand and filtered following method described in text. The average grain size is around 70µm. Although the upper mesh size is 65µm, it is impossible to stop some larger grains passing through the filter, especially if they are elongate needles. However, the maximum grain volume and the overall range of sizes is still greatly reduced in comparison to unfiltered samples.

4. create a stable environment for long duration experiments within limitations of equipment used.

Details of temperature and pressure conditions chosen for each system, and justifications of these, are given in individual chapters.

Experimental duration of static experiments

Experimental duration has a large effect on sample texture, particularly in hydrostatic experiments where annealing leads to recrystallisation and a move toward textural equilibrium. Dihedral angles can only be used as a measure of permeability in samples if the sample has attained textural equilibrium (VonBargen and Waff, 1986). Dihedral

angles measured should produce a normal frequency distribution about the median value.

A series of preliminary experiments carried out on the FeS-olivine system examined the importance of experimental duration for development of textural equilibrium in hydrostatic experiments (Berg, 2010). Experimental duration varied between 2 and 46 hours, while pressure and temperature remained constant. For each experiment, 150-200 dihedral angles were measured using ImageJ measuring tool on backscatter electron images of cut and polished quenched samples. The spread of dihedral angle data was compared to a cumulative frequency normal distribution curve in the form of

$$D(x) = 1/2[1 \pm erf\frac{|x-\mu|}{\sigma\sqrt{2}}] \tag{2.1}$$

following the method of Hustoft and Kohlstedt (2006), where μ = mean and σ = standard deviation. An increase in experimental duration shows a move towards textural equilibrium as the spread of dihedral angles moves closer to the calculated normal distribution (Figure 2.8). This supports the findings of Bagdassarov, Golabek, et al. (2009) who suggest an experimental duration of >25 hours is required for reliable dihedral angle measurement. The majority of static experiments carried out during this project were carried out over 48 hours, as we found this was required for a fully equilibrated texture.

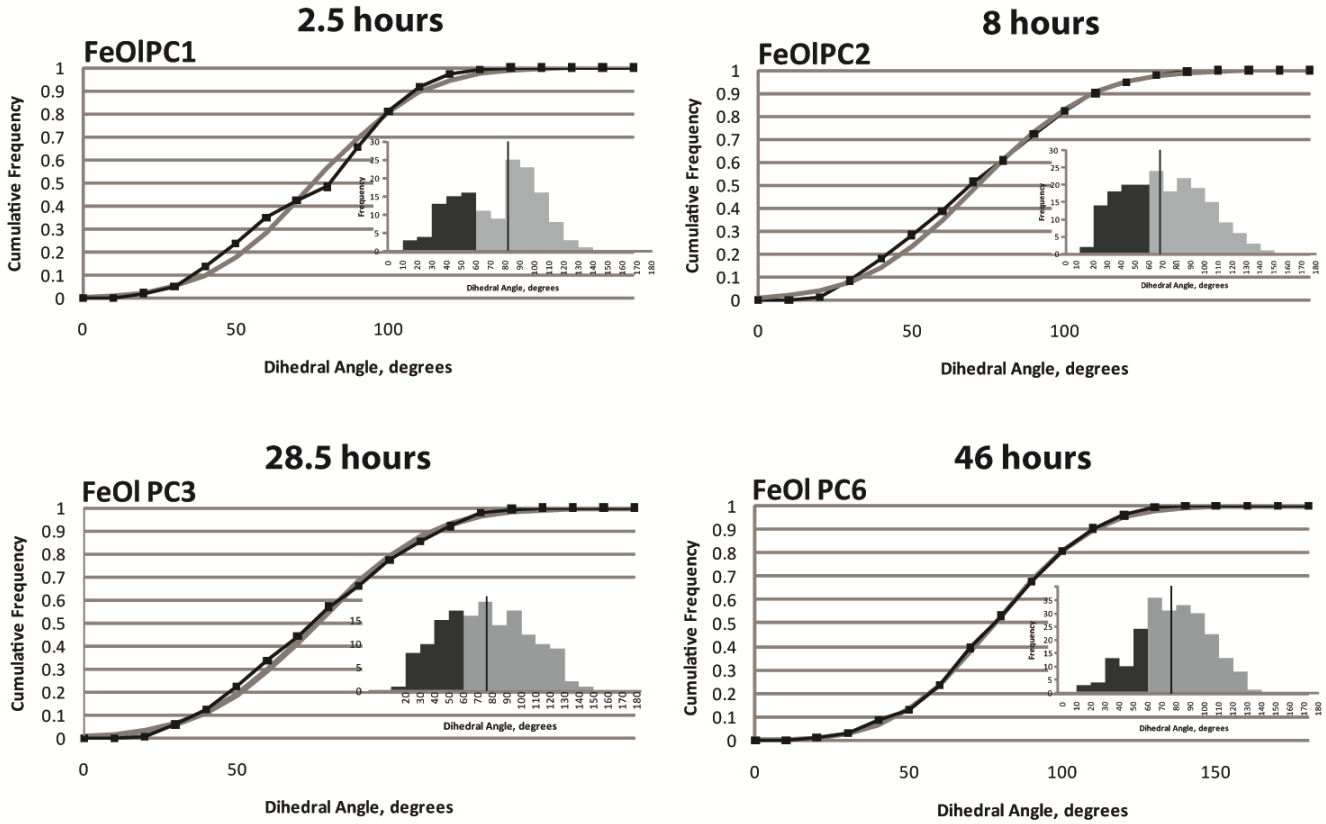

Figure 2.8: Dihedral angle analysis carried out on a series of preliminary experiments (Berg, 2010). All experiments were conducted at 2GPa, 1100°C with varying experimental duration. Dihedral angle distribution is shown in the form of cumulative frequency charts. The theoretical normal distribution cumulative frequency is plotted in the form of Equation 3.1 as a grey line, while data points joined by black lines show observed distribution. Histograms are also included for each dataset (insets). Darker grey shading indicates angles below 60°, lighter shades are above 60°. The median value is shown as a black line. Increasing annealing time leads to a move towards a more normal distribution and therefore a more reliable dihedral angle measure.

Experimental conditions in basaltic melt experiments should be chosen to be long enough to produce a reasonable equilibrium texture, as examined extensively in the SOM of Miller et al. (2014) to be produced on the order of ~135 hours. In addition, the experimental duration has to allow full dissolution and homogenisation of hafnia (HfO_2) crystals within the melt. However, issues with partial melting in experiments led to dynamic melt migration occurring despite hydrostatic conditions, precluding development of equilibrium textures after a certain length of experimental duration. These issues are discussed at length in chapter 4.

Deformation rates and time under strain in dynamic experiments

The requirement of textural equilibration is void for deformation experiments, which by definition cannot attain textural equilibrium. This is the reason dihedral angle analysis cannot be used for deformation experiments. Each experiment was annealed hydrostatically prior to deformation for at least 2 hours to allow the texture to begin equilibrating. Deformation time scales were varied in order to test the effect of experimental duration / total deformation on resulting textures.

The duration of experiments was limited due to limitations of equipment, particularly in higher strain-rate experiments which were inherently unstable due to the potential for breaking the graphite furnaces and of experimental blow-outs from the open centre of the rotoPEC. Our most stable experiments were those at very low strain-rates, giving experimental durations of >24 hours under strains of $<1x10^{-5}s^{-1}$.

Maximum strain and strain-rate was initially calculated from total rotation of anvils and duration of strain.

A number of definitions of strain exist which can be used to assess the extent of deformation. Engineering strain (e) is defined as a ratio describing the change in shape of an object in comparison to its original shape:

$$e = \frac{\Delta L}{L} \tag{2.2}$$

In the case of torsional deformation this can be calculated as no. of degrees rotated / total degrees in a circle (360°), i.e. a measure of the rotation of the sample relative to the original. A second definition is that of shear strain, γ, which is a measure of the angular rotation of a cylinder through torsion, calculated as

$$\gamma = r\frac{\phi}{L} \tag{2.3}$$

with definitions given in Fig. 2.9

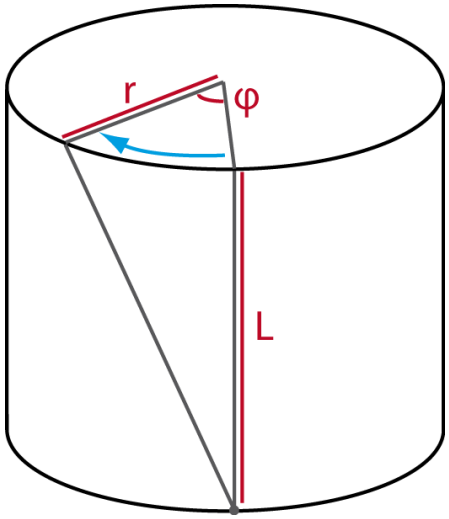

Figure 2.9: Schematic diagram defining terms used in calculation of shear strain γ. A cylinder of length L and radius r, is deformed in torsion to an angle ϕ. Angular shear strain is calculated as a ratio of angular rotation, in radians, as shown in equation 3.3

Strain is divided by total seconds under strain to calculate strain-rate (s^{-1}). The anvil strain-rate is constant for the input motor rpm, therefore strain-rate was calibrated to motor rpm for future experiments. Total strain of sample could be verified to a certain extent using platinum strain markers within some samples. These were removed from later experiments as their highly attenuating nature interfered with tomographic imaging.

The strain-rate of experiments was varied over orders of magnitude in order to test the effect of strain-rate on textural evolution. Strain rates ranged from $1x10^{-6}s^{-1}$ to $1x10^{-4}s^{-1}$. Specific deformation conditions are given in individual chapters.

2.3 Tomographic techniques and analysis

Computed microtomography (μCT) can be used to provide a 3D model of melt structures in the recovered samples, in order to examine the 3D network system and support conclusions made by 2D textural analysis. Three contrasting tomographic techniques have been used in this study and are described in detail in this section. The CT equipment used will be described, followed by description of processing carried out on images before and after the reconstruction process. The theoretical principles of the technique have been described in section 1.2.2.

2.3.1 In-house equipment

The in-house X-ray μCT system is a custom-built instrument, made up of a tungsten-filament cone beam X-ray source, a rotating turntable and sample holder, and a detector unit made up of an amorphous silicon detector (indirect) combined with a flat panel camera. Samples were mounted onto a graphite stick, held in place on the sample stage with a custom made tightening 3-jaw chuck or custom-made brass holder. The source-detector system is aligned manually, while the sample can be centred using a remote controlled nano-positioning piezometer stage located on top of the turntable. The turntable itself is computer-controlled and linked to the *in-house* acquisition software, allowing capture of several hundreds-thousands of images (projections) at accurate increments of 360°. The number of projections captured around 360° can be adapted to suit each scan. It is also possible to add or average two or more sets of projections from exactly the same orientation, which improve image quality by increasing the signal/noise ratio of an image. We have experimented with using different numbers of projections to optimise scan conditions. The number of projections taken is generally on the order of 1000, or 3000 if three images are averaged at every stop. To improve image quality further an external filter, consisting of a thin copper or aluminium sheet, was placed between the sample and detector on some scans. This filters out lowest energy X-rays, which can create beam hardening artefacts and degrade image quality (see section 1.2.2).

Scans carried out for this study were made using a low energy, high resolution head, which allows for highest resolution imaging as the spot size can be reduced, and the camera-sample distance can be minimised to maximise magnification. Generally, samples scanned were ~1-2mm diameter cylinders, with a camera-sample distance of ~2cm, giving a voxel size of 2μm. With improvement of the system it has been possible

to carry out scans of <1mm diameter sample sub-portions to attain CT volumes of submicron (0.7µm) voxel size.

Initial scans were recorded on a Teledyne Rad-Icon Shad-o-box CCD flatscreen X-ray camera, with 48 µm resolution and 12-bit depth. This camera was replaced in early 2014 with a Perkin Elmer XRD 0822 flat panel detector, with 16bit depth and 200µm pitch, which has significantly improved the imaging speed and noise levels within scans.

Reconstruction of 2D slices is performed by the University of Ghent's Octopus reconstruction software (Dierick et al., 2004). The software uses a filtered backprojection algorithm to create sinograms and 2D slices from the projections captured by the scanner (see section 1.2.2 for more detail of reconstruction process). The software allows for ring-artefact removal during creation of sinograms, beam-hardening reduction and simple noise filtering during reconstruction of slices.

2.3.2 Nano-CT equipment

The Manchester X-ray Imaging Facility houses a series of commercial micro- and nano-tomographic imaging devices which produce exceptional quality tomographic reconstruction at higher resolution than is achievable on our own in-house system. A series of successful runs were carried out over the course of two weeks on a variety of FeS and Olivine samples at different resolutions. High resolution is achieved by reducing sample size, therefore a certain amount of sample preparation was required to produce each image. Sample sizes were so small that sample preparation was in essence destructive, making the nano-resolution scans the last stage in the full series of analyses carried out on these samples.

Xradia Versa

The Xradia Versa is a commercial laboratory micro-CT unit designed with a dual magnification system that allows larger sample sizes to be scanned at higher resolution (it does not solely rely on the small sample size and close source-sample distance for magnification, but uses additional optical magnification, as shown in figure 2.10. Very high (submicron) resolution scans still require the lowest possible sample size. For a 1mm diameter sample a voxel size of 0.7µm was achieved. To prepare a 1mm diameter section for the Versa scanner, samples were cut in half then ground away at the edges to produce a 1mm x 1mm x >1 mm 'matchsticks'. These are mounted on toothpicks which are held with small chucks onto the sample stage.

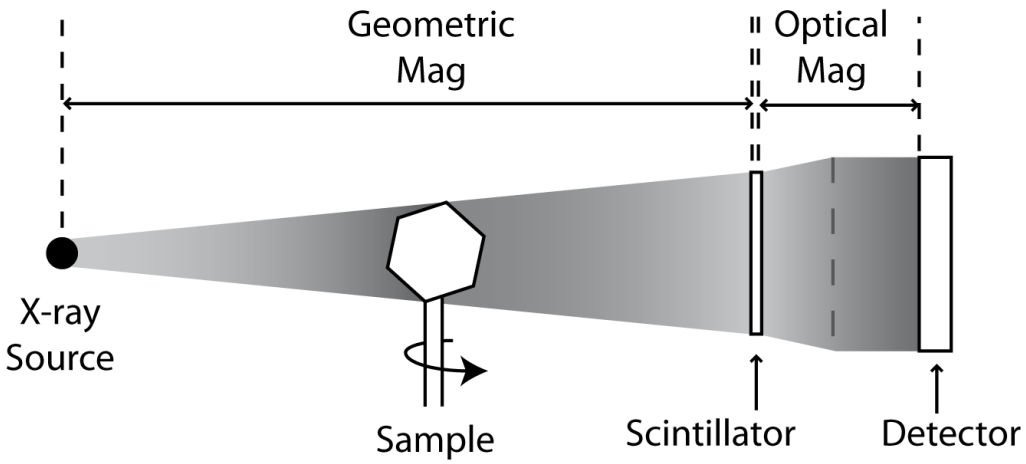

Figure 2.10: Zeiss Xradia Versa tomographic set-up, using two stages of magnification to reduce dependence of sample size to resolution. Samples are still required to be less than 1mm diameter to produce a voxel size of 0.7µm. Image adapted from *www.xradia.com*

Scans take on the order of several hours (depending on quality and resolution required) and projections are taken over 180°. To remove motion blurring artefacts from these scans a single ~1µm gold ball is attached to the sample top, which can be easily tracked on each projection and allows correction for any systematic shift. Due to the improved optics of the Versa scanner, and the effect of removing motion blurring / misalignment issues by gold ball tracking, the sharpness and therefore resolution of the Versa scans are a slight improvement of those made using our *in-house* system, despite a similar voxel size (see section 1.2.2).

Xradia Ultra nanoXCT

The Xradia nanoXCT scanner housed at Manchester X-ray Imaging Facility is the highest resolution laboratory CT scanner currently commercially available. The device can scan samples down to a minimum voxel size of 50nm. The very high resolution does require extremely small sample sizes however, which also clearly limits the effectiveness of this method to examine representative textures of a relatively large experimental sample. It also makes for challenging sample preparation.

Two resolution modes are available for use: A 'low' resolution mode with a 130nm voxel size and 65 µm field of view (i.e. maximum sample size) and a 'high' resolution mode with 50nm voxel size which requires a reduced field of view of 15µm.

A sample of 65µm was created by mounting a pre-polished sample flat side down on a glass slide using temporary Crystal Bond resin and grinding the other side to create a thick thin-section. This section was released from the resin and then further cut down to create tapered matchsticks using a sharp razor blade, and the best sections were chosen by examining pieces under a microscope.

A reliable cut of a 15 µm diameter was cut using a Focussed Ion Beam housed at the Centre for Science at Extreme Conditions (CSEC) at Edinburgh University. This allows more control to ensure that the maximum possible field of view is scanned. The sample is bombarded with a high energy beam of gallium ions that etches away the surface a few nanometers at a time. A thin-section of sample is created as above using temporary resin, but ground to 15 µm thickness. This section is imaged using the focussed ion beam at low energy setting to choose an appropriate area to cut. The area of interest is then cut out as a square (using the FIB like a 'cookie cutter'). As 15µm deep trenches are in fact relatively large for a focussed ion beam to cut, it takes about a day to cut the section. Figure 2.11 shows the process as a combination of focussed ion beam images, and later examination under the petrographic microscope.

The sample was later mounted on a fine tungsten needle or a plastic tipped mount - the latter is preferable as it is relatively X-ray transparent, meaning it will not affect attenuation significantly if it is in the field of view at any point.

Nano-scans of highest quality took on the order of 24 hours to complete, as lower energy X-rays were used and a higher exposure time was required to collect sufficient data. This means that drift during scans can be more of a problem than in faster scans. Again a gold-ball tracking method was used to correct for motion blurring, although in 15µm field of view scans this meant a significant volume scanned was taken up by this highly attenuating material, further reducing the amount of data collected.

All tomographic slices from Manchester scans were reconstructed using the Zeiss Xradia XMreconstructor software and additional *in-house* MATLAB code was used to correct for motion blurring and misalignment.

2.3.3 Synchrotron CT for in-situ X-ray tomography

Synchrotron X-ray sources were used during this project to allow *in-situ* high pressure-temperature analysis of partially molten samples. The synchrotron X-ray source is described in detail in section 1.2.2. Synchrotron X-rays are a far more intense source than obtainable from a laboratory source, allowing the beam to be significantly filtered to a smaller energy spectrum leaving a useable intensity of X-rays. The parallel

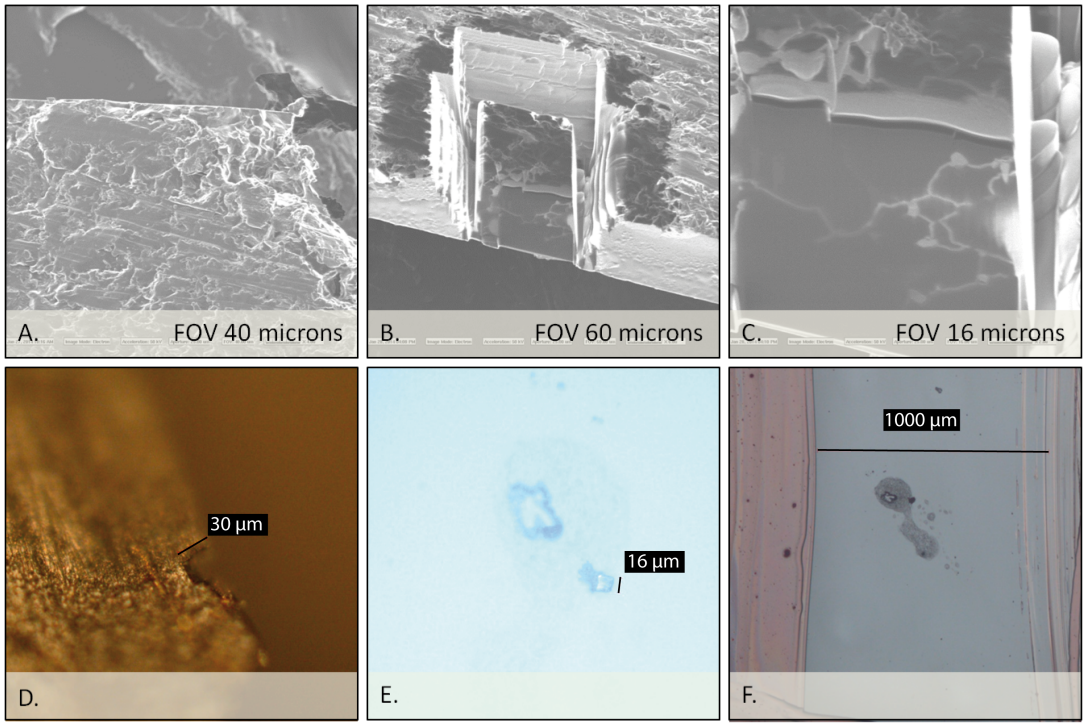

Figure 2.11: A series of images showing the process of cutting a 15µm section using the focussed ion technique. A-C are images taken by focussed ion beam imaging (resolution down to 5nm). A shows the chosen area of sample before cutting. B is an image of the cut area after cutting, C is a close-up of the cut area showing metal networks (light grey-white) within olivine (grey). D-F are images taken of the cut area (D) and the isolated sample (E,F) using petrographic microscopy. D and E are reflective light images, F is a plane polarised transmitted light image.

nature of the beam also simplifies reconstruction and reduces the number of artefacts produced in the scan.

Several weeks of beamtime were conducted during a number of visits to the European Synchrotron Radiation Facility, Grenoble, France and the UK DIAMOND facility in Oxfordshire to perform *in-situ* X-ray tomography at high temperatures and pressures. Each beamline specialises in a different technique, therefore the exact set-up used and preparation required is different for each beamline used. DIAMOND I12 is specifically designed to incorporate heavy engineering equipment for tomographic techniques, while ESRF ID27 is an engineering beamline mostly used for diffraction studies, and not specifically designed for tomographic work. The two beamlines used in this project, and methods used to acquire the data are described in more detail where relevant in chapter 5, section 5.2 of this thesis.

2.3.4 Estimating spatial resolution

As previously described in section 1.2.2, the true spatial resolution differs from the reconstructed voxel size, and is dependent, in a cone beam CT scan, on the geometric magnification of the sample from its position in the beam, the detector resolution itself, and the blurring caused by the spot size of the source. We have used the method of Feser et al. (2008) to gain an estimate of the spatial resolution of scans carried out over the course of this PhD:

Geometric magnification, M, is calculated as $M = \frac{a+b}{a}$ where a and b are source-sample and sample-detector distances respectively. The effect of blurring caused by magnificiation, r_s, can be calculated as $r_s = S(b/a)$, where S is the spot size, which is correlated with power of the X-ray source (This is illustrated in figure 1.10).

Finally, an estimate of the overall spatial resolution (r_{total}) can be calculated combining these effects with the effect of detector resolution, r_D:

$$r_{total} = \frac{\sqrt{r_D^2 + r_s^2}}{M} \tag{2.4}$$

A table of resulting resolution values of *in-house* CT scans can be found in appendix A.1.2. These estimates are used where applicable in appropriate chapters, referred to as estimated spatial resolution, as opposed to voxel size, which is generally smaller. However, the calculation is essentially limited to those scans carried out in the cone beam geometry of the University of Edinburgh in-house CT scanner. The calculation is not appropriate to nano-CT scans, used in chapter 3, where further optical focussing before and after the sample complicates the relationship between source-sample distance and blurring (section 1.2.2). Synchrotron tomography, which is the focus of chapter 5, has a parallel beam geometry and therefore resolution cannot be calculated using this technique. Therefore, in these chapters, where different scan types and geometries are used, I use voxel size for relative comparison of scan quality, in the knowledge that this does not represent spatial resolution, which is likely to be significantly lower.

It becomes apparent, in any case, that a calculated resolution estimate does not give a true comparison of the size of features that can be segmented in a dataset, affected significantly by artefacts such as doubling from misalignment, streak artefacts, and contrast between phases. Segmentation is discussed in section 2.3.5.

2.3.5 Noise reduction, filtering and image analysis

Image processing and analysis of tomographic datasets has been a vital aspect of data manipulation in this project. Figure 2.12 shows the series of steps required to produce data from a tomographic image. Segmentation of the dataset by assigning certain volumes to specific phases allows the dataset to be quantitatively analysed for geometric features and values such as phase connectivity. This section describes the techniques used during this project to filter and segment datasets. The exact processing stream depends on the dataset used and its quality, therefore changes with the sample scanned / CT system used for capture, and are therefore detailed in individual chapters.

Noise filters and artefact removal

Noise reduction occurs throughout the process of producing a tomographic dataset, from physical filters during image capture, to digital filtering of the final slices.

Image capture Physical filters can be used in laboratory CT to reduce the energy spectrum of X-rays hitting the CCD detector. This reduces the effects of beam hardening artefacts, although it also reduces the overall signal of the beam hitting the detector, which can increase the noise in a dataset. A way to enhance signal-noise ratio can be to increase the number of projections, or to take 2-3 images at each angle and average or sum them to produce a composite image for each step. However, longer scans are also likely to produce more noise due to shifts in beam quality or sample drift leading to misalignment, therefore there is a limit to the increase in quality attained by increasing projection numbers. Over the course of developing the *in-house* CT equipment the number of projections, and averaging, has been optimised to achieve the best scan quality while keeping scan time low to reduce artefacts caused by spot and sample drift (I. Butler, pers. comm.). Details of scan conditions are given in relevant chapters.

Reconstruction A series of steps can be made during reconstruction to reduce noise and reduce systematic artefacts within tomographic datasets. A key aspect of the reconstruction process is background removal and normalisation of raw projections. Background removal is carried out by capturing a series of images of the field of view with the sample removed (flat field projections, FF) and a series of images with the x-rays switched off (dark current projections, DC) and their average is subtracted from each raw projection. 10-20 each of FF and DC projections are usually taken, and must be carried out separately for each scan. This removes texture created by variations in sensitivity of the CCD detector panels. Additional normalisation is carried out by

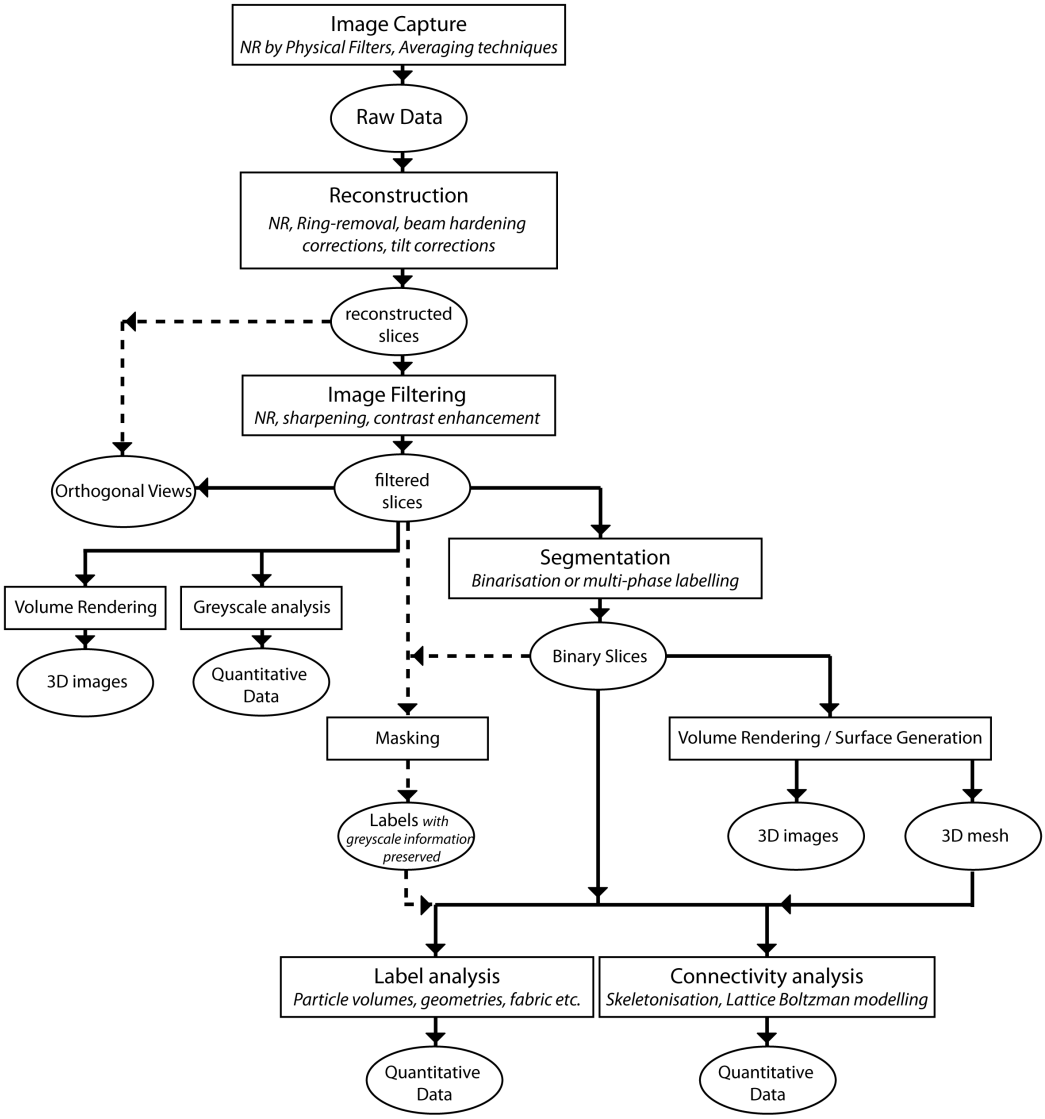

Figure 2.12: A flow chart showing processing steps of a tomographic dataset from initial data capture to final qualitative and quantitative products. Processing steps are given in rectangular boxes, while products are shown in ellipses. Noise reduction (NR) can be carried out at multiple stages including during image capture, reconstruction and post-reconstruction image enhancement using digital filtering techniques. After raw data has been enhanced by filtering, segmentation /binarisation of data allows more detailed analysis of phase geometry and connectivity and the production of quantitative data. Individual steps are described in detail in the text.

choosing a field of view within each raw projection that is free of attenuating sample. Any variation in signal within this area over the time of a scan is due to fluctuations in the X-ray beam or the sensitivity of the CCD - changes are averaged to ensure the greyscale across all projections reflects a similar X-ray attenuation. Octopus 8.7

(Dierick et al., 2004) gives additional in-built options for removal of common artefacts: Ring artefact removal can be carried out either during creation of sinograms or during back-projection reconstruction of slices, beam hardening corrections can be applied at this stage to normalise greyscale values between the sample centre and edge, and a simple noise filter can be added to reduce white noise.

Post-reconstruction image processing A large number of digital filters exist which can be used to reduce noise, sharpen an image or enhance edges of phases within a greyscale image or image stack. Over the course of this project I have made use of such filters available in two image processing software suites: The freely available ImageJ and its extension Fiji (Abramoff et al., 2004), and the commercial package AVIZO Fire^{TM}. I will briefly describe those filters used most commonly over the course of this project (example data in Figure 2.13):

- **Remove Outliers** (ImageJ) A simple but very useful way to remove speckled noise, which removes individual pixels or pixel groups that are significantly brighter or darker than the surrounding average. The size of pixel group and the acceptable range of greyscales is user defined. This works well for datasets where features of interest are significantly larger than the pixel/voxel size, but can lead to data removal if features are small. Using this for single pixel 'wild spike' removal is a useful initial processing step before further filtering takes place.

- **Median** (ImageJ and Avizo) The greyscale value of a pixel is replaced by the median value of pixels within a surrounding kernel of given size and shape. Using the median, rather than the mean, in an image helps to preserve edges to some extent as the value of the pixel must be the value of one of the pixels in the region - this removes the blurring effect caused by calculating the mean of a pixel found in a boundary region (Fig 2.13 C.). However, the median filter still blurs edges significantly in comparison to other edge-preserving filters (see below).

- **Bilateral** (ImageJ and Avizo) An edge-preserving filter, which smooths pixels according to the average of its surrounding neighbourhood pixels, except in regions where greyscale varies rapidly, indicating a potential boundary between phases. The size of the neighbourhood, and sensitivity to greyscale variation, are user defined (Fig 2.13 B.).

- **Non-local means** (Avizo Fire) This filter assigns a greyscale to a pixel by comparing its initial value to the weighted average of 'similar' pixels within the dataset (Buades et al., 2005). To reduce processing time, this dataset is reduced to a search window of a user-defined size. This filter is very effective at removing random white noise while avoiding the blurring of real features (although often artefacts are also enhanced in this manner). The use of the filter in this project has generally been restricted to small datasets, due to the intensive computational power required to carry out the filtering technique (Fig 2.13 D.).

- **Anisotropic Diffusion** (Avizo Fire) An edge-preserving filter based on a diffusion smoothing method which stops smoothing occurring across areas of the image where the greyscale gradient is above a defined threshold (Perona and Malik, 1990). In this project it has been used effectively where features are reasonably large and the dataset is too large to permit non-local means filtering (Fig 2.13 E.).

Segmentation

Segmentation is the process of assigning certain ranges of greyscale value within a dataset to a distinct phase. This can be simply binarisation - assigning areas of greyscale to either being of a phase (I) or being part of the exterior (0). Other segmentation software, such as the 'Edit New Label Field' tool pack, allows segmentation into multiple phases (e.g. air, capsule, olivine, iron sulphide) for more complex datasets. Segmentation enables the application of algorithms to measure the geometry and connectivity of regions of the sample volume, but unless a masking technique is used (see below) greyscale data is lost and replaced with a single label value for each phase. It is also important to note that data segmentation from a greyscale to a binary or multiple label dataset is inherently a slightly subjective process. Particularly in poor quality datasets, it is important to be aware of the errors involved in carrying out thresholding and segmentation in assessing quantitative data outputs produced by segmentation.

Over the course of this project, thresholding has generally been carried out using the AVIZO Fire^{TM} tools. A number of automatic, semi-automatic and manual tools are available, which can be used alone or in combination to reliably separate phases.

- **Global thresholding** The simplest thresholding technique whereby voxels across the image within a given greyscale range are assigned to a certain phase.

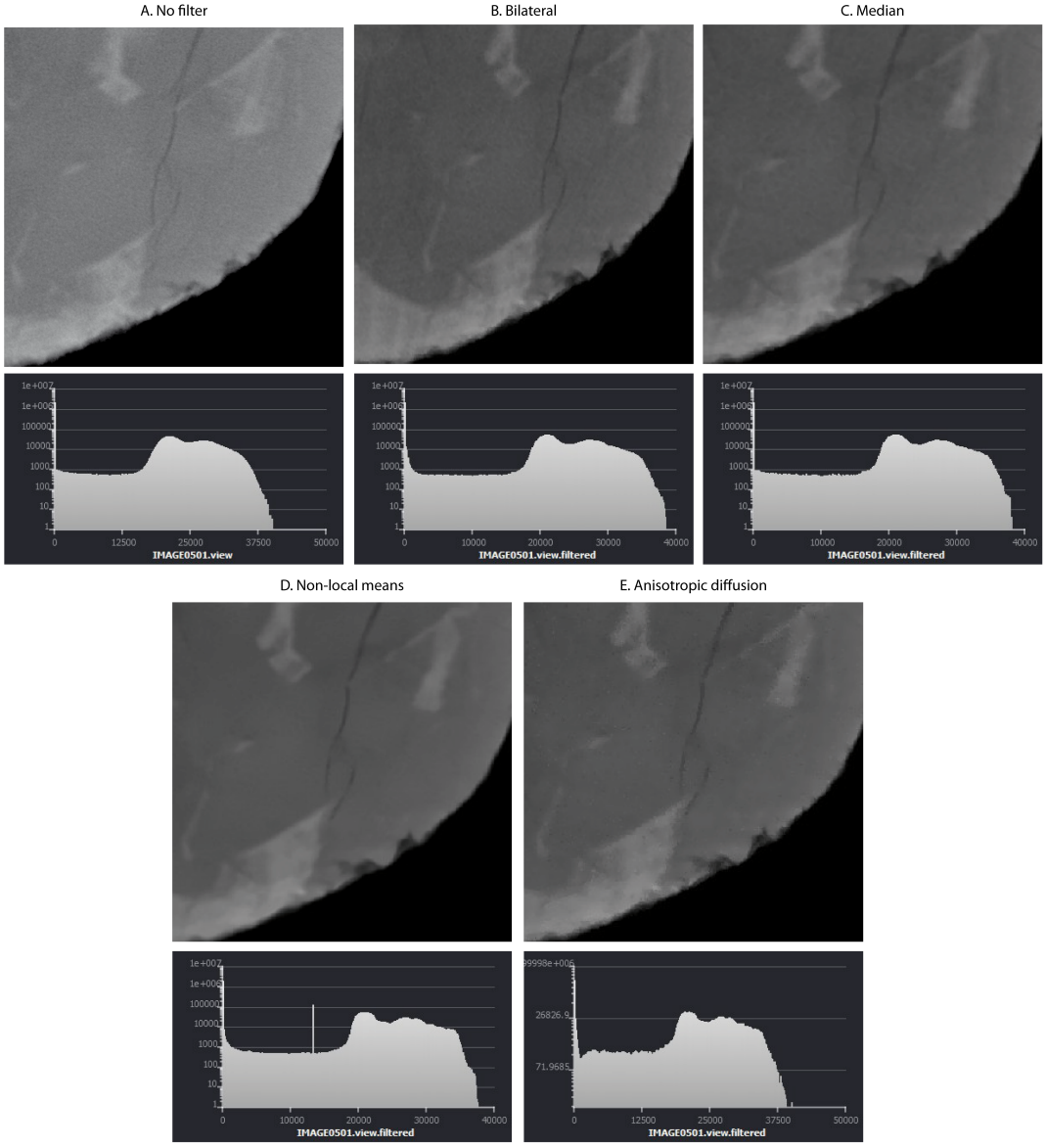

Figure 2.13: Examples of various noise filters available on Avizo Fire ™ on a close up of the same example slice from dataset OlBaVS3-hires, used in chapter 5 of this thesis. Field of view ~0.5mm, voxel size 2 µm. Details of the filters are given in the text. Each is accompanied by the image histograms to show how the filter affects the greyscale ranges of the dataset (single slice only). The filters generally enhance peaks on a histogram, suggesting contrast between phases is enhanced. The non-local means and anisotropic diffusion filter reduce white noise most significantly, but both can also act to enhance artefacts such as the central ring filter. All filters are supposedly edge preserving, but the non-local means filter appears to keep edges sharpest while still significantly reducing white noise within phases.

This works well if the contrast between phases is high enough that regional changes do not create overlaps in greyscale, and there is minimal regional change in brightness and contrast across the sample (e.g. caused by shadowing or beam hardening, Figure 2.14B.).

- **Tophat** The tophat segmentation selects regional maxima or minima within a dataset, searching for structures of a given maximum kernel size i.e. it will select areas that are brighter than their surroundings (above a user-defined threshold) and smaller than the user defined kernel size. This allows small features such as isolated melt pockets to be segmented even if their overall greyscale is lower than larger features due to partial volume effects (Figure 2.14)

- **Watershed** Watershed segmentation uses an intermediate greyscale gradient image to find the boundary between two phases at the point of the greatest rate of change. Areas of the image are chosen (by global thresholding or manual segmentation) that are 1) certainly within the phase of interest and 2) certainly outside, with an unknown intermediate range. The phases 'flood' the intermediate regions until they hit areas of maximum greyscale gradient (i.e. phase boundaries). This works well to separate large features, but often misses out on smaller particles (Figure 2.14).

- **Magic Wand** The magic wand tool is a semi-manual selection tool which allows a voxel to be chosen as a 'seed' point - all voxels connected to this point that are within a given threshold range are selected. This is a very useful technique for finding connected networks of voxels within a given greyscale range, but should be used with caution as it can miss areas of a phase that are not connected to a larger volume (e.g. small disconnected melt pockets).

- **Other segmentation tools** Other tools available within the tool kit allow for manual correction of the above automated segmentation techniques. In most cases, some manual correction will be required, particularly if there are significant artefacts within the dataset - ring artefacts, for example, are easy to spot by eye due to their regular shape and alignment, but are often segmented wrongly due to their sharp edges and intensities.

Figure 2.14 is a good example of how individual segmentation techniques are often limited in their ability to segment areas of interest. The tool kit allows these techniques to be combined, along with masking techniques, dataset cropping and label

smoothing / island removal adjustments, to correct and improve the segmentation until it is deemed reasonable for its requirements. The level to which the dataset is subjectively altered may depend on whether the dataset will be used for quantitative analysis, or qualitative volume rendering and imaging. An example of the final segmentation process is shown in figure 2.15.

Due to the different CT scanners used, very different scan qualities and varying compositional phases used over the course of the PhD, the filters used to improve data, and techniques to segment datasets, vary between scans. Combinations of processes often become complex to allow for accurate segmentation. Specific processing steps used in each dataset are described and justified in the relevant chapters. It is important to note that the final outcome will always be subjective to a certain extent, as the final segmentation needs to be judged 'by eye'.

Ground-truthing with BSE imaging

The preceding section shows that segmentation of tomographic images is often best completed by manual correction. The final outcome is, therefore, always subjective to a certain extent. To ensure the final segmentation is justified, textures observed in tomographic slices must be verified by comparison to 2D SEM / BSE imaging. 2D slices from tomographic imaging can be directly compared to the 2D polished section examined using an SEM at far higher (nano-scale) resolution. This analysis can be qualitative: to verify, for example, that features observed in the CT slices are also visible in the 2D section, e.g. the observation of wetted grain boundaries or very small spherical melt pockets. The process of segmentation can also be tested by comparing, for example, the quality of a segmentation of a 2D tomographic slice to a segmentation carried out on the high quality BSE image (see figure **??**, section 4.4.3). The assumption is that if textures can be verified by comparing the high quality 2D dataset of BSE images with a sample 2D section of the CT scan, the full 3D dataset segmentation can be assumed to be reasonably accurate. The combined use of BSE and EDS also allows verification phase composition, which is an important factor as a CT dataset is scaled only according to attenuation, meaning two distinct phases can have similar greyscale levels. In chapter 5, section 5.3.2 this is proven to be a particularly important step to fully interpret textures observed during *in-situ* experiments.

Visualisation

Visualisation of stacks of slices can be carried out by a number of different methods. The simplest is by re-slicing of the data to create a series of orthogonal stacks, allowing the data to be examined on 3 separate planes. This has been carried out using ImageJ (Abramoff et al., 2004) or Avizo Fire^{TM}. Alternatively, the dataset can be examined by volume rendering each voxel within a 3D matrix, assigning each with a given opacity and greyscale/colour thereby creating a full 3D image of the data of interest. In addition, for a segmented dataset, a surface can be extracted, defining the boundary between 2 phases (or a phase and its exterior) and created by a mesh of polygons (e.g. triangles). This surface can be used to input into modelling software to carry out e.g. Lattice Boltzmann flow simulations (section 3.3.4).

An additional useful way to image data in 3D has been to use a masking technique (Figure 2.12). A phase of interest is segmented from a dataset, and then recombined with original greyscale data to use as a clipping mask and only show greyscale data within the phase of interest. This allows the greyscale information of the segmented phase to be preserved while variations outside the phase of interest are removed. This has been useful in *in-situ* datasets where scan quality has been poor and artefacts can obscure data of interest if full volume rendering is used for imaging (chapter 5).

Quantitative analysis of segmented data

Once segmentation has taken place, individual particles (voxel clusters) within a binary dataset can be analysed quantitatively. This has been carried out using the Avizo Fire^{TM} Label Analysis tool, which can give data on volume, area, 3D distribution, aspect ratio/ elongation, orientation and potential particle alignment, and shape/geometry of individual particles. This information can be useful for examining the effects of deformation on particle texture. The alignment of melt and redistribution into melt rich/melt poor regions is known to be an effect of deformation on melt geometry and is evidence for localised melt redistribution and therefore interconnectivity (Kohlstedt and Holtzman, 2009). This may also be a way to show development of interconnectivity within a dataset even when resolution limitations mean that fine melt sheets between larger melt volumes cannot be imaged - the concavity/convexity of a melt pocket is thought to be an indicator of relative connectivity (i.e. similar to dihedral angle data) and a more complex, concave shape will be more likely to be part of a larger connected network than a near-spherical melt pocket (see section 3.3.2).

Melt network topology

To gain an understanding of porous network geometry and how this relates to permeability, it is often useful to simplify observed structures to simple geometric shapes, for example a series of tubes or sheets (Gueguen and Dienes, 1989). This helps to reduce a complex natural system to a simple numerical model to use for quantitative analysis. Many porous systems are described as a series of pores, which store the majority of the fluid, and narrow minima between them known as throats. It is the size of the throats that tends to limit permeability (Koplik et al., 1984).

It is desirable to be able to describe melt networks produced in experiments in similar terms in order to make the observed melt geometry comparable to previous studies, and potentially to characterise or even quantify to some extent permeability in our samples. This is not a trivial task, particularly as the majority of melt network studies of this type assume some form of textural equilibration in order to justify simplification of the system. Our deformation melt networks are, by definition, never at textural equilibrium, and observations always only represent a snapshot of textures that change constantly over time.

One way to simplify relatively complex networks is by the process of skeletonisation. This is a technique that has been used widely to characterise melt networks in 2-dimensions, and particularly in combination with tomographic reconstructions of 3D networks. A complex 3D network is reduced to a series of one-dimensional branches that connect to each other by a series of nodes. It is then possible to quantify the network by counting the number of branches, nodes, the number of branches that are attached to each node (co-ordination number) and the thickness of individual branches and nodes. Although the geometry of the melt network remains representative, this makes comparison of different melt networks easier.

Original data must be binarised to show only the melt network of interest. The process involves thinning the network shape to its central medial axis (Lindquist et al., 1996). Using Avizo Fire^{TM} software this is done by creating a distance map, a greyscale image of the network which is scaled according to distance from the edge of the binarised data. Data are then thinned incrementally until only a central 1-dimensional chain of pixels remains, keeping those areas that are connected in the binary image connected in the skeleton itself. A secondary re-dilation step then uses the distance map to get a minimum (i.e. limiting) thickness measure for each branch. In this way the topological interconnectivity of the network remains true to observations, but the geometry of individual pores and branches is lost. Figure 2.16 shows the

skeletonisation process as carried out using Avizo Fire^{TM} Skeletonisation module. Using the auto-skeletonisation function combines these steps to produce a spatial graph directly from binary data input.

The resulting dataset is known as a spatial graph. Avizo gives limited analysis options of the spatial graph dataset. Statistical analysis of the dataset is possible - the 'Analyse Spatial Graph' module of Avizo quantifies the dataset, splitting the dataset into different disconnected graphs, and giving the number of branches within each connected unit. Each graph is then given an individual spreadsheet of containing branches, which are quantified according to their length and thickness.

Data regarding connectivity of nodes (i.e. the number of branches connected to each node) cannot be collected using an Avizo module - To retrieve this data I used a Matlab code designed first to prune the skeleton data, and then create a histogram of the node co-ordination number. The code was written by Laurent Montési and Kevin Miller of the University of Maryland (Miller et al., 2014; Zhu et al., 2011). The cleaning process removes artefacts created during the skeletonisation process which do not contribute in a meaningful way to melt network geometry, for example removing loops (branches returning back on themselves to the same node), twins (a pair of branches linking between the same two nodes), and links shorter than 7μm. It is rarely possible to completely remove artefacts produced by large melt sheets, which can reduce the connectivity value of a network. This may partly explain why a fully connected basaltic melt network has a lower average node connectivity than that predicted theoretically (Zhu et al., 2011). A full description of the code function can be found in the supplementary material of Miller et al. (2014).

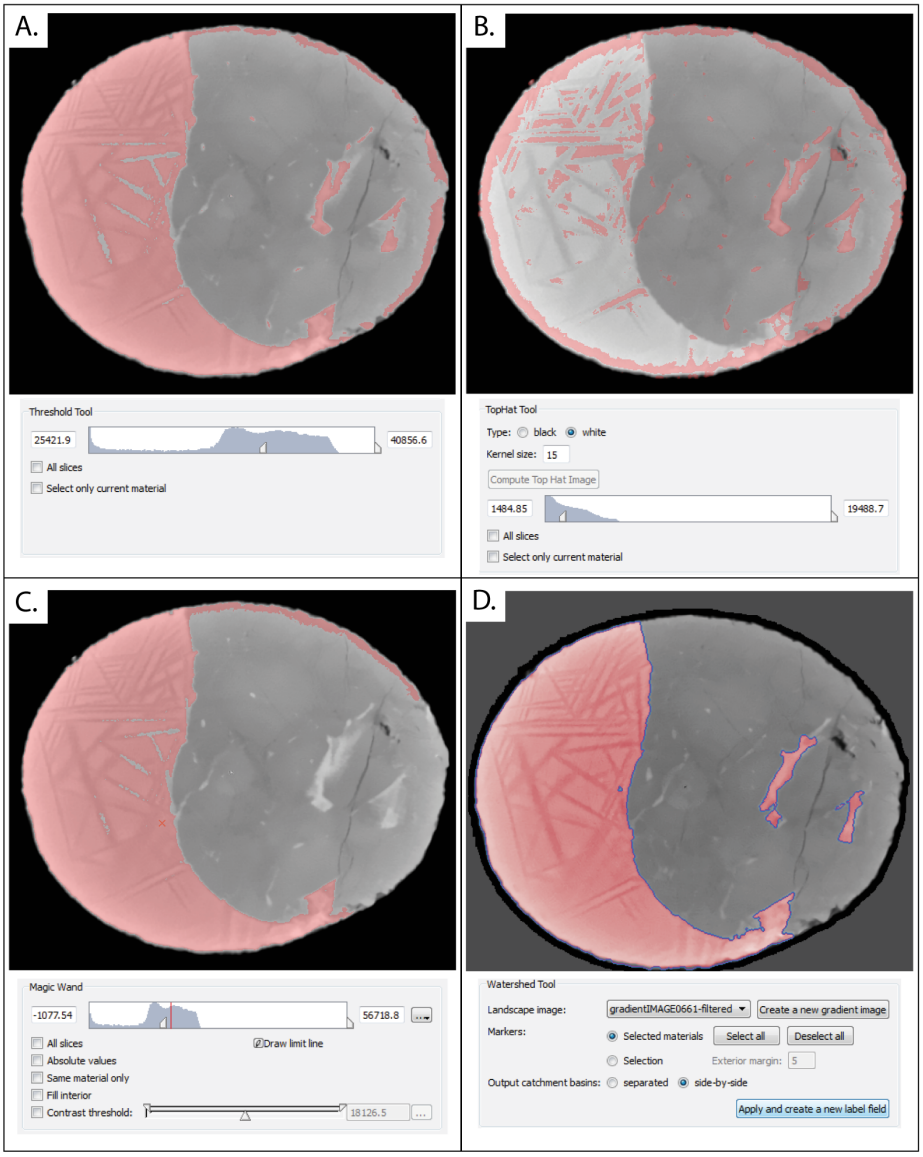

Figure 2.14: Example attempts to binarise a CT slice into melt phase (in this case Hf-doped basalt) and non-melt phase regions using segmentation methods as available within the Avizo Fire™ Edit New Label Field tool kit for segmenation. Pink areas are segmented as the melt phase (in this case skeletal crystals were taken to have been created during quench therefore are being segmented as part of the 'melt phase') The example slice has initially been filtered using a non-local means filter (see above) A. Global thresholding tool B. Top hat thresholding tool C. Magic Wand tool D. Watershed tool. See text for descriptions of each segmentation technique. This slice shows how even a subtle beam hardening effect, leading to brightening of the sample edges, can cause problems in segmentation. The watershed tool is most successful in removing this issue, as the gradient of greyscale edge by beam hardening is gentle. The tophat tool is good for picking out small inter-granular melt pockets. Although none of the techniques alone are successful in segmenting the melt phase, the toolkit allows combinations of techniques to be used along with manual correction to create more reliable binary datasets (see Figure 2.15).

Figure 2.15: An example of the same slice segmented by a combination of the watershed, tophat and global thresholding tools. A. Initial combination of segmentation tools, using a masking technique so that the tophat tool only segments areas previously segmented as non-melt (Figure 2.14D.) - the tophat tool picks out the finer melt pockets missed by watershed segmentation, although beam hardening artefacts mean segmentation is not successful at sample edges. B. Cropping sample edges using the Volume Edit technique is often the simplest way to ensure a reliable segmentation of the remaining dataset. C. A 'remove islands' function is used to remove clusters of less than 15 voxels within the dataset. The segmentation may be further improved by manual removal of segmented artefacts, e.g. central ring artefact that has been segmented as a melt pocket.

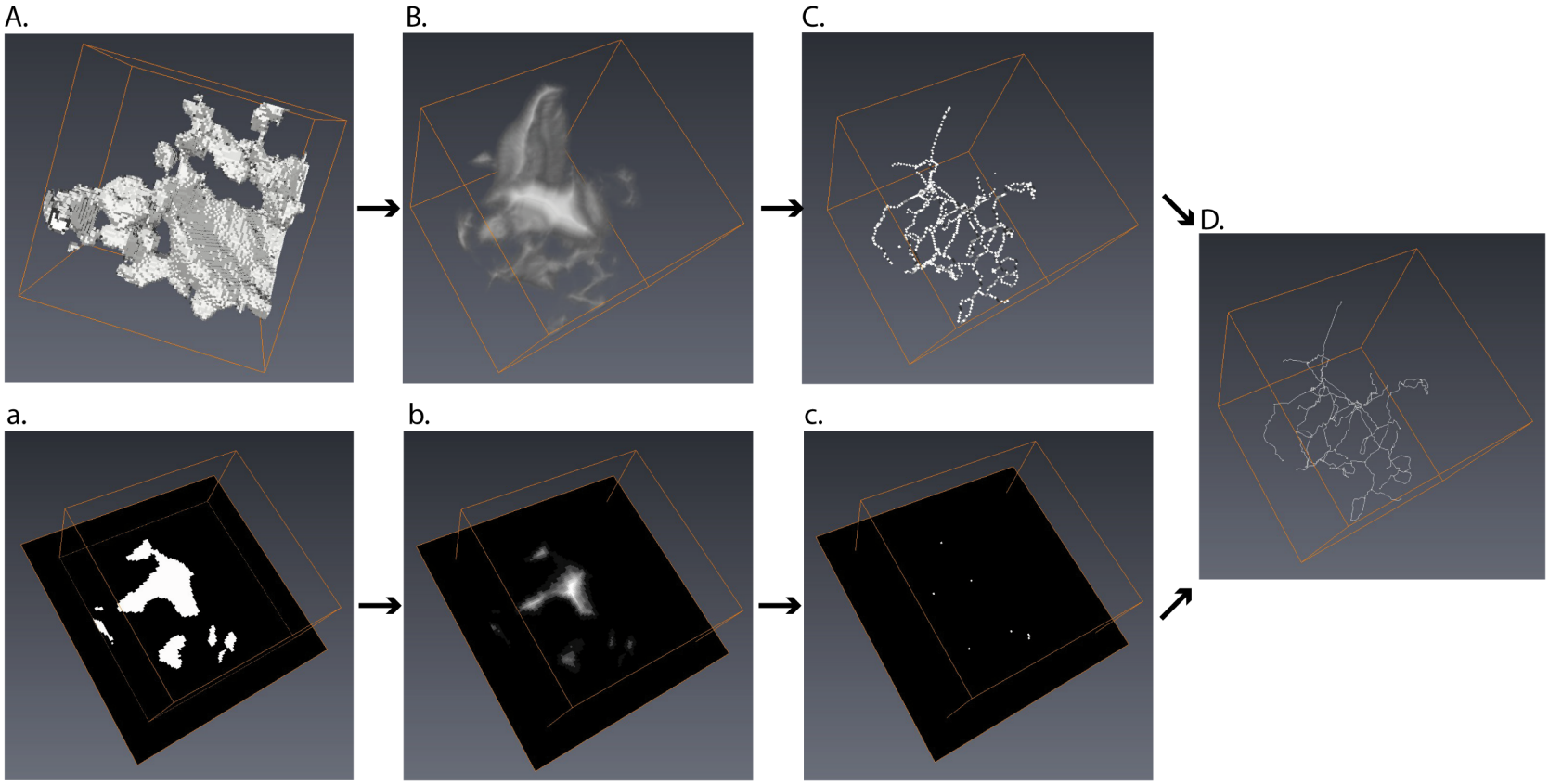

Figure 2.16: Step-by step images representing the process of skeletonisation using Avizo Fire 8. Steps A-D are undertaken automatically by the Auto-skeleton function used in this process. It is also possible to carry out each step individually for more control on the outcome. Capital letters show the process as it affects the 3D volume. Small letters show the same process occurring on an individual slice within the 3D volume. The volume in this case is a 200x200x200 voxel cube subsample of an individual FeS melt network (see section 3.3.4 for results) A. The input image of a segmented melt network - melt is rendered white, olivine is transparent. B. A distance map is computed of the melt volumes. A gradient of transparent to opaque represents volumes of melt close to the melt tube boundaries, and central areas respectively. The most opaque areas therefore represent the mid-points of the melt channels. C. The maxima of greyscales are picked from the distance map to produce a map of points representing the mid-point of melt channels. D. The final production of the topological skeleton joins these points to form skeleton branches and create nodes where these branches intersect or terminate. Information about mean branch thickness is also stored in the skeleton produced in Avizo, which is the average distance between the mid-point and melt channel edge for each branch.

2.4 Other analytical techniques

2.4.1 Diffraction patterns for in-situ temperature and pressure calibration

As X-rays pass through a crystalline material they interact with the crystal lattices, producing characteristic interference, or diffraction, patterns. The interaction of X-rays with a solid varies depending on phase composition and crystal orientation, but also varies in a reproducable manner with changes in pressure and temperature, as the crystal lattice expands and contracts in response to environmental conditions. The analysis of crystal diffraction patterns therefore allows pressure and temperature of a known solid phase to be estimated by comparison to previously calibrated standards.

X-ray diffraction patterns were analysed at the ESRF ID27 synchrotron beamline using a uniquely designed Soller slit system (multi-channel collimator) to intensify sample signal and reduce noise created by X-rays passing through the frame and sample gasket (Mezouar, Faure, et al., 2002). Figure 2.17 shows the set-up of the rotoPEC in the ID27 hutch with the diffraction system in place. An automated macro toggles between imaging mode and diffraction mode, and includes moving the soller slits into position, reducing the aperture of slits to reduce the size of the X-ray beam entering the sample, and adjusting the angle of the monochromator to produce a monochromatic beam of the required energy. It takes 5-10 minutes to switch from imaging to diffraction mode.

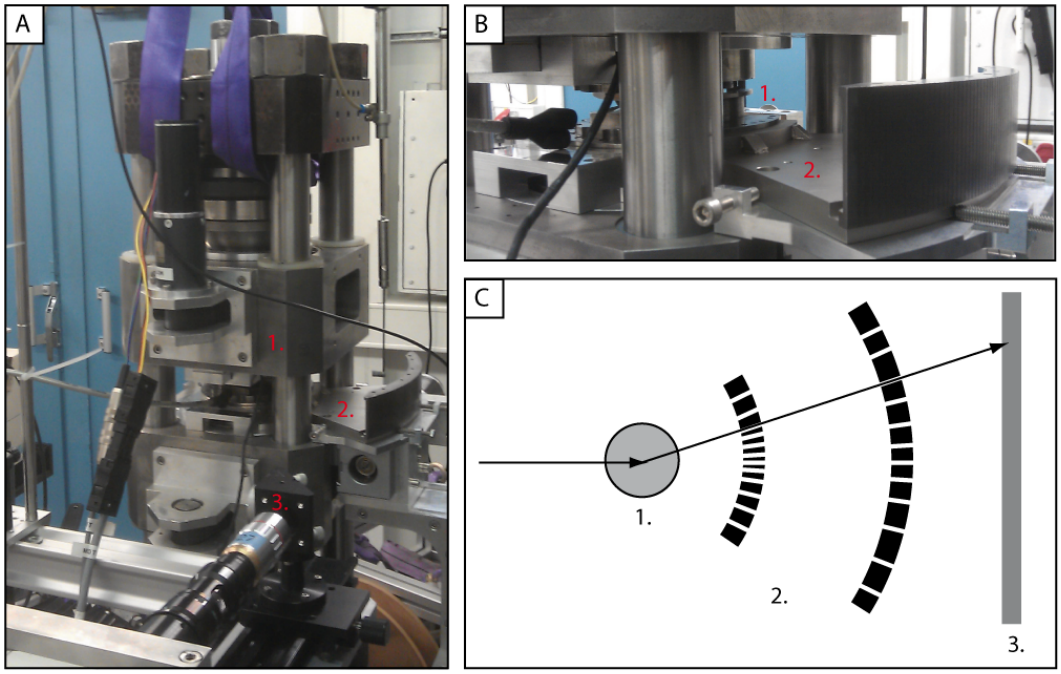

Figure 2.17: A series of images showing the X-ray diffraction set-up for the rotoPEC and other Paris-Edinburgh cells using Soller slits at the ID27 beamline at ESRF. A. shows the rotoPEC frame (1) in position with custom-built soller slits in-situ (2). The X-ray CT camera (3) can be seen at the edge in its offline position. An automated procedure moves the soller slits out and camera into position when toggling between diffraction and imaging mode. B. A close-up of the soller slits (2) in position, showing their proximity to the press (1). Soller slits are aligned semi-automatically by scanning beam intensity across several mm using the photo-diode and chosing the central position of highest intensity. C. A schematic plan-view diagram showing the function of the soller slits / multi-channel collimater, adapted from Mezouar, Faure, et al. (2002). X-rays (arrow) interact with the sample (1) and diffract. The collimator(2) ensures only the X-rays of interest intersect with the detector plate (3) and reduces noise created by material in the sample assembly

Diffraction patterns were captured by a 2D planar solid-state detector (SSD), with dimensions of ~50x50cm. A typical diffraction pattern of a polycrystalline powder is a series of concentric rings, produced as X-rays interact with a large number of crystals of the same phase but varying orientation. (A single crystal will produce a diffraction pattern of a series of points on a grid, the spacing of which is affected by d-spacing of the crystal lattice. A combination of crystals of the same phase but different orientations will create a series of points of the same spacing, but varying orientation, thereby combining to create a series of rings of characteristic spacing.) Due to the presence of the press blocking the upper and lower portions of the ring pattern, only the central section of the pattern was observed on the imaging plate in our experiments. An example of diffraction patterns produced by this set-up is shown in Figure 2.18.

Diffraction patterns were imaged and processed using a free *in-house* (ESRF) software package, Fit2D, which visualises, integrates and allows cross-calibration of diffraction plots with standards downloaded from online databases of crystal structure (Hammersley, 1998). The diffraction pattern can be observed qualitatively as an image, or integrated to produce a graph of angle of scatter (2θ) vs. signal intensity (Figure 2.18). Changes within the diffraction pattern can give an indication of melting or presence of amorphous glass (loss of sharp lines and presence of diffuse blurred patches on the scan), and recrystallisation (a 'spotty' diffraction curve indicates reduction in number of crystals / crystal orientations and therefore likely growth by recrystallisation). Peaks on integrated plots are characteristic for each mineral (each peak represents diffraction from a separate lattice plane), allowing phases to be identified and changes caused by pressure and temperature variations to be tracked. As a rule, an increase in pressure will increase the 2θ angle of a peak, while an increase in temperature will reduce the angle.

To match peaks effectively requires the composition of the sample to be relatively simple - using a complex mixture of materials makes it difficult to identify phases. In initial experiments at ESRF we were unable to track temperature and pressure quantitatively using this method due to the complexity of compositions (Figure 2.18A.). During phase two of experiments, sample compositions were simplified in order to allow quantitative estimates of pressure and temperature during experiments (Figure 2.18 B.). MgO and gold peaks are both well constrained by a number of studies over pressures of 2-3GPa and temperatures of 0-2000K (Anderson, Isaak, and Yamamoto, 1989; Fei, Li, et al., 2004; Jamieson et al., 1982), which are the range of interest in our experiments. Polycrystalline Boron Nitride, as used for capsule material in some experiments, has also been fully characterised at a range of temperatures and

pressures (Datchi et al., 2007).

2.4.2 Scanning Electron Microscopy (SEM)

Imaging of samples is carried out in two-dimensions on cut and polished samples using Backscatter Electron imaging on a Scanning Electron Microscope. This is mostly carried out after 3D scanning as it is a destructive technique. The majority of work was carried out on the Philips XL30CP Scanning Electron Microscope of the Edinburgh Materials and Micro-Analysis Centre (EMMAC). The inbuilt PGT Spirit X-ray analysis system was used to give preliminary, semi-quantitative compositions and distinguish between phases. Additional electron microscopy work was carried out using the XL30 LaB^6 ESEM suite at Heriot Watt University, for quantitative analysis of hafnium-doped basalt preliminary work (chapter 4) using the Oxford Instruments X-max 80 EDX detector. Later analysis was carried out on the new Carl Zeiss SIGMA HD VP Field Emission SEM at Edinburgh University, with the Oxford AZtec ED X-ray analysis system (EDS).

Deformed samples were sectioned as shown in Figure 2.19 to show textures from a range of angles. Due to the nature of torque experiments, strain-rate and total strain varies from a minimum (in theory zero strain) at the sample centre to maximum at the edges. Traditional analysis of 2-D textures is carried out by a tangential cut (Figure 2.19c) as this gives a view of the textures at maximum strain and simplifies the deformation to simple shear. Further cuts were made to examine changes in texture due to a change in strain-rate across the sample. In theory this allows textures to be analysed at greatly reduced strain-rates by examining the sample centre.

Samples were mounted in epoxy resin, then dried under pressure for 2 days. Samples were ground by hand then machine-polished using 0.3μm alumina.

2-D images were used to make qualitative observations of textures. Quantitative analysis could also be carried out, for example examining melt pocket distribution, 2D orientation, and melt pocket diameters using ImageJ software (Abramoff et al., 2004) to enhance contrast and/or to binarise images. Binarised images were used to examine the effect of polishing on samples and estimating the amount of material lost to plucking (chapter 3).

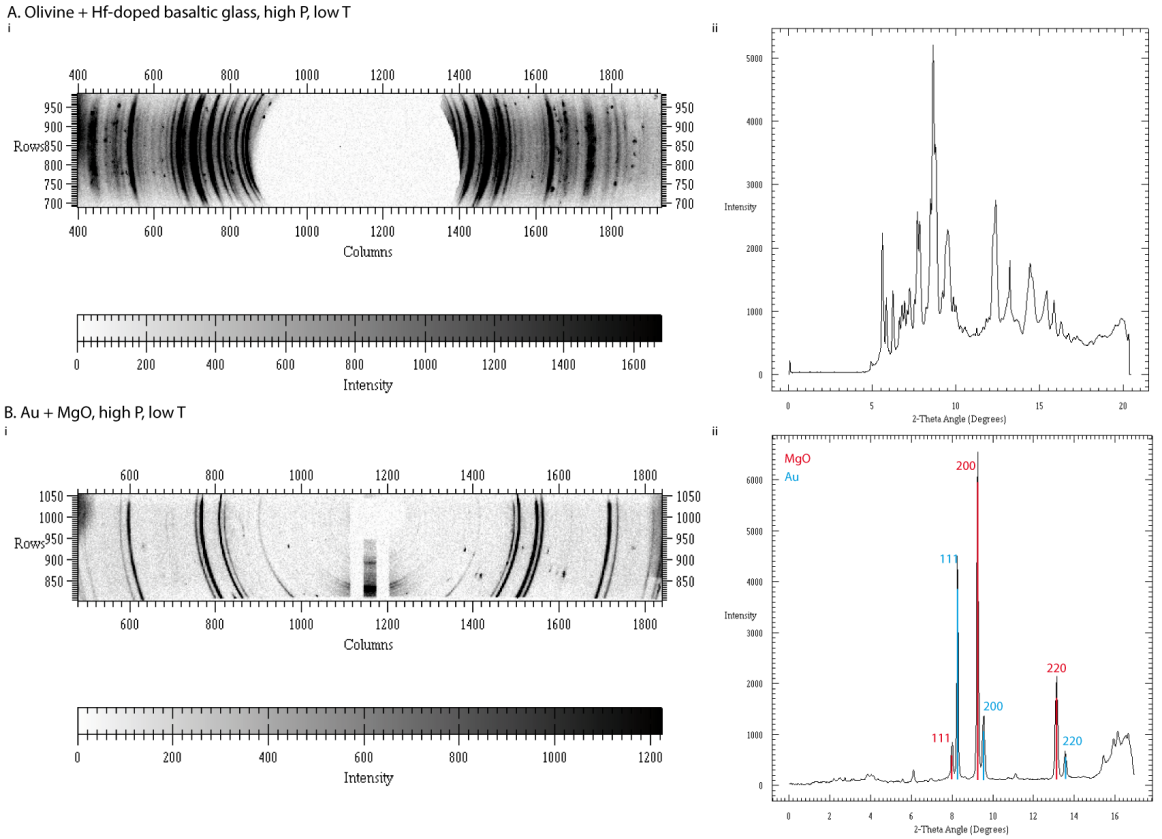

Figure 2.18: Examples of diffraction patterns produced at ESRF ID27 in phase 1 (A.) and phase 2 (B.) of experiments. In each case, the diffraction scan is shown on the left with accompanying greyscale-intensity key (this varies depending on the intensity of the pattern and can be rescaled to highlight weak peaks). A polycrystalline diffraction pattern is made up of concentric rings, but in this case the anvils of the press block the top and bottom of the pattern leaving a rectangular mid-section of crescents, which are symmetrical about the image centre. 'Rows' and 'Columns' are arbitrary spatial units from the imaging plate and intensity is a relative value. On the right is shown the integrated intensity-2θ plot created by Fit2D. The complexity of compositions in the first phase of experiments makes it impossible to identify individual peaks due to overlap of peaks for multiple phases present. In the second phase of experiments, compositions were simplified to allow peaks to be identified and indexed, which allows pressure and temperature to be roughly calibrated. Here, peaks have been labelled as MgO or gold, and individual lattices identified by Miller indices. This is carried out by matching peaks to existing standards.

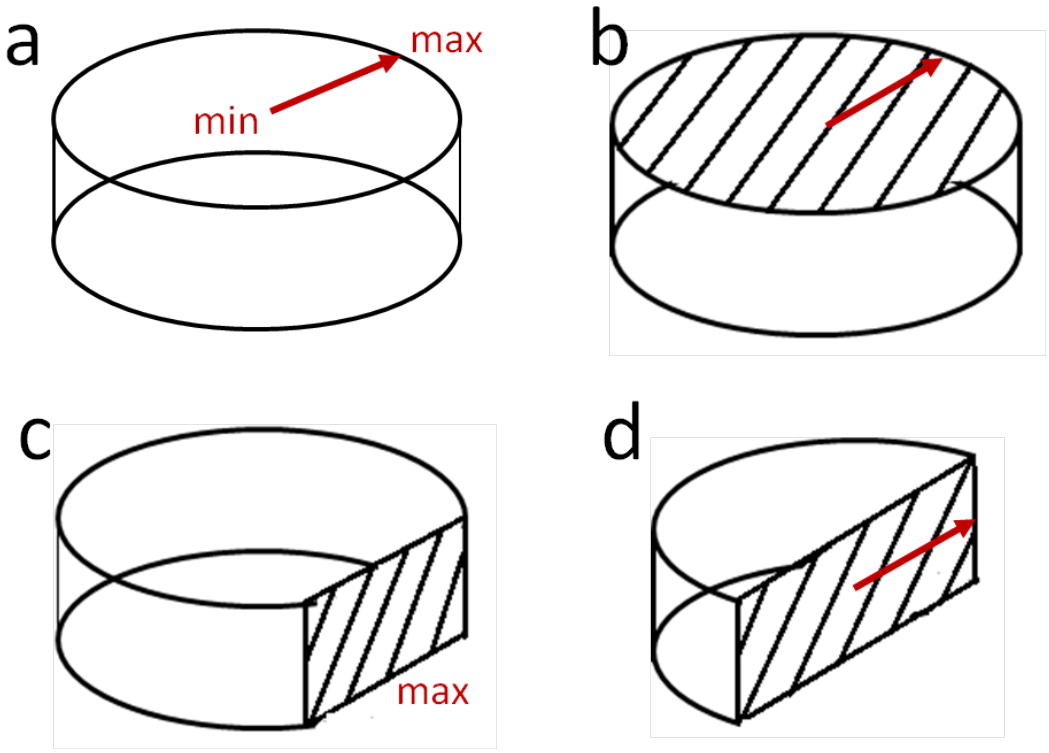

Figure 2.19: Orientation of sectioning used for scanning electron microscope imaging. a) original disk-shaped sample, diameter = 2mm. Red arrow indicates increase of strain from minimum at the centre (theoretically zero) to maximum at the edges of the sample. b) planar section, giving a large surface area for imaging and showing potential changes across the sample due to increase in strain. c) tangential cut, made to image textures at maximum strain only, essentially simplifying the system to simple shear. d) middle cross-section, cut to systematically image texture from minimum to maximum strain

2.4.3 Electron Probe Micro-Analysis (EPMA)

Fully Quantitative Analysis was carried out on a selection of samples using the CAMECA SX100 Electron Microprobe (Edinburgh Materials and Micro-Analysis Centre). This was to characterise the composition of the starting materials, as well as to test the extent to which diffusion takes place between differing phases. The equipment allows analysis of points and lines, as well as semi- or fully-quantiative element mapping of sample areas. This method is estimated to be accurate to 10ppm concentration (C. Hayward, pers. comm.).

An electron microprobe uses essentially the same system as an SEM, although the setup is optimised for quantitative sample analysis as opposed to imaging. As a beam of electrons hits the sample, samples emit characteristic X-rays that depend on their composition. The emitted X-rays are analysed and compared to a series of standards of known composition, which allows the composition of the sample to be quantified.

Sample preparation is similar to that required for SEM work. However, the system is more sensitive to relief, which can seriously affect accuracy of quantitative data, therefore often a regrind and polish is required to ensure the sample surface is of high enough quality to use for EPMA.

An example of data produced from EPMA analysis is shown in figure 2.20. Specific analyses and results are described in the relevant chapters.

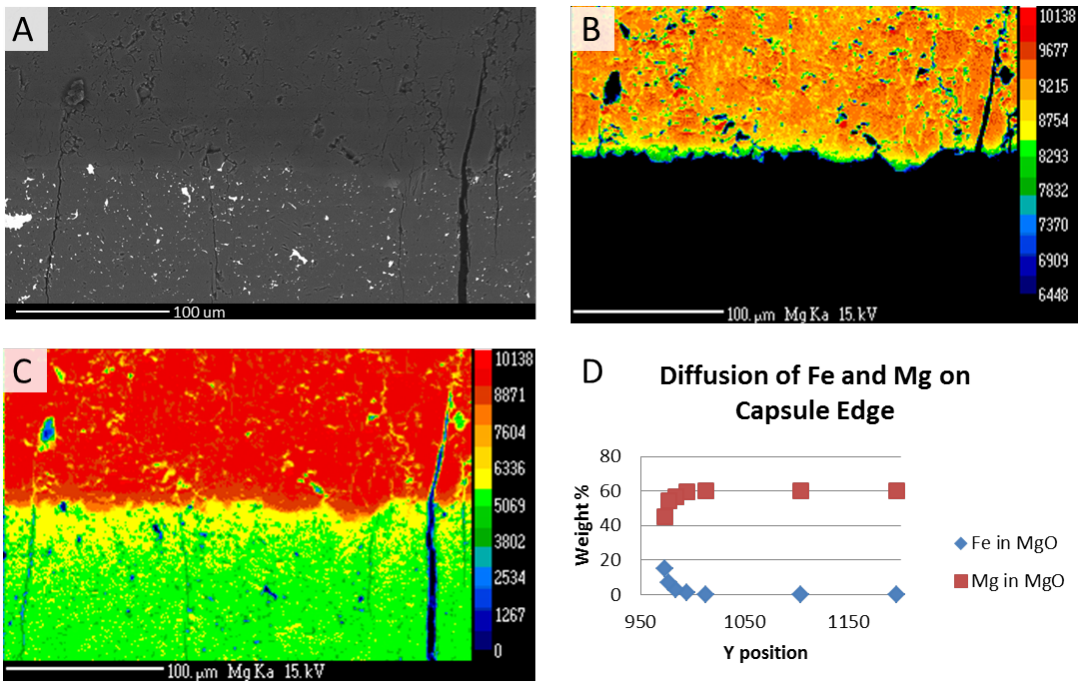

Figure 2.20: An example of quantitative analysis that can be carried out using Electron Probe Microanalysis. A) a backscatter image produced on the electron probe, used to choose points or lines for analysis, or in this case the location for an element map. Image shows the capsule (top) and sample edge (bottom) of sample FeOl1. B) semi-quantitative map showing relative concentrations of iron in A. C) semi-quantitative map showing relative concentrations of Mg in A. Quantitative maps can also be produced, but were not required in this case and take longer to scan. D) quantitative point analysis carried out on the MgO capsule closest to olivine. This combination of techniques was used to check for reactions taking place at the capsule edge.

2.4.4 Electron Backscatter Diffraction (EBSD)

The effect of deformation on the crystal structure and development of preferred orientation of olivine crystals in our experimental samples was examined by Electron Backscatter Diffraction. When a sample is bombarded with electrons in a scanning electron microscope, some backscattered electrons are scattered at low angles and are therefore diffracted by lattice planes within the sample. Some of these electrons will be scattered on a trajectory that satisfies Bragg's Law, leading to positive interference increasing electron intensity in these trajectories. This creates bands (in three dimensions cones) of positive and negative interference being produced from the sample that are characteristic of the structure and orientation of a crystalline material. An EBSD detector is situated at a low angle to the sample in order to detect these patterns, which are known as Electron Backscatter Patterns (EBSPs). Some structure can be directly interpreted from EBSP. For example, a band on an EBSP represents a lattice plane - as d-spacing within the lattice planes increase, the band width decreases. Areas where many bands intersect are major axis planes,and individual bands can be identified by miller indexing. A difference in orientation of the crystallographic structure will create a different position of the EBSP. EBSD software automatically indexes and orientates the crystals by comparing to a database of known crystal structures. The composition of the sample must therefore be known in order to carry out the analysis.

Sample preparation

For a good diffraction pattern to be imaged, pristine crystal lattices must be present within a few nanometres of the sample surface. In addition, the sample surface cannot have significant relief, as this can create shadows that hide local details and lead to mis-indexing. In addition to the standard polish for BSE imaging (see above), an additional mechanical-chemical polish of colloidal silica -SYTON (Fynn and Powell, 1979) is used to perfect the sample surface. The sample surface must also be completely free of dust and dirt before analysis takes place.

Output data

EBSD analysis can be made as points and lines, as for EPMA analysis, however the majority of data produced is in the form of a 2D Orientation Map (OM) of a chosen area of interest. The map contains orientation data for each pixel successfully analysed, and

can be colour coded according to overall orientation. This raw data can be processed in several different ways depending on the purpose of the analysis. Processing for this project was conducted using the EBSD processing software HKL-Channel5^{TM}, using a procedure for noise reduction and analysis developed by Elisabetta Mariani and Liverpool University. The process of noise removal must be carefully conducted to avoid leading to unrealistic grain growth or significant changes in shape caused by data extrapolation. This method is described in detail in Appendix A.1.1.

Data produced can be shown in a number of different formats, as shown below

- **Phase map** A 2D map showing distribution of different phases analysed.
- **Euler angle map** Orientation data can be colour coded by their Euler Angles. These are defined as the three successive orientations required to produce the orientation of a specific lattice plane from a fixed co-ordinate system within the sample. Maps can be coded by individual euler angles or a combination of all three (Figure 2.21C.).
- **Band contrast map** This image simply shows the quality of signal at each point - however, as this varies with crystal orientation and is particularly variable at grain boundaries, it can be used effectively to differentiate between grains within the sample area - better than a simple backscatter electron image. This data can be used to separate grains and conduct grain size analysis (Figure 2.21A.).
- **Mis-orientation maps** Misorientation is a measure of how much the orientation of an individual point varies from a selected reference point. One point is selected, and the map is colour coded by magnitude of deviation from that single point. This can be used, for example, to examine the extent and location of deformation within single crystals.
- **Grain boundary map** Grain boundaries are identified by a large mis-orientation value between neighbouring grains. It is possible to create a map of grain boundaries using Channel5 software, classifying boundaries of grains and sub-grains depending on the extent of mis-orientation (E. Mariani, pers. comm.) (Figure 2.21B.).
- **Pole figures** Data from the whole map or from sub-samples can be plotted onto pole figures (C5 Mambo) or inverse pole figures (C5 Tango), which can show if there is a preferred crystal orientation across the area scanned (Figure 2.22). It is important to note that initially every point scanned on the map will be input

as a data point - therefore larger crystal grains will skew results towards their orientation. If there is a large grain size variation, it is possible to plot only one point per crystal grain to improve analysis. Grain detection is carried out automatically using Channel5^{TM} and is reasonably reliable on a good quality dataset. Once grain separation has been carried out, it is also possible to filter grains according to size, and produce pole plots examining orientation of grains within a certain size range.

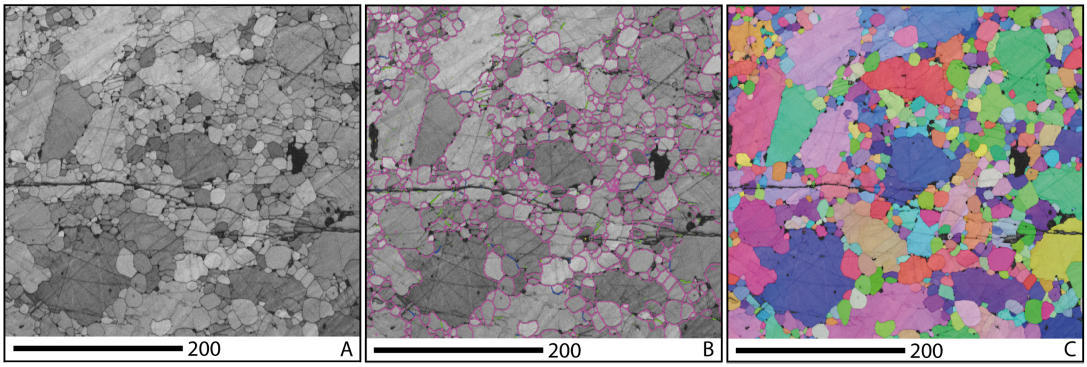

Figure 2.21: An example of the types of data map that can be produced by Electron Backscatter Diffraction. This is an example of a map made of an undeformed control experiment, FeOlPC5 (chapter 3) A. Band Contrast image, essentially portraying signal quality for each pixel mapped. B. Grain boundary map produced by highlighting boundaries between variations in orientation of a certain magnitude. Fuchsia >20°, Purple >15°, Blue >10°, lime green >5°, yellow >2°. C. Euler angle map: Map is colour coded according to variation in Euler angles. It is also possible to colour for each Euler angle individually.

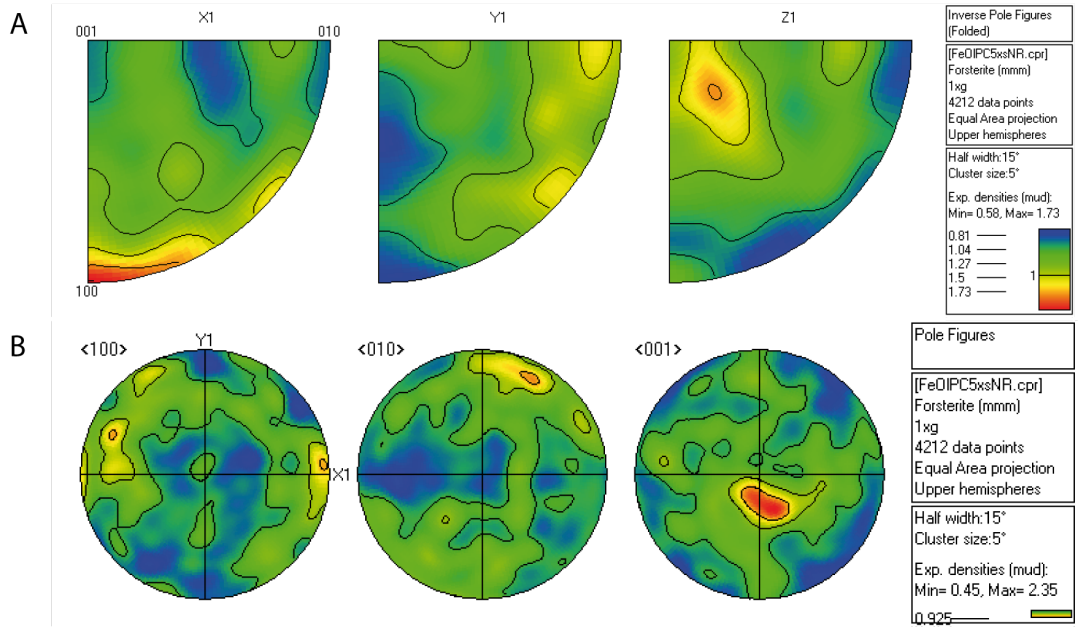

Figure 2.22: An example of the types of data plot that can be produced from EBSD data using Channel5 software. A. An inverse pole plot - the axes of the projection sphere are aligned with crystal directions. Axes of crystal lattices are plotted to show their alignment to a given reference orientation (e.g. stage orientation, or orientation of stress/compaction). The inverse pole figure can help visualise certain types of texture. B. A classic stereographic projection pole figure (one point per grain plotted). Three pole figures are drawn, each with a different orientation relative to the primary crystallographic axes.

CHAPTER 3

3D visualisation of core-forming melts

ABSTRACT

Deformation may significantly enhance permeability of small fractions of metallic melt in a solid silicate. This is an important factor in constraining processes of core formation, as a permeable network in solid silicate could have led to segregation of a core and mantle much earlier than previously thought, importantly long before the onset of a molten silicate 'Magma Ocean'. Few experiments examine effects of low strain-rate deformation at realistic conditions of core formation in small planetary bodies. In addition, 3D melt geometry and permeability is usually inferred indirectly from 2D textural analysis of polished sample slices. We conducted experiments on a synthetic solid olivine – liquid FeS system at extreme P-T conditions using the rotational Paris-Edinburgh Cell (roPEC), and analysed 3D melt geometry of quenched samples using micro- and nano-tomographic imaging. Deformation at strain-rates down to $10^{-6}s^{-1}$ aids grain boundary wetting and the formation of melt veins that appear to locally 'drain' certain sample areas. Results support theories of complex, multi-stage core formation in which pre-differentiated planetary bodies collided to form the Earth. These proto-cores may have sunk directly to the Earth's centre without re-equilibration with the mantle, which has major implications for the inferred geochemical composition of the lower mantle.

Author Contributions: Deformation experiments were conducted by G. D. Bromiley and Berg, in laboratories of S. Redfern, University of Cambridge. Hydrostatic experiments were conducted by Berg. CT scans at UoE were carried out by I.B. Butler and Berg. At University of Manchester, Berg carried out further CT scans including nanoCT with the assistance of R. Bradley and K. Dobson. FIB cutting for nano-CT was carried out by Mungo Frost, CSEC. EBSD was carried out at the University of Liverpool with the help of D. Tatham and E. Mariani, who also assisted with interpretation of results. LB modelling was carried out by J. Carr from University of Manchester. Skeletonisation software courtesy of Zhu et al., University of Maryland.

3.1 Introduction

3.1.1 Previous experiments in the metal-olivine system

In terrestrial bodies in the early solar system, metallic core forming material would have melted at significantly lower temperatures (1213-1233K) than surrounding silicate mantle (1450-1850K) (Sahijpal et al., 2007) giving a potentially substantial time-frame in which metals were in liquid form, surrounded by solid silicate material. Constraining the interconnectivity and permeability of such melts within a solid silicate matrix is therefore key to understanding the processes, timing and chronology of core formation in the early solar system.

Over the last two decades, a number of petrologic experiments have been conducted at various pressures, temperatures, compositions and timescales to determine the permeability of metallic melts (Fe ±Si, Ni, S, O) in a pure olivine or peridotite matrix (Shannon and Agee, 1996; Shi et al., 2013; Terasaki et al., 2007).

3D permeability has been classically estimated from 2D quench textures quantitatively using dihedral angle measurements (VonBargen and Waff, 1986). A dihedral angle of >60° means the system is impermeable below a certain threshold melt fraction (known as the pinch-off melt fraction), which increases with increasing dihedral angle. A value of <60° theoretically implies melt remains interconnected until the solid is completely drained.

The vast majority of studies on olivine solid- metallic liquid systems found that, when left to anneal to textural equilibrium, dihedral angles are consistently >60° (Shannon and Agee, 1996; Terasaki et al., 2005), with suggested values of the pinch-off melt fraction ranging from 5-40%, far greater than the value required to reproduce mantle compositions (Minarik et al., 1996). On the basis of these experimental studies, the general consensus is that the silicate portion of the early Earth must have been at least partly molten for the Earth to differentiate efficiently, giving rise to the 'Deep Magma Ocean Model' in which denser metal droplets drift to the bottom of a largely liquid silicate upper mantle (Ringwood, 1979).

As described in detail in the literature review section 1.2.1, problems have been encountered reconciling geochemical models of magma ocean core formation and the present-day composition of the Earth's mantle (Halliday, 2013). In addition, evidence from meteorites suggests that small planetary bodies such as asteroids are likely to be differentiated, making it harder to justify the sustained high temperatures required for magma ocean conditions (Taylor et al., 1993). These discoveries led to renewed investigation of the potential for percolative core formation at lower temperatures, before the onset of silicate melting (Bruhn et al., 2000).

3.1.2 Deformation-enhanced permeability of metallic melts

Aforementioned experimental work has been restricted solely to high P-T work in hydrostatic conditions. However, continuous bombardment during ongoing accretion and vigorous convection in bodies hot enough to melt their metallic component is likely to have resulted in a very dynamic, continually deforming environment in terrestrial bodies (Rushmer, Petford, et al., 2005), precluding the development of textural equilibrium. A growing number of studies have since been conducted in dynamic deforming systems. Experimental textures indicate that non-uniaxial stresses have been shown to change melt geometry significiantly and lead to grain boundary wetting, creating interconnected melt networks where melt remained isolated in a static system (Bruhn et al., 2000; Groebner and Kohstedt, 2006; Hustoft and Kohlstedt, 2006; Rushmer, Petford, et al., 2005). In a deforming system, differential stress could have a significant effect on melt permeability. In this case melt migration should continue to take place as long as differential stress acting to force melt along grain boundaries is greater than the effect of interfacial tension, acting to isolate melt pockets at triple junctions (Groebner and Kohstedt, 2006). The pinch-off melt fraction in a dynamic deforming system is therefore likely to be much reduced from that seen in samples in textural equilibrium (Hustoft and Kohlstedt, 2006), and has been proposed as an alternative / additional mechanism for core formation to take place before the onset of silicate melting.

However, due to limitations in experimental equipment, few deformation experiments have been conducted at high confining pressures appropriate to core formation conditions and it is disputed whether this effect would be an efficient mechanism in planetary interiors. Previous experiments have been limited in applicability due to large strain values (Bruhn et al., 2000), unrealistically high melt fractions (Rushmer, Petford, et al., 2005), and low confining pressures (Hustoft and Kohlstedt, 2006). The most recent published work by Walte et al. (2011) is the first study to be carried out at realistically high P-T and over a larger range of strain-rates. Their experiments appear to reveal a significant change in textures at low strain-rates, suggesting that differential stress becomes too low to create interconnected networks between small melt pockets. However, their study is heavily reliant on analogue experiments and the experimental geometry of axial compression may not encourage melt segregation.

Deformation-assisted percolation needs to be investigated more thoroughly over a wider range of strain-rates and durations and under conditions more applicable to core segregation in terrestrial bodies, in order to improve our understanding of this mechanism.

3.1.3 The importance of 3D visualisation

The majority of previous studies have relied on dihedral angle measurements to extrapolate from textures observed in 2D to estimates of 3D connectivity and permeability. Initial theory

of dihedral angle measurements assumes that crystals are cubic (maximum symmetry) and that the sample is texturally equilibrated (VonBargen and Waff, 1986). Studies have shown that olivine-melt systems take >25 hours annealing at high temperature and pressure to reach a state close to textural equilibrium (Bagdassarov, Golabek, et al., 2009).

Non-hydrostatic stress precludes the attainment of textural equilibrium, and deformed experimental samples are shown to be texturally heterogeneous, meaning dihedral angles cannot be used to predict 3D melt geometry (Groebner and Kohstedt, 2006). However, permeability and connectivity of samples is in essence a 3D geometric feature, therefore the ability to characterise melt geometry in three dimensions is crucial to constraining these processes further.

Studies have used different methods to extrapolate to 3D melt geometry in deformed samples, beyond qualitative interpretation of 2D melt textures: Samples can be cut into orthogonal sections (see methods section 2.4.2), giving a pseudo-three dimensional view of the sample interior (King et al., 2010). Serial sectioning techniques can be used to examine 3D geometry (Bruhn et al., 2000; Garapic et al., 2013) but this technique is destructive and time-consuming, meaning the sampled volume is often small, and a reduced resolution in the direction of polish can create a skewed 3D geometry with further interpolation required to estimate 3D geometry. The advancement of CT for use in the geosciences provides a non-destructive method to visualise the interior of partially molten samples directly using laboratory and synchrotron technologies. 3D reconstructions of iron melts in solid olivine systems have been conducted for hydrostatic systems (Watson and Roberts, 2011) and more recently in very high strain/ strain-rate deformation experiments (Wang, Lesher, et al., 2011), although textural interpretation is limited, as the fine features observed are still at the limits of resolution capabilities of standard micro-CT.

There remains a gap in data of deformation melt networks visualised directly in three dimensions, at high resolution, to allow full 3D characterisation of melt network geometry and interconnectivity.

3.1.4 Aims and objectives of work

Taking into account the gaps in knowledge described above, the aims of this chapter of work were therefore to

- use the rotational Paris-Edinburgh cell (described in Methods 2.2.1) to carry out controlled, very low strain-rate torsional deformation experiments under realistic high P-T conditions for core formation in planetesimals.
- visualise resulting melt textures using traditional 2D micro-analysis techniques, as well as high resolution micro- and nano-CT to visualise melt in three dimensions.

- evaluate analysis techniques that can be used to characterise melt interconnectivity and permeability using both 2D and 3D textural data.
- investigate techniques to extrapolate results to conditions of planetary interiors and evaluate potential implications for models of core formation in the early solar system.

3.2 Methods: Experimental techniques and tomographic analysis

3.2.1 Experimental techniques

Experimental samples were prepared from powdered gem-quality inclusion free olivine (Fo_{92}) and powdered troillite (FeS, making up 4 % by volume of the total mixture) and combined by grinding under ethanol for at least 3 hours to homogenise, creating a fine grained (<30μm) starting mixture. Early generation experiments (FeOlPC1-6, FeOl1, FeOlcam1, FeOlcam2) were carried out using a starting mixture of Olivine + 4vol% Fe_3S, using a combination of Fe metal and troillite to make up the metal melt composition.This initial starting material was of a more variable grain size.

Deformation experiments were carried out on the rotational Paris Edinburgh Cell (Figure 2) at the Dept. Earth Sciences, University of Cambridge and at the European Synchrotron Research Facility (ESRF), Grenoble, France. This device allows controlled deformation at simultaneous high pressures and temperatures (Bromiley et al., 2009), with capsules and gasket design as described in section 2.2. In all experiments, pressure was increased at a rate of 5 bars /min to the final run pressure. Once pressure had stabilized, temperature was then increased at a rate of 10-100°/min to the final run temperature. Samples were left to anneal for at least 2 hours, to relieve sample strain accumulated during initial compression. Samples were then deformed in torsion by rotation of the upper anvil at controlled strain-rates. Initial calibration of pressure and temperature was carried out by *in-situ* X-ray diffraction of MgO and Pt capsules at beamline ID27 (Bromiley et al., 2009). Offline experiments carried out here used these calibrations, applying the same power and pump pressure values, within an error range of ±1kbar for pressure, ±50°C for temperature.

Sample deformation in off-line experiments was measured during experiments by a digital measure of anvil rotation, and confirmed after the experiments had been recovered by examination of internal platinum strain markers. Run conditions for all experiments are given in Table **??**a. A comparison of strain-rate and total strain in our experiments compared to those of previous studies is shown in Figure 3.1. The majority of studies are at much greater strains and strain-rates. The most comparable study is that of Walte et al. (2011), which is also conducted at high pressures (3GPa). It is important to note, however, that the Walte study

was carried out under uniaxial compression, meaning the sample is deformed under pure shear, while our torsional equipment allows us to examine the effects of simple shear on the system.

Control experiments were performed under hydrostatic conditions using end-loaded piston-cylinder apparatus and a high-temperature talc-pyrex-graphite assembly. The starting mix was loaded into 4mm o.d. graphite capsules which were inserted into alumina sleeves and then loaded into the sample assembly. Experiments were pressurised and then slowly heated (100°/min) to the final run temperature. Temperature was measured using an R-type thermocouple adjacent to the capsule, and both temperature and pressure were monitored and maintained throughout the experiment. Samples were quenched by switching off power to the heating circuit whilst maintaining run pressure (quench rates >100°/s). Run conditions are given in Table **??**b.

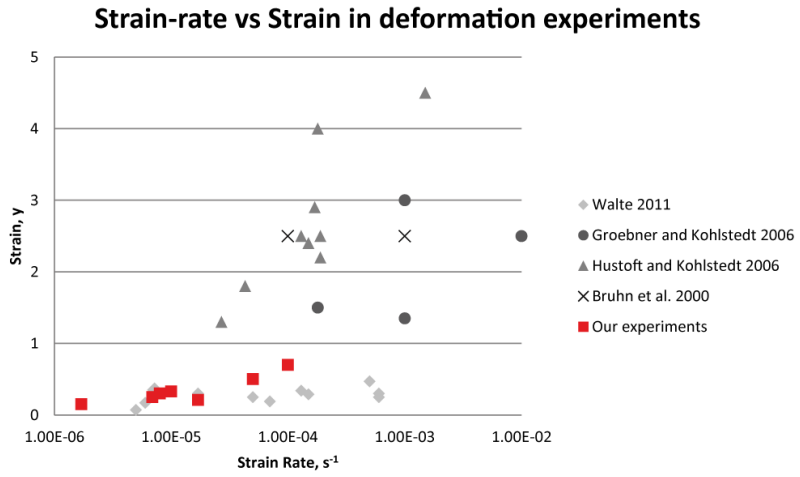

Figure 3.1: A comparison of strain-rate and strain of previous comparable deformation experiments. Stress and strain-rates of our experiments are comparable to those of Walte et al. (2011) (also the only other study to be conducted at high confining pressures), but our lowest strain-rate experiment has a strain-rate of $1x10^{-6}s^{-1}$, almost an order of magnitude lower than the lowest strain-rate experiment of Walte et al. (2011).

3.2.2 Analytical techniques

X-ray tomography

X-ray CT was used to provide a 3D model of melt structures in the recovered samples, in order to examine the 3D network system and support conclusions made by more traditional 2D textural analysis methods. The metal-melt, solid olivine system is particularly suited to CT

A.	Sample	Composition	T/°C	T $_{ann}$ / min	Tomographic Analyses
	FeOlPC1	Ol + 4 vol% Fe3S	1050	120	
	FeOlPC2	Ol + 4 vol% Fe3S	1100	480	
	FeOlPC3	Ol + 4 vol% Fe3S	1100	1710	
	FeOlPC4	Ol + 4 vol% Fe3S	1450	2820	Micro-CT (2µm)
	FeOlPC5	Ol + 4 vol% Fe3S	1300	1650	Micro-CT (2µm)
	FeOlPC6	Ol + 4 vol% Fe3S	1100	2790	
	FeOlPC8	Ol + 4 vol% Fe3S	1350	2880	Micro-CT (2µm) nano-CT (0.13µm)

B.	Sample	Composition	T/°C	T_{ann} / min	Tomographic Analyses	T_{def} / min	rot / °	γ	ε / s^{-1}
	FeOl3	Ol + 4 vol% Fe3S	1100	120		720	40	0.3	8.0 x 10 -6
	FeOl-Cam1	Ol + 4 vol% Fe3S	1400	120	Micro-CT (2µm)	180	60	0.5	5.0 x 10 -5
	FeOl-Cam2	Ol + 4 vol% Fe3S	1600	120		120	80	0.7	1.0 x 10 -4
	Cam3-FeOl1	Ol + 5 vol% FeS	1450	120	Micro-CT (2µm) Nano-CT (0.13µm) Ultra-nano CT (0.05µm)	1420	53	0.15	1.7 x 10-6
	Cam3-FeOl2	Ol + 5 vol% FeS	1450	120	Micro-CT (2µm)	200	75	0.21	1.7 x 10-5
	Cam3-FeOl3	Ol + 5 vol% FeS	1450	120	Versa Micro-CT (1µm) Nano-CT (0.13µm)	530	119	0.33	1.0 x 10-5
	Cam3-FeOl4	Ol + 5 vol% FeS	1450	120	Versa Micro-CT (1µm)	605	90	0.25	6.9 x 10 -6

Table 3.1: Table of samples and run conditions including details of tomographic scans carried out. A. Hydrostatic control experiments. B. Dynamic deformation experiments. T_{ann} = anneal time, T_{def} = deformation time, rot = total degrees rotated

analysis, because of its simple 2-phase nature and clear difference in density and composition of the two phases leading to a good contrast to distinguish the two materials.

Preliminary scans were made using the X-ray CT system built in-house within the Experimental Geosciences Facility, School of Geosciences. 1000 projections were made on a 360° rotation of samples, at 100kV, averaging three 1 second exposures at each projection. A copper foil filter was used to reduce beam hardening artefacts. Cone beam data was reconstructed using University of Ghent's Octopus software to produce 3D images at ~2µm voxel size.

Additional scans were performed at the Manchester X-ray Imaging Facility (MXIF) on the Zeiss Xradia Versa scanner. 2001 projections were made over an 360° rotation of the sample, at 80kV and 35 second exposure. A Low Energy filter (LE# 1) was used to reduce beam hardening artefacts. Samples were cut to 1x1mm matchsticks to maximize resolution. Slices were reconstructed using the Zeiss Xradia XM reconstructor software to produce 3D images at 1±0.2 µm voxel size.

Nano-tomographic scans were carried out on the Zeiss Xradia Ultra-810 equipment at MXIF, in which a sample was scanned at 0.13µm voxel resolution with a 65µm field of view. An additional scan of 50nm voxel size was carried out on a 15µm sub-section of deformed sample FeOl1. Table **??** gives a summary of tomographic scans carried out on each sample.

Image processing and segmentation

The reconstructed greyscale slices required edge-preserving filtering to reduce noise and to aid segmentation. A non-local means filter was applied to nano-scan reconstructions using VSG Avizo Fire^{TM} software (Figure 3.16). Larger volume scans could not be filtered using this method due computational limitations related to the size of dataset. These were filtered by an anisotropic diffusion filter, which is an edge-preserving filter based on a diffusion smoothing method which stops smoothing occurring across areas of the image where the greyscale gradient is above a defined threshold (Perona and Malik, 1990).

Image segmentation was carried out by a combination of techniques depending on the quality of the datasets, the purpose of the segmentation, and which software was used for analysis. These segmented datasets were used for volume rendering and a number of image analysis techniques in order to evaluate melt distribution, geometry and interconnectivity. These will be described in detail where appropriate in the results section.

SEM analysis

2D analysis on cut and polished sections was used in order to ground-truth interpretation of reconstructed tomographic slices. Samples were cut in three orientations to allow examination of textures: Two perpendicular cross-sections and a tangential slice to view an area affected

by pure shear of known orientation (see methods section 2.4.2). Qualitative 2-dimensional descriptions and grain size measurements were carried out using a Philips XL30CP Scanning Electron Microscope at the Edinburgh Materials and Micro-Analysis Centre, School of GeoSciences, University of Edinburgh. Backscatter Electron (BSE) images were used as well as the inbuilt PGT Spirit X-ray analysis system, in order to distinguish between phases during initial analysis.

EPMA compositional analysis

Quantitative analysis and element mapping was carried out on the CAMECA SX100 Electron Microprobe (Edinburgh Materials and Micro-Analysis Centre) to determine diffusion of iron or other elements between metal and silicate components during experiments. Element maps of iron, sulfur, silicon, magnesium, platinum and titanium were produced, as well as a series of manual points at the edges and centers of olivine grains close to large iron sulfide melt pockets and pure iron crystals. Elements analyzed and their respective standards were Mg, Al on Spinel, Si, Ca on Wollastonite, Fe on Fayalite, S on Pyrite, Ti on Rutile, Cr on Pure Cr, Mn on Pure Mn, Ni on Pure Ni, with a beam current of 10nA, voltage of 15keV and a beam size of 2.2 μm.

EBSD structural analysis of olivine crystals

Electron Backscatter Diffraction Analysis was carried out on polished sections of quenched samples in order to assess the effect of low degrees of deformation on olivine crystal preferred orientation and deformation of individual crystals. Samples previously prepared for SEM analysis were repolished using SYTON colloidal silica polish to perfect the sample surface. Analysis was conducted at the University of Liverpool using the CamScan X500 CrystalProbe FEG-SEM, at 20keV accelerating voltage, 40nA beam current. Error of measurements is $\pm$ 0.5°. The match unit used was the HKL Forsterite unit (Forsteri.cry), where unit cells were given as a= 4.7560, b=10.2070, c=5.9800 (i.e. b>c>a), equating the b axis to {001}. Maps were produced at a step size of 2μm.

3.3 Results

3.3.1 Observations of textures in two dimensions

Undeformed samples exhibit textures of evenly distributed, isolated melt pockets of similar size, which pinch out at high angles at grain boundary triple junctions (Figure 3.2). The 2D texture suggests melt is isolated and trapped at triple junctions, and dihedral angle analysis is in agreement with previous studies showing that dihedral angle is consistently >60° on average

(Shannon and Agee, 1996) and that increasing experimental duration leads to a more evenly distributed melt texture approaching textural equilibrium (Bagdassarov, Golabek, et al., 2009; Berg, 2010, see section 2.2.3).

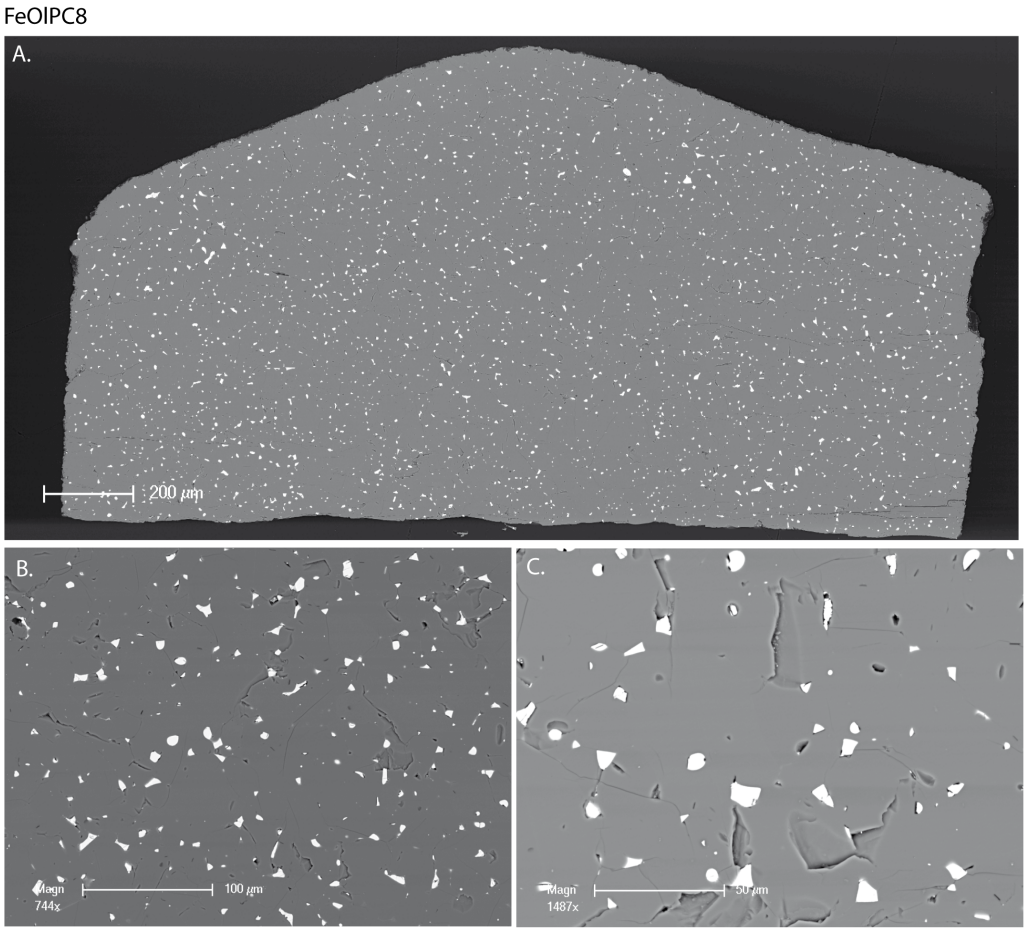

Figure 3.2: Backscattered Electron images of undeformed sample FeOlPC8 showing homogeneous melt distribution and melt pockets (white) at grain boundary triple junctions. Spherical melt pockets are also present in the middle of olivine grains (grey) suggesting grain growth during annealing has enveloped melt trapping it in crystal interiors.

We observe a distinct change in texture in deformed samples, although those observed are significantly different across the three samples cut for SEM analysis (Figure 3.3). Melt is generally more finely distributed across smaller melt pockets, which are not limited to grain boundary triple junctions. Melt veins of a range of sizes and extents are also present in each sample and melt is seen wetting grain boundaries in thin (sometimes <0.1 µm) sheets. These fine sheets are seen to connect larger melt pockets across multiple olivine grains. Melt distribution is more variable across the sample, with areas of significant melt accumulation, as

well as areas that are relatively 'drained' of melt populated with very fine near-spherical melt pockets (Figure 3.4). This suggests a localised redistribution of melt into melt-rich and melt-poor zones is taking place. Three orthogonal cuts show the effect of deformation at different orientations within the sample. Tangential cuts are traditionally used in torsional experiments as they remove the complexity of rotational strain and essentially show the effect of simple shear on the sample. Planar and cross-sectional sections allow a view over a larger portion of the sample, and represent a change from maximum shear at the edges, to (theoretically) zero shear stress/ strain in the centre, therefore allowing observation of changes with decreasing strain-rate. Qualitatively, there does not appear to be a systematic change in melt textures, or frequency of interconnected melt veins across sections, except for an area within 30μm of the capsule edge which has an anomalous texture due to reaction with MgO (see section 3.2.2) - this area was avoided for further analysis.

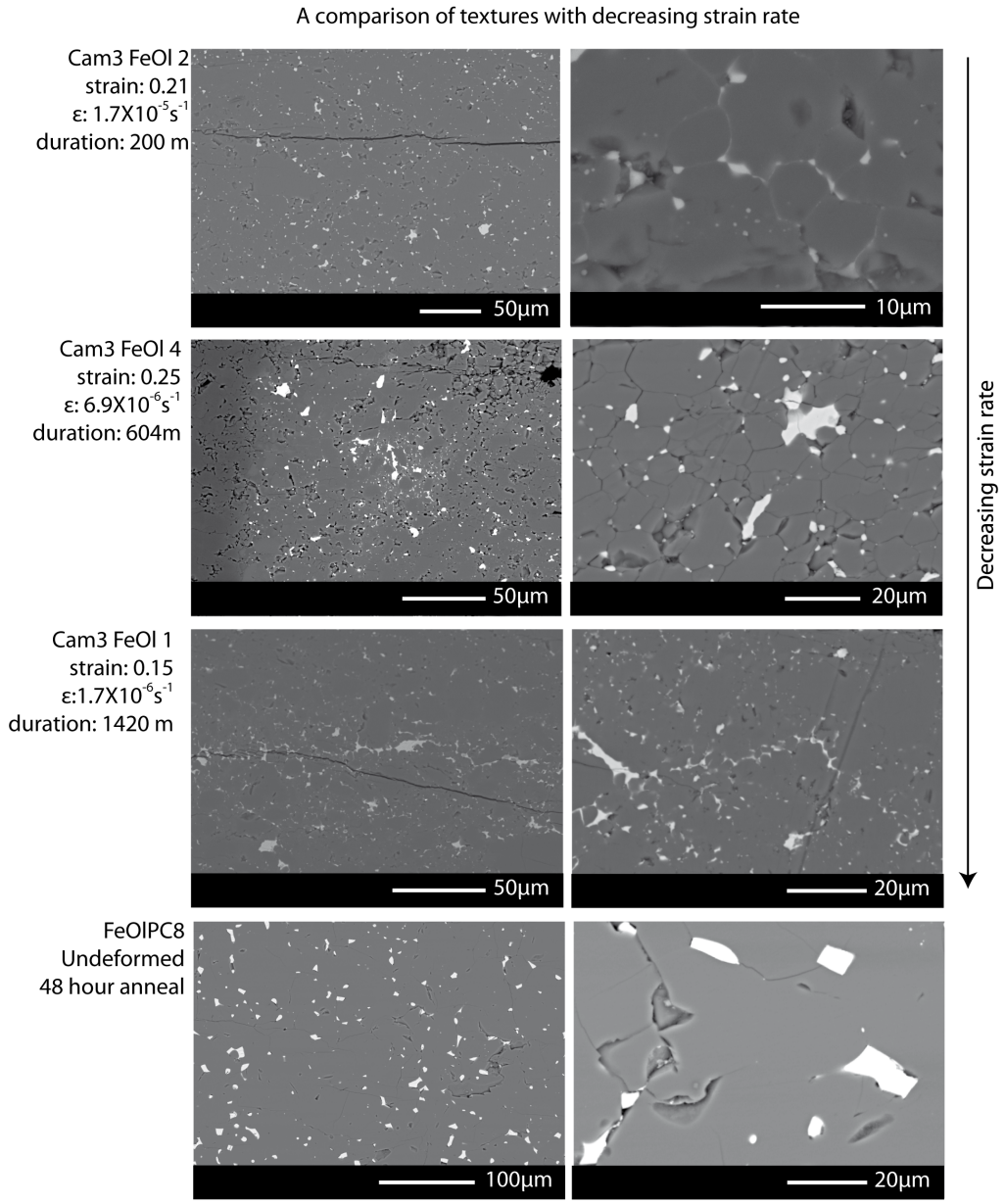

Figure 3.3: Examples of texture across samples with varying strain-rate. Previous studies suggest strain-rate affects the ability of FeS melt to produce melt networks and become interconnected. However, we do not see a clear correlation of textures and strain-rates, or even total strain. Instead the experimental duration has the greatest influence on textures in our experiments.

On tangential and mid-section cuts it is possible to see that large melt accumulations, where present, are aligned sub-horizontally, i.e. sub-parallel to the direction of maximum shear stress. The exact orientation of these melt accumulations does appear to vary from the edges to

the centre of the sample. The largest melt vein is observed on a planar cut within FeOl1, which is seen to be interconnected over >300μm in length, 100μm width, on this 2D plane alone.

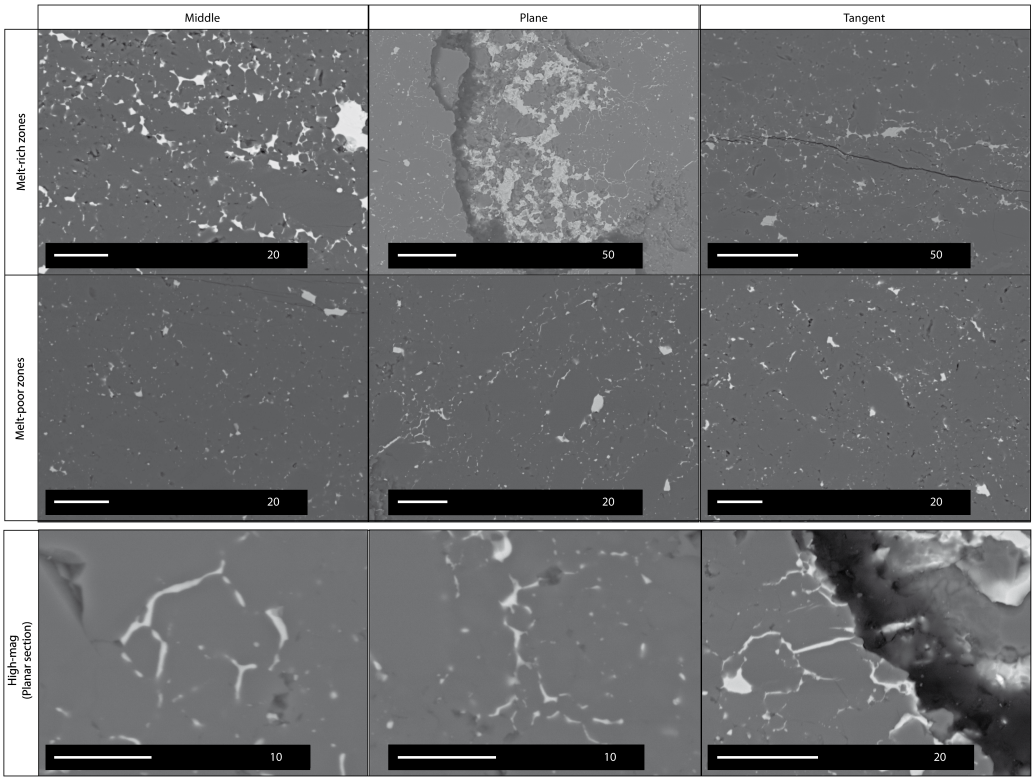

Figure 3.4: Examples of textures developed in sample FeOl1, our longest duration, lowest strain-rate sample (24hours under strain, $10^{-6}s^{-1}$, deformed to ~90° in torque). Examples of melt rich veins and relatively drained areas are shown in middle, planar and tangential cuts. The lower row of images shows high magnification examples of wetted olivine grain boundaries with melt sheets 1 μm or less. The bottom right image is of melt veins close to a larger melt vein (see planar melt-rich zone) and exhibits small melt filled fractures within olivine crystals. These only develop close to the largest melt accumulations. The large crack associated with the very large melt accumulation is most likely a post-quench decompression feature localised around the melt vein due to metal being softer than surrounding olivine.

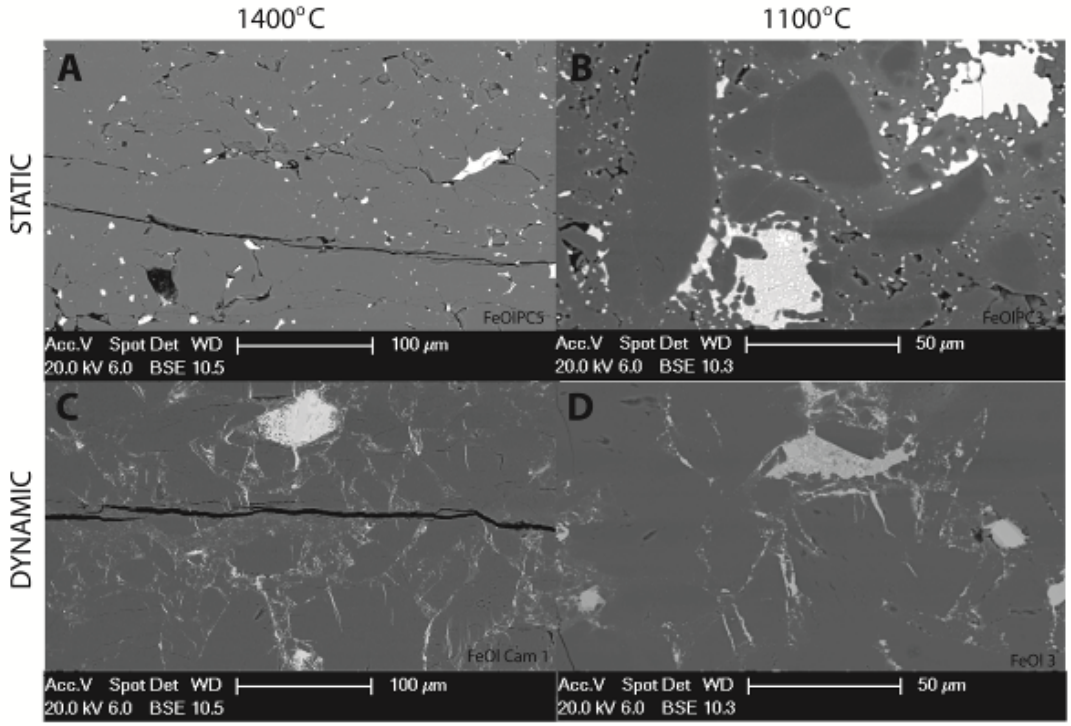

Figure 3.5: Examples of textures from first generation experiments carried out on starting mixtures of olivine + 5 vol%Fe_3S with a more variable starting grain size (Berg, 2010). Conditions are as follows: A. static 1300°C 1650m duration, B. static, 1100°C, 1710m duration, C. deformed, 1400°C, 180m duration, ($5x10^{-5}s^{-1}$) D. deformed, 1100°C, 720m duration ($8x10^{-6}s^{-1}$). Melt pocket size is variable in both static and deformed samples. See text for discussion.

The described features are significantly more widespread and clearly developed in our longest duration, lowest strain-rate experiment. Figure 3.4 shows examples of melt textures within FeOl1. Although melt veins are present in each of the deformed samples, they are not widespread in the sections cut of FeOl2 and FeOl4 (Figure 3.3). Although melt is more finely distributed in these samples, melt is only rarely seen to wet grain boundaries.

A distinct difference can also be seen in the textures developed in our first generation preliminary samples (Figure 3.5, Berg, 2010). The starting mixture of these experimental samples had a coarser, more variable grain size (<5μm - >100μm diameter), which may have affected melt distribution, both in static and deformed samples. There is a more variable size distribution of melt pockets in static samples, which is thought to be due to a heterogeneous starting grain size of Fe_3S. In deformed samples, olivine crystals appear to be damaged internally, with widespread melt-filled cracks entering single olivine grains. This is inferred to be due to hydro-fracturing of grains, and commonly occurs close to larger melt pockets. This may be caused by fluid overpressure caused by expansion of the FeS on melting. The process of hydro-fracturing does not necessarily promote interconnectivity of melt, and complicates the processes observed in samples. In addition, the larger initial melt pocket variation has made it more difficult to analyse early samples for melt distribution changes. Therefore second generation samples were produced with a more homogeneous starting FeS/olivine distribution and smaller grain size (starting grain size generally in the range of ~20-30μm in diameter). The resulting textures show far less evidence of hydro-fracturing grains, and more wetting of grain boundaries. Fractured olivine grains are still observed in some areas where a large amount of melt has accumulated (e.g. at the edges of the large melt vein observed in FeOl1, Figure 3.4).

An important feature in early generation samples is the use of Fe_3S for melt composition. This composition is more realistic as a starting point for early planetesimals (McCoy et al., 2006). Runs at 1100°C (Figure 3.5 B,D) show that exsolution occurs at sub-liquidus temperatures, and interconnected networks can form even below the Fe_3S liquidus. This also shows networks form at a liquid proportion of significantly less than 5vol%, as a significant proportion of Fe_3S remains trapped as solid Fe. The eutectic composition of FeS was chosen to reduce complexities introduced by this process, to make the system more comparable to previous studies, and ensure a 2-phase system to simplify analysis of features in CT.

3.3.2 Quantitative 2D analysis

To support the qualitative observations made from BSE imaging, some 2D image analysis has been carried out on these quenched surfaces. Analysis has been carried out in order to

- Evaluate the effect of annealing time / experimental duration on the quality of sample polish and therefore the reliability of textural observations from polished sections in two-dimensions.

- Analyse two-dimensional particle shape and area, for comparison to previous studies that have concentrated on 2D techniques, and in order to compare these analyses with 3D information gained from X-ray tomographic techniques.
- Assess development of a fabric of aligned melt and olivine grains

The main advantage to using two-dimensional analysis is the extremely high resolution available to image features at very high magnification.

Plucking analysis of deformed samples

Differences in texture observed in experimental samples of different experimental duration may be partly due to the difficulties of creating a well-polished slice of quenched samples that have only annealed for a short time. FeS metal is soft relative to olivine and therefore the polishing process can lead to this phase being removed preferentially during sample preparation. The process of polishing can also pluck out whole olivine grains, a process which may be enhanced if individual grain boundaries are wetted by a softer melt. To test the extent of plucking within samples, image analysis was carried out on 2D polished sections using ImageJ software (Abramoff et al., 2004). Figure 3.6 shows this process: For each cut made, 10 images of similar resolution were selected. Images have been chosen to reflect the overall texture of the sample, but to avoid large cracks created by decompression (e.g. Ai). A simple global thresholding was used to create two binarised images, to segment areas of FeS melt (Aii), and voids (Aiii). The ImageJ Measure tool was then used to give a % of total area covered by melts and voids respectively.

The amount of melt in both FeOl2, and FeOl4 is significantly lower than expected to be present, while the area of voids is very large, suggesting significant plucking of FeS relative to olivine may have taken place. FeOl1, the longest duration experiment, has the highest quality polish with only a small % of voids. The improved polish of FeOl1 could be due to longer annealing time making the sample more cohesive, although other factors may play a role, such as the exact polishing process, or the speed of depressurisation changing the extent of decompression features.

The % of melt within FeOl1 slices studied also varies significantly more than in FeOl2 and FeOl4, however, suggesting there may be a true variation in melt distribution which is not seen in other samples. Additional 2D and 3D quantitative analysis of melt distribution, alignment and shape factors do suggest that there is a true difference in textures between the samples analysed, which may also be due to experimental duration affecting the development of deformation textures and therefore melt connectivity. The analysis does show that sample preparation for SEM analysis could affect textural interpretation, and is another reason to carry out tomography to examine sample interiors without the need for grinding or polishing.

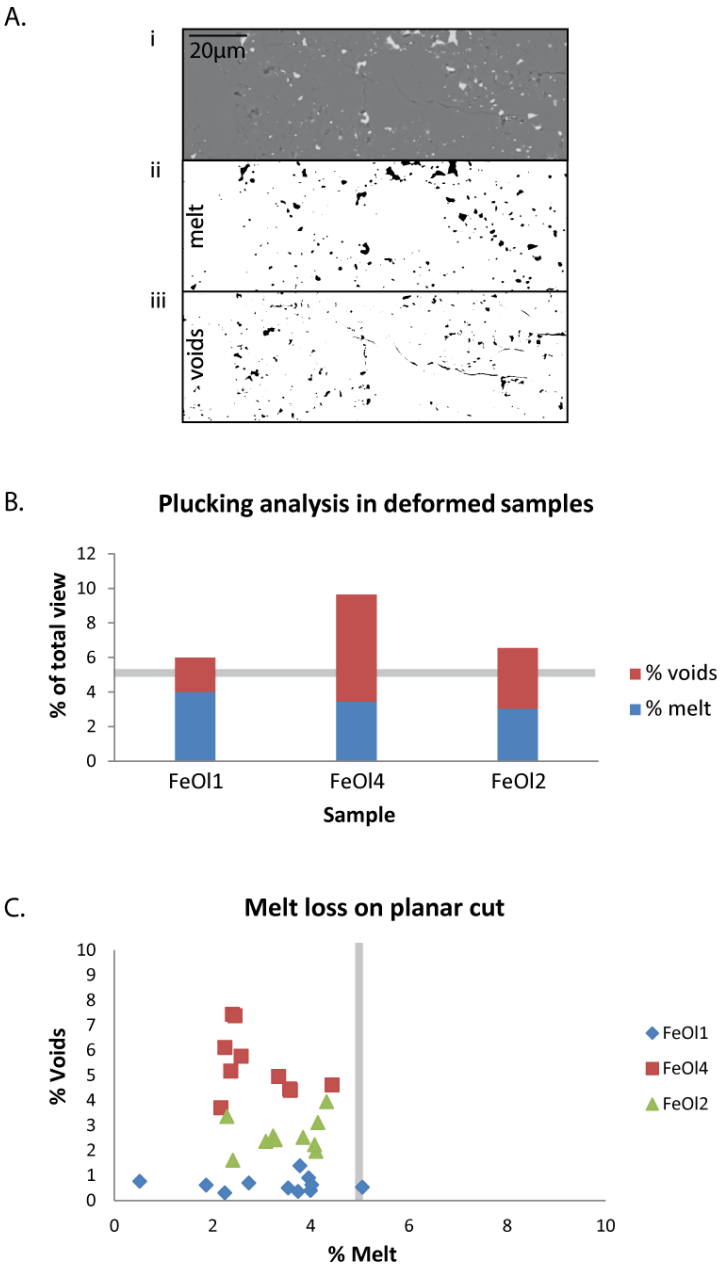

Figure 3.6: The percentage of material lost through plucking during preparation of polished sections. A. examples of the image process: i) raw image ii) binarised (black=melt) iii) binarised (black = voids) B. Chart giving the proportion of cracks /voids vs. melt, as area%. Expected melt content (5 area%) is shown by the grey bar in each image. C. Graph showing results of individual image analyses from planar sections in each of the deformation experiments. Experimental duration for FeOl1, FeOl2 and FeOl4 is 1420, 200 and 605 min respectively.

2D particle analysis

In order to investigate quantitatively the variation of sample texture, 2D melt distribution, melt pocket size and melt geometry of samples, backscatter electron images were used to carry out particle analysis using ImageJ (Abramoff et al., 2004) on cropped binarised images. The 'analyze particles' tool was then used to get data on melt pocket diameters, area, axis ratio (elongation) and orientation for each individual melt pocket. Additional analyses were carried out to evaluate particle shape, using measures of circularity, calculated as $4\pi x[Area]x[Perimeter]^2$ where 1 is a perfect circle and 0 is a straight line. A second measure of Solidity was also used, measured as $[Area]x[ConvexArea]$, which measures how embayed or pitted the pocket is. Each pocket is individually labelled and located in X and Y direction, allowing melt pocket distribution to be measured quantitatively. Analysis was carried out on FeOl1, FeOl2, FeOl4 and the undeformed control FeOlPC8, on all three orientations of cuts. Additional analyses were carried out on tangential sections of earlier generation samples FeOlPC4, FeOlPC5 and FeOlPC6 (Berg, 2010).

Figure 3.7 shows some results for particle analysis combining results from all three slice orientations for melt pocket diameter, aspect ratio, circularity and solidity. The difference between deformed and texturally equilibrated undeformed samples is very clear in terms of maximum diameter. The diameter of melt pockets in undeformed samples show a clear bell-shaped distribution of relatively large pocket size. Undeformed samples on the other hand exhibit a more skewed and variable distribution, with a large percentage of liquid in very small melt pockets down to 1 μm and less, but also a significant proportion of melt in larger melt accumulations. This suggests that deformation acts to distribute melt into smaller melt pockets but also leads to coalescence to larger melt veins. This is similar to the pattern seen in higher strain-rate experiments in Walte et al. (2011), but our lowest strain-rate, longest duration experiment exhibits the most marked difference in melt pocket diameter compared to undeformed samples. We do not see a change in melt pocket diameter distribution correlating with a change in strain-rate, as observed by Walte et al. (2011).

The distinction between deformed and undeformed samples is less clear in measures of aspect ratio, but FeOl1 shows a smaller majority of near circular pockets and a larger range of elongation. The distribution of shape and elongation of pockets in FeOl2 and FeOl4 is similar to the distribution observed in the undeformed sample, and has an average closer to 1, but FeOl1 shows a very distinct distribution with a larger proportion of liquid in less circular pockets with lower solidity values.

It is important to note that, although the melt distribution is much finer in deformed samples, even very small melt pockets may in fact be connected in three dimensions. 2D diameter analysis will not give the correct diameter of a melt pocket, even if the pockets are known to be spherical (Heilbronner and Barrett, 2013), which they are not in this case . Direct

3D analysis must be used to assess connectivity in deformed samples.

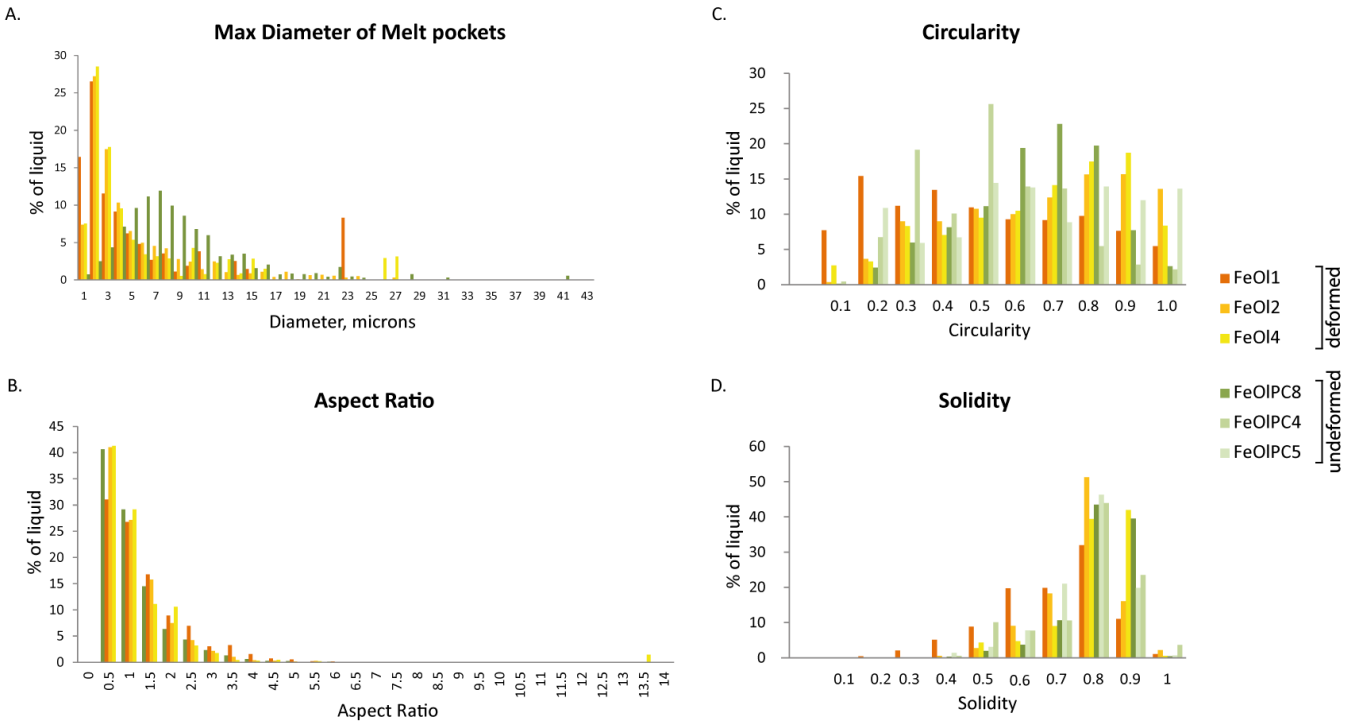

Figure 3.7: Particle analysis of melt pockets carried out on binarised 2D backscatter electron images of deformed and undeformed samples. A. Max. diameter of melt pockets (Feret diameter). B. Aspect Ratios of melt pockets C. Circularity, which is a measure of particle shape where 1 is a perfect circle and 0 is a straight line. For very small particles this value can be invalid, which may explain occasional values of >1. D. Solidity of each particle, where higher values indicate convex, spherical shapes and lower values indented, concave shapes. See text for full discussion of results.

Auto-correlation function analysis of fabric strength

In order to assess the strength and orientation of any fabric within experimental samples, auto-correlation function (ACF) analysis was carried out on 2D sample sections using ImageJ plugin Jazy_ACF (Heilbronner and Barrett, 2013). The auto-correlation function describes the heterogeneity of an image by comparing it to a direct copy of itself, at varying displacement from its original position. A homogeneous, isotropic texture will repeat itself regularly, and equally in all directions, producing a circular ACF function. A fabric with a distinct alignment will show higher correlation in a certain direction, producing a non-circular ACF with its long axis parallel to foliation. Figure 3.8 shows the intermediate processing steps involved in ACF analysis. Composite backscatter electron images were used in order to cover as large an area as possible at high resolution. Although ACF can be produced directly from greyscale images, the presence of linear decompression cracks throughout the sample affect the ACF produced. To avoid this, the image was cropped to avoid large cracks, and binarised to highlight the melt phase (Figure 10B). ACF analysis can only be carried out on square sub-sections of an image, but Jazy_ACF software allows tessellation of multiple ACFs across the full image. A region of interest of 128 pixels was chosen, which gave a dataset on the order of 200-400 data-points across the composite images, therefore allowing a clear comparison of textures as a function of location within each sample. Resulting ACFs are shown in Figure 3.8C. This image is thresholded to leave only the ACF centre for each tile. The size, aspect ratio and orientation of these images is then analysed using the particle analysis tool of ImageJ (Abramoff et al., 2004).

The most useful results were found from analysis of cross-sectional cuts, where it is possible to see changes with changing magnitude and direction of maximum stress from one edge to the other. Figure 3.9 shows graphed results for FeOl1, FeOl2, FeOl4 and the undeformed FeOlPC8. To clarify datasets, ACF centres smaller than 10 pixels are removed (these produce anomalous orientation results), and point colour is scaled to magnitude of aspect ratio (i.e. elongation). The undeformed sample has a large number of data points, reflecting the larger melt pocket sizes and increased spacing between melt pockets leading to larger ACFs. Orientation of the ACFs is random across the sample, as expected for the relatively isotropic nature of the undeformed sample fabric. Large, elongate ACFs in deformed samples are generally aligned between 0-30° and 150-180°, i.e. at low angles to the horizontal, implying a weak fabric created sub-horizontal to the shear direction. FeOl1 shows a clear change from high angles on the left edge, to low angles on the right, with horizontal alignment in the centre, which may be an indication that the fabric orientation is changing in response to the maximum strain (which is in opposite directions at either end of the sample and at a minimum in the centre). Further 3D analysis has been carried out on fabric orientation to investigate whether this is indeed a response to changing differential stress orientation (section 3.3.3).

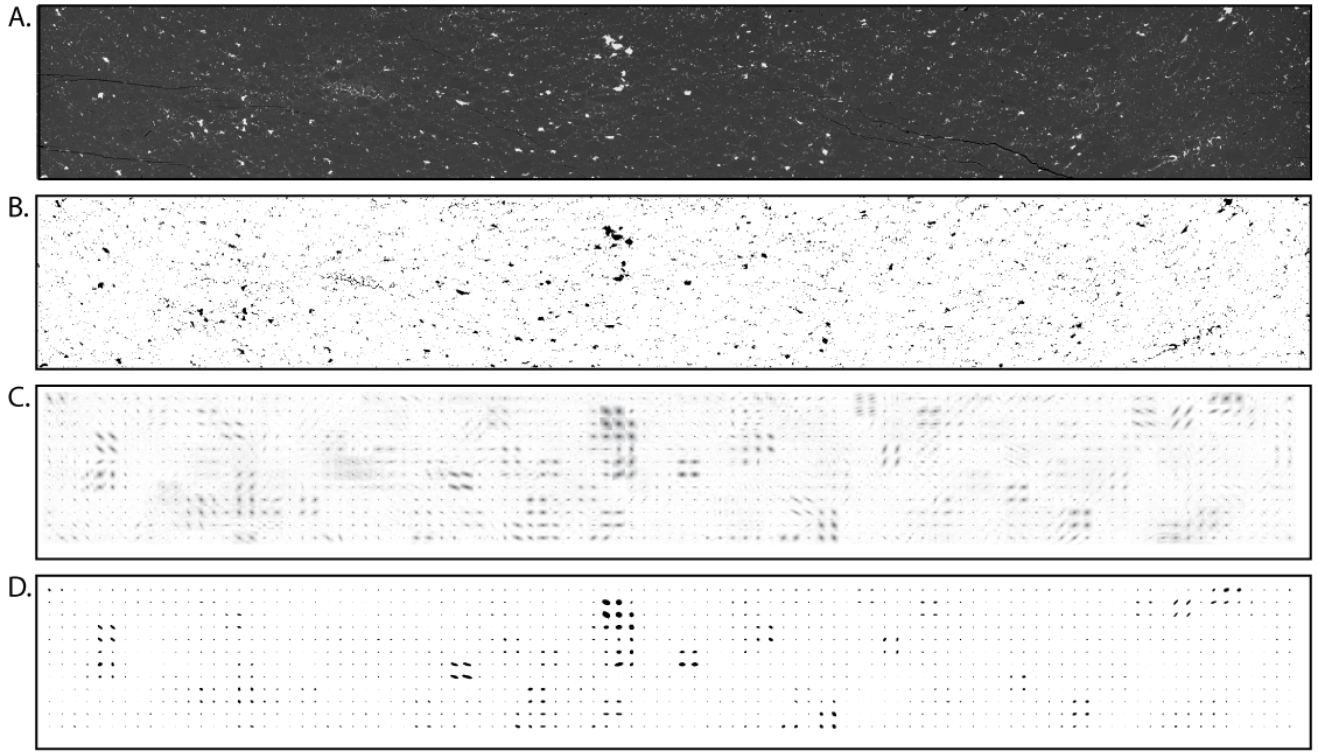

Figure 3.8: Example of the process of analysing textures using the Auto-Correlation Function (ACF) using sample FeOl1. A. Backscattered electron image of FeOl1, a composite image produced from 5 separate higher magnification images, spanning the width of the sample. The image has been cropped to avoid major decompression cracks which could affect ACF results. B. A binarised image showing melt in black, produced by simple global thresholding. This was done to stop voids and cracks affecting the ACF. C. Auto-correlation functions with a region of interest of 128 pixels, which was found to be large enough to be representative of the overall texture, while still producing enough data-points for a valid comparison. D. ACFs thresholded at 39%, leaving only ACF centres, which can be analysed for size, aspect ratio and orientation. ACF size is correlated with size of melt pockets, while orientation and elongation are related to alignment and strength of fabric within the image. The field of view in each image is 1700 x 300 µm.

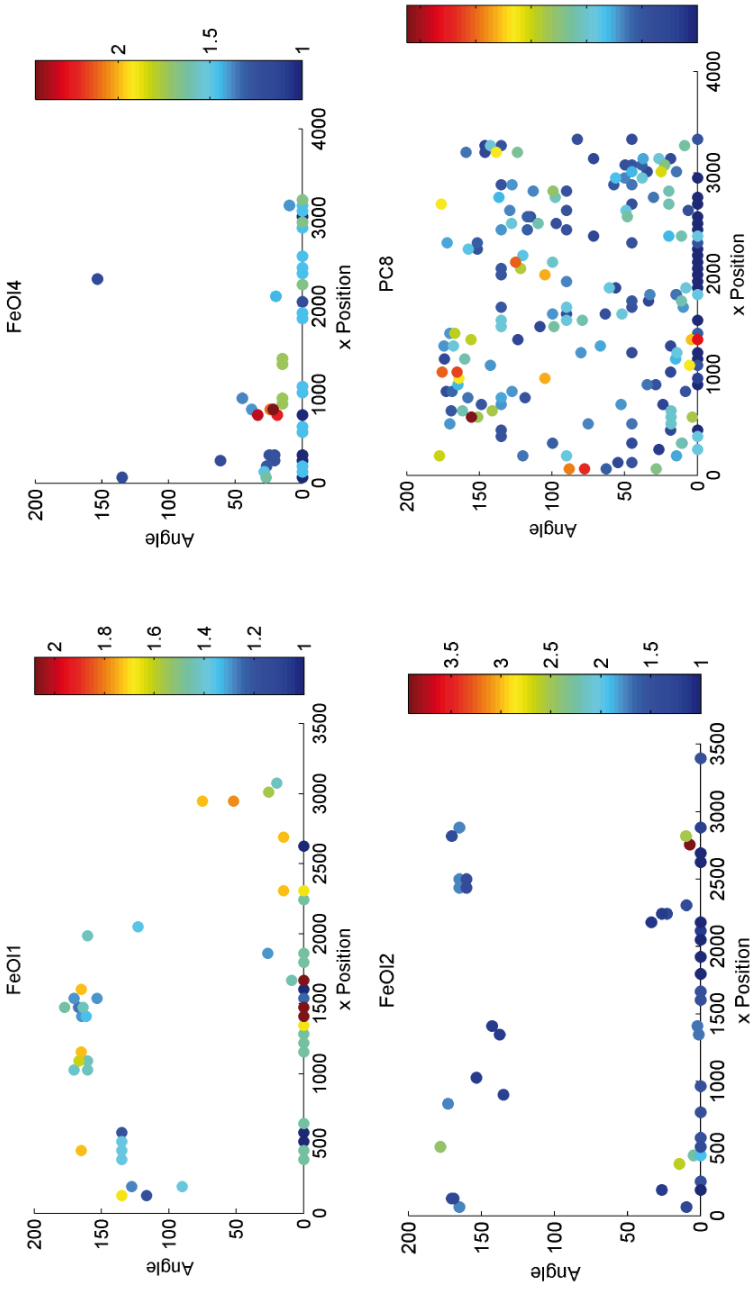

Figure 3.9: Graphs showing analysis of orientation vs. location of thresholded ACF centres, indicating presence or absence of a repeated pattern or fabric within samples. Colour of points is scaled to aspect ratio of ACF centres, indicating strength of fabric. ACF centres below 10 pixels in size generally produce anomalous results, therefore these plots show larger centres only. The undeformed sample shows an entirely random fabric orientation, while deformed sample ACFs all show a tendency to have a sub-horizontal alignment. In FeOl1 there appears to be a rotation towards higher angles at the sample edges, with opposite edges showing opposite orientation of alignment. This may be a response to the change in stress orientation across mid-sections, with maximum stress at either edge acting in opposite directions, and minimum stress in the centre. This correlation is less clear in the mid-section cuts of FeOl2 and FeOl4. There is no clear correlation of aspect ratio vs. orientation, suggesting there is no clear increase in fabric strength at the edges of deformed samples.

Summary of 2D textural observations

A summary of 2D textural observations are as follows:

- A significant change in textures is observed between deformed and undeformed samples. Melt in undeformed samples is found in homogeneously distributed, isolated melt pockets, while melt in deformed samples is more widely distributed into finer melt pockets, with a more variable size and shape.
- Our longest duration, lowest strain-rate deformed sample shows the most pronounced development of melt veins and the most extensive grain boundary wetting, although this could be in part explained by an improved polish on longer duration samples. 3D analysis is required to test whether the textural difference observed is genuine or due to the quality of polish.
- Deformed samples show a subtle development of fabric sub-horizontal to the plane of maximum shear stress.

Two-dimensional textural analysis is able to give significant information describing the relative differences in textures across deformed and undeformed samples, including apparent particle size, distribution and orientation of a specific fabric. However, in deformed samples where equilibrium is not attainable and stress magnitude / orientation are variable across the sample, there are serious limitations as to the validity of information gained from a single section across the sample. Even the analysis of three orthogonal sections will not fully reveal the 3D texture of the sample. This is particularly true for analysing the true connectivity of potential melt networks in deformed samples. In any 2D section, there is no way of knowing if and how individual seemingly isolated melt pockets are connected in three dimensions. Traditional 2D dihedral angle analysis cannot be used on deformed samples, as it requires textural equilibrium to be reliable. Dihedral angle analysis even after long duration experiments lead to an irregular dihedral angle distribution and fail to provide a meaningful result (Berg, 2010). Direct 3D visualisation of melts is required to draw conclusions about 3D melt geometry and interconnectivity.

3.3.3 Melt distribution analysis from X-ray micro-CT

3D analysis using micro- and nano-tomographic imaging allows direct visualisation of 3D melt distribution, geometry and interconnectivity. X-ray micro-CT analysis carried out using the Edinburgh University in-house CT equipment has been able to produce datasets ranging in voxel size of 2-3μm for 2mm F.O.V. whole-sample scans. Although this voxel size is coarse in comparison to textures observed in quenched sections, we have been able to use these scans to gain valuable 3D information regarding

- Melt volume distribution and therefore potential localised melt migration in response to thermal or pressure gradients / strain localisation within the samples.
- Orientation of any fabric produced in response to the orientation of stress tensors and changes in magnitude of stress across deformed samples.

3D melt distribution

3D reconstructions of experimental samples from four deformation runs, as well as the undeformed control sample, are shown in Figure 3.10. As previously observed in 2D images, melt distribution is more variable in the deformed samples, with a fabric created by alignment of larger melt accumulations, although there are also variations in melt distribution observed across the undeformed sample. Partial volume effects are significant in these micro-CT scans, caused by relatively large voxel size relative to size of textural features. This means that large volumes segmented as the melt phase are likely to be a combination of fine melt veins surrounding small olivine grains, as observed in 2d textures, rather than single large melt pockets. These large volumes still represent areas of higher melt % however, therefore analysing their distribution can give information about potential localised segregation into melt-rich and melt-poor regions. To quantify this melt distribution, the volume % of the segmented melt phase was calculated from segmented images per slice in X, Y, and Z directions as shown in Figure 3.11.

Overall the undeformed sample appears less variable than deformed samples, particularly in the Z direction, although the difference is subtle. FeOlPC8 does show an inherent variability although the range of volume % are small in the X and Z directions, and the variability appears to be in broader peaks, especially in the Z-direction, suggesting a more gradual increase and decrease in melt % over a larger area. FeOl1 shows very high variability, particularly in the Z and Y directions. There is a clear peak of melt % in the central portion of the sub-volume examined, both in Z and X directions – this may show some tendency for melt to move to the middle of the sample, but more analysis is required to see if this is due to some form of gradient, or if it is a coincidental redistribution. The remaining deformed samples do not show as large a variation in volume distribution, particularly in the X and Y direction – in fact, in the case

of FeOl2 melt appears to be more finely distributed than in the undeformed sample, showing no sign of melt accumulation or migration. This matches with qualitative observations, as textures do not appear to have changed significantly in these shorter timescale experiments. There appears to be a systematic change in melt concentration within sample FeOl1, as there is a clear increase in melt % in the centre of the sample in both Z and X directions.

In order to investigate whether this accumulation is related to stress / strain, the vol% melt was calculated for cylindrical shells moving from the centre to the edge of sample FeOl1. In theory, the sample edge experienced maximum strain and strain-rate, and the centre minimum (zero). If melt has migrated in response to this strain gradient it may be possible to see a gradual change in melt % across the sample reaching the centre. This analysis was carried out by using the Volume Edit function in Avizo Fire^{TM} to crop cylindrical sub-portions of the sample at decreasing radii and using the material statistics function to calculate volume %. Results are shown in Figure 3.12. Across shells of around 100µm thickness, there is a general trend of increasing melt % towards the sample centre. This would be expected if melt was moving towards areas of lower pressure/strain (Kohlstedt and Holtzman, 2009). However, thinner 20µm shells show that the distribution is more variable locally, so this analysis alone may not be sufficient to infer melt migration in response to this gradient.

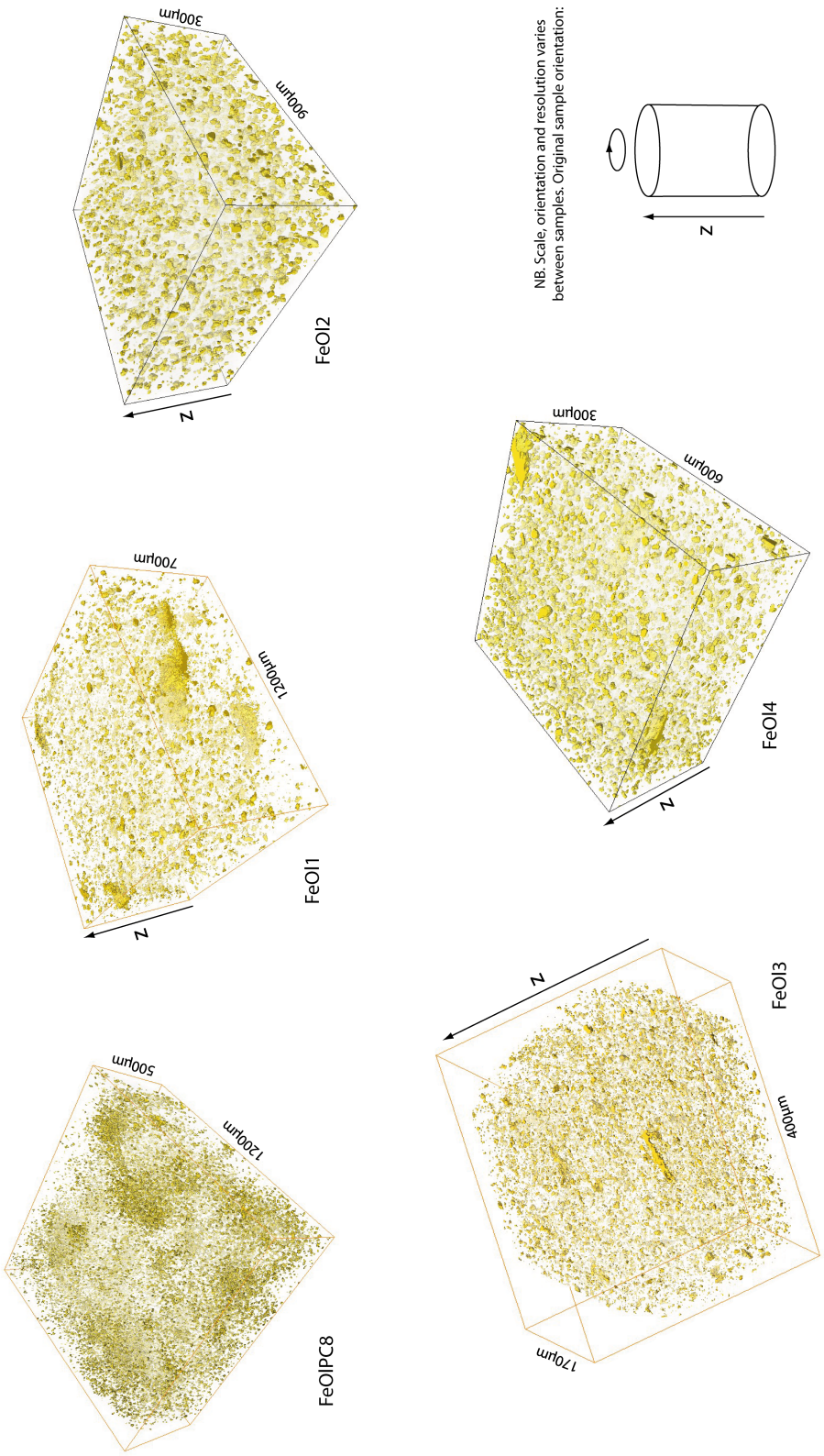

Figure 3.10: Volume renderings of melt (gold) in micro-CT reconstructions of experimental samples FeOl1-4. Olivine matrix has been rendered transparent. Orientation of the sample Z axis (parallel to torsional axis of rotation) is shown by arrows to orient each deformed sample. See text for details.

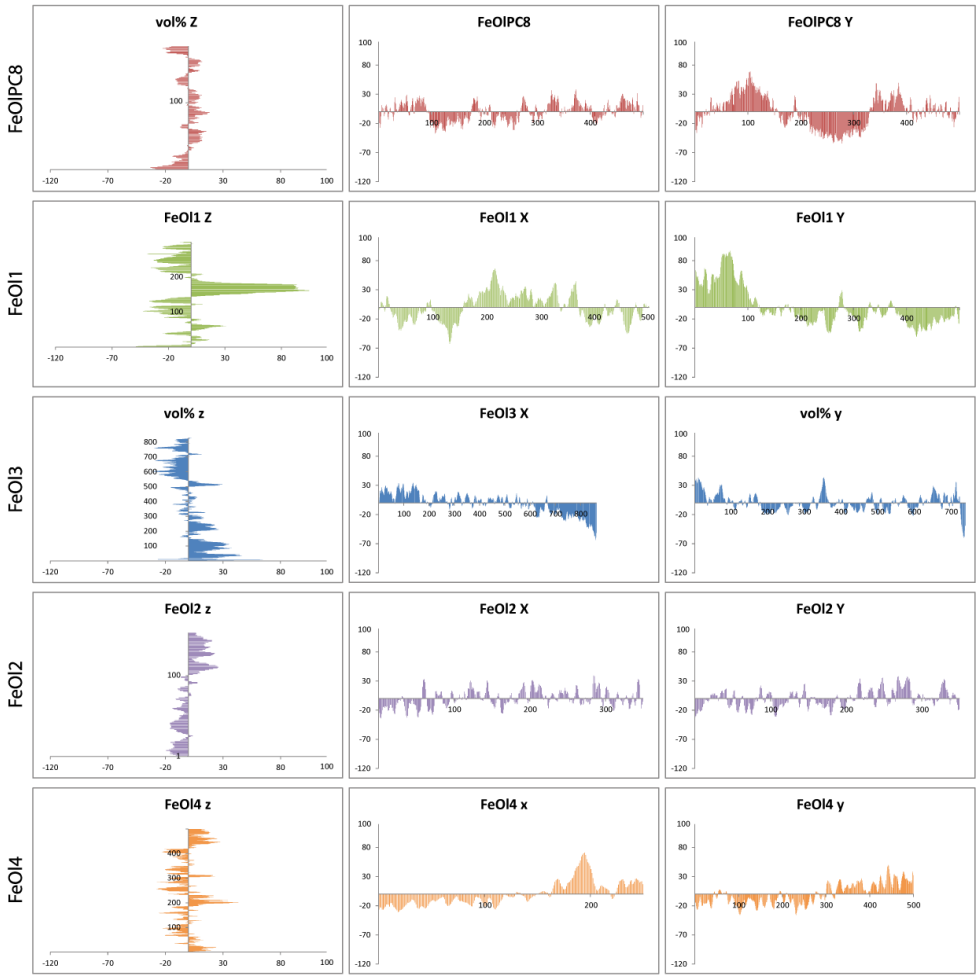

Figure 3.11: Relative melt distribution across the sample in terms of volume percentage of melt present across slices in three orthogonal directions. Processing involved 1) noise reduction by removing outlier pixels and applying a minor smoothing filter, 2) segmentation into melt vs. olivine using a global threshold and/or tophat segmentation algorithm. 3) re-stacking original z-slices (x-y plane) to two new orthogonal (x-z,y-z plane) stacks using ImageJ (Abramoff et al., 2004) 4) Extracting area % melt phase in each slice using Avizo Fire^{TM} 'material statistics' function. For comparison between samples this result was converted to % change from the average vol% in the whole volume. Z direction is chosen as the original orientation of slices (see Figure 3.10). Orthogonal X and Y directions have been chosen to ensure slice area is similar across samples, as the area of the slice analysed will affect variability of volume distribution. For Z direction (graph on left), vertical axis is slice number, and X axis represents % change from average volume fraction of the whole sample – in X and Y directions (middle and right-hand graphs) these axes are inverted. Results are discussed in the text.

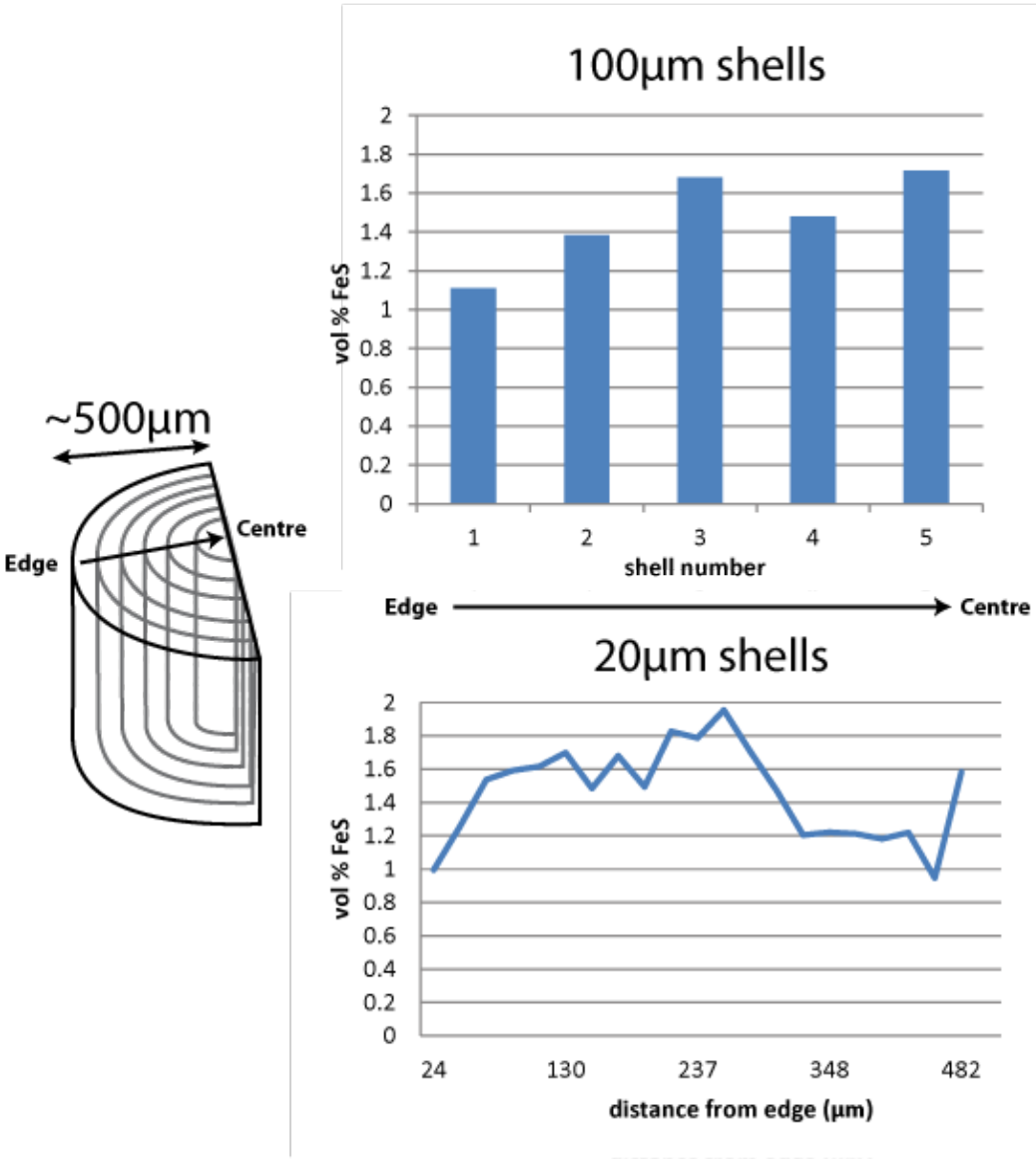

Figure 3.12: Volume distribution across FeOl1 measured as shells across the semi-circular sub-volume (see schematic insert). This should show if there is any net melt migration in response to a stress or strain gradient. Analysis was carried out using large ~100µm thickness shells to show large scale distribution (top), and again on a smaller scale with 20µm thickness shells to show more localised distribution (bottom). Large scale shells do appear to show a general increase towards the sample centre, the location of minimum stress, but small scale shells do not show a similar trend, showing a more general variability with a peak towards the middle shells – this is harder to explain by changes in stress magnitude.

3D melt alignment and orientation

Strength and orientation of fabric in three dimensions was analysed using two distinct shape tensor analysis methods. The first used the open source software Quant 3D created by University of Texas CT (Ketcham, 2005a), which allows detailed analysis of fabric in three dimensions using three measures of shape anisotropy and orientation (Figure 3.13):

- **Mean Intercept Length (MIL)** This creates a grid of lines of a certain orientation and measures the mean intercepts between phases – this is repeated for grids of different orientations and results are shown for each orientation. In this case there is no phase of interest and the MIL for the inverse thresholding would be identical.
- **Star Length Distribution (SLD)** uses a similar grid of parallel lines, but only measures the mean distance across the phase of interest. SLD specifically analyses the shape, rather than distribution of particles.
- **Star Volume Distribution (SVD)** uses a grid of points (in this case a uniform distribution) – lines protruding from each point are measured in length and a mean length is produced for each orientation.

Pre-thresholded slices were inputted into Quant3D software using a uniform grid of 513 orientations, with random rotation and dense vectors (recommended settings). 2000 points were analysed for each tensor method. Results are shown in Figure 3.13 and Figure 3.14 in the form of 3D rose diagrams showing relative elongation of tensors in each orientation direction, along with an image showing sample orientation. The most useful tensors in this case appear to be SLD and SVD, as they do not take into account the shape of the non-melt volume. The MIL value is affected by the sample shape and presence of cracks rather than melt fabric alone.

The undeformed sample FeOlPC8 shows a subtle fabric, with slight elongation in one direction to create rod-shaped melt alignment. This is unexpected, as the fabric is observed to be isotropic in qualitative observations. The alignment shown in deformed samples, however, is clearly stronger in every case except that of FeOl2, in which there appears to be only a very weak fabric. Melt alignment is most pronounced in FeOl1 and FeOl4, which are the two longest duration experiments, again suggesting that experimental duration appears to have the greatest effect on textural development within our samples. Alignment appears to be at a low angle to maximum shear, supporting 2D findings from ACF analysis. This includes a suggestion of two orientations of elongate melt pockets at ~160° and ~20° from horizontal (plane of max shear stress). Again this was found in ACF analysis in 2D, where melt orientation varied from horizontal in both directions at either end of the sample, suggesting the orientation is dependent on stress orientation. In this case, analysis was carried out on the whole sample, so there is no way to comment on localised alignment of melt pockets within the sample.

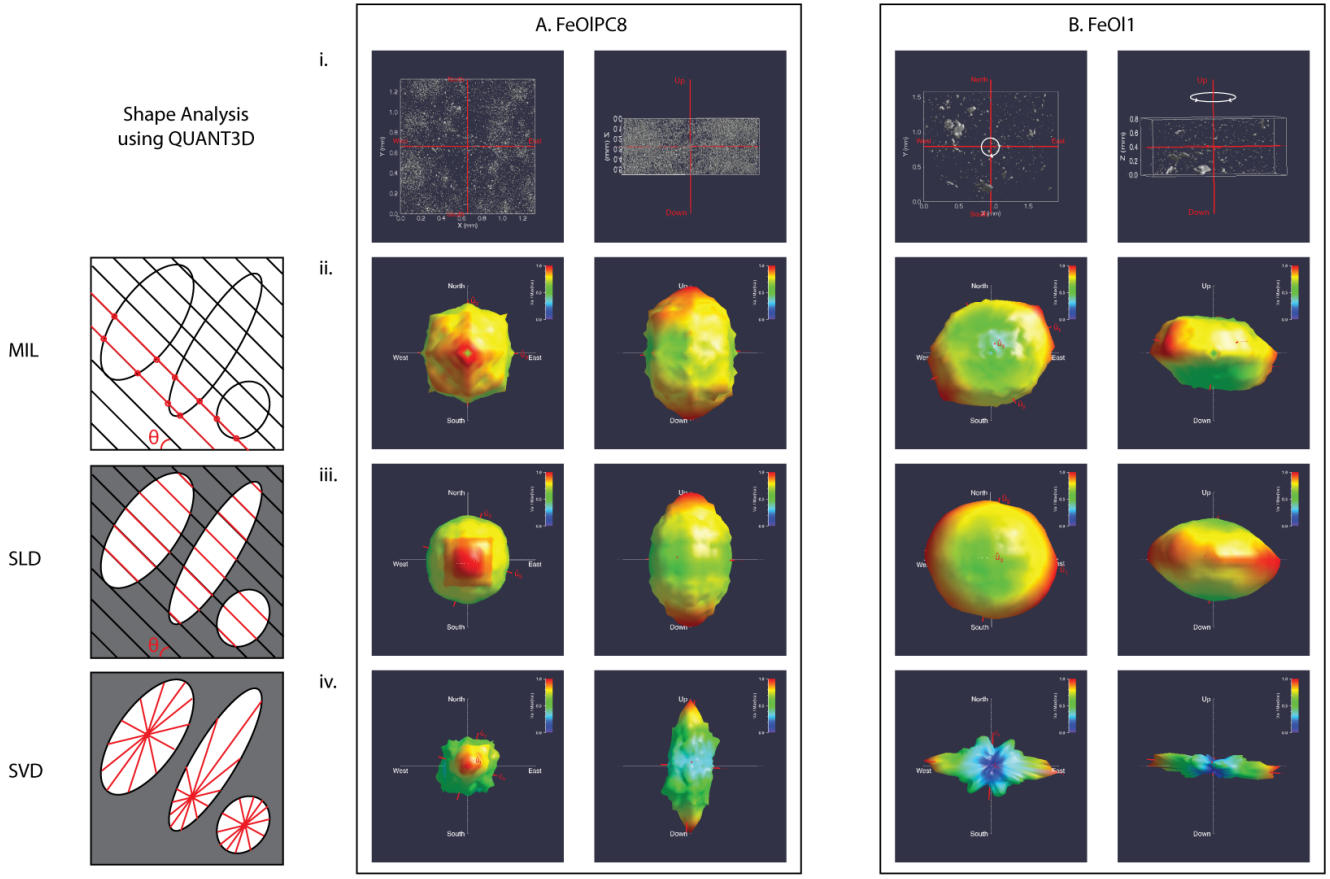

Figure 3.13: Quant3D analysis (Ketcham, 2005b) investigating alignment of melt by analysis of particle shape for undeformed FeOlPC8 (A.) and FeOl1 (B.) using Mean Intercept Length (ii), Star Length Distribution (iii) and Star Volume Distribution factors (iv). Schematic diagrams show a 2D example of how each analysis is carried out (see text). Results are shown in the form of a 3D rose diagram, from two orthogonal perspectives. The scale is of relative mean length, with a blue coloured lengths being around 10x shorter than the red colours (Ketcham, 2005b). An image showing the orientation of these results relative to the sample volume are shown for each sample (i). White ellipses show orientation of plane of torsional deformation.

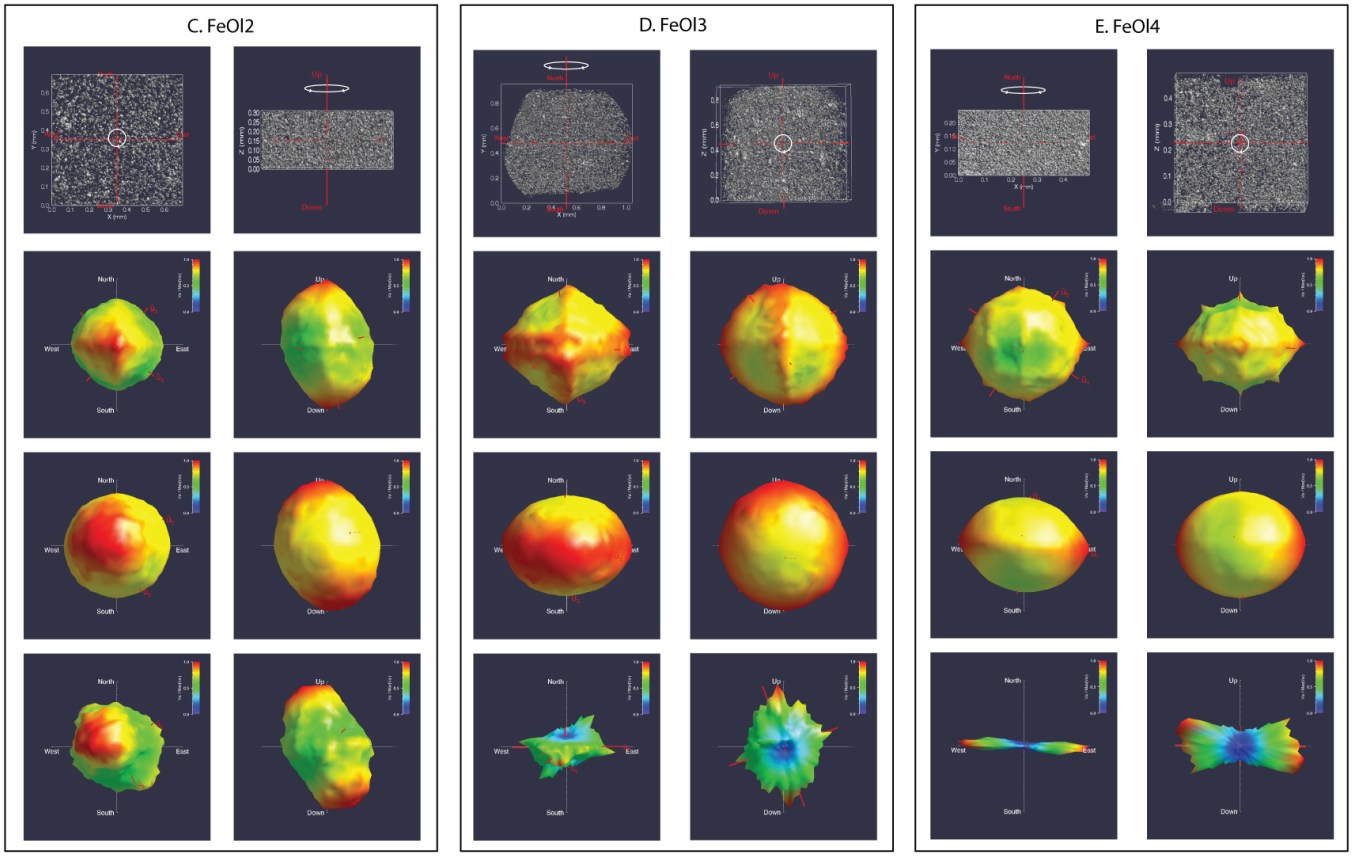

Figure 3.14: Continuation of figure 3.13 showing the particle alignment of FeOl2 (C.), FeOl3 (D.) and FeOl4 (E.). See text for descriptions.

In order to examine the geographical distribution of melt pocket alignment, particle analysis was carried out using the open source software Blob3D (Ketcham, 2005a), which uses an ellipsoid-fitting technique to give a value for particle elongation and orientation of long axes for individual segmented particles in a 3D volume. Each particle is located in x- y- and z-directions thereby allowing analysis to be carried out by region within the sample.

Results of orientation are initially given as three direction cosines, then converted to plunge and trend in order to plot onto a stereonet with points representing the orientation of long axes of fitted ellipses. Results are shown in Figure 3.15, showing the full dataset, and the data split into NW, NE, SW and SE quadrants of the sample (down X axis) using only elongate particles with axis ratios >2. Although results clearly show the same trend of sub-horizontal samples, there is no clear change seen in results from different quadrants, suggesting overall there is no correlation between exact trend and plunge of particles and the orientation of applied stress. It may be that the variation from horizontal is of a random nature associated with general undulation of melt particles about the horizontal plane, rather than being directly affected by orientation of shear stress. There are limitations to this analysis however. The fitting of ellipses requires a simplification of melt pocket shape, which, in the case of these deformed samples could lead to the loss of information, particularly in large melt bands which change in orientation across the volume, or shapes that include multiple melt veins coalescing. ACF analysis carried out on 2D sections may lead to a more reliable measure of fabric, as it summarises the fabric using the entire dataset rather than fitting an ellipse to individual melt pockets.

Limitations of micro-CT analysis

Micro-CT analysis is able to show a marked change in melt distribution between undeformed and deformed samples, and significant evidence for alignment of melt within deformed samples parallel to the shear plane. There is, however, a limit to the usefulness of data at this resolution. SEM images reveal a very fine distribution of melt, particularly within deformed samples, where fine melt sheets of less than 1μm are ubiquitous. These cannot be visualised successfully with a voxel size of 1-3μm. Partial volume effects will act to 'smear out' these fine features changing both volume and shape and making them essentially impossible to segment even manually. This problem is made worse by issues of misalignment within CT scans, particularly as these scans were taken early on in the development of the in-house CT equipment when this issue was more pronounced.

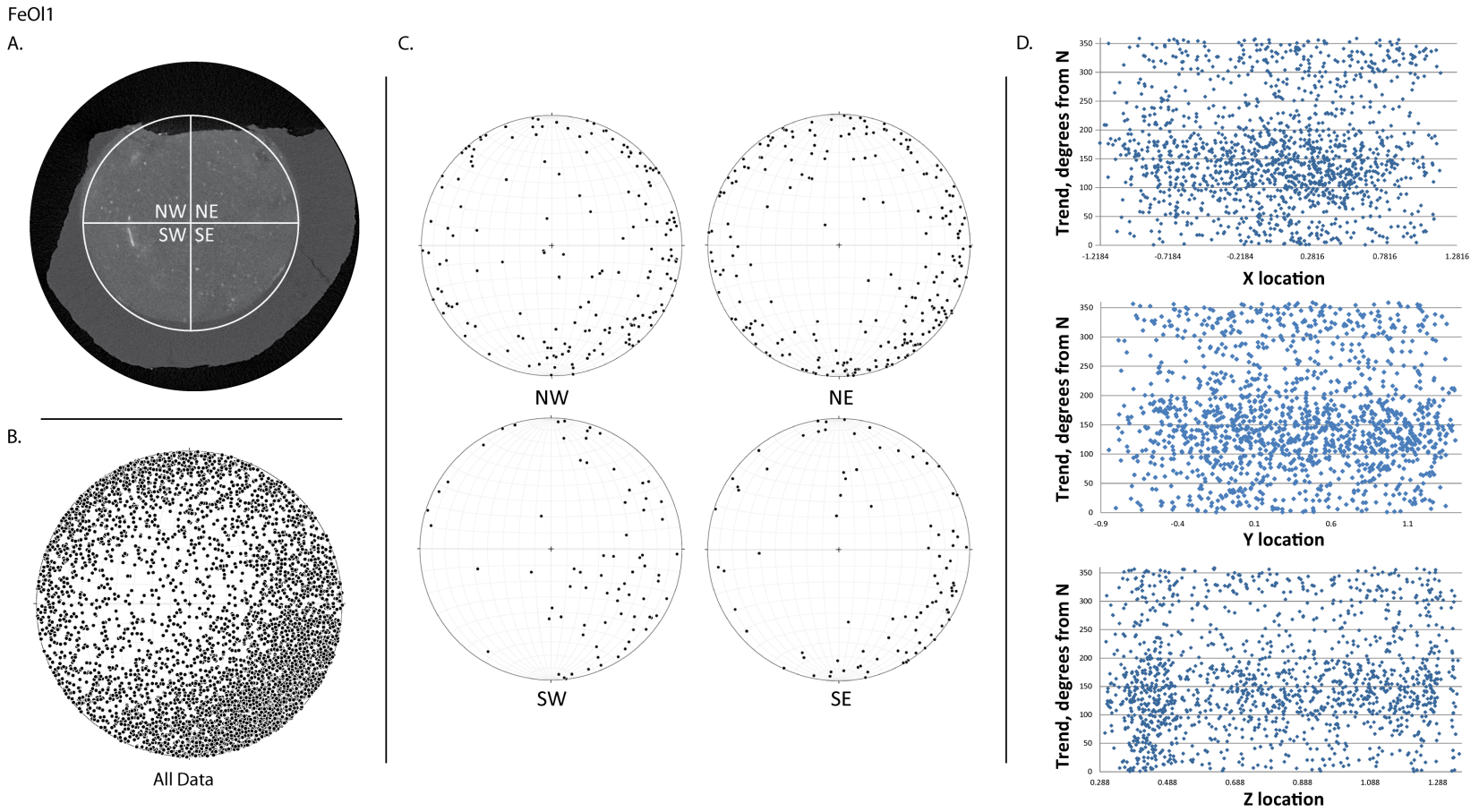

Figure 3.15: Blob3D orientation analysis of FeOl1. A. Slice through sample at orientation of analysis, such that the direction of shear is in the plane of the stereonet horizontal. The quadrants used in part C are shown. B. Plot of full dataset. There is a clear distribution of long axes about the horizontal, with fewer axes at higher angles to the shear plane. This is in agreement with previous analyses. C. Long axis orientations of particles with high aspect ratio only (AR>2) split per quadrant of sample. There is no clear correlation between the location of the particle within the sample and long axis orientation, other than the fact that the SW quadrant has a lower number of west-plunging axes. In each quadrant the majority of axes appear to be plunging SE, although in the NE and NW quadrants the trend of the plunges appears to be random. D. Trend of long axes of elongate particles (AR>2) with changing location across orthogonal X, Y and Z axes. Z axis is perpendicular to sample slices and therefore the plane of maximum shear stress. Again there is no regular trend observed from the centre to the edge, suggesting no relationship between stress orientation and trend of long axes.

3.3.4 Melt geometry and connectivity from X-ray nano-CT

Nano-resolution CT scans were carried out on small sub-volumes of samples FeOl1, FeOl3 and undeformed FeOlPC8, for 65x65x65µm sample volumes at 130nm voxel size, and one additional ultra-nano scan of FeOl1 at 15x15x15µm sample volume at 50nm voxel size. Equipment and required sample preparation is described in section 2.3. This technique essentially allows a 'zoom' into an area of interest within the sample to examine geometry and melt interconnectivity in great detail, but only into a small selected volume of the sample (Figure 3.17). Slices were filtered using non-local means filtering. Filtered slices were segmented by binarising the greyscale data into melt and non-melt areas. This was carried out by a combination of simple global thresholding and the watershed segmentation technique. Additional adjustments were made using the magic wand tool which automatically selects adjacent voxels within a certain greyscale range. An example of a slice from the FeOl1 nano-CT scan, and the filtering and segmentation process is shown in figure 3.16.

Nano-CT analysis is very useful for detailed analysis of melt network geometry. Resolution of these scans is high enough to allow much improved phase segmentation with a smaller partial volume effect. Melt pocket shape can be characterised effectively and the volume fraction of melt can be estimated more reliably from these scans, allowing better quantification of local melt fraction distribution across samples. However, there are also limitations to the technique. Difficulty of sample preparation essentially means the process is destructive, and the large expense of single scans mean that we have only been able to prepare a small number of nano-tomographic scans. The information collected cannot therefore be confirmed to be representative of the full sample volume. Sample preparation also makes it difficult to pre-select certain areas of interest for further study, although an improved technique of combining lower magnification micro-CT scans with laser ablation or focussed ion beam milling to remove a pre-selected area could be used in the future to allow selection of a specific region of interest. However, in combination with the larger scale CT scans and 2D ground-truthing, the scans give valuable additional information regarding shape of melt pockets, and melt geometry. Importantly, for the first time we are able to confirm the presence and examine in detail the topology of three-dimensional melt networks along wetted grain boundaries of FeS within an olivine matrix.

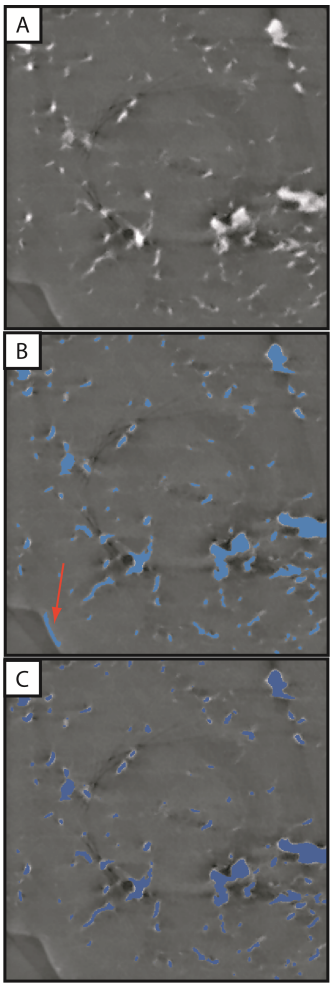

Figure 3.16: Tomographic imaging, processing and segmentation. A. Filtered tomographic slice produced from nano-tomographic scan. Voxel size is 0.13µm, FOV is 65x65µm. White = FeS, dark grey = olivine. The image displays beam hardening artefacts, causing the edges to be brighter than the centre of the image. B. Example of segmentation carried out by automated watershed segmentation. Generally the method segments phases well, but it is evident that some segmentation has been carried out incorrectly – e.g. Ol mis-identified as FeS in corners that are brighter due to beam hardening (see arrow). Some very fine melt networks are also missed by the automatic segmentation and need to be added manually. C. The final segmented area.

Qualitative observations

Initial observations of nano-CT scans highlight the difference in textures between deformed and undeformed samples (Figure 3.18). Particle shape within undeformed FeOlPC8 is relatively uniform, and melt pockets are close to spherical with clear angular edges on melt pockets representing the melt pinching off at high dihedral angles to the olivine grains. Smaller spherical particles are likely to represent melt trapped within olivine grains that have grown during annealing, which were also observed in 2D SEM analysis. Deformed particles have less uniform shapes, most showing a more concave nature with convolute margins and narrower sheet-like structures. Even at this fine scale it is clear that the melt within deformed samples, although distributed more finely overall, also accumulates to form very large melt pockets. In the case of FeOl1, one of these melt pockets stretches diagonally from one end of the scanned volume to the other – its total length within the volume is around 100μm, but the likely extent of the melt network is likely to be much greater. A reconstruction of this large interconnected melt pocket is shown in Figure 3.19. It is possible to see very fine individual melt sheets joining together to connect two larger melt accumulations. Fine melt sheets are likely to represent melt wetting small olivine grain boundaries, connecting together to form a network of sheet-like veins. Small isolated melt pockets are still present within sample volumes, but they represent a smaller proportion of total melt than in the undeformed sample (see section 3.3.4). Sample FeOl3 shows similar melt geometry and volume distribution, but there is no large interconnected melt pocket cutting across the sample, and overall there are fewer large melt pockets. A larger proportion of the melt is trapped in isolated grains. However, this is most likely due to the area being relatively drained of melt, as shown in section 3.3.4.

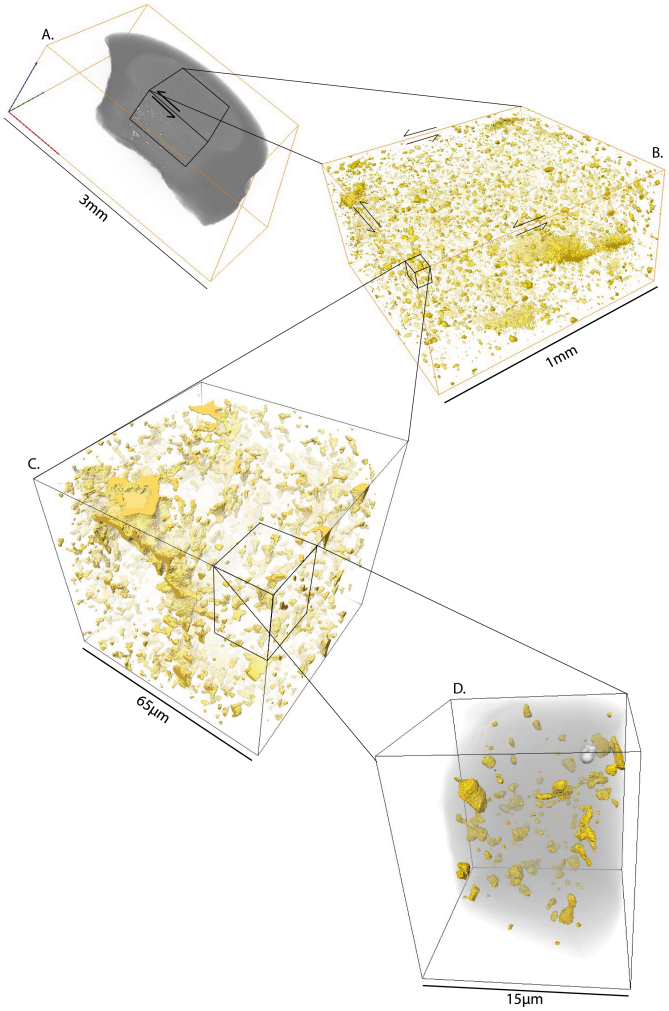

Figure 3.17: Reconstructions of deformed sample FeOl1 at varying levels of magnification from micro-, nano-, and ultra-nano CT scans. In each case, olivine is rendered transparent and FeS metal is rendered yellow. A. and B. are from in-house scans of the whole sample at 2.4µm resolution. A. shows the sample exterior including remaining traces of the platinum strain marker which allow orientation of sample strain to be correlated with the orientation of the melt phase. B. shows the cuboid volume of interest used in a number of melt distribution and fabric orientation analyses. C. nano-CT scan carried out of FeOl1 at MXIF (0.13µm voxel size). Due to sample preparation process the original orientation of the subvolume with respect to the whole sample is no longer known. D. Ultra-high resolution (UHR) scan of a 15x15x15µm sample fragment at 50nm resolution. See text for details.

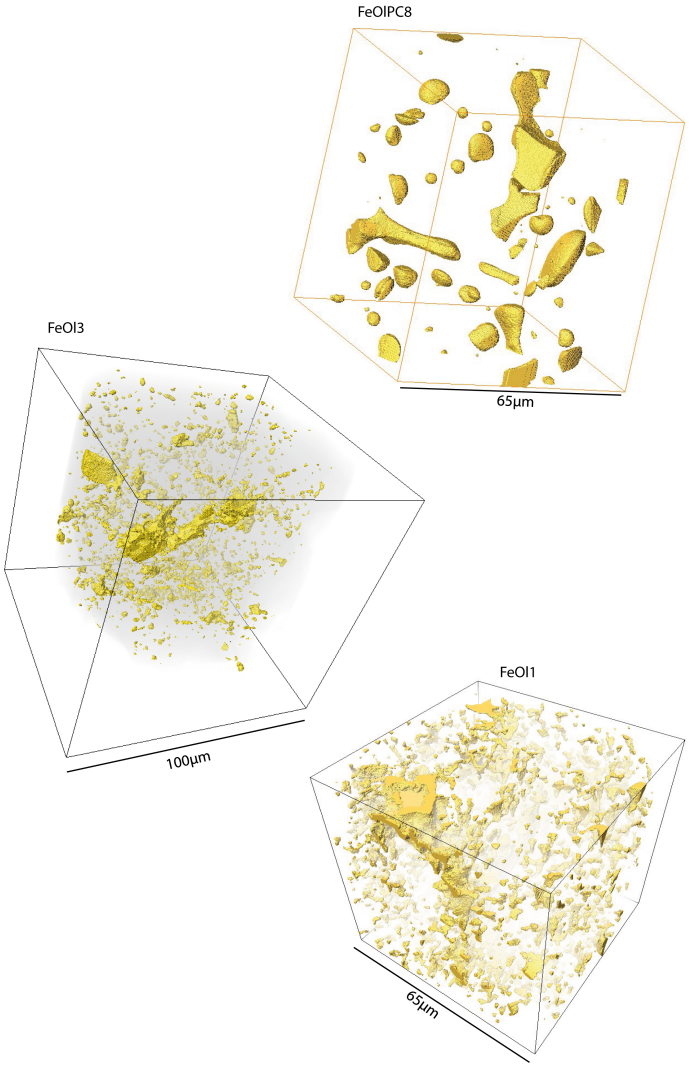

Figure 3.18: Reconstructions of melt within nano-CT scans carried out at MXIF. Olivine is rendered transparent (faint grey in FeOl3 to show sample outline) and FeS gold. FeOlPC8 is an undeformed sample while FeOl3 and FeOl1 are deformed. Differences in texture are described in the text.

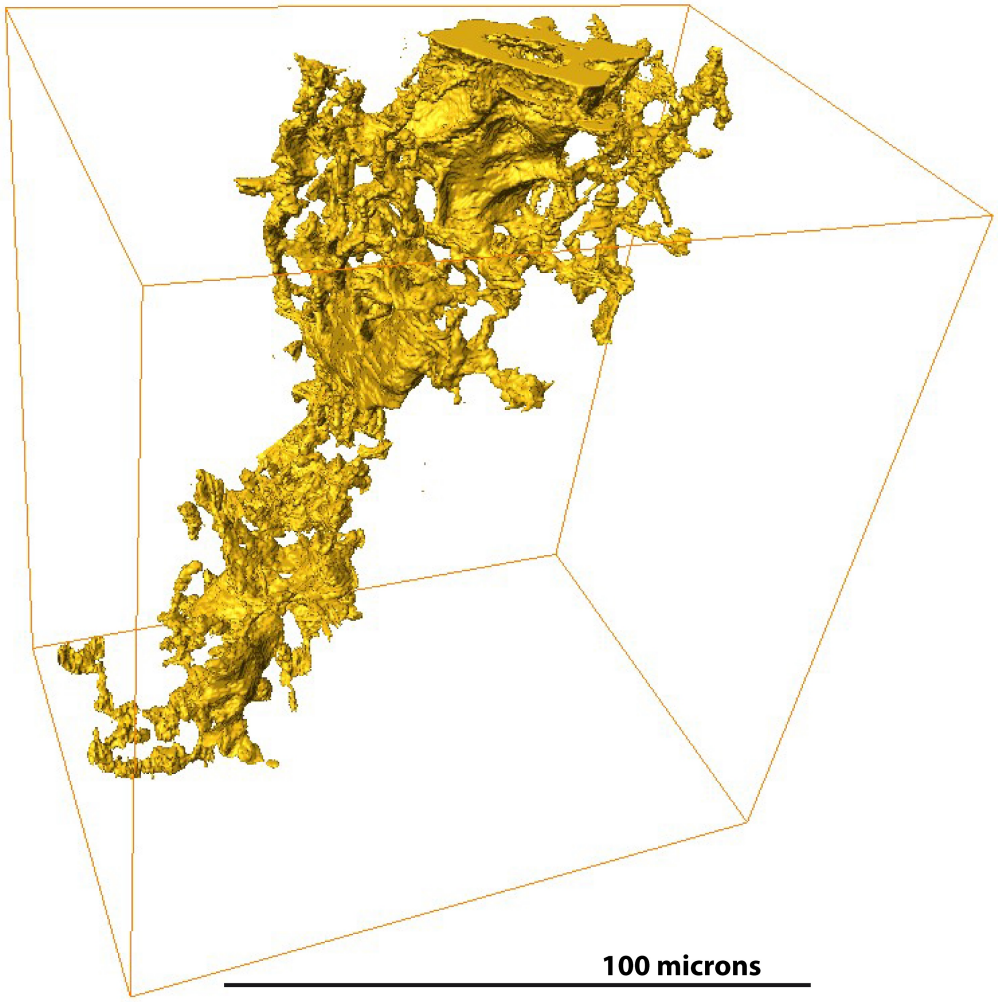

Figure 3.19: 3D nano-tomographic reconstruction of a deformation melt network. A. Reconstruction of the largest interconnected FeS melt accumulation within a small sub-volume of FeOl1 at a resolution of 130nm. This represents around 1/3 of the melt in the volume scanned (Full reconstruction shown in Figure 4A). Note fine sheets of melt joining larger melt accumulations.

Particle shape analysis

High resolution nano-CT scans give an opportunity to examine geometry of individual melt pockets to investigate how deformation may act to change melt textures and how this may be related to melt connectivity.

Melt connectivity is thought to relate to melt geometry by concavity / convexity of a particle shape. A melt pocket of more convex nature is more likely to be isolated than a particle with a concave, more convolute shape, in essence describing the shape's specific surface area (Bear, 1972,p.50). Therefore an important parameter to investigate is the relationship

between melt pocket volume, and surface area, which can indicate how convex a shape is. This is particularly the case where thin melt sheets may be missed in segmentation that would otherwise connect two melt volumes. The shape of the disconnected melt pockets can give an indication of their potential connectivity, even if the actual network is unresolvable.

Two parameters for testing this relationship have been used using Avizo Fire 8 analysis modules on segmented melt reconstructions:

The first uses the parameter of Fragmentation Index (FI), a calculation which compares the relationship between volume and surface area of a phase within a binarised image before and after a voxel dilation has taken place. FI is defined as

$$FragmentationIndex = \left(\frac{P_b - P_a}{A_b - A_a}\right) \tag{3.1}$$

where P = perimeter, A = area and subscripts b and a refer to those values *before* and *after* dilation, respectively. Lower fragmentation index values should indicate a more convex shape and therefore a more interconnected melt geometry. Input into the analysis module is in the form of a pre-segmented binary image (in this case, melt and non-melt phases) and a kernel size, which specifies the number of voxels the binarised images are dilated by. Output is in the form of an average value to describe the full dataset. This analysis has been carried out on both micro- and nano-CT scans to examine differences caused by variation in resolution.

Results of this analysis are shown in Figure 3.20. The chosen Kernel size has a large impact on the resultant fragmentation index, with differences between samples generally much greater at low kernel sizes, potentially making these the most useful for analysis. In micro-CT analysis the undeformed sample FeOlPC8 does show a much higher fragmentation index at low kernel size of dilation, which is expected as the texture suggests more convex melt pockets and isolated melt. However, at a kernel size >1 this relationship breaks down, and FeOlPC8 is shown to become more interconnected. This may be due to a combination of dense spacing of melt pockets and a low resolution scan, leading to a quick increase in connectivity by melding of pockets at higher kernels of dilation. Deformed samples show a lower fragmentation index at small K values, and each follows a similar pattern, maybe reflecting some similarity in melt texture.

Analysis reveals initially unexpected results in nano-scans. The undeformed sample FeOlPC8 shows the lowest FI and therefore theoretically highest interconnectivity, followed by FeOl1 ultra-nano samples. From textural observations it is clear that this does not match with the concavity of melt particles observed in the sample. The reason for this apparent disparity may be the fact that FI is carried out on the sample as a whole, examining the relative difference in melt volume and area of all melt pockets. This does not take into account the proportion of melt in each particular melt pocket. Melt in deformed samples is spread across a larger number of small melt pockets, but a large majority of melt resides in large volume accumulations. The

results of this analysis are therefore unlikely to represent true connectivity of the majority of melt in deformed samples.

An alternative technique was used to carry out individual analysis of melt pocket shape using the Label Analysis feature on Avizo Fire, and the in-built shape factor Shape_VA3d, defined as

$$Shape_VA3d = \frac{(Area3D)^3}{(36x\pi xArea^2)} \tag{3.2}$$

Where Area3D is the measured 3D surface area of the particle, and Area is the area of the particle shape cross-section. In this case, a higher value indicates a higher surface area to volume ratio and therefore a more concave, or convolute melt pocket shape. Individually labelled particles can be filtered using the Analysis Filter module, allowing groups of particles to be visualised within a specific range of shape values. Analysis was only carried out on nano-CT scans as these show true melt volume shape. Results are shown in Figure 3.21 and Figure 3.22 for all nano-CT scans carried out, showing volume reconstructions of melt pockets filtered to ranges of SV value of <2, 2-10, and >10.

Shape factor value correlates well with visual appearance of melt pockets. Shapes of factor 2 are convex and close to spherical. This category is inferred to represent stranded melt in tiny spherical melt pockets as observed in 2D observations of deformed samples and in previous studies (Nichols, 1976). Those of SV >10 have more complex convolute shapes indicating melt sheets and tubes, that suggest interconnectivity across multiple olivine grains. Intermediate SV values of 2-10 represent relatively flattened melt sheets of intermediate size. Examining these intermediate melt pockets qualitatively, particularly in sample FeOl1 there appears to be a fabric produced by alignment of these melt sheets, which could reflect the overall sample fabric observed in micro-CT analysis (section 3.3.3). Although these melt pockets are isolated within the nano-CT reconstructions, it may be reasonable to assume, due to their shape, that they represent melt wetting grain boundaries and therefore that they have the potential to connect together with ongoing deformation.

As seen in Figure 3.21, a correlation exists between melt shape and melt volume in deformed samples, with near-spherical melt pockets being solely restricted to very small melt pocket volumes, and more complex convolute shapes restricted to larger melt volumes. In contrast, the undeformed sample FeOlPC8 (Figure 3.22) shows a weaker correlation, with larger melt volumes also having near spherical convex shapes. FeOlPC8 does not have any melt particles with a shape factor greater than 10, supporting the observation that the undeformed sample is made up of mostly high dihedral angle, isolated melt pockets and that the percolation threshold is high in undeformed samples. The ultra-nano CT scan of FeOl1 appears to have a similar melt geometry to FeOlPC8, but the scale of individual melt pockets is in fact an order of magnitude smaller. This reflects the tendency for deformation to distribute melt more finely

across the sample.

Nano-CT resolution gives a relatively reliable measure of melt volume %, therefore the fraction of melt within each shape category can be used to get a rough idea of melt fraction within samples that is stranded in isolated near-spherical melt pockets in deformed vs. undeformed samples. Results of shape distribution vs. melt volume across the nano scans are shown in Figure 3.23. These results have been normalised to the max. melt content of 5 vol% expected in each sample. This is to take into account the fact that the scans are a random volume within a sample of variable melt distribution and that variability is caused by localised redistribution of melt. For example, the total melt vol% within reconstruction FeOl1 is 4.1%, which is close to the 5 vol% average. However, the scan in FeOl3 only contains 1.3 vol% melt. Therefore the nano-scan of FeOl3 is likely to represent a relatively drained volume of the sample. This can be seen reflected in the shape - volume distribution, as the relative proportion of small spherical pockets of melt of FeOl3, FeOl1 and the UHR scan of FeOl1 are all very similar when normalised to the average melt content of the sample. Therefore the amount of melt that is isolated in small spherical melt pockets is similar across the samples, but FeOl3 and FeOl1 UHR scans do not have any larger melt veins present in the volumes of interest (they are likely to be elsewhere in the samples). The undeformed sample shows a very different distribution, with >20% of total melt fraction found in pockets of near-spherical shape.

A tentative prediction of stranded melt fraction can therefore be made from these results. Assuming that melt in near spherical (SF<2) melt pockets is definitely isolated, and that melt in highly convolute pockets (SF>10) are definitely connected across multiple grains, it can be inferred that the stranded melt fraction lies somewhere in the region of 0.5-2vol%. As described previously, alignment and flattening of the intermediate geometry melt pockets within FeOl1 suggest there is at least potential for these melt pockets to become interconnected. Taking into account that the melt observed here is a sample quenched during ongoing deformation, my estimate for a stranded melt fraction would lie closer to the minimum of this estimate.

Individual analysis of melt pockets helps to explain why results from the Fragmentation Index were inconclusive. The Fragmentation Index does not take into account volume of individual shapes analysed, therefore the large frequency of spherical melt pockets within deformed samples leads to a high FI value. However, label analysis indicates that the amount of melt within these numerous small melt pockets is only a small fraction of the whole, making individual melt pocket analysis a more reliable indicator of connectivity.

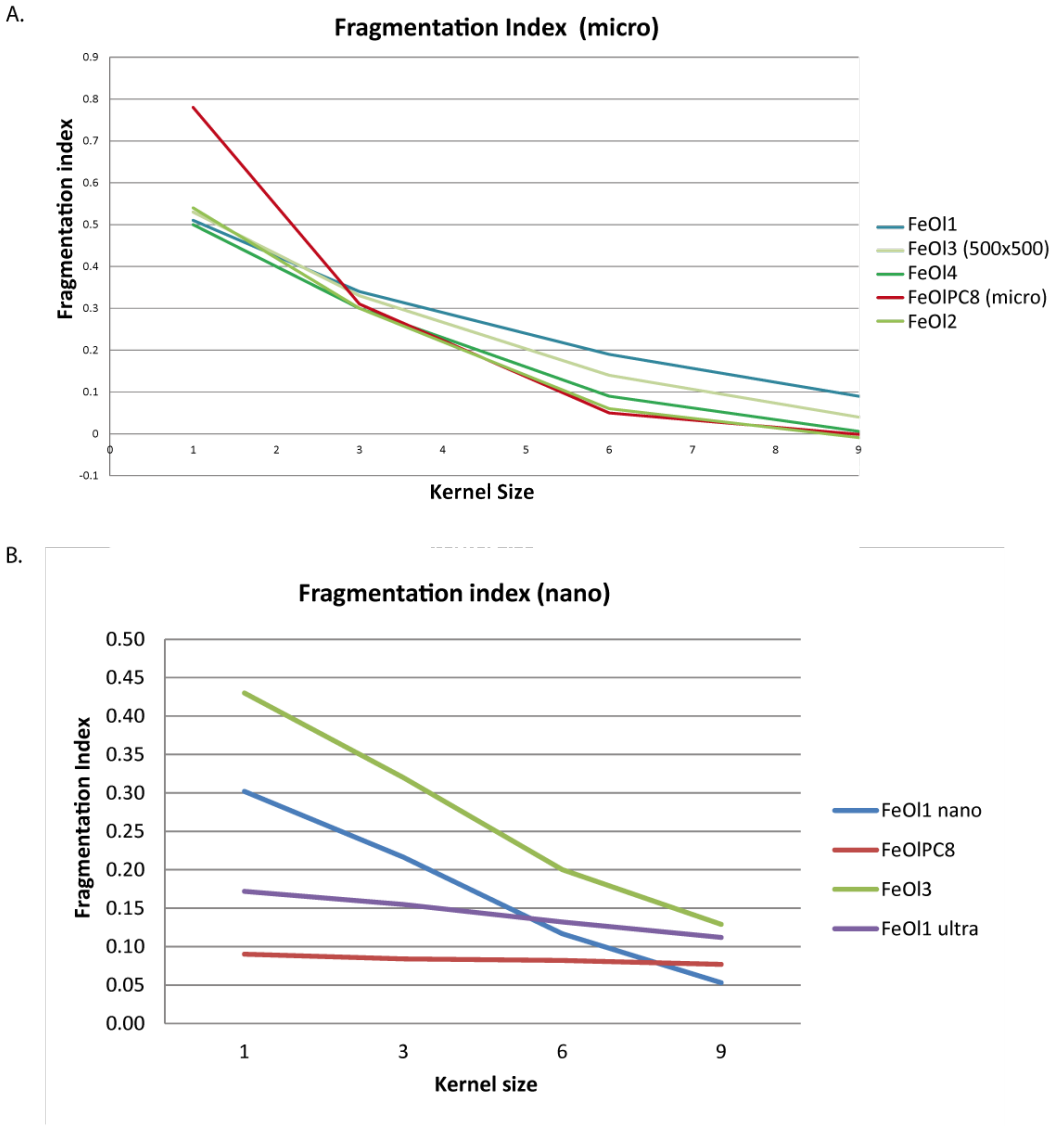

Figure 3.20: Fragmentation index (FI) analysis of micro- (top) and nano-CT scans (bottom), using Fragmentation Index module from Avizo Fire 8. Analysis is carried out on the full segmented dataset and represents the average fragmentation index across all melt pockets. Kernel size indicates the number of voxels the segmentation is dilated by as part of the analysis. A lower fragmentation index should theoretically indicate higher overall connectivity. However, as this analysis is carried out on the whole dataset and does not take into account melt volume, further investigation shows these values cannot be seen as representative of actual sample connectivity (see text).

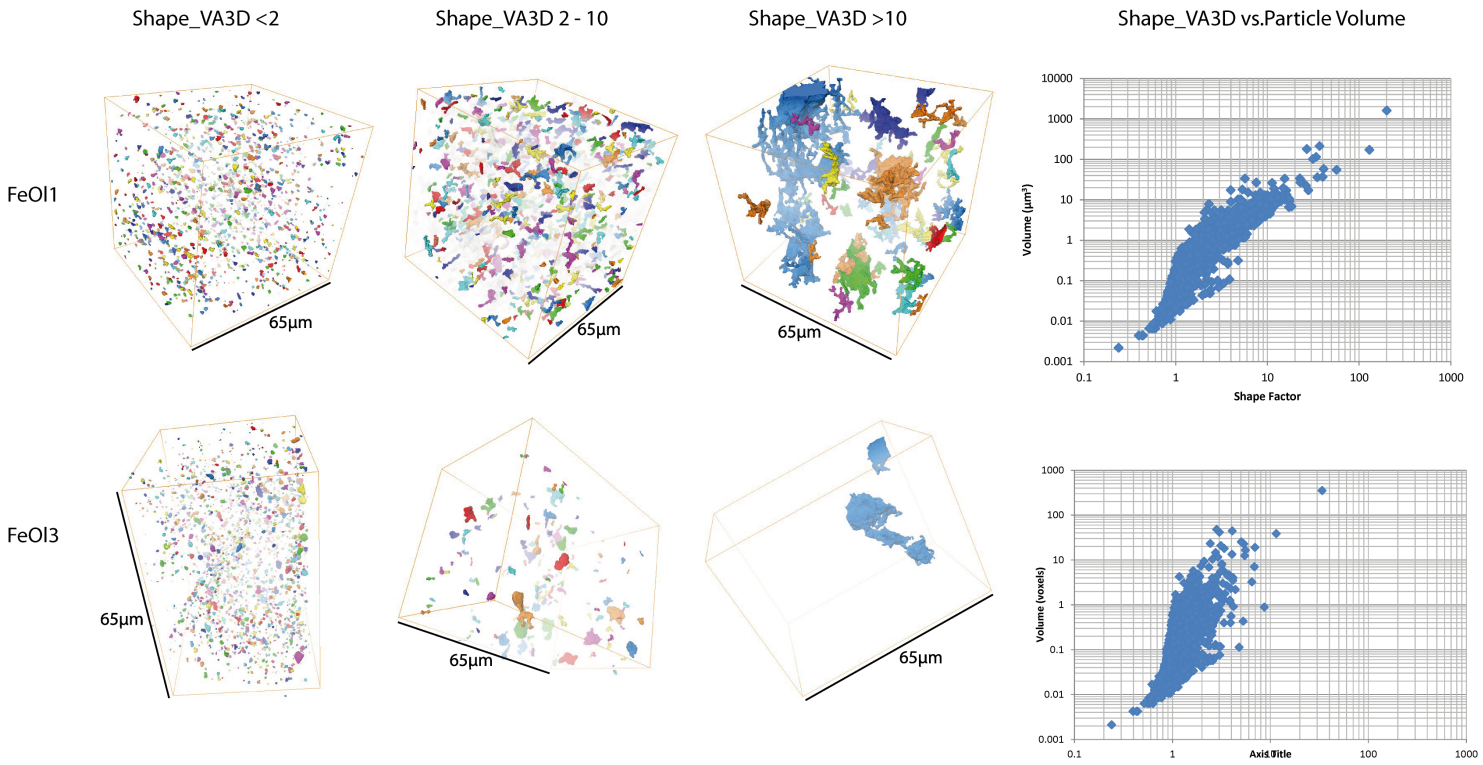

Figure 3.21: Analysis of shape factor Shape_VA3d (Avizo Fire ^{TM}) on nano-CT reconstructions of deformed samples FeOl1 and FeOl3. For each sample, a volume rendering of segmented melt is shown which has a shape factor of <2 (left), 2-10 (middle), and >10 (right). In addition, a plot showing relationship between segmented volume and shape factor is given for each sample. Total melt fraction in FeOl1 is 4.1vol%, in FeOl3 1.3vol%. The average melt% across the sample is 5vol%. This variation is expected as melt distribution is shown to be highly variable from micro-CT analysis. The difference in melt shape distribution across both deformed samples can to some extent be explained by the varying melt fraction observed in each sample – see text for details.

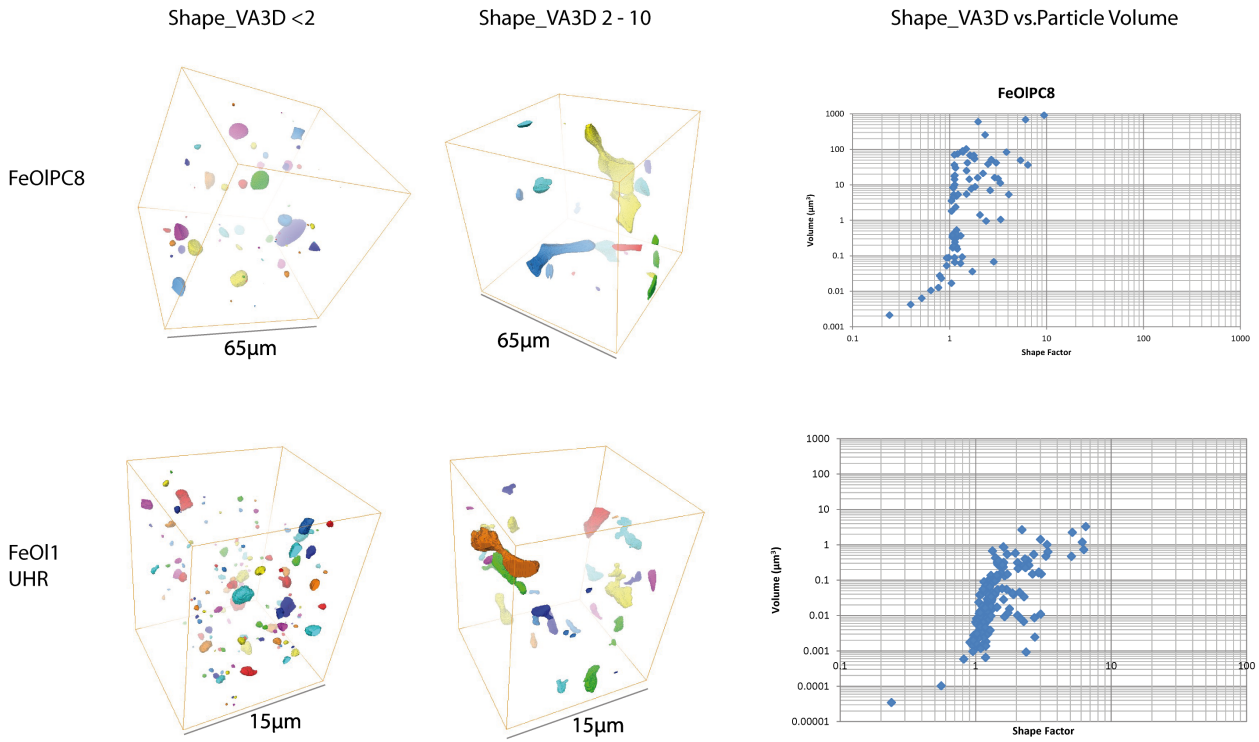

Figure 3.22: Shape analysis and filtered images showing variation in Shape_VA3d value of nano-CT reconstruction of undeformed FeOlPC8, and ultra-high-resolution scan of FeOl1 (15µm field of view). Volume renders of particles with shape factors of <2, and 2-10, are shown, along with a graph of volume vs. shape factor for each sample. Both samples show a reduced range of shape factors compared to those of deformed samples in Figure 3.21. The UHR scan of FeOl1 represents an area that is relatively drained of melt, with melt taking up only 1.3vol% of the total sample volume. In FeOlPC8 melt represents 2.7vol% of total sample volume.

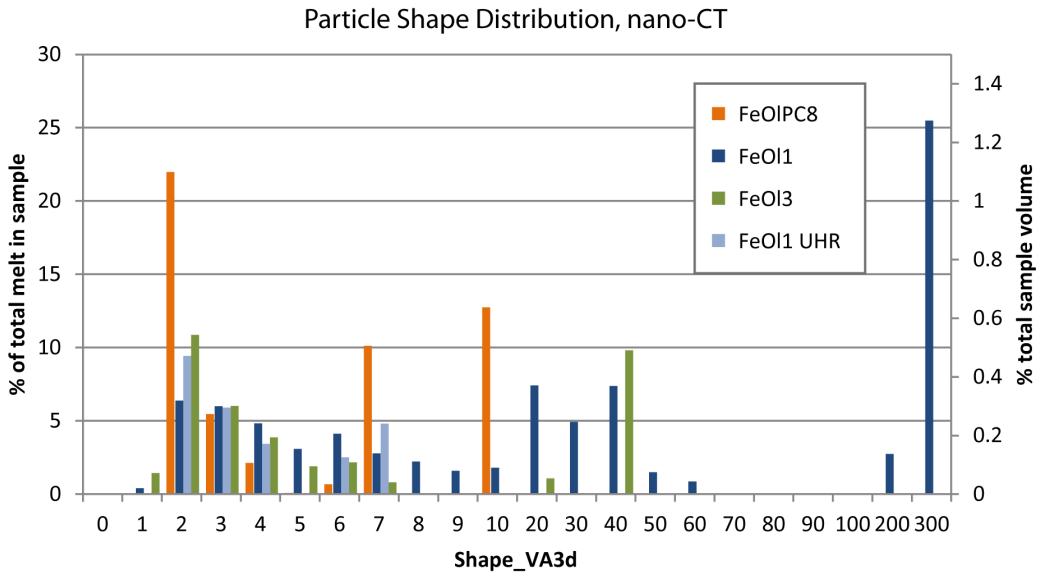

Figure 3.23: Distribution of melt across pockets of varying shape within nano-CT reconstructions of experimental samples. Each sample is expected to contain 5vol% melt on average. Melt proportions have been normalised to show the proportion of melt observed relative to this average melt content (left) and as a % of the total sample volume (this assumes the relationship between melt geometry and melt pocket volume is roughly constant across the sample). This allows a better comparison between the scanned volumes, which each have a different melt fraction due to random selection of volumes from samples which have an inherent variability in melt fraction. It is clear that, despite only showing a small fraction of melt within samples FeOl3 and FeOl1 (ultra-high resolution), both samples follow the distribution of deformed sample FeOl1, suggesting that a similar proportion of melt may be stranded in small isolated melt pockets. In each case the proportion of melt in near spherical melt pockets (2 or less) is less than 10%. In comparison, undeformed sample FeOlPC8 has >20% of melt in pockets of near spherical shape.

Skeletonisation to characterise melt connectivity

Geometry of melt pockets can be used indirectly as a proxy to assess melt connectivity in terms of concavity of a surface, although this can only be used to assess relative connectivity and is not enough to support definite conclusions regarding melt connectivity. A process of skeletonisation has been used to further characterise connectivity of the reconstructed nano-resolution melt geometry in FeOl1 compared to undeformed sample FeOlPC8. Skeletonisation involves reducing a complex 3D network to a series of one-dimensional branches which follow the center-lines through the structure, and nodes where branches intersect or terminate and allows quantification of melt network interconnectivity directly from 3D images. The theory and process of skeletonisation is described in section 2.3.5.

Skeletonisation was carried out using the AVIZO Fire 8 Skeletonisation module, using default auto-skeletonisation settings. Input was in the form of previously segmented nano-resolution data of our slowest strain-rate experiment FeOl1, and undeformed sample FeOlPC8, both of which were scanned at the same resolution of 0.13µm. The single largest interconnected network from FeOl1 (Figure 3.19) was also examined individually to compare its connectivity to the full melt volume. The resulting topological spatial graphs were analysed for their branch length, thickness and volume. Cleaning of data and node connectivity analysis was carried out using using SkeletonCleaner software, written by Laurent Montési and Kevin Miller of the University of Maryland (Miller et al., 2014; Zhu et al., 2011).

Figure 3.24 shows the results of the skeletonisation of the FeOl1 nano-tomographic dataset (full reconstruction), along with the undeformed control sample FeOlPC8. Figure 3.25 shows the quantitative average of these two examples.

An ideal fully interconnected melt network of tubules along triple junctions is predicted to have four branches per node (VonBargen and Waff, 1986), although natural basaltic melt networks studied have an average closer to three, even at textural equilibrium, which may be in part an artefact of the skeletonisation process (Zhu et al., 2011). The fact that our melt networks are clearly anisotropic also means that an average of 4-fold connectivity should not be expected. Only isotropic melt networks would be expected to show a 4-fold connectivity, as this represents a fully symmetric geometry (Zhu, pers. comm.).

The undeformed sample has a very low number of melt pockets within the volume scanned, and frequency of nodes is an order of magnitude lower than in the deformed samples. The undeformed melt pockets show the largest majority of individual dead-ends, as expected, and average connectivity is lower than in the full network scan of the deformed sample. It may be that the connectivity is still over-estimated however, as a number of small dead-end melt pockets appear to have been removed as part of the skeletonisation process (compare Figure 3.24 C., i) and ii).)

The full 3D dataset of deformed sample FeOl1 (Figure 3.24A) produces a skeleton with

a majority of dead-ends, although one third of nodes are three-fold connections (Figure 3.24 Aiii). An average connectivity of 1.9 suggests that melt is interconnected, although less than in an ideal theoretical network, as expected for an anisotropic system, far removed from textural equilibrium. The measured connectivity is likely to be a lower estimate as very fine (<0.1μm thickness) melt sheets connecting regions of melt are missed in segmentation due to resolution limitations.

The fully interconnected network has a higher average connectivity of 2.4, with a majority of 3-fold co-ordination nodes present. The average connectivity is still lower than that in basaltic networks found in Zhu et al. (2011), but this is expected due to anisotropy of the melt network.

It is possible that connectivity is underestimated, because of the difficulty of segmenting fine melt networks. Some very thin branches that should be connected may have been cut off by the process of segmentation into separate pockets. To test this, we have examined the effect on the skeleton of dilating and eroding the segmented network by 1 and 2 voxels in the 3D volume. Theoretically, any networks that have been cut off by the segmentation process may be re-joined by dilation, thereby increasing network connectivity. Figure 3.26A shows the results of this analysis, both before and after pruning of the skeleton. There does appear to be an increase in connectivity with dilation of the segmented network, but this is only significant in the pre-cleaned skeleton, suggesting the increase may be due to an increase in the number of artefacts produced than in the connection of real networks, and that the segmentation process has segmented the majority of melt networks effectively.

A Region of Interest (ROI) analysis was carried out examining using small sub-samples of the segmented melt network to examine the effect of sample volume on the connectivity. Results are shown in Figure 3.26B. Average connectivity of nodes is higher in smaller sub-volumes, and decreases regularly with increasing ROI. This is particularly marked in the examination of the single melt network skeleton. We see no levelling off of the network connectivity value, suggesting we have not reached a sample size representative of connectivity in the full sample. However, reaching a constant connectivity in an anisotropic deformation melt network is not expected. A large melt network is likely to be immediately surrounded by a 'drained' region of reduced connectivity, which this analysis may be capturing. It does show, however, a limitation in this analysis. Due to the small sample size of our nano-tomographic scan we cannot predict quantitatively the connectivity of the surrounding full sample. The observation of frequent veins in 2D analysis and the presence of large melt accumulations in lower resolution CT scans suggests connectivity is likely to be highly variable with localised maxima across the sample.

The skeletonisation process also stores information about branch length and mean thickness, allowing a simple analysis of shape variation within a single segmented melt pocket / vein. This can be difficult to achieve without skeletonisation, as other 3D label analysis

treats each melt pocket as one object, and only the total shape is analysed, which is too large a simplification for complex melt networks with multiple branches. The results shown in Figure 3.27 highlight the geometric differences between melt in deformed and undeformed samples. In deformed samples melt is distributed across multiple branches creating a total length of branches that far exceeds the total length of the melt pocket, as suggested by the observed visual geometry.

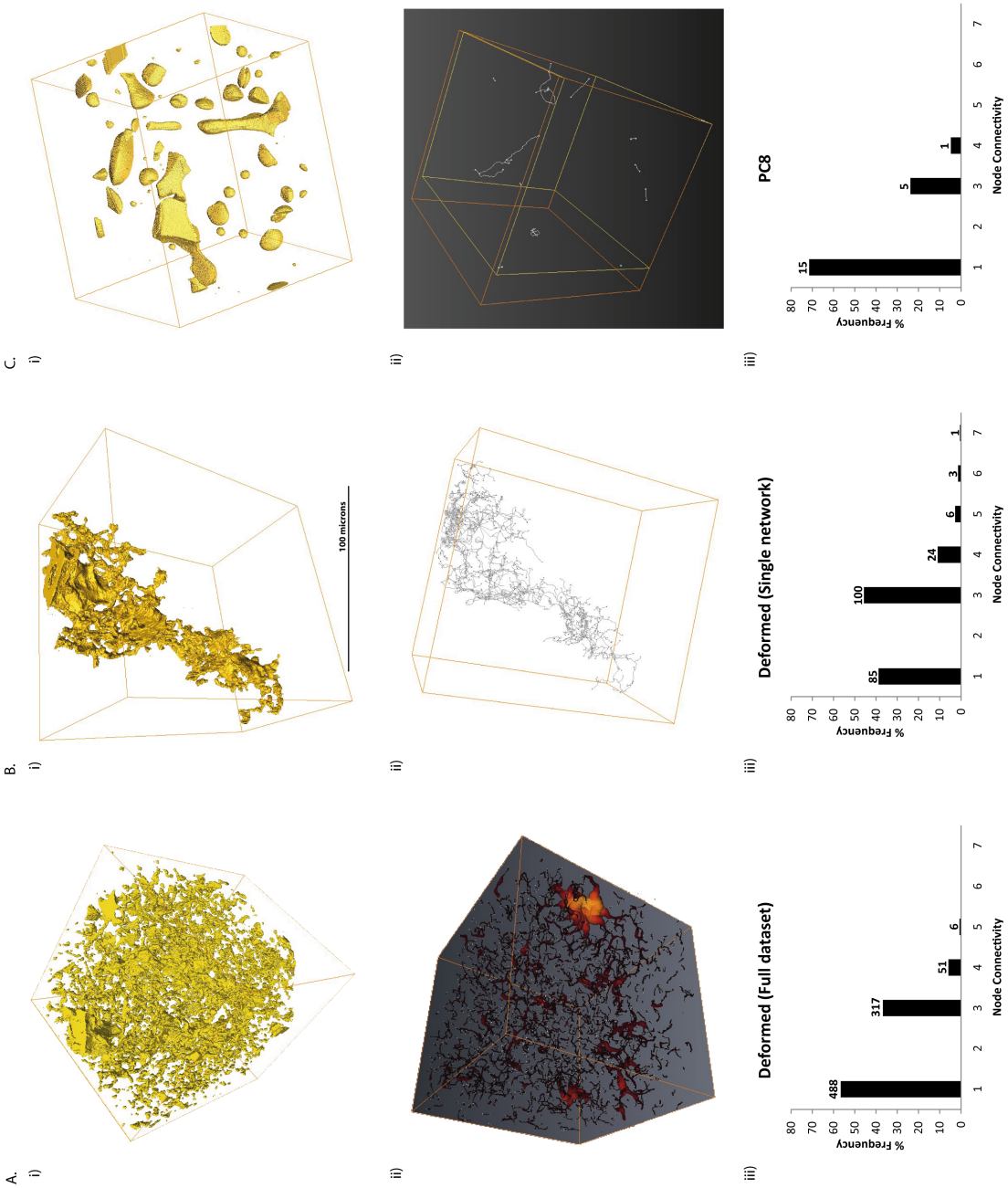

Figure 3.24: Caption on next page

Figure 3.24 ***(preceding page)*****:** Skeletonisation results from A. Deformed sample FeOl1: full dataset. B. Deformed sample using only largest single interconnected network. C. Undeformed sample PC8. In each case i) represents the original segmented dataset (melt rendered gold, olivine transparent), ii) represents the skeleton produced. The skeleton in A. also shows the average thickness of individual branches as calculated during the skeletonisation process. iii) a graph of node connectivity vs % frequency of the skeleton networks as calculated from a 300x300x300 voxel region of interest using the Scobacleaner software (see section 2.3.5). The frequency of nodes is given above each column. The single network has a majority of 3-fold co-ordination nodes, while the full network has a larger number of disconnected single node dead-ends. This shows there are a significant number of dead-end pockets still present in the sample. The total frequency of nodes in the undeformed samples is an order of magnitude less than in the deformed sample. Also, the proportion of disconnected single node networks is greatest in the undeformed sample. However, by comparing C i) and ii) it is clear that not all segmented melt pockets have been interpreted as branches by the skeletonization software, therefore the proportion of dead-end branches is likely to be even higher in undeformed samples.

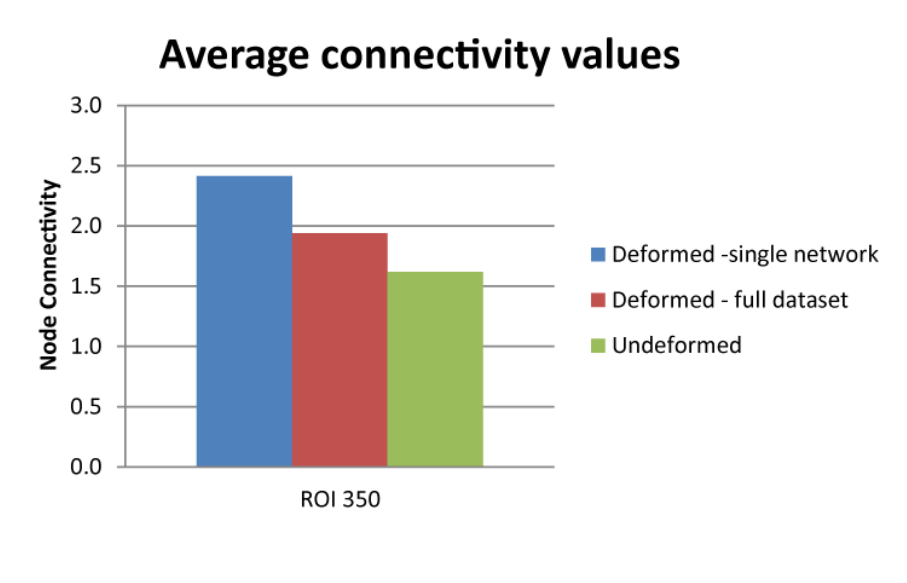

Figure 3.25: The average connectivity of deformed vs undeformed samples from skeletonization analysis for regions of interest shown in Figure 3.24. The single network has, as expected, a higher connectivity than the full dataset of the deformed sample, which includes numerous isolated melt pockets. Again, full dataset analysis does not take into account the higher proportion of melt within larger interconnected channels, therefore is likely to underestimate connectivity within deformed samples.

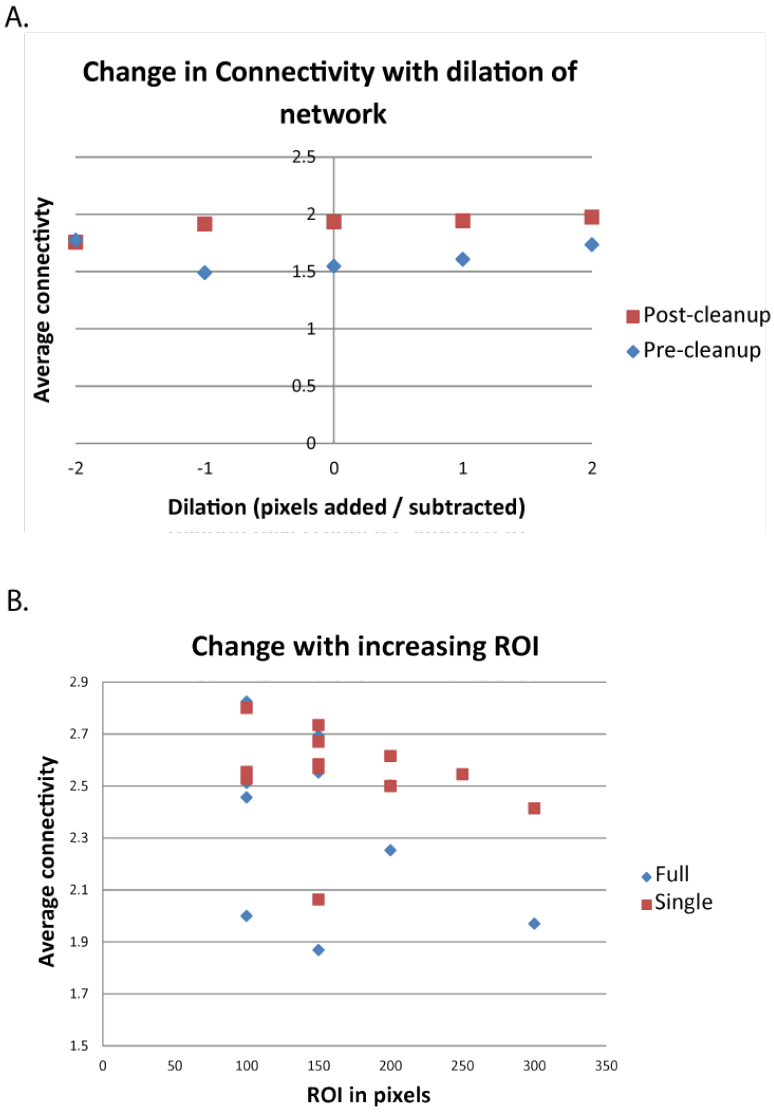

Figure 3.26: Graphs showing quantitative results of skeletonisation connectivity analysis and evaluation of error. A. The segmented images (input to the segmentation process) were dilated/reduced by 1, 2 pixels at the melt edges, to examine the effect of over/under thresholding the original greyscale image. This has a larger effect on the skeleton before processing in the skeletonwrapper software, which suggests that a mis-thresholding leads to an increased number of artefacts rather than a true increase in connectivity . Overall changes in connectivity after processing are negligible. B. Datasets were split into sub-volume Regions of Interest (ROIs) to examine changes in connectivity with increasing volume of network examined. A general trend is seen of decreasing connectivity with increasing ROI. Connectivity values do not level off suggesting the region scanned is not large enough to be representative of the whole sample. However, connectivity within the sample is likely to be highly variable, dictated by the local variability of melt fraction within the sample.

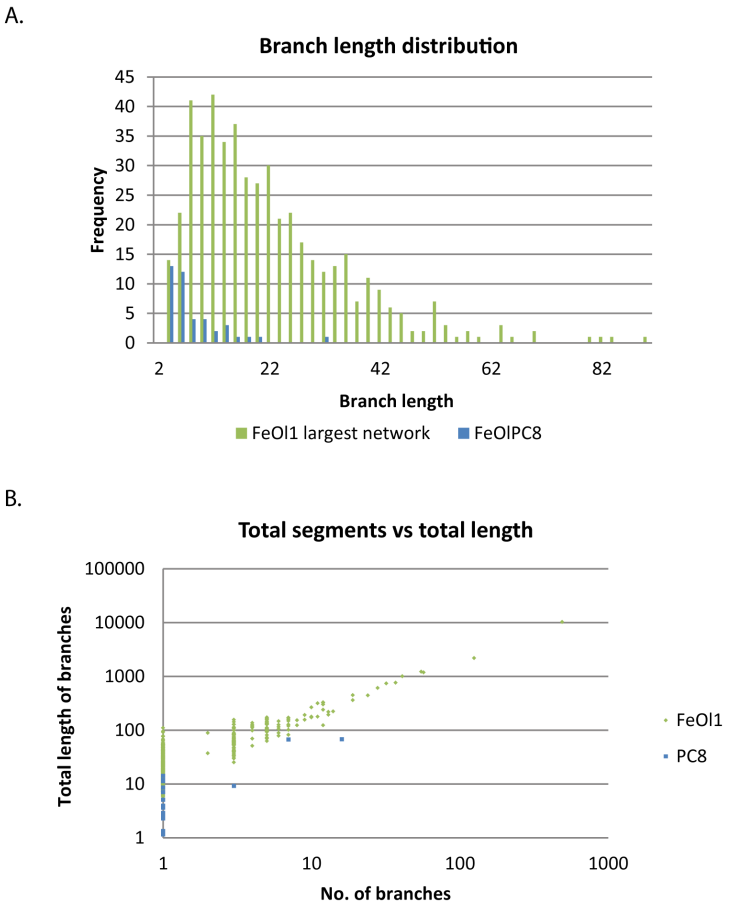

Figure 3.27: Branch length analysis from skeletons of deformed and undeformed samples. A. A comparison of the distribution of branch lengths in the largest connected network of FeOl1, and the full FeOlPC8 segmentation. Only the largest connected network was examined in FeOl1 because of the difficulty of processing all 1000 individual graphs to analyse mean length distribution. Branch length overall is much greater in the deformed sample. Also, the number of branches within the single deformed network is orders of magnitude greater than the number of branches in the total undeformed segmented sample (made up of 18 individual isolated skeletons). This reveals the complexity of the deformed melt network, being made up of numerous larger melt pockets connected by wetted grain boundaries between numerous small olivine grains. B. The total number of branches in each isolated graph vs. total length of branches summed for each graph. Total length of branches in the deformed networks is almost 2 orders of magnitude greater than the largest skeleton observed in the undeformed sample. Lengths are in voxels, each voxel representing a length of 0.13µm.

Qualitative modelling of fluid flow within a deformation melt network

In order to examine preferential fluid flow through deformed melt networks, a Lattice-Boltzmann simulation of fluid flow was carried out through a mesh created from volume renderings of the fully connected melt network dataset of FeOl1 (Figure 3.19). Modelling was carried out by James Carr, University of Manchester. The segmented image of the iron melt was surface meshed using AVIZO and exported as a STereoLithography (STL) surface. The volume meshing and simulation was performed using the Open Field Operation and Manipulation (OpenFOAM) Computational Fluid Dynamics (CFD) toolbox. Volume meshing was performed using the snappyHexMesh utility to form a Finite Element mesh consisting of hexahedra and split-hexahedra. A pressure gradient was applied as boundary conditions across adjacent bounding faces of the volume which intersect the segmented iron melt. A transient solver for incompressible laminar (non-turbulent) Newtonian flow was run to solve for a velocity field within the mesh.

Figure 3.28 A. shows the initial pressure gradient conditions input into the model. Flow is in the positive x direction (see axes in bottom left corner). Figure 3.28 B and C show the resulting flow pattern developed after a given time of flow. Due to the very fine nature of melt sheets within the reconstructed network it proved difficult to gain quantitative data from the model. Results show that melt is able to move from one edge of the sample volume to the other in orthogonal directions. Preferred paths of melt flow indicate that melt is required to flow through fine sheets between grains and cannot bypass these through larger 3-grain boundary tubules, in contrast to results inferred from basaltic melt networks (Zhu et al., 2011). This means fine sheets are likely to limit the permeability of the system, which needs to be taken into account in simple permeability models (see discussion). It may be possible to carry out quantitative analysis by Lattice-Boltzmann modelling by refining the model. However, it is unclear how representative these results would be of melt migration within deforming melt networks. Lattice-Boltzmann techniques assume a static network, but our sample is a quenched snapshot of a melt network evolving through time. In addition, this melt network is from a very small sample volume and is unlikely to reflect overall permeability (i.e. it is not a representative elementary volume). It may be possible to model flow by incorporating aspects of an evolving melt network within a deforming matrix (Rutqvist et al., 2002) but this is beyond the scope of this study.

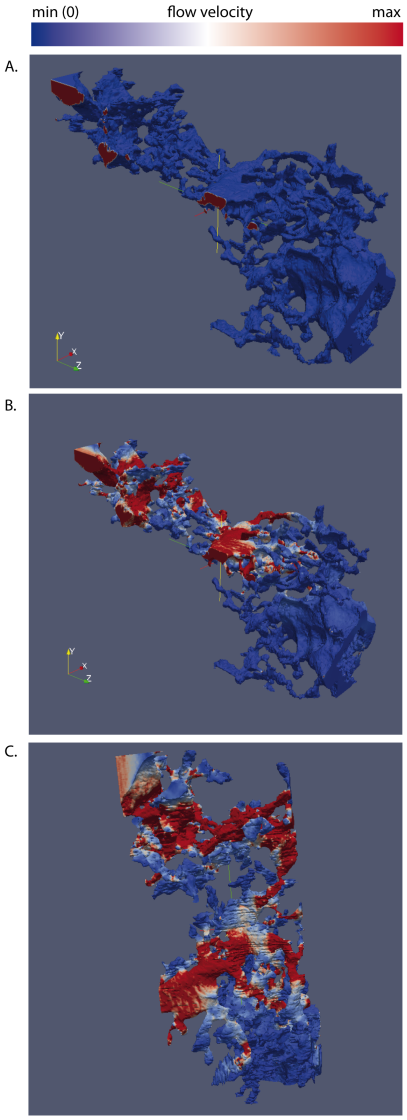

Figure 3.28: Lattice Boltzman model of fluid flow through the largest interconnected melt network in sample FeOl1. The colour scale key for all images is shown at the top. A. The initial boundary conditions showing max. pressure at the X- origin plane. B. Flow conditions after a time x. Melt has flown through the melt network showing preferential high velocity fluid pathways in larger volume spaces. However, high velocities are also seen in very fine tubules and sheets, indicating melt is forced to flow through these fluid pathways and therefore that permeability will be limited by these narrow bottlenecks. C. A view of the same flow in the Y direction showing the flow from X-min to X-max planes and flow through narrow melt pathways.

3.3.5 Summary of results from 3D analysis

Using a combination of micro- and nano-CT analysis allows us to combine broader low resolution data of melt distribution and texture across the full sample volume with more detailed characterisation of melt geometry and connectivity, in order to fully characterise differences within deformed and undeformed samples. A summary of the key results follow

- Melt in deformed samples is more finely distributed throughout samples in finer melt pockets, although overall melt distribution is more variable, suggesting local melt migration is taking place leading to melt-rich areas vs. relatively drained areas. The undeformed sample does show more variability in melt distribution than initially expected from 2D analysis, but variation is of a more even undulation and from 3D reconstructions it appears these are caused by clusters of isolated melt pockets, rather than connected melt veins.

- Fabric strength and orientation analysis suggests deformed samples generally do produce a fabric sub-horizontal to the maximum shear stress produced by torsional deformation. We do not see a clear correlation between stress orientation and the plunge and trend of melt pockets, as initially suggested by 2D ACF analysis of FeOl1 (section 3.3.2). Sample FeOl2 may have a fabric no stronger than that seen in the undeformed sample.

- Overall 3D analysis supports evidence that FeOl1 shows the greatest interconnectivity of our deformed samples, and that differences observed in 2D textures are not only produced by a poor polish. Sample FeOl2 appears to show the least changes from undeformed textures – this sample is from our shortest duration experiment (200min) suggesting experimental duration is an important factor in producing deformation melt textures.

- Analysis of melt geometry from nano-CT scans show fundamental differences in texture and scale of melt pockets in deformed and undeformed samples. Although a large number of melt pockets in deformed samples are spherical and appear isolated, these are of a much finer scale than in deformed samples and represent a much smaller volume fraction of melt. This disparity between melt pocket frequency and volume leads to a biased result in whole-sample connectivity analysis. Despite this, skeletonisation analysis indicates that deformed samples show a greater overall connectivity than undeformed samples.

- We have shown that deformation clearly acts to enhance connectivity in a liquid FeS-solid olivine system. Experimental duration, rather than total strain or strain-rate, appears to have the greatest impact on melt textures produced.

3.3.6 EBSD analysis of olivine crystals in experimental samples

We have used Electron Backscatter Diffraction (EBSD) in order to examine the preferred crystal orientation, internal crystal deformation and grain size of olivine crystals within our samples. This data could potentially help us to investigate

- deformation mechanisms occurring in our samples – *knowing the mechanism of deformation and the slip-system in which olivine deforms helps to compare results to natural samples*
- strain partitioning between melt and liquids in the sample - *it may be possible to infer interconnectivity by assessing how much strain has been taken up by melt as opposed to olivine grains. The presence of melt can change CPO by leading to strain partitioning in melt-rich and melt-poor zones or facilitating crystal rotation; the effect it has is shown to vary according to system permeability (Holtzman, Kohlstedt, et al., 2003, section 1.2.1).*
- processes affecting grain growth and recrystallisation in deformed and statically annealed samples - *Do we see a change in processes in deformed vs undeformed samples in terms of olivine grain growth? Is there a change in grain size? If so is this due to dynamic recrystallisation or the pinning of grains leading to decreased grain growth?*

Results of EBSD analysis conducted for this study are shown in Figures 3.29-3.34, in the form of All Euler maps, pole figures showing alignment of the main three crystallographic axes in 3D space, and inverse pole figures showing the preferential alignment of specific axes towards the three reference axes of the sample (see section 2.4.4).

EBSD maps and CPO development

The undeformed sample scanned shows a very bimodal distribution of crystal sizes (Figure 3.29). The bimodal nature of grain-size distribution may have developed by Ostwald ripening enhancing the size distribution of an already variable grain-size during annealing, as large crystals grow at expense of smaller (Karato, 2008). However, this sample is of an earlier generation in which grain size was more variable initially and so cannot be directly compared to deformed samples. The general crystal orientation is close to random, as expected for an undeformed sample, although larger grains show some evidence of dispersion of 100 and 010 axes along small circles (Figure 3.29B), which are interpreted as kink-bands formed by dislocation slip (Burnley et al., 2013, E. Mariani, *pers. comm.*). These may be caused by initial compaction damaging larger grains.

In comparison to undeformed samples, all deformed samples show a stronger crystal preferred orientation. Due to the orientation of sample sections care must be taken when interpreting the exact processes creating them:

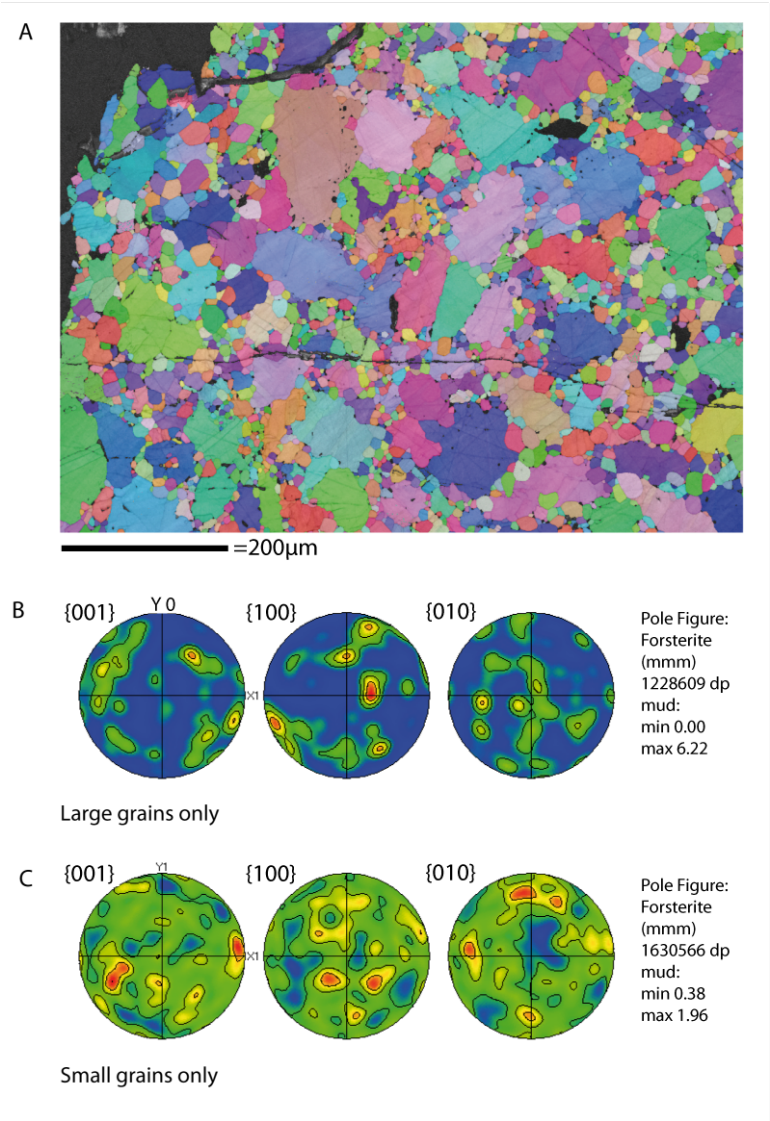

Figure 3.29: Band contrast map of FeOlPC5 sub-area with all euler angle colours overlain (similar colours generally represent a similar orientation). The map highlights individual grains - There is a clearly bimodal grain size distribution in the sample. B. Pole figures of large grains (>10µm). There is a weak tendency for axes to be dispersed over small circles within large grains, which is a sign of deformation by dislocation creep (formation of kink bands - see section 3.3.6). This may have occurred during compaction C. the distribution of small grains within the undeformed samples is essentially random, as expected from a sample that has annealed under hydrostatic confining pressures.

FeOl1 and FeOl4 were investigated on their mid-section cut. This means the shear stress will be at a maximum at the edge closest to the capsule, and theoretically close to zero at the sample centre. If the cut is directly through the mid-section, the shear plane will be

perpendicular to the slice examined, coming out of the page. It is likely, however, that the mid-section cut is not directly through the exact sample centre, but is instead somewhere between a direct mid-section and a tangential slice. Also, strain partitioning within the sample may mean that horizontal shearing could be taking place directly through the sample centre. In this case, the shear plane would be horizontal in the resulting pole figures, and therefore directly comparable to those used in Holtzman, Kohlstedt, et al. (2003) and other previous studies (King et al., 2010; Tkalcec et al., 2013).

FeOl2 analysis was conducted on a planar section of sample, i.e. looking down onto the top of the shear plane. The rotational axis is perpendicular to the plane of cut. This means that theoretically, deformation changes from a maximum of simple shear, oriented N-S at the edge of the capsule, to being at its minimum, and rotational (constantly changing direction of maximum stress in the sample centre, see diagram Figure 3.32). To compare the resulting pole figures to FeOl1, FeOl4 and previous studies, two 90° rotations must be carried out to make sure the shear plane is oriented horizontally. Of course, the data is not truly 3-dimensional, therefore this rotation is not showing the true CPO as measured from an alternative orientation. Taking EBSD data from three orthogonal cuts would improve interpretation of true 3D crystal CPO.

Figure 3.33 A. shows schematic pole figures summarising CPO developed to allow comparison between samples, following the same method as Tkalcec et al. (2013). In each case, therefore, two schematic pole figures have been created - one where the shear plane is assumed to be already horizontal, and one rotated assuming initial sample orientation as shown in results figures. This should allow comparison to summaries of classic CPO observed in olivine, created by Tkalcec et al. (2013), and shown in figure 3.33B.

Assuming the pole figure needs to be rotated (i.e. the plane is a true mid-section cut), the alignment of FeOl1 suggests A-slip deformation, although the alignment of a axes is in more of a diffuse girdle than seen in the classic A-slip system. If, however, the sample is already oriented so that the shear plane is horizontal (see discussion above), the pattern looks similar to that of partial melt deformation in a reduced permeability system, where strain partitioning has caused back-rotation of olivines in melt-depleted areas (Figure 1.4, section 1.2.1). In either case, there is an apparent back-rotation of the olivine grains with respect to the shear plane. This would be consistent with the relative permeability of the FeS-olivine system, and the observed development of melt rich and 'drained' areas, although melt bands are more subtle in our samples than observed in high strain-rate, high strain studies (Holtzman, Kohlstedt, et al., 2003).

The CPO of FeOl4 is different to FeOl1 even if possible rotation is taken into account. Essentially there appears to be a switch in the alignment of 010 and 100 axes between FeOl1, and FeOl4, suggesting two contrasting slip systems are active. FeOl1 has evidence for A-slip being active, while the FeOl4 pattern is not clearly comparable to any of the systems shown

in B. The change in slip system may be caused by a change in temperature or strain-rate (see Figure 1.3, section 1.2.1). Although initial pole figures suggest FeOl2 and FeOl4 have different CPOs, once both figures are rotated the CPOs appear consistent - it is therefore likely that the same slip system is dominant in both of these samples.

It is possible that an initial CPO develops on compaction/ uniaxial compression, which is overprinted by torsional deformation, which may explain the difference observed. The level of overprinting may vary with experimental duration. To test this, sample FeOl2 CPO was plotted on separate vertical sections across the map area to see if there was any change in CPO towards the sample centre (Figure 3.32). If there was an initial CPO caused by compaction it may be expected to be consistent across the sample, or stronger in the centre, whereas a CPO created by shear deformation should become weaker towards the centre. There does appear to be a weakening of fabric in the observed CPO from the edge to the centre of the sample, therefore the CPO observed is created from shear stresses, rather than being a remnant of CPO created during compaction.

The strength of CPO has been compared for grains of different sizes in samples FeOl1 and FeOl4 (Figures 3.30,3.31). Theoretically there may be a difference in CPO development expected for large grains and small grains if they are undergoing different mechanisms of deformation, or if small grains are newly recrystallised within the strain field (AveLallemant and Carter, 1970). However, in both cases there is no clear difference and the strength and orientation of CPO are roughly similar.

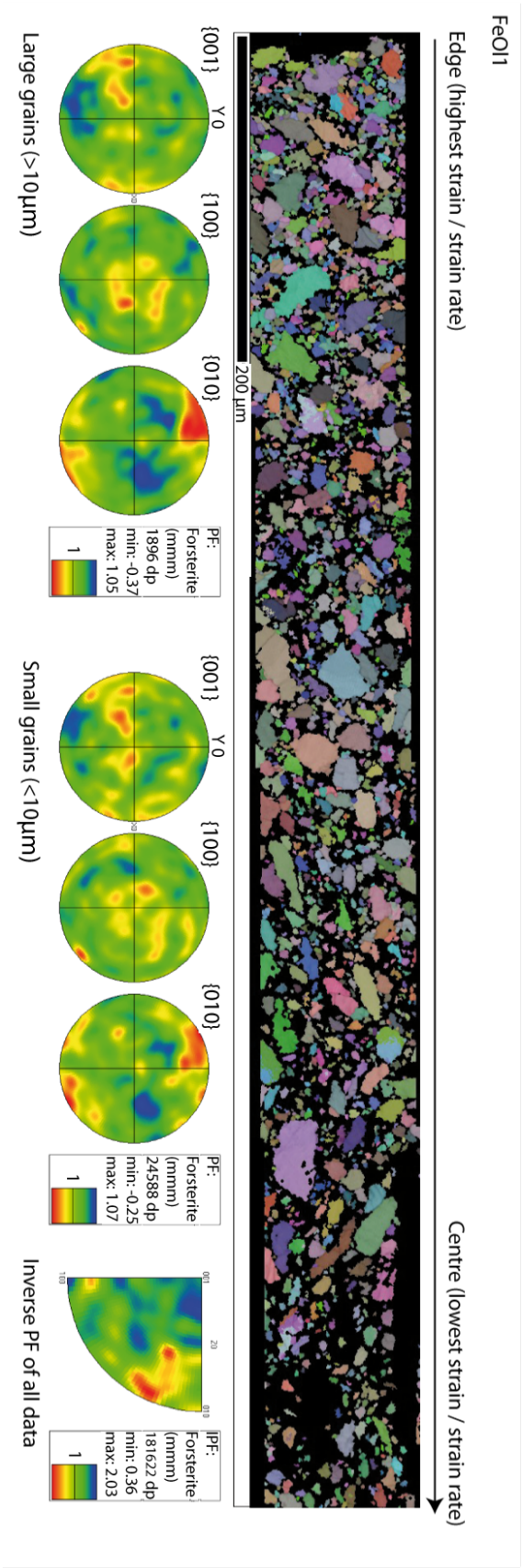
FeOl1
Edge (highest strain / strain rate)
Centre (lowest strain / strain rate)
200 µm
{001}
Y 0
{100}
{010}
PF: Forsterite (mmm) 1896 dp min: -0.37 max: 1.05
1
Large grains (>10µm)
{001}
Y 0
{100}
{010}
PF: Forsterite (mmm) 24588 dp min: -0.25 max: 1.07
1
Small grains (<10µm)
IPF: Forsterite (mmm) 181622 dp min: 0.36 max: 2.03
1
Inverse PF of all data

Figure 3.30

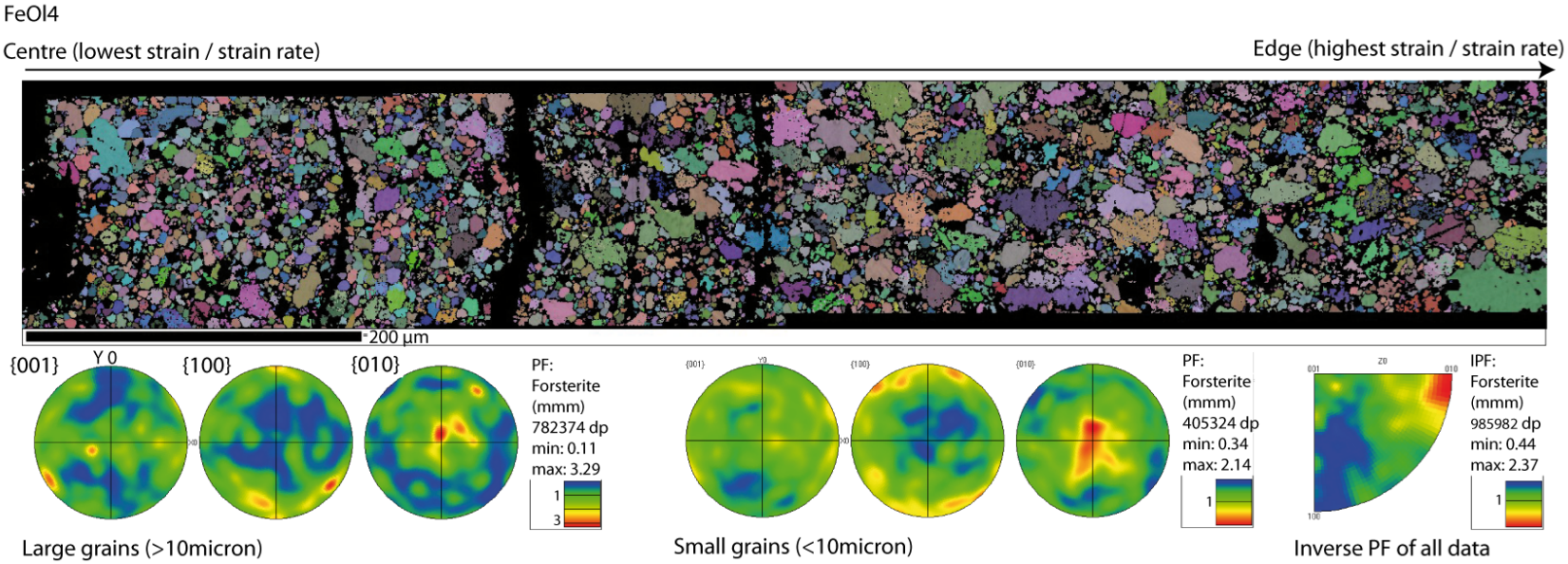

Figure 3.31: EBSD analysis of FeOl1 and FeOl4, both of which have been cut through the mid-section. The plane of maximum shear is therefore in and out of the plane of section, and maximum at the capsule edge. A map of band contrast overlain with All Euler colours is shown, along with pole figures showing the orientation of large grains, small grains, and an inverse pole figure showing the overall distribution of grain axes within the sample. Results are described in the text.

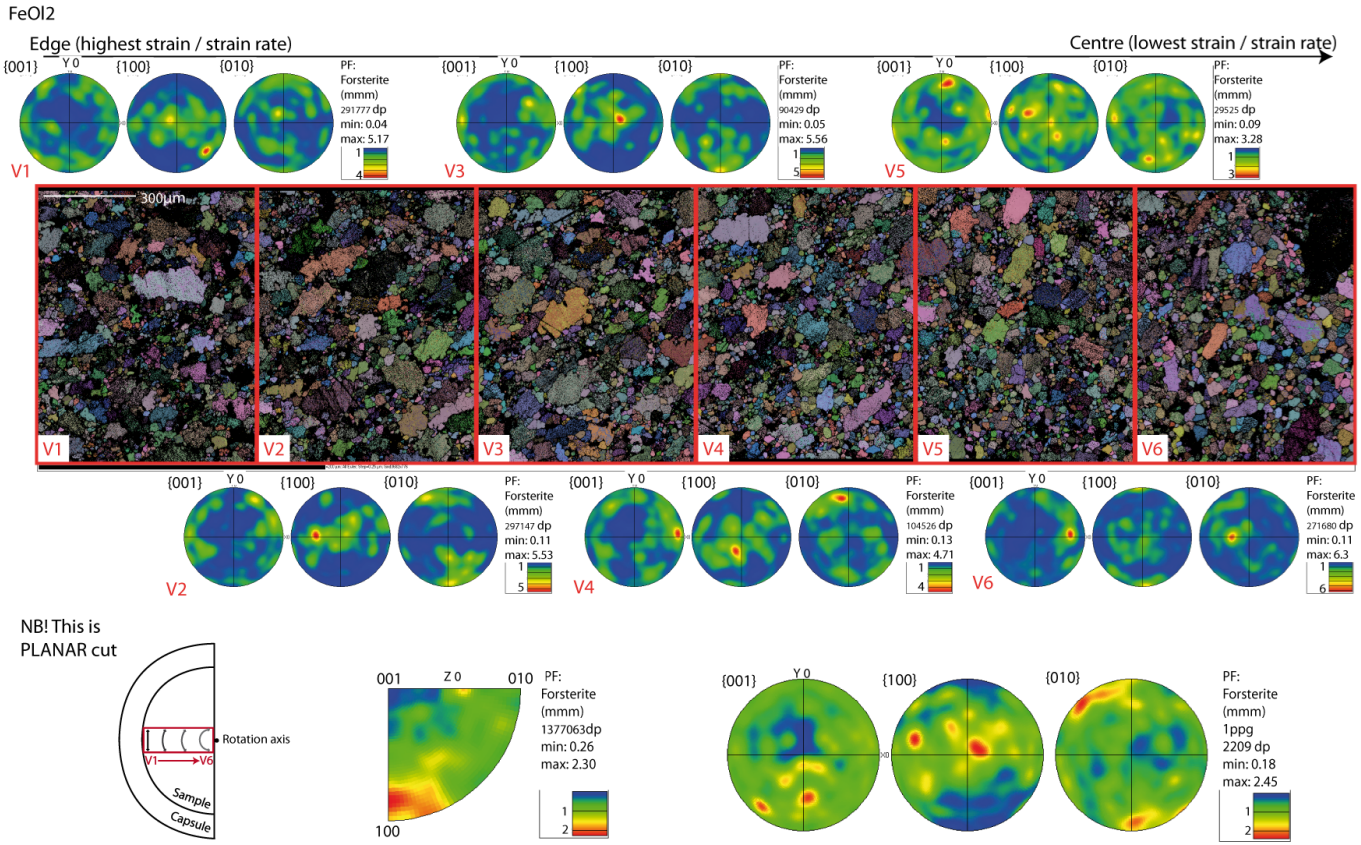

Figure 3.32: FeOl2 EBSD analysis, carried out on a planar cut where maximum shear direction is in the NS direction at the sample edge, reduces to theoretical zero at the sample - see schematic diagram bottom left. A euler map showing band contrast overlain with euler pole colours is shown, along with pole figures of grain orientation for vertical sections V1-V6 moving from the sample edge to centre. Crystal orientations are shown by the inverse pole figure and pole figures at the bottom.

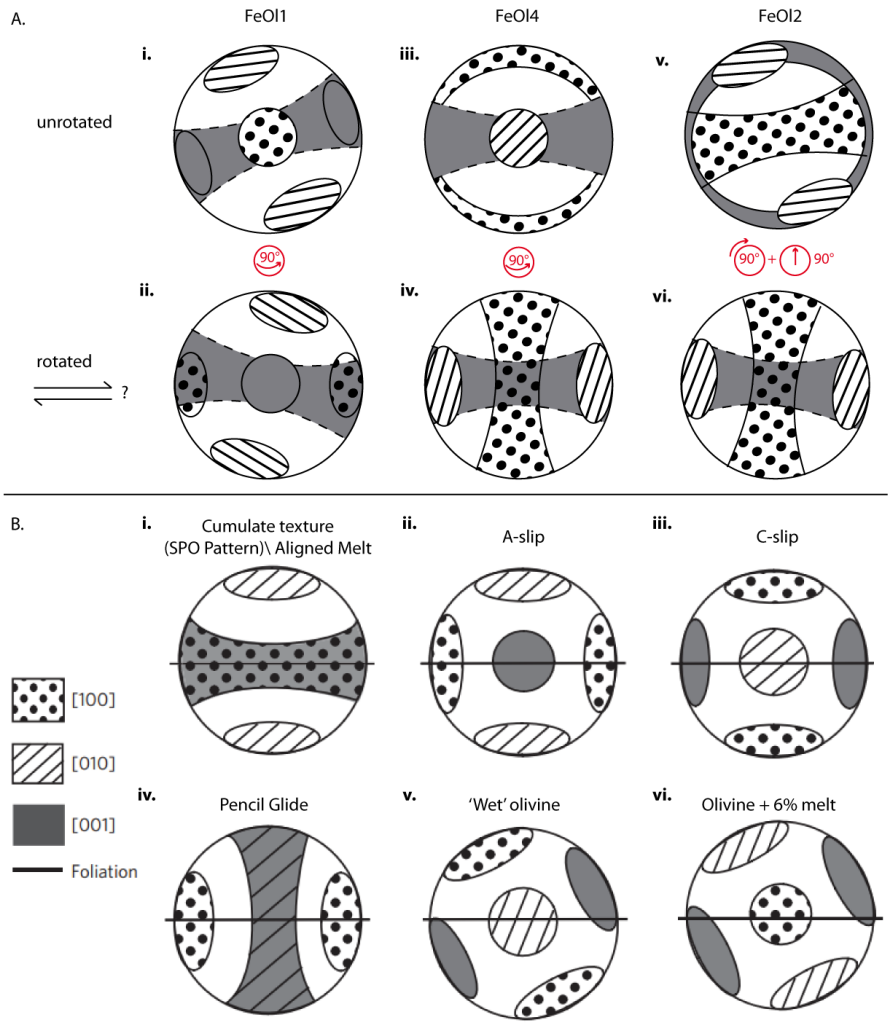

Figure 3.33: A. Schematic summaries of CPOs developed in samples FeOl1,2 and 4 using method of Tkalcec et al. (2013). i,iii, and v show the data in its raw, unrotated format. Due to the cuts used during EBSD analysis, the shear plane is not aligned horizontal, and data has to be rotated to align the shear plane horizontally and allow comparison to previous work (see text). ii, iv, vi show data that has been rotated. NB. Depending on strain partitioning and the accuracy of the mid-section cut, it may be that the CPO developed in i, iii is formed from a horizontal shear plane, therefore these pole figures may already be directly comparable to previous work (see text). B. Summary of olivine CPOs developed in different scenarios adapted from Tkalcec et al. (2013). i) Cumulate texture created by shape-preferred orientation (Boudier, 1991) - also equivalent to the texture observed by Holtzman, Kohlstedt, et al. (2003) for deformation with 6% basalt melt in highly permeable systems. ii) Classic A-slip system: (010)[100] (Ismail and Mainprice, 1998; Tommasi et al., 2000) iii) C-slip: (100)[001] (Frese et al., 2003) iv) Pencil Glide, {0kl}[100] (Tommasi et al., 2000) v) Slip observed in 'wet' olivine (Jung and Karato, 2001). vi) olivine +6% melt in a reduced permeability system undergoing strain partitioning (Holtzman, Kohlstedt, et al., 2003). These are compared to A. in text.

Kink bands / twinning

In all deformation samples, a number of large crystals show evidence of dislocation creep structures. Internal deformation is evident by the presence of kink bands. Examples are shown in Figure 3.34. These can be seen in misorientation maps of individual grains, showing a distinct change in orientation across different areas, and is very pronounced in pole figures of individual grains, where grain orientation is shown to split into distinct orientations rotated about a single plane. In each case rotation appears to occur about one axis, e.g. about {100} in the case of the majority of grains in FeOl1 and FeOl2. The poles of orientation of the other two axes are spread about a great circle which is the plane of the {100} axis. Internal deformation within each twinning orientation is also observed, up to ~10% mis-orientation showing minor internal deformation. This deformation appears to be at a near perpendicular orientation of the plane of rotation on which the axis poles lie. The actual location of the different orientations within the crystal itself is not clearly structured, which lead to the original thought that this may be a mis-indexing error of the software. However, similar behaviour has been characterised in olivines and olivine analogues in a number of experiments (Burnley et al., 2013; Raleigh, 1968) and is interpreted as evidence of dislocation creep. Kink bands will preferentially form in crystals orientated with their preferential slip planes oriented sub-parallel to the sense of shear, meaning they could potentially be used to infer the orientation and sense of shear in a sample if the orientation is unknown.

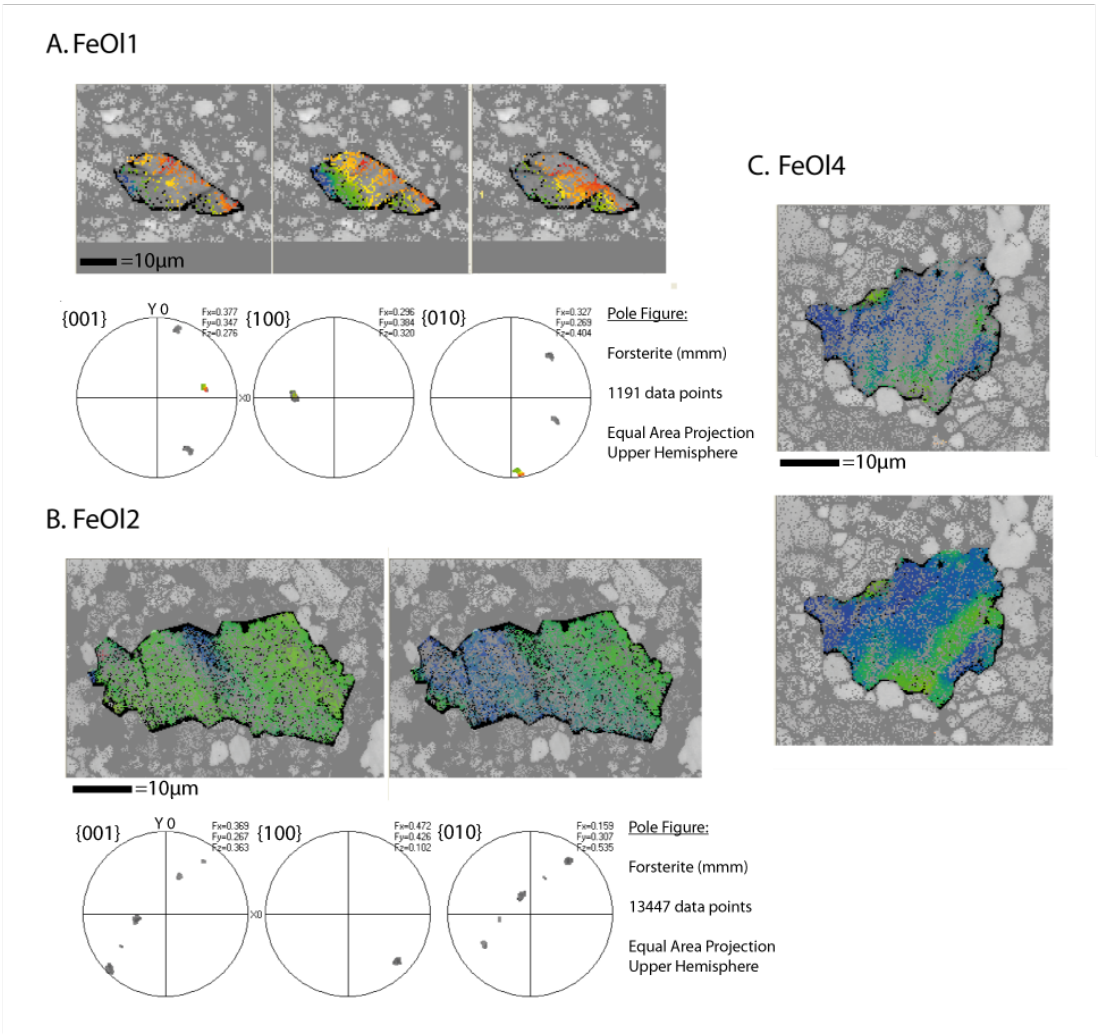

Figure 3.34: An example of grains exhibiting a pattern interpreted as deformation twinning, taken from A. FeOl1, B. FeOl2 and C. FeOl4. Maps are individual misorientation maps of isolated grains. A single point is selected as a reference orientation, and a colour scale assigned to represent orientations deviating from 0° (dark blue) to a maximum of 15° (red) from this point. Grey areas within the grain are zones in which orientation differences are >15° (i.e. a kink, or twin). Subsequent maps of the same grain show the internal misorientation in each of the twin zones. The pole figures show orientation of crystallographic axes within each of the pictured crystals. There is a systematic rotation of {001} and {010} axes about the rotation axis of {100}. In FeOl1, the {100} rotation axis is oriented at ~40° to the shear plane .

Conclusions of EBSD analysis

EBSD analysis shows that

- **There is a clear development of CPO in deformed samples, and evidence of dislocation creep in large grains** (although this is also seen in undeformed samples, presumably from compaction). Evidence of CPO development in small grains could be evidence of their deformation by dislocation creep, although this would be unexpected at the strain-rates used here and studies have shown CPO to develop even in the diffusion creep regime (Miyazaki et al., 2013), so this is not conclusive. The lack of in-situ stress and strain measures during experiments mean it is not possible to find the stress-strain relationship to test n-values and know the deformation mechanism for certain.
- **The CPO developed in response to deformation is likely to be consistent within deformed samples FeOl4, and FeOl2, but FeOl1 shows a different slip system active.** It is unclear what causes the differences in CPO observed across deformed samples. Changes in strain-rate lead to different slip-systems being activated (Raleigh, 1968): CPO observed in FeOl1 may be consistent with the deformation pattern observed for systems of low permeability (relative to basaltic melt + olivine (Holtzman, Kohlstedt, et al., 2003)), which would be expected in a system containing lower mobility FeS melt. The CPO development in the other deformed samples is not directly comparable to those observed in their study, or in fact any of the common slip systems of olivine.

Due to the orientation of cuts used for EBSD analysis (mid-section and planar cuts) it is difficult to compare the results directly and it is difficult to draw strong conclusions. This is a result of EBSD analysis being carried out after BSE imaging required cutting of orthogonal sections. Future EBSD work would be best carried out initially using tangential sections as used in most torsional deformation studies (King et al., 2010), as the shear direction is in the plane of section and is roughly constant. Further orthogonal cuts could be used to allow pseudo-3D analysis of olivine structure.

3.3.7 Compositional analysis of samples using electron probe micro-analysis

Compositional analysis of experimental sample slices reveals compositions are mostly as expected (Table 3.2) and show that there have been no significant reactions taking place between FeS and Olivine. Table 1 shows average compositions of the constituent materials after the three experimental runs. The Aheim olivine composition away from the sample rim is calculated as $(Mg_{0.93}Fe_{0.7})SiO_4$, which is within 1 % of its original composition. FeS composition is also shows no significant change, with equal molar proportions of each element calculated.

Element mapping shows a significant reaction taking place between olivines and the MgO outer capsule (Figure 3.35). MgO appears to leach olivines of iron in the proximity of the capsule-sample boundary. Quantitative analysis (Figure 3.35d) shows that the iron content reduction is at a maximum directly at the capsule edge and falls to a minimum around 100μm from the edge. This reaction is found to affect sample texture. A rim of 30μm at the boundary between MgO and olivine is found to have an unusual reaction texture in each sample. For this reason we have avoided using this area as part of the textural analysis. The platinum strain marker appears to take up some iron from surrounding olivines (Figure 3.36D) but there is negligible diffusion of Pt into the surrounding sample (Figure 3.36C). The effect of the platinum is restricted to <30μm from the metal boundary. This area of sample is not easily analysed in 3D due to the shadowing caused by high attenuation of platinum, so the area is not used in textural analysis.

Material	Na		Mg		Ca		Ti		Mn		Fe	
	wt%	δ	wt%	δ	wt%	δ	wt%	δ	wt%	δ	wt%	δ
Ol (starting)*			**30.41**		**0.04**				**0.13**		**5.46**	
Ol (central)	**n.d**	0.006	**31.13**	0.254	**0.04**	0.091	**0.003**	0.003	**0.07**	0.010	**5.68**	0.46
Ol (edge)	**n.d**	0.008	**31.55**	0.923	**0.07**	0.087	**0.003**	0.006	**0.06**	0.022	**4.72**	1.28
FeS					**0.01**	0.008	**0.004**	0.004	**0.02**	0.016	**64.23**	5.65

Material	Ni		Si		O		S		Total		n
	wt%	δ	wt%	δ	wt%	δ	wt%	δ	wt%	δ	
Ol (starting)*	**0.27**		**19.56**		**45.13**				**101.00**		
Ol (central)	**0.26**	0.079	**19.48**	0.14	**44.43**	0.186			**101.10**	0.33	15
Ol (edge)	**0.20**	0.114	**19.44**	0.18	**44.37**	0.443			**100.43**	0.85	13
FeS	**1.22**	0.588	**0.33**	0.73			**33.09**	6.67	**98.90**	1.59	9

Table 3.2: Average compositions of the constituent materials from 3 experimental runs (FeOl1, 2 and 4) given in weight %. Ol (central) are defined as measurements of olivine made >100 μm from the capsule edge, Ol (edge) are those <100 μm from the edge. Reported values are averages of a number of points, n. Standard deviations, δ are calculated incorporating instrumental and population error. More details of error calculation and compositions of individual samples can be found in Appendix A.2.2 n.d.= not detected (value below detection limit). There is no significant difference between the composition of olvines and FeS in any of the experimental runs. The FeS used appears to become slightly enriched in Fe. S does not appear to be taken up by olivine grains however. There is a significant reaction rim near the sample edge around the olivines, therefore the average composition of olivines is best taken from olivines not positioned close to the sample edge (central). Olivines situated at the edge of the sample have a slightly lower iron content. *Starting composition of olivine from wet chemical analysis by Sibelco Europe, no error values available.

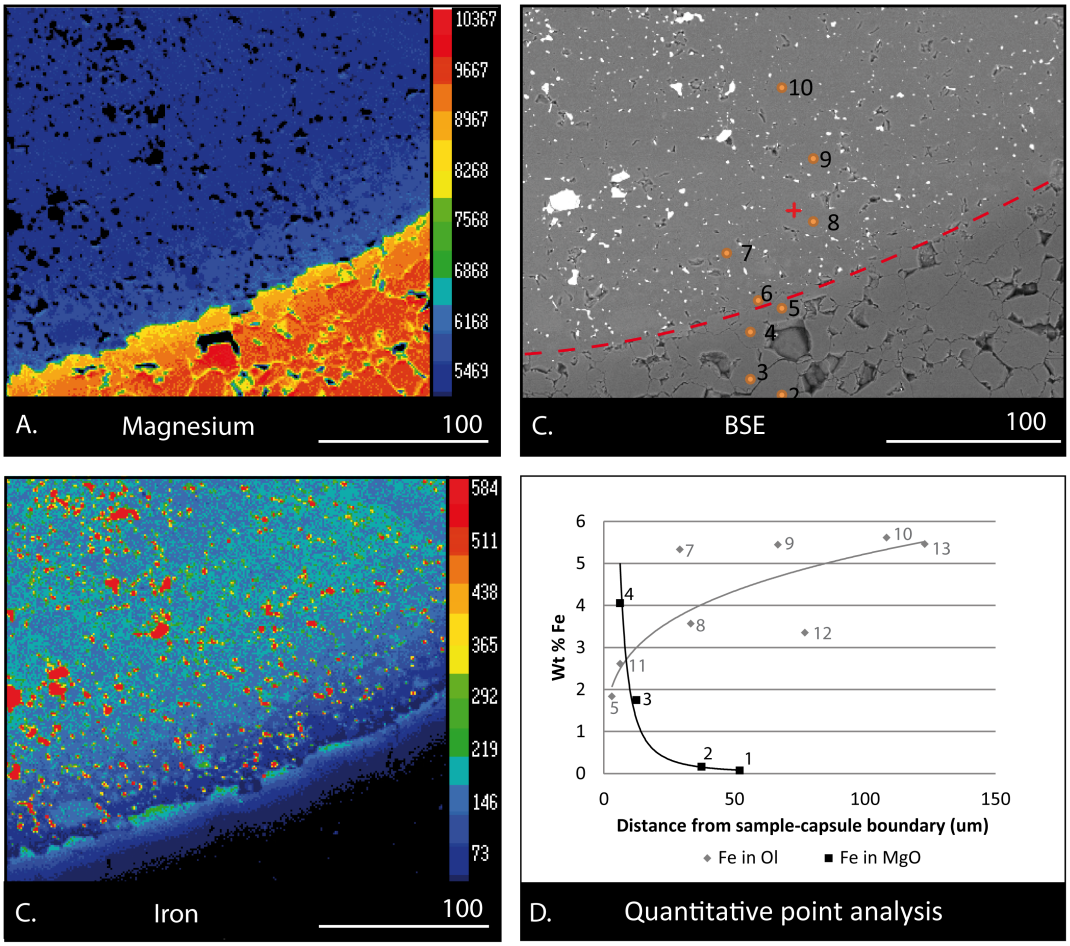

Figure 3.35: Electron microprobe analysis of experimental sample FeOl2 close to the experimental capsule. Compositional maps (A,B) are qualitative, and rainbow scale shows relative concentration of each element. A: Compositional map of magnesium showing sample (top-left) and capsule (bottom-right). There is a subtle enrichment in magnesium visible at the edge of the sample. B. Iron content. The boundary effect is clear in this map, which shows a distinct enrichment in iron at the capsule edge, but also a drop in iron content at the edge of the sample. This reaction does not appear to reach further than 50 µm into the sample. C. shows a backscatter image of the same area with quantitative point analyses marked on. D. A graph of the quantitative analyses from C. showing the change in iron content in the MgO capsule (black) and sample olivine (Grey). Additional points 11-13 are from another analysis area within the same sample. The drop in Fe near the sample edge is evident. The edge effect disappears within 100µm of the sample edge in the olivines. This reaction does seem to be associated with a change in texture of the melt, suggesting this edge should not be used for textural analysis of melt geometry.

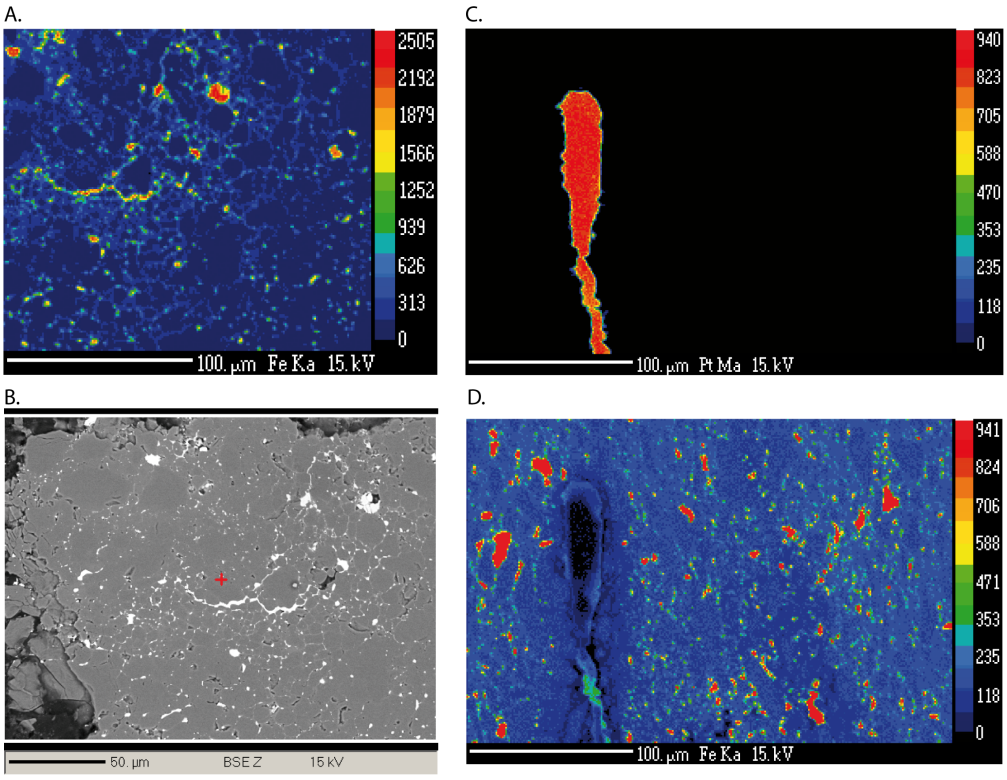

Figure 3.36: Other features of note revealed from EPMA element mapping. A. A melt vein and surroundings showing relative Fe content. From FeOl2. The melt vein is shown clearly with a large increase in iron. There is a very fine rim around each olivine crystal (<1µm) which is due to the presence of a very fine layer of melt wetting grain boundaries, as seen in the backscatter image of the same area in B. There is no clear evidence that there is any uptake of iron into olivine from the FeS liquid. C. Relative platinum concentration in and near platinum strain marker in FeOl1. There is negligible spread of platinum into the surrounding capsule although there is minor diffusion at edges but this is only a few µm in thickness. D. The relative Fe-concentration near the platinum strain marker does show some uptake of Fe within the platinum, and a minor reduction in iron concentrations in olivines within 20µm of it.

3.4 Applications to core formation in the early solar system

3.4.1 Connectivity of FeS melts in solid silicate - comparison to previous work

Detailed analysis in 2 and 3D has allowed full characterisation of melt geometry within our experimental samples. We believe there is sufficient evidence to suggest that within laboratory experiments, deformation aids grain boundary wetting and the formation of extensive melt networks. Our experiments support suggestions of previous studies that this mechanism is a viable way to initiate metal-silicate segregation before the onset of silicate melting (Bruhn et al., 2000; Groebner and Kohstedt, 2006; Hustoft and Kohlstedt, 2006; Rushmer, Petford, et al., 2005; Wang, Lesher, et al., 2011; Watson and Roberts, 2011). Previous observations of melt migration below the solidus of olivine at experimental conditions have been contested by many as non-viable as a core formation mechanism due to experimental limitations including unrealistically low confining pressures, very high strain-rates (Bruhn et al., 2000), large melt volumes and the complexity of using natural samples (Rushmer, Petford, et al., 2005). Our results cannot be contested by any of these arguments, and still show evidence for enhanced connectivity. However, the exact geometry of features does appear to differ significantly from those observed in higher strain-rate experiments (Bruhn et al., 2000). For example, we only see a subtle localisation of melt into melt-rich and melt-poor zones, and instead see evidence of wide-spread grain boundary wetting throughout our sample in very thin sheets. 3D visualisation allows us to show directly that deformation enhances connectivity, despite a lack of strong melt preferred orientation fabrics. The lack of significant melt redistribution is likely to be due to the lack of a significant gradient (thermal or pressure) causing the melt to migrate. For example, in previous experiments conducted using simple shear deformation equipment and serrated pistons, regions of compression (high pressure) and tension (low pressure) develop, with melt pooling in low-pressure regions (Hustoft and Kohlstedt, 2006).

Our experiments suggest that grain boundary wetting is particularly pronounced in our lowest strain-rate, longest duration experiment. In this respect our results are also contradictory to the findings of Walte et al. (2011), a study conducted at comparable P-T conditions and relatively low strain-rates. This group do not see evidence of stress acting to change textures in experimental samples at strain-rates of less than $10^{-4}s^{-1}$ in their deformed FeS-olivine samples. In our experiments we clearly see stress-dominated melt sheets, which are finer than 1μm in our lowest strain-rate ($10^{-6}s^{-1}$) experiment.

The appearance of interconnected networks in our samples at lower strain-rates than observed by Walte et al. (2011) may be due to:

1. The longer experimental duration of our very low strain-rate experiment, which could allow more time for samples to develop textures.

2. Differences in experimental geometry: Textures are likely to develop differently in the pure shear, axial compression experiments of Walte et al. (2011) compared to the simple shear in our torsion experiments (Kohlstedt and Holtzman, 2009 and references within). For example, pure shear may not encourage redistribution into melt-rich and melt-poor regions, as seen in geometries that apply significant simple shear deformation (Bruhn et al., 2000; Hustoft and Kohlstedt, 2006).

Experimental geometry may therefore be an important factor in the development of textures within deformed samples. The small number of deformation experiments conducted mean that there is still insufficient data to confirm this, and it is clear that further experiments are required to fully characterise the response of low mobility melts to different deformation mechanisms.

3.4.2 Extrapolation to core forming conditions

Despite this uncertainty, results from our experiments suggest that application of differential stress may act to enhance connectivity of FeS melt in an olivine matrix, over a greater range of experimental strain-rates than previously expected. However, for this mechanism of deformation-aided percolation to segregate core and mantle material in the early solar system, it must be possible to scale these observations to realistic conditions of planetary interiors. For core formation to be fully complete before the onset of silicate melting, melt must be able to drain from a silicate mantle to leave behind a fraction of 1vol % or less in order to reproduce observed geochemical signatures (Groebner and Kohstedt, 2006), and be able to segregate melt within realistic timescales (Kleine, Touboul, et al., 2009). Previous studies have examined this process of extrapolation to investigate the potential efficiency of percolative core formation at realistic time-scales and strain-rates (Groebner and Kohstedt, 2006; Walte et al., 2011).

Any extrapolation from laboratory experiments to core forming conditions must take into account

- **the significant reduction in strain-rate and therefore differential stress acting on melt pockets at planetary conditions:** Deformation in proto-planets is expected at low strain-rates due to convection (10^{-12}-$10^{-14}s^{-1}$, Walte et al., 2011), medium strain-rate from potential tidal forces and high strain-rates in localized events from ongoing bombardment/accretion ($10^{-11}$to $>10^{-7}s^{-1}$, Rushmer, Petford, et al., 2005). Lowest strain-rates in experiments are $10^{-6}s^{-1}$ (our study).

- **significant increase in timescales under high P-T and exposure to differential stresses:** Core formation is likely to have taken place over millions to tens of millions

of years (Kleine, Touboul, et al., 2009), vs. laboratory experiments on the scale of hours to days.

- **the increase in grain size expected in planetary materials:** Grain size in planetary bodies is expected, from textural observations of meteorites, to be on the mm-cm scale (Mittlefehldt et al., 1998), vs. μm-scale in laboratory experiments.

Whether deformation creates interconnected melt networks depends on an interaction between differential stress, which acts to force melt out of isolated pockets and onto grain boundaries, and the interfacial tension between liquid melt and solid grain boundaries, which, in the case of iron-rich melts, acts to isolate melt pockets at grain boundary triple junctions.

Groebner and Kohstedt (2006) suggest that, for deformation enhanced segregation to take place, the following inequality must be true:

$$\frac{\sigma}{\gamma_{s-l}/r} > 1 \tag{3.3}$$

Where σ is the differential stress, γ_{s-l} is the interfacial energy between solid and liquid, and r is the melt pocket size. r is related to grain size, d and melt fraction ϕ by the expression

$$r = \pm \frac{d}{\sqrt{2}} \sqrt{\frac{\phi}{F(\theta)}} \tag{3.4}$$

Where F is a geometric function of the dihedral angle (θ), and the positive and negative streams are for dihedral angles above and below 60° respectively. Taking into account that γ_{s-l} is equivalent to $\gamma_{s-s}/2cos\theta$, the above equations can be combined to calculate the potential melt fraction remaining after core formation has taken place by percolation, Φ_{def}:

$$\phi_{def} > \frac{1}{2} F(\theta) \left(\frac{\gamma_{ss}}{d\sigma cos(\theta/2)} \right) \tag{3.5}$$

ϕ_{def} is calculated for experimental conditions, where $d = 10^{-5}m$ and $\sigma = 10^{8}Pa$ ($\dagger\sigma = 10^{3}mPa$), with γ_{ss} as a known constant of 1J/m (Cooper and Kohlstedt, 1982) resulting in a melt fraction of 10^{-4}, suggesting core formation is efficient to very low melt fractions (two orders of magnitude below that stranded in hydrostatic conditions). Scaling to planetary conditions, differential stress decreases to 10^{-6} Pa, but the increase in grain size to 10^{-3}m reduces the influence of interfacial tension. Overall, $d\sigma$ remains constant, therefore the fraction of melt stranded should be the same in both cases. The study concludes that deformation experiments can be essentially directly extrapolated to core forming conditions, and that deformation-aided percolation is an inherently efficient and rapid process (Groebner and Kohstedt, 2006). Quantitative analysis carried out on 3D volumes of our lowest strain-rate sample suggests the stranded melt fraction, at least in experimental samples, of 0.5-2%, which is lower than estimates made of the interconnectivity threshold in Hustoft and Kohlstedt (2006). Therefore

our experiments appear to suggest the mechanism is, if anything, more efficient at lower strain-rates, and therefore in agreement with the suggestion that this process could be highly efficient at core forming conditions.

This method is directly disputed by Walte et al. (2011). Their extrapolation approach is based on their observations of isolated melt textures at low strain-rates in the olivine-FeS system, supported by *in-situ* observations of at ambient conditions on analogue norcamphor-H_2O experiments. Again, textures are inferred to be controlled by the interplay between differential stress and surface tension, but in this case the inequality is not based on unity, as in equation 1, but instead on a scaling factor R, which is inferred from the relationship between melt pocket size and shape observed in their experiments. R is related to the balance between differential stress (or strain-rate ε) and overpressure in a melt pocket ΔP, which depends on its size (radius, r) and its surface energy (γ_{s-l}), therefore:

$$R = \frac{\Delta P}{\Delta \sigma} \rightarrow R = \frac{2\gamma_{s-l}}{rA\varepsilon^{1/n}} \rightarrow r = \frac{2\gamma_{s-l}}{RA\varepsilon^{1/n}} \tag{3.6}$$

Where A is a pre-exponential factor, and n is the stress exponent as found from a stress-strain-rate curve during deformation. As strain-rate decreases, the size of the melt pocket which is affected by deformation is inferred to increase, with the boundary between the stress-affected, and surface-tension dominated regimes forming a line of slope n on a double-logarithmic graph of strain-rate vs grain size (Figure 3.37). A broad intermediate region lies around the boundary, where both surface tension and differential stress have an effect on textures of melt pockets. Active segregation is thought only to take place in the stress-dominated regime. The effect of differential stress is to reduce melt pocket size, while surface-tension dominant regimes will increase melt pocket size, therefore leading the system to converge towards the intermediate regime. This linear relationship between strain-rate and melt pocket size can be scaled up to core forming conditions, to investigate whether at low strain-rates planetary melt pockets are likely to be stress- or tension- dominated. From their experimental data in the FeS-olivine system and the norcamphor analogue, n is found to be 3.5, which is compatible with a system deforming by dislocation creep. At high dihedral angles, only high strain-rate events such as impacts lead to melt segregation, while at moderate dihedral angles (the Fe-S system) vigorous convection in planetesimals could also cause some melt segregation. Walte et al. (2011) argue that this method is more accurate than extrapolation of Groebner and Kohstedt (2006), as it relies more on empirical experimental observations, and less on assumptions of other inferred melt characteristics such as viscosity or solid-liquid interfacial energy, where estimates vary widely in the literature. However, as previously discussed, our observations differ from those of Walte et al. (2011) at low strain-rates (Figure 3.37), and are therefore incompatible with this extrapolation technique. The effects of changing deformation to simple shear, and increasing timescales of experiments appears to change

textures significantly. Basing scaling factors used for extrapolation on a small number of experiments using a unique deformation geometry is unlikely to truly constrain mechanisms occurring in planetary interiors.

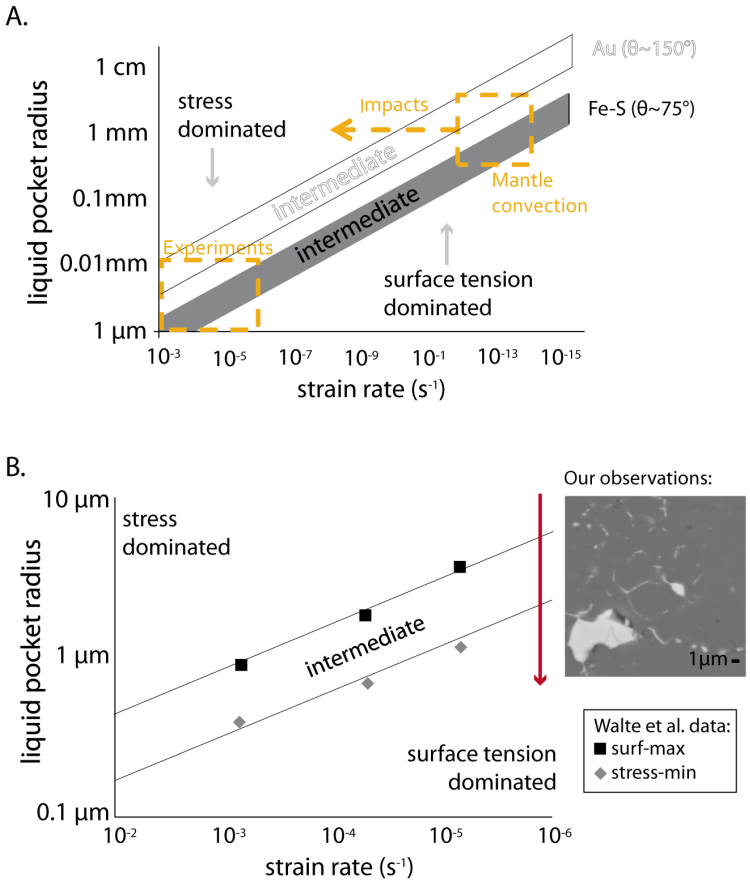

Figure 3.37: A comparison of our data to the extrapolation technique of Walte et al. (2011), which predicts deformation aided core formation is not efficient at planetary conditions. Both graphs are adapted from Walte et al. (2011) A. Graph showing inferred linear boundary between stress-dominated, interconnected melt pockets, and surface-tension dominated isolated pockets, which can be extrapolated to lower strain-rates and larger grain sizes expected at the planetary scale. Both high dihedral angle results, from Olivine-Au system, and moderate dihedral angle results from the Olivine-FeS system are shown. B. A comparison between the experimental results of Walte et al. (2011) in the FeS-Olivine system, on which this extrapolation technique is mainly based, and the textures observed in our experiments. The Walte study sees a minimum melt pocket size of 1 µm affected by deformation at low strain-rates. Below this, all pockets are dominated by surface tension and non-wetting. We clearly see very fine, submicron melt in sheets wetting grain boundaries (see inset), therefore our data is incompatible with this extrapolation.

In fact, our experimental results are not easily compatible with either extrapolation

technique described. We see wetting of grain boundaries down to the submicron scale, but there is only subtle redistribution of melt and creation of melt rich zones, contrary to observations in studies by the Kohlstedt group. We see a number of fine melt sheets wetting grain boundaries, but in all samples there are also larger melt pockets that are not clearly elongate. We do not observe a correlation of textures with strain-rate or total strain. Instead, the most interconnected textures are observed at very low strain-rate and total strain, in our experiment of >24 hour duration.

For this reason it is difficult to extrapolate our results quantitatively to core forming conditions using a viable extrapolation technique. However, our results imply that core formation should be more efficient than suggested by previous studies, and gives no reason to doubt that the mechanism of deformation-aided percolation of metallic melts could potentially take place within the time scales associated with core formation.

3.4.3 Prediction of permeability and timescales of core formation

Assuming that percolation of Fe-rich melts through an interconnected network is a viable mechanism for core formation in dynamic systems, the following equation can be used to estimate permeability in the partial melt system (Gueguen and Dienes, 1989; Hustoft and Kohlstedt, 2006)

$$k = \frac{d^2 \phi^n}{C} \tag{3.7}$$

where k = permeability, d = grain size, ϕ = percolation threshold and C and n are geometric factors dependent on melt network geometry, with n = 2 for a network of interconnected tubules and n = 3 for interconnected sheets (Gueguen and Dienes, 1989). Our 3D textures indicate geometry of mostly interconnected sheets, and qualitative modelling suggests melt is forced to flow through these fine networks. This suggests that n is likely to lie closer to 3. Estimated C values for partial melt networks are highly variable, with estimates lying between 10 and 1000 (Connolly, Schmidt, et al., 2009; McKenzie, 1984) although the majority of studies agree at a value between 10 and 20. The velocity of melt migration can be calculated as

$$V_m = \frac{k \Delta \rho g}{\phi \mu} \tag{3.8}$$

Where $\Delta\rho$ = density difference between solid and melt, ϕ=melt fraction, μ= viscosity of melt, g=acceleration due to gravity.

Permeability of melt networks has been calculated for the full range of estimated C and n values to examine how much permeability estimates vary with these parameters. The velocity of melt migration for a planetary object the size of the Earth, Moon, and Vesta is then calculated using these maximum and minimum permeability estimates. A very rough estimate of core formation timescale can then be made by calculating the time taken for metal to migrate from the edge of a planetary object to its centre. Calculated permeability and estimated timescales of percolative melt migration for the Earth and Vesta are shown in Figure 3.38. The radius and gravity of a planetary body does not appear to affect core formation timescales significantly (the reduction in radius is cancelled out by the decrease in g reducing melt velocity). Initial calculations carried out by Hustoft and Kohlstedt (2006) give a more generous estimate of velocities, mostly from assuming larger melt fractions (0.1-0.3) suggesting cores could form within 15-150 years. Our calculations show that even with very low permeability estimates, core formation could take place within planets and planetesimals well within constraints for timescales of core formation of 30Myr or less (Kleine, Touboul, et al., 2009). Reducing melt fraction does significantly change permeability estimates (3.38 C.), and at very low melt fractions permeability decreases to minimal levels - however, assuming estimates of C of

<200 are reasonable (Hustoft and Kohlstedt, 2006), even small melt fractions will be able to drain to the cores of planets in less than 1Ma. Essentially, as long as a melt network is interconnected, permeability estimates suggest that it should be possible to form a core within imposed timescale constraints.

Min. permeability/ m^2	3×10^{-14}		
Max. permeability/ m^2	1×10^{-10}		
Melt viscosity (Pa s)	0.04 [1]		
$\Delta\rho$	3500 [2]		
Melt fraction	0.03 [2]		
	Earth	**Moon**	**Vesta**
Gravity, g (m/s^{-2})	9.81	1.62	0.25 [3]
Radius (km)	6371	1750	250 [4]
P at centre (Gpa)	360	5	0.12 [3]

Table 3.3: A table of parameters used for calculating velocities and timescales of core formation in planetary bodies in the solar system (Figure 3.38). Minimum and maximum estimates of permeability are taken from the full range of estimates for geometric factors C and n, for a melt fraction of 0.03 (see figure 3.38A). Other sources: 1:*Terasaki, Kato, et al., 2001* 2:*Hustoft and Kohlstedt, 2006* 3: *Ruzicka et al., 1997* 4:*Russell et al., 2012*

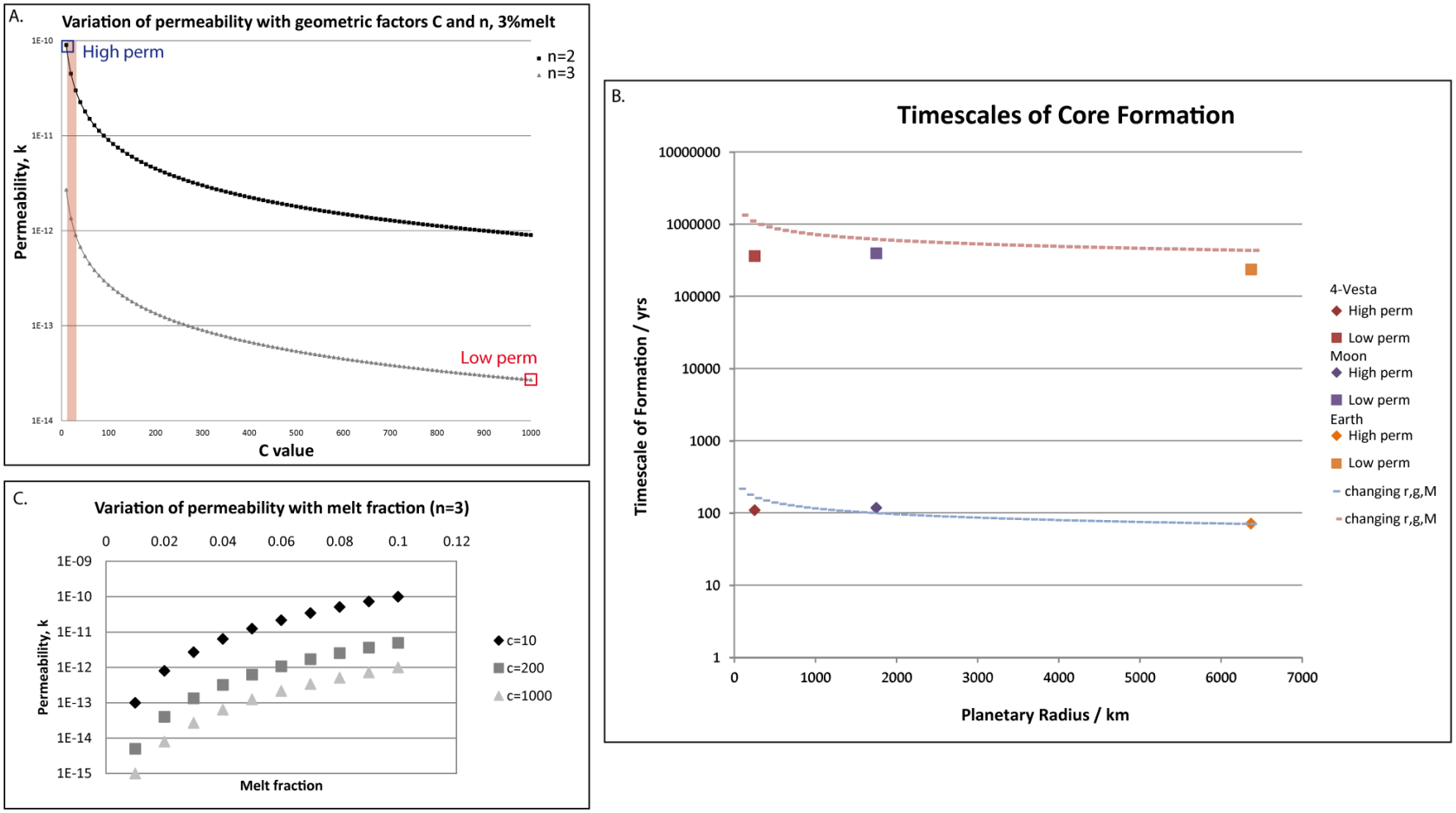

Figure 3.38: A. Investigation into variations of permeability calculations using different estimates for geometric parameters C and n, calculated using equation . The most common estimates of C are highlighted in red (see text) giving relatively high permeability estimates. B. Estimates of velocity calculated using minimum and maximum estimates of permeability from A., and parameters for melt characteristics, and planetary radii and g, as given in Table 3.3. Dotted lines show estimated timescales changing g, r and M of a hypothetical terrestrial planetary body. Initial velocities are calculated using equation 3.8. Timescales are estimated by dividing velocity, in kmyr^{-1} by planetary radius.

These calculations assume a stable, fully interconnected melt network. Use of quench experiments cannot provide meaningful insight into the longevity of melt networks in a dynamic deforming system, so these calculations provide an upper estimate of rates of deformation and high-pressure aided Fe-melt segregation. The equation also does not take into account the anisotropy of the melt network, an important factor affecting melt permeability. Assuming melt is in sheets rather than tubes also makes permeability estimates highly anisotropic, as melt fractions will be very different depending on direction of flow (Hustoft and Kohlstedt, 2006). Anisotropy may enhance melt network formation however – for example at the edges of diapirs which create shear as they sink through plastic mantle material (Lev and Hager, 2008), which could encourage melt network formation parallel to their edges.

Another method to calculate core segregation rates could be to model melt flow through realistic melt networks such as those produced in our experiments, following methods similar to those used by Miller et al. (2014) for basaltic melt. The small volume of the nano-scan reconstruction has made quantitative modelling through a Lattice Boltzmann simulation difficult to achieve and beyond the scope of this investigation. It may also be too simplistic to assume this specific quenched melt network is representative of the full network volume or that melt networks remain consistent over time within a continuously deforming system. This method could be pursued and evaluated in further work.

3.4.4 Could core formation be completed without the need to invoke a magma ocean?

The extrapolation of the Kohlstedt group described above suggests that percolative core formation could theoretically be a highly efficient process in planets and planetesimals, and that metallic melt could be segregated to melt fractions of 10^{-4}. The small fraction of stranded metal has been invoked to explain the siderophile abundances in meteorites (Groebner and Kohstedt, 2006). Percolative core formation may also explain differentiation in icy satellites of Jupiter, which show evidence of having metallic cores, but have too many volatiles on their surface to infer large-scale melting during their accretionary history (Hustoft and Kohlstedt, 2006).

It is important to note that initial theories of magma ocean core formation were created under the assumption that metallic melts were unable to segregate from solid silicate, as tested under laboratory conditions. Original theories of percolative core formation (Elsasser, 1963) were dismissed due to laboratory experiments conducted in hydrostatic conditions (Ballhaus and Ellis, 1996; Shannon and Agee, 1996). Our experiments show that under the range of possible laboratory strain-rates, metal-silicate segregation is viable under the influence of non-hydrostatic stress. Even if we cannot be entirely confident that our results can be extrapolated to the long timescales and low strain-rates of core formation models, our results add to a building

body of evidence that this initial negative assumption can no longer be accepted as valid. This includes a number of experiments showing the potential for metallic melt networks to form at very high confining pressures (>50GPa) (Shi et al., 2013; Takafuji et al., 2004).

This is not to imply that large-scale silicate melting did not occur in the majority of terrestrial planetary bodies. Geochemistry of asteroid samples gives evidence for significant silicate melting (Greenwood et al., 2005), and abundant heat sources in the early solar system mean that temperatures were likely to rise above the silicate solidus (McCoy et al., 2006; Tonks and Melosh, 1993). However, the attempt to reconcile geochemical signatures with equilibrium core formation models led to the need to infer the equilibration of metal and silicate liquids at the base of long-lived magma oceans to large depths in planetary objects to reproduce observed isotopic signatures (Wade and Wood, 2005; Wood et al., 2006). Although short-lived isotopes (mainly ^{60}Fe and ^{26}Al) may have provided enough heat to induce some silicate melting in smaller bodies (McCoy et al., 2006), dynamic multi-phase models suggest these could only have caused significant melting in planetesimals that were accreted within a few half-lives of ^{26}Al, i.e. within 2 Ma of solar system formation (Sramek et al., 2012). Long-lived magma oceans are harder to explain in small planetary bodies due to the heat-sink effect of early melt via dykes and fractures on initial silicate melting (Wilson and Keil, 2012).

Our results, in combination with those of previous studies, show that the initiation of metal-silicate segregation is likely to occur before the onset of silicate melting. Melting of planets on a large scale is still a likely aspect of planetary evolution, but it may not be a requirement for core formation to initiate and to drain to small melt fractions. Sub-silicate-solidus melt migration provides an alternative mechanism for more widespread core formation, potentially as part of a multi-stage core formation process both before and after widespread silicate melting.

The discussion in section 3.4.2 highlights uncertainties in extrapolating from laboratory to core formation scenarios, particularly in terms of quantitative estimations of the fraction of melt left stranded from deformation-enhanced percolation mechanisms, and the time-scales of melt migration. Our experiments suggest that the process is likely to be more efficient than previously expected, although more experiments would have to be carried out to quantify this further, and even with continued experimentation the uncertainty of extrapolation will not be removed. Results do suggest, however, that metal-silicate segregation in newly accreted bodies is likely to have initiated once temperatures were high enough to melt Fe-S, even if the process is not efficient enough to completely drain core-forming melts without further large-scale melting.

The presence of interconnected melt networks is enough to invoke some separation of metal from solid silicate, meaning there is the potential for melt segregation to occur in response to external gradients over longer time-periods on planetary scales. Initial segregation could theoretically lead to a number of processes of melt localization, first in response to strain

gradients, and then leading to large scale melt segregation in response to gravitational gradients. Wetted grain boundaries are likely to lead to reduced strength and therefore localized focusing of deformation (Holtzman, Kohlstedt, et al., 2003), with the potential to enhance conditions for segregation, leading to a run-away segregation process. Once melt has accumulated sufficiently, melt may sink under its own weight as diapirs (a process that has long been part of the magma ocean theory), or permeability may be further enhanced by high pressures through the lower mantle to the core (Shi et al., 2013).

If core formation was initiated below the solidus of silicate, mantle and core material cannot be expected to have equilibrated significantly as a process of the core formation mechanism, and the subsequent geochemistry of these layers will not reflect any particular core formation mechanism. Early, low temperature onset of core formation makes it likely that initial planetesimals collided into proto-planets with pre-formed cores, which are suggested by numerical models to have merged directly without re-equilibration (Rudge et al., 2010). This may make it very difficult to reconcile the geochemistry of the terrestrial mantle with any particular core formation process. Invoking this sub-solidus segregation mechanism as part of a multi-stage model of core formation explains the lack of agreement in previous geochemical studies (see section 1.3.1). Composition of core and mantle material if equilibrated between two high temperature liquids as invoked in the magma ocean model (Wood et al., 2006), will be very different to compositions inferred from sub-solidus core formation models. This change in baseline model could therefore have significant repercussions for other theories regarding mantle and core composition of the Earth, such as studies examining the 'late veneer' hypothesis (Holzheid et al., 2000), which often start with the assumption of magma ocean equilibration. Suggesting that this assumption is invalid has a significant impact for a huge number of geochemical studies.

We can currently only speculate regarding the initiation and extent of these sub-solidus processes. Numerical modelling, similar to that carried out by Neumann et al. (2012), can help to constrain the potential for these melt extraction mechanisms and, although beyond the scope of the present study, should be carried out more extensively to gain a proper understanding of exactly how and when core formation takes place in proto-planets and planetesimals. An important objective of future planetary modelling work should be to incorporate these multiple stages of core formation into models of planetary evolution.

3.5 Conclusions

There follows a summary of key results from this chapter's work

- Deformation experiments have been shown to encourage wetting of grain boundaries and development of pervasive intergranular melt networks in a liquid FeS- solid olivine

system at low melt fractions. These networks are most strongly developed in very low strain-rate experiments of long duration.

- 3D visualisation has been successful in characterising these melt networks, using a series of CT scans at varying sample size and resolution, to examine sample-scale melt distribution and to 'zoom in' to finer geometries.

- Our results are not directly compatible with previous attempts to extrapolate to core forming conditions, as textures are slightly different from those observed in previous studies. However, if anything our results suggest the process is more efficient than previously expected, particularly in comparison to the work conducted by Walte et al. (2011). The difference in textures is likely to be due to varying deformation mechanisms and timescales of experiments.

- As long as melt networks remain interconnected, velocities of melt migration are shown to be relatively fast even taking into account the full parameter range of calculations, and timescale estimates lie in the range of timescales predicted by Hf-W isotope constraints on core formation in the early solar system.

- We speculate that initiation of metal-silicate segregation by deformation enhanced percolation, before the onset of silicate melting, is feasible as part of a multi-stage disequilibrium model of core formation.

CHAPTER 4

Visualisation of basaltic melt networks in an olivine matrix

ABSTRACT

Experimental work performed at a range of strain-rates indicates that differential stress can significantly alter the geometry of basaltic melt in a solid matrix at small melt fractions. This effect has been proposed to explain geophysical anisotropy in the upper mantle and as a process to extract and focus melt beneath spreading ridges, but the exact effects of partial melt on mechanics of upper mantle systems are disputed, partly due to the difficulty of characterising 3D melt geometries from 2D quench textures. In this chapter, I show results of experiments conducted on a basaltic melt-solid olivine partial melt system, where basaltic melt has been doped with heavy element Hf to increase contrast in standard X-ray CT. High P-T experiments have been conducted at a range of melt fractions in both hydrostatic and dynamically deforming systems, using rotoPEC torsional deformation equipment. The doping technique proves to be a promising method for visualising basaltic melt networks, although problems with the presence of solid HfO_2 crystals make reconstruction a challenge in some samples.

Author Contributions: Starting mixtures were prepared by the PhD student, assisted by GD Bromiley. Deformation experiments were carried out at Universite de Pierre et Marie Curie, France, with the assistance of Yann LeGodec & Julien Phillippe who designed the novel rotoPEC equipment. CT scans were conducted on the UoE *in-house* system with the assistance of I. Butler. Further sample preparation, analysis and evaluation was carried out by the PhD student.

4.1 Introduction and Aims

4.1.1 Basaltic melt in the upper mantle: Summary of debates

Basaltic melt is the primitive melt produced in the mantle and is, therefore, inferred to be present within the mantle where the solidus has been exceeded, either by decompression of hot mantle material from upwelling, or by the addition of volatiles lowering the melting temperature (McKenzie, 1984). Its geometry and permeability at small melt fractions is likely to play a key role in a number of processes occurring within the upper mantle, including

- The seismic character and rheology of the upper mantle (low velocity zone), important in the mechanics of plate tectonics (Forsyth et al., 1998).

- The mechanics of melt extraction at mid-ocean ridges, in particular the velocity and efficency of initial melt movement at depth (Langmuir and Forsyth, 2007).

In addition, experimental work performed at a range of strain-rates indicates that differential stress can significantly alter the geometry of basaltic melt in a solid matrix (Jin et al., 1994). This effect has been proposed to explain geophysical anisotropy in the upper mantle (Holtzman and Kendall, 2010) and as a process to focus melt at mid-ocean ridges from broad regions of melting to narrow zones of eruption at the surface (Gregg et al., 2012).

The summary of these processes in the literature review (section 1.4) highlights the uncertainties caused by a lack of constraint on low degree partial melts in terrestrial systems. The majority of textural studies have been conducted on 2D sections via dihedral angles and detailed qualitative analysis of 2D features. It has been disputed whether small fractions of basaltic melt (<2vol%) wet two-grain boundaries at upper mantle pressures and temperatures, or whether melt is mostly located in triple junction tubules. It is difficult to determine whether this dispute is due to melt geometry varying at different P-T conditions, or whether the discrepancy is due to difficulty in interpreting 2D textures. For example, Faul et al. (1994) claimed melt is present in disk-like sheets which become interconnected at a certain permeability threshold (around 1%), but this has been attributed by a number of authors to be due to the incorrect interpretation of linear features in 2D melt networks as sheets, rather than tubes that have been cut parallel to their long axis (Kohlstedt and Holtzman, 2009). The investigation of deformation melt geometries in particular calls for direct visualisation of 3D melt geometries, as the majority of 2D-3D extrapolation techniques assume the sample is homogeneous and at textural equilibrium (VonBargen and Waff, 1986).

4.1.2 Previous 3D visualisation of basaltic melts

Recent studies have examined the potential for direct visualisation of melt in 3D using serial sectioning techniques, which, although time consuming, do allow a direct visualisation of melt textures in a third dimension. However, the resolution in the third dimension will always be far lower than in the other two, leading to a slightly distorted view of the melt geometry e.g. at best 1.6μm in Z vs. 20nm in X and Y in a recent study (Garapic et al., 2013). In addition, the time consuming nature of the work, the field of view with depth is often also limited e.g. 40μm total view in Z direction vs. 200-200μm in X and Y directions (Garapic et al., 2013).

The use of CT scans to visualise basaltic melt is made difficult by the low contrast between basalt melt and olivine crystals in X-ray radiographs. The density and composition of the two materials are very similar making greyscale values within reconstructed slices impossible to separate for segmentation. The images of basaltic melt created by Zhu et al. (2011) demonstrate the potential for visualising basaltic melt networks using phase contrast imaging, but this requires specific X-ray techniques best suited to synchrotron beams, and most standard laboratory CT equipment is not set up for this technique. Synchrotron beamtime is expensive and time-limited, therefore a simple technique to image melt networks using laboratory CT equipment could provide a valuable resource.

The majority of 3D visualisation so far has been carried out on undeformed samples, although deformation studies have recognised the need to examine melt in 3D due to the heterogeneous nature of experimental samples (King et al., 2010; Kohlstedt and Holtzman, 2009). By carrying out a serial sectioning technique, Holtzman and Kohlstedt (2007) estimated 3D permeability of melt in deformed networks, but due to its time-consuming nature the technique was only conducted on one experimental sample and then extrapolated to further experiments. A number of deformation experiments have used orthogonal cuts through quenched samples to gain some 3D information (King et al., 2010), but at the time of writing there has been no published work showing direct 3D geometry of deformed basaltic melt networks.

4.1.3 Aims of the study

The aims of this chapter are to

1. develop a simple methodology to visualise basaltic melt networks within an olivine matrix from quenched experiments using the in-house CT equipment.

2. use this technique to compare, in three dimensions, melt geometry in deformed and undeformed samples in samples of varying melt fractions, and assess changes in melt geometry with varying textural equilibration and in response to torsional deformation.

3. examine olivine crystal response to deformation using electron backscatter diffraction techniques, investigating the effects of melt fraction and geometry on olivine crystal deformation.

4.2 Preliminary method development

4.2.1 Hf-doping

In order to visualise material effectively in 3D, the attenuation of X-rays through two phases must be significantly different. As described in section 1.2.2, this could be due to a large difference in density, or differences in composition (at low beam energies).

Iron sulphide and olivine have a large attenuation contrast due to the large difference in density and mean atomic number between the two materials, making these experiments particularly well suited to CT analysis (chapter 3). The olivine-basalt mixtures required for upper mantle studies are more problematic. Basaltic glass / melt is compositionally similar to olivine crystals, and the attenuation of both materials are very similar. An example tomographic slice of a basalt-olivine sample is shown in Figure 4.1 A. - olivine and basalt are almost impossible to distinguish. This similarity can also be seen in Backscatter Electron (BSE) scans of quenched slices (Figure 4.1 B).

To enhance contrast between crystals and melt we have doped the basalt starting mixture with hafnium metal (Hf). Hf has a large atomic weight and partitions strongly into basaltic melt. To verify the doping method we had to ensure that the addition of Hf to basalt did not significantly change the properties of the liquid, and therefore the applicability of experiments to real terrestrial problems. This includes the melting temperature, and the interfacial energies between olivine and basaltic liquid, which can be measured in texturally equilibrated samples using average dihedral angle measurements. We conducted a series of piston cylinder experiments using a dual capsule design (Figure 4.2) to directly compare textures in doped and non-doped basaltic melts in an olivine matrix.

10wt% hafnium was added to milled mid-Atlantic ridge N-MORB (major oxide compositions by weight: 50.76% SiO_2, 14.32% Al_2O_3, 10.74% FeO, 9.11% MgO, 11.77% CaO, 1.84% Na_2O, 1.108% TiO_2) and the mixture melted in a tube furnace at 800°C. Variable wt % mixtures were later created by combining this ground powder with more milled basalt, effectively diluting the mixture. The resulting glass was ground to a fine powder and combined with polycrystalline olivine (30-75μm) as a starting mixture (see Table 4.1 for quantitities). The capsule design as shown in Figure 4.2 allowed two starting materials to be directly compared in a single experiment. Table 4.1 shows the experimental conditions of each experiment.

Experimental samples were quenched and images analysed using the SEM at Heriot Watt, including quantitative EDS analysis. Preliminary 2D X-ray shadowgrams were taken

Test name	Sample compositions	Temp / °C	Pressure / GPa	Duration/ hrs
Hf-test-1	Ol + 10vol% basalt /doped basalt (10wt%Hf) (original coarser grain size)	1400	2	1
Hf-test-2	Ol + 10vol% basalt /doped basalt (10wt%Hf)	1600	2	1
Hf-test-3	Ol + 2vol% basalt/ doped basalt (10wt%Hf)*	1400	2	48
Hf-test-4	Ol + 10vol% hf doped basalt (5wt%) / 10vol% hf doped basalt (2.5wt%)	1400	2	1

Table 4.1: Hafnium doping test runs and conditions. All were conducted using dual capsules on both non-doped and doped basalt for direct comparison

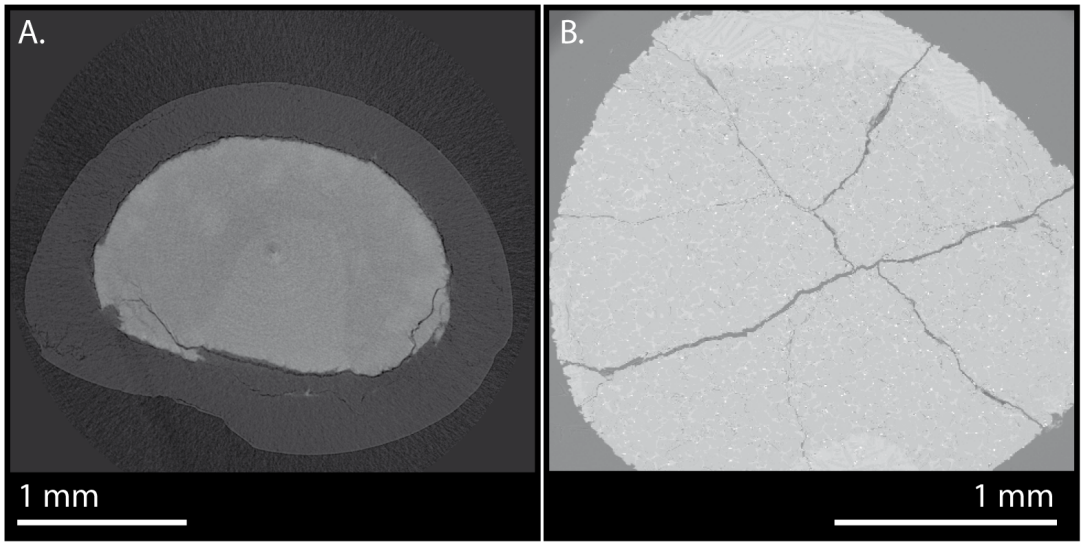

Figure 4.1: Contrast between basaltic melt and olivine A. Tomographic slice of a mixture of olivine and basaltic glass. The outer rim is MgO (dark grey) - the olivine and basalt is distinguishable on a coarse scale (lighter grey shades) but the contrast is not high enough to segment phases reliably. B. BSE image of basalt and olivine. Basalt is slightly lighter in these images due to the iron content of the chosen MORB. Even at this higher resolution the contrast is not significant and automatic segmentation is difficult.

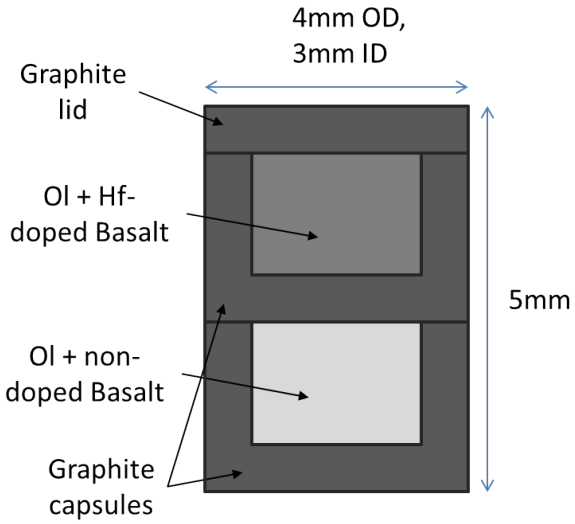

Figure 4.2: Graphite capsule designed to directly compare two liquids under exactly the same experimental conditions. A graphite lid stops the two liquids from being able to mix.

of cut samples using in-house CT equipment to examine differences in contrast during X-ray tomography.

Preliminary results

Initial experiments showed Hf to successfully increase contrast between olivine and basaltic melt as long as it remained fully dissolved in the melt phase. Figure 4.3 shows an example comparing undoped basalt in olivine (a.) and basaltic melt doped with 10wt% Hf (b.) demonstrating the drastic improvement in contrast between the samples in backscatter imaging. Figure 4.4 show preliminary shadowgrams of the Hf-doped basalt vs non-doped basalt samples. Although no full 3D visualisation was attempted at this time, greyscale differences were measured in order to check if there was an observable difference between the melt and olivine crystals at different Hf-contents of melt. The normalised shadowgram containing Hf shows a greater variability in greyscale, promising successful differentiation of phases within such samples in full CT scans.

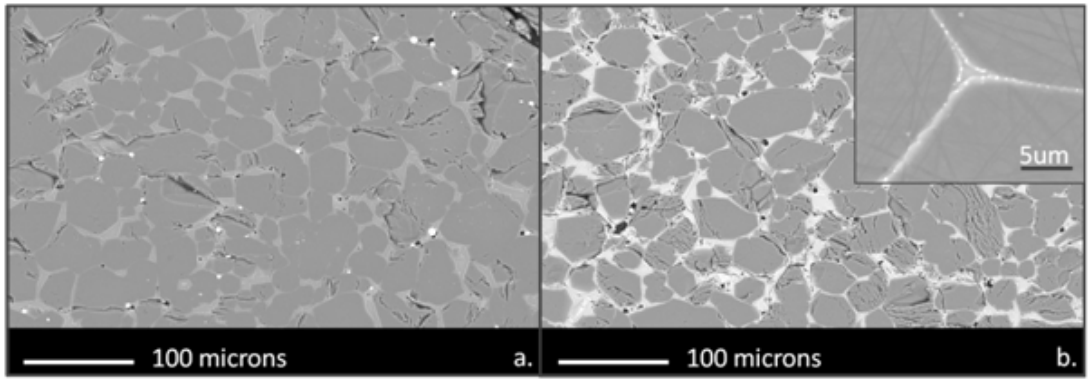

Figure 4.3: A comparison between a. non-doped basalt and b. doped basalt, annealed for 1 hour at 1600°C. The difference in contrast between the melts is clear. Basalt is more attenuating than olivine in both cases, but in b. the difference is much more pronounced. In undoped basalt, ~10 μm diameter spherical iron melt blebs are present (white) which are not apparent in b. However, much smaller solid iron crystals / spheres are still present in the doped basalt, and found at olivine grain edges, where they create embayments, clearly reacting with the olivine and creating a ragged edge effect (see insert). It is unclear whether the difference in iron bleb size is due to a difference in the original starting mixture or an effect of the hafnium. There are no large hafnia crystals in the doped sample, which may be due to a combination of reduced starting grain size and higher temperatures. The total Hf content in the doped melt is 9wt% on average.

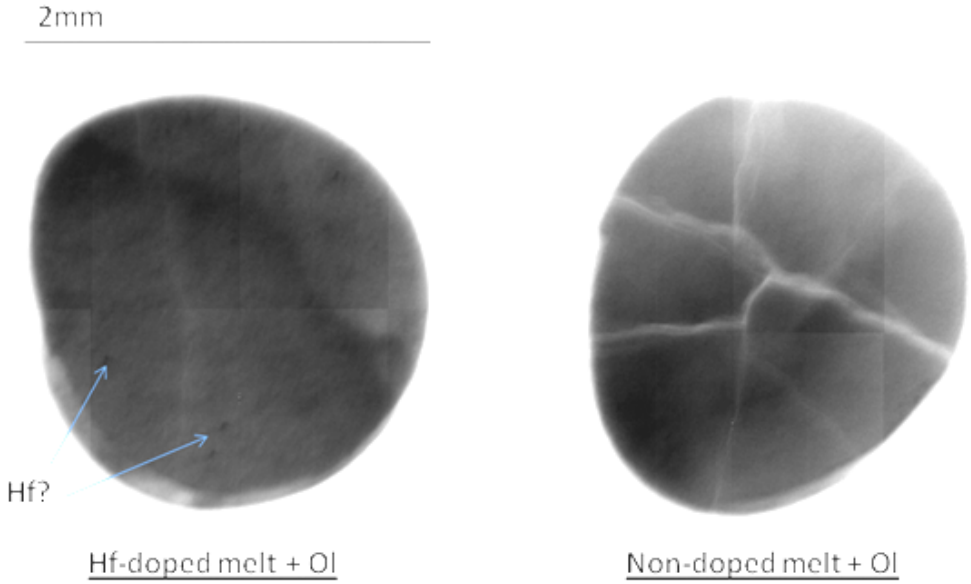

Figure 4.4: Preliminary X-ray photographs of hafnium doped vs. non-doped samples, normalised using ImageJ software. The variability within sample mass is higher in the Hf-doped samples, with dark patches presumably representing melt rich areas. The appearance of the non-doped sample is smoother. Larger scale variations are caused by fractures (pale) and variations in sample thickness (very dark areas are thicker than light areas).

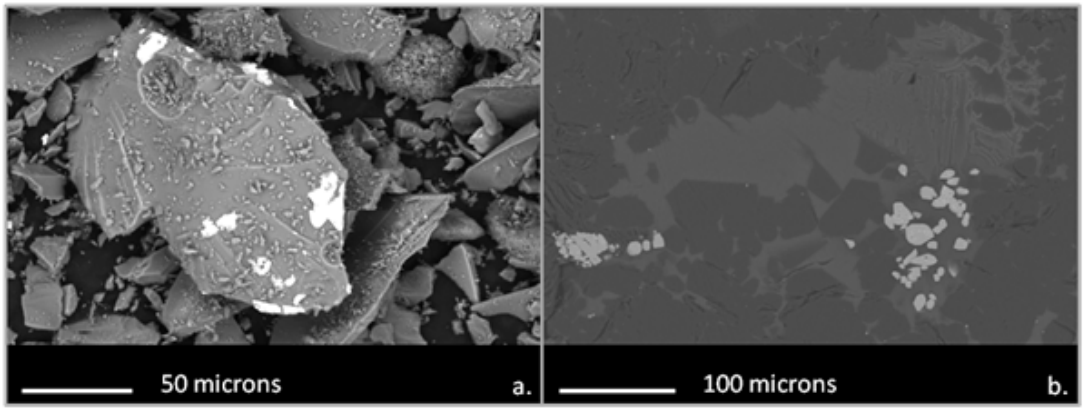

Figure 4.5: Hafnium doped basalt - a. BSE image of original starting mixture showing whole Hf crystals (white) in a single 100µm glass fragment. The glass fragment is surrounded by more fine grained olivine (smaller crystals) showing the disparity in grain size. b. The same starting mixture after 1 hour annealing at 1400°C . The light-grey melt contains 8 wt% Hf, and there is a visible difference in contrast between olivine and hafnium-doped glass. However, solid hafnia crystals are more pronounced (white crystals) and cluster. It is likely these would show up far more effectively in CT scans than the doped melt itself.

Lower dilutions of Hf in basalt, as expected, decreased contrast between liquids significantly. As the majority of tests showed 10wt% Hf could be fully taken up by the liquid and did not leave solid remnants, and there were no clear effects on melt behaviour, this weight% was chosen for future experiments.

Some samples (Hf-test-1 and Hf-test-4) revealed the presence of solid HfO_2 crystals present within the melt phase. This is to be avoided as it reduces the contrast of the melt phase (where Hf content is reduced) and increases complexity of the samples by adding a third phase. Factors contributing to the presence of Hf-crystals were found to be as follows:

- **Starting grain-size** - First generation Hf starting mixtures, including those used at ESRF, were coarsely ground. Analysis of this starting mixture showed that there were some large HfO_2 crystals within the starting glass (Figure 4.5 a.). These did not disappear from the glass after two hours of annealing at high temperatures and pressures (Hf-bas-test-1, Fig 4.5 b.). Later experiments were carried out using a finer grained starting mixture, which reduced the occurrence of solid Hf oxide crystals.

- **Temperature** - In the run carried out at 1600°C no solid HfO_2 crystals are present. It may be that the solubility of hafnia in basalt is temperature dependent, and higher temperatures were required to dissolve the Hf-basalt (e.g. Fig 4.3). However, the grain size had already been reduced for this run, which may be the main cause of increased solubility.

- **Annealing time** – Initial experiments carried out with only a 1 hour anneal were shown to contain undissolved HfO_2 crystals. Textures over longer anneal times showed full dissolution into the melt phase. However, an anneal time of only 1 hour at high temperatures and with a finer starting grain size proved to be enough to dissolve hafnia crystals fully in the melt phase.

The 48 hour run was also carried out in order to make dihedral angle measurements and check for variability between the two melts. Only 2 wt % basalt in olivine was used as small fractions of melt are most sensitive to interfacial energies, and development of textural equilibrium takes the longest time in these samples. Dihedral angle measurements (Figure 4.6) show there is no statistically significant difference between mean or median dihedral angles within the doped and non-doped samples. Given the small number of experiments performed, this analysis gives only a preliminary constraint on sample textures and further analysis may be necessary to ascertain if there are any subtle but consistent changes in texture between doped and non-doped samples. Generally, textures appear similar enough to allow textural comparison between Hf-doped samples and non-doped basaltic melt behaviour.

Hf uptake in olivine was also examined to check for significant reactions that could affect olivine and melt behaviour. From BSE imaging and EDS analysis there is no evidence of any

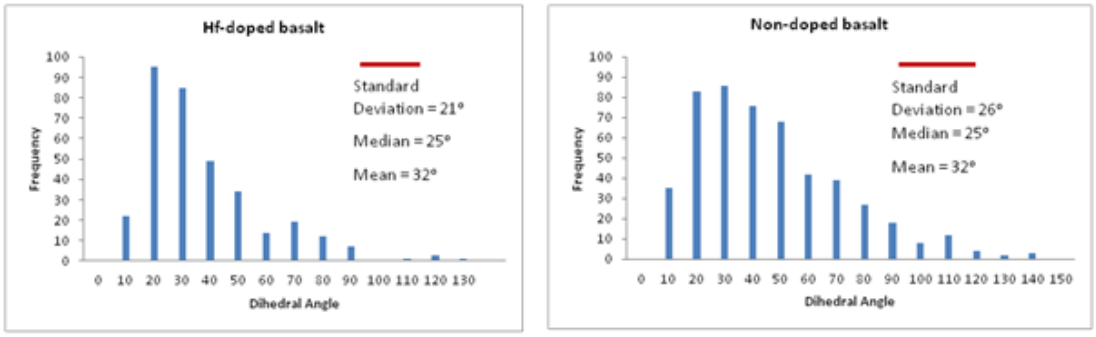

Figure 4.6: Dihedral angle distribution of A. Hf-doped basalt and B. Non-doped basalt measured BSE images of 2D quenched slices using ImageJ software. Although averages differ by 10°, the variation is not statistically significant. More analysis would have to be carried out to see if the subtle difference is significant across more samples.

significant reaction between Hf and olivine, at any temperature or run duration. The outer edges of olivine crystals appear to be enriched in iron, which may be due to a reaction taking place between olivine and Fe-rich basaltic melt (basalt contains ~9wt % FeO). This reaction is more pronounced in the Hf-doped melt, where iron melt is more evenly distributed in smaller pockets throughout the melt (Figure 4.3). The effect is limited to within <1μm of the crystal edge, and the olivine interior appears to have a very homogeneous composition.

This preliminary work has allowed us to test effectiveness of Hf doping of basaltic melt in improving contrast, and to test for any differences in liquid properties of Hf-doped and non-doped basaltic liquids. We found that the addition of 10wt% Hf to MORB glass, once finely ground, greatly improves the contrast between olivine and basaltic liquids both for backscatter electron microscopy and tomographic imaging. Important factors to ensure good dissolution of Hf, and therefore the best contrast, are to grind starting mixtures finely, and ensure annealing time of >2 hours to ensure Hf fully partitions into the melt.

4.3 Methods

4.3.1 Experimental methods

Final starting mixtures were prepared from ground gem-quality San-Carlos olivine (Fo_{95}) and Hf-doped MORB basalt. Four starting mixtures were prepared with quantities of basalt ranging from 1.6-30vol%. Olivine crystals were ground and filtered to ensure a grain size of 30-50 µm. This relatively large crystal range was again chosen to ensure that features would be larger so easily recognisable in lower resolution tomographic scans (section 2.2.2).

Hydrostatic experiments were carried out using end-loaded piston-cylinder apparatus and a high-temperature talc-pyrex-graphite assembly, as described in Methods section 2.2.1. Starting mixtures were packed into 2x3mm i.d. graphite capsules. Samples were pressurised and slowly heated (100 $°s^{-1}$) to run temperature. All experiments were conducted at 2GPa pressure and 1400°. Anneal time was generally >48h to ensure reasonable equilibration of textures, except in time series experiment TS1, which was left for only 2 hours to examine the textures expected at the point at which deformation begins in dynamic experiments. Samples were quenched at rates of >100$°s^{-1}$ by cutting power supply to the system.

Deformation experiments were carried out using the rotoPEC adapted Paris Edinburgh design, with a pyrophyllite-graphite-steel ring gasket (section 2.2.1). Experiments were carried out offline at the Universite de Pierre et Marie Curie in Paris, France. No direct measurement of temperature or pressure was possible, and both were estimated from previous calibration experiments (see Figure 2.5, section 2.2.1). A power of 400W and oil pressure of 124 bars was considered roughly equivalent to 1400°and 2GPa, and calibration suggests an error of ±50°and ±1kbar for pressure (although the uncertainty may be greater than initially realised - see Chapter 5). Samples were quenched by cutting power to the rotoPEC equipment. Thermocouple experiments indicate quench time is very fast (<1s for 1000°drop) Exact compositions and conditions of experiments are shown in Table 4.2.

4.3.2 Analytical techniques

Tables 4.3 and 4.4 give details on the CT scan and reconstruction parameters for individual scans carried out on experimental samples. Quenched deformed samples were initially scanned within experimental gaskets at a coarse resolution (spatial resolution ~6µm) to ensure melt had not escaped the gasket itself and to examine the effect of deformation on the full sample assembly. Samples were later removed from their external casing and 1.5-2mm diameter samples were scanned at a higher resolution of 2.5-3µm to examine features within the scans in more detail. Table 4.3 gives scan conditions and table 4.4 reconstruction parameters for each scan carried out.

Deformed samples								
Sample Name	**Vol% basalt**	**Anneal Time**	**Rotation/deg**	**Time under strain**	**Strain**		**rate**	
					e	**y**	**e.**	**y.**
Pdef1*	30	16	41.91	451	0.1	0.4	4E-06	1.4E-05
Pdef2*	1.5	2	55-123	618-1320	0.2-0.3	0.5-1.1	4E-06	1.4E-05
Pdef3*	15	2	106-136	1195-1441	0.3-0.4	0.9-1.2	4E-06	1.4E-05
Pdef4	15	2	180	429	0.5	1.6	2E-05	6.1E-05
Pdef5	1.5	2	180	429	0.5	1.6	2E-05	6.1E-05
Pdef6	15	2	180	960	0.5	1.6	9E-06	2.7E-05
Pdef7	1.5	2	180	960	0.5	1.6	9E-06	2.7E-05
Pdef8	1.5	2	200	1067	0.6	1.7	9E-06	2.7E-05
Pdef9	1.5	2	200	2152	0.6	1.7	4E-06	1.4E-05
Undeformed samples								
OlBaPCts1	15	2						
OlBaPCts3	15	48						
OlBaPCvs1	30	48						
OlBaPCvs3	1.5	67						
OlBaPCvs4	5	69						

Table 4.2: Table of experiments conducted using synthetic mixtures of natural olivine and MORB basalt. All experiments were conducted at 1400°C and 2GPa conditions. For deformed experiments, the temperature was indirectly measured from previous calibration experiments, making the error for these measures greater than for piston cylinder experiments, where a thermocouple was used for direct measurement. The deformed samples marked with a * are those which have been further analysed and which the results chapter focuses on. Further experiments had issues with furnace fracture and large scale melting of gasket material.

BSE analysis was carried out on ground and polished sections to groundtruth CT data and analyse composition semi-quantiatively using EDS analysis. Further analysis was carried out on a number of samples using EBSD to examine the structure of olivine in deformed and undeformed samples.

Scan									
Sample name	**Camera**	**Scan type**	**x-s /mm**	**Beam energy /kV**	**Power /W**	**Exposure /s**	**Frame averaging**	**No. projections**	**Physical filter**
Pdef1*	Old	Gasket	40	100	2.7	3	1	500	0.8mm Al
Pdef2*	Old	Gasket	40	100	2.7	3	1	500	0.8mm Al
Pdef3*	Old	Gasket	40	100	2.7	3	1	500	0.8mm Al
Pdef4	Old	Gasket	40	100	2.7	3	1	500	0.8mm Al
Pdef5	Old	Gasket	40	100	2.7	3	1	500	0.8mm Al
Pdef6	Old	Gasket	40	100	2.7	3	1	500	0.8mm Al
Pdef7	Old	Gasket	40	100	2.7	3	1	500	0.8mm Al
Pdef8	Old	Gasket	40	100	2.7	3	1	500	0.8mm Al
Pdef9	Old	Gasket	40	100	2.7	3	1	500	0.8mm Al
	Old								
Pdef1*	Old	hi-res	10	120	2.8	1.5	2 (sum)	2000	0.8mm Al
Pdef2*	Old	hi-res	12	120	2.7	3	2 (sum)	500	0.8mm Al
Pdef3*	Old	hi-res	17	120	2.8	1.5	2 (sum)	2000	0.8mm Al
Pdef4	Old	hi-res	17	120	2.8	1.5	2 (sum)	2160	0.8mm Al
Pdef5	Old	hi-res	12	120	2.7	3	2 (sum)	500	0.8mm Al
Pdef6	Old	hi-res	12	120	2.7	3	2 (sum)	500	0.8mm Al
Pdef8	Old	hi-res	12	120	2.7	3	2 (sum)	500	0.8mm Al
OlBaPCts1	New	hi-res	5.5	100	2.8	1	2	2000	none
OlBaPCts3	New	hi-res	4	80	2.8	0.5	2	2000	none
OlBaPCvs1	New	hi-res	4	80	2.8	0.5	4	2000	none
OlBaPCvs3	New	hi-res	4.5	100	2.8	1	2	2000	none
OlBaPCvs4	New	hi-res	4.5	100	2.8	1	2	2000	none

Table 4.3: A summary of conditions of computed tomography scans carried out for the basaltic melt study. All were conducted using the *in-house* CT equipment, as described in section 1.3.1. 'Old' camera refers to Teledyne Dalsa Shad-o-box CCD flatscreen X-ray camera and 'new' camera refers to Perkin Elmer XRD 0822 flat panel detector. The replacement of the camera led to significant improvements in scan quality (section 2.3)

Reconstruction							
Sample name	**Voxel size/µm**	**Spatial res /µm**	**NF (%)**	**BH filter**	**Ring Filter**	**Output scaling**	**Spot Shift**
Pdef1*	6	6.3	50	0.3	(8, pre-sino)		
Pdef2*	6	6.3	50	0.3	(8, pre-sino)		
Pdef3*	6	6.3	50	0.3	(8, pre-sino)		
Pdef4	6	6.3	50	0.3	(8, pre-sino)	0-20	
Pdef5	6	6.3	50	0.3	(8, pre-sino)		
Pdef6	6	6.3	50	0.3	(8, pre-sino)	0-20	
Pdef7	6	6.3	50	0.3	(8, pre-sino)		
Pdef8	6	6.3	50	0.3	(8, pre-sino)		
Pdef9	6	6.3	50	0.3	(8, pre-sino)		
Pdef1*	1.5	2.9	0	0	5,30	0-12.5	
Pdef2*	1.8	3.0	50	0.3	5,30	0-10	
Pdef3*	1.8	3.0	50	0.7	5,30	0-20.127	
Pdef4	2.6		50	0.7	5,30	0.2-11	
Pdef5	1.8		0	0.1	5,50	0.2-15	
Pdef6	1.8		0	0.3	0	0-19	
Pdef8	1.8		0	0.5	5,50	"-0.2-27.91	
OlBaPCts1	2.0	2.4	0	0.8	5,50	0-20	Spot shift -2y, +3x
OlBaPCts3	2.0	2.4	0	0.8	4,45	0-20	
OlBaPCvs1	2.0	2.4	0	0.9	4,45	0-20	
OlBaPCvs3	2.2	2.9	0	0.8	5,50	"1-8	Shift -10x
OlBaPCvs4	2.2	2.9	0	1	8,45	"1-8	Shift -10x

Table 4.4: Conditions of all reconstructions carried out on basaltic melt samples. All CT reconstructions were carried out using the University of Ghent's Octopus reconstruction software, with variables as described in methods section 1.3.1. Noise filter is given as a % value. BH filter refers to beam hardening filter. Ring filters can either be applied during the creation of the sinogram (pre-sino), where the value refers to the intensity of the fourier filter or during the reconstruction process, where two values describe the thickness of potential rings, and their maximum angle. Spatial resolution is calculated as described in section 2.3.4, see Appendix A.1.2 for full table of parameters.

4.4 Results

4.4.1 2D analysis of undeformed samples

Textural changes with anneal time

Samples OlBaPCts1 and OlBaPCts3, both initially contained 15vol% melt, but were annealed for 2 and 48 hours respectively to compare textures with increasing anneal time. BSE images of these samples are shown in figures 4.7 and 4.8. Textures indicate that processes are more complex than initially expected.

Sample OlBaTS1 is inferred to reveal the starting textures of a deformation experiment, as those carried out in this study mostly begin with a 2 hour annealing time. The texture of the sample is relatively homogeneous with no clear change in melt fraction across the sample. Olivine grain size is variable and poorly sorted. A significant proportion of HfO_2 crystals are present (as expected due to the short anneal time), generally surrounded by melt, suggesting incomplete dissolution or reprecipitation of hafnium in the form of hafnia HfO_2. The melt hafnium content is around 6wt%, suggesting around 40% of input Hf is still present in solid hafnia crystals. Melt does not fully wet all olivine grain boundaries, instead clusters of olivine grains are surrounded by larger melt patches. It is possible that the melt has not had time to locally migrate and wet all grain boundaries, suggesting melt network connectivity may be affected. Some olivine grains are faceted suggesting some recrystallisation may have already taken place, but grains have not grown significantly from their initial size.

Sample OlBaTS3 was expected to show textural equilibration due to longer anneal times. In a hydrostatic system with no melt migration gradients, this would be expected to lead to melt distributing itself evenly along grain boundaries as expected for a low dihedral angle liquid. The sample instead reveals a clear gradient in melt fraction, revealing significant migration of melt has taken place. An interesting negative correlation is observed between the number of solid HfO crystals present and the melt fraction (Figure 4.9) suggesting that melt migrated away from the top of the sample before complete Hf dissolution could take place. Remaining solid crystals were taken up as inclusions by rapidly recrystallising olivines. Although density differences between basalt and olivine may be the cause of melt migration, thermal gradients are a more likely cause, as observed in previous partial melt studies to be a stronger force for migration (Lesher and Walker, 1988). There is some evidence for textural change with annealing despite the presence of melt gradients. Wetted olivine grain boundaries are more prevalent than in OlBaTS1, even in the 'drained' area of the sample with a very small melt fraction, suggesting that melt has become more evenly spread into grain boundaries over time. Sheets of melt in low melt fraction areas are <1μm thick, and appear to be wetting 2-grain boundaries, with only very small pockets at triple junctions. Some grain boundaries

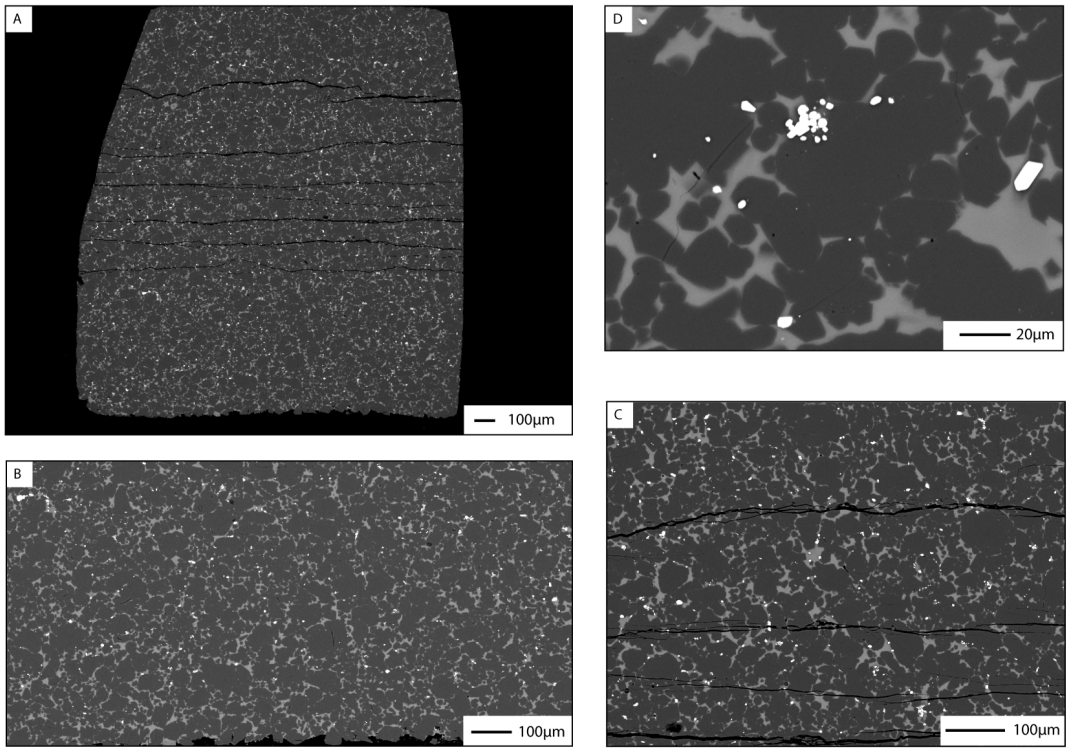

Figure 4.7: BSE imaging of Undeformed sample OlBaPCTS1, 15 vol % hafnium-doped basalt, annealed for 2 hours at 1400°C and 2GPa. A. shows the full sample section, images B-D show the texture of the sample at increasing magnification. Dark grey areas are olivine, light grey is doped basaltic melt (the lighter grey colour indicating melt has a different atomic density to surrounding olivine) and bright white crystals are hafnia (HfO_2). Textures are described in detail in the text.

remain dry even in high melt fraction zones. Olivine crystals show marked grain growth and recrystallisation with increased anneal time. Grain size is more homogeneous and a large number of crystals appear faceted. There is some evidence of olivine melting/dissolution and rapid quench crystallisation at the very base of the sample, as shown in high magnification images E and F in figure 4.8, but these textures are not widespread in this sample.

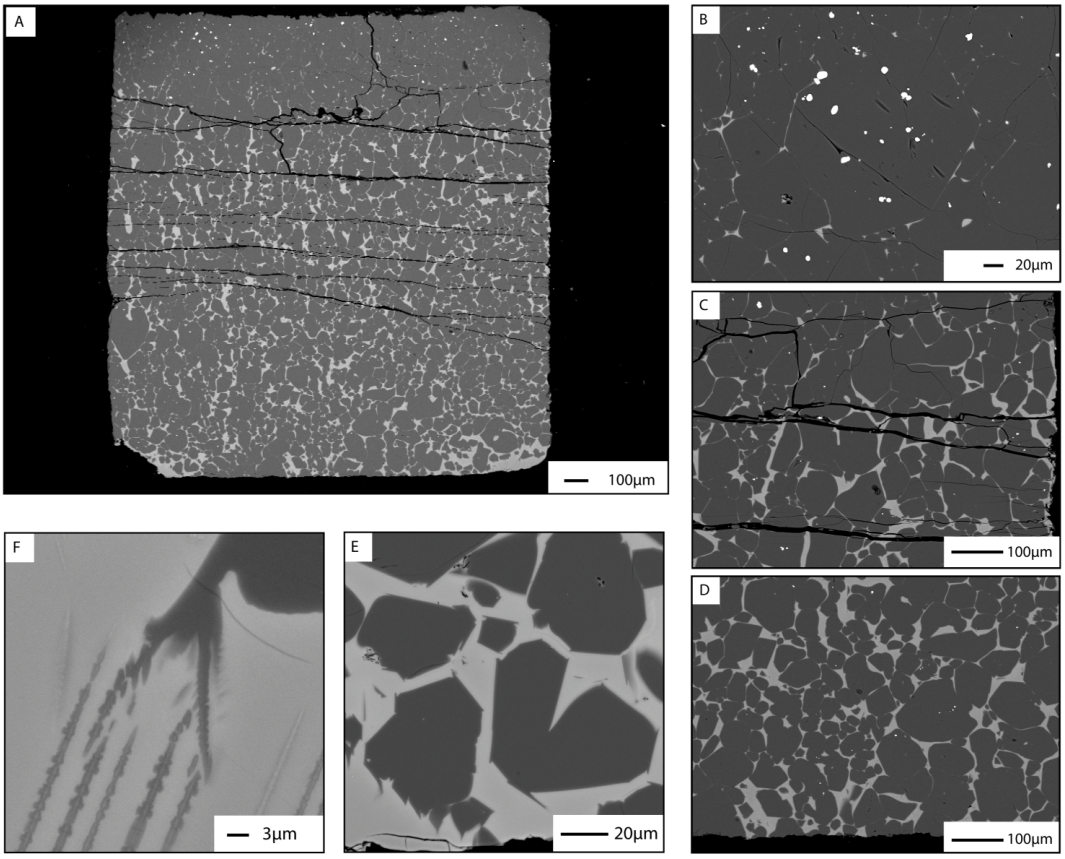

Figure 4.8: BSE imaging of Undeformed sample OlBaPCTS3, 15 vol % hafnium-doped basalt, annealed for 48 hours at 1400°C. and 2GPa. Dark grey=olivine, light grey= Hf-doped basalt, white= HfO_2 crystals. A. shows the full sample section. A clear gradient in melt fraction exists between the top and bottom of the sample, with pools of melt at the base. However, we do not definitely know that the sample is the 'right way up' in this image, it may be inverted. B. close-up of relatively drained area of the sample, showing melt present in pockets at grain triple junctions but also in fine sheets of ~1µm thickness. Hf crystals are abundant and appear in the centre of olivine grains. C. and D. show areas of the centre and base of the sample, with increasing melt fraction observed towards the base. Hf crystals are less abundant than at the top of the sample. E. and F. are high magnification areas of the 'melt pools' seen at the very base of the section, showing olivine embayment and presence of quench crystals suggesting some olivine melting did occur in localised volumes.

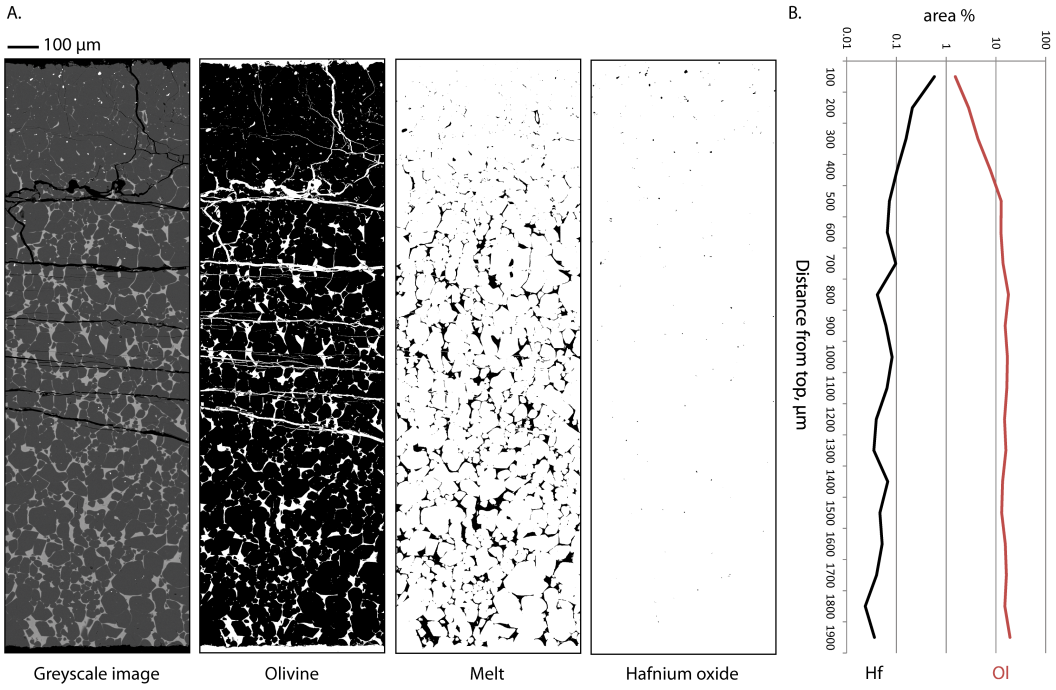

Figure 4.9: 2D image analysis of melt vs. Hf Oxide distribution across sample OlBaTS3. A. Images are binarised to pick out phases of interest and measured using the 'particle analysis' tool on ImageJ. B. Area % is calculated by summing total area and dividing by the sum of olivine, melt, and Hf crystals (thereby avoiding the influence of cracks in the sample on the calculation). By carrying out analysis across 100 µm horizontal strips, changes in phase proportions are analysed along the length of the sample. The change in melt concentration across the sample is not uniform. Instead there is a sharp increase in melt across the first 500µm, followed by a relatively steady melt fraction of around 15%, (the average melt fraction across the sample). There is a striking negative correlation between the proportion of HfO_2 crystals present and the melt fraction, with the majority of Hf crystals found in areas that are relatively drained of melt. HfO_2 crystals are often found as inclusions in olivine crystals in drained areas, suggesting they were incorporated during grain growth.

Volume series VS1-4: Textures at varying melt fractions

Samples OlBa VS1, 3 and 4 were all annealed for >48 hours. Different starting melt fractions were used in the hope of allowing direct comparison between equilibrium textures at varying melt fractions, with melt fraction increasing from VS3, VS4 to VS1. Unfortunately, partial melting and significant melt migration limited possible comparison. In all cases there are very few solid HfO_2 crystals remaining - as well as the increased anneal time, it is possible that the additional melting helped to ensure melt was not saturated, aiding dissolution. BSE images are shown in figures 4.10-4.12. All samples have large 'pools' of 'melt' at their edges, populated with skeletal quench crystals. The total melt fraction in each case is significantly larger than within the initial starting mixture, suggesting partial melting of olivine has taken place in this melt zone. The boundary between melt and non-melt areas is generally very sharp, with a clear transition between melt-dominant quench textures, and the expected equilibrium textures of fine melt networks wetting grain boundaries. In sample VS4, there is a clear gradient of melt within the remaining sample, with drained areas of «5vol% melt in areas furthest from the melt 'pool', and higher melt fractions closest to it, suggesting melt was dynamically migrating towards the melt rich zone at the time of quench. The migration gradient in this case is horizontal, ruling out density differences as the cause of migration. Observation of fractured grains suggests the melt gradient is large enough to create local fluid overpressures that cannot be overcome by flow along grain boundaries, causing grain hydrofracturing (Parfitt and Wilson, 2009).

In areas relatively unaffected by melt, it is possible to make some comparison of textures that are close to textural equilibrium. Melt is observed wetting grain boundaries at all melt fractions, with sheet thickness varying depending on initial melt fraction. Melt appears to be relatively spread out within 2-grain and 3-grain boundaries and there is little evidence, at least from 2D textures, that melt is pooling at triple junctions at very low melt fractions (i.e. dihedral angles are very low) e.g. figure 4.10B. Olivine crystals are very large in each sample, due to increased anneal time (up to >500μm diameter in sample VS3), and texture shows well developed triple points between grains. Spherical melt inclusions are found in the centre of some larger grains in VS3 and VS4.

Overall, although complications arise due to presence of solid hafnia, melt gradients leading to dynamic melt migration, and significant partial melting, there are volumes of the majority of undeformed samples that can be used to compare textures, at least qualitatively, at varying melt fraction and anneal time. Large enough volumes are available to allow CT scans to compare 3D melt geometries in these relatively unaffected areas (see section 4.4.3), at least for preliminary comparison and testing of doping techniques. Given more time and some experimental adaptation, it may be possible to create more reliable samples showing melt at textural equilibrium.

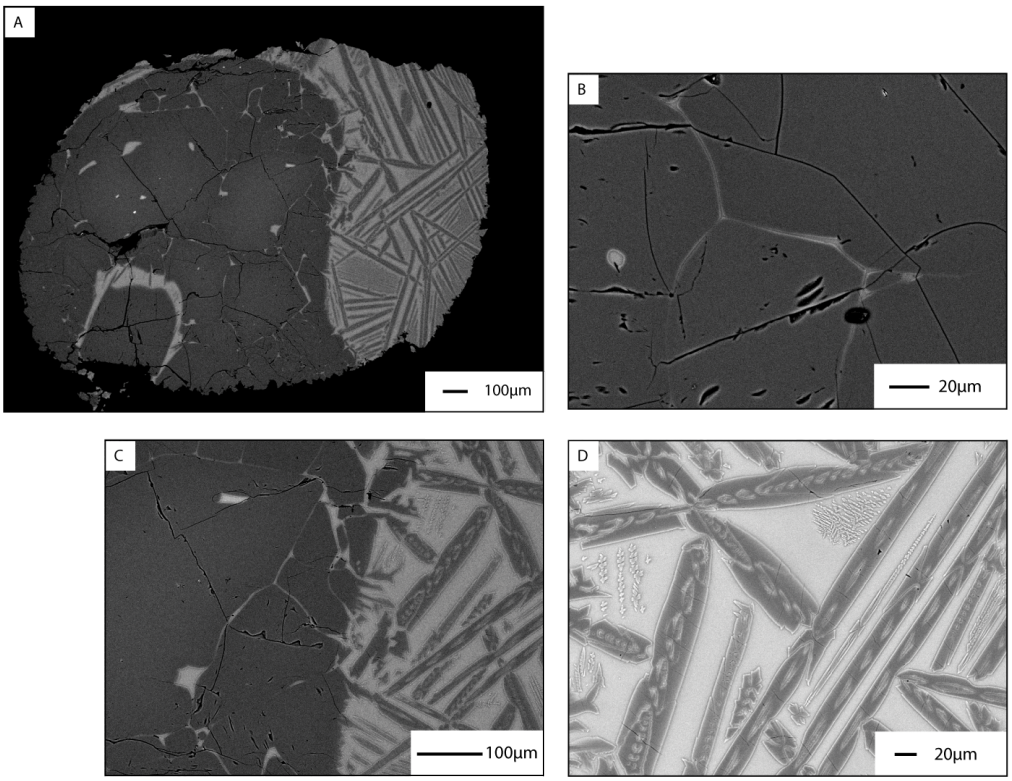

Figure 4.10: BSE imaging of undeformed sample OlBaPCVS3, starting mixture of 1.5 vol % Hf-doped basalt, annealed for 69 hours at 1400°C and 2GPa. A. shows the full sample section, showing that significant silicate melting has taken place at one edge of the sample producing skeletal olivine crystals during rapid quenching (as seen in D). B. shows melt wetting grain boundaries in very fine sub-micron sheets, in a recrystallised olivine matrix of well developed triple junctions. C. The edge of the 'partial melt section' showing the sharp boundary between euhedral olivine crystals with interstitial melt on left, and large melt fractions with skeletal quench crystals on the right. D. Example of fine skeletal textures in the quench area. Dark grey = olivine, light grey = basaltic melt. In the 2D section imaged, there are no remnant HfO_2 crystals.

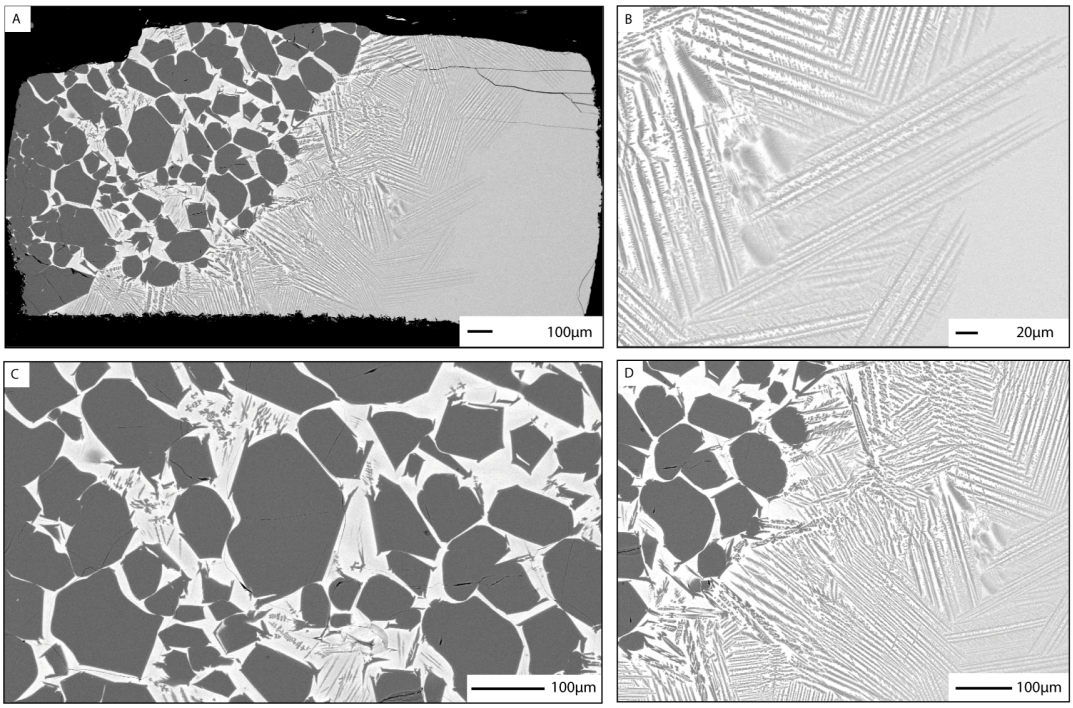

Figure 4.11: BSE imaging of undeformed sample OlBaPCVS1, 30 vol % Hf-doped basalt, annealed for ~72 hours at 1400°C and 2GPa. Dark grey = olivine, light grey = basalt melt. Brightness is an indicator of hafnium enrichment in the melt phase. A. shows the full sample section. Again, significant silicate melting has taken place on the right half of the slice. B. Texture in melt pool transitions into uncrystallised glass with crystal edges becoming less defined and composition between liquid and solid becoming less contrasting due to enrichment in Hf of liquid where quench crystals form. C. Quench crystals nucleate on remaining olivines. D. Sharp edge between partial melt zone and remnant olivines is present, but less well defined in this sample.

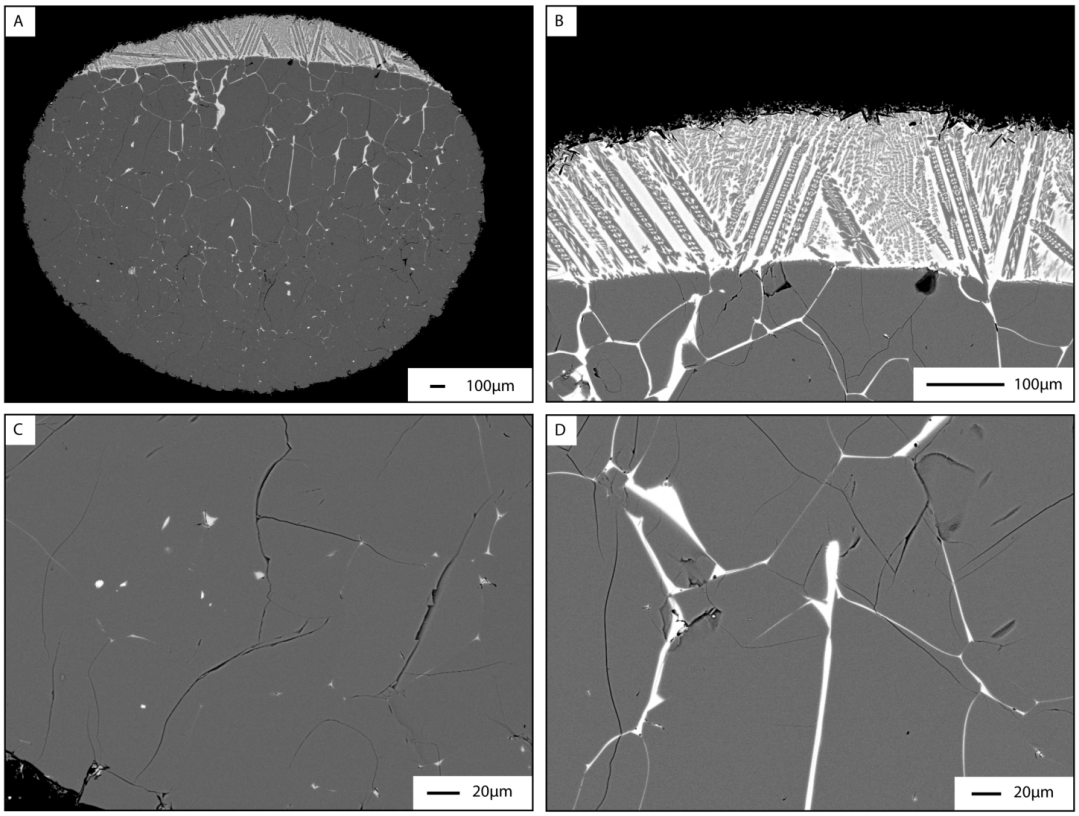

Figure 4.12: BSE imaging of a planar section of the undeformed sample OlBaPCVS4, 5 vol % hafnium-doped basalt, annealed for 67 hours at 1400°C and 2GPa. A. shows the full sample section, in this case cut in the X-Y plane of the cylindrical capsule. In this case, olivine melting is limited to one edge of the sample, with a very sharp melt front boundary as shown at high magnification in B. Olivine crystal shape at the edges is clearly defined by the melt front boundary, which is more evidence that olivine crystals have undergone partial melting. Images C and D are high magnification insets of a melt poor and melt rich area of the sample respectively. More details given in text.

4.4.2 2D analysis of deformed samples

A total of nine experiments were carried out using the rotoPEC to deform samples of varying melt fraction and at various strain-rates. However, due to a flaw in the gasket design, a number of these experiments failed producing large scale melting and reactions between the sample gaskets, capsules and samples themselves, rendering the majority of experiments unusable. These reactions were initially observed qualitatively at a gasket scale in low-resolution CT scans, and later analysed semi-quantitatively for chemical compositions using EDS analysis combined with backscatter imaging. 2D BSE images of these failed experiments are shown in Figures 4.13 and 4.14. In each case it appears that high strain-rates and strains led to the possible fracturing / rupturing of the sample capsule, and surrounding graphite furnace, which may have caused a sudden increase in resistance and therefore temperature spiking in certain areas of the sample, including on the steel contact rings at the top and bottom of the sample. This lead to large scale melting and mingling of various gasket components. In sample Pdef8 there is significant growth of a number of reaction crystals of intermediate composition, including elongate minerals interpreted from their composition and clear cleavage to be biotite. In some cases, such as samples Pdef4-6, there are some areas where original olivine and melt relationships can still be recognised, but the areas are limited and it is unclear how much deformation actually reached the sample rather than being taken up in deforming the gasket itself, therefore these samples are not useful for further analysis.

Three initial samples were found to be relatively unaffected by large-scale melting, namely Pdef1 -3, which were all of relatively low strain-rate and low strain deformation. This suggests that the deformation equipment may be limited to low strain-rate experiments to produce the best results, at least in high T runs. The three deformation experiments deemed a 'success' are described in more detail in this section, accompanied by figures of 2D analysis. Each deformed sample has been cut in a tangential section so that the slice examined is effectively deformed in simple shear, with the shear direction horizontal in each case.

Pdef1

Sample Pdef1 has a starting composition of 30vol% melt. This is the only deformed sample with a long initial anneal time of 16.5 hours, before any deformation took place. Deformation was carried out to a total shear strain of γ=0.4 at a strain-rate of $1.4 \times 10^{-5} s^{-1}$. Olivine crystals show a distinct pale rim due to iron enrichment, suggesting some reaction may have occurred with the surrounding melt. Some reaction appears to have taken place between the sample and capsule, but it seems to be limited to within 20μm from the capsule edge and does not affect the rest of the sample (Figure 4.15). Despite long anneal times, Hf is not dissolved into the basaltic melt as seen in undeformed samples. This could be explained by a slower quench time allowing hafnia to reprecipitate. Alternatively, ongoing deformation damaging the graphite furnace may have changed resistivity enough to reduce overall sample

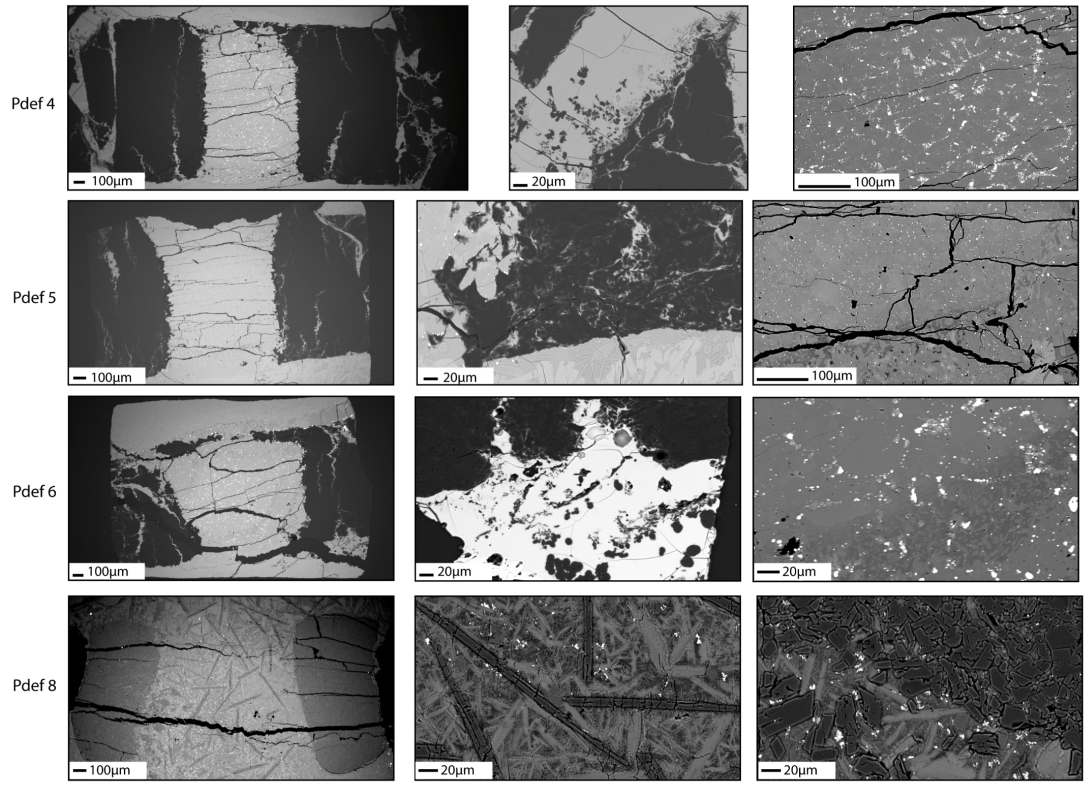

Figure 4.13: BSE imaging of a tangential sections of other experimental samples, showing significant damage and whole-scale melting has taken place rendering these samples unusable for further analysis (as prediced by CT scans). See text for details.

temperature (despite constant power). Temperature may have dropped enough to begin to precipitate HfO_2 crystals before the sample was quenched.

Interestingly, despite the long initial anneal time there is no evidence of thermal gradients causing localised melt migration prior to deformation, with melt relatively homogeneously distributed across the sample slice examined. It is possible that the same localised thermal gradients are not present in the rotoPEC assembly, or that the effect of deformation complicates melt gradients. For example, thermal gradients may draw melt towards sample edges, while deformation acts to push melt into the sample centre due to pressure gradients (Kohlstedt and Holtzman, 2009).

There is no clear evidence for formation of melt-rich bands. The high melt fraction puts this sample close to the rheologically critial melt fraction (RCMF); therefore deformation may be mostly taken up by relatively free rotation of olivine crystals, leaving melt textures relatively unaffected. Initial observations indicate that there is a subtle fabric created by olivine shape orientation, but this requires further, high resolution quantitative analysis.

Pdef2

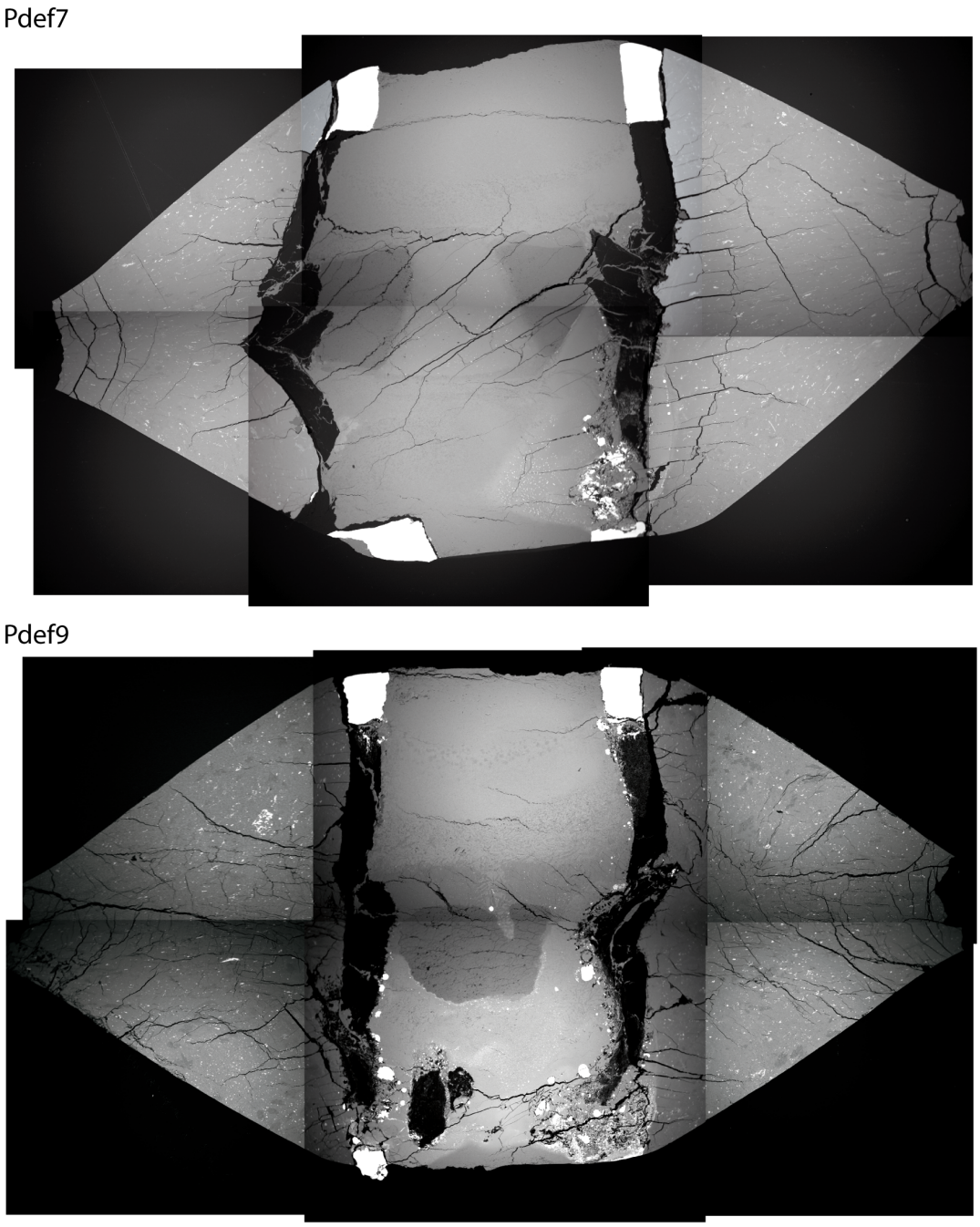

Figure 4.14: BSE imaging of a full gasket sections of two failed experimental samples, showing the extent of damage to the sample and surrounding capsules (see text for details).

Pdef2 has the lowest initial melt fraction of 1.5vol%, annealed for 2 hours before being deformed at a strain-rate of $1.4 \times 10^{-5} s^{-1}$. Due to a motor power failure, the length of time and

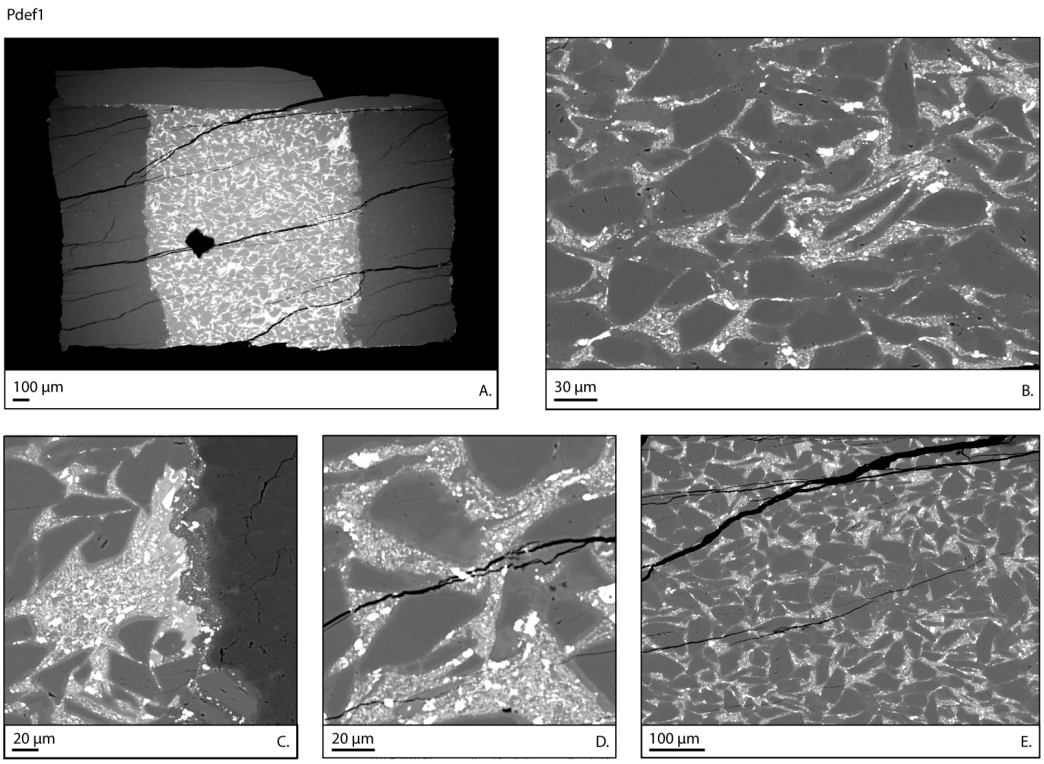

Figure 4.15: BSE imaging of a tangential section of deformed sample Pdef1. Dark grey = capsule, mid-grey = olivine, light grey = basaltic melt, white = hafnia (HfO_2) crystals, black = carbon surface contamination. A.shows the full sample section surrounded by alumina capsule. B. close-up showing three phase olivine + melt + hf-crystal texture. There is evidence for a shape preferred orientation of olivine crystals, with long axis aligned sub-horizontally. C. and D. show close-ups of the melt phase with HfO_2 crystals of variable size within them. Olivine show a rim of brighter material that is due to iron enrichment. E. a medium-scale image showing potential subtle fabric development.

total strain deformed is not known in this sample, with a possible range of shear strains of 0.5-1.1, although the total strain is likely to be low (comparable to that of Pdef1) as there is little damage observed to the surrounding capsule, compared to those seen in samples deformed to higher strains. 2D textures are shown in Figure 4.16. There is evidence for some reaction taking place between the boron nitride capsule surrounding the sample and the alumina spacers (Figure 4.16B.) and some reaction at the top and bottom of the sample (e.g. top left of fig 4.16 C.) as evidenced by a slight discolouration of olivine. Central portions of the sample remain unaffected, however. Again, solid hafnia crystals reveal that hafnium is only partially dissolved into the melt, which may be an effect of slow quenching and re-precipitation. This makes it difficult to differentiate between melt and olivine even in 2D backscatter electron imaging due

to the low contrast between olivine and basalt. Close analysis of textures reveal little evidence for wetting of 2-grain boundaries. There may be a very subtle alignment of melt pockets sub-parallel to the shear direction, but there is no development of clear melt bands. In fact, there appears to be little connectivity, at least from 2D textures.

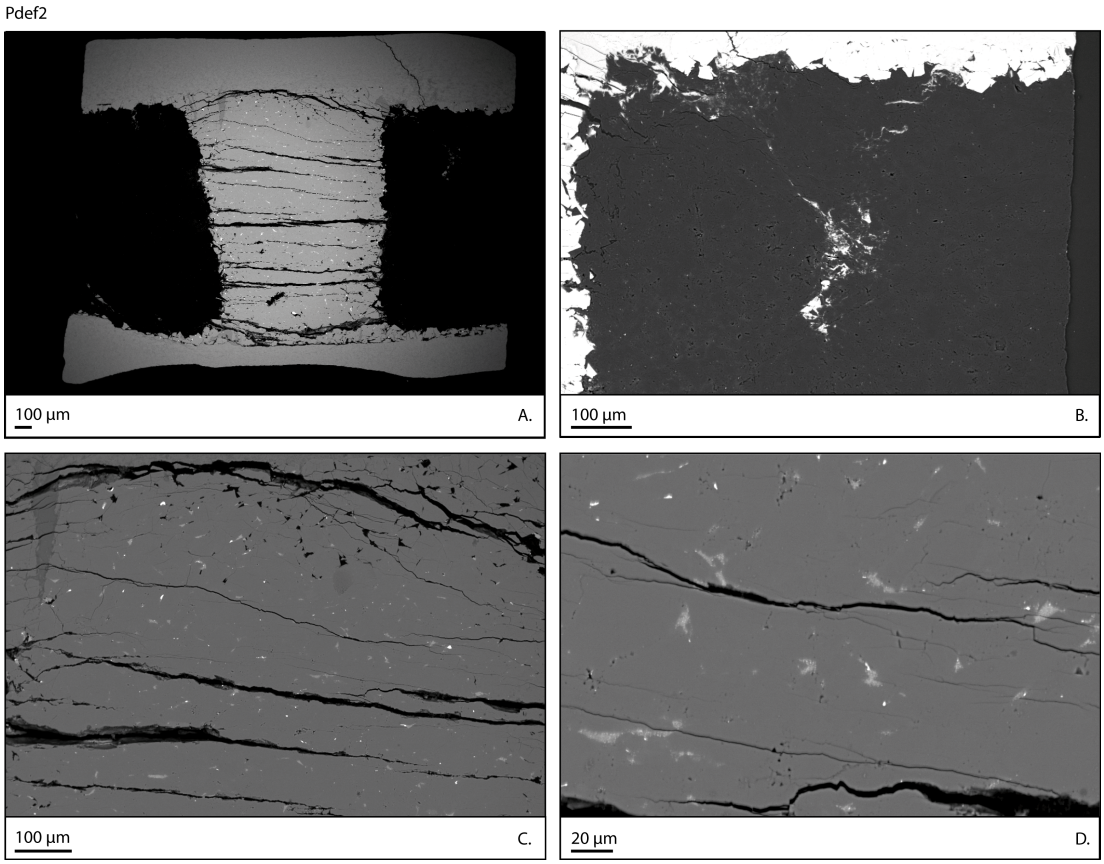

Figure 4.16: BSE imaging of a tangential section of deformed sample Pdef2. A. shows the full sample: Central area is olivine + melt + Hf sample. The surrounding dark area is low density BN capsule. Light grey areas at top and bottom are alumina spacers. B. an example of textures within BN capsule with enhanced contrast. Alumina and olivine on top and left are bright with clipped greyscale. There is clear evidence of mingling of capsule and spacers suggesting melting has taken place, but this does not appear to have affected the sample significantly. C and D show textures within the sample itself, showing low contrast between melt and olivine. Bright white spots are HfO_2 crystals.

Pdef3

Deformed sample Pdef3 contains 15vol%, annealed for 2 hours after which it was deformed at a comparable strain-rate to previous samples to a total strain of 0.9-1.2. Again the capsule is

relatively undamaged allowing reliable analysis of textures. A substantial proportion of Hf is once again present as a separate phase (HfO_2) and not dissolved in the quenched basaltic melt. The presence of undissolved HfO_2 in each deformed sample makes it likely that this is an effect caused by a feature of the rotoPEC equipment. In this sample, there is a marked difference between textures at the centre and edge of the sample, with a significantly reduced melt content close to the capsule edge. This texture may be similar to that observed in OlBaTS3, with a large number of remnant Hf crystals suggesting melt migration may have taken place before Hf crystals were able to dissolve in the melt. These areas are present at the lateral edges of the capsule however, rather than at the top, suggesting melt may have migrated towards the sample centre, as might be expected for torsional deformation experiments (Kohlstedt and Holtzman, 2009). Qualitative observation suggests there may be a very subtle alignment of melt pockets, but again there is no evidence of the formation of melt bands.

Due to experimental limitations we have been limited to examining samples deformed to low strains and at low strain-rates only. In the samples described in detail above, we have not seen significant development of melt bands or even clear alignment of melt pockets to suggest melt has been affected significantly by deformation. This suggests that either: melt is too mobile to create shear bands on a scale observable within the sample i.e. compaction length is too great (Holtzman, Kohlstedt, et al., 2003), or that strain has not been sufficient / over a long enough time-scale to lead to partitioning into melt-rich and melt-poor regions. Previous torsional deformation experiments in basaltic systems have been to very large strains (γ = 1.5-7) (King et al., 2010). If the current design of the rotoPEC is limited to low strain-rate, low strain experiments, it may be that the equipment is not best suited to produce these melt bands.

There are significant differences observed between characteristics of individual melt pockets in deformed samples compared to undeformed, however. Grain boundary wetting is not clearly observed in Pdef2 (1.5vol% melt) or Pdef3 (15vol%), while in areas of equivalent melt fraction in undeformed samples, very fine melt sheets (<1μm) between grain faces are abundant. It may be that in a basaltic system, deformation acts to reduce connectivity by increasing anisotropy of the fabric (i.e. increasing the amount of melt in some boundaries, while pushing melt out of others). An alternative reason for reduced permeability could be the abundance of solid crystals within the 'melt' phase. Permeability of the melt system has been reduced in previous studies by the addition of solid chromite (Holtzman, Kohlstedt, et al., 2003), and the hafnia crystals, if they were in the melt during deformation, may have a similar effect. Further 3D analysis is required to constrain these differences further and test whether fabric is completely disconnected, or has a marked permeability anisotropy.

It is clear that the complexity of processes within all samples produced may preclude their use to constrain real Earth processes. A large number of further experiments would be required to create a reliable dataset of deformed and control samples, which is beyond the scope of this study. However, the potential for 3D visualisation of melts using a doping technique can still

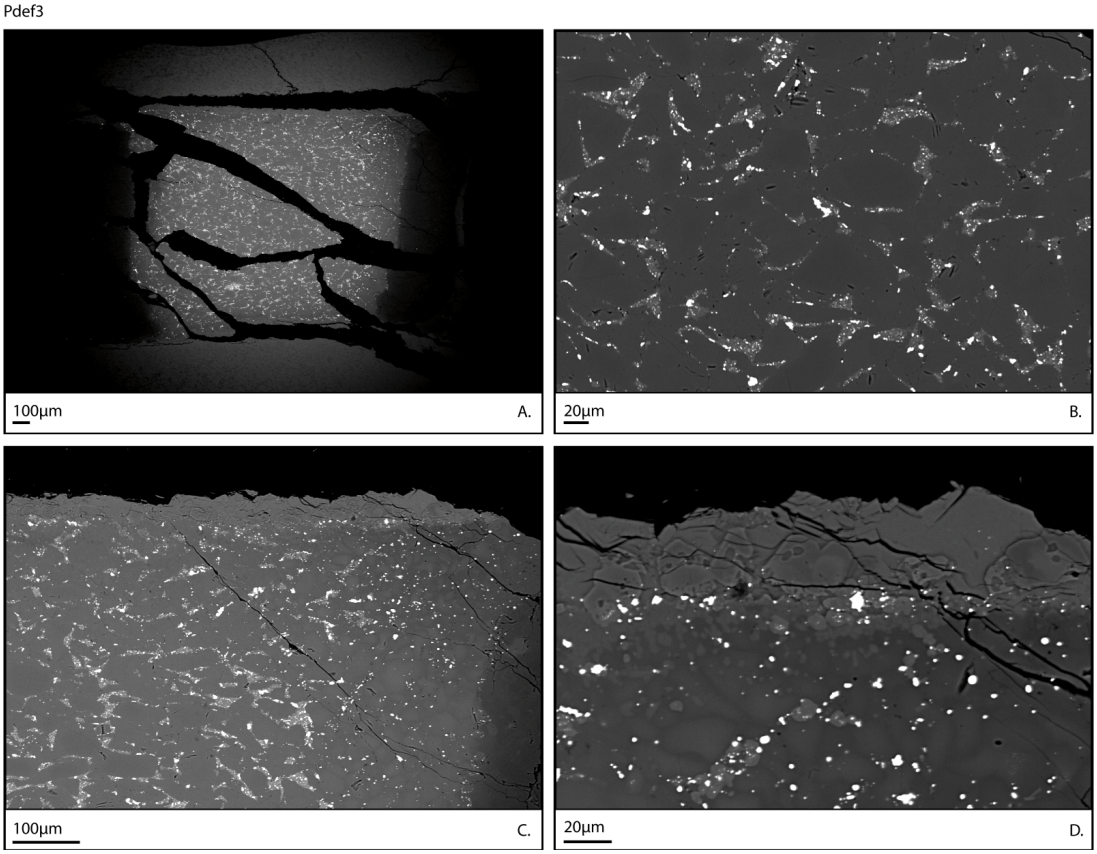

Figure 4.17: BSE imaging of a tangential section of deformed sample Pdef3. Dark grey = capsule, mid-grey = olivine, light grey = basaltic melt, white = HfO_2 crystals. A. shows the full sample including surrounding capsule and spacers. B - D are high magnification areas of interest. The right edge of C. and image D. both show the change in texture observed at the sample edge with a reduced melt content and a large number of HfO_2 crystals. This is similar to the 'drained' melt area observed in TS3 suggesting melt migrated away from the sample edge. See text for details. However, the mottled appearance of olivine and lack of a clear boundary between the sample and capsule observed in D. also suggest a reaction may have taken place affecting the sample edge, therefore differences in texture are not simply due to melt migration.

be fully evaluated using these samples, and will be described in the following section.

4.4.3 Tomographic visibility

The experimental samples described above in two dimensions have all been scanned using in-house CT equipment to attempt segmentation of the melt and crystal phases. The success of segmentation depends on individual sample characteristics. In figure **??** I have carried out a qualitative comparison between the segmentation of phases possible with the 2D backscatter electron image, compared to an equivalent CT slice through the 3D dataset. In each case the CT scan and the BSE image have been filtered using non-local means filtering and segmented using a semi-manual technique combining global thresholding and manual correction. Generally, samples where Hf has separated significantly from the melt are more difficult to segment, not only because the melt itself is less concentrated in Hf, but also because the bright HfO_2 crystals can cause streak artefacts and shadowing. An additional characteristic to improve segmentation is the olivine grain size. An example of a close-up section of OlBaTS1, with a small and variable grain size, is shown in Figure 4.20, both from a high magnification BSE image and from 'zooming in' to an equivalent slice in the CT scan. The area in the red rectangle is thought to represent the same feature in both slices. In the CT slice, a large number of fine olivine grains appear to be missed in the segmentation and the complexity of the melt network between these grains is lost. In contrast, melt is easily separated from olivine grains in a sample such as OlBaVS1, where a large grain size combined with a large melt fraction leads to larger features that are easier to pick out by eye and more easily segmented by automated methods. The best CT reconstructions are therefore produced from undeformed samples, with large melt fractions, that have been annealed for long time periods. This evaluation of segmentation quality highlights the limitation of comparing scan quality using voxel size or resolution alone (see section 2.3.4). Many other factors limit the ability to segment these datasets, making comparison between scans, even if they are of similar resolution, limited in these circumstances.

There follow a series of images showing successful segmentation of undeformed samples. In each case a large sample volume was segmented using an automated watershed segmentation to show general melt distribution across the samples. Although these segmentations are on too large a scale to complete full manual correction, the quality of CT scans ensures a reasonably reliable segmentation, although in the case of small melt fractions (OlBaVS3 and VS4), some fine melt sheets may have been missed in this coarser segmentation. A further sub-volume of each sample was selected to best reflect a volume of sample unaffected by large-scale olivine melting, to show the potential of such segmentation for analysis of basaltic melt networks in a crystalline silicate matrix. Although automated methods were used for initial segmentation, manual correction was carried out on each slice individually to ensure an accurate representation of the melt geometry. As shown in Figure **??**, the segmentation of these undeformed samples is reasonably reliable, and could potentially be used for quantitative

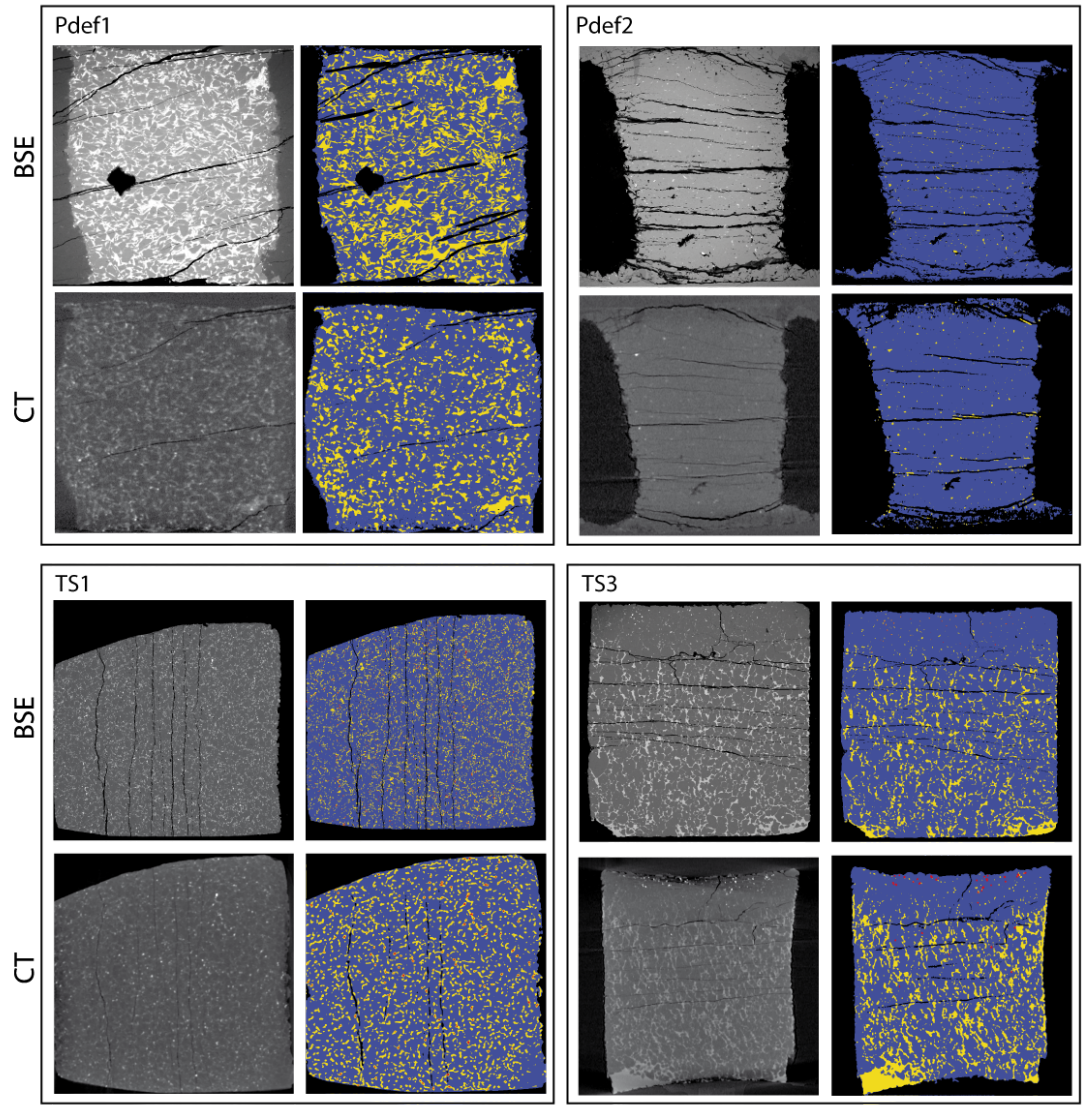

Figure 4.18: Comparison of resolution and sharpness of 2D BSE slices vs. equivalent CT slices of deformed and undeformed samples. In each case, the CT slice was chosen to be as close as possible to the cut section imaged in two dimensions. Orthogonal slices (all but slices VS3 and VS4) were selected using ImageJ ortho-views feature, allowing stacks to be viewed on z-x and z-y planes. Each image is paired with an image showing the best segmentation possible of the same slice, as carried out on Avizo Fire ^{TM} using 'edit new label' tool kit by a combination of global thresholding, tophat segmentation, and manual correction using the paint brush tool. In each case the colour key is as follows: blue = olivine, yellow = basaltic melt, red = HfO_2 crystals.

comparisons of connectivity and melt geometry.

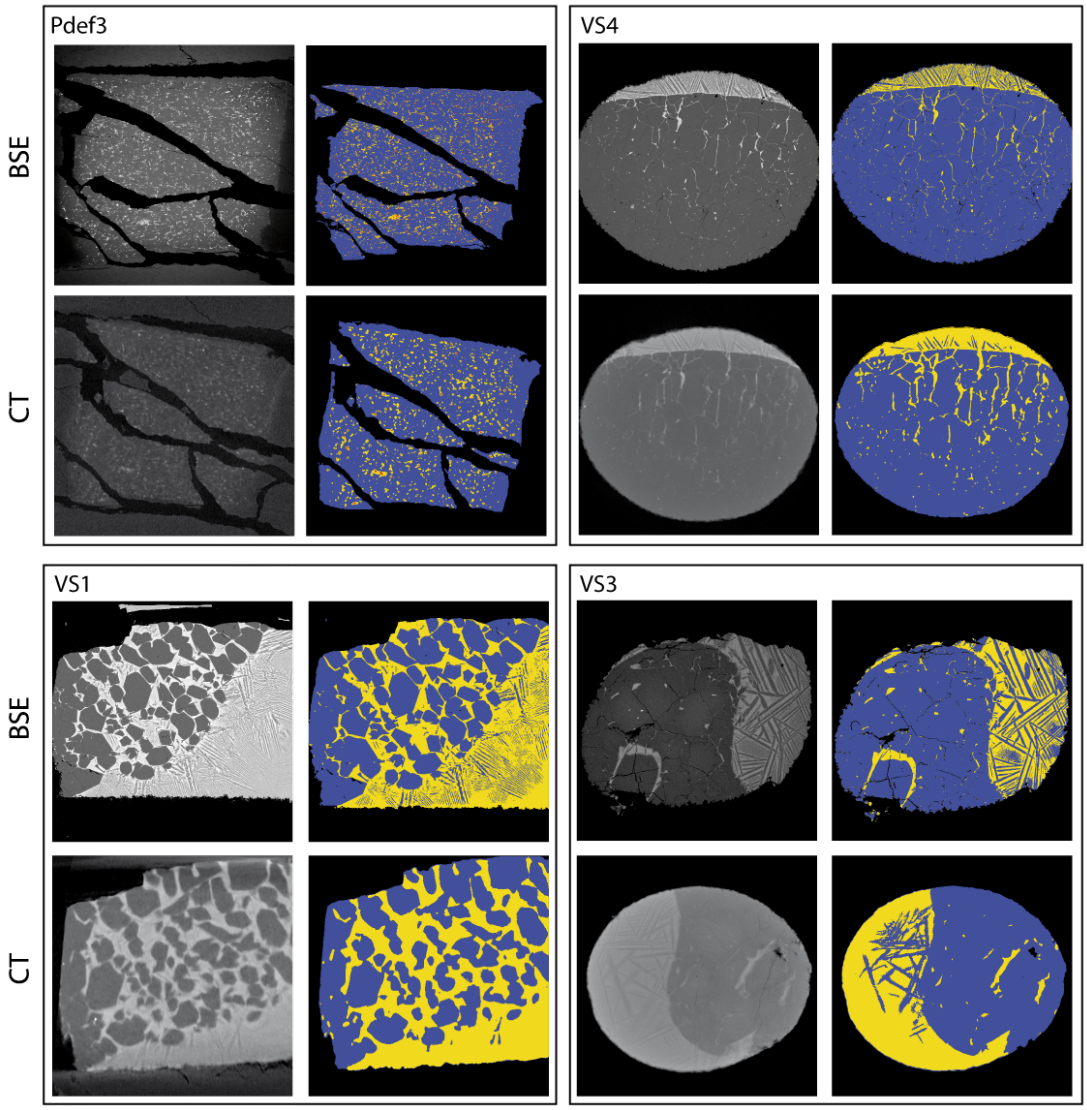

Figure 4.19: BSE vs. CT slice comparisons continued. See previous image for caption

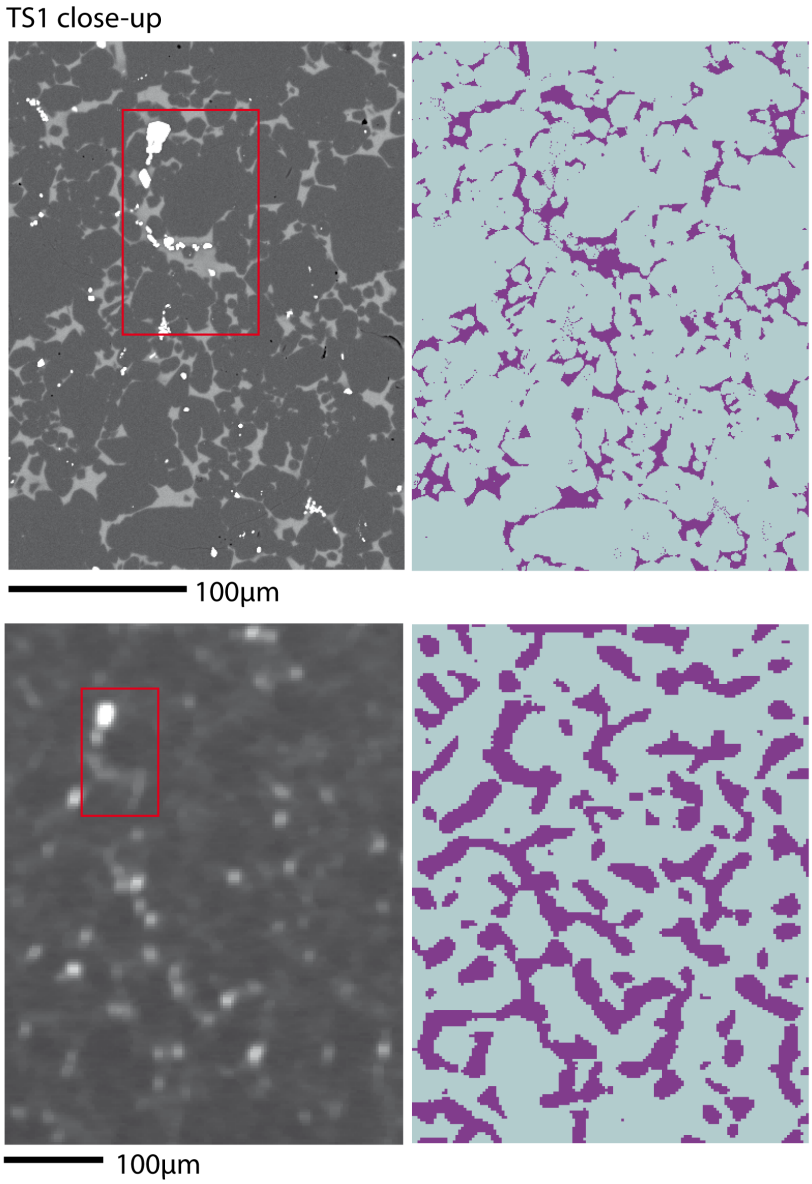

Figure 4.20: An example of segmentation of a small high-magnification area of sample TS1 of BSE image (Top) and roughly equivalent CT slice (bottom) with respective segmentations on the right. Although the CT slice is in fact at a smaller scale than the BSE image, the segmentation suggests larger features as the presence of small olivine grains within melt-rich areas is not at all visible in the poor quality CT scans. The difficulty is caused by a) lower resolution, b) the lack of dissolution of Hf crystals into the melt reducing contrast between melt and olivine and c) the small grain size of olivine crystals creating features that are too small to be imaged using CT scans. Therefore data collected from CT scans such as these are of limited value unless resolution can be improved significantly.

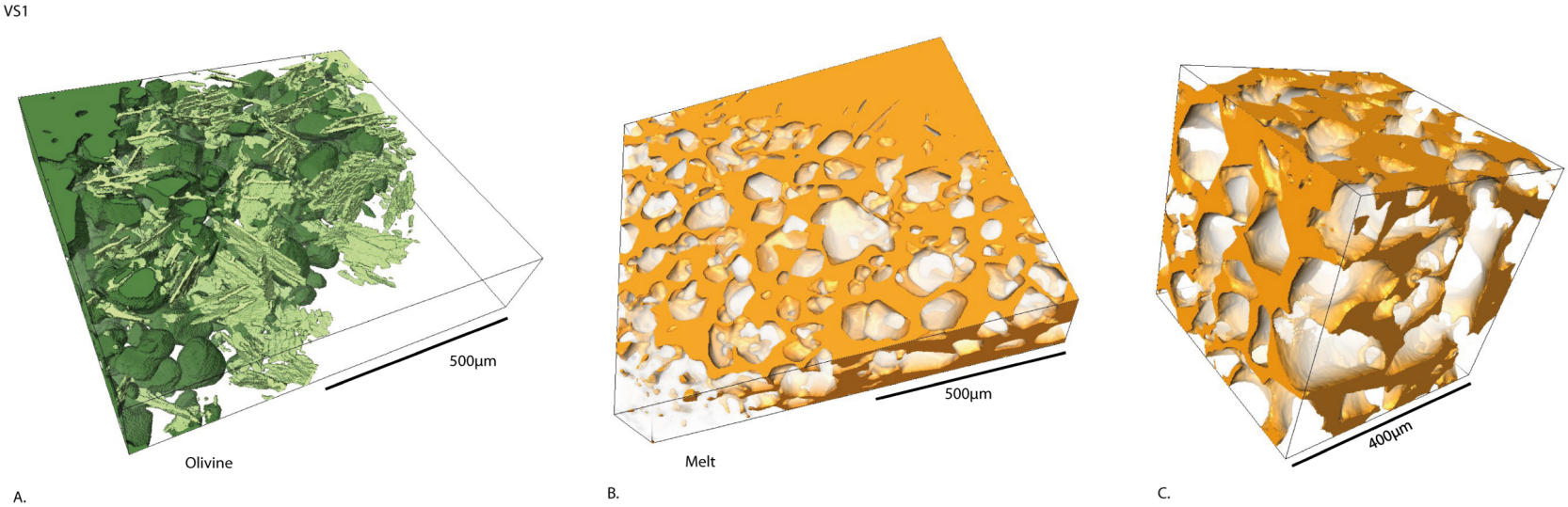

Figure 4.21: 3D reconstructions of melt from sample OlBaVS1: A. a large scale reconstruction of olivine crystals including skeletal quench crystals (light green) using automatic watershed segmentation combined with additional manual correction. The large size of features in this volume make manual correction across a larger sub-volume feasible. It is possible to see how individual sheets of crystals have nucleated on existing crystals and grown in branching sheets from them, although detailed structure of skeletal crystals is not resolved. B. The melt phase of the same reconstructed volume in A, showing a gradient of melt fraction increasing from the bottom left to the top right corner of the sub-volume. C. A smaller sub-volume segmented from the central portion of the sample showing melt network geometry in an area relatively unaffected by large scale melting. Melt has a sharp boundary with faceted crystal edges. Needle-like overgrowths appear on some crystal edges, observed in BSE imaging as initiation of skeletal crystal growth, presumably during quench (Figure 4.11 C). Very fine quench crystals observed in BSE imaging are not segmentable from CT scans.

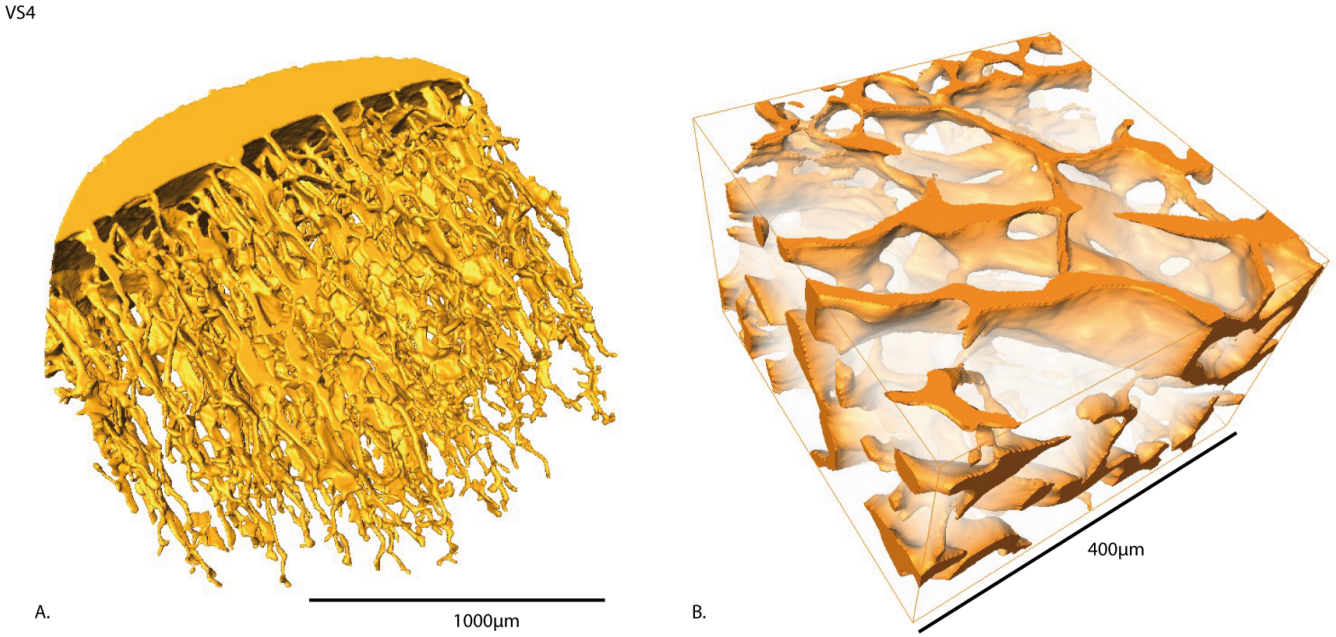

Figure 4.22: 3D reconstructions of melt from samples VS4 with initial basalt content of 5vol%. A. Full volume segmentation using automatic watershed segmentation. This full segmentation has missed finer melt networks within the low melt volume areas, but shows overall melt distribution including the clear gradient in melt fraction, and presence of parallel melt-rich fractures perpendicular to the melt rich zone, suggesting significant lateral melt migration was taking place. B. shows a smaller sub-volume with further manual correction to improve the segmentation. The volume is chosen to be relatively central and unaffected by cracking, to allow best characterisation of the true basaltic melt network. However, the anisotropy of the melt network is evident from the thickness of melt sheets aligned left to right, compared to the thickness of those aligned top to bottom. The large melt pocket is positioned to the right of the volume as oriented here.

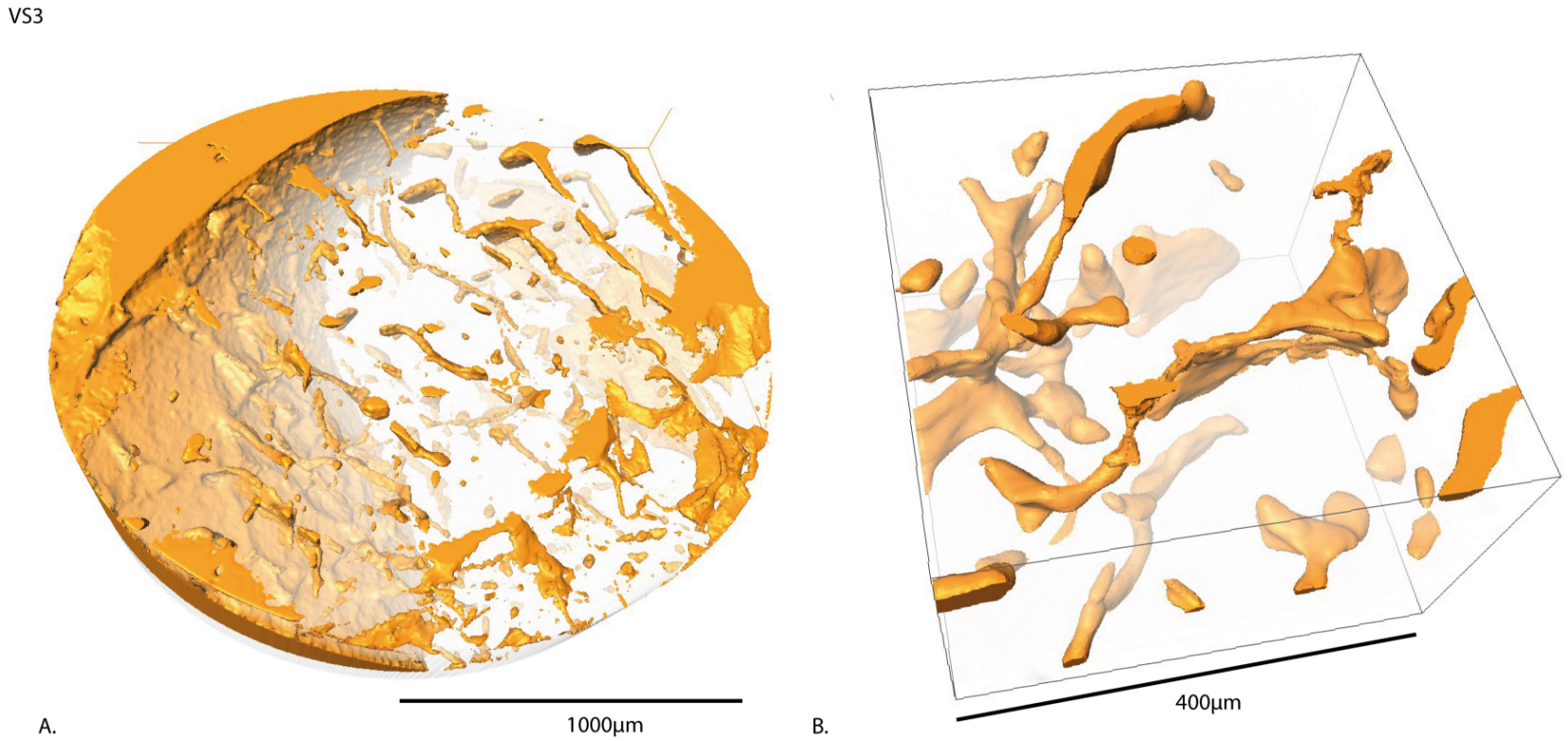

Figure 4.23: 3D reconstructions of melt from sample OlBaVS3 with initial basalt content of 1.5vol%. A. represents a full volume automated segmentation and B. a smaller sub-volume improved by manual correction. The full volume shows the significant amount of melting undergone by olivine within the sample. Only the central area is relatively unaffected by olivine melting, with melt accumulations picking out grain triple junction tubules between olivine grains (transparent). The anisotropy of the system is clear, with tubules preferentially perpendicular to the melt rich zone on the left. Exact geometry of melt is better picked out by manual segmentation (B.). Some wetting of 2-grain boundaries is observed, although the majority of melt is still in grain boundary tubules. It is possible that melt is missed even in manual segmentation, as a 2µm voxel size will not be sufficient to resolve sub-micron sheets of melt between 2-grain boundaries.

Comparison of undeformed basalt across volumes

Samples which have annealed for long time periods at high temperature, and have undergone rapid quench, have been segmented successfully giving a series of reliably segmented melt networks at varying melt fractions for comparison. In figure 4.24 cubic sub-volumes of basaltic melt at increasing melt fraction are shown. In the corresponding figure 4.25, skeletonisation analyses are shown of each cubic sub-volume to compare interconnectivity of the melt at varying melt fractions. This was carried out using the skeletonisation algorithms of Avizo, and analysed using the Scobacleaner software, as described in section 2.3.5.

Changes in connectivity can be observed across the volumes, although there is no clear correlation between melt connectivity and melt fraction. The lowest melt fraction here may include melt sheets that are too small to be easily segmented from a CT scan with an estimated spatial resolution of 2.5-3μm, or whether there are actually fewer wetted grain boundaries. The Scobaclean software also has problems identifying true connectivity of melt sheets and large melt volumes as described in S.O.M. of Miller et al. (2014), which may explain the lower mean connectivity of the high melt fraction sample.

Given the inhomogeneity of the remaining sample, and clear evidence for melt migration, results from this analysis do not reflect the characteristics of a melt network at textural equilibrium, therefore these results are not necessarily comparable to those of previous studies (Miller et al., 2014; Zhu et al., 2011), where basalt melt was left to equilibrate for >132 hours without evidence of significant melt migration. I would be hesitant to apply our preliminary results directly to terrestrial processes. However, the doping methodology used could be used in future for a detailed characterisation of realistic basaltic melt networks.

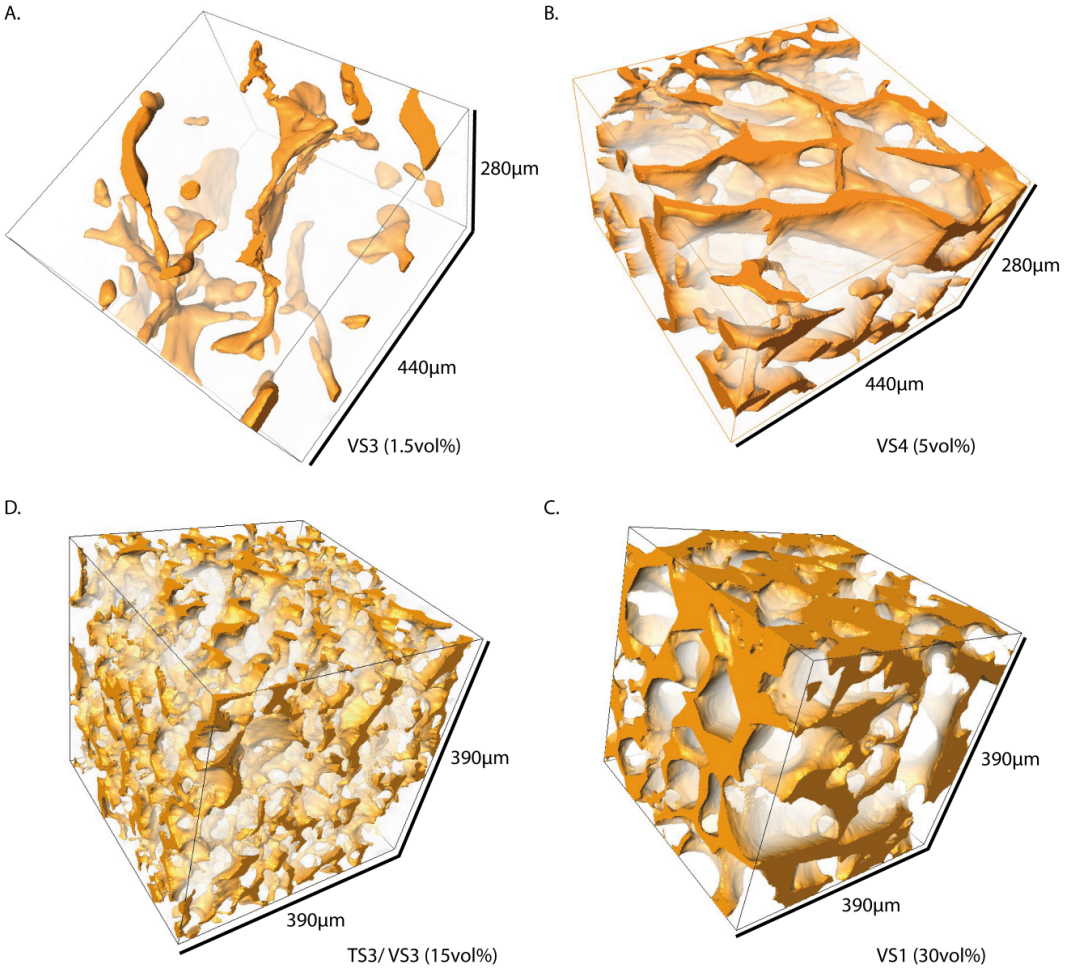

Figure 4.24: 3D reconstructions of melt from samples VS3, TS3, VS3 and VS4 as a series of changing basaltic melt volumes. All samples have a relatively large grain size and sharp CT scans mean melt can be segmented relatively reliably. Segmentations were carried out by a combination of watershed segmentation followed by manual correction of slices.

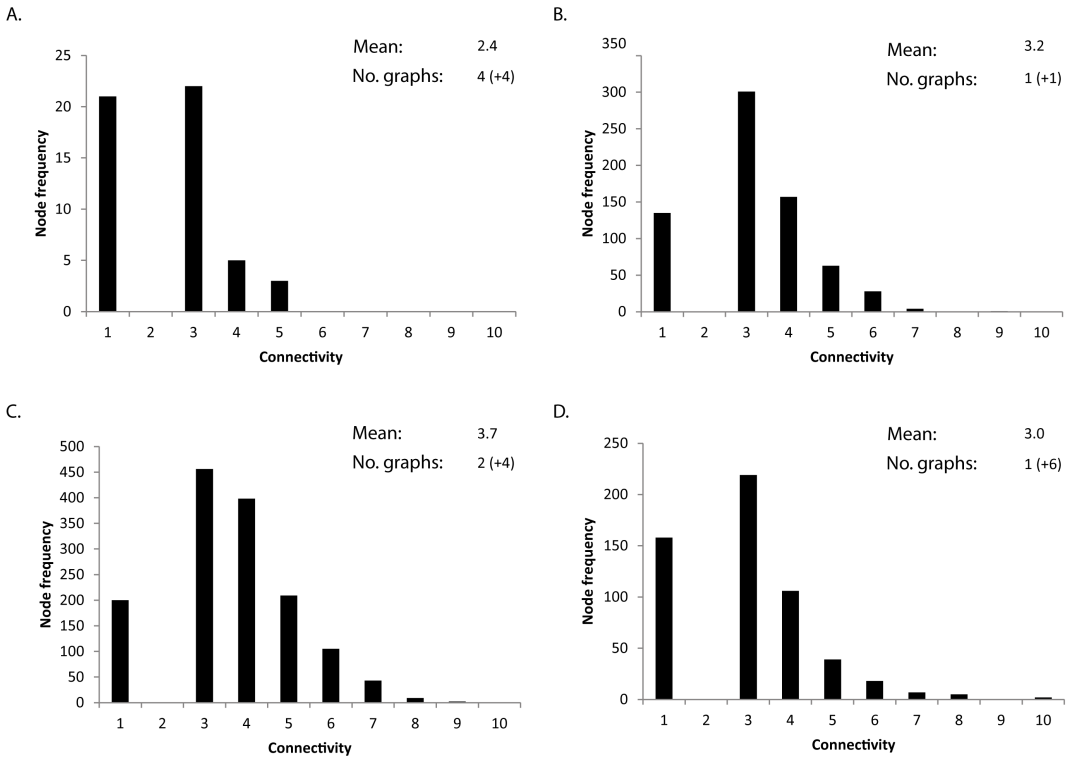

Figure 4.25: Skeletonisation data from the above 3D reconstructions of melt with changing melt volume. Skeletons were created using Avizo Fire skeletonisation data and analysed using Scobacleaner software as described in section 2.3.5. No. of graphs were taken from skeleton statistics information attainable from Avizo, given as the number of graphs containing 2 or more segments, with no. of single-segment graphs given in brackets. In each case minimum length threshold was 10 voxels.

Comparison of basalt with changing anneal time

Segmentations of the melt phase are shown in figure 4.26, from sample OlBaPCTS1, which has been annealed for 2 hours, compared to OlBaPCTS3, annealed for 48 hours. In this case segmentation has been carried out using simple global thresholding, which includes some error caused mainly by partial volume effects on the olivine crystal - melt boundary. Therefore a minimum and maximum boundary of melt has been shown in each case. The % of total sample volume which is represented by the melt phase is given in each case - the possible range of total melt is larger in experiment TS1 because of the greater error segmenting melt that is segregated from HfO_2 crystals (see Figure **??**). The increased grain size of the olivine over greater anneal time is evident from the larger gap between grains, although it has proven difficult to separate olivine grains effectively to conduct 3D grain size analysis, particularly in TS1, where 2D analysis shows that melt does not wet all grain boundaries - and dry boundaries are almost impossible to pick out on CT slices. Essentially, 3D images of TS1 and TS3 are not able to show the subtle differences in texture observed in 2D imaging. An advantage of phase contrast imaging over doping is that these boundaries can still be seen, therefore making grain size analysis in 3D more feasible.

Comparison of deformed vs. undeformed basalt

As evident from figure **??** the segmentation of deformed samples is significantly less successful than in the previously described undeformed samples. This is partly due to the presence of HfO_2 crystals, and reduced hafnium content in basaltic melt, as described previously. Another factor is the variable grain size, in this case presumably caused by dynamic recrystallisation of olivine along grain boundaries. This is particularly evident in Pdef1 (see EBSD analysis in the following section) and complicates the features within the sample, making them more complex to segment.

Figure 4.27 shows the reconstructions of Pdef1-3, with an orthogonal cut through the experimental gasket from low resolution CT scans (A.), and a qualitative volume rendering of the sample volume from higher resolution scans (B.). C shows a sub-volume of interest reconstructed using semi-automated thresholding of the highest resolution scans (see table 4.3), with D. showing the equivalent analysis of melt network topology. There are no evident 3D fabrics, although potentially there is some alignment of the melt in Pdef1 and Pdef2 sub-horizontally, but any alignment is very subtle. Average connectivities are shown to be generally lower than in undeformed samples, potentially reflecting a more anisotropic melt fabric. In each case, the minimum connectivity has been used as for the undeformed samples, to allow the best possible comparison. However, as shown in analysis of Pdef 1, figure 4.28, using different thresholding techniques creates different melt geometries and therefore different connectivities, suggesting these results are not very reliable, limiting constraints on melt geometry in this case.

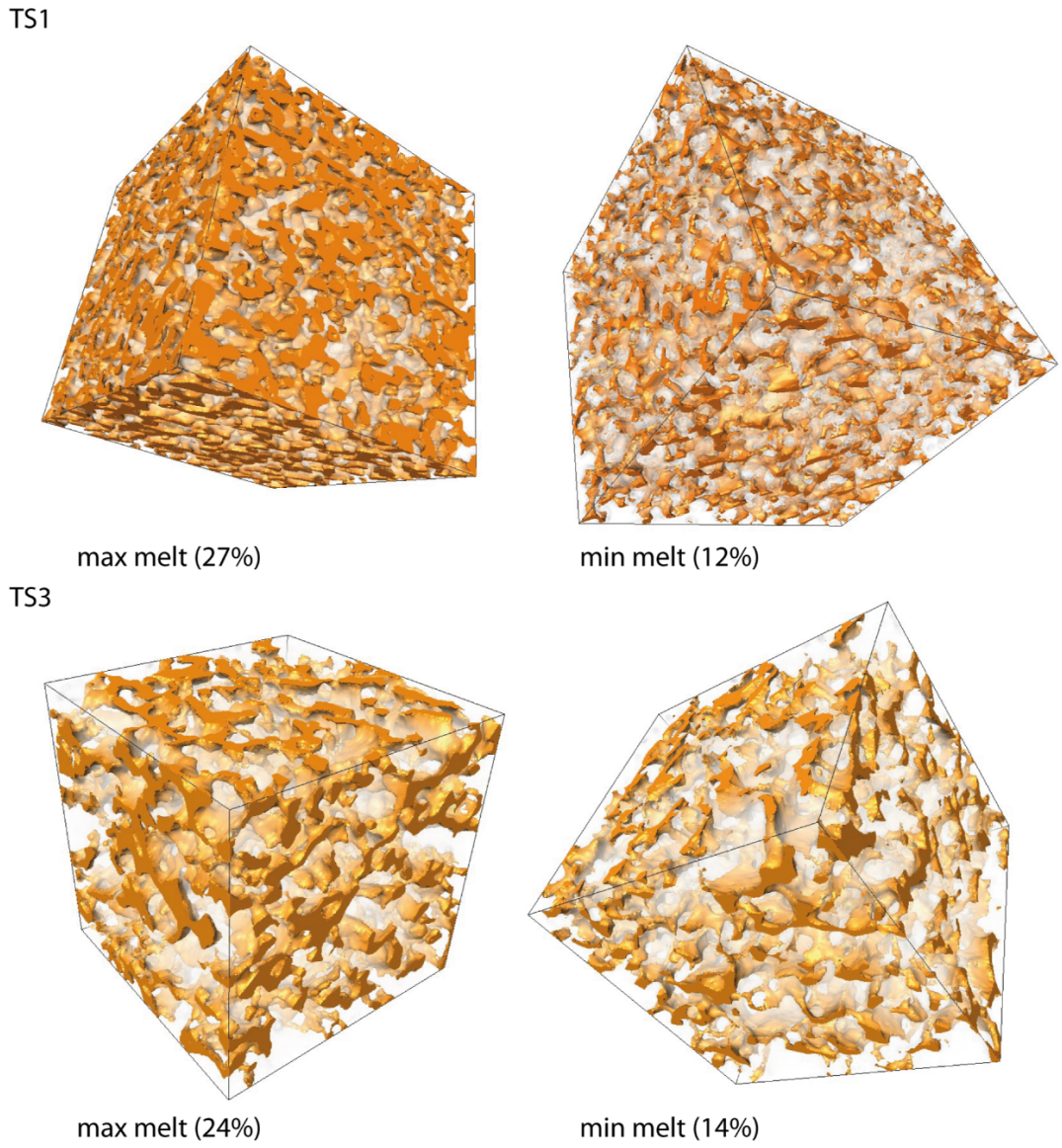

Figure 4.26: 3D reconstructions of melt from samples TS1, annealed for 2 hours, vs. TS3, annealed for 48 hours. Two segmentations have been carried out for each sample, for a minimum (left) and maximum (right) estimate of melt volume. The errors of segmentation are large for both samples, but the error is reduced in TS3, which has larger grain sizes from increased annealing. As previously described, segmentation of TS1 does not show fine features such as melt between smallest olivine grains. In each case the vertex length of the field of view is 390µm.

The dissolution of Hf in basalt needs to be improved in deformation experiments to allow full 3D characterisation of textures. Due to the finer features developed in these recrystallised samples, nano-tomographic imaging could be used to visualise these melt networks fully.

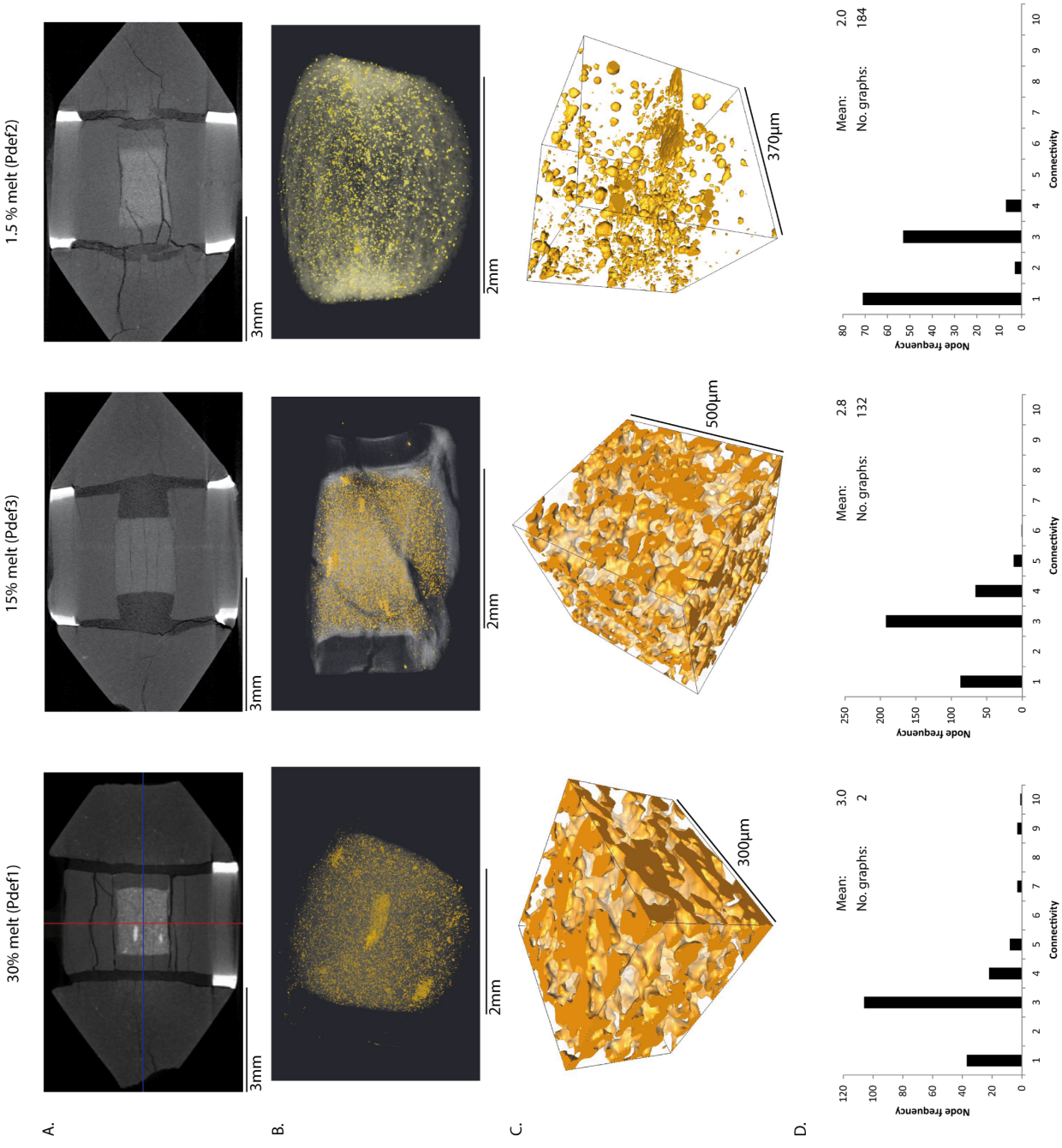

Caption on next page

Figure 4.27:

Figure 4.27 ***(preceding page)*****:** 3D reconstructions of deformed samples Pdef 1, 2, and 3 representing deformation of 40-100 degrees of basaltic melt volumes from 30 vol% down to 1.5 vol%. A. shows example orthogonal sections from low resolution full-gasket scans. B. shows a reconstruction of the full sample volume from the high-resolution slices, using simple global thresholding for 3D visualisation. C. shows small sub-volumes that have been segmented using a combination of thresholding techniques. D. shows the connectivity of 128x128x128 voxel sub-sections of these samples.

4.4.4 Comparison of olivine structures using EBSD

EBSD analysis has been carried out on a number of deformed and undeformed samples to compare olivine grain size, shape and crystallographic preferred orientation across experiments. This can give further insight into processes affecting the samples, and the effect of melt presence on olivine crystal orientation and deformation.

Results of each analysis are given in figures 4.29-4.34. In each case, a map showing the band contrast (i.e. signal quality) is shown overlain with euler colours indicating crystal orientation (similar colours indicate similar orientation). Additional maps are shown to highlight grain characteristics, including a map of grain boundaries overlain onto band contrast, and a local mis-orientation map showing local variations in orientation, thereby highlighting sub-grain development in olivine crystals (see section 2.4.4). Pole figures, showing orientation of the three main olivine axes within 3D space, and inverse pole figures, showing any alignment of those axes to the external reference axes X, Y and Z, are given of different data subsets, as described in the figure captions. Two additional figures, 4.35 and 4.36, show internal deformation within single olivine grains in undeformed and deformed samples.

'Undeformed' samples

OlBaPCTS1 Figure 4.29 shows EBSD analysis of sample OlBaPCTS1, reflecting the texture after a relatively short 2 hour anneal. The short anneal time of this sample means the olivine grain size is probably close to that of the initial starting mix grain size. Grain size is variable, but not bimodal. There is no clear fabric or sorting of grain sizes, the sample is homogeneous across the sample (only a small sub-area of the sample was chosen for EBSD analysis due to the homogeneous sample texture). The crystallographic orientation appears random, as expected in an undeformed sample. Interestingly, the grain boundary and local mis-orientation maps show that large olivine grains have more internal sub-grain boundaries compared to those in longer annealed samples. Figure 4.35 shows examples of grains showing various stages of internal deformation within each sample. The initial subgrains in shortly annealed samples may reflect damage to grains caused by the grinding process that may have healed by recrystallisation in samples annealed for longer time periods.

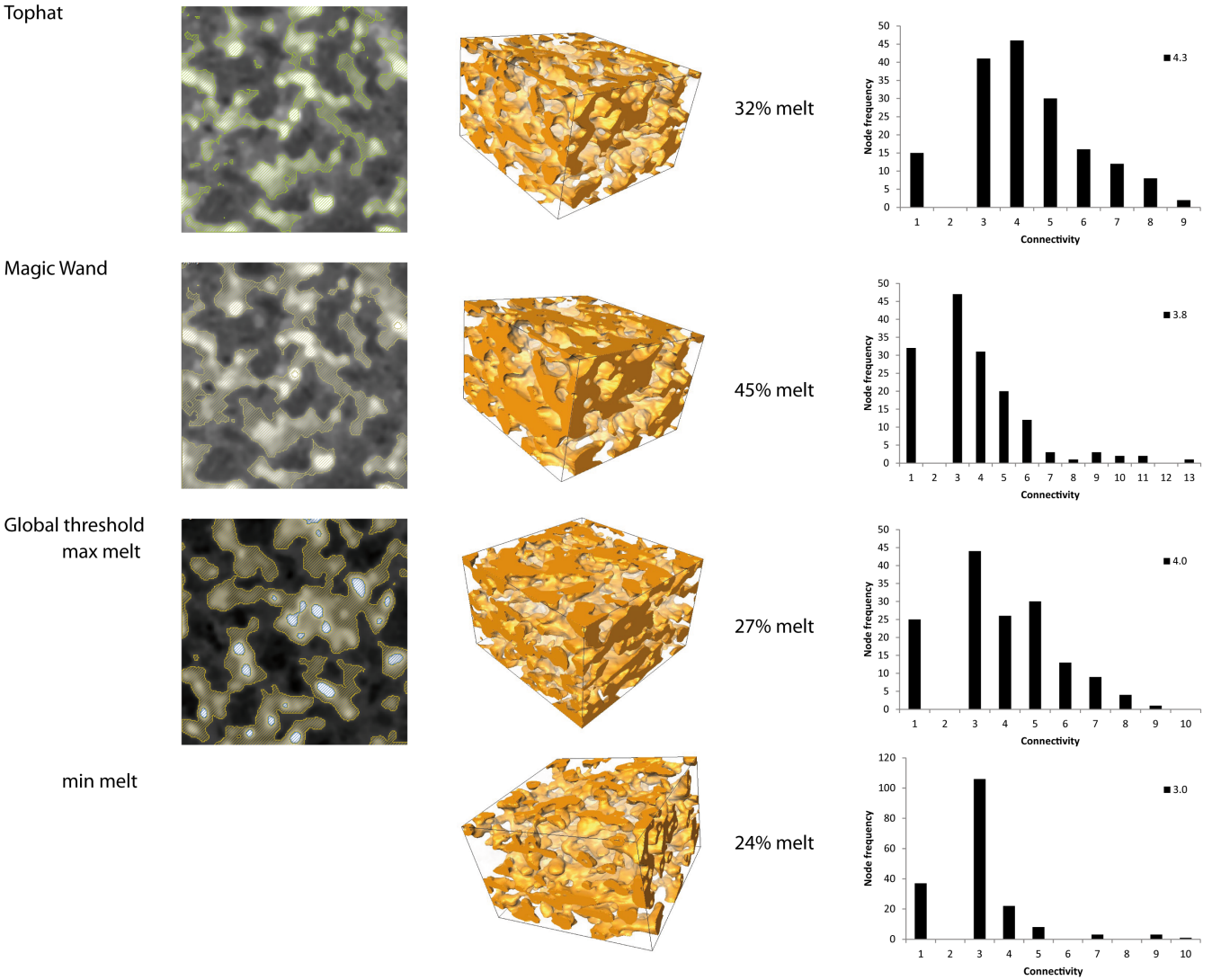

Figure 4.28:

Caption on next page

Figure 4.28 ***(preceding page)*:** Evaluation of segmentation accuracy on deformed sample Pdef1. Three different automatic thresholding techniques were used to segment the same 200x200x128 voxel subvolume. A: An example 200x200voxel CT slice (field of view = 390μm) with hatched overlay representing areas segmented as melt and hafnia. B: Reconstructed sub-volume, with melt shown in orange and olivine /HfO_2 transparent, with %total sub-volume segmented as melt, and calculated connectivity of the segmented subvolume. Melt geometry and connectivity are affected significantly by the segmentation method used, therefore results from this analysis for deformed samples are not reliable.

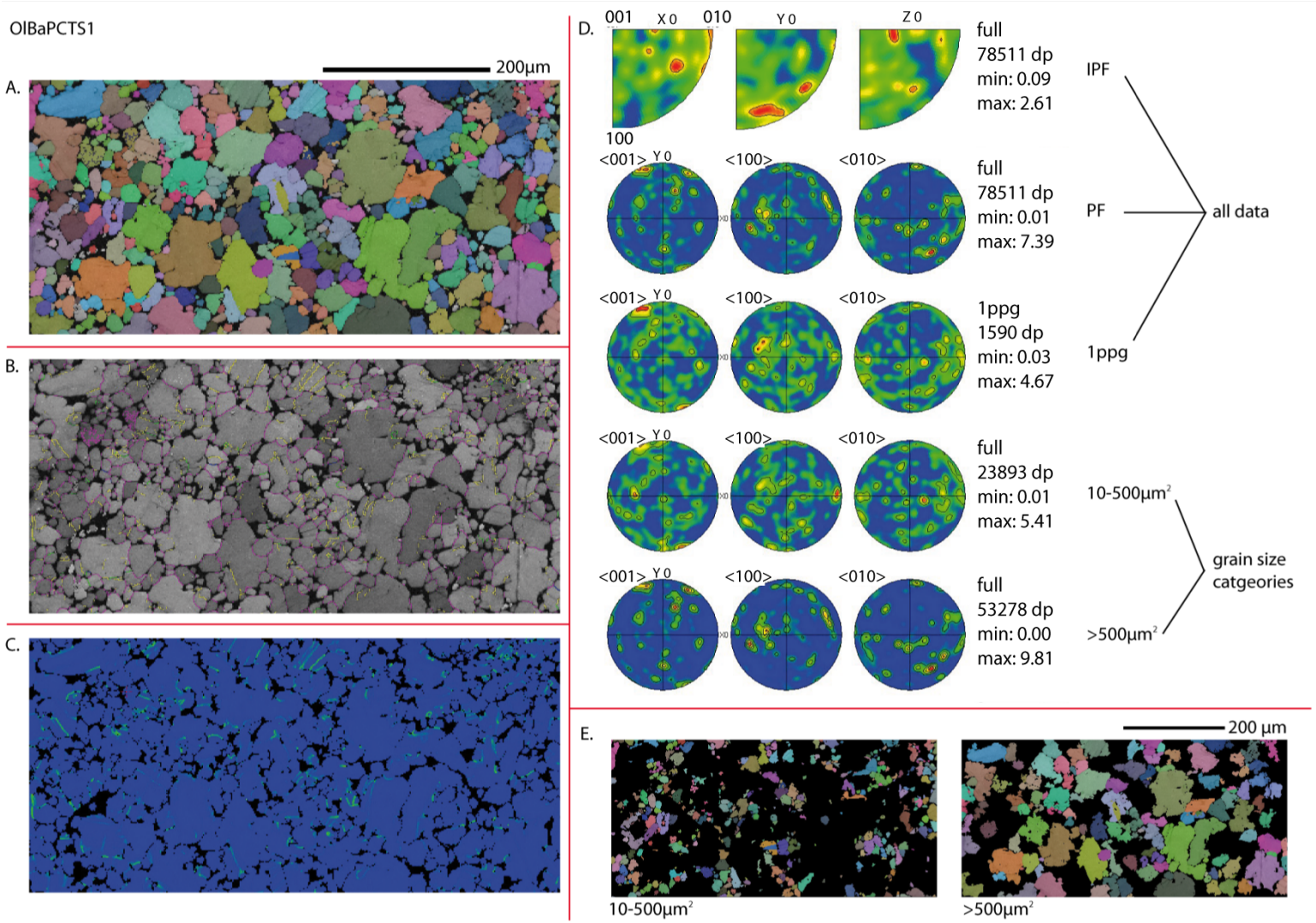

Figure 4.29:

Caption on next page

Figure 4.29 ***(preceding page)*:** EBSD analysis summary of sample OlBaPCTS1, with an initial melt fraction of 15 vol%, annealed for 2 hours under hydrostatic P-T conditions. A. All Euler map of crystal orientations. B. Band contrast map with overlying grain boundaries with colour key as follows: Fuchsia >20 % orientation difference, purple >15%, blue >10%, lime green >5%, and yellow >2% orientation difference. C. local mis-orientation map showing local deviation from the average crystal orientation and therefore highlighting internal deformation of crystals. Green areas indicate higher local mis-orientation = sub-grain boundaries. D. An inverse pole figure, showing the alignment of crystallographic axes with the external reference directions X, Y and Z respectively, and a series of pole figures showing the orientation of major crystallographic axes in 3D space, showing alignment of i) full data set, ii)1 data point per grain, iii) data from small grains only, iv) from large grains only. E. 'All Euler' map (as in A.) showing i) small grains, and ii) large grains only. In pole figs, min and max refers to exp. densities (mud).

OlBaPCTS3 The longer anneal time of this sample is reflected in the increased grain size of olivines, as shown in Figure 4.30. Grain size is generally larger, although some small grains remain suggesting development of a bimodal grain size by a process of Oswald ripening (Karato, 2008). As described previously from Backscatter imaging, there is a clear gradient in melt fraction from one side of the sample to the other (NB. the sample here is flipped so that the 'top' of the slice shown in figure 4.9 is now on the right hand edge of the EBSD map). The texture generally shows recrystallisation of olivines towards an equilibrium fabric. The relatively 'dry' area of melt on the right side is shown by the lack of gaps between olivine crystals and a neater triple junction fabric within the olivines. There are fewer sub-grains within olivine crystals than seen in TS1, suggesting grains may have undergone healing from damage caused by crushing. Where sub-grains are present, their shape is more equant suggesting recrystallisation has taken place (Figure 4.35).

There is evidence for crystallographic preferred orientation developed in the olivines, with 100 crystallographic axes aligning in a girdle parallel to the Y axis. The orientation of <001> axes appears almost random, while there is a subtle (X) alignment of <010> axes. As the sample is rotated 90°, this means the the crystallographic long axes, <100>, are aligned with the direction of compression. It is possible that this is a result of initial compaction of the sample, but in that case we may expect to see this alignment in other undeformed samples. Inferred melt migration direction within the sample is horizontal, therefore perpendicular to <100> and parallel to <010>. Melt flow is known to create a shape preferred orientation in elongate crystals (Vernon, 2000), however to create such an alignment requires crystals to be able to rotate as flow occurs, which seems unlikely at low melt fractions and high confining pressures. It is hard to draw firm conclusions when it is unclear what gradient caused the initial melt migration.

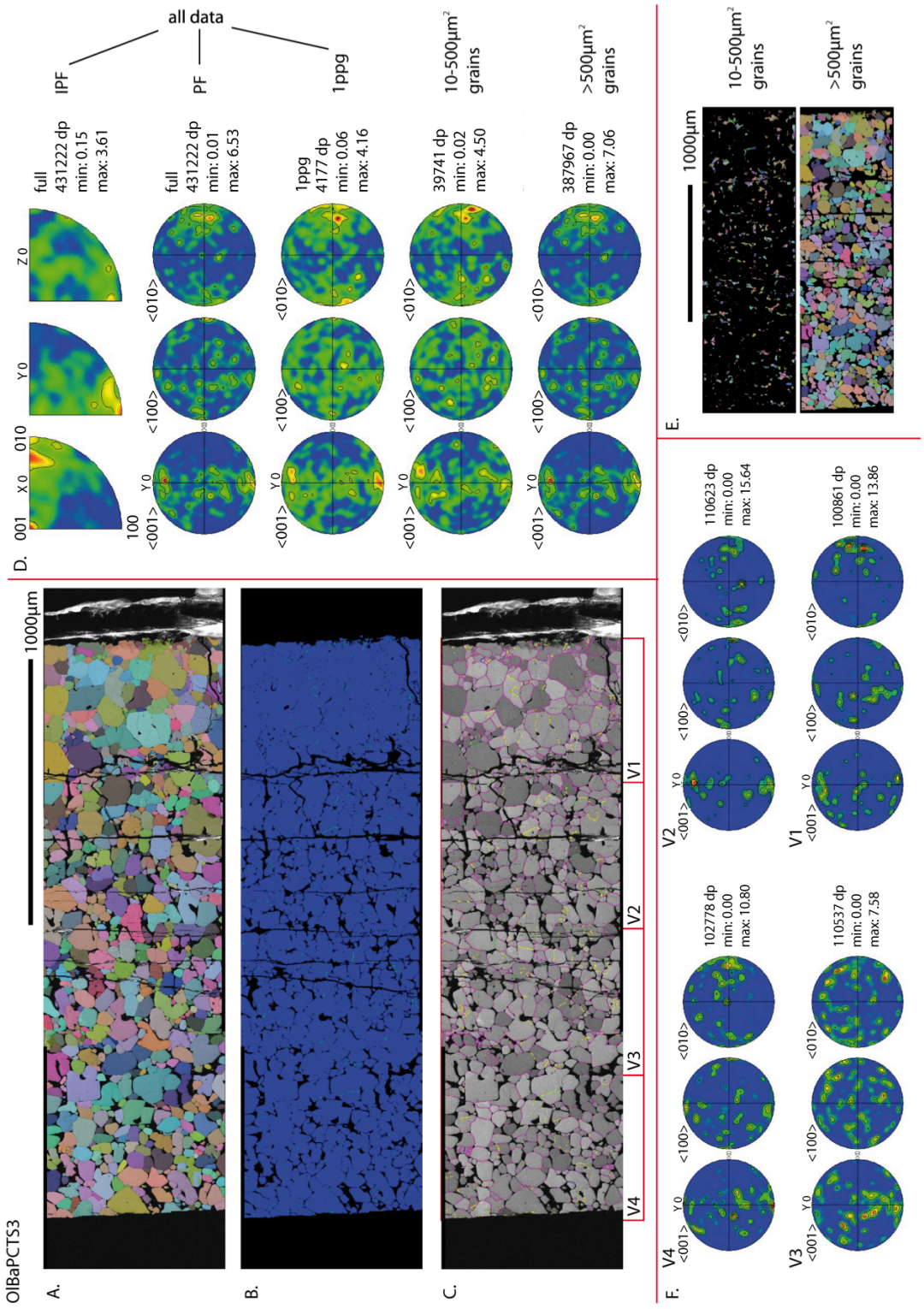

Figure 4.30: EBSD analysis summary of sample OlBaPCTS3, with an initial melt fraction of 15 vol%, annealed for 48 hours under hydrostatic P-T conditions. See Figure 4.29 for key to image sections.

OlBaPCVS4

Sample VS4 has a very large grain size reflecting the extra anneal time of the sample of 69 hours. The shape of olivine grains is close to equilibrium texture, with a large number of triple junctions. There are very few sub-grains developed, compared to less annealed samples, although some crystals do show some minor sub-grains. The reduction in the number of sub-grains from the least to most annealed samples reflects the recrystallisation process leading to large undeformed sub-grains. An example of a hydraulic fracture is seen in the mapped area (Figure 4.31), cutting through a central large olivine crystal. Olivine crystal structure appears unaffected by this fracturing, suggesting it is an entirely brittle process. In addition, the EBSD map also shows clearly how quench crystals have grown in the zone of partial olivine melt during quench. Crystals nucleate from a point on an existing solid olivine grain, then grow outward in the same crystal orientation. Internal mis-orientation mapping shows a subtle change in crystal orientation with growth away from the initial nucleation (Figure 4.35). There is little evidence of any CPO development within this sample, although the large crystal size compared to the map area means sample size is too small to say this conclusively.

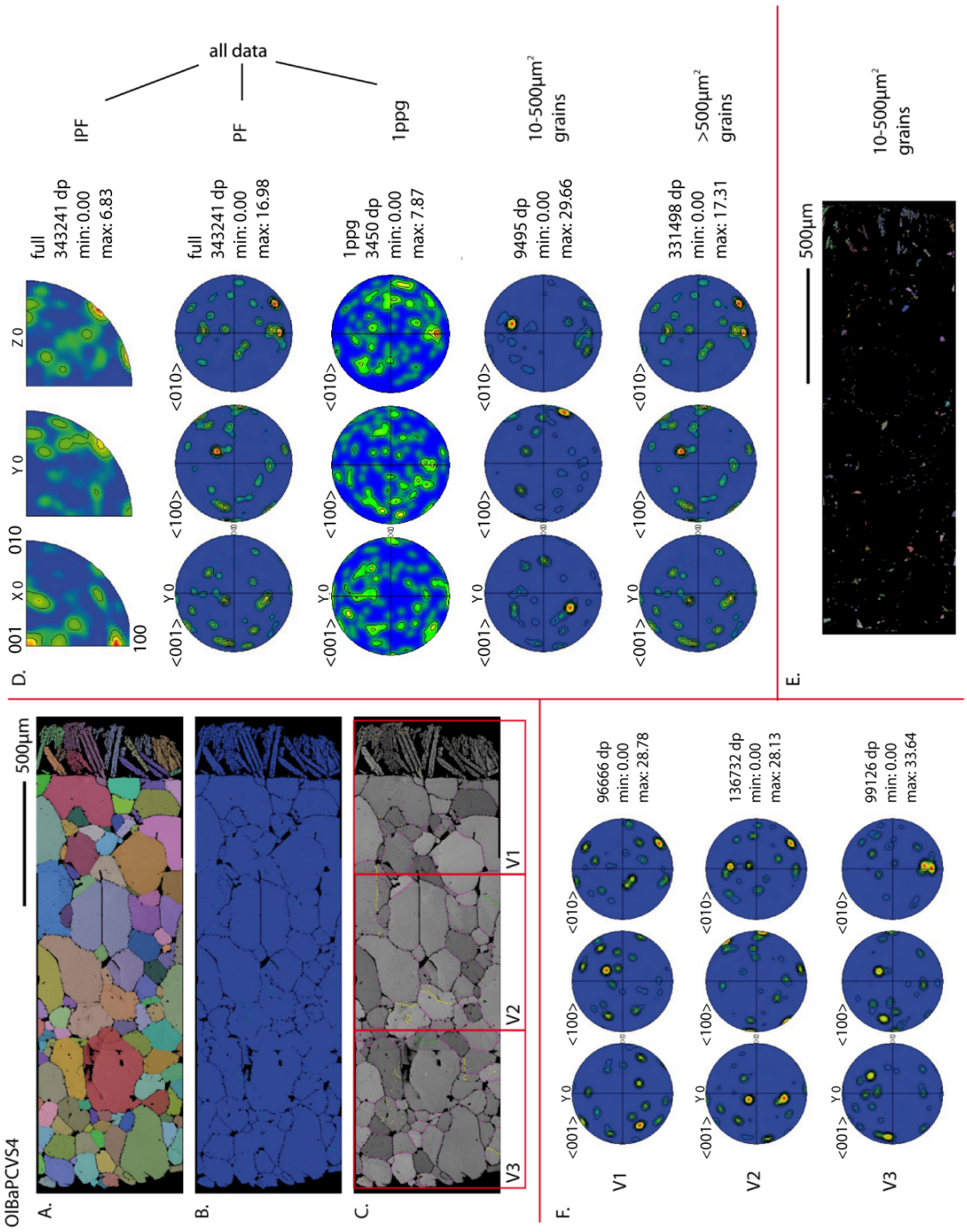

Figure 4.31: EBSD analysis summary of sample OlBaPCVS4, with an initial melt fraction of 5 vol%, annealed for 69 hours under hydrostatic P-T conditions. See Figure 4.29 for key to image sections.

Deformed samples

Deformed samples show significant differences in texture, shape orientation and grain size compared to undeformed samples, and in most cases development of CPO is more evident. Olivine grain size distribution is shown to be bimodal, thought to represent the effects of dynamic recrystallisation during deformation. In each case the sample cut is tangential to the axis of torsion, therefore the section is in a plane where deformation is essentially simple shear aligned horizontally.

Interpretation of the results is complicated by uncertainties caused by experimental equipment failures - in the case of Pdef2 and Pdef3, the motors applying torsional deformation cut out while the experiment was unattended, making it unclear to what extent the sample was deformed, and importantly how long the sample was left to anneal at high P-T after deformation took place. This uncertainty must be taken into account when drawing conclusions from these data.

In this section I will describe data from each sample individually as shown in the following three figures, as follows: A. full dataset, B. crystals larger than 100μm only, and C. crystals of size 6-100μm. In each case data are represented as i) Map of crystallographic orientation (Euler angles) of olivine crystals overlain onto a band contrast image, ii) Inverse Pole Figure, iii) Pole Figure. D. Shows the data split into four vertical subsections to look for changes across the tangential sample slice. The final figure (4.36) shows the development of sub-grains within each sample.

OlBaPdef1 Sample Pdef1 shows a strong bimodal olivine grain size distribution, with large crystals surrounded by 'ribbons' of smaller grains. This texture suggests some dynamic recrystallisation has taken place as expected for deformed olivines and previously observed in other deformation studies and natural samples and inferred to be evidence for solid state flow (Vernon, 2000). The texture suggests a shape preferred orientation exists where crystal long axes are orientated sub-parallel / at a low angle to the shear direction. A crystallographic preferred orientation is also present, particularly evident in the inverse pole figure (Fig. 4.32 A. ii) showing a clear alignment of 100 axes in the X-direction. This is represented as a girdle on the corresponding pole figure. A more subtle alignment of <001> in the Z direction (i.e. perpendicular to the plane of the map) is shown in the pole figures, and a subtle linear alignment of the <010> axis towards north and south of the Y direction (i.e. perpendicular to the shear direction). The CPO appears to be stronger in the small crystal population than the larger, suggesting either that small olivine crystals are rotated more easily towards the preferred orientation, or that their recrystallisation orientation was dictated by the existing stress field (AveLallemant and Carter, 1970). The sample CPO is generally similar to the CPO observed in the olivine + MORB 'aligned melt' sample from studies by Holtzman, Kohlstedt, et al. (2003) (see figure 1.4, section 1.2.1). This is expected as the melt is highly mobile, and the

lack of melt-rich and melt-poor bands suggests there has been no strain partitioning in the sample. A similar CPO is observed in picritic cumulate magmas, inferred to be due to settling of olivine crystals at the base of a magma chamber creating a shape preferred orientation (SPO) by aligning long axes perpendicular to settling direction (Boudier, 1991). There is a distinct SPO observed in this sample, so it is possible that the large melt % means crystals are able to rotate passively to align with deformation and produce the SPO/CPO observed. However, this is not easily compatible with evidence for dynamic recrystallisation ribbons indicating significant solid deformation.

NB. in this case the alignment of the data during EBSD mapping was such that the sample edges were rotated several degrees from normal to the frame of mapping. The Channel5 'virtual chamber' was used to re-orient the samples by 2.5°to ensure the reference axes X,Y and Z were aligned with the shear and compaction directions of the sample.

OlBaPdef2 Sample Pdef2 underwent a 2 hour anneal, followed by torsional deformation of 55-123°. Figure 4.33 shows EBSD analysis results. The uncertainty of the deformation comes from equipment failure (described above). This also means there has been an unknown length of time for the sample to anneal after deformation has taken place (between 0 and 12 hours), which may have affected sample textures.

Again olivine crystals show a distinct bimodal grain size distribution. The distribution of small grains as ribbons is less evident than in Pdef1, but overall there is a similar number of small grains compared to Pdef1. The average size of the 'small' crystal population is slightly larger than in the first sample, and shape appears more equant, which may be due to a period of hot-pressing after deformation allowing deformed olivine grains to begin to re-equilibrate. Therefore the texture may be the result of a combination of deformation followed by annealing leading to some recovery of crystal shape. Large crystals again show an SPO with crystal long-axes appearing to align with the shear direction. CPO is very weak in sample Pdef2, although inverse pole figures, particularly of the small crystal population, indicate a slight preference for <001> and <100> axes to align to the horizontal (parallel to shear) and 010 to align to the Y direction.

OlBaPdef3 Sample Pdef 3 (Figure 4.34), contained 15vol% melt and was deformed for 100-140°, with a potential post-deformation anneal time of up to 4 hours. Deformation was theoretically more extensive than in the previous two samples. However, textures do not show much evidence of extensive deformation. Olivine crystals do not show any clear shape preferred orientation, many appear equant and show a clear triple junction texture, particularly on the left edge of the sample in the area observed to be relatively drained of melt. The olivine texture is similar to that observed in undeformed sample OlBaPCTS3, although the overall grain-size is smaller, and there is a more bimodal distribution of grains. However, small grains are more evenly distributed across the sample than in the other deformed samples, with no evidence for development of ribbons or any deformation-parallel fabric. The CPO is similar

to that observed in Pdef2, although even more subtle and only observable on the inverse pole figures.

Figure 4.36 shows local mis-orientation maps of individual crystals within Pdef1-3, showing the extent of sub-grain development within each sample. Pdef1 shows a large number of strained olivines with undulose deformation, and the most extensive ribbon recrystallisation. Pdef2 contains less elongate olivine with more equant sub-grains where they are developed. Pdef3 shows very few sub-grains developed, with a large number of grains showing no internal deformation at all, and no undulose textures observed in any grains on the slice.

The different texture of Pdef3 could be interpreted as being created from initial deformation (creating bimodal grain size and CPO), followed by significant re-equilibration during later hot-pressing, allowing the sample to recover significantly towards a new textural equilibrium. However, in this case we would expect to preserve any CPO developed, and there is no other evidence that the sample was deformed significantly more than samples Pdef1 and 2, although theoretically it was left longer to attain a larger strain. The lack of CPO developed in samples could simply be due to low strain - previous studies have observed a lack of significant CPO in partially molten systems at less than 30% strain (Zimmerman et al., 1999).

Further experiments would have to be carried out to test the speculative hypotheses explaining crystal structure in these deformed and undeformed samples. In each case, too many processes could be affecting olivine structure in each sample. Future experiments could systematically vary anneal time before and after deformation, and be more accurate in documenting deformation taking place within each sample. In fact, the system monitoring the rotoPEC equipment has already been improved significantly since these experiments were carried out, where the extent of deformation is automatically recorded if the motor stops, allowing more accurate knowledge of the state of sample deformation.

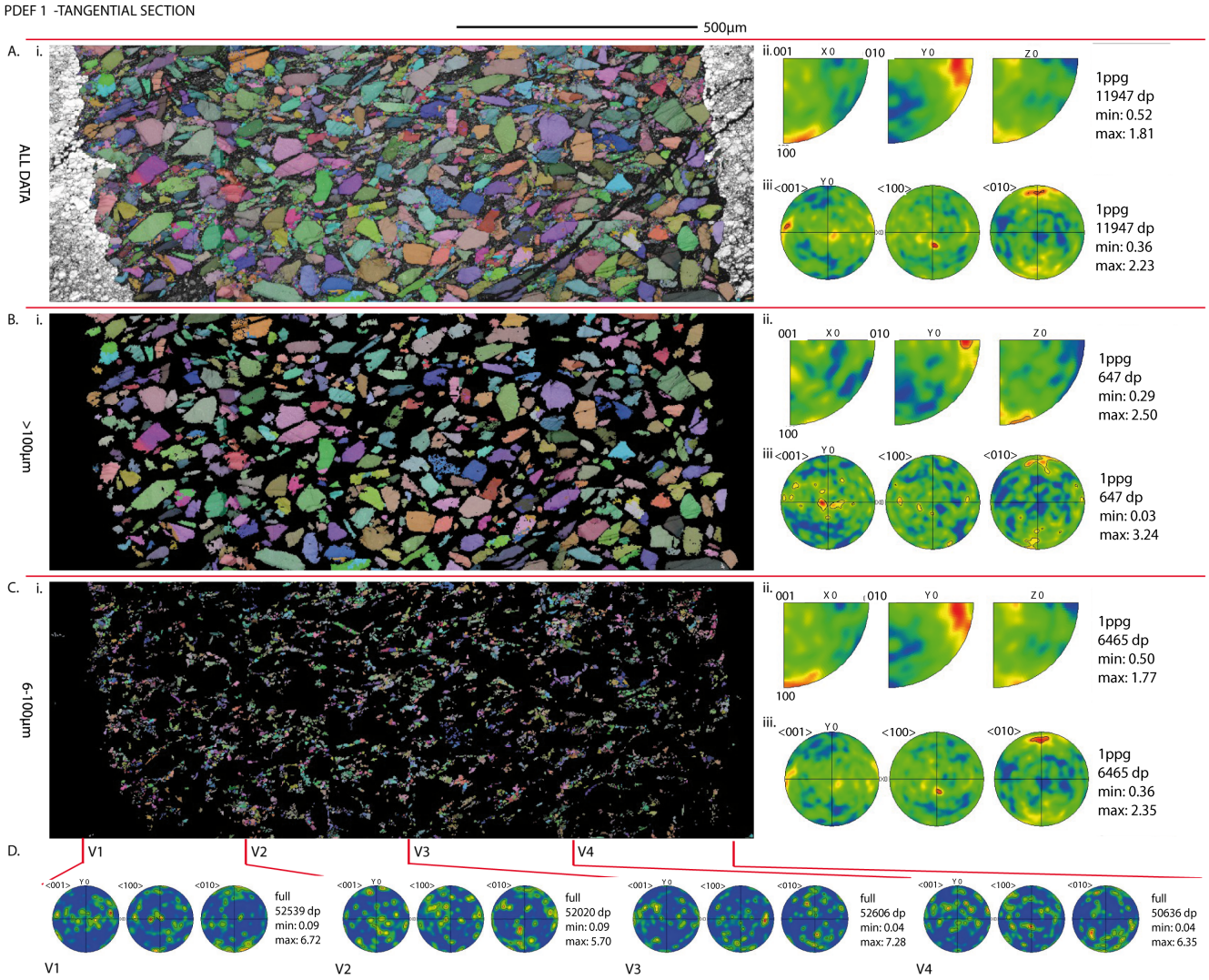

Figure 4.32: EBSD analysis summary of deformed sample Pdef1, with an initial melt fraction of 30 vol%, deformed to 42°after annealing for 16.5 hours. Data are represented as described in the text. White areas in A. i) are alumina capsule, in B. i) and C. i) data outside the grains of interest are included in black background)

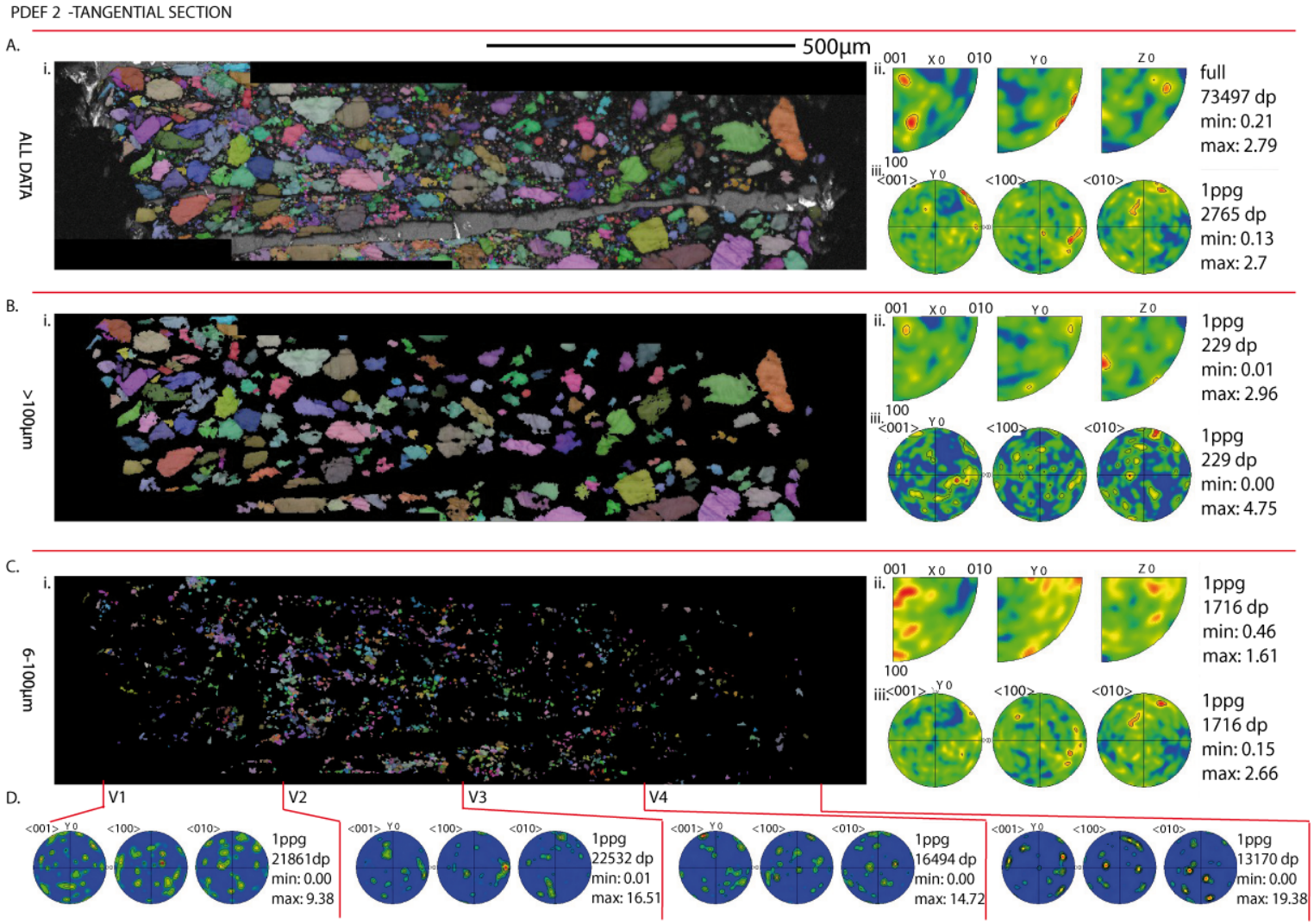

Figure 4.33: EBSD analysis summary of sample Pdef2, containing 1.5vol% melt and deformed for 55-123deg following a 2 hour anneal. A full description is given in the text.

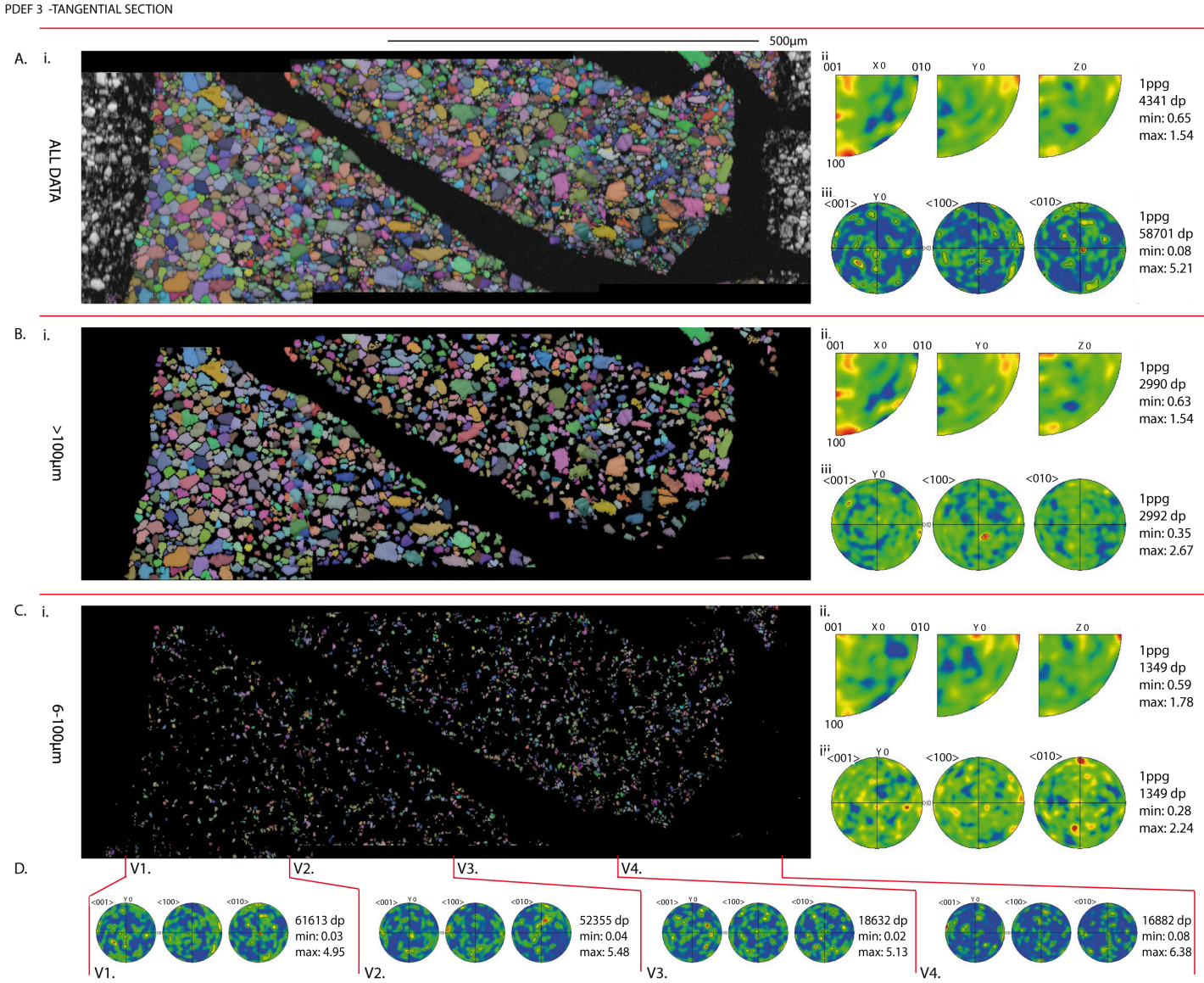

Figure 4.34: EBSD analysis summary of sample Pdef3. See text for key and detailed description.

Figure 4.35: EBSD analysis: Examples of sub-grains within undeformed samples annealed for different lengths of time. Individual crystal maps created by using 'textural component' mapping tool, which uses a reference orientation (selected from crystal of choice) and mapping any changes in orientation from that reference on the colour scale shown. Any uncoloured areas have a deviation larger than the maximum indicated on the scale.

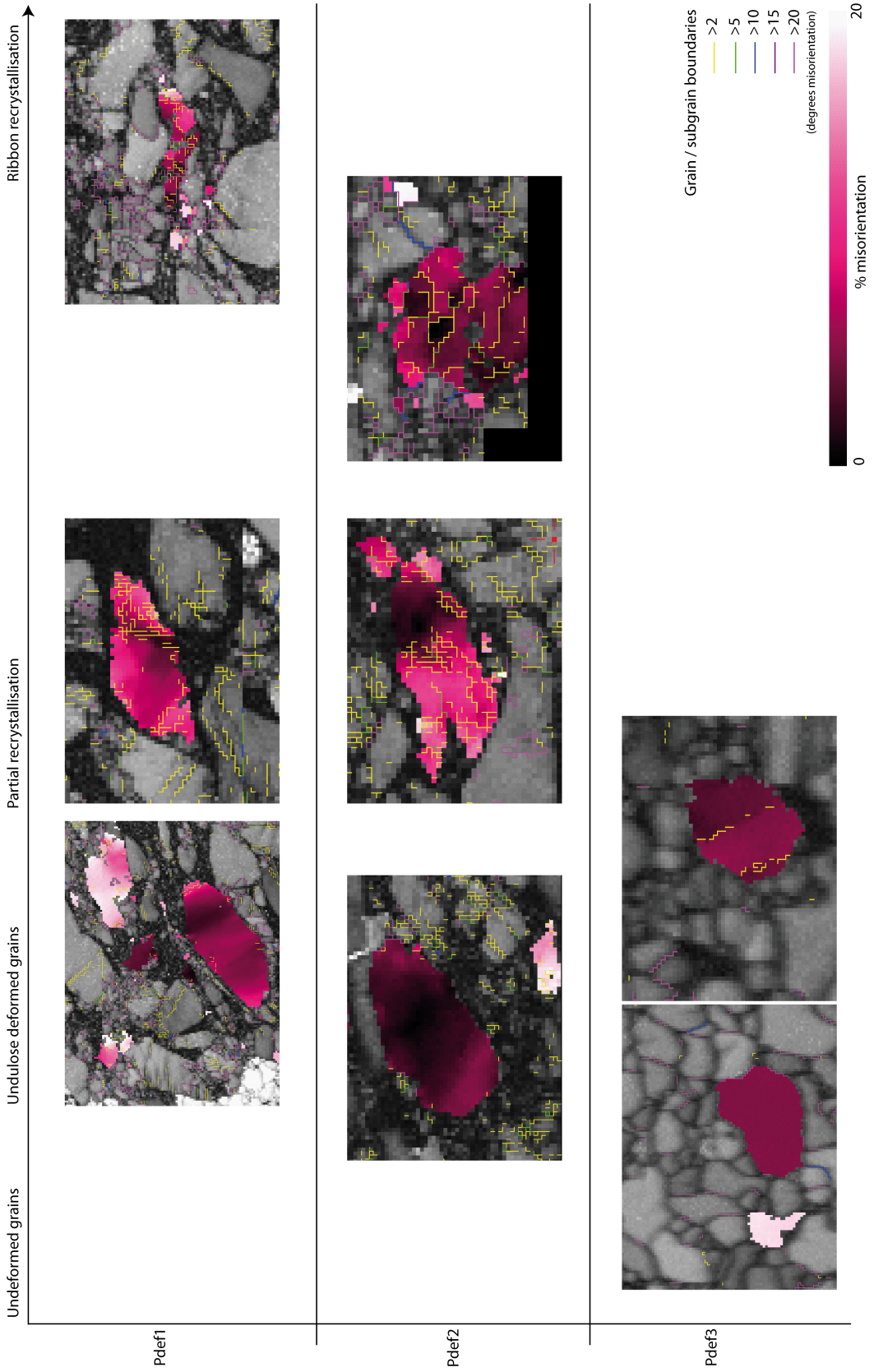

Figure 4.36: Grains and subgrains developed within deformed samples Pdef1 -3. See text for details.

4.5 Discussion and conclusions

4.5.1 is Hf-doping a useful technique for visualisation of melts in three dimensions?

The study carried out in this chapter has been of a preliminary nature, to test the potential of a new doping method to allow quick visualisation of basaltic melts using standard CT equipment. This is not only a useful technique for laboratory CT, but is also required to carry out *in-situ* deformation experiments, which cannot be carried out using phase contrast imaging (chapter 5). Results described in this chapter show that the technique can be very successful in enhancing contrast, but the precipitation/ lack of dissolution of solid HfO_2 crystals in certain samples has meant that some samples could not be visualised successfully.

As discovered in preliminary experiments, the melt phase had to be finely ground initially to allow full dissolution of the Hf within the sample. In addition, a long anneal time was found to help an even distribution of Hf purely in the melt phase, and across the sample, allowing better phase segregation in tomographic slices. A limitation of the Hf-doping technique compared to phase contrast imaging, as used by Zhu et al. (2011), is that non-wetted grain boundaries are impossible to visualise, making individual olivine grains hard to segment unless all grain boundaries are wetted - this means that long anneal times, where melt has had time to spread across grain boundaries, and large melt fractions, where melt films are thick, lead to better indirect visualisation of olivine grain boundaries.

Initially the quench time of rotoPEC experiments was thought to be the cause of Hf crystals in melt, suggesting that HfO_2 crystals may have had time to reprecipitate on cooling of basaltic liquid. However, calibration experiments indicate the quench time is thought to be relatively fast (<5s) from thermocouple experiments and comparable to piston cylinder experiments (Yann LeGodec, unpublished data). Later *In-situ* experiments, discussed in the following chapter, revealed that a drop in temperature can occur at constant power levels in long duration experiments, presumably due to changes in resistivity of the sample assembly. It is possible, therefore, that the temperature of the experiment dropped sufficiently to precipitate HfO_2 crystals before final experimental quench. This would mean that Hf crystals were present during deformation, which could affect permeability of the system.

Comparing the work directly to the phase contrast imaging of basalt carried out by Zhu et al. (2011), our melt network reconstructions are of similar quality for undeformed samples at large melt fractions, but at low melt fractions the limited resolution of the CT system exacerbates the problem of resolving very fine melt networks that was discussed by Garapic et al. (2013) whereby very fine melt sheets wetting grain boundaries are almost impossible to observe. Phase contrast imaging may be limited in picking out these very fine melt sheets, as

the technique highlights phase edges, which would be very close together in fine melt sheets. Although the above experiments cannot yet resolve the finest melt sheets, our doping technique combined with nano-tomographic imaging could serve to solve this problem, with a voxel size down to 50nm combined with Hf doping serving to highlight melt sheets between crystal boundaries (if present).

4.5.2 Application of results to real Earth systems

Results of both 3D and 2D visualisation of undeformed samples highlight the difficulty of achieving textural equilibrium within partially molten basaltic melt samples even in hydrostatically annealed samples. We have found that the majority of experiments for a long anneal time have revealed a significant melt gradient within the sample, rather than homogeneously distributed melt. This is likely to be due to the mobility of basaltic melt - even a small difference in temperature or melt concentration across the sample will lead to significant concentration of melt within certain areas. In addition, full 3D visualisation revealed significant partial melting of olivine crystals, potentially caused by the presence of graphite creating CO_2 gas, which can lower olivine melting temperatures (Eggler, 1976). Quenching of these partial melts have led to the formation of skeletal quench crystals in a significant number of samples, further complicating processes occurring within the experimental samples. Due to these complications, the results from these experiments are difficult to interpret fully and apply to real Earth scenarios. However, these preliminary experiments show the potential for 3D visualisation using our Hf doping technique, highlighting its successes and failures. Future use of the same doping technique on better controlled basaltic melt experiments is likely to lead to more geologically significant results.

An initial aim of the study was to use novel visualisation of basaltic melt in deformed and undeformed samples to draw conclusions about the response of melt networks at various fractions of partial melt to low strain-rate deformation. However, due to the complexity of processes ongoing in the sample it has proven difficult to draw any certain conclusions about the effects of deformation of melt network texture, and the melt networks themselves have not been visualised satisfactorally in deformed samples due to precipitation of Hf from the liquid phase. Improvements in quench rates in deformation samples could allow the collection of improved deformation datasets to visualise deformation textures more reliably.

The bias of melt visualisation quality in certain samples, as described above, makes it difficult to compare results accurately across melt fractions, annealing time as well comparing the effects of deformation. For example, large grain sizes and large melt fractions produce larger textural features that lend themselves well to direct 3D visualisation (large grain size, large textural features, large melt fraction), but these are not necessarily the most applicable to real Earth scenarios, particularly not those of interest in upper mantle basaltic melting. The

majority of studies have tried to limit olivine grain size in order to balance out the issues of high strain-rate and short timescales of laboratory experiments (Kohlstedt and Holtzman, 2009). As large melt fractions are particularly well suited to this visualisation technique, it may be possible in the future to use the technique for studies of magma chamber processes and crystal mush deformation. Nano-scale tomographic imaging could be used to get more reliable 3D geometry data from low melt fraction samples, and those with a smaller olivine grain size.

4.6 Conclusions

- Doping basaltic melt with Hf has successfully been used to enhance contrast of the melt in an olivine system. The system works particularly well in experiments at relatively high temperatures, annealed for long durations, and with large melt fractions, which ensure HfO_2 crystals are fully dissolved in the melt.
- Olivine grain growth is very pronounced in undeformed experiments, which also aids reconstruction of samples annealed for a long time, as features are increased in size, improving segmentation quality.
- Issues with solid HfO_2 crystals were particularly pronounced in deformation experiments, potentially because experimental temperatures were not as high as initially thought. This meant reconstructions of deformation experiments were less successful, limiting potential for comparison between deformed and undeformed partial melt 3D textures.

CHAPTER 5

In-Situ melt migration using synchrotron X-ray tomography

ABSTRACT

The aim of this chapter's work was to explore the potential of carrying out *in-situ* melt migration experiments using the novel rotoPEC equipment in combination with a synchrotron X-ray source. The equipment was successfully installed on two separate synchrotron beamlines, and CT scans carried out over the course of experiments successfully tracked sample geometry and any changes in melt distribution for three contrasting partial melt systems. Experimental design was optimised to ensure melt migration was visible over laboratory timescales, stable within the limitations of equipment, and easily tracked using CT scans. The final experiment, conducted on a liquid gold-solid BN system, showed significant melt migration during the experiment. It was possible to characterise changing 3D geometry of melt-filled fractures during the experiment using tomography, and also estimate melt migration velocities by capturing dynamic movement using 2D radiography.

Author Contributions: Nic Odling assisted with design and production of sample capsules. Experiments conducted at DIAMOND synchrotron I12 beamline were carried out with the assistance of GD Bromiley, Dr Kate Dobson (University of Manchester), Yann LeGodec and Julien Phillippe (UPMC, Paris). During ESRF phase I and II, we were accompanied by GDB, YLG, JP with Frederic Bergame (UPMC) asstisting for 2 days during phase I. Beamline scientist was Mohammed Mezouar. During beamtime, sample preparation was mostly conducted by the PhD student and GDB, with some assistance from YLG particularly during the final phase of experiments. Installment of rotoPEC equipment into beamlines was carried out by YLG, JP and beamline scientists. We are grateful for the support from a number of additional workers at DIAMOND and ESRF who assisted with the set-up of the rotoPEC in the hutch and programming of motor coupling and automated tomographic capture system.

5.1 Introduction to in-situ analysis of melt migration

The movement of small volumes of melt through a solid matrix (rock) plays a key role in many fundamental geological processes, from planetary formation in the early solar system to present day volcanism. However, the behaviour of low melt fractions in terms of connectivity, segregation velocities, and melt geometry at the extreme P-T conditions of planetary interiors remains poorly understood. Although recent advances have been made in high resolution 3D tomographic imaging (Shi et al., 2013; Zhu et al., 2011), constraints on these processes are still mostly reliant on the analysis of post-quench run products (Holtzman and Kohlstedt, 2007). Estimating permeability and melt migration velocities from textural interpretation of final run products is the equivalent of using a still-frame photo in the middle of a 100m sprint to estimate the speed of runners, and the final outcome of the race. The uncertainties of these methods of interpretation mean that quantities are still poorly constrained within models of melt migration in the upper mantle and for estimates of core formation timescales. Estimates of permeability and melt velocity are still reliant mostly on poorly constrained numerical models (Hustoft and Kohlstedt, 2006). Simulation of fluid flow by Lattice-Boltzmann modelling has been carried out using real 3D melt network geometries (Miller et al., 2014), but again these are based on images of quenched run products, and this is only possible with the assumption of textural equilibrium and a steady state system. This assumption is not valid in deformation or melt migration experiments, where the texture will be constantly changing (section 1.2.1). Direct visualisation of small partial melts from laboratory samples while at high temperatures and pressures could help to empirically constrain melt migration velocities, limits of melt connectivity and the importance of melt migration along grain boundaries in comparison to transport of melt through fractures and other pre-existing planes of weakness.

This chapter outlines a series of investigations carried out on experimental samples of varying composition and design, aimed at producing some of the first *in-situ* 3D tomography of partial melt movement at extreme P-T conditions. These experiments were carried out using the novel rotational tomography Paris-Edinburgh cell (rotoPEC), uniquely adapted for use in *in-situ* experiments at synchrotron beamlines (section 2.2.1).

The work was carried out over 1 week at the DIAMOND synchrotron, Didcot, Oxfordshire in October 2013, and over two separate weeks at the European Synchrotron Radiation Facility, ESRF, Grenoble. Additional preliminary work and follow-up analysis was carried out at the University of Edinburgh and EMMAC. Due to the preliminary nature of these studies, significant method development and experimental design adaptation took place over the course of this work. For this reason the chapter will examine the results for the most part in chronological order, and evaluate successes and experimental limitations at each stage of method development.

5.1.1 Previous *in-situ* investigations of partial melt geometries

3D visualisation of partial melt geometries at concurrent high P-T is an area that is currently the focus of continued development. Equipment adaptations to allow this to be carried out have been previously described in chapter 1. The majority of existing published studies are in the developmental, proof of concept stage. Previous *in-situ* deformation work on multi-phase systems has been carried out using the Drickamer apparatus investigating the effects of deforming Fe-Ni-S in solid olivine to extreme values of torsional strain (Wang, Lesher, et al., 2011; Wang, Uchida, et al., 2005), but was limited to sub-solidus temperatures of both materials.

The work carried out in this chapter is the first carried out using the novel rotoPEC design. The work incorporates significant method development, to examine the feasibility of melt migration experiments with in-situ imaging of melt migration, in static and dynamic systems. It is therefore of a preliminary nature, investigating the potential scope of future investigations carried out with this equipment.

5.1.2 Geological applications

The ability to visualise 3D melt geometry in laboratory samples *in-situ* at extreme pressures and temperatures has the potential to elucidate processes ongoing in a number of geological settings including those examined in the previous two chapters:

- **Core Formation in the Early Solar System** Previous work carried out during this project and in some previous studies (Bruhn et al., 2000; Hustoft and Kohlstedt, 2006) has shown that even low strain-rate deformation can significantly enhance metallic melt connectivity in a solid olivine matrix, which could have significant constraints on theories of core formation in the early solar system (chapter 3). Deformed samples in the previous study showed localised redistribution of melt on the grain scale and a subtle alignment of melt sub-parallel to the shear direction. The enhanced connectivity of the samples suggests a potential for melt to migrate on a larger scale in response to external gradients of e.g. temperature or pressure (Hustoft and Kohlstedt, 2006), but estimates of melt migration velocity have been limited to simple calculations based on generalisations of melt geometry (Hustoft and Kohlstedt, 2006). During preliminary investigations (Berg, 2010), melt was observed within the external MgO capsule wall, suggesting movement over the scale of several mm over the course of an experiment (Figure 5.1). By conducting further experiments using the same FeS-Olivine system, combined with *in-situ* visualisation techniques, it may be possible to track this motion in real time, observe textural changes across the experiment and potentially quantify velocity of deformation-enhanced percolation.

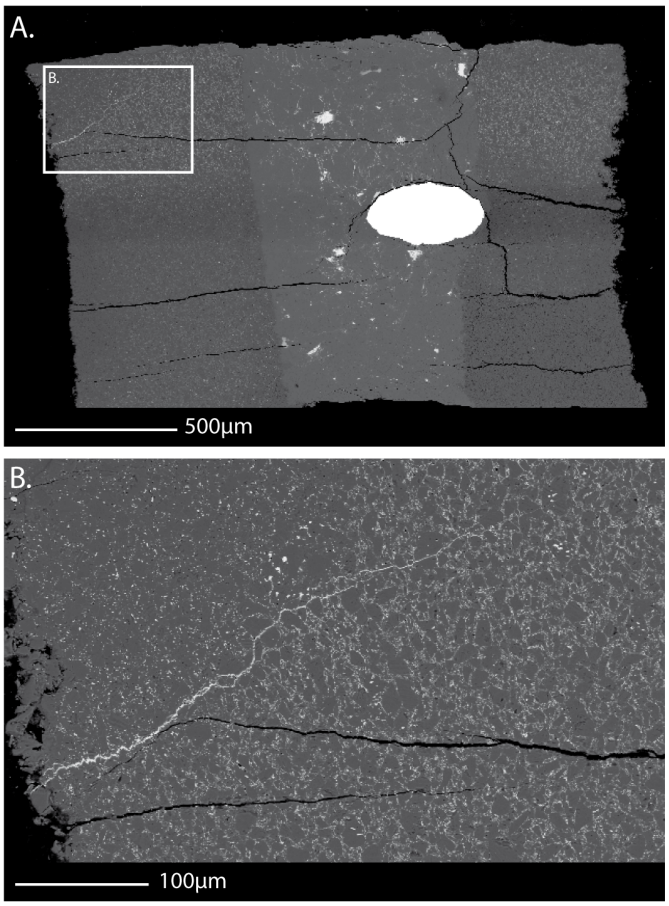

Figure 5.1: BSE images showing evidence for melt escaping from the original sample zone within a preliminary experiment (FeOl-Cam2) conducted using roPEC equipment (Berg, 2010). A. Image of full quenched polished section. Central 1/3 is original sample zone. Grey=olivine, white = Fe_3S. Central large white area is a platinum strain marker. Slightly darker areas on the edge are alumina capsule. B. shows a close-up of the edge of the alumina capsule (see inset in A.) and shows significant wetting of alumina grains by FeS melt, including a large vein on a scale of >300µm extending to the edge of the capsule. This melt must have originated from the centre of the capsule, indicating movement on the scale of ~1mm over the timescale of a laboratory experiment. This suggests there is potential for this melt migration to be imaged and its velocity measured using the rotoPEC adaptation for *in-situ* high P-T imaging and synchrotron X-ray sources.

- **Basaltic melt in the Upper Mantle** - As described in detail in chapter 4, a large number of studies have investigated 'dual porosity' theories of melt migration on the grain scale and through larger conduits to reconcile geochemical and geophysical evidence of very rapid melt extraction under spreading ridges. It is known that basaltic melt is

highly mobile on a grain scale in a solid olivine matrix from experiments examining post-quench material (Cooper and Kohlstedt, 1982; Hirth and Kohlstedt, 1995), as also evident from our work in chapter 4. However, mainly due to experimental equipment limitations, there have been no published studies as yet examining melt migration in real time at upper mantle P-T conditions. *In-situ* experiments could help to constrain melt migration velocities, the presence or lack of an interconnectivity threshold at very low melt fractions and the importance of fracture flow vs. grain-scale melt migration of basaltic melt under upper mantle conditions. The work carried out in chapter 4 also shows that quench experiments can only give limited information on processes occurring within runs, and *in-situ* observations are the only way to fully characterise experiments.

For work described in this chapter, sample composition has been varied to investigate both of these geological systems. Initial work carried out at Diamond I12 was focused on the problem of core formation in early solar system, examining the liquid FeS- solid olivine system and emphasising effects of deformation on melt geometry and grain-scale interconnectivity. In phase I of ESRF work, experimental design was adapted taking into account initial limitations of DIAMOND experiments, to examine more mobile basaltic melt making work applicable to the upper mantle geological system. This chapter essentially outlines a series of preliminary investigations to investigate the feasibility of tracking melt migration and changes in melt geometry over the course of a high P-T experiment, each of which could be taken further to investigate each geological system of interest.

5.1.3 Outline of aims

Taking into account the novel aspect of these experiments, the general aims of this chapter's research were of a broad preliminary nature, and flexible in the knowledge that aims may develop along with experimental method development. Broad objectives were to

1. design experiments to encourage macroscopic melt migration that could potentially be traced during in-situ experiments using rotoPEC equipment and be relevant to one or more geological applications described above.

2. carry out *in-situ* experiments at a synchrotron beamline using the rotoPEC equipment. This involved installation of ~200kg equipment in the beamline hutch, correlating rotoPEC rotation and motor control with the control of the X-ray camera for tomographic scans, alignment of the sample in the beam, and testing reconstruction quality at varying experimental conditions.

3. investigate best methods and processes for capturing movement of melt and changing melt geometries in 2 and 3 dimensions using radiography, X-ray diffraction and tomographic techniques.

4. develop analytical and processing techniques that could be applied to tomographic and radiographic time-series data to allow quantification of melt movement and development of melt connectivity.

5.2 Methodology and method development

The following section outlines specific methods used in carrying out experiments at synchrotron beamlines DIAMOND I12 and ESRF ID27. This includes development of starting mixtures, experimental capsule designs, and the specific work required to incorporate the rotoPEC equipment into each individual beamline and assimilate its functions with the tomographic software in each beamline.

5.2.1 Capsule designs

The rotoPEC equipment and gasket design used in our experiments is shown in figure 2.3, section 2.2.1. The sample volume is a cylinder of 3mm od. Although the height of this cylinder is 2mm, only the central 1mm is within the field of view of X-rays during experiments; this reduces in size as the anvils close over the course of an experiment. Taking into account these factors, we developed a series of interior capsule designs to encourage melt migration on a scale visible during *in-situ* radiography and tomography (Figure 5.2). Designs were developed and adapted taking into account results of the previous phase.

Capsules were made using polycrystalline MgO, synthetic forsterite or (in the final experiment only) boron nitride. Capsules for DIAMOND and ESRF phase I experiments were drilled individually at the University of Edinburgh using a small laboratory lathe, or using the ID27 *in-house* lathe at ESRF. Holes within the capsules, created to contain the metal-rich starting mixture, were drilled to be much smaller than the total 3mm diameter available, in the hope that high fluid pressure in the melt-rich region would cause melt to migrate outward into the remaining polycrystalline capsule. Initial experiments showed that the capsule lid may act as a conduit and lead to preferential flow, but this was generally out of the field of view of X-rays. This led to the dual capsule design (Figure 5.2B) in which two symmetrical capsule halves were used to ensure the join, and potential melt conduit, were placed in the vertical centre, ensuring it remained within the field of view throughout the course of an experiment. The final capsule design (type C) was a development to enhance stability and prevent blow-outs (this was successful in combination with a change in capsule composition - see following section).

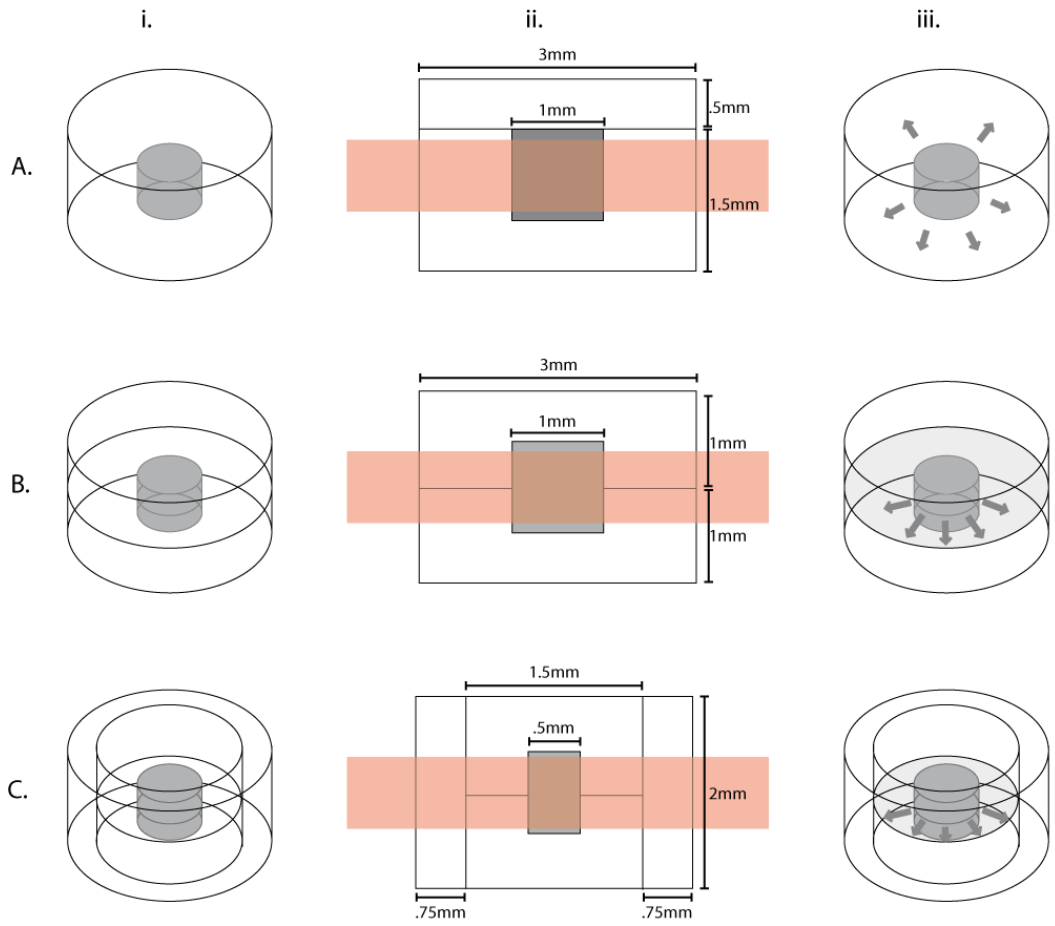

Figure 5.2: A series of diagrams showing the development of capsule designs over the course of the experiments described in this chapter. i. 3D sketch of the capsule (in white) with the central hole shown in grey in the centre of each. ii. cross-section through the capsule centre with key dimensions indicated and the volume of the sample remaining visible between the anvils is highlighted in pink. iii. expected dominant melt migration direction shown by arrows. A. the central capsule design used during DIAMOND I12 experiments. Melt is placed in the central hole. The high melt % in the centre of the sample was expected to cause melt migration, where melt would flow from the melt-rich centre to the melt-poor sample edge. B. The initial adaptation of the sample to create a dual capsule design. The gap between top and bottom capsules could create a weak plane /pre-made fracture to encourage the melt to flow along it. Placing this in the centre of the sample meant this preferential flow path remained in the field of view throughout the experiment. C. A further adaptation of the dual capsule design to provide greater stability and reduce experimental failure, with a smaller central sample volume and an additional external cylinder to support the central sample structure (Y. LeGodec, pers. comm.)

5.2.2 Composition of starting mixtures

The range of starting mixtures and capsule compositions used in experiments in this chapter reflect the ongoing developmental aspect of the work. Factors to take into account when chosing starting compositions include their relevance to geological scenarios, the contrast between phases in terms of X-ray attenuation and the ability for the materials to be easily identified from their diffraction patterns. In addition, our aim to capture movement over the course of an experiment lasting several hours meant that compositions had to be adapted to encourage melt migration to take place at the right timescale i.e. changing melt mobility if necessary to increase or reduce the melt migration velocity within samples.

An aspect of the work was to encourage melt migration into the external polycrystalline capsule, therefore these had to be made of a suitable geological analogue. Initial capsules used during experiments at DIAMOND and ESRF were made of sintered forsterite ($MgSi_2O_4$), synthesised from constituent oxides (see section 2.2.2). Later experiments used machineable MgO, which is the Mg endmember of the second most common mineral in the Earth's interior and therefore also representative of deep Earth materials. The final experiment conducted during ESRF phase II used a capsule material of hexagonal BN, mainly chosen to provide stability and due to its high thermal conductivity to ensure efficient heat transfer to the sample volume.

Tables 5.1 and 5.3 below give the compositions used in each experiment over the course of the three phases of beamtime. In some situations, last minute decisions to change sample composition forced material proportions to be a rough estimate - these estimated percentages are marked with a *. Other starting mixtures were measured out by weight using precise digital scales, and ground thoroughly to homogenise. As the reasons for adapting compositions are influenced mainly by the results of the previous phase of experiments, I will describe these factors in detail at the end of each results section.

5.2.3 Synchrotron beamlines, rotoPEC installation and tomographic set-up

Due to the weight of the rotoPEC deformation equipment, the equipment cannot be installed on the majority of beamlines set up specifically for micro- or nano-tomographic scans. Instead we made use of beamlines that are set up for large scale engineering work and are used to incorporating large equipment and machinery. Several days of beamtime were required in each case to install the rotoPEC equipment and set up the CT system. The exact method used varied considerably at the two beamlines visited, as described below.

Diamond I12

During this project we made use of I12, the Joint Engineering, Environmental and Processing (JEEP) beamline at the DIAMOND synchrotron in Oxfordshire, UK. This beamline is multi-functional, with two experimental hutches which allow different imaging and diffraction techniques to be applied to varying materials, including large scale, heavy duty engineering experiments in hutch 2. The beam makes use of X-rays created at an undulator (wiggler) on a straight-line segment of the synchrotron ring, rather than those produced at a polygon vertex (see fig 1.7, section 1.2.2). The energy range of the beam is 50-150keV, but energy can be tuned with a monochromator. Our experiments were able to make use of the inner hutch, giving us a higher flux of X-ray, which is important for imaging of high density materials such as metals.

Carrying out tomographic scans at the I12 beamline involved installation, alignment and set-up of the rotoPEC press inside the I12 inner hutch. The 200kg rotoPEC equipment was installed on a specially prepared aluminium alloy stage on the optics stage to ensure the centre of the sample would be at the height of the beam (Figure 5.3). A chain-operated crane was used to manoeuvre the rotoPEC into position on the optics bench (Figure 5.3 B). The optics stage was motorised, allowing adjustment of position in the x, y and z positions to allow exact alignment of the rotoPEC with the beam and camera. It can also be adjusted to correct for a slight tilt in X and Y directions in the axis rotation of the sample (in this case the rotoPEC) which can cause noise and artefacts in reconstructions.

A portable sanchez pump was used in combination with a gas cylinder to pump to confining pressure (both available on-site). Two transformers were used to apply a voltage to the equipment to heat the sample to the correct temperature. Both temperature and pressure had to be applied manually in the experimental hutch, and could not be adjusted at the same time as the hutch shutter was open (i.e. during a tomographic scan). Motors for the top and bottom anvils were controlled remotely from the control room. An air-blown cooling system was attached to the frame of the rotoPEC to stop motors from overheating during rotation (Figure 5.3C.). In this case we did not use diffraction methods to directly measure temperature and pressure - instead calibrations from previous *in-situ* diffraction experiments were used (see section 2.4).

The device rotational axis was aligned with the X-ray beam and camera using a small platinum sphere (~0.5mm) attached onto a test gasket/assembly at rtp. The rotoPEC motor rotation and camera shutter were controlled using separate software. In order to obtain tomographic scans, the rotoPEC anvils were continuously rotated to 180° at a known speed, and the X-ray camera programmed to take projections at the correct time interval to ensure 1501 projections were taken over the 180° rotation of the sample. Where the sample was left to anneal for several hours, the system was left to rotate and collect projections continuously, and later projections were split into groups of 1501, each representing a 180° rotation to be

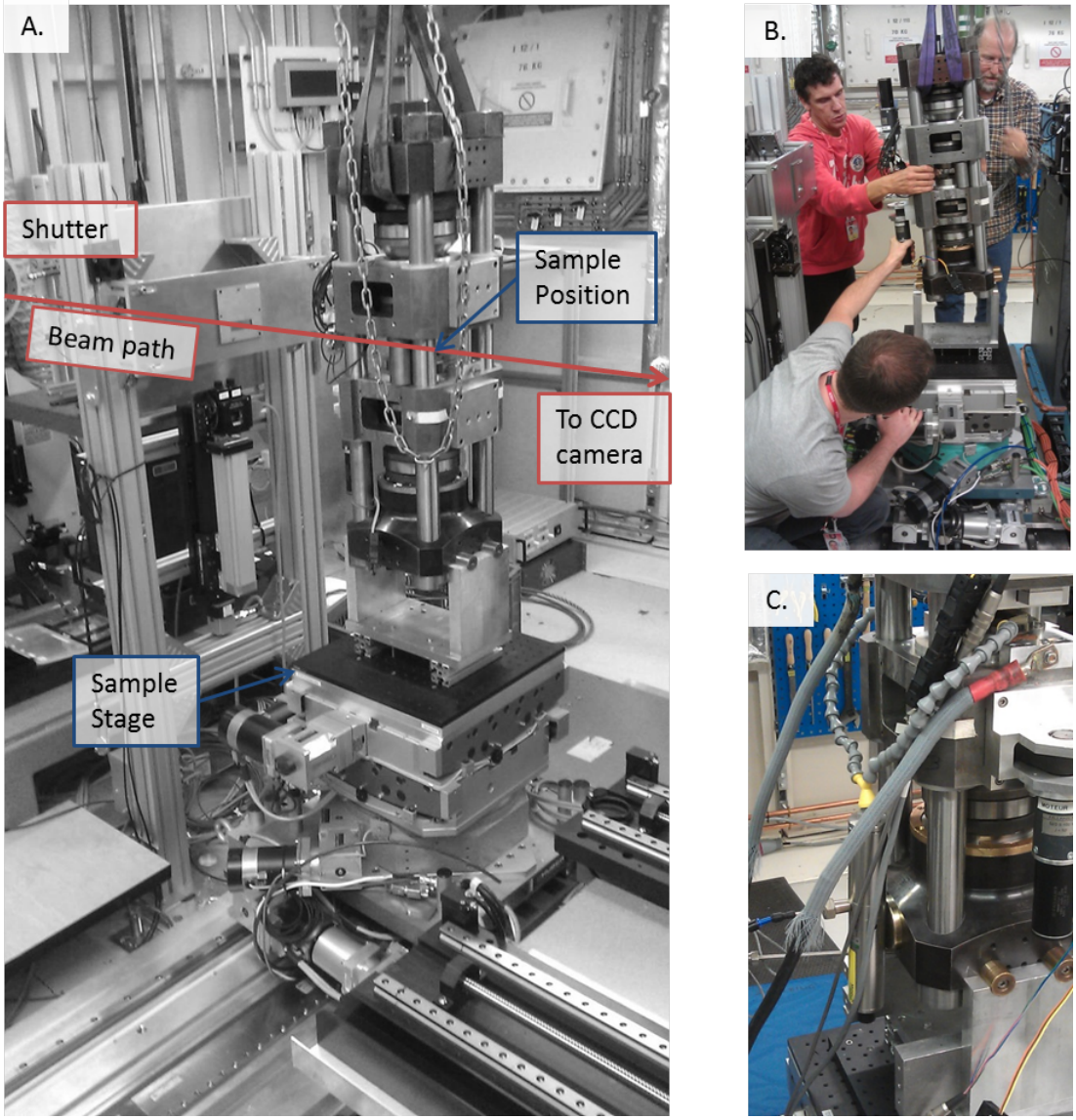

Figure 5.3: The inner hutch at Diamond showing rotoPEC set-up. A. The rotoPEC in position on the sample stage of the inner hutch. The beam path is shown by the red arrow. The inner shutter is shown at the very left of the image, while the CCD is out of view to the right (not currently in position for scans). B. Positioning the rotoPEC onto the sample stage and aluminium alloy supports using the ceiling crane. C. The portable cooling system (yellow and grey attachment), attached to the rotoPEC using a strong magnet. The equipment uses compressed air to cool the anvil motors.

reconstructed into a full tomographic scan. This allowed us to track potential changes in texture over several hours. A small number of radiographs were also taken without rotation to record potential movement in the sample in two dimensions.

The anvil motors were found to become unstable at high speed whilst samples were under load, limiting scan speed to 1.5 hours for 180°. Exposure time was set to 1.73s, which was

adequate for good imaging, and an additional 0.43s wait time was programmed into the camera between each projection to ensure the camera and rotoPEC were temporally correlated. The movement of the motors over the 1.73s of exposure time did not significantly affect projection quality. Before and after each scan, 40 flat field and 40 dark current images were taken to normalise projections. The majority of tomographic scans were carried out at 53kV energy. For a monochromatic beam this describes the peak of X-ray energy, rather than the maximum limit of X-ray energy as in laboratory CT systems. Therefore this energy is roughly comparable to a beam of 120kV in our *in-house* CT system.

A relatively small sample-detector distance of 300mm was used to ensure attenuation contrast was high. This works well for the high contrast between FeS melt and olivine as used in these experiments. Larger distances enhance the phase contrast effect in synchrotron experiments (see chapter 1, sectionX) but we found this technique was not useful for *in-situ* experiments as it reduced the contrast between phases of interest, and also reduced the transparency of the boron-epoxy sample gasket, which was outside the region of interest of our scans and therefore interfered with reconstructions.

All scans were reconstructed using Diamond *in-house* software using a filtered back-projection algorithm. A total of 1.9 TB of data was produced over a four day period, including raw projections and reconstructed slices. Final scans were produced with a voxel size of ~2μm, therefore resolution was roughly equivalent to that achieved in the university of Edinburgh laboratory CT equipment.

Tomographic scans were taken of samples at room temperature and pressure, at various stages during annealing at high P-T, and concurrent with deformation at high P-T. Scans were also carried out at low temperature, high pressure, to examine the effects on scan quality by potential motion blurring. A final tomographic scan was carried out of the quenched sample at room temperature (but confining pressure as this increased the stability of the sample during rotation). Samples were removed if possible and later scanned again using the in-house laboratory CT at Edinburgh University, both to compare scan qualities, and also to allow examination of those parts of the sample volume otherwise obscured by the rotoPEC anvils. Table 5.1 shows a summary of all samples produced during Diamond beamtime, and Table 5.2 lists all tomographic data produced.

Sample Name	Composition	Capsule Type	Pressure on line / kbar	Inferred P / GPa	Power / W	Inferred T / K	Initial Anneal Time / min	Deformation rate / rpm	Total strain / degrees	Total time at T-P / min	Summary of Experiment
DLS1	Ol + 4wt% FeS (plus plat grain for alignment)	Synthetic Ol	80	1	84	1200				60	Heated and pressurised and used for alignment, but not continued as Sample-detector distance meant little contrast between phases.
DLS2	Ol + 4wt% FeS	MgO	80	1	284	1200	480	200		780	300rpm for 10min, rotation stopped as too fast. 200rpm for 50min, anneal for 4hrs
DLS3	Synthetic Olivine + 20 vol% FeS	Synthetic Ol	120	2	350	1600	470	100	123	1035	1600K for 10min, 870K for 96 min, 1600K for 60min, 870K for 60min, 1600K for 400min, deformation at 100rpm for 40 minutes, 1600K for 30min, 870K for 90min, 1600K for 90min, deformation at 100rpm for 45min, 1600K for 60min, deformation at 100rpm for 60min, 1600K for 4 hours
DLS4	Synthetic Olivine + 20 vol% FeS	Synthetic Ol	120	2	350	1700	110	20	22	560	20rpm for 45min, anneal for 60min, 20rpm for 45min, anneal for 5hrs
DLS5	Synthetic Olivine + 10 vol% FeS	Synthetic Ol	120	2	350	1700	160	20	61	1272	20rpm for 55min, anneal for 60min, 20rpm for 68min, anneal for 54 min, 20rpm for 75min, anneal for 150min, 20rpm for 110min, anneal for 60min, 20rpm for 60min, anneal for 7hrs
DLS6	Synthetic Olivine + 10 vol% FeS	MgO	120	2	350	1700	120	100/20	94	1188	100rpm for 25 min, 120m anneal, 20rpm(?) for 107min, 120m anneal, 20rpm for 61min, 60m anneal, 20rpm for 70min, 75m anneal, 20rpm for 70min, 6hrs anneal

Table 5.1: A summary of samples produced at I12 synchrotron with T-P conditions, deformation rates and total strain. A summary of the full experiment is also included.

Scan no.	Sample Scanned	P-T Conditions	Deformation / rpm	Sample Strain	no. of projections	Scan time / min	FF	DC	
27909	DLS3	low T, high P	0	0	1501	48	27909,27910	27911	
27913	DLS3	high P-T	0	0	1501	96	27912,27914	27915	
27917	DLS3	low T, high P	0	0	1501	96	27916,27918	27919	
27921	DLS3	high P-T	0	0	1501	96	27920,27922	27923	
27926	DLS3	high P-T	0	0	1501	96	27924,27927	27928	
27930*	DLS3	high P-T	0	0	7257	245	27929,27931	27932	6 frames
27934	DLS3	low T, high P	0	0	1501	96	27933,27935	27936	
27938	DLS3	low T, high P	0 (post 100rpm deformation)	34	1501	96	27937	27940	
27942	DLS3	high P-T	0	34	1501		27941,27943	27944	
27946	DLS3	high P-T	100	72	1510	48	27945,27947	27948	
27950	DLS3	high P-T	0	72	1510	48	27949,27951	27952	
27954	DLS3	high P-T	100	115	1510	48	27953,27956	27957	
27967	DLS3	high P-T	0	123	1510	48	27966,27968	27969	
27974	DLS4	high P-T	0	0	1510		27973,27975	27976	
27978	DLS4	high P-T	20	6	1510		27977,27979	27980	
27983	DLS4	high P-T	0	6	1510		27981,27984	27985	
27987	DLS4	high P-T	20	11	1510		27986,27988	27989	
27991	DLS4	high P-T	0	11	1510		27990,27992	27993	
27995	DLS4	high P-T	0	22	1510		27994,27996	27997	
27999	DLS5	high P-T	0	0	1510		27998,28000	28001	
28003	DLS5	high P-T	0(post 20rpm deformation)	0	1510		28002,28004	28005	
28007	DLS5	high P-T	20	10	1510		28006,28008	28009	
28011	DLS5	high P-T	0	24	1510		28010,28012	28013	
28015	DLS5	high P-T	0	31	1510		28014,28017	28018	
28023	DLS5	high P-T	0	51	1510		28022,28025	28026	
28027	DLS5	high P-T	0	61	1510		28026,28028	28029	
28031*	DLS5	high P-T	0	61	11500		28030,28032	28033	4 frames
28035	DLS6	high P-T	0	0	1510		28034,28036	28037	
28039	DLS6	high P-T	0	0	1510		28038,28040	28041	
28043**	DLS6	high P-T	100	22	1510		28042,28045	28046	
28044	DLS6	high P-T	0	22	1510		28042,28045	28046	
28048	DLS6	high P-T	0		1510		28047,28049	28050	
28052**	DLS6	high P-T	20	32	1510		28051,28053	28054	
28057	DLS6	high P-T	0	42	1510		28055,28058	28060	
28061	DLS6	high P-T	0	42	1510		28060,28062	28063	
28067	DLS6	high P-T	0	52	1510		28065,28068	28066	
28071	DLS6	high P-T	0	64	1510		28070,28072	28073	
28074*	DLS6	high P-T	0	64	10096		28072,28075	28076	6 frames

Table 5.2: A summary of tomographic scans carried out at Diamond I12 beamline.

ESRF ID27

ID27 Beamline at the ESRF is a beamline specifically designed to allow high pressure *in-situ* experiments to be carried out using diamond anvil or larger volume high pressure cell apparati. The roPEC has been installed on the beamline previously to carry out radiography of melt migration and deformation experiments, and to produce a temperature-pressure calibration curve using X-ray diffraction techniques (Bromiley et al., 2009).

The rotoPEC was placed onto a custom-built stage which was able to move in X,Y, and Z directions to align the stage with the X-ray beam. A diffraction system was in place which included soller slits purpose built for use with Paris-Edinburgh cells (Mezouar, Faure, et al., 2002), a large diffraction plate and beam stop, with a simple macro control to toggle between imaging mode and diffraction mode (see section 2.3).

The ID27 beamline is used extensively for radiography and diffraction, but has rarely been used for tomography. During phase 1, an automated system was set up to couple the X-ray camera with the rotoPEC software controlling the anvil motors. The coupled system allows a projection to be taken for incremental angles of rotation (e.g. every 0.02°). This allowed the collection of a defined number of projections over 180°, without the need to adjust the camera wait time if there was a change in the speed of anvil rotation. This is more accurate than the simple timing technique used at Diamond I12, but the technique initially took several days to set up.

Scans and scan conditions are given in table 5.3. Exposure time and beam energy were adapted depending on the attenuation of the material used. Additional flat-field scans and dark current scans were taken before and after each scan. Reconstruction was carried out using the University of Ghent's Octopus 8.6 software, as licensed through the University of Edinburgh (Dierick et al., 2004). Simple 2D radiography was also used in some cases to track movement of the rotoPEC anvils and check for migration of melt within the sample, in which case flat fields and dark currents were taken to normalise the images, also using Octopus 8.6 software.

Beam wavelength used was 37 Angstroms, equivalent to ~33kV beam energy. Exposure time for all projections was 100ms.

Table 5.3 shows the samples produced during both phases of beamtime at ID27 at ESRF.

	Sample Name	Composition	Capsule	Max Power / W	Est. Temperature / K	max pump P /bars	Est. sample P / GPa	Duration* / min	Comments
Phase I	MgFe1	20vol% FeS +synthetic Ol	MgO (off-centre)	350	1700	110			Quenched overnight. Minor Blowout after 2nd heating.
	MgBa1	Hf-doped basalt (100%)	MgO (centre)	230	1500	100			Only reached 240W due to blowout.
	OlBa1	20vol% Hf-doped basalt in natural Olivine	Synthetic Ol dual capsule	340	1600	120	2		V slow heating (over 16 hours). Left overnight at 270W.
	OlBa2**	20vol%* Hf-doped basalt in natural Olivine	Synthetic Ol dual capsule	400	~2000	120	2	240	Heated over 3 hours. Movement seen in this sample!
Phase II	Au-Mg-1	MgO + 4vol% Au (/37%)	MgO dual capsule	300	1150	140	5		blow-out before max. temperature reached
	AuMg2	MgO + ~2vol% Au (/20%)*	MgO dual capsule	560	1700	100	2.5		BN spacers led to difficulty heating sample interior? Gasket softened and anvils closed before melting of gold was achieved.
	AuMg3	MgO + ~2vol% Au (/20%)*	MgO dual capsule	280	1500	100	2.5		blow-out before max. temperature reached
	AuMg4	MgO + ~2vol% Au (/20%)*	MgO dual capsule in MgO capsule	250	1500	100	2.5		blow-out before max. temperature reached
	AuBN1**	BN + ~2vol% Au (/20%)*	BN dual capsule in BN capsule	400	1800	100	2.5	420	Successful melting!

Table 5.3: A summary of samples produced in two phases of work carried out at ID27, ESRF, Grenoble. A large number of samples failed to reach melting temperatures before blow-outs occurred. Starred experiments indicate successful melting of sample material. These are the samples used for further analysis. P,T in Phase I are estimates from previous calibration. Phase II P,T are taken from direct estimates based on *in-situ* gold and MgO diffraction patterns.

5.3 Results and discussion

5.3.1 Diamond I12 - Investigating grain-scale melt migration

Over the course of beamtime at DIAMOND I12, we were successful in producing tomographic reconstructions during several experimental series, producing time-series datasets of samples under high P-T over several hours of annealing, and subsequently over step-wise deformation of the samples at a range of strain-rates. The following section outlines the results of these experiments, and limitations of observations made during this first phase of experiments.

Quality of tomographic scans

Scans produced at DIAMOND produced sharp, high quality tomographic reconstructions with a voxel size of ~2μm, which is high enough to track any significant changes in melt texture should they take place over the course of an experiment. However, the sharpness of individual scans was variable, which caused problems tracing very subtle changes in a quantitative manner (see section 5.3.1). Examples of reconstructions produced at I12 are shown in Figure 5.4, accompanied by sinograms of the slices prior to reconstruction.

Scans were carried out at rtp, high pressure and low temperature, at high temperature and pressure, and at high temperature and pressure with ongoing deformation. Scan quality was compared in order to find conditions which produced the best reconstructions. Results indicate that the sharpest scans are produced when the sample is under concurrent high pressure and temperature. All scans suffer some reduction in quality from an inherent 'judder' presumably caused by a stepwise motion of the anvils in the rotoPEC. This is most evident in the sinograms, where the regular movement can be seen to create a 'frilly' edge to sinogram image (Figure 5.4). Within each sinogram, each 1D horizontal line of pixels represents a single projection at a given angle. The wavelike edge of the sinogram therefore represents a systematic 'back and forth' translation of the whole sample volume as the motors rotate the stack. The wave is more pronounced in the low temperature scan than at high temperatures, potentially because the sample has a more elastic response to motion at lower temperatures. This is reflected in the quality of the reconstructed slice. In the syn-deformation sinogram, the waveform is more asymmetric, and overall the lines are less sharp, which is probably due to the inherent movement of the sample during the tomographic scan, causing further blurring in the scan reconstructions (Figure 5.4 C.). Movement is not necessarily redistribution of melt, but is inherently caused by motion from the full sample gasket deforming as the upper and lower anvils rotate at different speeds.

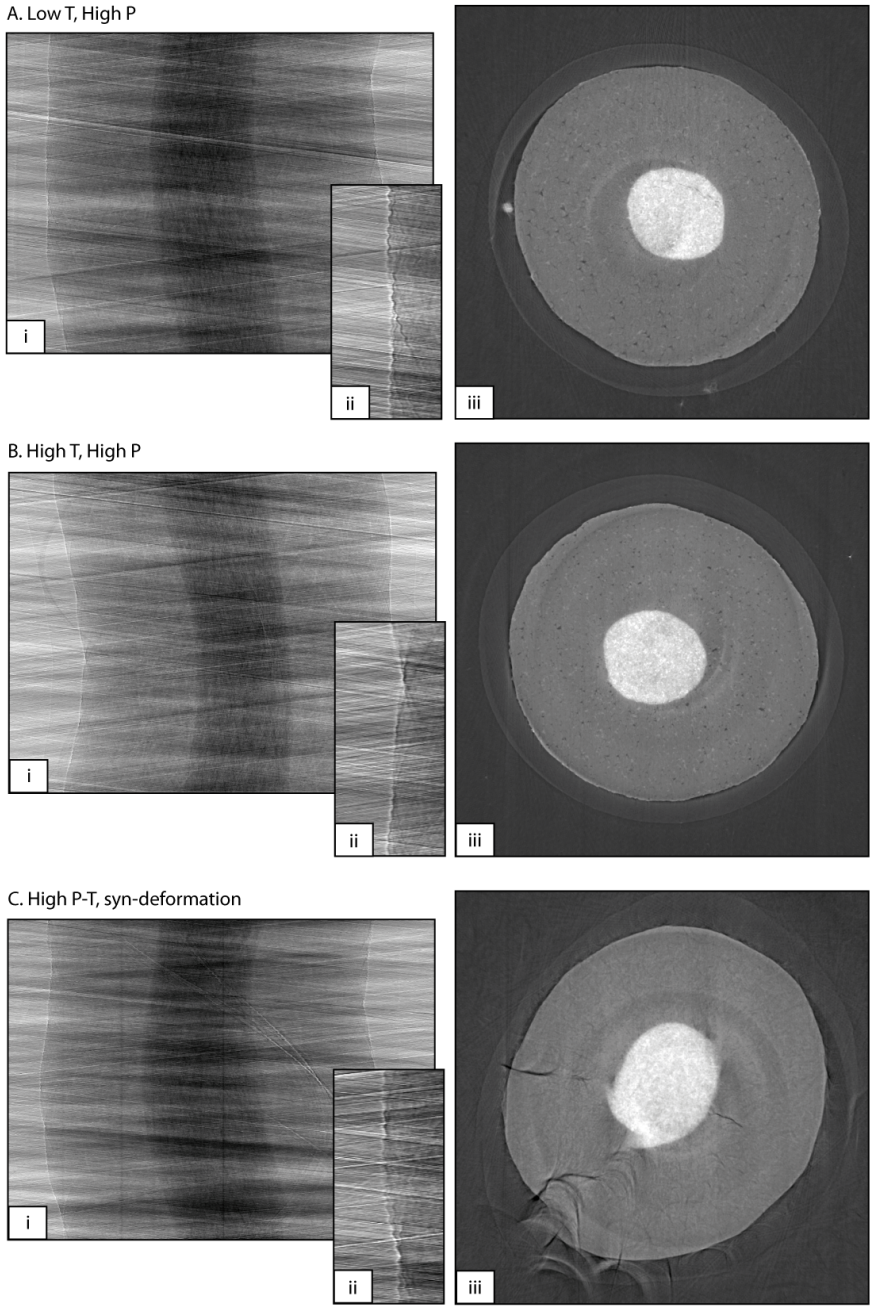

Figure 5.4: Examples of scan quality from a number of scans made of sample DLS3 during DIAMOND beamtime for A. a high pressure, low temperature scan, B. a high pressure, high temperature scan and C. a tomographic scan taken while deformation was ongoing. In each case, i. is the intermediate sinogram image of the image (see section 1.2.2), ii. is a close-up of the sinogram edge showing the systematic 'frilly edge' inherent in each image, iii. is the resulting slice from each sinogram. See text for details.

Textural changes with annealing and deformation

Figures 5.5 - 5.8 show example orthogonal slices of tomographic reconstructions from experimental samples DLS3-6, as a time series over the course of each experiment. Using ImageJ (Abramoff et al., 2004) for post-reconstruction processing, scans have been rotated to ensure the same sample orientation for each orthogonal slice, and greyscale ranges have been normalised for each scan. In addition, a quick volume reconstruction of the central melt-rich zone has been created by using the 'magic wand' seeding tool combined with global thresholding to pick out the central bright volume from the Avizo Fire^{TM} segmentation tool kit.

Due to the large melt fraction in the centre of the sample, theoretically significantly above the estimated percolation threshold for FeS-olivine systems (Yoshino et al., 2004), and the large strain-rates used during deformation, we were expecting to see significant changes in melt texture and potential sample-scale melt migration taking place. However, no significant movement was observed relative to the solid matrix. Instead, overall ductile deformation of the sample, as well as macroscopic brittle fractures were observed during deformation. If any melt migration was occurring, it was on a very fine grain-scale and therefore not immediately observable in reconstructions. Details of results from individual samples are given in the figure captions. Overall, deformation of 20rpm ($10^{-5}s^{-1}$ strain-rate) or less appears to lead to ductile deformation of the sample gasket, while 100rpm deformation ($10^{-3}s^{-1}$) causes brittle fracturing. The reduction in height (in z direction) observed in each sample is caused by the closure of the anvils during the course of the experiment due to softening and flow of the gasket material.

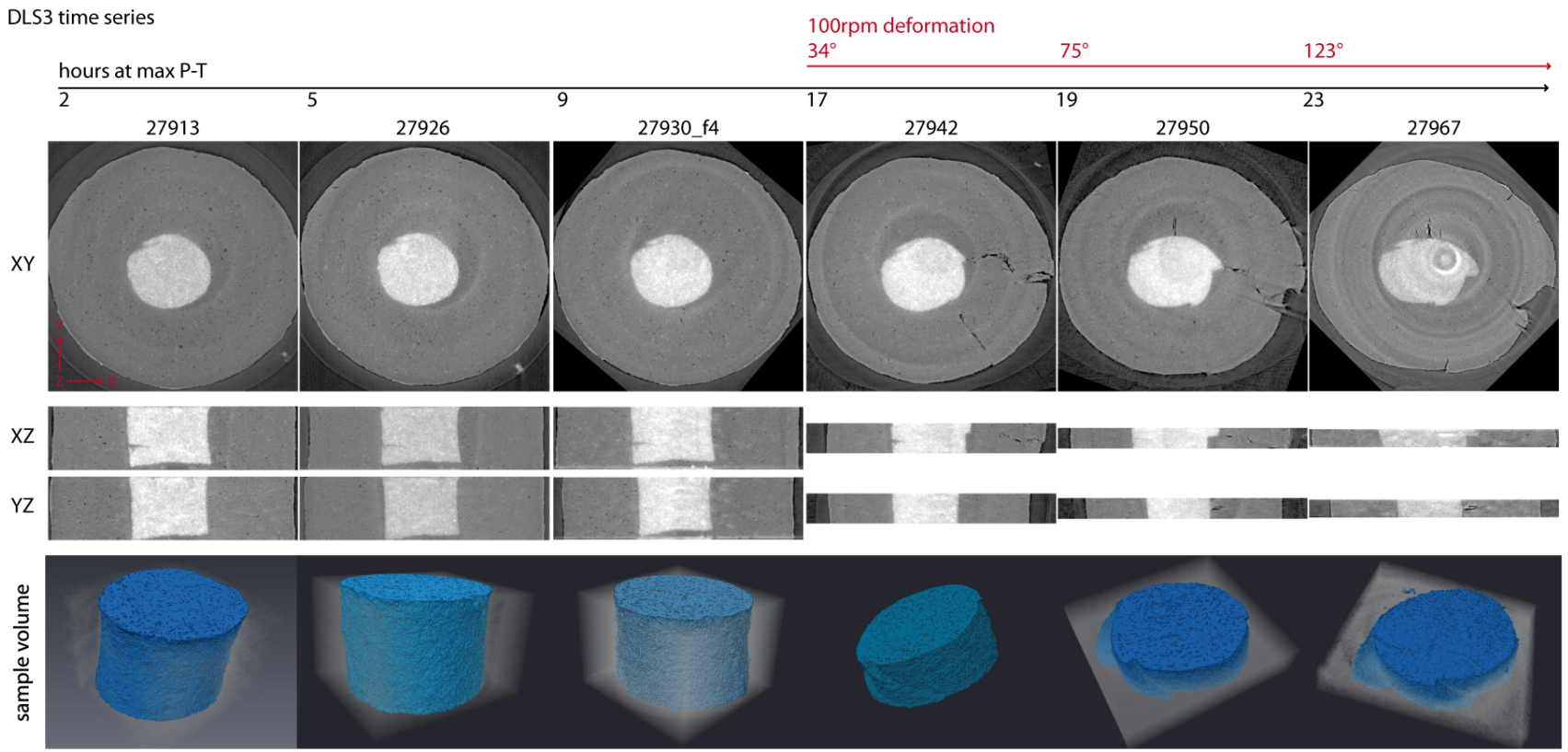

Figure 5.5: Textural changes in sample DLS3, shown by orthogonal slices through tomographic reconstructions, and the segmented central melt-rich zone to show changes in 3D shape. Orthogonal slices are zoomed into the central sample portion (field of view is 3x3mm) - white areas are FeS melt, grey is forsterite and dark grey surrounding the central capsule is graphite capsule and BN gasket material. There are no clear changes occurring with annealing, and no evidence for melt migrating from the central area. The addition of 100rpm deformation leads to brittle fractures within the sample leading to discrete changes the shape of the capsule, including the melt rich sample volume.

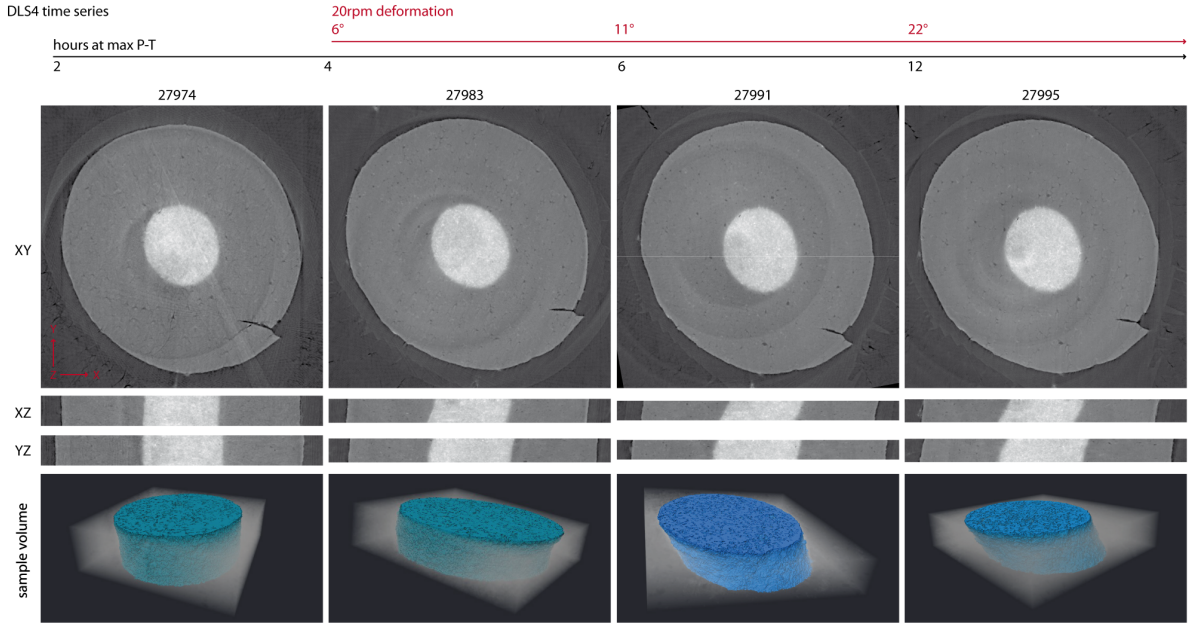

Figure 5.6: Textural changes in sample DLS4 (key as in Fig 5.5) In this case, a fracture (bottom left of capsule on X-Y slice) is present from early on during the experiment (presumably created during initial compaction). The fracture does not widen, instead appears to heal over the course of the experiment. The central melt-rich volume undergoes a significant change in shape, suggesting a ductile response to deformation. Again, there is no evidence of melt migrating away from the melt-rich zone.

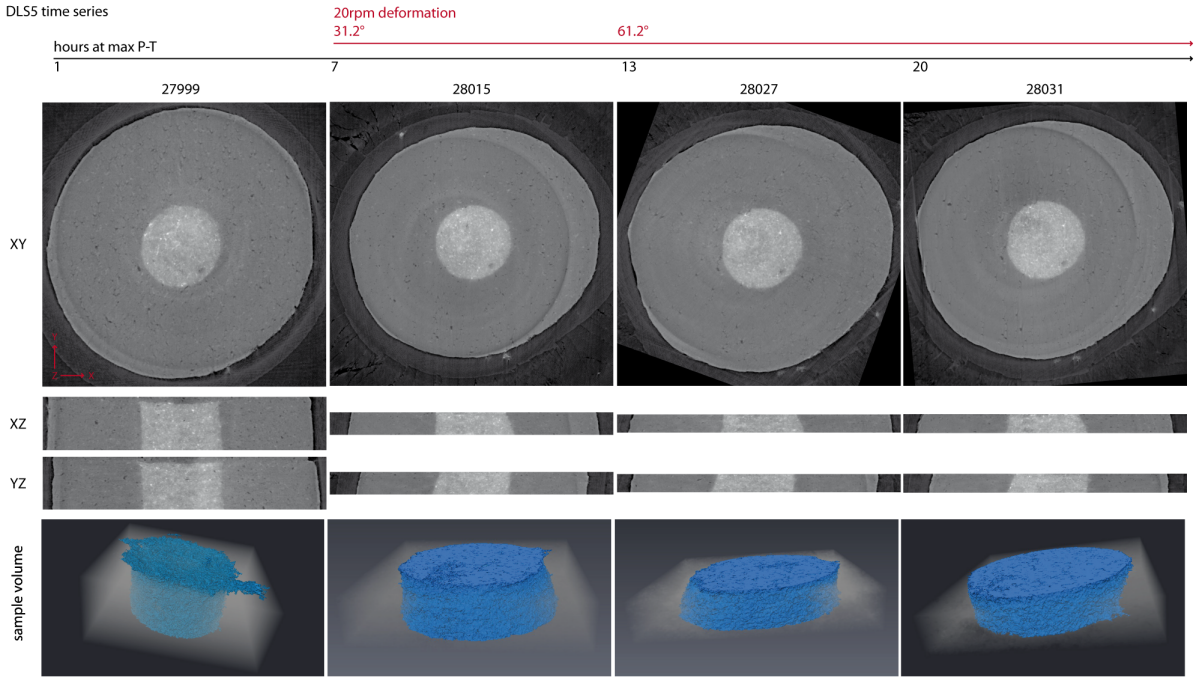

Figure 5.7: Textural changes in sample DLS5, key as in Fig 5.5. Again the sample undergoes ductile deformation in response to the 20rpm rotation speed. There is a change in overall capsule shape, as well as the shape of the central melt rich zone. The first scan shows some metal-rich material is smeared out along the capsule lid (top of sample volume shown in 3D reconstruction), but this area moves quickly out of the field of view as the anvils close.

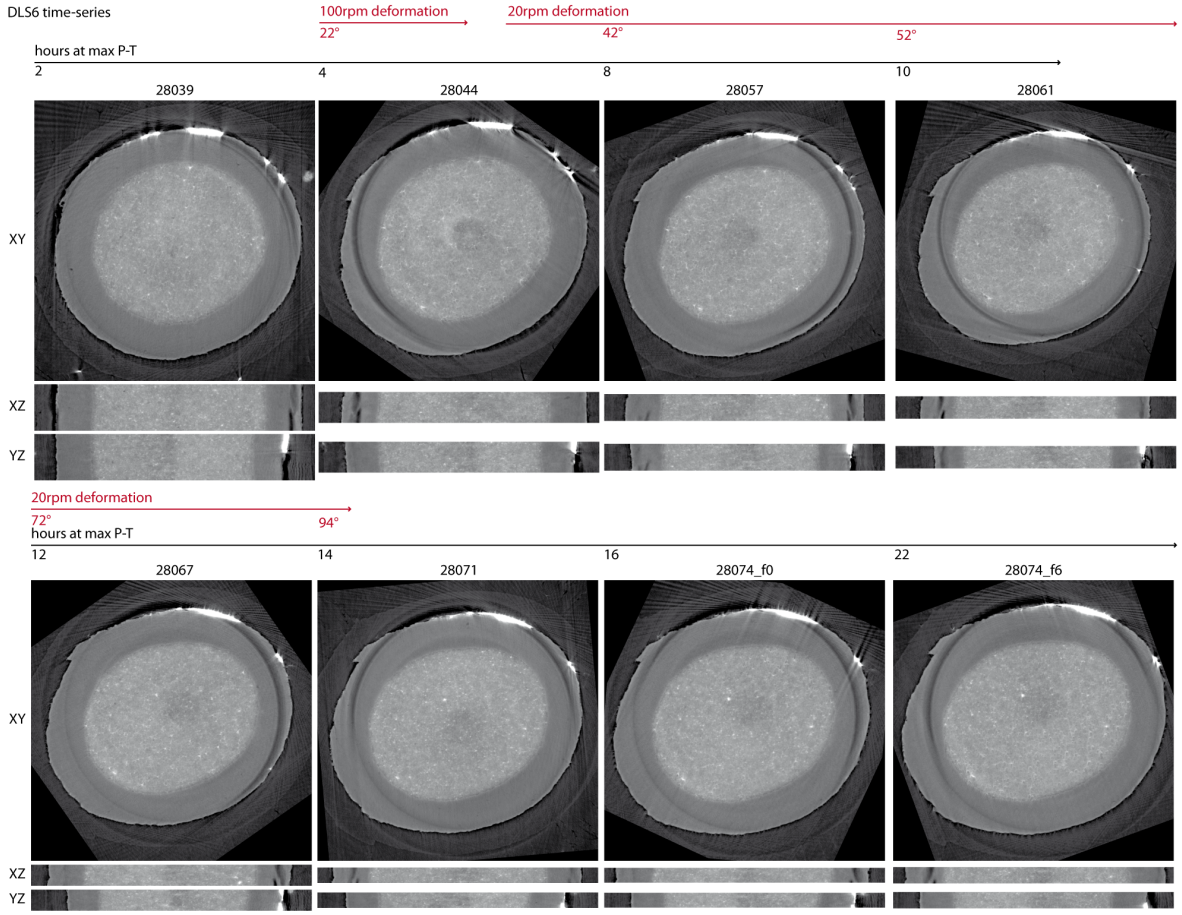

Figure 5.8: Textural changes in sample DLS6, key as in Fig 5.5. The larger sample volume is evident in these scans (a standard MgO capsule with a 2x2mm cylinder central hole was used in this case). There is an additional bright phase present on the capsule edge which was emplaced by accidental contamination. Despite an initial deformation of 100rpm we do not see significant brittle response to deformation in this sample (although the majority of deformation is carried out at 20rpm). The lower metallic vol% (10vol%) in the sample allows a better view of the textures within the melt-rich zone. Particularly evident is the lack of change in textures within the sample between scans 28067 and 28074_f6 where the same large melt pockets can be picked out from one scan to the next with no significant change in their location. This suggests very little melt movement has taken place over 10 hours at (theoretically) high P-T.

Quantitative analysis of particle shape

Although no large scale movement was observed in the scans, it is possible that melt was re-organising itself on a local grain-scale in a way that is too subtle to see on immediate examination of tomographic reconstructions. Quantitative analysis was carried out on binarised images of the central melt portion to test for such subtle changes, using the 3D shape factor (Shape_VA3D), which uses a ratio of surface area and volume of a voxel cluster to assess how concave or convex a segmented volume is, and may be used as a proxy for connectivity (see section 3.3.4).

To ensure effective comparison could be made between scans, image processing steps were kept constant for each scan. The procedure for processing tomographic scans was carried out using Avizo8 Fire^{TM} as follows:

1. Crop scan to a volume of interest, which was the area of the sample visible between the two closing anvils at any time, and unaffected by significant artefacts caused by close proximity to the anvils.

2. Use global threshold segmentation (methods section 2.3.5) to isolate the central melt-rich area of the sample (using a 'remove islands' function to ensure the full sample area was selected)

3. Use a top-hat segmentation tool on this central melt-rich portion to highlight local greyscale maxima and thereby segment volumes inferred to be melt-filled pockets. The same segmentation kernel was used in each scan to ensure similar areas were segmented, but the exact threshold parameter was varied for each scan to ensure the same vol% of melt was segmented in each case. Total melt % segmented was chosen to be around half of the true volume % initially inserted into the capsule. This was to ensure the full segmented volume was definitely melt, and that blurring and partial volume artefacts were less likely to affect quantitative results.

4. Carry out label analysis on the segmented melt to gain information on particle volume, area, aspect ratio and a value for the Shape_VA3D parameter.

5. Create a graph of volume vs. Shape_VA3D to compare the relationship between melt pocket size and concavity over time in each experimental sample.

Figures 5.9 to 5.12 show results of particle analysis carried out for each DLS sample using a series of scans from different times during the experiment. In each case, the smallest volumes, numbering fewer than ~10voxels (25μm), show artificial results produced by the cubic nature of voxels, therefore trends are best observed in particles of larger volume.

If connectivity is enhanced during the experiment due to deformation, this should be reflected in each graph by a shallowing of the gradient of the volume-particle shape curve

(i.e. smaller volumes will have more concave surfaces, so larger shape factor values). In fact, although changes are observed over time during experiments, each sample appears to show a different trend, or very little change (see figure captions), making it difficult to draw conclusions regarding connectivity in samples.

In particular, it becomes apparent what a large effect scan quality can have on segmentation. Blurring, star and ring artefacts are difficult to avoid in segmentation and may contribute to skewing a dataset significantly. If all datasets are used, any potential trends can be obscured by differences in scan quality. For example, sample DLS3 shows a slight increase in gradient as deformation progresses (Figure 5.9 D-F), implying a decrease in connectivity. However, comparing these results to orthogonal slices in figure 5.5 it becomes apparent that the quality of scans significantly decreases with onset of deformation. The change in trend most likely reflects the reduction in scan quality rather than a true change in particle shape.

Sample DLS 4 has a sharper dataset (5.6) and shows the clearest change across the time-series as seen in Figure 5.10. A large proportion of melt in the melt-rich zone appears to be initially interconnected in one large volume of metal, and over the course of the experiment the largest volume grows, seemingly at the expense of particles of moderate volume and shape factor value, which could be inferred as observing these particles being taken up in the largest interconnected volume. However, this effect could also be created by compaction moving particles closer together, making them join up artificially due to partial volume effects.

A technique like this could be used to compare future datasets however, particularly if the quality and sharpness of scans improves and becomes more reliable across datasets.

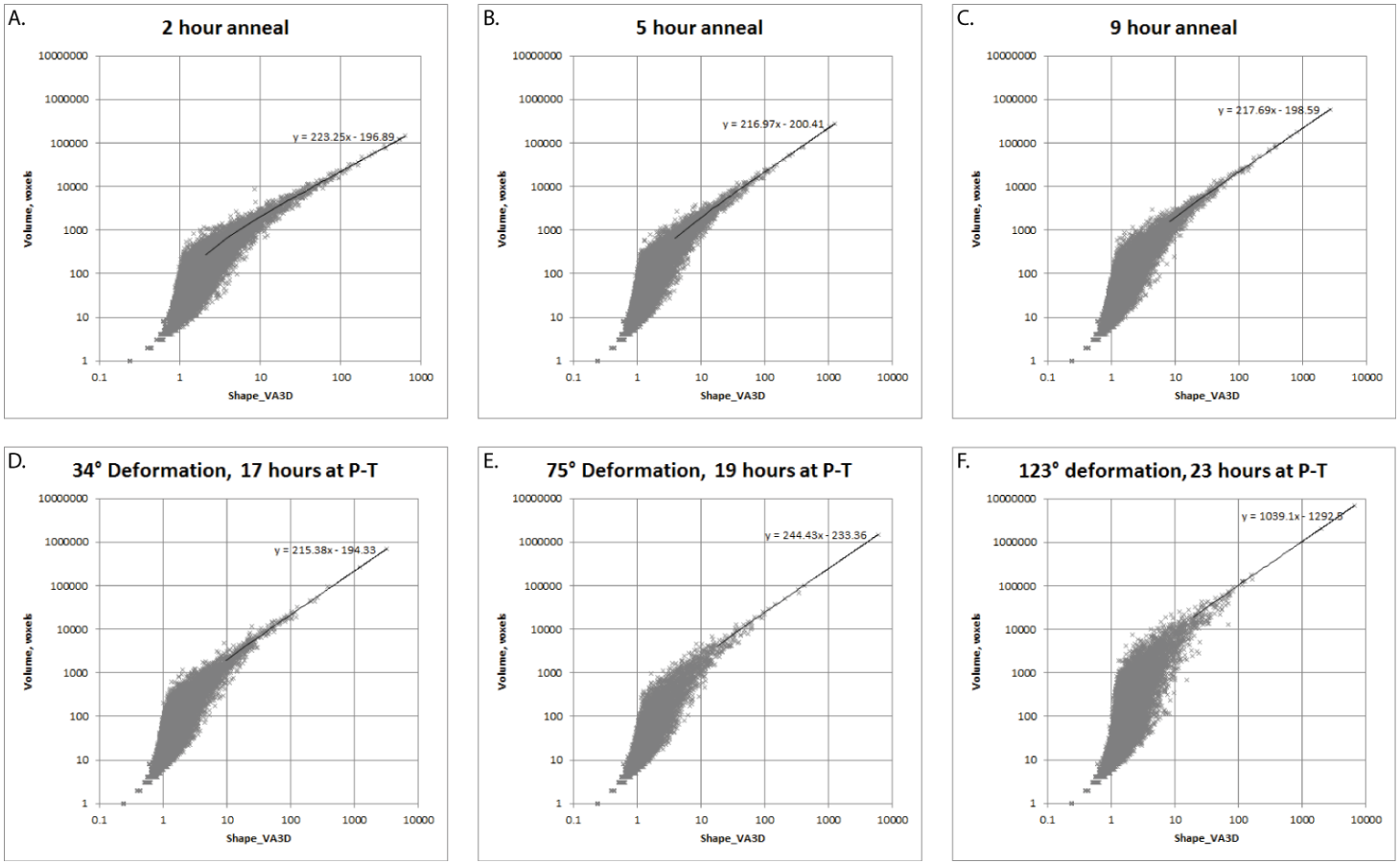

Figure 5.9: Graphs of particle shape factor vs. particle volume across segmented melt volumes within sample DLS3. A high shape factor value suggests a more concave shape and therefore potentially greater connectivity. A trend is fitted to the graph to show any potential changes in slope occurring during the experiment. With ongoing deformation, the slope of the graph appears to increase, which would suggest larger particles are becoming more convex in shape. However, by comparison to Figure 5.5 we can see that the final figures also show a significant blurring and an increase in ring artefacts. Therefore this change in segmented particle shape could be due to the loss of scan quality over the course of the experiment.

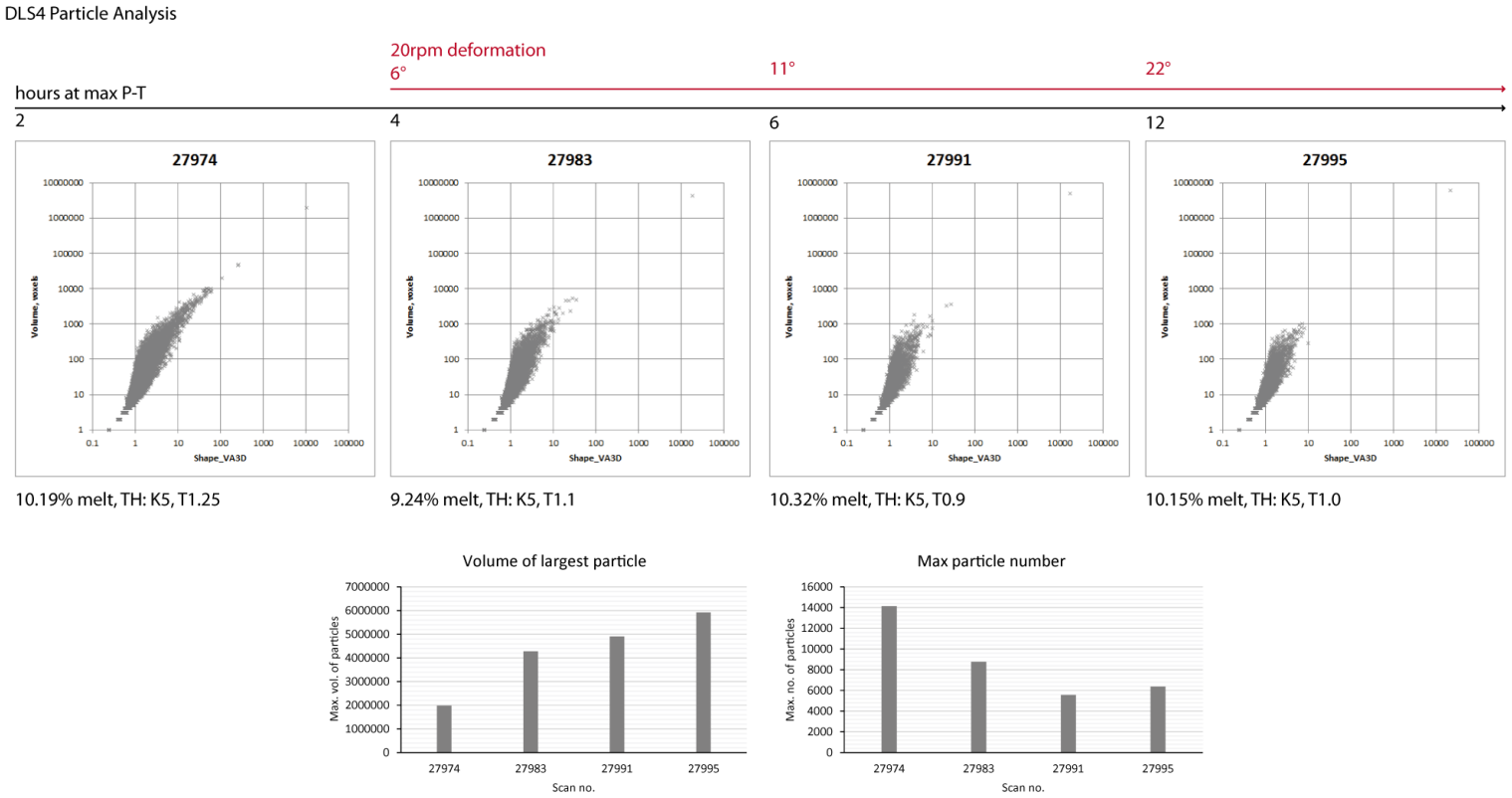

Figure 5.10: Graphs of particle shape factor vs. particle volume across segmented melt volumes within sample DLS3. A loss in the number of particles of moderate shape factor (~10-100) is observed at the same time as the largest volume of particle increases in size and concavity. This is the strongest evidence observed for enhanced connectivity during an experiment in this series. This effect could however be caused by simple compaction (see text)

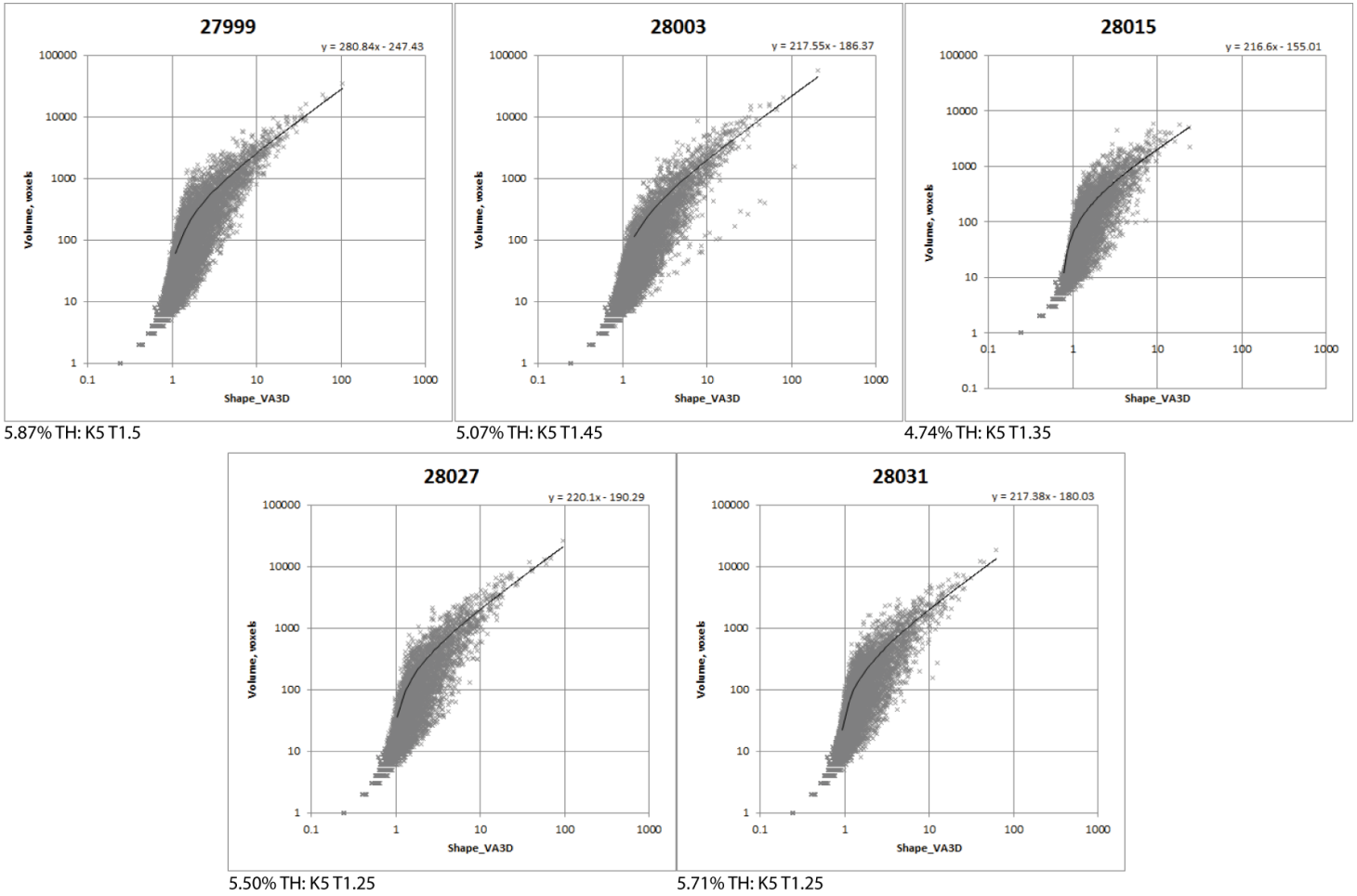

Figure 5.11: Graphs of particle shape factor vs. particle volume across segmented melt volumes within sample DLS3. Sample DLS5 shows very little change in volume-shape trend over annealing or deformation, although there is a subtle drop in gradient overall, particularly at the beginning of the experiment. A deviation of some particles from the normal trend is observed in 28003, but these are not seen in the remaining analysis, suggesting they may be caused by an artefact in the CT scan such as accidental segmentation of ring artefacts.

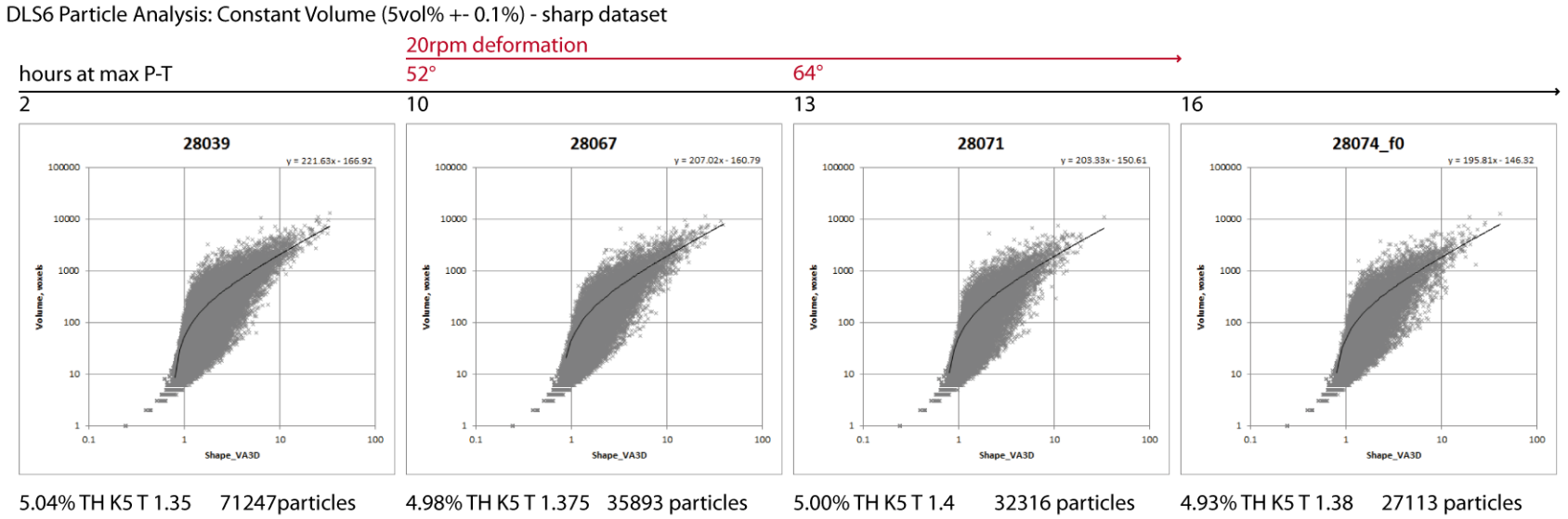

Figure 5.12: Graphs of particle shape factor vs. particle volume across segmented melt volumes within sample DLS3. Only the four sharpest scans were chosen to remove the effect of scan quality on analysis results. There is very little change in particle shape with annealing and time. There is a subtle reduction in gradient, which may suggest an increase in connectivity, but the change is not signficiant enough on its own to draw firm conclusions.

Quantitative analysis of fabric development

Quant3D (Ketcham, 2005b) analysis was carried out on binarised images (see thresholding process above) in order to test for development and orientation of fabric within the samples by annealing or deformation. A detailed description of the software is given in section 3.3.3. The Star Length Distribution (SLD) calculates the mean length of an object in various orientations, from a number of arbitrarily generated points within the dataset. Lengths from 2000 points were analysed over 513 orientations, of uniform distribution. The rose diagram reflects the distribution of lengths at these different orientations. The SVD (star volume distribution) works similarly but uses 3D cones emanating from points of origin, rather than lines, therefore describing more of the texture of the binarised particles. An anisotropic fabric will produce an anisotropic rose diagram. Neither analysis should be affected by the total shape of the dataset. Results of this analysis are shown in Figures 5.13 - 5.16. In each rose diagram, the up- down axis is the Z axis of the sample (i.e. axis of rotation during tomographic scans). The horizontal plane is parallel to deformation.

All samples show flattening of fabrics during experiments, suggesting particles may become more elongate aligned parallel to the plane of torsional deformation (perpendicular to compaction). Some flattening occurs before the onset of deformation, although it becomes more pronounced after onset of deformation (e.g. figure 5.13). There is no clear evidence that a fabric is developed at an angle to the shear plane, therefore it is unclear whether the fabric developed is similar to development of shear bands in deformation experiments of partial melts (Kohlstedt and Holtzman, 2009). Anisotropic alignment of melt particles is not expected to occur, as torsional deformation of a cylindrical sample means the orientation of stress is not constant. In fact this may explain the reduction of anisotropy observed in samples DLS4 and DLS5. Sample DLS3 shows the development of anisotropy over the course of the experiment, although this could be explained by the development of the large scale brittle fracture observed to develop in the sample, which may skew the SVD and SLD results.

Overall, the development of a fabric suggests that the material in the samples is responding in some way to compaction and deformation over the course of these experiments, although it is not clear whether this is due to alignment of melt, or deformation of solid multi-phase material.

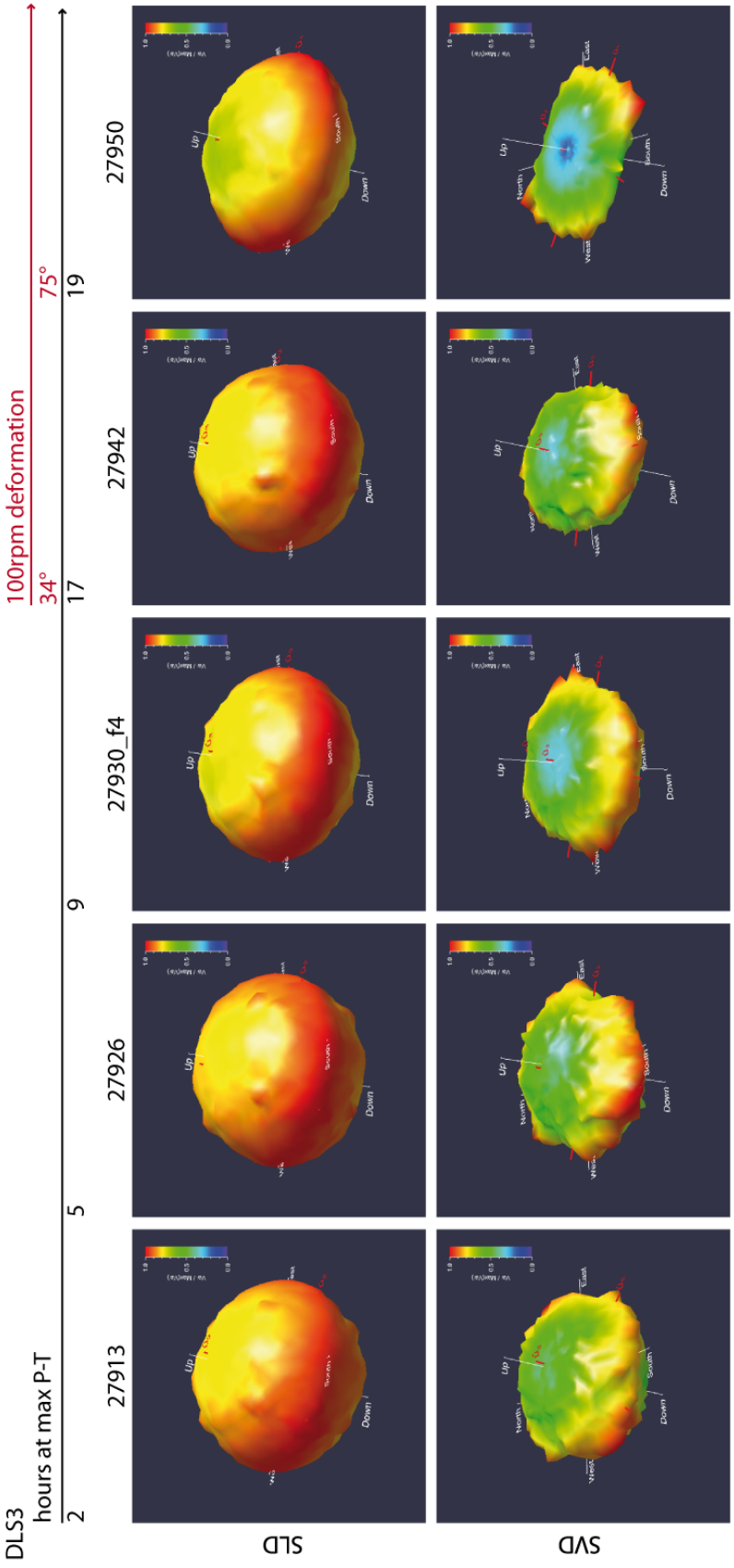

Figure 5.13: Fabric analysis of sample DLS3 using Quant 3D software (see section 3.3.3 for details of method). Both fabric indicators suggest a horizontal fabric may be created in the particles during annealing which is enhanced during deformation.

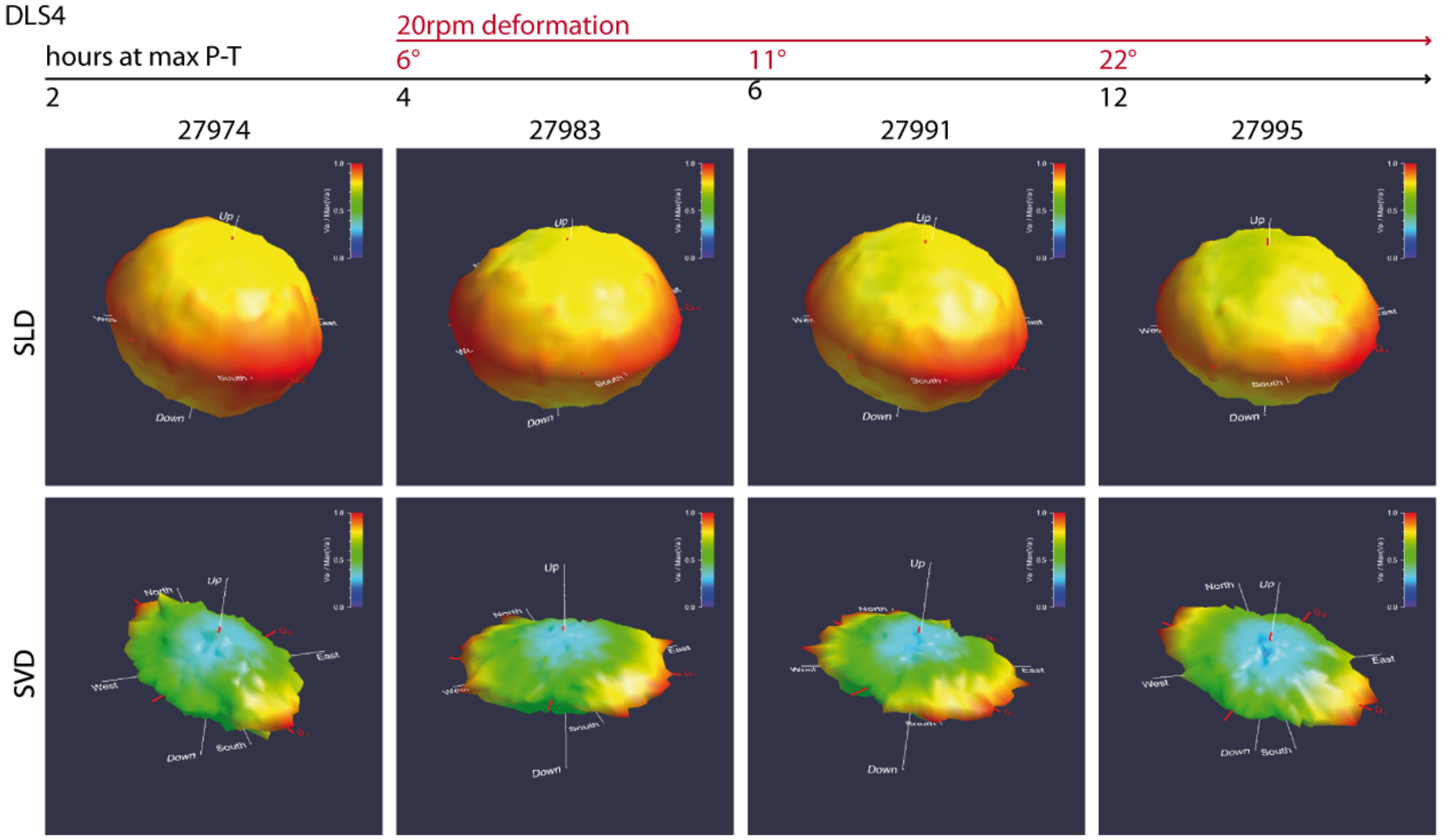

Figure 5.14: Fabric analysis of sample DLS4 using Quant 3D software. Again a very subtle flattening is observed over the course of the experiment, but in this case there is already a subtle anisotropy /fabric after annealing which does not change significantly during the experiment.

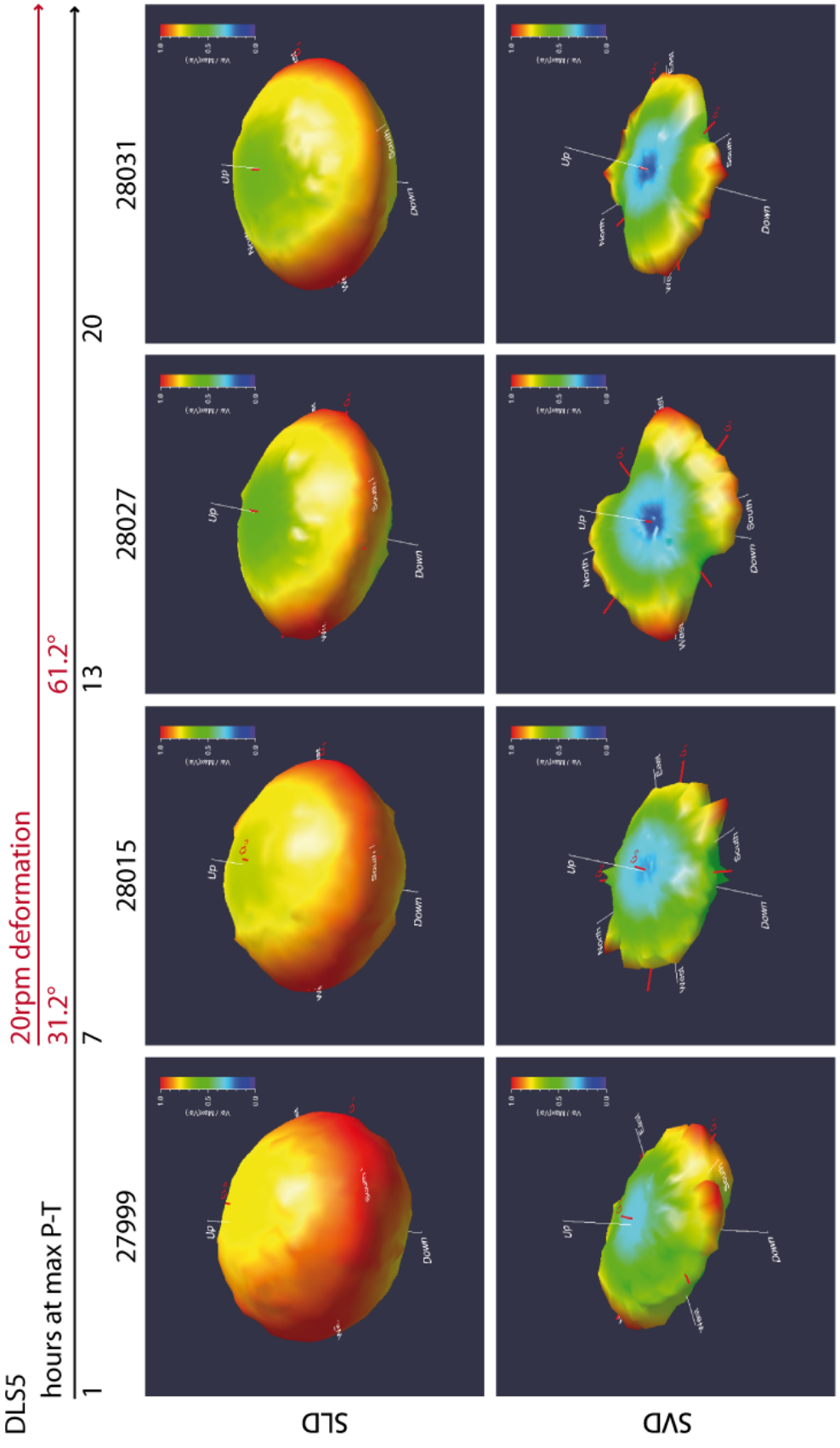

Figure 5.15: Fabric analysis of sample DLS5 using Quant 3D software. As well as an overall flattening suggesting development of a horizontal fabric parallel to the shear plane, the SVD rose diagram suggests there is a movement away from an initial anisotropy towards the NW/SE and a move towards a more even distribution of orientations, potentially with a subtle extension of particles in the West-East direction.

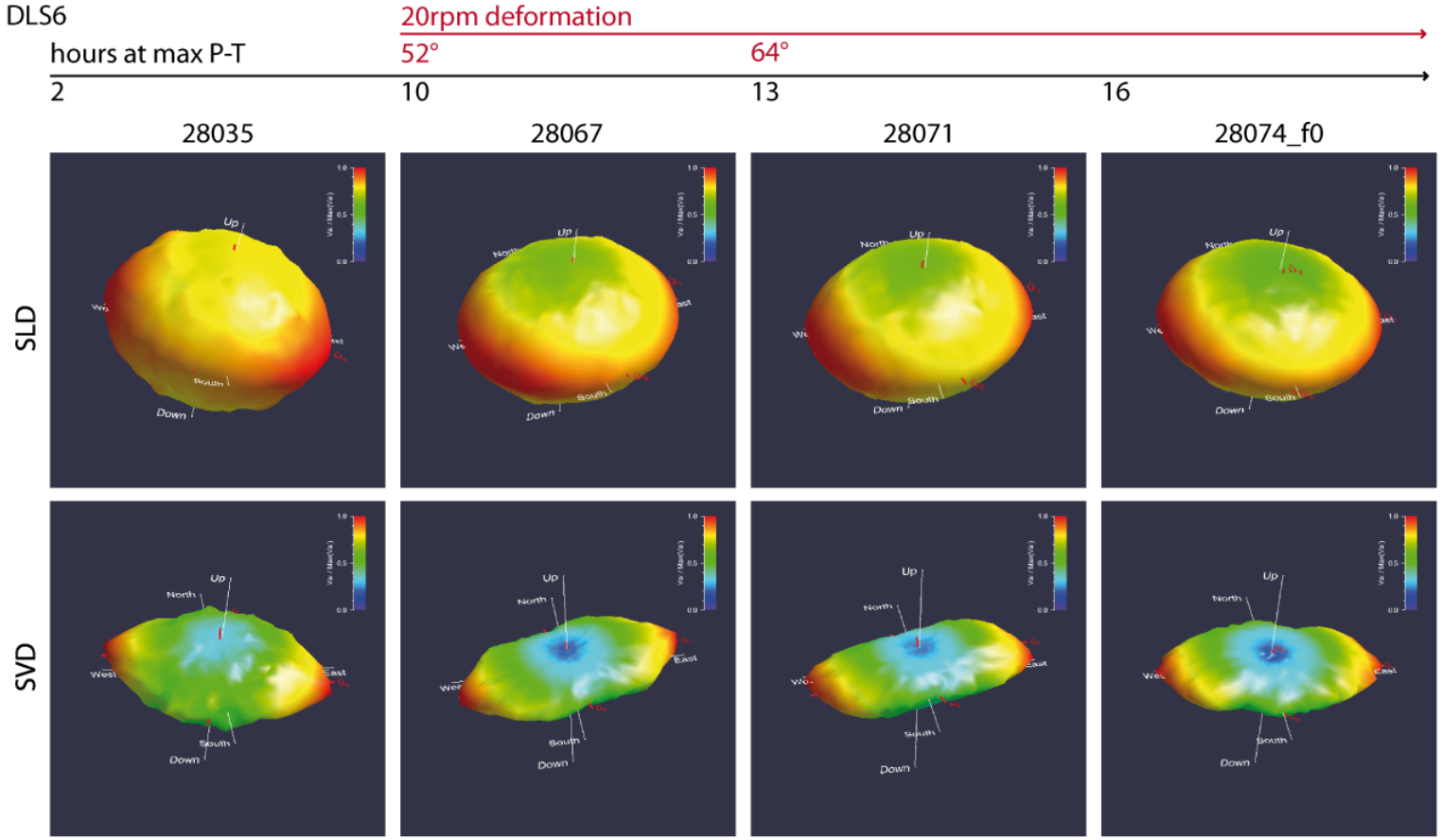

Figure 5.16: Fabric analysis of sample DLS5 using Quant 3D software. Sample DLS6 shows a similar flattening of the course of the experiment, and a potential strenghtening of a pre-existing fabric over the course of the experiment. The final scan represents continued annealing after deformation, and there is a subtle reduction in the aspect ration of the SVD rose diagram. This may be a reflection of the fabric produced during deformation becoming less strong during the annealing process. However, the change is very subtle, so could be caused by minor changes in segmentation / differences in scan quality.

SEM analysis and groundtruthing

Only two samples (DLS5, DLS6) were recovered sufficiently to conduct later SEM analysis and ground-truth 3D textures observed in tomographic scans with very high resolution 2D backscatter imaging of a quenched and polished cross-section. DLS 3 and DLS4 were both affected by blow-outs which meant the sample was either not recovered, or the textural changes occurring during the blowout would have been too great to provide meaningful ground-truthing for the previous time-series. Both recovered samples were cut as tangential slices to reveal a slice essentially affected by simple shear deformation. Figures 5.17 and 5.18 show examples of the textures observed. BSE imaging highlights some important features to constrain processes during these experiments

1. There is no clear evidence of any FeS migrating from the initial melt rich zone into the surrounding olivine capsule, even at the high resolution of BSE imaging.

2. There is a fabric observable in the tangential slice of DLS 5, sub-parallel to the horizontal direction of shear (Figure 5.17B.). This supports the idea that the changes in SLD and SVD shown by Quant3D analysis are caused by fabric development. DLS6 does not show a strong fabric.

3. A noticable difference to previous experiments is the very fine grain-size of both sample and capsule - grain size of synthetic olivine and metallic powder is so fine that even BSE imaging, with a resolution on the nm scale has difficulty resolving individual grain-boundary geometries. For this reason it is difficult to confirm even with high resolution BSE images whether the FeS was molten or not.

4. The bright rims of metal (iron) at the edges of the capsule in DLS6, emplaced as a result of accidental contamination, do show some evidence of melting with the presence of veins and intrusion into the outer Boron epoxy gasket (Figure 5.18 B.) which suggests the melting point of iron was reached during these experiments, at least at the capsule edges.

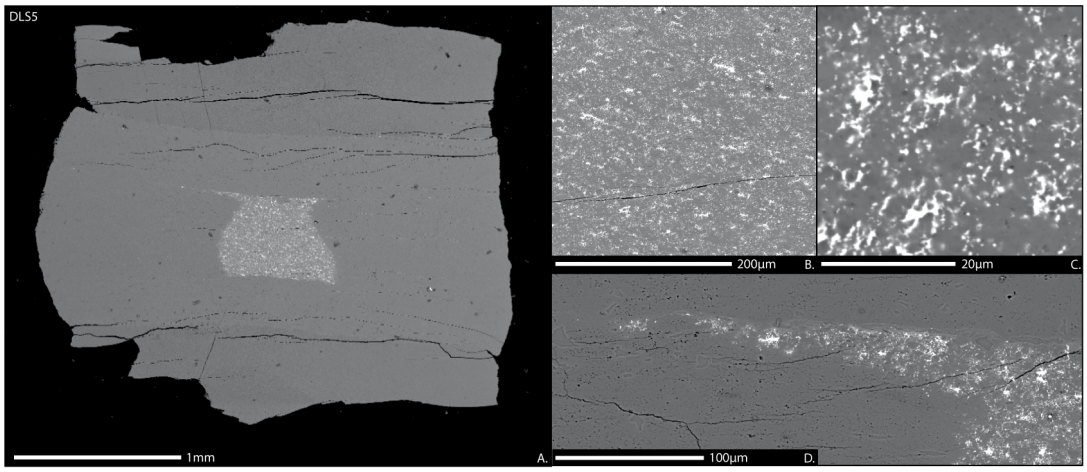

Figure 5.17: BSE images of quenched recovered sample DLS5. A. whole sample including capsule edge. B. An example of texture within the initial melt-rich zone, revealing a subtle fabric sub-parallel to the shear direction. C. A close-up of sample textures. D. A close-up of sample material within the crack between capsule and capsule lid, initially interpreted to be potential evidence for melt migration along a plane of weakness, but here shown to be caused by the smearing out of starting material (including olivine grains) rather than caused by actual melt migration.

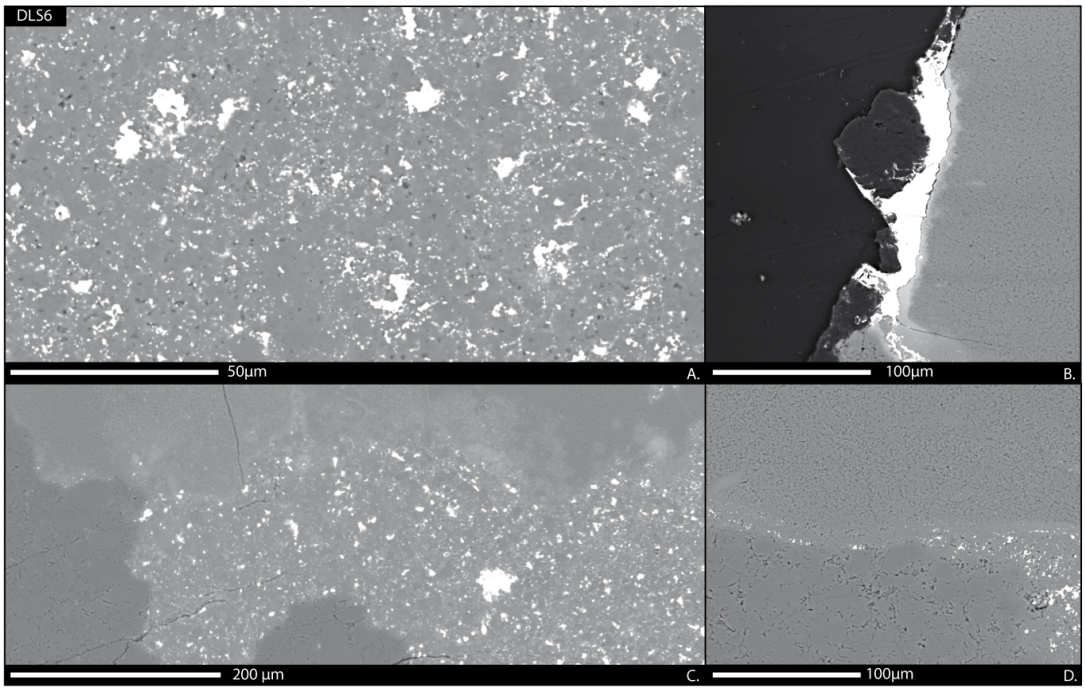

Figure 5.18: BSE images of quenched recovered sample DLS6. A. An example of textures from the central melt-rich zone. The fine-grained nature of material is evident. B. Textures observed in the metallic (iron) rim between the olivine capsule (grey, right) and the boron epoxy gasket (dark grey, left). There is evidence of veining and intrusion of the metal into surrounding capsules, suggesting the metal has melted over the course of the experiment.

Discussion

Although experiments carried out at DIAMOND I12 show the potential for *in-situ* tomographic scans using the rotoPEC equipment, achieving high quality reconstructions of whole samples and melt geometry, the lack of textural changes within samples over the course of the experiments was surprising. No clear movement was observed of the FeS metal away from the central melt-rich zone, despite large melt fractions of iron which should encourage melt mobility and potentially lead to melt pressure gradients even without the effect of deformation (Yoshino et al., 2004).

The lack of motion of FeS melt could be explained by a number of different hypotheses:

- The FeS was not molten. A distinct limitation of rotoPEC equipment is the lack of direct measures of temperature and pressure within the sample itself. During DIAMOND experiments, the lack of availability of X-ray diffraction meant that temperature within the sample was estimated from previous calibration experiments carried out at ESRF ID27. The strongest evidence that some samples were not at high temperature/pressure come from the brittle response to deformation, leading to open fissures and fractures, evident as dark areas in tomographic slices. In some cases these features are not immediately filled with melt where you may expect them to be (e.g. figure 5.5, scans 27942 and 27950). SEM analysis shows evidence of iron melt at least at the capsule edge (Figure 5.18C), but the very fine-grained nature of the starting material makes it difficult to conclude with certainty that the central portion of metal had melted.

- FeS was molten, but gradients within the sample were insufficient to cause melt migration. Initial capsules were designed with melt in the centre of the sample, assuming that melt would migrate outward due to pressure gradients from melt-rich to melt-poor zones (Kohlstedt and Holtzman, 2009). However, the centre of the capsule experiences the least deformation within a torsion experiment, therefore it is possible that deformation strain-rates in this portion of the sample were too low to affect melt geometry significantly, or that pressure gradients from torsional deformation drive flow towards the centre of the capsule (Kohlstedt, pers. comm.), therefore the gradient may even be acting to inhibit flow away from the sample centre.

- FeS was molten, but melt migration velocities were too slow to be observable over laboratory timescales. This hypothesis assumes that melt has the potential to be mobile and that pressure gradients did exist for melt to begin to move, but that we are unable to observe its motion due to low velocities. The fine-grained nature of the starting material could have contributed to decreasing mobility of melt pockets, as a small grain size will enhance the effect of interfacial tension to inhibit melt flow (Hustoft and Kohlstedt, 2006).

Successes and limitations

Work at Diamond demonstrated technically that tomography at in-situ high temperatures and pressures is feasible. Examples of quantitative textural analysis are shown which could potentially track changes in the sample should they occur. However, due to experimental limitations it is difficult to constrain reasons for lack of motion as discussed above.

It is clear that the lack of a direct measure of temperature from scans causes large uncertainties in textural interpretation, and this must be improved in order to draw real conclusions from these scans.

In addition, the fine grain sizes of starting materials, and potentially the capsule design itself may have inhibited movement of melt (if present) or reduced its velocity to too low a level to be observable in these experiments. Several adaptations in experimental design were carried out before the second phase of experiments, to try to increase the scale of movement within the sample and improve visualisation of this potential melt migration (see below).

5.3.2 ESRF 1 - basaltic melt migration along cracks

Experimental summary

The first phase of beamtime at ESRF ID27 was carried out in October 2013, only one week after beamtime at DIAMOND. Despite limited time between sessions, we were able to adapt the experiment taking into account the limitations observed during experiments at DIAMOND:

- basaltic melt used as a more mobile alternative to FeS, as it is known to have a low viscosity reflected in dihedral angle values of 25-50° (Kohlstedt, 1993), significantly below the theoretical threshold limit of 60°. Basalt was doped with Hf to improve contrast between crystals and melt, although the short time between beam-times meant we were unable to fully assess doping methods as described in section 4.2, and a preliminary mixture was used that was more heterogeneous.
- The capsule was adapted to the 'dual capsule' design (Figure 5.2 B.), to provide an existing central conduit for the melt to travel along preferentially and ensure melt migration takes place within the field of view of *in-situ* tomography. Migration is also more likely to take place on a larger scale that is resolvable in tomographic scans.
- The capsule design, and use of a more mobile melt, meant deformation was not necessarily required to observe melt movement, thereby reducing complexity of processes within the sample.

A distinct advantage of beamline ID27 was its X-ray diffraction capabilities, specifically designed for use with large volume Paris-Edinburgh presses (Mezouar, Faure, et al., 2002).

This allowed tracking of pressure and temperature increases, and unambiguous evidence for melting of material in the field of view, reducing uncertainty in assessing melt migration processes (section 2.4.1).

Several days were required to set up the rotoPEC with the beamline X-ray camera. Initial run failures and instability meant that we were unable to reach the melting point of the partial melt phases for a number of initial experiments (table 5.3), but with further experimental design optimisation we successfully imaged melt movement *in-situ* in 3D during the final experiment, OlBa2.

OlBa2 experimental summary and data collection

Sample OlBa2, containing 20vol% Hf-doped basalt within the central sample portion of the dual capsule design (made of synthetic olivine) was pressurised over half an hour to 120bars (~2GPa). An initial tomographic scan was taken at high pressure but low temperature to show starting geometry. The sample was heated slowly over the course of 5 hours, to an overall power of 400W, taking continuous diffraction patterns to track recrystallisation and look for evidence of melting (Figure 5.19). As diffraction scans showed that melting temperatures were being approached (Figure 5.19C), the set-up was switched to imaging mode and the X-ray camera left on to capture any potential melt movement. As it takes 5 minutes to toggle between the two modes this meant no further diffraction patterns were taken during onset of melting. When motion was observed by radiography it was very sudden. Over the course of no more than 10s, a highly attenuating near spherical volume of material appeared at the capsule edge where previously there had been only low attenuation capsule material, around 1mm away from the central sample zone containing the attenuating doped basalt. Unfortunately the movement was not recorded. Some further growth of this new attenuating volume took place over ~30s, after which motion appeared to cease. A series of tomographic scans were taken at this point, at concurrent high temperature and pressure, to attempt to capture any further changes in melt geometry in three dimensions. It takes 45 minutes to carry out each tomographic scan, therefore each represents 45 minutes of potential movement within the sample.

In addition to this *in-situ* data collection, further scans were made of the quenched run product using the University of Edinburgh *in-house* CT system in order to image the full gasket (voxel size 6 μm), in order to capture volumes of the sample outside the field of view during *in-situ* scans. A further high resolution scan was taken of the central sample and olivine capsule after removal from the gasket, at a voxel size of 1.5μm. Finally, the sample was cross-sectioned and polished to allow BSE imaging for ground-truthing.

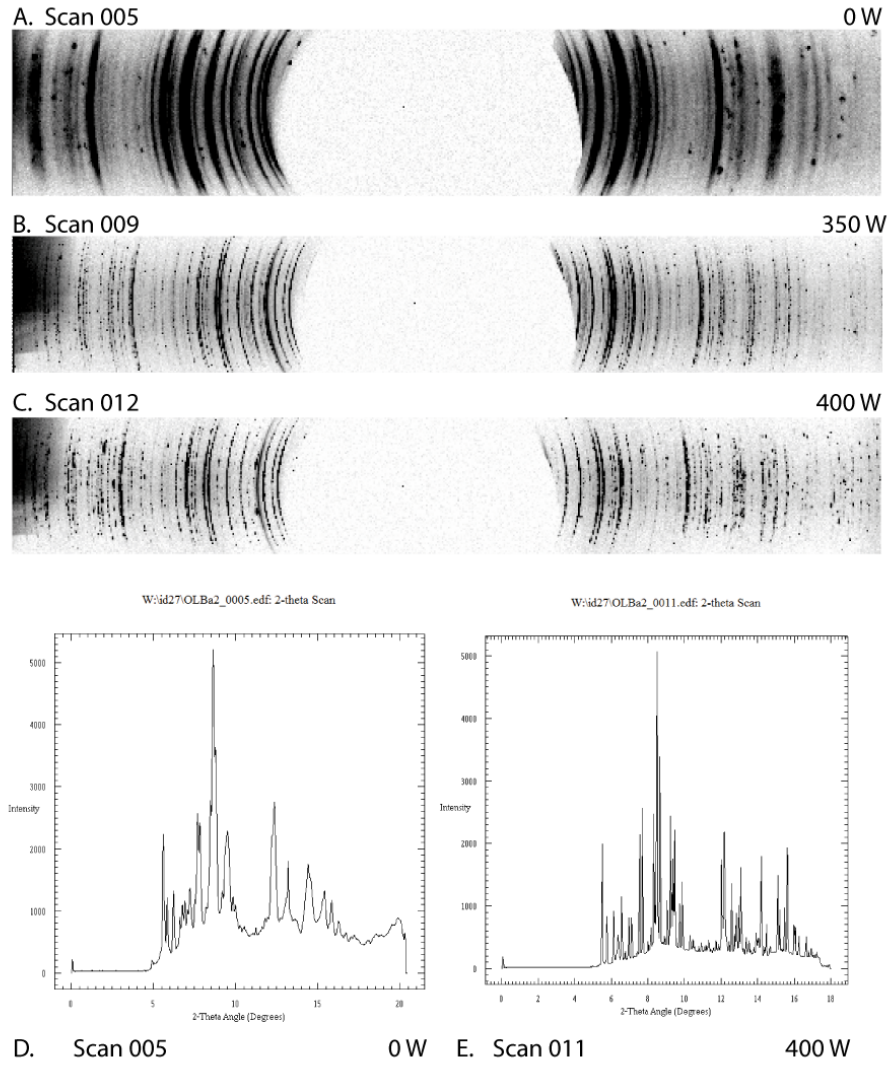

Figure 5.19: Examples of how diffraction patterns were used in experiments in phase I at ID27, for sample OlBa2. A-C show unprocessed diffraction patterns at three points during the scan of the sample at high pressure, but varying temperature. The centre of the scan is obscured by a diode used to protect the imaging plate being damaged by the main X-ray beam. D and E show integrated plots. At room temperature (A) the scan shows very soft, blurred diffraction lines, apparent as a diffuse raised area without peaks in the integrated plot D. This is due to the presence of glass powder within the sample and is similar to the pattern expressed by melt - diffuse diffraction produced by X-rays passing through amorphous material. As temperature increases through B. and C. the diffraction pattern loses this diffuse base and becomes more spotted, indicating significant recrystallisation is taking place within the basaltic glass during slow heating. C. is at the point of incipient melting, although the diffuse pattern expected from the presence of melt is not clearly observed here (shortly after this, motion is observed within the sample using radiography.)

In-situ tomographic scans

Figure 5.20 shows the sequence of tomographic reconstructions from scans carried out during experiment OlBa2, before heating (A) and at temperature: 5min (B), 1hour (C) and 2 hours (D) after initial melt movement. The following key features are highlighted

- The starting geometry (A) shows melt is mostly restricted to the central portion of the sample, although the crack between the two samples is faintly observable due to a small amount of the more attenuating phase contaminating its surface during loading (red planar feature in volume reconstruction). An intermediate greyscale in the central capsule suggests an intermediate phase may be present, but this could also be explained by a fine-grained portion of the basalt and olivine starting mixture. Later scans do not show the same clear intermediate greyscale.
- Melt motion has only taken place in one direction, along a narrow conduit, widening out to a larger volume at the edge of the capsule. The conduit appears to be within the in-built plane of weakness, but the attenuating phase clearly does not take advantage of the full 2D plane.
- Significant blurring is observed in scan B, initiated several minutes after initial motion, particularly within the narrow channel and larger volume channel 'head', created by a large number of streak artefacts emanating in multiple orientations from the more attenuating phase. This type of artefact is considered as evidence of melt movement occurring during the scan.
- Despite the input power remaining at 400W for the duration of tomographic scans B-D, there is no evidence for further large scale melt movement. The overall geometry of melt in scans B-D remain essentially identical, except for the increased motion blur in B suggesting localised redistribution of melt occurs during the scan. In scans C-D, the increase in scan sharpness, and reduction of streak artefacts, suggests motion reduces to minimal levels by 2 hours after melting temperature was reached.

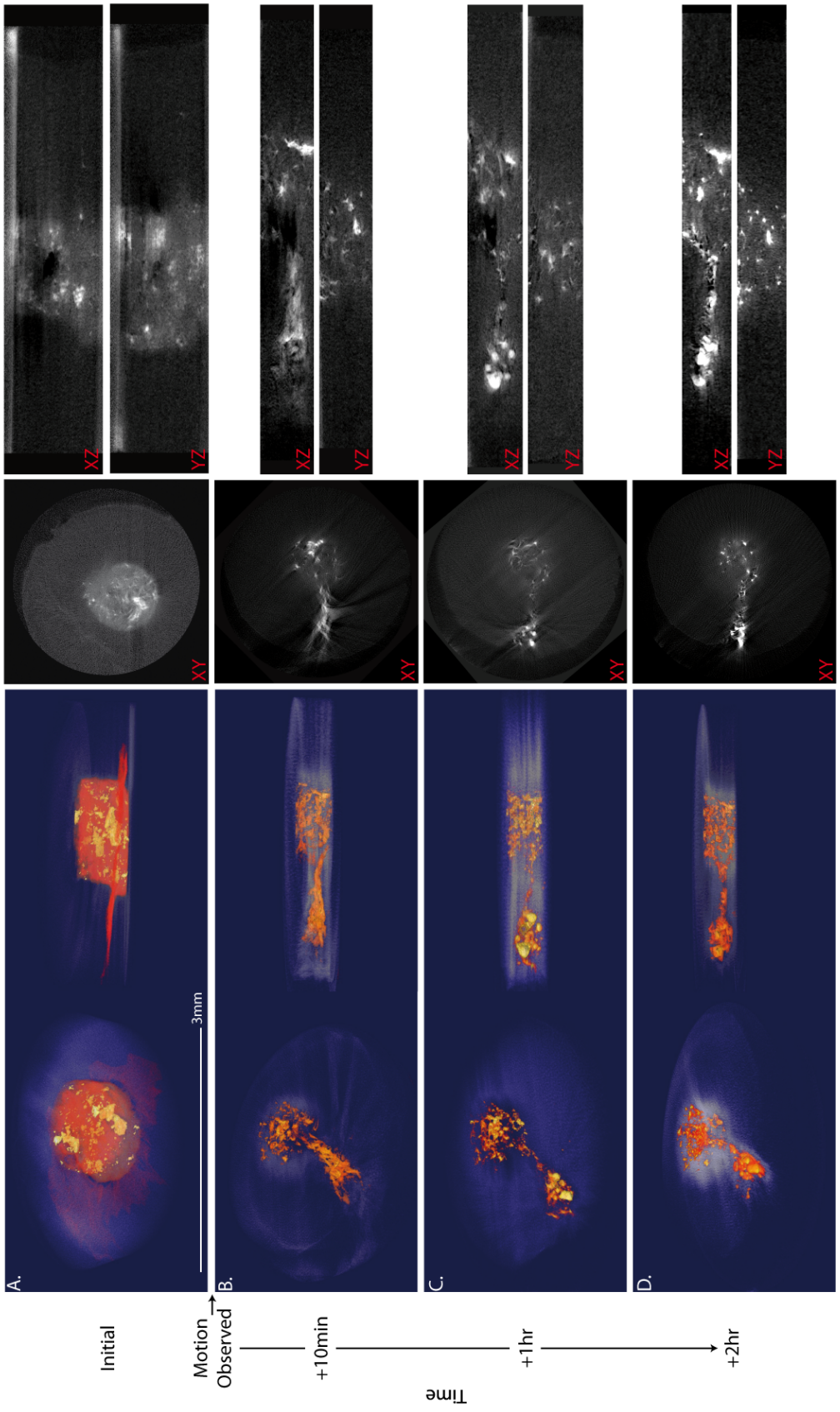

Figure 5.20: Caption on next page

Figure 5.20 ***(preceding page)*:** 3D reconstructions (left) and orthogonal slices (right) of changes in melt distribution of sample OlBa2, during ESRF phase 2 experiments. Voxel size is 2.8μm. In each case, orthogonal slices are shown on the right (bright areas = more highly attenuating) and a 3D volume render is shown on the left. Volume renders are carried out with masking used to preserve greyscale within melt areas (see section 2.3.5). The dataset is recoloured on a scale from red - yellow - white, and simultaneous increase in opacity, to show the change in greyscale within the segmented area. An additional white volume rendering of the full dataset at 1 % opacity was used as a background to add depth and show the full extent of the imaged volume. All scans were carried out at high temperature and pressure, therefore melt was mobile during scans. A. the initial geometry of the sample, with the attenuating phase in the centre. Reconstructions B., C. and D.: melt texture 10 minutes, 1 hour and 2 hours after the initial movement was observed. See text for details.

Further constraints from post-quench analysis

3D reconstructions of post-quench scans taken using the University of Edinburgh *in-house* CT system are shown in Figure 5.21. Good alignment and lack of movement during rotation also make these scans sharper, therefore easier to interpret, leading to improved resolution of features in comparison to ESRF *in-situ* scans.

These sharper scans allow important constraints to be made about processes occurring at high P-T:

1. There is clear evidence for a third phase of intermediate attenuation present in the sample that was not reliably resolvable in initial scans. It is brighter than the surrounding boron epoxy and olivine, but darker than the brightest attenuating phase, and is found within the central sample volume, and surrounding the brightest attenuating phase. This intermediate attenuation cannot be caused by partial volume effects dimming the brightness of the most attenuating phase, as it is clearly shown to produce its own unique features - this is clear in C ii. where the intermediate phase, in translucent red, is shown to spread laterally away from the brightly attenuating volume at the capsule edge in two fine sheets. In contrast, the most attenuating phase is shown to have a spherical 'globular' geometry. These textural features are reminiscent of the texture created by two immiscible liquids (e.g.Pak et al., 2015), with the brighter spherical 'blobs' representing a less mobile melt phase within the liquid of intermediate attenuation.

2. There is a large volume of the most attenuating phase (directly surrounded by the intermediate phase) outside the central capsule area within the boron epoxy gasket. The orthoslice in Figure 5.21 B shows that this material is outside the graphite furnace, which is broken at the centre. The brightest phase is not physically joined to bright phases in the capsule centre, but the intermediate phase does form a channel joining areas in the centre to the edge, and through the broken graphite furnace. This is interpreted as evidence that the two melt phases have moved over scales of >3mm between the capsule and the outer gasket.

These interpretations are further complicated by BSE imaging (5.22) with EDS analysis to identify phases. The brightly attenuating phase within the centre of the sample is in fact shown to be made up of two separate phases, which cannot be resolved in tomographic scans: The majority of the bright phase in the central sample is solid, euhedral hafnia (HfO_2), presumably residue undissolved crystals within the Hf-doped basalt. The second bright phase, which is found mostly at the base of the sample and represents 100% of the bright phase observed at the capsule edge, is pure Fe metal. The metal tends to form small round spherules, as suggested by 3D geometry, which is good evidence for the presence of two immiscible fluids within the sample at high P-T. At the capsule edge some of the iron is seen to form linear features,

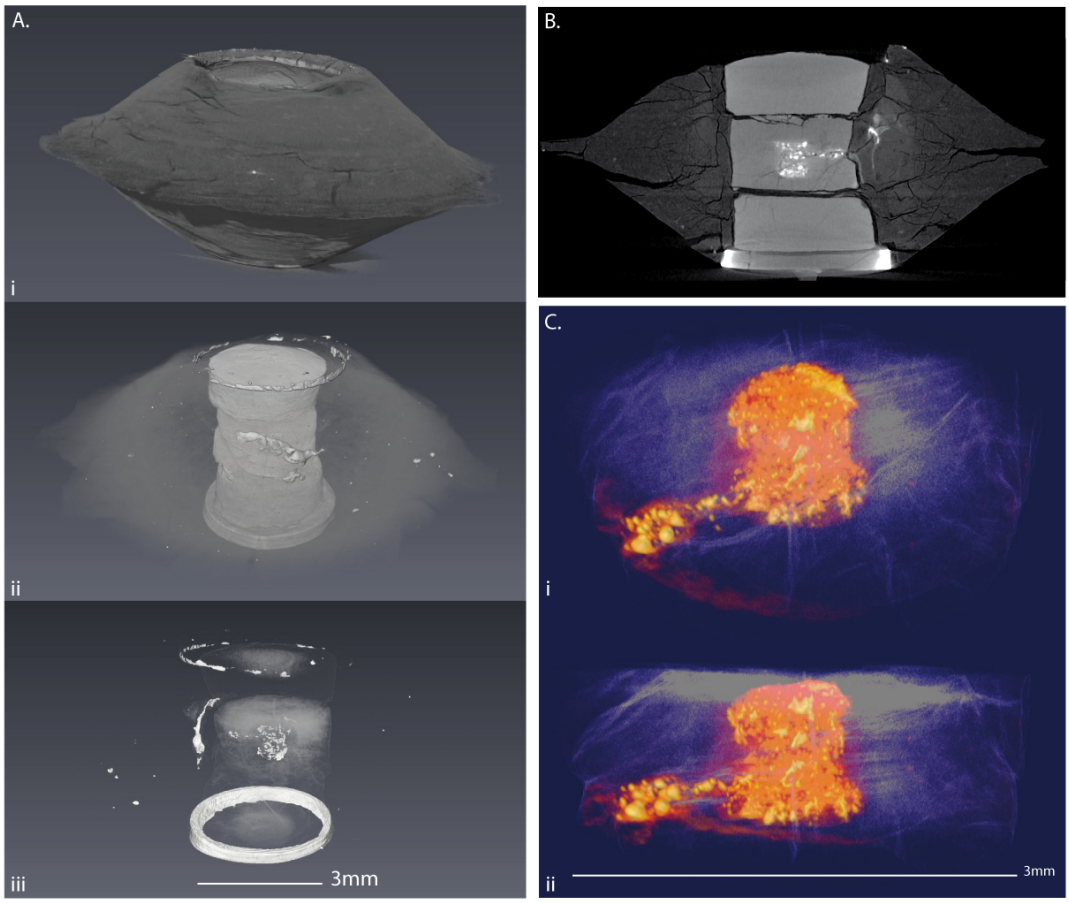

Figure 5.21: 3D reconstructions of sample OlBa2, after quench, taken using the University of Edinburgh *in-house* CT system. The first scan was taken of the full sample gasket (voxel size = 6μm). A. volume reconstructions of the recovered gasket at increasing transparency: i) exterior, ii) interior capsule and spacers, and iii) highly attenuating phases only - this includes the Fe contact rings at the sample base (top ring is no longer present). B. an orthogonal section through the gasket showing the interior of the capsule. C. volume render of the high resolution scan (voxel size = 1.5μm) of the central 3mm of sample capsule. Again, segmented areas have greyscales preserved by the process of masking, and rescaled: Yellow opaque areas are the most attenuating, while red translucent volumes have a relatively low attenuation (although still higher than background levels).

apparently indicating some wetting of grain boundaries. Basalt does not appear to have mixed effectively with Hf, making basalt glass very difficult to differentiate from olivine even in BSE images. However, where it is observed, there is evidence that a small amount of Hf has been dissolved in the glass, making it slightly more attenuating than surrounding olivine. Very little basaltic glass appears to be present within the central sample zone. A small quantity is observed in the zone of melt at the capsule edge (Figure 5.22 C), evidence of melt migration away from

the sample centre.

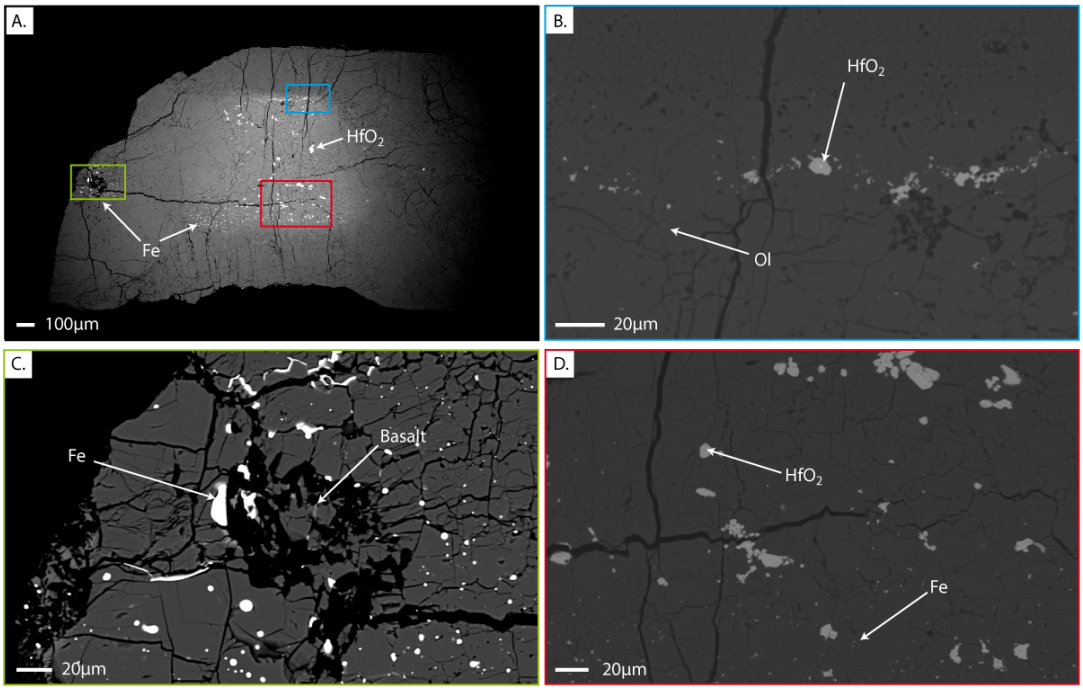

Figure 5.22: BSE images showing quenched and polished slice of sample interior of OlBa2. EDS analysis was carried out to gain qualitative compositional information, in order to identify phases as labelled. A. shows the whole sample, with the central sample portion visible as slightly paler than surrounding capsule. This suggests the central sample olivine is slightly denser than surrounding capsule, which is unexpected as they are made of the same material. This may be caused by reaction with the metallic or basaltic melt with the olivine in the starting mixture. B. shows a close-up of pale (dense) crystals at the top of the sample. These are all found to be hafnia crystals. C. a close-up of the capsule edge showing bright Fe, which forms mostly spherical blobs, with some wetting of olivine grain-boundaries also observed (linear features). The dark grey shown is olivine, but some lighter grey areas are shown to be basaltic melt. D. shows an area at the base of the melt-rich zone where both bright hafnia crystals and quenched Fe are observed. The hafnia appears as larger crystals, with a roughly euhedral shape, while Fe appears as spherical blobs and are more abundant in the lower half of the image.

Discussion/Textural interpretation

Off-line CT scans and BSE analysis suggest that melt migration processes within the sample were more complex than the simple single stage of melt motion inferred from initial *in-situ* observations. The initial simple two phase system of olivine + basalt has shown to be made up of four phases, in order from least to most attenuating:

1. Olivine (solid phase 1)
2. Basaltic melt with low levels of Hf (highly mobile liquid phase)
3. Solid hafnia (HfO_2) crystals (solid phase 2)
4. Iron melt (lower mobility liquid phase)

Unless the starting mixture was significantly contaminated, the most likely source of the iron is in fact the contact ring at the top of the gasket. This would suggest that the iron melt in fact travelled from outside the gasket into the centre, in the opposite direction to the basaltic melt. It is unclear exactly how initial mingling of the two liquids took place, but there is significant evidence for two phase flow and significant volumes of iron are found in the central capsule, suggesting the liquid was highly mobile and able to migrate significant distances (several mm). It is the movement of the iron melt that was presumably observed within radiographic imaging and is most evident in tomographic reconstructions. Basaltic melt may have been flowing for significantly longer than the iron melt, potentially explaining the motion blurring observed within scans B and C, without further changes to the geometry of the highly attenuating phase (iron). In fact, the lack of basaltic melt in the sample centre in quenched cross-sections suggests the melt may have mostly drained from the interior, leaving iron melt as stranded spherules. The lack of change in the central sample zone is also explained by this, as the majority of the attenuating phase here is the solid hafnia, left stranded after initial melt migration. It is possible that a thermal gradient has drawn the melt to sample edges, close to the graphite furnace. The break in the furnace structure suggests there may have been uneven heating creating hot-spots which could produce a significant thermal gradient to encourage melt migration in one particular direction.

This significant change in inferred processes shows the importance of ground-truthing X-ray CT work before significant interpretations are made. X-ray CT imaging can only give information about relative attenuation of materials, which can lead to misinterpretation if the exact phases within the sample cannot be confirmed.

Limitations

During this initial week of experiments at ESRF ID27, the rotoPEC press was successfully automated together with tomographic software after several days of set up. Despite initial run

failures, we were successful in observing significant *in-situ* melt migration within a sample at extreme temperature and pressure, and capturing these changes in texture over a series of tomographic scans. A number of technical difficulties limited the success of experiments, which could be improved in further experiments:

- The use of complex compositions caused problems both with analysis of diffraction data, and complexity of processes at high temperature and pressure. In particular, the fact that we were unable to make Hf-doped basaltic glass without remnant solid HfO_2 caused additional complexity and meant that basalt melt itself did not have a large enough contrast against the olivine solid matrix.
- Contamination of Fe, potentially from contact rings, was unexpected at the time but was later found to be a problem in further experiments (Chapter 4). Use of metal rings with higher melting point (e.g. molybdenum) should ensure this type of contamination cannot occur in future experiments.
- Experimental failures were common, and temperatures that were required to reach melting point of basalt (and iron) were close to the limits of stability of the rotoPEC equipment. The use of melt phases of lower melting point could improve experimental stability.

5.3.3 ESRF Phase 2 - Gold melt movement along fractures

Experimental adaptations

A second phase of experiments was carried out at ESRF ID27 over a week of beam time in January 2015. Although initial set up of equipment was fast, a number of experimental issues and inherent instability led to a number of blow-outs and experimental failures, and several last-minute design adaptations were required to solve these issues. In the final experiment, AuBN1, we were finally able to cause melting and observe several episodes of melt migration. Final adaptations for this successful experiment were as follows:

- Adaptation to the final type C capsule design (Figure 5.2) improved stability of the sample.
- The use of gold as a melt phase meant that melt was easily identifiable in diffraction patterns (Figure 5.24). Gold also has a lower melting point compared to FeS and basalt, meaning experiments could be carried out at more stable temperature conditions. It has a high dihedral angle (150° in olivine system) and is therefore a good analogue for low mobility end-member of melt migration processes (Bruhn et al., 2000; Walte et al., 2011).

- Polycrystalline capsule material was changed to a more simple composition for X-ray diffraction processes. Initially, MgO was used, as its diffraction behaviour at high P-T is well constrained (Tang and Dong, 2010) and it is a good simple analogue for the behaviour of polycrystalline material in the Earth's deep interior (Cordier et al., 2012). This was changed to boron nitride (BN) in the final run to try to further improve stability and improve thermal transfer to the central sample. Cubic BN can also be used effectively to track P-T by diffraction (Datchi et al., 2007).

- Additional changes were made to the gasket in order to improve stability, and efficiency of heat transfer to the sample. Initial experiments used BN as a spacer material, but its high thermal conductivity meant it became difficult to heat the central sample. Spacers were replaced by MACOR^{TM} ceramic, which has a low thermal conductivity and so improves thermal insulation. Molybdenum was used to make the contact rings, which has a significantly higher melting point than Fe.

AuBN1: Experimental outcomes and data collection

A schematic graph detailing experimental conditions and data collected during experiment AuBN1 is shown in figure 5.23. After pressurisation, the sample was successfully heated to the melting point of gold three times. Unfortunately, misalignment of the press with the soller slits meant that no diffraction patterns were available during initial pressurisation and heating of the experiment, but later diffraction patterns show clear evidence of melting (Figure 5.24); the first melting event is inferred from a series of still images, which, once normalised, show evidence of melt migration (Figure 5.26). The power input required to melt gold increased over the course of the experiment, suggesting an increase in resistance of the furnace and gasket meant the temperature-power relationship was changing. This suggests that pre-calibration of power-temperature curves is not hugely reliable and should be used with caution in future experiments, as the exact relationship may change over the course of an experiment. Direct measurements will always be more reliable and should be used where possible.

When melting did occur, it became evident that melt migration velocities were too fast to be tracked using tomographic scans, which take 45-60min to complete. Instead, melt movement itself was captured by 2D radiography, taking a still frame at intervals of 10-20s. Between melting events, temperature was dropped to just below the melting point to carry out tomographic scans in order to track changes in melt geometry. A summary of the movies and tomographic scans created during experiment AuBN1 is given in table 5.4. This combination of 2D *in-situ* radiography, and lower temperature static tomography scans allowed us to track 3D melt geometry and concurrently track melt motion in real time.

There were significant issues with tomographic scan quality, particularly during initial scans 2-5. The field of view of tomographic imaging meant that a proportion of the sample left

the field of view during the scan. In addition, rotoPEC motor failure meant that new motors were used to rotate the press. These had a different gear-ratio therefore the exact rotation speed required to rotate the sample to 180° was initially unknown. For the first 5 scans, the sample was only being rotated to ~165°, affecting scan quality significantly. Successful reconstruction was carried out for scans 1,5,7 and 8 only. Although voxel size of scans is 2.8 μm, the actual resolution is significantly lower. Example orthoslices are shown in figure 5.25.

2D projections had an exposure time of 100ms. A time interval of 20s between projections was found to be sufficient to capture melt migration events. Figures created below show example projections to highlight changes observed. The original projections for each movie have been normalised using flat field and dark current images on Octopus 8.7 software (Dierick et al., 2004), to improve contrast of the images and enhance signal-noise ratio. To highlight changes within each projection, an initial reference frame, p_0 is subtracted from each of the following frames to create an image, $p_x - p_0$, carried out using ImageJ's Image Calculator function (Abramoff et al., 2004). Greyscale therefore represents changes in attenuation between the reference and the new projection: Black areas indicate a relative increase in attenuation, and therefore appearance of melt, and white areas a decrease and therefore loss of melt. Full datasets for each movie can be found in digital appendix B1.

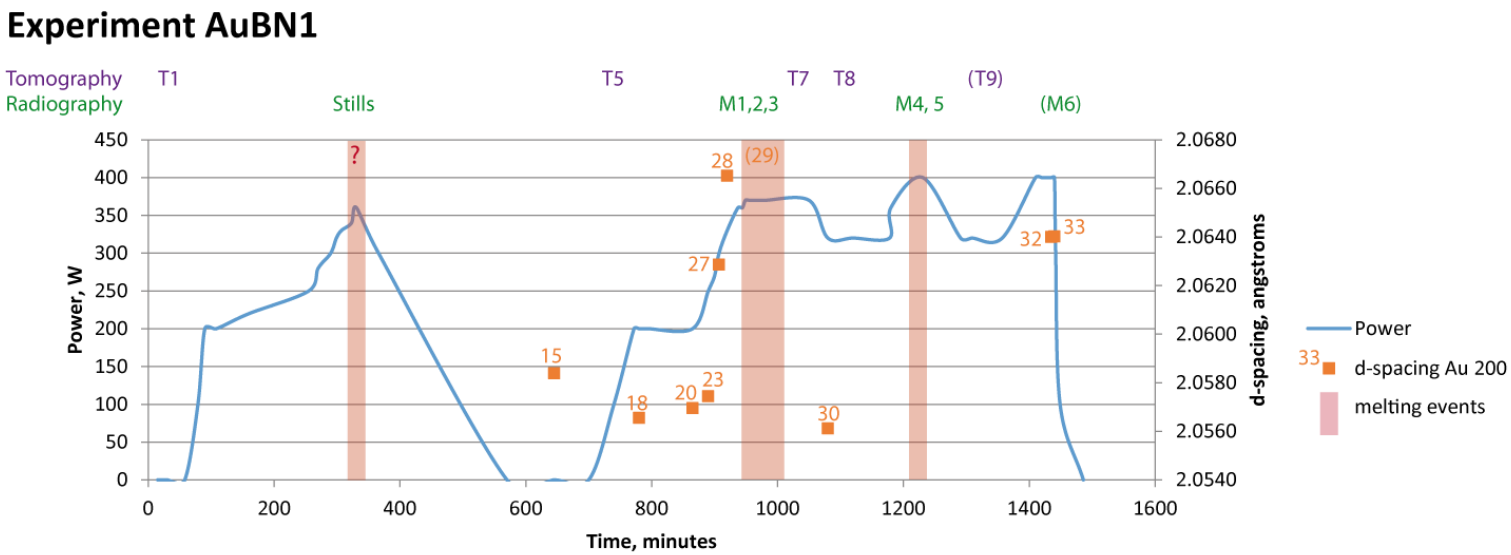

Figure 5.23: A graph showing changes in power over time during experiment AuBN1. In addition, d-spacing of the 200 Au lattice plane is shown from diffraction scans taken during the experiment, labelled with their scan number (the initial 700 minutes of the experiment were carried out without successful diffraction as the press frame was incorrectly aligned with soller slits). The timing of 3D tomography scans, and 2D radiography is also given. Times when the sample is shown to be molten are highlighted in red: the initial melting (marked with ?) was not confirmed with diffraction patterns but inferred by movement observed in the sample. Although power and d-spacing appear to increase at a similar rate during initial heating, after 1200 minutes the power required to melt the sample rises. This suggests resistance in the furnace may have changed during the experiment.

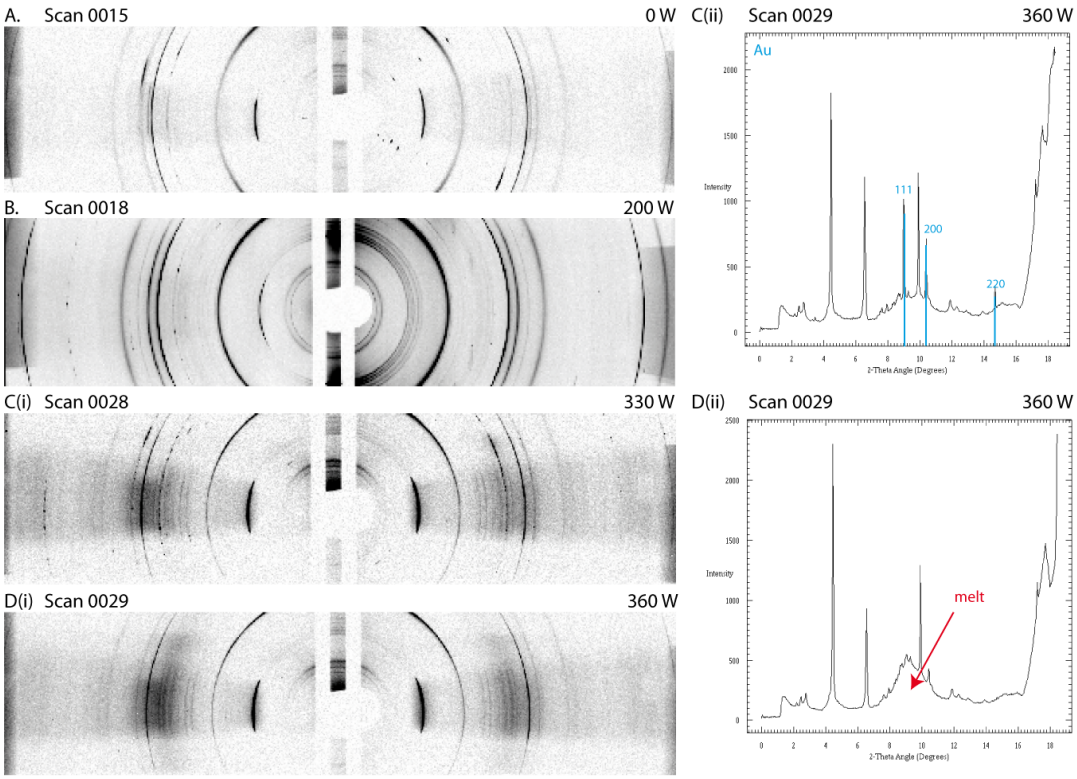

Figure 5.24: AuBN1 diffraction patterns taken A. at low T (at this point the scan was slightly misaligned reducing the strength of patterns observed) B. at 200W, with a clear pattern showing both gold and BN peaks, C. at the point of incipient melting (330W) - gold lines are still visible but very spotty and a diffuse background is already present suggesting some melt is already present. D. Scan above the melting point of Au, with gold peaks completely absent and a broad diffuse background indicative of a melt phase. C (ii) and D (ii) show the integrated Fit2D ((Hammersley, 1998)) plots from scans C (i) and D (i) respectively. Gold peaks, labelled in C (ii) disappear completely in D (ii) and are replaced with a diffuse background rise in attenuation (see arrow). Remaining peaks are those of BN.

			XP conditions		Scan properties			CT properties	Movie properties	
Name	**Date**	**Start time**	**P / W**	**V**	**wavelength, Å**	**exp /ms**	**no. proj.**	**degrees rotated**	**t interval, s**	**Comments**
AuBN1_1	25/01	23:00	100	0	45	100	930	165		diffraction patterns misaligned during heating, unable to observe peaks
AuBN1_2	26/01	01:18	100	200	45	100	930	165		gold leaves fov
AuBN1_3		02:10	100		45	100	930	165		gold leaves fov
Au BN1_4		03:36	100	300	45	100	1800	165		Dropped T to do tomo to 300 (NB the flat fields were wrong shape also gold moved out of FOV so cannot reconstruct.
AuBN1_5		11:15	0	0	55	100	930	165		Tomo at pressure, low T, slits widened so more in field of view, can hopefully reconstruct
AuBN1_6		12:45	100	200	55	100	930	165		after this scan, evidence for melting in diffraction pattern at 360W
movie1		15:14	100	360	55	100	1000		1	no clear melt movement
movie2		15:19	100	370	55	100	1000		1	very small movement observed between frames 600-800
movie3		15:26	100	370	55	100	1000		1	anvil closes slightly: only observable motion in scan
AuBN1_7		15:50	100	370	55	100	930	180		NB changed rotation value from 214 to 240 as we think we are rotating much less than we should be (prev scans only rotated to 164 degrees)
AuBN1_8		18:10	100	320	55	100	930	180		
movie4		19:10	100	360	55	100	179		10	no clear melt movement
movie5		20:01	100	400	55	100	130	180	20	at least 3 discrete melt movement event captured during radiography
AuBN1_9		21:19	100	320	55	100	930	180		Anvil closed during scan so unusable
movie6		22:07	100	400	55	100	300		20	only observable movement is anvil closing - diffraction shows gold peaks despite low T, has Au crystallised? Furnace resistance may have changed as anvils closed

Table 5.4: A table detailing the 3D tomographic scans and 2D radiographic movies created during experiment AuBN1 during the second phase of experiments at ID27.

Characteristics of observed melt movement and changes in geometry

Figure 5.25 shows ortho-slices from tomographic scans, in XY, XZ and YZ orientations produced from each of the successfully reconstructed scans. Resulting 3D reconstructions are shown in Figure 5.27, with a close-up of the sample base shown if Figure 5.29.

Figures 5.28, 5.30 and 5.31 show examples of movement captured in 2D radiographic imaging.

Important characteristics of melt migration observed are as follows

- Melt movement occurs through localised fractures, not by diffuse grain boundary percolation. A geometry of interconnected fractures is observed in 3D reconstructions, emanating from the central melt rich zone. These fractures vary in shape, from fine 2D sheets, to tortuous tubular features. Their thickness also varies, from several μm, up to ~20μm (exact estimates are impossible due to poor scan quality; measurements are likely to be maximum estimates).

- Melt migration is episodic. 2D radiography captures melt migration ocurring through fractures in a series of discrete events, rather than a continuous flow. Movement events occur over a time frame of 5 minutes (e.g. fig 5.30) to half an hour of continuous flow (e.g. fig 5.31), followed by gaps of several minutes - hours where no movement is observed.

- The initial melt migration event was preceded by movement of sample material just below the gold solidus. The end of this movement is captured in figure 5.26, followed by the first *in-situ* observation of melt migrations (1. and 2. in fig 5.26). This creates an offset micro-fault feature in the lower half of the melt rich zone, as seen in orthoslices and 3D reconstructions of scans 5-8.

- The majority of melt-filled fractures observed are present from scan 5- scan8, with little change in melt geometry (Figure 5.27). This combined with above movement may suggest that the fracturing observed just before melting may have created fractures that are later filled with melt (fractures with no melt in them are hard to pick out on tomographic scans). However, between scan 5 and scan 7, taken before and after the second melting event, a large new melt-filled fracture is observed to form below the melt-rich zone (see arrow, figure 5.29), which correlates with melt movement observed in movie 2, figure 5.28. This suggests that the melt is creating at least some of its own pathways.

- There is evidence that two episodes of melt migration can occur along the same fracture. Melt movement M2, as shown in Figure 5.31, shows how melt already present in a fracture is removed by another flux of melt through the same conduit.

- Interestingly, the pre-made plane of weakness from the dual capsule design does not seem to have been a conduit for significant melt migration. The fracture is observable in scan 1 showing starting geometry due to remnants of melt entrained within it, and the amount of melt present does not appear to increase significantly. It may be that the fine-grained nature of BN capsules used meant this fracture was efficiently sealed on compression.

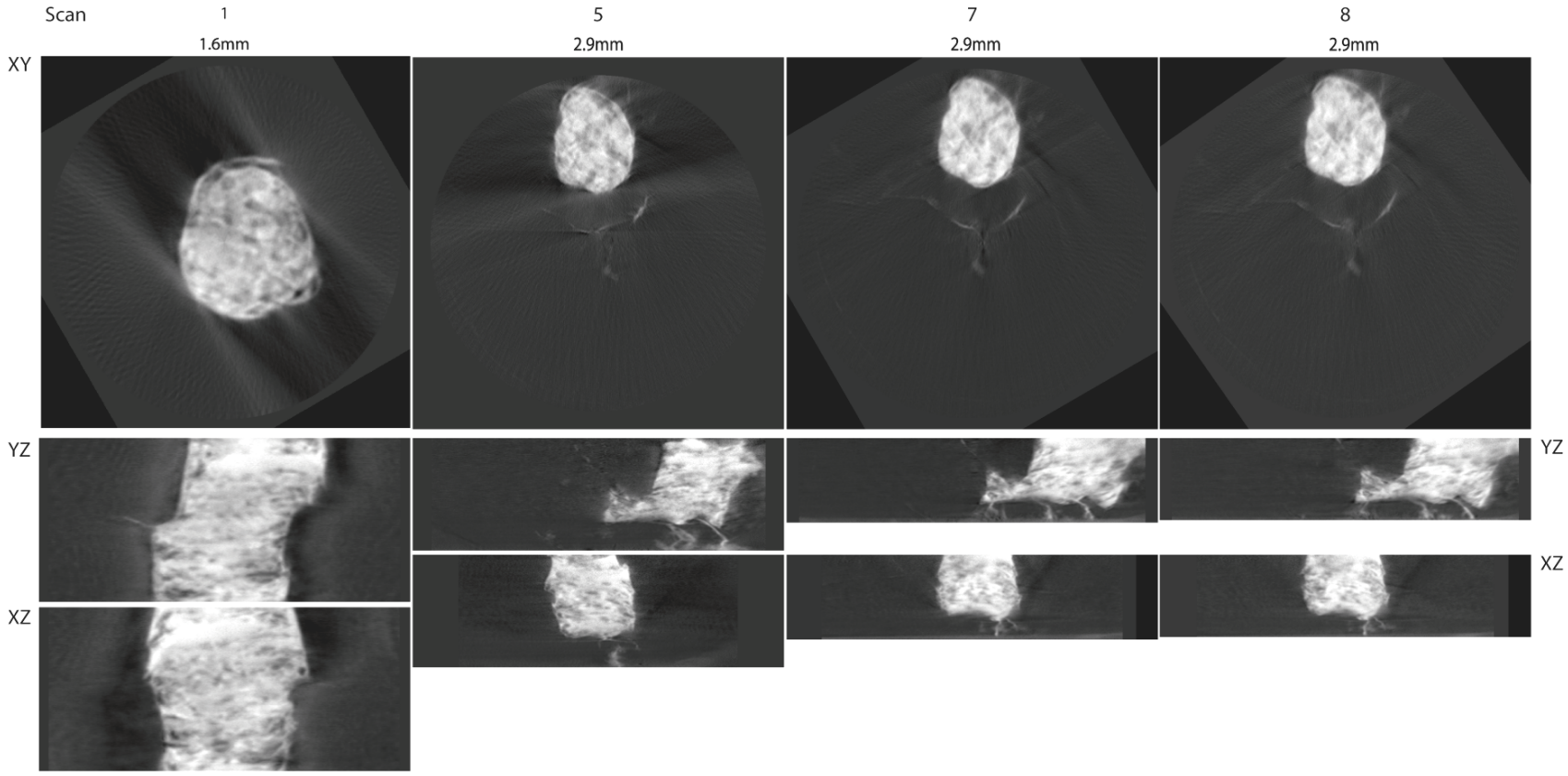

Figure 5.25: Orthoslices of tomographic scans 1,5,7 and 8 produced during experiment AuBN1. Dark areas are BN capsule, while pale areas are gold. Scans have been rotated so that each is shown at roughly the same orientation. Scan 1 shows the initial geometry of the sample, with scans 5-8 showing the development of fracture networks after melt migration events. The majority of fractures are observed below the gold rich zone.

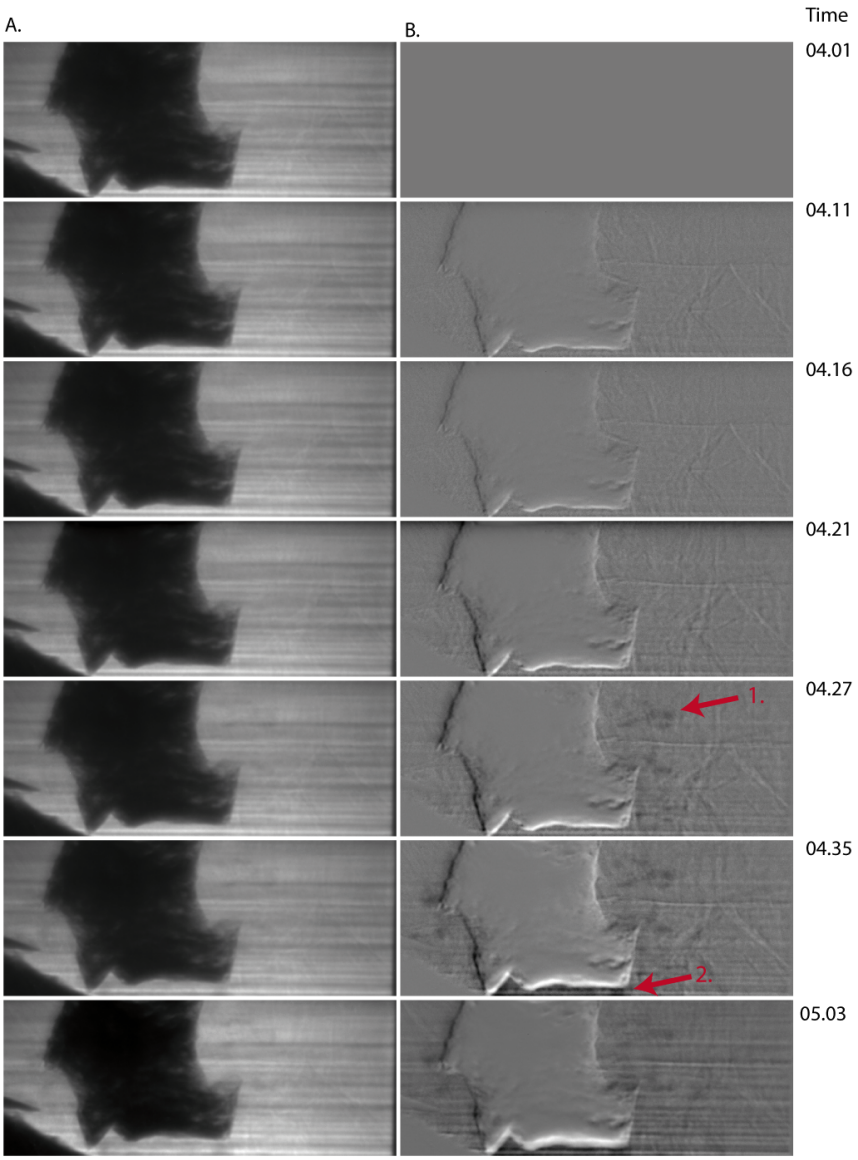

Figure 5.26: Still frames of sample AuBN1 taken over initial heating, showing the normalised and $p_x - p_0$ projections (dark areas show an increase in attenuation, light areas a decrease). Time of each still frame is indicated. The stills are taken at the end of the period of movement, so the majority of the change of shape has already taken place. An overall upward movement of the sample base is observed, as highlighted in the $p_x - p_0$ projection by a growing white band. At 04:27 and at 04.35 increases in attenuation away from the central sample zone are interpreted as evidence of melt movement.

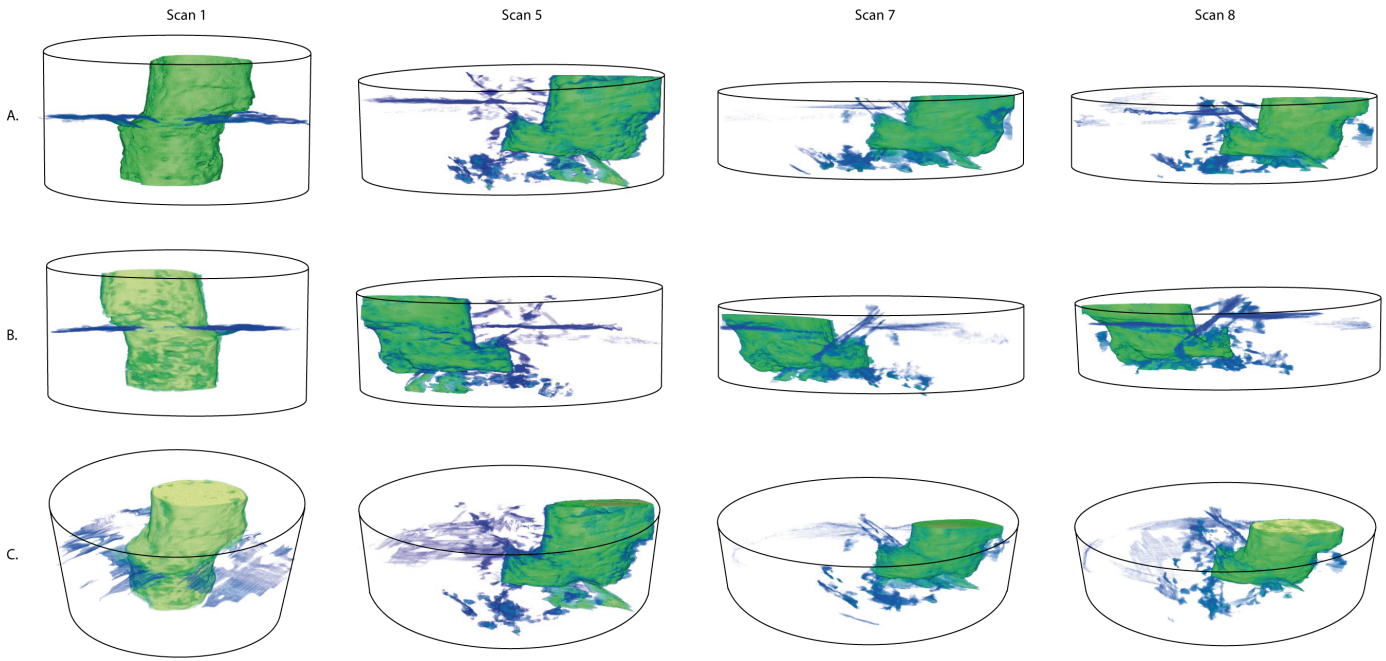

Figure 5.27: Volume rendering of scans 1 and 8 at three contrasting orientations (A, B and C). A masking technique has been used to segment volumes of interest, but preserve greyscale values within segmented areas and therefore attenuation value of volumes of interest. An LUT has been applied to the preserved greyscale, with blue transparent volumes representing the lowest greyscale values: blue = low relative attenuation, green/yellow = high attenuation (exact scaling in each case is subtly different, but similar enough for qualitative comparison). Scan 1 shows the initial sample geometry after pressurisation but before heating. The central melt rich zone is shown: the two cylinders containing the starting mix are not exactly aligned creating a pre-existing offset between melt-rich central cylinders. The crack between the two sample halves is also faintly visible due to traces of gold left on the sample surface during loading. Scan 5 was taken after the initial sample movement and melt migration event. It shows both an off-set within the bottom melt-rich zone, and a series of melt-filled fractures emanating from the source zone. The thickest fractures are at the base of the sample. Scans 7 and 8 are taken after melt movement 2. Decrease in vertical field of view is caused by anvils closing over the course of the experiment.

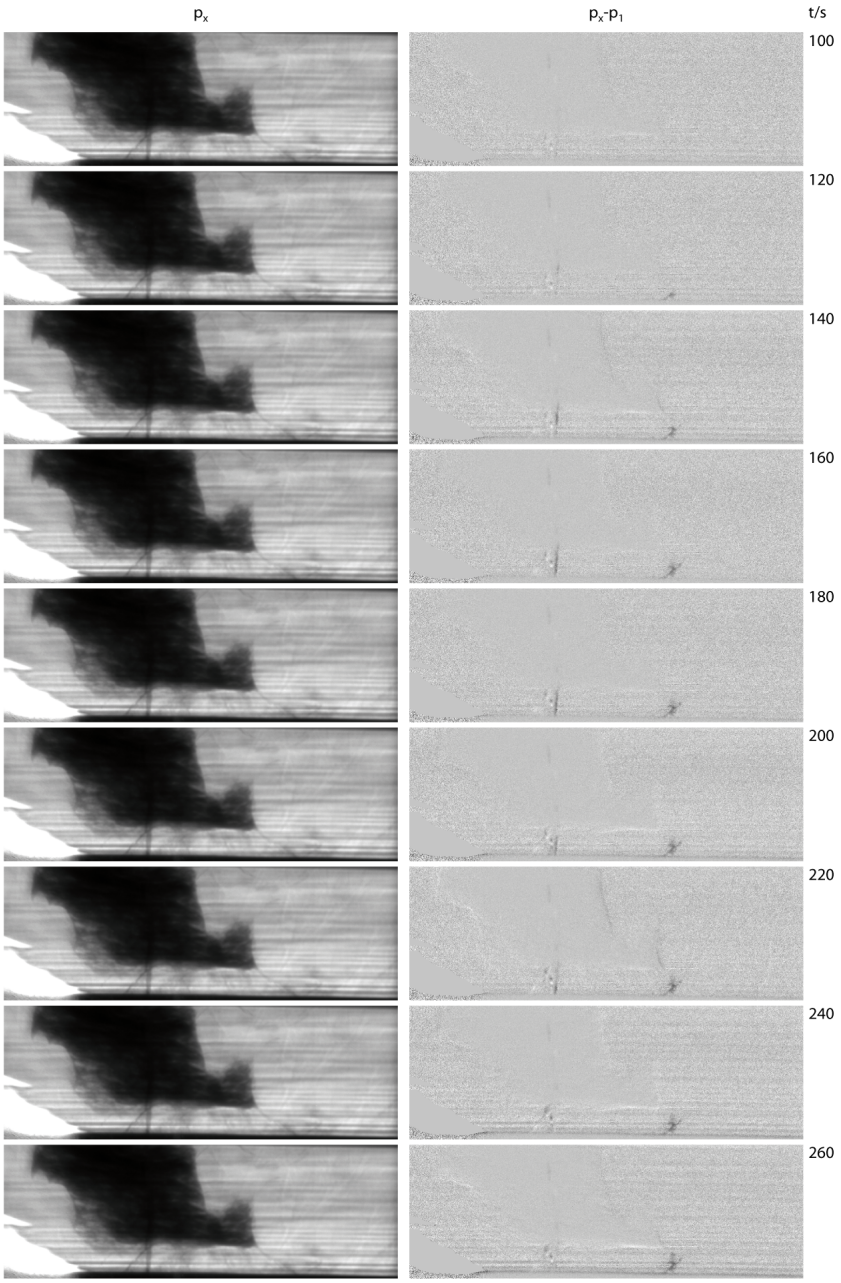

Figure 5.28: A series of projections highlighting changes in melt position observed in movie2, which is recorded between tomographic scans 5 and 7. Normalised projections, p_x, do not show changes clearly, but the processed images px-p0 highlight melt movement. Two discrete motions are apparent: A central, apparently vertical flow from the melt-rich zone downwards, and a concurrent flow at the right edge of the melt-rich zone, moving upward from an area outside the field of view, to join a pre-existing fracture network attached to the right edge of the central melt zone.

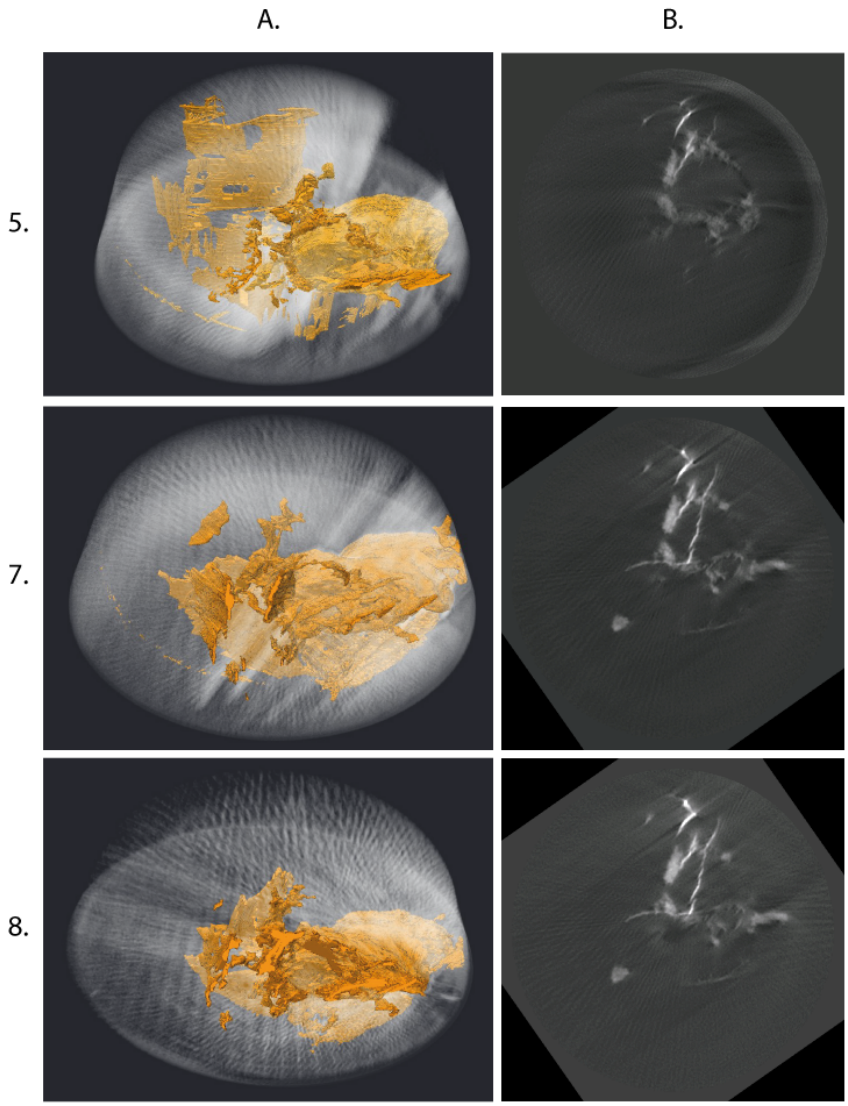

Figure 5.29: Figure showing the basal view of the sample from scans 5-8, to highlight geometry of the fractures at the bottom of the sample. The bottom of the scan reveals a large concentration at the base of the sample representing gold melt moving down and out of the field of view. There is very little change between scans 7 and 8.

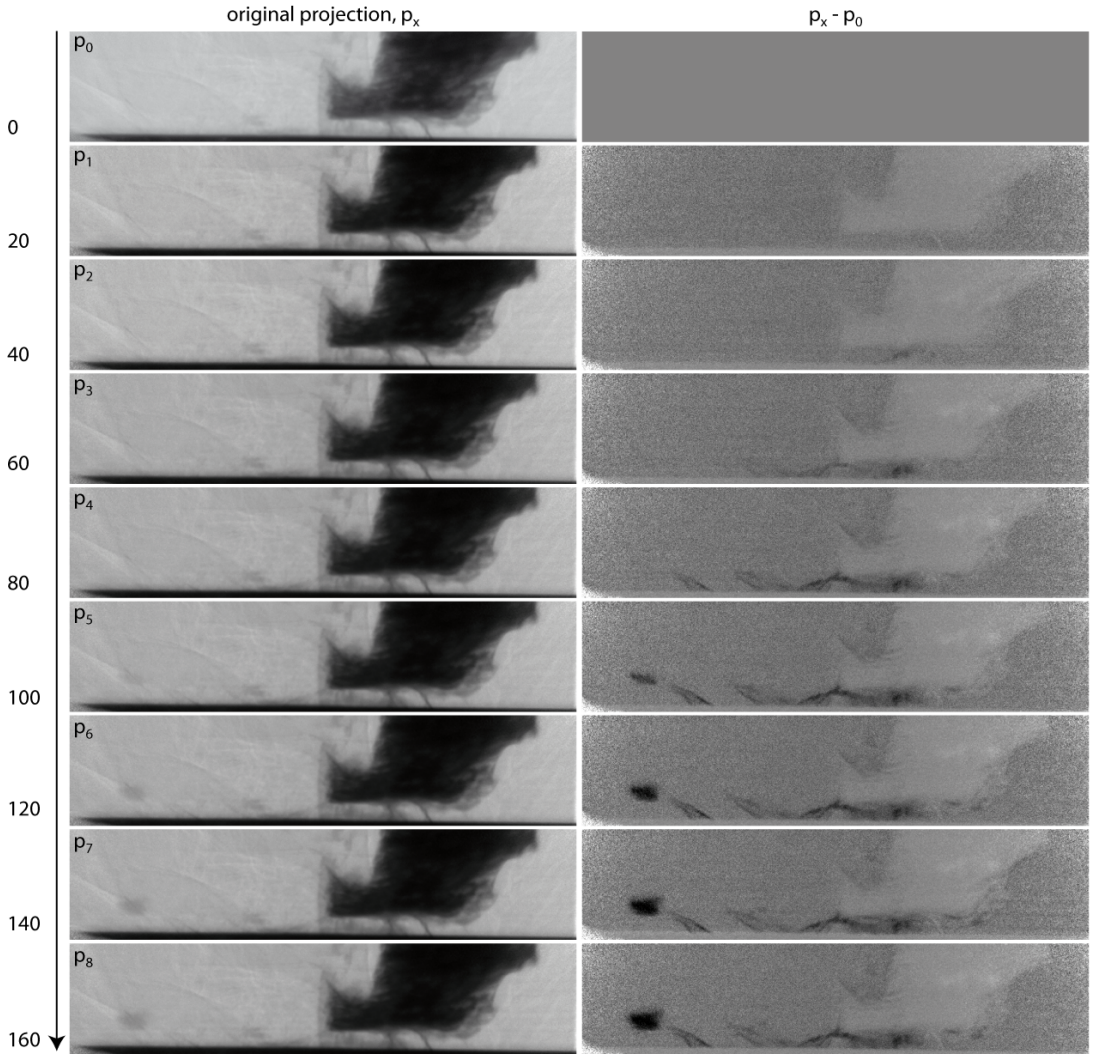

Figure 5.30: A series of radiographic projections capturing melt migration occurring during movie5, while the sample is at 400W input power. Projections are at an interval of 20s - the time interval is therefore a total of 160s. After this, motion ceases in this area, and there is a gap of 5 minutes before further significant motion is observed elsewhere in the sample (see Figure 5.31). Melt moves in and out of view over the base of the projection, but overall the movement appears to be horizontally from the centre to the edge of the image.

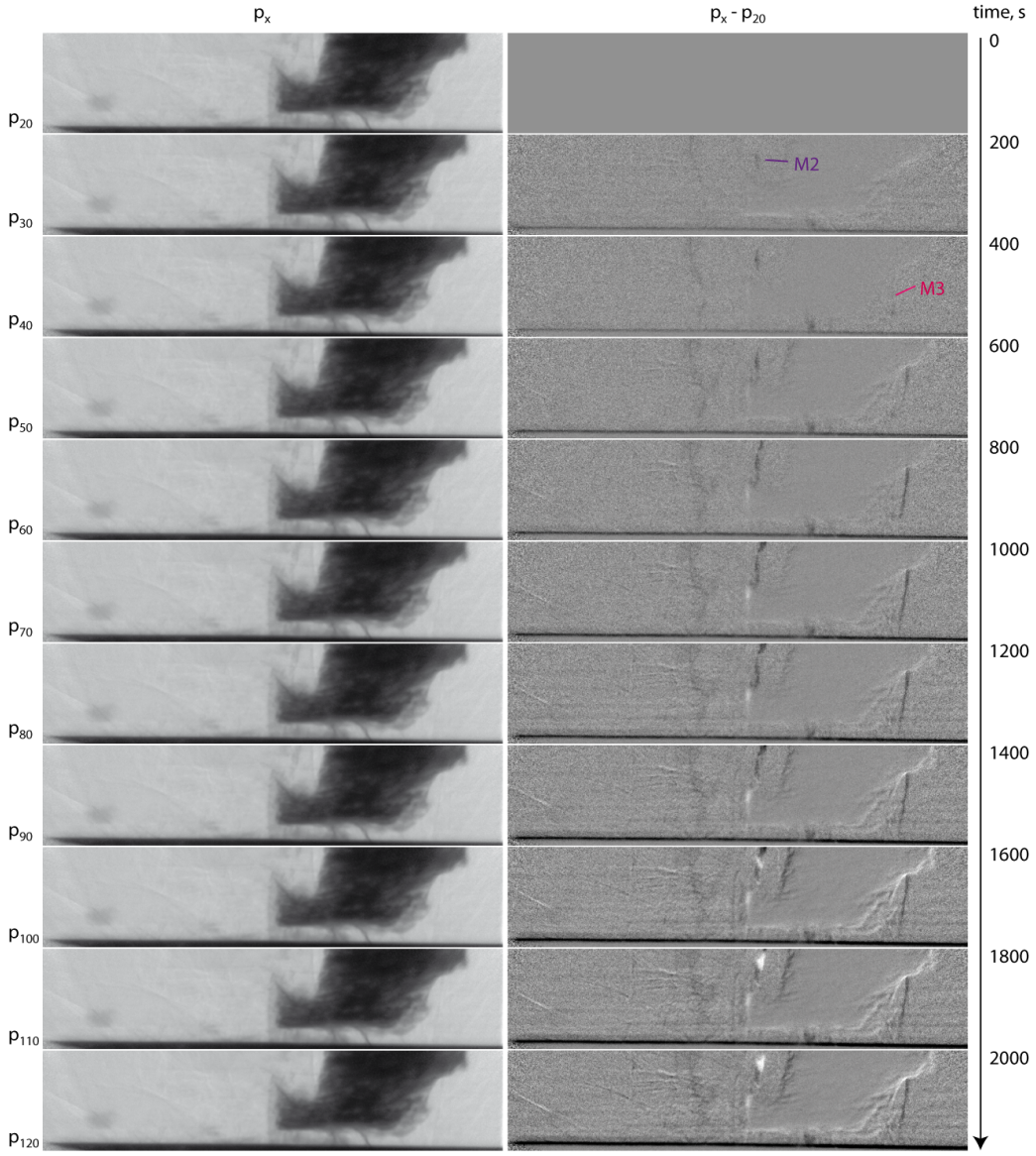

Figure 5.31: A series of radiographic projections capturing melt migration occurring during movie5, at 400W input power. Processes of creating images are similar to those described in Figure 5.30 but the initial reference frame for the right-hand column is chosen as p_{20} to highlight changes of interest. Also, movement takes place over a larger number of frames, therefore every 10th frame has been chosen to represent the motion observed. Discrete melt movements M2 and M3 are labelled on the projections where a change is first observed. Further melt movement may be occurring to the left of movement M2, where a sub-vertical melt vein appears. However, the orientation of it relative to the 2D plane makes it harder to track this motion effectively. The anvil can be seen moving upward as a growing black band at the base of the projections. This also explains why the full texture of the image becomes more apparent in $p_x - p_0$ projections over time, as the full sample material moves up and therefore changes position relative to the reference frame p_{20}.

Calculating melt migration velocity

The melt movement observed with 2D radiography gives an opportunity to estimate the velocity of melt moving along fractures by tracking melt movement across different projections. Initially this can be carried out by simply tracking melt movement within the 2D radiographic projection to get an estimate the minimum distance moved by the melt front, and thereby giving an estimate of the minimum velocity of melt migration. Movement M2 was chosen to examine in detail because melt movement is easily tracked across a series of projections, with a sharp edge between the melt and background. The process of estimating displacement, and resulting velocities are shown in figure 5.32.

Results show that estimates of velocity are not constant, but instead show a marked apparent acceleration in the central 200s of movement. This could be an artefact of seeing the movement in 2D (the fastest velocity could represent movement that is closer to perpendicular to the viewing plane and therefore represent an estimate closer to the true velocity), but could also reflect true variation in melt migration speeds caused by e.g. a narrowing of the melt channel. An estimate of the minimum velocity of the total movement observed, taking into account uncertainty from thresholding estimates, is $0.35 \pm 0.1 \mu m\ s^{-1}$.

Adding the third dimension to this analysis can give further constraint to melt velocity estimates. Using the 3D reconstructions of fracture geometry, it may be possible to make a more realistic estimate of the real distance of melt migration by matching 2D 'shadows' of melt fractures to their 3D fracture counterparts. This has been attempted using movements M1 and M2 as observed in movie5, and the reconstruction of fractures in scan AuBN1_8. Figures 5.33 and 5.34 show the process used to attempt to match 2D and 3D data and get maximum estimates of melt migration distance.

Movie5 was recorded after scan AuBN1_8, therefore it is possible that the melt has created a new set of fractures to move along and fractures in AuBN1_8 do not show the true flow path. However, there is little change in fracture geometry between scans 5 and 8, and there is good evidence that movement M2 is utilising a pre-existing melt flow channel (see above). Once a post-quench scan can be carried out it will be possible to compare the fracture networks before and after melt motion and test this assumption.

Even if the above assumption is correct, there are still a number of flow paths available that could represent the true path of the material observed in 2D radiography. In each case, a minimum and maximum estimate of velocity has been made assuming melt flow along maximum and minimum displacement estimates. These estimates are shown in table 5.5. An additional maximum velocity estimate taken directly from the 2D radiograph (i.e. assuming velocity perpendicular to the viewing plane) has also been included.

Despite the uncertainty of this analysis, it is clear that the motion observed in M2 is at least an order of magnitude lower than motion M1 even when the maximum velocity estimate of M2

is compared to the minimum of M1. Therefore the differences in movement speed are not just due to different orientations of motion, but instead represent true variation in melt migration velocity. The estimated timescales of velocity lie in the range of 0.6-60μm s^{-1} varying over 2 orders of magnitude. Scaled up to more intuitive dimensions this translates to 0.04mm-3.45mm per minute, or 0.1-5 m per hour. The question of scaling to true Earth scales, for flow through larger fractures, may not be this simple, however, as examined in the following discussion.

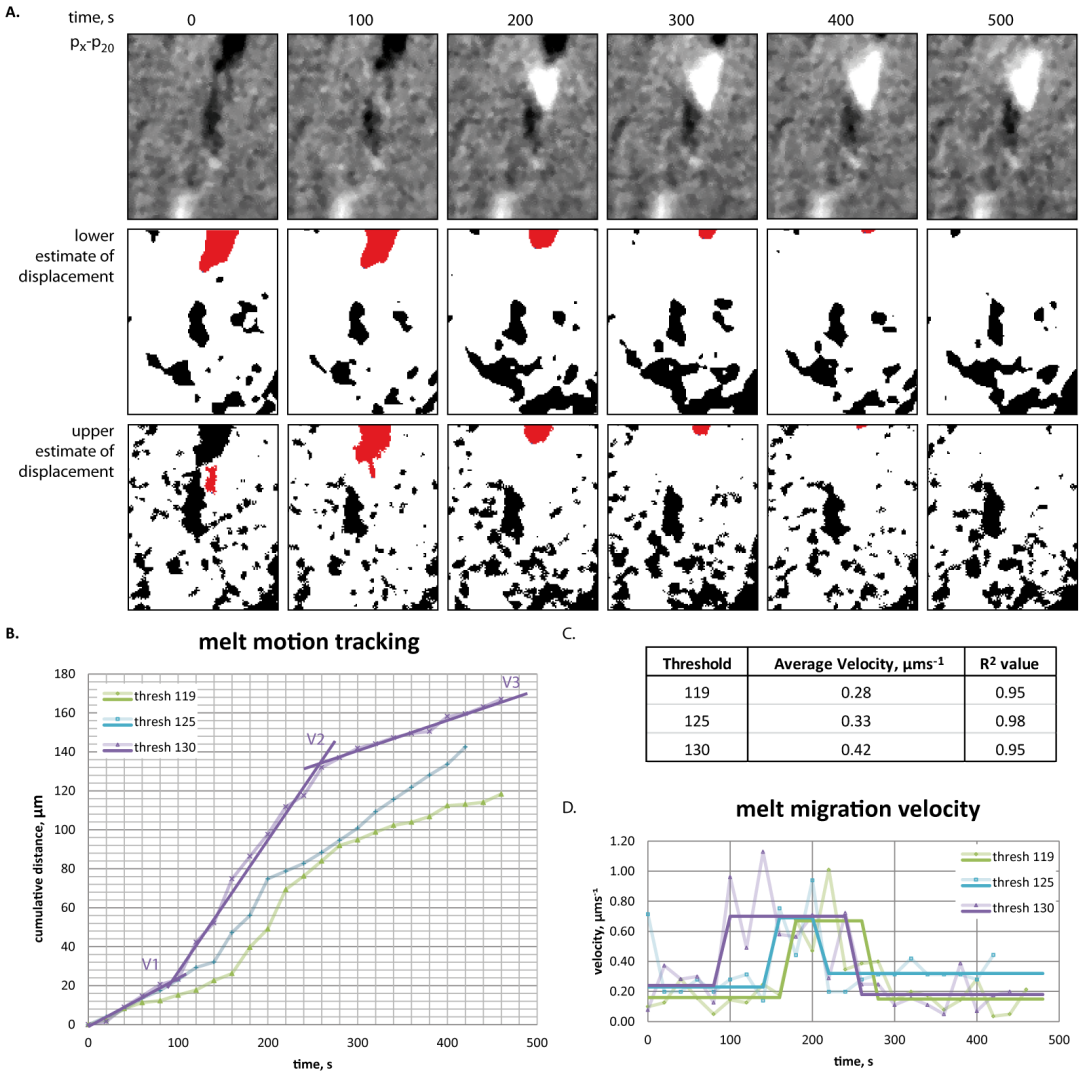

Figure 5.32: Melt motion tracking by image analysis of 2D radiography, with melt motion M2 as an example. A. A series of stills showing the motion of interest over a time interval of 500s: i) A greyscale image $p_x - p_{20}$ showing changes from a starting point of projection 20 which highlight melt movement (see text). Image has been filtered on ImageJ using 'remove outliers' function to reduce noise. ii) The same image thresholded at a minimum greyscale estimate and iii) maximum estimate, with the melt volume of interest highlighted. In each case, the min x and min y (bottom left) pixel location was measured. The maximum melt threshold leads to a slightly larger estimate of displacement. B. A time-displacement graph of the tracked point for three different threshold values. Although the overall displacement varies between the three measures, the overall shape of the three graphs is similar, all revealing a sharp increase in apparent velocity in the middle ≈200s. The line of threshold 130 is labelled with these three stages as V1, V2 and V3. C. gives a table of the average velocities of the full 500s measured. D. shows a graph of the velocities measured between each datapoint for each dataset (pale line) with the average velocity measured for v1, v2 and v3 shown as the darker line.

	distance / µm	time / s	speed / µms^{-1}
M1a short	300	20	15.0
M1a mid	900	20	45.0
M1a long	1150	20	57.5
M1b short	300	20	15.0
M1b long	800	20	40.0
M2 2d	350	540	0.6
M2 short	400	540	0.7
M2 mid	500	540	0.9
M2 long	1500	540	2.8

Table 5.5: A table of melt velocity estimates for gold melt flowing along fracture planes, using different estimated flow paths. The process of estimating distance is described in figures 5.33 and 5.34.

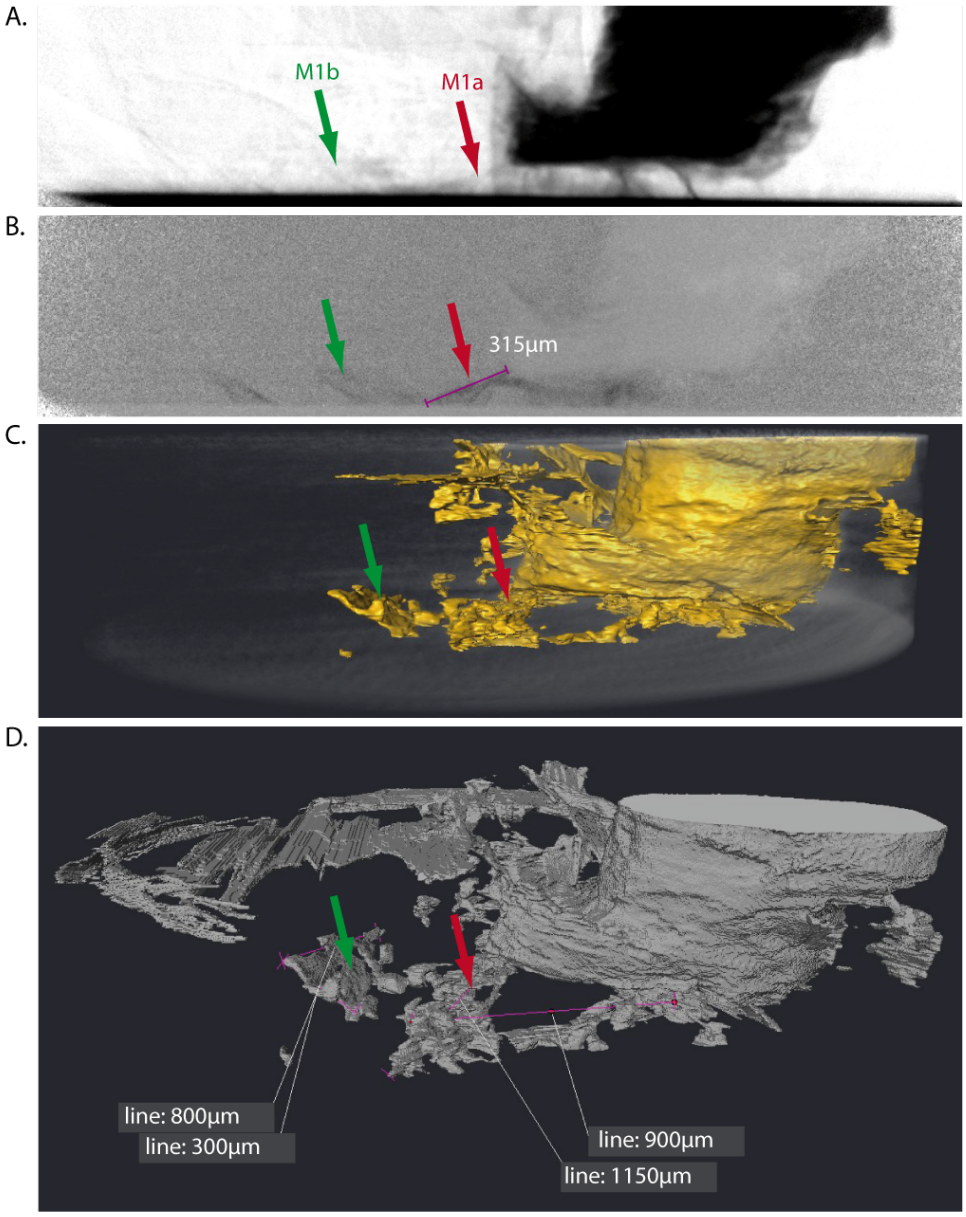

Figure 5.33: Figure showing the process of matching melt migration observed in 2D radiographs to 3D tomographic reconstructions of the existing fracture network in AuBN1_8. A. Example of an original radiographic projection (p_5), with areas of interest labelled. B. Image $p_5 - p_0$ highlighting initial movement M1 in the image. The minimum path the melt has taken is the direct 2D path taken as shown in purple, measured at ~300µm. This movement is shown to occur between two projections (see fig 5.30), therefore can be constrained to take place in 20s or less. C. 3D reconstruction of AuBN1_8 with arrows showing suggested location of melt migration (assuming no new fracture has been created) D. Measures made using Avizo Fire ^{TM} '3D Measure' tool showing estimated displacement of paths taken along the 3D fractures (voxel size = 2.8µm). Due to partial volume effects and significant artefacts, reducing certainty of segmentation, therefore distances have been rounded to the nearest 50µm (±~10 voxels).

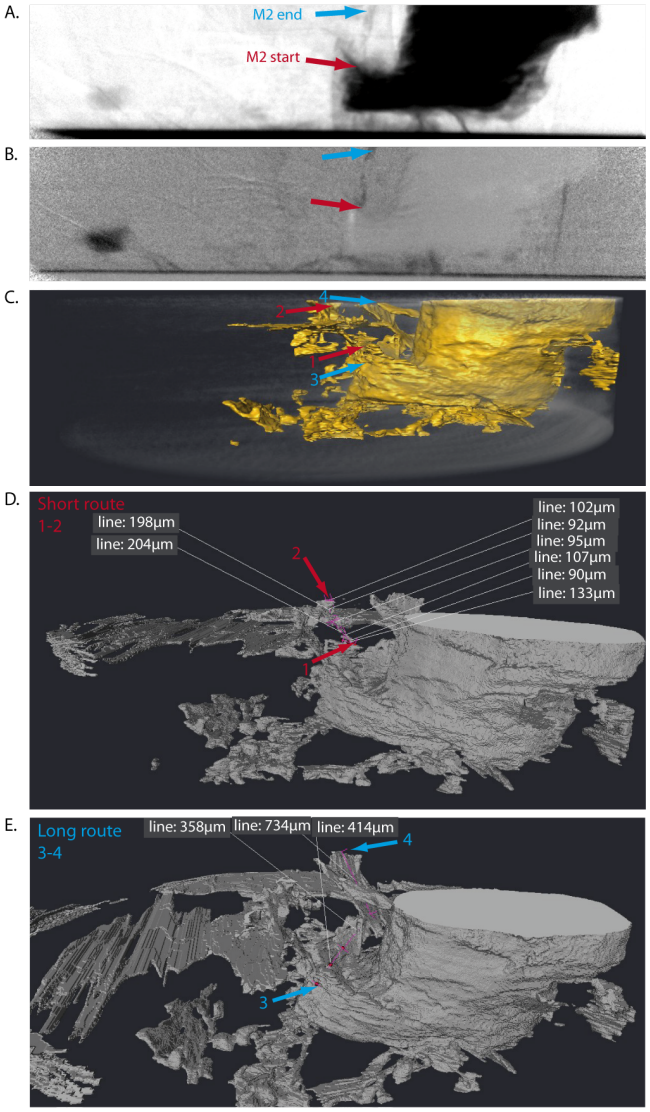

Figure 5.34: Figure showing the process of matching melt migration M2 as observed in 2D radiographs to 3D tomographic reconstructions of the existing fracture network in AuBN1_8. A. An example of an original radiographic projection (p_{70}), with the approximate start and end of observed motion labelled -see figure 5.31 for full movement. Complete motion from this start and end point is observed over a total of 27 projections, a total time of 540s. B. Image $p_{70} - p_0$ highlighting melt movement in the image. C. 3D tomography of AuBN1_8. It is difficult to match the observed movement to an existing fracture network and there are multiple potential starting and finishing locations. Estimates of the shortest and longest routes are shown. In this case, 2D radiography shows good evidence for melt movement occurring along a pre-existing fracture network (figure 5.31) D. shows measures of the shorter route from location 1 to 2, with an intermediate, slightly more convolute route with the same start and end point (mid-estimate) E. shows measurement of the longest estimated path, from the sample middle (3) to the edge of the field of view (4).

Explaining characteristics of gold melt migration

Notable characteristics of gold melt migration observed within sample AuBN1 include:

- Relatively fast movement observed, despite the high interfacial tension and therefore inferred low mobility of gold melt.
- Apparent brittle behaviour of melt migration through sheet-like fractures, as opposed to slow permeation of melt along grain boundaries.
- The episodic nature of these melt migration events, interspersed with periods of several minutes of apparent quiescence, which are not clearly correlated with a drop in temperature or power.

The following discussion will attempt to explain these characteristics in terms of simple models of fluid flow and fracture propagation. Bearing in mind the unique properties of gold melt, we will compare these processes to those occurring in other *in-situ* investigations in this chapter, carried out in different partial melt systems.

Possible driving forces for melt migration

In experiment AuBN1 the melt front was observed to move through fractures at rates of ~10^{-6}-10^{-5}ms^{-1}. Gold was expected to have a low mobility, due to its high dihedral angle of 145° in the cubic BN system (Ricci and Novakovic, 2001), and in comparison to previous studies of melt migration carried out over the course of this project, these flow velocities were higher than we were initially expecting.

Melt movement observed has been modelled using a simple Darcy's law flow calculation of sheet flow along a single planar fracture (The cubic law):

$$q = \frac{\rho_l g}{\mu} \frac{w^3}{12} \frac{\delta h}{\delta L} \tag{5.1}$$

where q = advective velocity, ρ_l = density of liquid, w = fracture aperture, μ = viscosity of liquid and $\frac{\delta h}{\delta L}$ is the hydraulic gradient. h is the hydraulic head, which can be expressed as a combination of the elevation head (z) and the pressure head $\frac{P}{\rho g}$, defined as $h = z + \frac{P}{\rho g}$.

At high T but ambient pressure, μ of liquid Au is estimated at 0.04Pa s (Ofte, 1967), and ρ_l at 17,310kgm^{-3}. In experimental samples $L \approx 0.001$m, and $z \approx 1$mm. If flow was produced simply by a change in elevation (i.e. $\frac{P}{\rho g} = 0$), q is calculated to be on the order of 10^{-12}ms^{-1}, at least 6 orders of magnitude lower than observed in our experiments. Although these calculations are simplistic, they do tend to overestimate flow rates, with additional factors such as fracture roughness and tortuosity acting to slow migration velocities. An additional driving force is clearly required to produce the melt flow observed.

By varying values of δP, the hypothetical fluid overpressure required to produce melt migration on the order observed in our experiments can be estimated over a range of feasible aperture values (10-20μm), giving a range of solutions of 0.001-5 MPa to explain minimum and maximum velocity estimates (Figure 5.35).

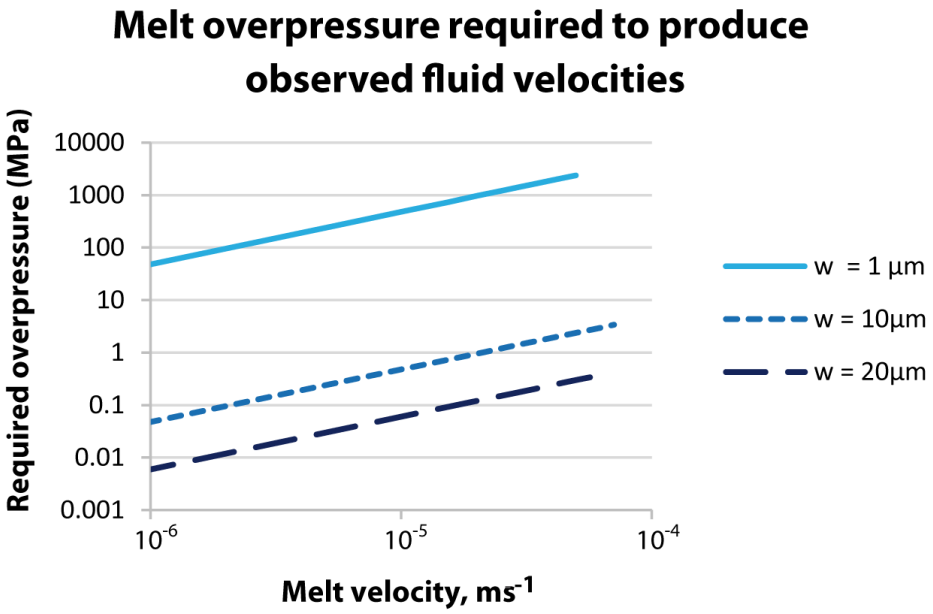

Figure 5.35: Range of overpressures calculated using equation 5.1 for different fracture apertures (w), fitted to observed range of velocities from experiment AuBN1

A solid-liquid phase change at atmospheric pressure will generally lead to a volume expansion as density decreases on melting. The phase transition is therefore likely to lead to an overpressure pushing outward from the melt-rich zone. Assuming the solid is incompressible, the overpressure value will be equivalent to the pressure difference, ΔP, between the pressure required to compress the liquid from its theoretical density at atmospheric P, ρ_l to the density of the solid state ρ_s, and the background confining pressure (P_c):

$$\Delta P = \left(K_T \frac{\Delta \rho}{\rho_l} \right) - P_c \tag{5.2}$$

where K_T is the bulk modulus, or resistance to compression of the material, and $\Delta\rho$ is the difference in density between solid and liquid states. Assuming Au ρ_s = 19,300kgm^{-3}, ρ_l = 17,310kgm^{-3}, and the bulk modulus of liquid gold is 63GPa at 1600K (Blairs and Joasoo, 1980; Steeb and Bek, 1976)[1]. Taking into account that the system is already at 3 GPa confining

[1]Steeb and Bek (1976) measure a value of adiabatic compressibility for gold κ_S at 1x10^{-12} cm.s^2/g. This has been converted to isothermal compressibility, $\kappa_T = \gamma\kappa_S$ where γ is ratio of isobaric vs. isochoric

pressure, the overpressure associated with this phase change is around 3 GPa. This value drops to 2 GPa when taking into account the fact that the gold in the centre is diluted with solid BN in a ratio ~1:3 (density 2100kgm^{-3}), but is still several orders of magnitude higher than that required to cause flow of the velocities observed, for aperture values of 1-20μm.

If overpressure is the sole cause for melt migration we may expect to see movement in all directions from the capsule. We certainly do observe melt migrating in multiple orientations, but there appears to be a preference for melt to move downward. This suggests there may be an additional melt gradient encouraging flow in a particular direction. The density difference between gold and BN is large (~15000kgm^{-3}), which will create a subtle melt gradient, although the driving force is much lower than that of fluid overpressure, as previously discussed above. A thermal gradient may also be present, known to cause significant melt movement in other partial melt experiments (Lesher and Walker, 1988). Once a full sample scan is available, it may become more apparent what is causing melt to flow in a particular direction.

Why do we see brittle movement and fracturing at high P-T?

The large melt overpressure calculated may explain the mechanism of brittle fracturing observed to be the main mechanism of melt propagation. Our experiments are conducted at pressures of 3 GPa, and temperatures of 1400°C, which should place the system well into the ductile regime of deformation. Initial movement observed during experiment AuBN1, shortly before the onset of melting, was thought to be in the form of plastic deformation due to the speed of motion. As melting occurs, the gold is clearly observed to move along fine sheets with the geometry of fracture planes, rather than a pervasive percolation along grain boundaries, suggesting a change to brittle behaviour.

Brittle processes occurring at extreme pressures and temperatures have been observed in laboratory experiments from micro-structures (DellAngelo and Tullis, 1988) and from acoustic emission observations (Dobson et al., 2002). Observations in real rock exposures show ductile fabrics implying high TP, overprinted with evidence of contemporaneous brittle fracturing by melt. These can be explained by a process of 'melt-enhanced embrittlement' (Davidson et al., 1994), again linked to overpressure created by melting. Brittle processes are thought to occur when the overpressure is higher than can be relieved by percolative flow along grain boundaries. This process is therefore more common in low permeability systems, and would be expected to occur here where the melt source is a large volume of a high surface-tension liquid, where flow along grain boundaries is limited and significant pressures can build up.

From natural rock textures, Davidson et al. (1994) calculated that only a small differential stress (<20MPa) is required for hydraulic fracture to take place in a basaltic melt system, at high pressures. The pressure required to initially fracture the surrounding BN in our samples is

heat capacity, estimated at 1.5 for gold (Blairs and Joasoo, 1980). κ_T is inverted to find isothermal bulk modulus, $K_T = 1/\kappa_T$

complex to calculate, as it may depend on pre-existing weaknesses, but the high overpressures calculated from initial phase changes (2-3 GPa) do suggest that there could be enough force available for hydrofracture to take place. It is unclear whether the melt movement is taking place by true hydrofracturing through BN grains, or by prising apart of grain boundaries (figure 5.36). There is evidence to suggest that both processes take place (figure 5.36 E,F). Further BSE analysis of micro-structures may clarify the processes occurring. Which path the melt takes most likely depends on an interplay of grain size and the precise orientation of melt pockets in relation to grains.

Why is melt migration episodic?

Episodicity requires a mechanism for fluid flow to cease along fractures, for renewed overpressure to build up, and a renewed release of melt to occur in a cyclic pattern. The discussion above suggests that a fluid overpressure from volume expansion could explain melt flow velocities. As melt flows out of the sample volume, this would release the overpressure and therefore remove the driving force, which will slow the melt flow and maybe halt it entirely. For this process to explain the observed episodicity would require repeated solidification and remelting of the system to produce repeated volume expansions within the system.

Episodicity is a constant characteristic of dyke emplacement on Earth as observed by episodic seismic tremor (White et al., 2012, and references within). The majority of laboratory and field studies conducted suggest refreezing of dyke tips is the cause of episodicity, due to the dyke entering a relatively cool source rock (Ozerov et al., 2003; White et al., 2012) and freezing, allowing pressure to build up behind them until they re-fracture.

In our experiments melt and matrix are thought to be at thermal equilibrium, therefore solidification will not occur due to cooling upon entering the host material. It is possible that minor, localised temperature fluctuations could reduce the temperature to below the solidus in some areas of the sample. However, there is no clear change in the process observed even when power is increased significantly beyond initial melting temperature of gold. An alternative speculation is that pressure increases at fracture tips could cause temporary solidification of melt, although it is unclear what pressure changes would be required to cause this (an increase in pressure will increase the solidus temperature).

However, it may be possible to explain the episodicity without having to invoke localised solidification. The following calculation examines the overpressures required to keep a fluid filled crack expanded and flowing (Lister and Kerr, 1991)

$$\Delta P_e \sim \frac{(\mu/(1-v))w}{l} \tag{5.3}$$

where μ = shear modulus, v = poisson's ratio of the material and w = aperture. For a fracture in hexagonal polycrystalline BN ($\mu \approx$ 300GPa, $v \approx 0.17$ (Green et al., 1976)), the

overpressures required are calculated on the order of several GPa. As the overpressure created on melting will be released as soon as fluid flows, fractures will not remain dilated beyond initial movement, and are likely to seal quickly again after initial fluid flow. High interfacial tension of remnant melt in narrow fracture entrances may also act to seal existing flow paths, without solidification of melt.

A mechanism is required to recharge fluid overpressures to a large enough level to create renewed flow surges of relatively high velocity. As seen by the physical movement of the anvil, the sample assembly is constantly undergoing shortening during the experiment. As fluid and solid will compress at different rates, continued compression could lead to re-pressurisation of the melt rich source. The cycle of episodicity could hypothetically be produced by a combination of initial hydrofracture caused by volume changes on melting, pressure drops halting fluid flow and resealing of fractures, followed by renewed pressure build up from uneven compression of the sample assembly to levels required to force fluid flow back through pre-existing fractures.

This would suggest that the overpressure of secondary melt migration events may be significantly lower than the original hydraulic fracturing event, leading to lower fluid flow velocities. This would be compatible with observations made in movie 5, where melt movement M1, the first observed on onset of melting, is much faster than movement M2, which is observed to flow along a pre-existing melt network.

The above discussion makes a number of significant assumptions. Observations are limited to one sample, and further experiments would have to be carried out to test these hypotheses. Speculatively, however, characteristics of melt movement could be explained by the mechanical properties of liquid gold in combination with large initial melt fractions in the source region.

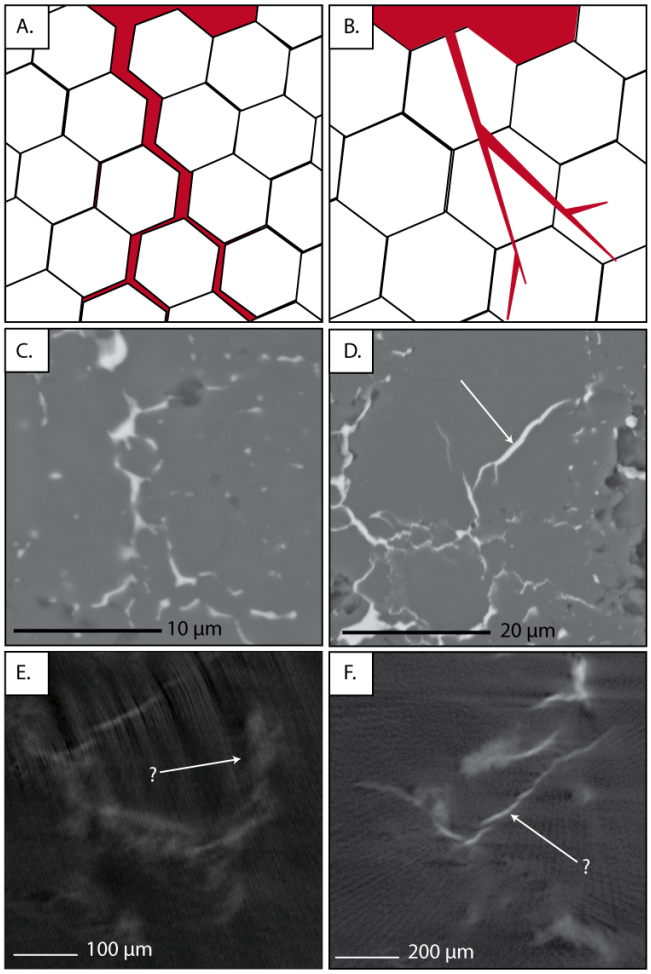

Figure 5.36: Figure showing two endmember mechanisms by which melt can propagate via fractures into a polycrystalline material. A. Migration by 'prising apart' grain boundaries. B. Fracture propagation by brittle fracture and internal splitting of individual crystals. In both A. and B., the melt source is shown at the top, with melt migrating downwards. C. and D. show examples from BSE imaging of each of these processes occurring in the deformed FeS-olivine system relevant to core formation (experimental sample FeOl1, described in detail in chapter 3). Pale grey areas are FeS melt, dark grey crystals are olivine. E. and F. show examples of fractures observed within tomographic scans of AuBN1, interpreted as convolute wetted grain boundaries (E.) and more brittle, potential grain splitting boundaries (F.). The poor quality of scans makes this identification highly speculative and higher quality data is required to confirm this. Pale grey is gold melt phase, and dark areas are polycrystalline BN. NB the scale associated with tomographic scans (E, F) is significantly smaller than SEM images. The exact grain size of BN is unknown but thought to be very fine, while fracture features are much larger than observed in the FeS-olivine system. It is possible that the sharper fractures are still following grain boundaries of very fine, unresolvable BN grains.

5.3.4 Comparison between *in-situ* experiments in different partial melt systems

During experiments described in section 5.3.1, FeS melt was not observed to move over timescales observable over the course of *in-situ* experiments. As previously suggested, the lack of movement could simply be due to the fact that temperatures were lower than initially estimated and melting had not taken place.

However, the properties of the liquid, combined with the lower melt fraction used, may also be the cause of the lack of movement observed, even if the FeS was fully molten. Table 5.6 shows some key properties of liquid FeS in comparison to liquid gold. Important differences in material properties are the density differences between liquid and solid, and the bulk modulus of the liquid, which indicates resistance to compression. Although FeS should expand more on melting than gold (the ratio of $\delta\rho/\rho_i$ dictates the extent of expansion of the material during melting), the higher compressibility of the volatile-rich liquid means that potential overpressures built up on the phase change are far lower. Using equation 5.2 and assuming a central melt rich zone of 20% FeS + 80vol % olivine as used in DIAMOND experiments, the final pressure difference is a negative underpressure of ~1GPa (at 2GPa confining pressure). Even if the centre of the sample was 100% FeS the melt overpressure would be 0.1 GPa, significantly lower than in the gold melt experiments. Even if the material was molten, it may not have had a significant driving force to cause melt migration away from the central melt-rich zone, even with the addition of non-hydrostatic stress.

	ρ_s	ρ_l	$\Delta\rho_s$	**Bulk modulus (liquid),** K_T
FeS	5100 [a]	3800 [a]	0.25	$5.4\text{x}10^{10}$ [a]
Au	19300	17400 [b]	0.1	$1.8\text{x}10^{11}$ [c]

Table 5.6: A table showing properties of density, viscosity and compressibility for FeS in comparison to Au liquid, used as parameters in equation 5.2 to estimate potential overpressures created during volume expansion. References: a) Urakawa et al., 2001 b) Paradisa et al., 2008 c) -see footnote 1.

Rushmer, Petford, et al. (2005) estimate the order of magnitude of potential overpressures produced by shear deformation for melt fractions of 10-20% at strain-rates of 10^{-5} to $10^{-6}s^{-1}$ will produce differential stresses within individual melt pockets on the order of 0.1-100MPa, several orders of magnitude less than the overpressures produced from phase changes on melting of gold. According to these values, differential stresses produced in low strain-rate experiments are unlikely to produce the large scale fracturing observed in gold melt migration experiments. However, melt overpressures from deformation may still act to cause fluid flow into grain boundaries. Assuming differential stress is the only driving force for melt migration,

velocities calculated using Darcy's law (equation 5.1) for flow along a planar sheet into grain boundaries of around 0.1 μm, melt migration velocities are on the order of 10^{-11} - 10^{-9} ms^{-1}, and distances melt may be expected to migrate in an experiment lasting 1 hour may be on the order of 0.1-10μm, and therefore may be too low to be resolved in CT scans. These calculations also tend to significantly over-estimate melt velocities, therefore migration distances may be much lower than this. Also, there is no clear reason for the pressure differences to encourage melt movement away from the central melt-rich zone, and rearrangement within this central melt zone is difficult to see due to small grain sizes.

This difference in liquid properties does suggest that gold melt may not be the best analogy for melt migration during core formation, and the melt movement characteristics observed may be unique to this specific partial melt system. Comparison between different partial melt systems will be discussed further in the following chapter.

5.4 Conclusions

- We have successfully incorporated rotoPEC equipment into two synchrotron beamlines to carry out *in-situ* high temperature and pressure experiments, carrying out a series of tomographic scans to track changes in 3D sample geometry over the course of an experiment.

- Experiments carried out at DIAMOND on samples in the FeS-olivine system, did not show significant changes in melt geometry over the timescales of a single experiment. This may be due to a lack of melt migration gradients to encourage melt redistribution, or very low melt velocities, although could also be due to the experiment being at lower temperatures than suggested by previous calibrations. The uncertainty in experiments is due to a lack of a direct temperature measure during these experiments.

- Phase I experiments at ESRF used a dual capsule design to encourage large-scale movement of melt along a pre-existing plane of weakness, using a more mobile Hf-doped basaltic melt. Movement was observed to take place, and was faster than initially expected. However, on further analysis of the sample after quench, the movement was observed to be of a complex multi-phase Fe-rich and basaltic melt fluid. The complexity of results highlight the need for thorough post-quench analysis and SEM groundtruthing to remove uncertainty of interpreting processes from CT scans alone.

- The final experiments conducted in the gold melt system showed the greatest success in characterising melt movement through a solid matrix. A combination of 2D radiography to capture melt movement, and 3D CT scans to capture intermediate melt geometries, was shown to give a more thorough understanding of the melt migration processes

occurring in the sample. The rapid melt migration, episodicity and brittle nature of melt migration events observed in the final experiment may be explained by the high melt fractions used in combination with unique fluid properties of gold melt. This may make these specific experiments less applicable to real Earth systems.

CHAPTER 6

Synthesis, conclusions and critical evaluation

6.1 Introduction and chapter structure

This chapter aims to summarise, compare and evaluate work carried out over the course of this PhD project. First, each chapter's key findings will be examined in the context of previous work, specifying how our results impact the current standing of research into partially molten systems. The next section attempts to compare between different experimental samples in the three chapters of the PhD, taking into account differences in experimental design, to assess melt textures and structural differences across different partial melt systems, what comparisons can be drawn and where differences in melt characteristics change processes of textural development. There follows a critical examination of the techniques used over the course of this PhD and an evaluation of experimental limitations, and a final section detailing ideas for future research and method development to improve reliability and broaden applicability of the preliminary work described in this thesis to real geological systems.

6.2 Summary of results in the context of previous work

6.2.1 Chapter 3: connectivity of FeS in olivine and applications to planetary geology

Chapter 3 details experiments carried out on the FeS melt-solid olivine system at small fractions of partial melt (5vol%), using the novel rotoPEC experimental equipment to investigate the effects of torsional deformation on dynamic melt mobility. We have found that deformation does enhance the mobility of FeS melt in a polycrystalline olivine matrix, leading to wetting of 2-grain boundaries and initiating localised melt segregation. These results contribute to a building body of evidence that dynamic deformation enhances permeability of melts that would otherwise be immobile in hydrostatic high P-T systems, as originally suggested by the Kohlstedt group (Bruhn et al., 2000; Groebner and Kohstedt, 2006; Hustoft and Kohlstedt, 2006) and supported by work carried out on natural meteorite samples (Rushmer, Petford, et al., 2005).

Our main contribution to this research area is two-fold:

1. Our experiments have been conducted at lower strain-rates, total strain and longer duration than previous experiments (see figure 3.1, section 3.2.1), at concurrent realistic high P-T conditions. In fact, we find the best developed textures in our longest duration, lowest strain-rate experiment. Our results appear contradictory to the findings of Walte et al. (2011), the only other study to conduct deformation experiments in this system at high confining pressures, who do not see the development of melt networks at strain-rates of $<10^{-5}s^{-1}$. This difference may be due to increased experimental duration

allowing textures to develop more fully, or due to differences in deformation mechanism (pure shear triaxial compression vs. simple shear in our torsional deformation experiments), which may affect textural development.

2. Our study is the first to use 3D visualisation of experimental samples using both micro- and nano-CT techniques to examine the FeS-olivine partial melt system. Although tomographic imaging has been used to visualise small melt fractions in this partial melt system in order to estimate percolation thresholds in hydrostatic systems (Watson and Roberts, 2011), and to examine multi-phase solid distribution in deformation experiments conducted to very high strains (Wang, Lesher, et al., 2011), our analysis of melt textures at multiple resolutions has allowed more thorough characterisation of 3D geometry than possible in previous deformation studies.

The results from our experiments alone are insufficient to confirm that this mechanism can be extrapolated to core forming conditions to fully form the core without the need to invoke further silicate melting. However, in contrast to Walte et al. (2011) we see no evidence to suggest that the segregation mechanism changes with decreasing strain-rates and that the process should become less efficient with decreasing strain-rates, if balanced out by increasing grain sizes reducing the effect of interfacial tension (Groebner and Kohstedt, 2006). Simple calculations of timescales of core formation across a range of permeability values suggest that, assuming interconnectivity of the FeS network, percolation of melts would be highly efficient and metal could drain to the core within 1Ma of melting, even at very low estimates of permeability. Even if the mechanism is not 100% efficient, deformation enhanced percolation is likely to have initiated core formation before the onset of silicate melting, and may be part of a protracted, complex, multi-stage process initiating in planetesimals accreting to form the rocky planets (Halliday, 2013). The geochemistry of the Earth probably reflects the disequilibrium nature of the core formation process (Rudge et al., 2010).

6.2.2 Chapter 4: basaltic melt in olivine at conditions of the upper mantle

The aims of work carried out in chapter 4 were to

1. Develop a simple doping methodology to enhance contrast between olivine and basalt, to allow visualisation of basaltic melt networks using standard CT machines.

2. To compare the 3D geometry of basaltic melts at varying melt fractions, and experimental durations, in static and dynamic deforming systems.

By doping basaltic glass with 10vol % Hf, volume reconstructions of basaltic melt experiments in hydrostatic systems were created that were comparable in quality to those of

Zhu et al. (2011). Although recent reviews suggest the potential for doping silicate melts (Rushmer, Dixon, et al., 2015), to date there is no published work using this technique in the context of CT scans of partial melt systems. The doping method used may have some advantages over phase contrast imaging, in that grain boundaries wetted by basaltic melt will be more easily distinguishable from dry grain boundaries (which may also be enhanced by phase contrast imaging), even if melt sheets are very thin. In addition, the technique can be used on any XCT system, including high P-T *in-situ* work, as described in chapter 5. Although resolution of BSE images is still far higher, doping methods in combination with high resolution CT scans could help to constrain melt geometry at very low melt fractions, as a faster, alternative method to laborious serial sectioning carried out in previous studies (Garapic et al., 2013). However, the doping technique requires improvements to remove excess hafnia (HfO_2) and ensure full dissolution into the basaltic liquid, as deformed samples in particular were unable to incorporate hafnium leading to a complex 'granular' melt phase which complicated segmentation of CT images.

Interpretation of 3D geometry of undeformed samples is complicated by the lack of textural equilibrium, which generally makes textures anisotropic, with the quench product capturing dynamic melt migration. Grain boundary wetting occurs in all undeformed samples, even at very small melt fractions (some areas are drained to <2vol% melt). At low melt fractions the majority of melt does appear to reside in triple junction tubules, supporting the argument of Zhu et al. (2011) that melt sheets in 2-grain boundaries probably do not limit permeability significantly. The presence of hydrofractured grains parallel to apparent melt flow in samples of low melt fraction, however, suggests that melt flow along triple junctions may still be insufficient to overcome fluid overpressure caused by melt migration gradients in the sample (Davidson et al., 1994). These textures suggest that at a certain grain size, melt will create its own pathways by hydrofracturing if the permeability of the grain-scale network is insufficient, supporting theories that melt-enhanced embrittlement may increase permeability and be an efficient method of melt extraction (Connolly, Holness, et al., 1997). This brittle process also enhances the anisotropy of the melt network, thereby significantly changing the geometry of the melt network without the influence of deformation. Our results suggest that deformation may not be required at all to produce this effect, as long as a sufficient gradient exists to encourage melt migration, although more experiments would have to be carried out to constrain exact processes creating observed migration gradients within our piston cylinder experiments.

Due to the difficulties of segmenting deformed basaltic samples and issues with experimental failures, the comparison of 3D deformation melt geometries to previous studies was limited in its extent. Combining 2D analysis and 3D melt distribution textures suggests that melt textures do change significantly with the addition of non-hydrostatic stresses. In comparison to previous work, we do not see pronounced alignment of melt pockets (Hier-

Majumder et al., 2004). The apparent decrease in connectivity and grain boundary wetting observed in deformed samples in 2D analysis may be caused by an increased anisotropy of melt networks rather than a reduction in overall permeability, but this hypothesis cannot be confirmed yet due to the difficulty of segmentation from tomographic scans. The differences in textures in comparison to previous work are probably due to low strains achieved in experiments. Melt alignment, for example, is observed from 100-500% shear (Holtzman and Kohlstedt, 2007), whereas our successful experiments are less than 50% total shear. It is clear that a distinct change in melt geometry does occur with application of differential stress, even at low strain-rates and over short time periods. It would be interesting to fully characterise these changes in three dimensions by improvement of the doping methodology, to examine the intermediate geometry in realignment of the melt to produce a melt-preferred orientation, or localised segregation. However, due to the complexity of processes occurring within the sample (presence of solid hafnia, evidence for other reactions, damage to the capsule etc.), the work in its current state is not enough to say for certain that textures developed are solely due to deformation.

6.2.3 Chapter 5: *In-situ* melt migration using synchrotron technologies

Work in chapter 5 represents a series of preliminary feasibility studies to investigate the scope of possibilities for *in-situ* work using the newly designed rotoPEC equipment. Our research group is one of a number of groups interested in adapting high pressure-temperature devices to carry out X-ray microscopy, all of whom are at a similar stage of method development, with the majority of published work being in the form of 'proof of concept' studies (Gotou et al., 2015; Rushmer, Dixon, et al., 2015; Wang, Lesher, et al., 2011). Work of Wang, Lesher, et al. (2011) was able to track large-scale geometric changes over time in a multi-phase solid system undergoing deformation. Resolution limitations were similar to ours, although they were able to carry out experiments to very high strains therefore changes were less subtle. These experiments did not have the additional instability of a partial melt phase, which may explain why experiments were more stable. Gotou et al. (2015) have shown the potential for tracking phase segregation using 2D radiography in an adapted multi-anvil device, in this case in an iron-rich melt - silicate multiphase liquid system. Although the combination of 2D radiography and 3D imaging is mentioned as a potential future step by Gotou et al. (2015), to the best of our knowledge no research has been published that combines 2D radiography with 3D tomography to track the evolution of sample geometry and migration of partial melt in a solid matrix. Our study of gold melt migration, in which we are able to capture migration through apparent micro-fractures and estimate velocity of the migrating melt front, therefore represents the next step forward in terms of *in-situ* partial melting experiments.

Key melt migration characteristics observed in this experiment, in particular the apparent brittle behaviour and episodicity of melt migration, may be due to the unique properties of gold melt, combined with large melt fractions used, and may therefore be difficult to compare to off-line partial melting experiments of other melt compositions. However, the direct observation of melt migration throughout an experiment does highlight limitations of the classic ex-situ post-quench analysis of samples (Bruhn et al., 2000; Hustoft and Kohlstedt, 2006; Walte et al., 2011). Episodicity of melt flow, for example, is something that is impossible to observe by this type of analysis, and it is feasible that the development of melt veins and networks such as those observed in previous deformation studies could have been created by discrete pulses of movement, rather than a gradual development of textures. *In-situ* work such as ours represents a unique opportunity to observe time-resolved evolution of a dynamic system such as melt migration.

6.3 Comparison of results across chapters: textural comparison in different partial melt systems

6.3.1 Comparison of the FeS-olivine and basalt-olivine partial melt systems

The work carried out in chapters 3 and 4 gives us the opportunity to compare textures produced in partial melt systems of contrasting mobility and composition. Detailed 2D and 3D characterisation of melt textures has been carried out, as well as analysis of compositions and structural effects on olivine crystals, both during annealing and in response to deformation. Here I will briefly discuss differences observed between the two systems to examine how these factors are affected by melt characteristics.

Static textures

Differences in static textures were generally as predicted by previous studies. Figure 6.1 A-C show textures of two samples that were each nominally 5vol% liquid. FeS, at melt fractions of 5vol% studied, is stranded in isolated, high angle melt pockets at triple junctions, with an average dihedral angle consistently >60°. In contrast, basaltic melt is observed to wet grain boundaries in very fine sheets, even at very low melt fractions (the area in B. has been drained to <2% melt). Textures are similar in areas of higher melt fraction (C.) but melt sheets are thicker. A significant number of spherical FeS inclusions are found within olivine grains, absorbed as liquid inclusions during growth. In contrast, the basaltic system has few liquid

inclusions within grains. This may be an effect of increased mobility - basaltic melt is able to move fast enough to avoid being engulfed by growing olivine grains (Karato, 2008).

Dynamic textures at low melt fractions

In the FeS-olivine system, deformation acts to enhance the connectivity of an initially immobile melt by pushing melt into 2-grain boundaries and allowing networks to form (Figure 6.1 D.). In the basalt-olivine system, the effect is less clear (Figure 6.1 E,F.). In fact, at low melt fractions (Pdef2), deformation appears to reduce the number of wetted grain boundaries (although it is important to take into account the reduction in contrast of basaltic melt due to the lack of Hf uptake - some very fine melt sheets may be difficult to observe even in BSE imaging). Analysis of melt topologies highlights this change: In the FeS system, melt networks increase in mean node connectivity, while basaltic melt generally shows a decrease in connectivity, with both moving towards an average of around 2 (assuming, as supported by 2D textural analysis, that the change is not solely due to worse segmentation of CT scans). This is compatible with the assumption that shear deformation enhances the anisotropy of a melt network (W. Zhu, pers.comm.). In this sense, the addition of non-hydrostatic stresses may lead to convergence of textures in both systems, despite initial starting geometries being at opposing ends of the spectrum of melt mobility. However, this is unlikely to be a realistic way of looking at these textural differences. The mobility of basaltic melt is very high, therefore the addition of non-hydrostatic stresses will cause the melt to respond very differently, presumably encouraging immediate large-scale movement if facilitated by any gradient in melt fraction (in an open system). Although tangential textures at low strains may appear to resemble those of undeformed FeS melt, the true three-dimensional geometry may be highly anisotropic. The presence of a fabric is suggested by 3D reconstructions, although segmentation quality is too low in these scans to confirm that this is due to true melt geometry.

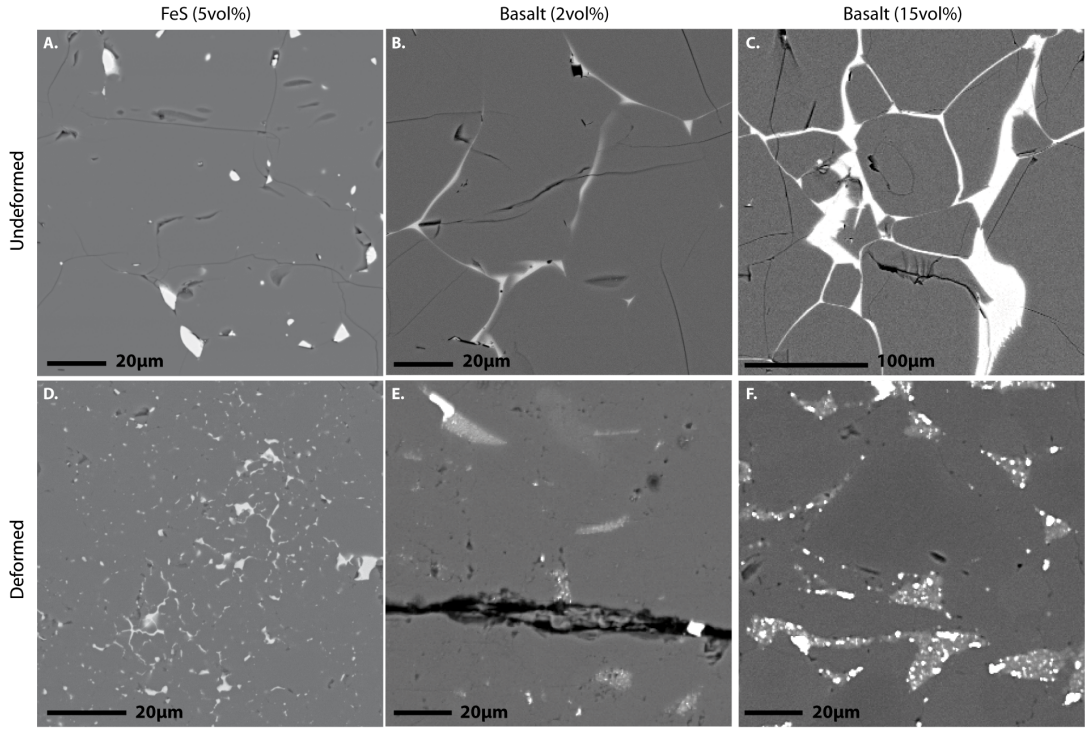

Figure 6.1: A comparison of partial melt textures in FeS-olivine (low mobility system) vs. basalt-olivine (high mobility system). A. FeS (white) in polycrystalline olivine matrix (undeformed), B. Hf-doped basalt (pale grey) in olivine, at low melt fractions (<2 % melt) C. Basaltic melt textures at melt fraction of ~15%. D, E and F show respective textures in a deformed system. In our experiments, deformed textures of basalt actually resemble the undeformed textures in the FeS-olivine system, at least in the tangential slices observed. The difference in textures of deformed samples is more pronounced than expected.

Olivine structure

The structure of olivines within both FeS and basaltic melt samples was examined by EBSD mapping, highlighting differences in grain size, internal deformation of grains and CPO development. The response of olivine crystals to both annealing and deformation was very different in both partial melt systems:

- **Grain growth during annealing.** Olivines are shown to grow significantly during annealing in samples containing basaltic melt. Maximum grain diameters in sampled areas are 85, 150 and 275 μm with annealing times of 2, 48 and 69 hours, respectively. Figure 6.2 shows a comparison of undeformed olivine textures from EBSD analysis. Although a direct comparison to the olivines in the FeS starting mix is limited due to a difference in initial starting grain size, evidence from textures in FeOlPC5 (6.2 A.) suggests different mechanisms of grain-growth are occurring in samples. Olivine grains in the FeS sample show a distinctly bimodal grain size, inferred to be caused by Ostwald ripening (Karato, 2008, p.238). In contrast, olivine grains in the basaltic melt series begin with a relatively heterogeneous grain size and appear to converge towards a more homogeneous distribution (6.2 B-D). This is due to the difference in solubility of olivines in basaltic melt in comparison to FeS - a low solubility enhances the effect of Ostwald ripening. In addition, overall grain-growth may be limited in the FeS-olivine system. The presence of inclusions on the edges of large crystals explains this - the lower mobility of FeS liquid means olivine is forced to engulf liquid FeS to form inclusions, a process known to reduce grain-growth (Karato, 2008, p. 237).

- **Development of CPO**. Deformation of the FeS-olivine system produces a clear CPO, although the slip system activated seems to be different in the lowest strain-rate, longest duration experiment FeOl1. Deformation in the basaltic melt - olivine system has only produced a clear CPO in Pdef1. This is not the highest strain experiment, but is the sample with the largest melt fraction (30vol%). The variation in CPO developed suggests differing mechanisms to produce them: FeOl1 shows a back-rotation of 010 poles, which may be evidence of strain partitioning as a result of melt segregation (Holtzman, Kohlstedt, et al., 2003) reflecting the reduced permeability of the system. The basalt system more closely resembles the 'aligned melt' CPO observed by Holtzman, Kohlstedt, et al. (2003), but it is also identical to the SPO orientation observed in picritic cumulates (Boudier, 1991); it is possible that the large melt volume allows crystals to rotate and align themselves to the shear direction. The lack of a clear CPO in the other two basaltic melt experiments, despite higher total strain, does suggest that the high melt fraction is the main cause for the CPO development in Pdef1. Pdef2 and Pdef3 (basalt) and FeOl2 (FeS) have comparable total strain and strain-rates, but CPO is less well developed in basaltic melt experiments. One possible reason for this

difference could be that these low strain levels are taken up by readjustment of melt in the high permeability system, while in the lower permeability FeS system, olivine crystals take up more of the strain by deformation. Although the exact cause of CPO developed in each system is not known, the results do suggest that mechanisms of deformation are different in each system, potentially caused by differences in permeability and melt mobility. However, other important variables may also affect CPO, for example the different starting grain size of olivines, and the complexity of an additional phase (hafnia) in the deformed basaltic melt samples.

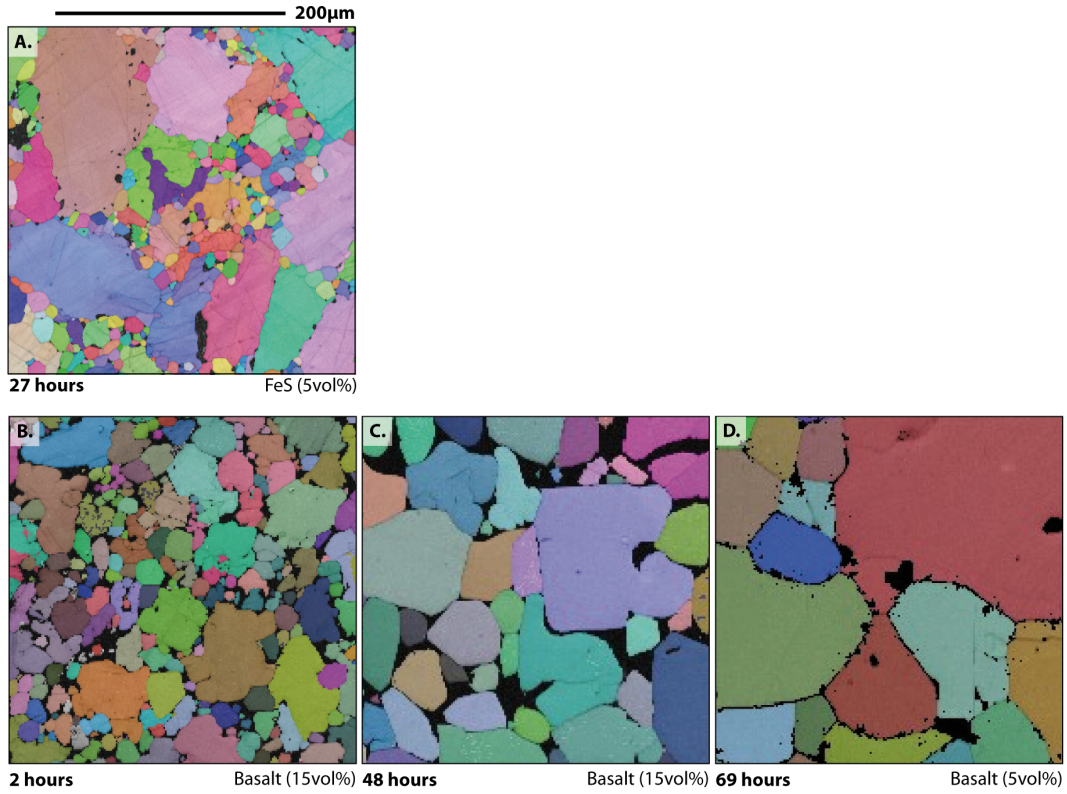

Figure 6.2: A comparison of grain-growth with annealing in hydrostatic experiments. A. FeS-olivine system, annealed for 27 hours. B-C are basalt-olivine samples, annealed for 2, 48 and 69 hours respectively. Grains are falsely coloured according to Euler orientations, and the melt phase is in black. The same scale is used throughout. Although different initial starting mixtures were used, there is enough evidence to suggest that different mechanisms and rates of grain-growth were acting, which is expected from the two contrasting systems.

Comparison between these two systems shows that textural differences are not solely caused by changes in melt mobility. The composition of basaltic melt, and the increased solubility of olivine in silicate melts also has a significant impact, particularly evident with olivine grain-growth. It may be that the process of migration of lower mobility FeS melts

occurs by very different mechanisms, and it is too simplistic to compare the two systems in terms of a 'sliding scale' of melt mobility, with deformation leading to convergence of the textures of the two materials.

6.3.2 Comparison of off-line experiments to *in-situ* observations

In-situ observations of melt migration were carried out across three different partial melt systems, although differences in experimental design still do not allow simple comparison between textures. Experiment OlBa2, carried out in the basaltic melt system, was shown to be highly complex, with multiple phases of melt present, thereby making it difficult to compare to other partial melt experiments in this thesis. However, it is interesting to compare the features (or lack of features) observed in FeS-olivine *in-situ* experiments to those quench textures observed in off-line experiments (Chapter 4), and compare these to the unique melt migration characteristics observed in the final experiment, AuBN1.

A comparison between FeS and Au melt is previously made in section 5.3.4, showing that characteristics of melt migration in the AuBN experiment may be due to the properties of gold melt and therefore are not directly comparable to FeS melt migration experiments, at least under conditions studied here. Fluid overpressures within FeS-olivine experiments in DIAMOND experiments are unlikely to have been sufficient to cause melt migration gradients alone, and the additional pressures created by low strain-rate deformation may not have led to significant movement (in relation to scan resolution) even if stresses were acting to encourage melt flow away from the melt-rich zone. Differences between off-line FeS-olivine experiments and those carried out *in-situ* include a much lower grain size, which will act to significantly reduce permeability of the system. In addition, experiments at DIAMOND were conducted by deforming the sample over short timescales (45min-1hour) at larger strain-rates, after which the sample was left to anneal for several hours. It may be that the application of continuous strain and low strain-rates over long timescales is more conducive to encouraging melt migration. For example, by calculations of velocity in section 5.3.4, assuming similar potential overpressures produced by deformation, over the course of 24 hours, melt may be able to move up to 10^2 μm in response to these pressure gradients, not taking into account changes in grain size. This order of magnitude of melt migration velocity may be sufficient to explain the small-scale redistribution of melt observed in off-line experiments. Theoretically, therefore, melt migration observations within these samples could be reconciled if both systems are molten, and the lack of melt migration observed may be due to the method of deformation, small grain size, and very low melt flow velocities within *in-situ* samples.

The episodicity of melt migration in the AuBN1 experiment is thought to be caused by a cyclic build up and release of overpressure. As discussed previously, melt could be moving in discrete migration events within off-line deformation experiments, a characteristic that is

missed due to limitations of post-quench analysis. Melt veins observed within FeOl1 could theoretically be created in discrete pulses of melt movement, rather than a gradual evolution of texture. A speculative mechanism for this would be overpressure build-up due to non-hydrostatic stresses, until it is possible to overcome interfacial energies and force melt along grain boundaries. The presence of some small-scale hydrofracture within FeOl1 (Figure 3.4) suggests at least some build up of overpressure occurred, although it is unclear whether this was during the onset of melting or at some other point during the experiment. Clearly this hypothesis requires further *in-situ* examination of FeS systems to be investigated further.

The importance of hydrofracture in different partial melt systems

Interestingly, evidence for hydraulic fracturing has also been observed throughout all experiments, and within all partial melt systems. Even for high mobility basaltic melt wetting all grain boundaries, at low melt fractions (2-5vol%) and under hydrostatic conditions, melt was seen to fracture solid olivine grains instead of bypassing crystals on wetted grain boundaries (sample OlBAVS4, chapter 5). This shows brittle behaviour takes place even when the system is highly mobile and permeable.

Brittle behaviour occurs when overpressures are too large to be compensated for by permeable flow. These can be created by sudden increases in volume e.g. phase change, as hypothesised in experiment AuBN1, but can also be created by large gradients of melt migration i.e. fracture will occur if melt percolation cannot take up excess strain. A large grain size is likely to encourage hydrofracture as the path to bypass the grains by permeable flow is longer and therefore overpressures are more likely to build up. This may play a role in the observed hydrofracture in the basaltic melt system during our experiments. The causes of hydrofracture, therefore, very between different partial melt experiments.

Brittle behaviour appears to be enhanced by the presence of melt even at high pressure and temperature conditions and it is likely that, in a real Earth system of large and variable grain size, brittle behaviour will play an important role in melt distribution and geometry. For example, the effect of hydrofracture may be important for core forming systems. Speculatively, it seems likely that in a system such as a young, heterogeneously mixed planet of variable grain size undergoing partial melting as temperature increases, there will be conditions leading to melt enhanced embrittlement and microfracture. The fact that the Fe melt – solid olivine system has a low permeability to begin with, at least in a hydrostatic system, makes it more likely that brittle fracturing processes may take place (Davidson et al., 1994). In an experiment examining reaction-induced micro-fracturing by granitic melt (Connolly, Holness, et al., 1997), melt overpressure induced fracturing is calculated to enhance permeability by four orders of magnitude in comparison to the original metamorphic rock system, showing microfracture could significantly enhance permeability relative to pervasive flow along grain boundaries.

This mechanism could allow melt to accumulate to significant volumes in response to a flow gradient, which could be enough to initiate large scale diapirism and long-distance melt migration required for core formation to be viable through a solid matrix.

6.3.3 Are melt migration processes comparable across different partial melt systems?

This section has attempted to compare melt migration processes across different partial melt systems, which vary according to melt and solid compositions, melt fraction and capsule design. Although similarities are found, and attempts are made to correlate differences with the extent of liquid mobility, or melt fraction, it becomes clear that the individual fluid properties are often too complex to allow a direct comparison. Not only does textural development rely on liquid mobility (i.e. interfacial tension), other characteristics such as melt density, viscosity and composition will also directly affect textures and migration dynamics in a system. Some of these factors may be interrelated (e.g. composition will affect solubility in a specific solid system, affecting interfacial tension), but others do not have a clear correlation (e.g. viscosity is not correlated with interfacial tension). Even if the melt composition was the sole variable across these experiments, it would be impossible to vary only one of these factors at a time. It may be a simplification to assume, for example, that gold melt will always act in a similar way to a reduced mobility iron-rich melt (predicted to be present in more reducing conditions during core formation), as has been previously suggested by experimental work (Groebner and Kohstedt, 2006). Density and compressibility differences are large and reactions with solid crystals will be considerably different. It may also be unrealistic to assume that a deformation melt network in an Fe-S system will lead to similar percolation as observed in highly interconnected basaltic melt systems, simply due to an increase in connectivity. These caveats should be taken into account when comparing results across different melt systems.

6.4 Critical evaluation of equipment and methodologies

The following section outlines some of the limitations of methodologies and techniques used to carry out experiments during this project. Emphasis will be on CT equipment and 3D visualisation, which has been the main focus of development during this project, particularly with respect to the advancement of the UoE in-house CT scanner.

6.4.1 Computed tomography

Development of in-house techniques

The in-house CT scanner at the University was relatively new at the time of starting this PhD project, and the custom-built system has been continuously developed over the ~3.5 years of its use for analysing our experimental samples. The improvement of scan quality is apparent from examination of example tomographic slices over time (Figure 6.3). Improvements have been made in several areas: issues with misalignment were evident in early scans, due to the need to manually align the source-sample-detector system, which have been partly solved by improving the mechanism of alignment and recognising the need to ensure alignment was accurate to within several μm. Improving alignment means that higher magnification scans have produced sharp reconstructions - by reducing the sample size and source-sample distance scans have been achieved down to a voxel size of 0.7μm (spatial resolution 2.1 μm), with a sharpness comparable to commercial CT scanners such as the Xradia Versa (Figure 1.12, section 1.2.2). Significant improvements were made with the purchase of a new X-ray detector system. Although the overall resolution of the new camera is lower, the speed of acquisition has been reduced allowing more projections to be captured in a smaller time-frame. This has enhanced scan quality as the effects of potential drift of the sample or X-ray spot source are decreased by shorter scan times, reducing misalignment/movement artefacts. Finally, an upgrade to the Octopus reconstruction software improved refinement of variables to optimise scan quality, and an improvement to several artefact reduction algorithms (including a more effective ring filter).

However, the issue of manual alignment remains, in that scan quality is variable depending on the exact accuracy of the alignment process (see Figure 6.3 C.). Future planned changes include installation of a more accurate alignment mechanism, which involves placing the rotary table on two orthogonal linear slide pairs, both driven by motors to allow full alignment and adjustment of sample position to be carried out remotely. Alignment will therefore be possible using the sliding mechanism while X-rays are on, to allow more accurate fine-tuning.

Methods to improve visualisation

In addition to these physical improvements to scan quality, several general methodological adaptations have been used to improve visualisation where possible in experimental samples. For example, using a more homogeneous, generally slightly larger starting grain size increases overall size of features and therefore makes them more resolvable in scans of several μm voxel size. The dual capsule design used in *in-situ* experiments was also created to ensure melt movement was on a large enough scale to be resolvable despite the low scan quality during

ESRF beamtime. Another important factor is ensuring contrast is high, but not too high to create streak/star artefacts or shadowing. The FeS-olivine system is at the limit of contrast and relatively high X-ray energies, in combination with physical filters, had to be used to ensure minimal shadowing. Initial experimental samples included platinum strain markers, but these were found to cause significant shadowing, complicating reconstructions, and were removed from later experiments. In terms of the doping technique used, it was clear that certain experimental conditions were required to minimise the presence of hafnia crystals, reducing complexity and allowing more reliable segmentation.

These adaptations are not always directly compatible with appropriate experimental design, which is a limitation of the CT technique. A compromise has to be made between optimising visualisation and making experiments comparable to earlier studies / realistic to Earth conditions. The increase in grain size in basaltic samples, for example, may have changed processes occurring within the sample (e.g. increasing the frequency of hydro-fracture). This also means comparisons between scans are sometimes ineffective. For example, the growth of grains in undeformed samples made scans easy to segment and produced high quality 3D geometries, while dynamic recrystallisation in deformed samples made textures difficult to characterise fully. At current resolution limitations, it may be sensible to design future experiments taking into account these variations, to ensure samples are fully comparable. This may mean limiting experiments to undeformed samples, or large melt fractions, unless nano-tomographic techniques are available to fully constrain geometry of finer features. These have the additional flaw of requiring a very small field of view, which may be too small to truly constrain features in undeformed samples of large grain size. A multi-resolution approach will allow the best comparison between samples of varying feature size.

CT vs. other visualisation techniques

X-ray CT was chosen as a method to visualise experimental samples over techniques of serial sectioning due to the non-destructive nature of the technique, and ability to create a large number 3D datasets of isotropic resolution with relative ease. This is certainly true for sample volumes in micro-CT. Over the course of the project it became clear, however, that certain features were too small to be resolvable using micro-CT resolution. Nano-CT preparation requires sample sizes of 65 or 15 μm diameter, which makes sample preparation destructive, therefore this advantage is lost, but in comparison to the latest serial sectioning work by Garapic et al. (2013), the isotropic resolution is still an advantage to avoid interpolation, and the relative ease of sample preparation makes it more realistic to scan several samples for comparison. At the ultra-nano resolution the advantage is less clear. The 15μm field of view requires sample preparation using a focused ion beam, a technique which could theoretically also be used for high precision serial sectioning. Several studies have used dual FIB-SEM equipment for serial

sectioning of samples of up to ~50μm diameter, with 100nm thickness layers (2nm precision), which also allows full characterisation of each layer by SEM/BSE, EDS and EBSD (Groeber et al., 2006; Uchic et al., 2006). It may be that the advantages of serial sectioning at this sample size outweigh those of ultra-nano-CT, particularly as CT scans at this scale are often reduced in quality due to even very small sample drift. A combination of micro-CT scans, followed by serial sectioning in combination with EDS and EBSD techniques, may allow a more thorough ground-truthing and near-3D characterisation of structure and composition of experimental samples.

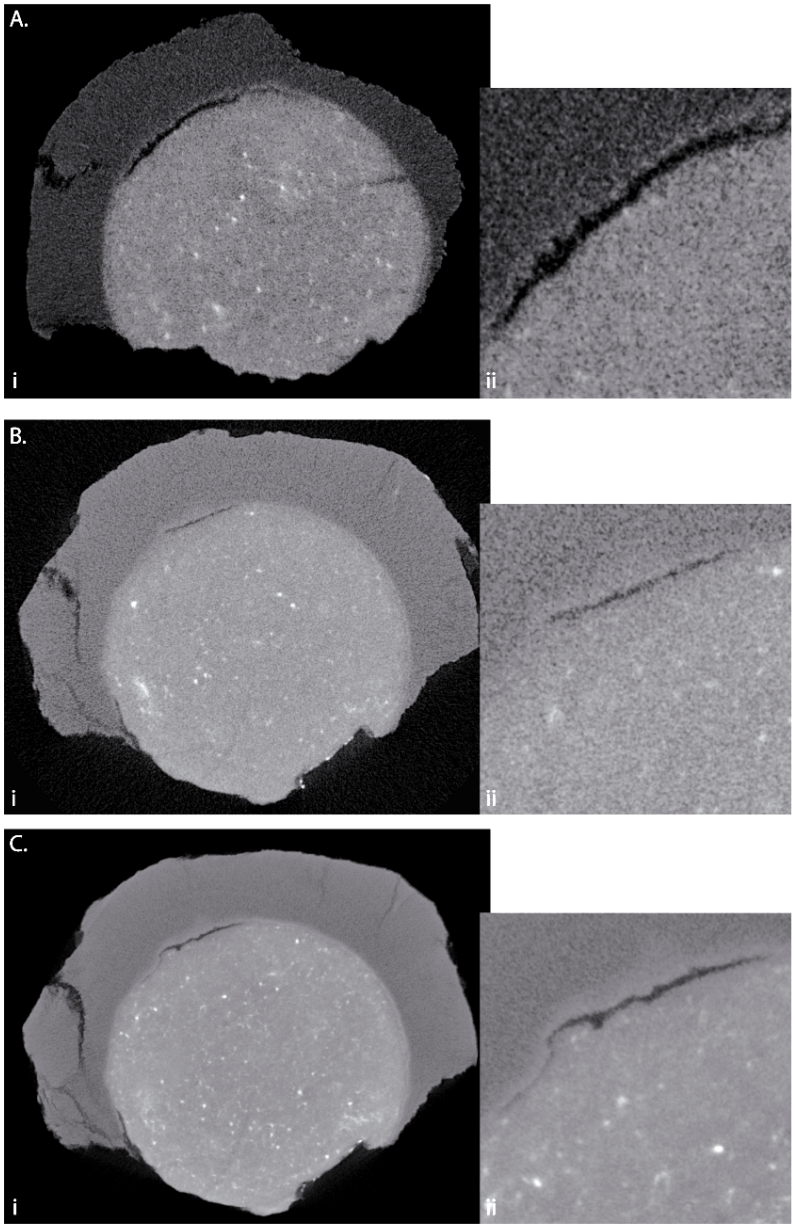

Figure 6.3: Comparison of two CT scans produced using the Edinburgh University *in-house* microCT system of the same sample FeOl2. The sample is of the FeS-olivine system (central section) surrounded by external MgO capsule, inner diameter of capsule is 2mm. i. full slice, ii. larger scale inset. A. Scan from February 2012, voxel size 2.2µm, estimated spatial resolution 3.0µm. B. Scan from August 2013, voxel size 1.8µm, sr 2.8µm. Improved resolution comes from improved methods of alignment, which also allows the sample to be moved closer to the source, increasing magnification. C. Scan using new camera, October 2014. Voxel size is 2.5µm, sr 3.5 µm. Although resolution is calculated as lower, quality of segmentation is actually improved in this final scan due to the reduction of noise and artefacts, mostly from faster scan speeds, and the use of new filtering algorithms in Octopus 8.7 (Dierick et al., 2004). A doubling effect is observed in this reconstruction from slight misalignment, although this is not present in every scan.

6.4.2 Experimental equipment

Piston cylinder for static experiments

In general, the piston cylinder experiments have given reliable results, to allow development of equilibrium textures as a standard to compare to deformation experiments. However, some issues were found, particularly in basaltic melt experiments, with partial melting of olivines at temperatures significantly below the expected solidus. This occurred both in the FeS-olivine system and in basaltic melt experiments, and may be due to the presence of graphite and talc in the sample assembly creating reducing conditions (G. Bromiley, pers. comm.). The fact that melting occurs mostly at the sample edge supports the link to the graphite capsule. Another issue was the lack of textural equilibrium in basaltic samples due to a thermal (or melt fraction) gradient (section 5.3). It may be that this is related to the previous issue, as basaltic melt is seen to flow towards regions of partial melt, therefore using different capsule materials to control the oxygen fugacity could improve both factors in future experiments. If a thermal gradient from temperature variations within the sample assembly is the cause of the melt migration, it may be more difficult to find a solution to the issue.

roPEC and rotoPEC equipment in relation to partial melting experiments

The newly designed rotoPEC and roPEC equipment for torsional deformation have been thoroughly evaluated over the course of this work. The equipment has been shown to have distinct advantages and limitations:

Advantages

- roPEC and rotoPEC equipment allows stable experiments to be carried out at very low strain-rates at high P-T and over long durations, making it possible to conduct experiments at more realistic conditions than possible in previous deformation experiments.
- the transportable nature of the rotoPEC design has allowed its installation in two different synchrotron beamlines using *in-house* equipment available to carry out CT scans using the dual rotation of motors within the confining pressure frame.

Limitations

- Deformation experiments above a certain strain-rate have been shown to cause damage to the sample assemblies in high T runs, including the graphite furnaces (Chapter 4) suggesting experiments to high strains and strain-rates may be difficult to achieve using this equipment at these conditions. This means experiments are not easily comparable to

many previous studies of partial melt and deformation, and certain features, such as melt bands or strongly aligned melt pockets in basaltic melt experiments will not be easily achievable (Chapter 4). Unless the design can be improved to increase stability, it may be that experimental design will have to take this limitation into account, potentially limiting the application of this equipment to certain geological systems.

- The lack of a direct temperature measure has been shown to be an issue during deformation experiments. Although off-line experiments using temperature calibrations appeared effective for roPEC experiments, experiments carried out on the rotoPEC for *in-situ* work (chapter 5) highlighted problems of uncertainty in temperature measurement, which may also have affected basaltic melt experiments in previous work (section 5.3). It is possible that the power-temperature relationship changes over the course of an experiment, requiring a direct measure of temperature for individual experiments to accurately constrain P-T conditions.

- The motors were found to be limited to relatively low speeds of rotation, meaning truly *in-situ* 3D tomography capturing melt migration was limited. In its current design, melt migration is still best observed using 2D radiography.

The rotoPEC is a new design in its second iteration, and is still in development (Julien Phillippe, doctorial thesis, *in prep*). There is scope to improve equipment for *in-situ* melt migration techniques. Some potential future developments are already in progress and could be useful, particularly to improve *in-situ* melt migration experiments:

- Using sintered diamond anvils to increase vertical field of view and stop the reduction in field of view by anvils closing over the course of the experiment. These anvils already exist for other Paris-Edinburgh presses and could potentially be used in future experiments.

- Various improvements could be made to decrease tomography scan time, which may eventually allow collection of true 4D data from rotoPEC experiments. Using more powerful motors could increase speed of stable rotation, although the high confining pressures used put motors under a large amount of strain so the improvements that can be made here are likely to be limited. An alternative method would be to place the rotoPEC equipment on a tomographic stage with its own rotation. The stage would rotate the full frame, causing problems with the confining metal frame blocking X-ray transparency. Algorithms have been developed to allow reasonable tomographic reconstruction even with missing data (e.g. with a 160° rotation), so it may be possible to cope with the loss of data, although scan quality will be compromised. This may be an alternative if time-resolved data of large changes in feature geometry is more important than getting the best quality tomographic data.

6.5 Ideas for future work

The broad scope and developmental nature of this PhD project means each chapter is to a certain extent preliminary. There follow some ideas for development and expansion of ideas for each area examined in chapters 3-5.

6.5.1 Core formation work

Expansion of work from chapter 3 will mostly involve confirming reproducability of experiments. The experimental results obtained are taken as evidence for the enhancement of melt permeability from deformation at lower strain-rates than previously examined, but the limited number of experimental samples limits the certainty of conclusions. More experiments have to be carried out to confirm the behaviour of samples at experimental conditions. This is particularly true as our results contradict previous studies (Walte et al., 2011) and support ideas of percolative low temperature core formation long assumed improbable by many experimentalists (Wood et al., 2006). Experiments carried out over longer timescales and potentially even lower strain-rates will help to strengthen arguments in favour of deformation-enhanced percolation of iron-rich melts. Changing melt composition (e.g. varying Fe_xS_y), and melt fractions would be simple ways to expand experimental variability and examine their effects on deformation mechanisms and melt textures.

The use of FIB serial sectioning techniques, as described in section 6.4, could be a way to further improve 3D characterisation of FeS-olivine samples, particularly with respect to olivine structure in response to deformation and changing melt permeability.

6.5.2 Basaltic melt - upper mantle work

The doping technique developed in chapter 4 still needs improvement to be a viable method for reliable comparisons between samples. It may be possible to reduce the amount of solid hafnia in samples after quench by reducing total Hf content of the melt, and/or by using a controlled atmosphere furnace to fully incorporate Hf and produce a doped glass before creating a starting mixture. An alternative may be to experiment with different heavy elements as a doping agent, such as barium or caesium, as used in previous doping experiments (Ikeda et al., 2004), or to use a different element which is more soluble in basaltic liquid (or where solubility is less temperature dependent). Once the doping technique has been optimised, it may be possible to use the method in combination with nano-CT techniques to gain high resolution images of 3D melt geometry of small regions in both deformed and undeformed samples. The increased resolution will help to reduce the uncertainty of comparing samples of varying grain-size, and, if the doping agent is fully incorporated, the melt will highlight even very finely wetted grain

boundaries. Additional changes could be made to the experimental design to encourage melt band formation, for example by adding a further solid phase to reduce permeability of the melt system, as utilised by King et al. (2010) and Holtzman and Kohlstedt (2007).

6.5.3 Ideas for development of *in-situ* work

Preliminary results from chapter 5 have already highlighted differences in melt migration processes that may have been missed due to post-quench analysis of off-line deformation studies, such as episodicity and unexpectedly high velocities of migration. Due to the limited number of successful runs, further work is required to draw firm conclusions. Although experiments had to be significantly simplified to ensure experimental success, it may now be possible to gradually increase the complexity of experiments to suit investigations of a number of geological systems (including those described above), and to systematically change variables. Ideas for further experimental adaptation include:

- For a single melt phase, change melt fraction or the volume of the source region. Is there a point at which the melt stops moving in response to its own melt overpressure? Is there a predictable relationship between melt overpressure and melt velocity?
- Change melt systems to examine *in-situ* processes with different melt mobilities / viscosities / compositions. Is there a simple correlation between melt viscosity and velocity, or do other factors complicate the relationship, as discussed in section 6.3.
- Change the composition of polycrystalline material – Sintered forsterite or MgO would be a more realistic composition than BN to represent crystalline material in the deep Earth and would therefore be a better option in terms of applicability of earth systems, if capsules can be stabilised.
- Change the grain size of the polycrystalline material to examine its effect on melt migration, formation of fractures and melt network geometry geometry. Does this change the extent of melt-enhanced embrittlement vs. plastic flow?
- Techniques such as digital volume correlation could be used to track changes in melt / fracture geometry over time. This is a technique that is becoming more popular in medical CT, which allows changes in 3D geometry to be quantified in features changing in scans of the same features over time (Bay et al., 1999). This could be used to investigate the development of fractures, changes in melt pocket volume, or changes due to deformation over the course of an experiment.
- Examine the effect of deformation on melt migration. In this case the sample capsule could be adapted to feature an off-centre hole (Figure 6.4), ensuring the melt-rich zone

undergoes maximum strain-rate deformation. The cylindrical melt-rich zone may also act as a deformation marker as it deforms. It will be possible to see if deformation promotes melt migration and, if so, whether it affects the direction of melt migration and location of flow gradients. As differential stress is known to affect the brittle behaviour within partially molten rocks, it will be particularly interesting to examine the effect of changing strain-rates on the occurrence of fractures and frequency / characteristics of melt propagation events. This will allow comparison of *in-situ* experiments to off-line deformation experiments carried out in chapters 3 and 4.

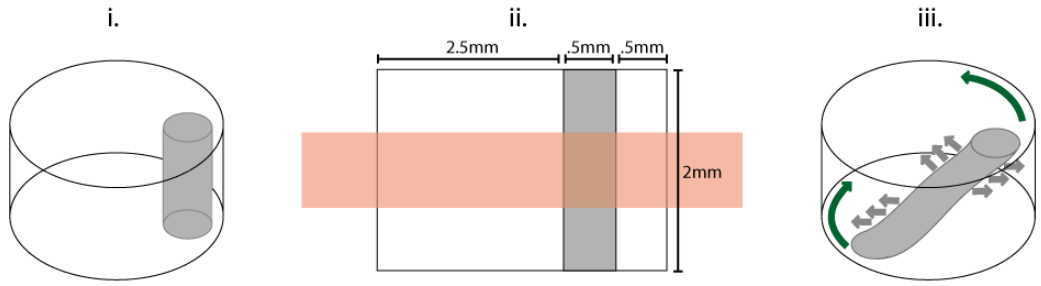

Figure 6.4: A potential design for *in-situ* deformation experiments involving an off-centre hole to contain the melt-rich starting mixture. Pink shaded areas show the area visible by X-ray during *in-situ experiments* i. 3D diagram of initial capsule design ii. cross-section showing important dimensions. iii. Schematic showing potential results of a deformation experiment. The melt-rich zone (grey) is at the edge of the capsule so that it experiences maximum intensity of deformation (green arrows). The full cylinder will be deformed, acting as a strain marker. Melt may begin to migrate away from the melt rich zone (grey arrows). The direction in which it moves may be influenced by deformation direction.

References

Abramoff, M. D., P. J. Magelhaes, and S. J. Ram (2004). “Image Processing with ImageJ”. In: *Biophotonics International* 11.7, pp. 36–42.

Anderson, D. L. and R. L. Kovach (1968). “The composition of the terrestrial planets”. In: *Earth and Planetary Science Letters* 3, pp. 19–24.

Anderson, O. L. and D. G. Isaak (2002). “Another look at the core density deficit of Earth’s outer core”. In: *Physics of the Earth and Planetary Interiors* 131.1, pp. 19–27.

Anderson, O. L., D. G. Isaak, and S. Yamamoto (1989). “Anharmonicity and the equation of state for gold”. In: *Journal of Applied Physics* 65.4, pp. 1534–1543.

Arbaret, L., M. Bystricky, and R. Champallier (2007). “Microstructures and rheology of hydrous synthetic magmatic suspensions deformed in torsion at high pressure”. In: *Journal of Geophysical Research: Solid Earth* 112.B10.

Arzi, A. A. (1978). “Critical phenomena in the rheology of partially melted rocks”. In: *Tectonophysics* 44.1, pp. 173–184.

AveLallemant, H. G. and N. L. Carter (1970). “Syntectonic recrystallization of olivine and modes of flow in the upper mantle”. In: *Geological Society of America Bulletin* 81.8, pp. 2203–2220.

Bagdassarov, N., G. J. Golabek, G. Solferino, and M. W. Schmidt (2009). “Constraints on the FeS melt connectivity in mantle silicates from electrical impedance measurements”. In: *Physics of the Earth and Planetary Interiors* 177.3, pp. 139–146.

Bagdassarov, N. and H. Pinkerton (2004). “Transient phenomena in vesicular lava flows based on laboratory experiments with analogue materials”. In: *Journal of Volcanology and Geothermal Research* 132.2, pp. 115–136.

Bai, L., D. R. Baker, and M. Rivers (2008). “Experimental study of bubble growth in Stromboli basalt melts at 1 atm”. In: *Earth and Planetary Science Letters* 267.34, pp. 533–547.

Ballhaus, C. and D. J. Ellis (1996). “Mobility of core melts during Earths accretion”. In: *Earth and Planetary Science Letters* 143.1-4, pp. 137–145.

Bay, B. K., T. S. Smith, D. P. Fyhrie, and M. Saad (1999). “Digital volume correlation: Three-dimensional strain mapping using X-ray tomography”. In: *Experimental Mechanics* 39.3, pp. 217–226.

Bear, J. (1972). *Dynamics of fluid flow in porous media*. American Elsevier Publishing Company.

Beghein, C. and J. Trampert (2004). “Probability density functions for radial anisotropy: implications for the upper 1200 km of the mantle”. In: *Earth and Planetary Science Letters* 217.1, pp. 151–162.

Berg, M. (2010). *Core Formation in Deforming Terrestrial Planets and Planetesimals*. Misc.

Berger, M. J., J. H. Hubbell, S. M. Seltzer, J. Chang, J. S. Coursey, R. Sukumar, D. S. Zucker, and K. Olsen (1998). “XCOM: photon cross sections database”. In: *NIST Standard reference database* 8.1, pp. 3587–3597.

Bizzarro, M., J. A. Baker, H. Haack, and K. L. Lundgaard (2005). “Rapid timescales for accretion and melting of differentiated planetesimals inferred from Al-26-Mg-26 chronometry”. In: *Astrophysical Journal* 632.1, pp. L41–L44.

Blairs, S. and U. Joasoo (1980). “Sound velocity and compressibility in liquid metals”. In: *Journal of Inorganic and Nuclear Chemistry* 42.11, pp. 1555–1558.

Boudier, F. (1991). “Olivine xenocrysts in picritic magmas”. In: *Contributions to Mineralogy and Petrology* 109.1, pp. 114–123.

Bromiley, G. D., S. A. T. Redfern, Y. Le Godec, G. Hamel, and S. Klotz (2009). “A portable high-pressure stress cell based on the V7 Paris-Edinburgh apparatus”. In: *High Pressure Research* 29.2, pp. 306–316.

Bruhn, D., N. Groebner, and D. L. Kohlstedt (2000). “An interconnected network of core-forming melts produced by shear deformation”. In: *Nature* 403.6772, pp. 883–886.

Buades, A., B. Coll, and J.-M. Morel (2005). “A non-local algorithm for image denoising”. In: *Computer Vision and Pattern Recognition, 2005. CVPR 2005. IEEE Computer Society Conference*. Vol. 2, pp. 60–65.

Burnley, P. C., C. J. Cline II, and A. Drue (2013). “Kinking in Mg2GeO4 olivine: An EBSD study”. In: *American Mineralogist* 98, pp. 927–931.

Canup, R. M. (2008). “Accretion of the Earth”. In: *Philosophical Transactions of the Royal Society A: Mathematical, Physical and Engineering Sciences* 366.1883, pp. 4061–4075.

Carlson, W. D., T. Rowe, R. A. Ketcham, and M. W. Colbert (2003). "Applications of high-resolution X-ray computed tomography in petrology, meteoritics and palaeontology". In: *Geological Society, London, Special Publications* 215.1, pp. 7–22.

Carter, N. L. and H. G. Ave'Lallemant (1970). "High temperature flow of dunite and peridotite". In: *Geological Society of America Bulletin* 81.8, pp. 2181–2202.

Cheadle, M. J., M. T. Elliott, and D. McKenzie (2004). "Percolation threshold and permeability of crystallizing igneous rocks: The importance of textural equilibrium". In: *Geology* 32.9, pp. 757–760.

Chen, J., Y. Wang, S. Duffy, G. Shen, and L. P. Dobrzhinetskaya (2011). *Advances in high-pressure techniques for geophysical applications*. Elsevier.

Chou, C.-L. (1978). "Fractionation of siderophile elements in the Earth's upper mantle". In: *Lunar and Planetary Science Conference Proceedings*. Vol. 9, pp. 219–230.

Coble, R. L. (1963). "A Model for Boundary Diffusion Controlled Creep in Polycrystalline Materials". In: *Journal of Applied Physics* 34.6, pp. 1679–1682.

Connolly, J. A. D., M. B. Holness, D. C. Rubie, and T. Rushmer (1997). "Reaction-induced microcracking: An experimental investigation of a mechanism for enhancing anatectic melt extraction". In: *Geology* 25.7, pp. 591–594.

Connolly, J. A. D. and Y. Y. Podladchikov (2007). "Decompaction weakening and channeling instability in ductile porous media: Implications for asthenospheric melt segregation". In: *Journal of Geophysical Research-Solid Earth* 112.B10.

Connolly, J. A. D., M. W. Schmidt, G. Solferino, and N. Bagdassarov (2009). "Permeability of asthenospheric mantle and melt extraction rates at mid-ocean ridges". In: *Nature* 462.7270, pp. 209–212.

Cook, R. L., C. A. Herbst, and H. E. King (1993). "High-pressure viscosity of glass-forming liquids measured by the centrifugal force diamond anvil cell viscometer". In: *The Journal of Physical Chemistry* 97.10, pp. 2355–2361.

Cooper, R. F. and D. L. Kohlstedt (1982). *Interfacial energies in the olivine basalt system*, pp. 217–228.

Cordier, P., J. Amodeo, and P. Carrez (2012). "Modelling the rheology of MgO under Earth's mantle pressure, temperature and strain rates". In: *Nature* 481.7380, pp. 177–180.

Craddock, P. R., J. M. Warren, and N. Dauphas (2013). "Abyssal peridotites reveal the near-chondritic Fe isotopic composition of the Earth". In: *Earth and Planetary Science Letters* 365, pp. 63–76.

Daines, M. J. and D. L. Kohlstedt (1997). “Influence of deformation on melt topology in peridotites”. In: *Journal of Geophysical Research-Solid Earth* 102.B5, pp. 10257–10271.

Daines, M. J. and F. M. Richter (1988). “An experimental method for directly determining the interconnectivity of melt in a partially molten system”. In: *Geophysical Research Letters* 15.13, pp. 1459–1462.

Datchi, F., A. Dewaele, Y. Le Godec, and P. Loubeyre (2007). “Equation of state of cubic boron nitride at high pressures and temperatures”. In: *Physical Review B* 75.21, p. 214104.

Davidson, C., S. M. Schmid, and L. S. Hollister (1994). “Role of melt during deformation in the deep crust”. In: *Terra Nova* 6.2, pp. 133–142.

Deer, W. A., R. A. Howie, and J. Zussman (1992). *An introduction to the rock-forming minerals*. Vol. 696. Longman London.

DellAngelo, L. N. and J. Tullis (1988). “Experimental deformation of partially melted granitic aggregates”. In: *Journal of Metamorphic Geology* 6.4, pp. 495–515.

Dierick, M., B. Masschaele, and L. Van Hoorebeke (2004). “Octopus, a fast and user-friendly tomographic reconstruction package developed in LabView (R)”. In: *Measurement Science and Technology* 15.7, pp. 1366–1370.

Dobson, D. P., P. G. Meredith, and S. A. Boon (2002). “Simulation of subduction zone seismicity by dehydration of serpentine”. In: *Science* 298.5597, pp. 1407–1410.

Drake, M. J. and K. Righter (2002). “Determining the composition of the Earth”. In: *Nature* 416.6876, pp. 39–44.

Duliu, O. G. (1999). “Computer axial tomography in geosciences: an overview”. In: *Earth-Science Reviews* 48.4, pp. 265–281.

Dziewonski, A. M. and D. L. Anderson (1981). “Preliminary Reference Earth Model”. In: *Physics of the Earth and Planetary Interiors* 25.4, pp. 297–356.

Eggler, D. H. (1976). “Does CO2 cause partial melting in the low-velocity layer of the mantle?” In: *Geology* 4.2, pp. 69–72.

Elsasser, W. M. (1963). “Early history of the Earth”. In: *Earth science and meteorites*, pp. 1–30.

Faul, U. H. (2001). “Melt retention and segregation beneath mid-ocean ridges”. In: *Nature* 410.6831, pp. 920–923.

Faul, U. H., D. R. Toomey, and H. S. Waff (1994). “Intergranular Basaltic Melt is Distributed in Thin Elongated Inclusions”. In: *Geophysical Research Letters* 21.1, pp. 29–32.

Fei, Y. W., C. M. Bertka, and L. W. Finger (1997). “High-pressure iron sulfur compound, Fe3S2, and melting relations in the Fe-FeS system”. In: *Science* 275.5306, pp. 1621–1623.

Fei, Y., J. Li, K. Hirose, W. Minarik, J. Van Orman, C. Sanloup, W. van Westrenen, T. Komabayashi, and K. Funakoshi (2004). “A critical evaluation of pressure scales at high temperatures by in situ X-ray diffraction measurements”. In: *Physics of the Earth and Planetary Interiors* 143, pp. 515–526.

Feser, M., J. Gelb, H. Chang, H. Cui, F. Duewer, S. H. Lau, A. Tkachuk, and W. Yun (2008). “Sub-micron resolution CT for failure analysis and process development”. In: *Measurement science and technology* 19.9, p. 094001.

Forsyth, D. W., D. S. Scheirer, S. C. Webb, L. M. Dorman, J. A. Orcutt, A. J. Harding, D. K. Blackman, J. P. Morgan, R. S. Detrick, Y. Shen, C. J. Wolfe, J. P. Canales, D. R. Toomey, A. F. Sheehan, S. C. Solomon, W. S. D. Wilcock, and Melt Seismic Team (1998). “Imaging the deep seismic structure beneath a mid-ocean ridge: The MELT experiment”. In: *Science* 280.5367, pp. 1215–1218.

Frese, K., V. Trommsdorff, and K. Kunze (2003). “Olivine 100 normal to foliation: lattice preferred orientation in prograde garnet peridotite formed at high H2O activity, Cima di Gagnone (Central Alps)”. In: *Contributions to Mineralogy and Petrology* 145.1, pp. 75–86.

Funakoshi, Ken-ichi and Akifumi Nozawa (2012). “Development of a method for measuring the density of liquid sulfur at high pressures using the falling-sphere technique”. In: *Review of Scientific Instruments* 83.10.

Fusseis, F, X Xiao, C Schrank, and F De Carlo (2014). “A brief guide to synchrotron radiation-based microtomography in (structural) geology and rock mechanics”. In: *Journal of Structural Geology* 65, pp. 1–16.

Fynn, G. W. and W. J. A. Powell (1979). *The cutting and polishing of electro-optic materials*. Hilger.

Garapic, G., U. H. Faul, and E. Brisson (2013). “High-resolution imaging of the melt distribution in partially molten upper mantle rocks: evidence for wetted two-grain boundaries”. In: *Geochemistry, Geophysics, Geosystems* 14.3, pp. 556–566.

Gluckstad, J. (2000). *Phase contrast imaging*.

Gotou, H., T. Yagi, R. Iizuka, and A. Suzuki (2015). “Application of X-ray radiography to study the segregation process of iron from silicate under high pressure and high temperature”. In: *High Pressure Research* 35.2, pp. 130–138.

Green, J. F., T. K. Bolland, and J. W. Bolland (1976). “Theoretical elastic behavior for hexagonal boron nitride”. In: *The Journal of Chemical Physics* 64.2, pp. 656–662.

Greenwood, R. C., I. A. Franchi, A. Jambon, and P. C. Buchanan (2005). "Widespread magma oceans on asteroidal bodies in the early Solar System". In: *Nature* 435.7044, pp. 916–918.

Gregg, P. M., L. B. Hebert, L. G. J. Montesi, and R. F. Katz (2012). "Geodynamic Models of Melt Generation and Extraction at Mid-Ocean Ridges". In: *Oceanography* 25.1, pp. 78–88.

Groeber, M. A., B. K. Haley, M. D. Uchic, D. M. Dimiduk, and S. Ghosh (2006). "3D reconstruction and characterization of polycrystalline microstructures using a FIB-SEM system". In: *Materials Characterization* 57.4, pp. 259–273.

Groebner, N. and D. L. Kohstedt (2006). "Deformation-induced metal melt networks in silicates: Implications for core-mantle interactions in planetary bodies". In: *Earth and Planetary Science Letters* 245.3-4, pp. 571–580.

Gueguen, Y. and J. Dienes (1989). "Transport properties of rocks from statistics and percolation". In: *Mathematical geology* 21.1, pp. 1–13.

Gutenberg, B. (1948). "On the layer of relatively low wave velocity at a depth of about 80 kilometers". In: *Bulletin of the Seismological Society of America* 38.2, pp. 121–148.

— (1954). "Low-velocity layers in the Earth's mantle". In: *Geological Society of America Bulletin* 65.4, pp. 337–338. DOI: 10.1130/0016-7606(1954)65[337:LLITEM]2.0.CO;2.

Gutenberg, Beno (1926). "Untersuchungen zur Frage, bis zu welcher Tiefe die Erde kristallin ist". In: *Z. Geophys* 2, pp. 24–29.

Halliday, A. N. (2013). "Earth science: Small differences in sameness". In: *Nature* 497.7447, pp. 43–45.

Hammersley, A. P. (1998). *FIT2D V9.129 Reference Manual V3.1*. ESRF97HA02T. ESRF Internal Report.

Hammond, W. C. and E. D. Humphreys (2000). "Upper mantle seismic wave velocity: Effects of realistic partial melt geometries". In: *Journal of Geophysical Research: Solid Earth* 105.B5, pp. 10975–10986.

Hebert, L. B. and L. G. J. Montesi (2010). "Generation of permeability barriers during melt extraction at mid-ocean ridges". In: *Geochemistry Geophysics Geosystems* 11.

Heilbronner, Renee and Steve Barrett (2013). *Image analysis in earth sciences: microstructures and textures of earth materials*. Vol. 129. Springer Science.

Herring, C. (1950). "Diffusional viscosity of a polycrystalline solid". In: *Journal of Applied Physics* 21.5, pp. 437–445.

Hier-Majumder, S., P. H. Leo, and D. L. Kohstedt (2004). “On grain boundary wetting during deformation”. In: *Acta Materialia* 52.12, pp. 3425–3433.

Hirth, G. and D. L. Kohlstedt (1995). “Experimental constraints on the dynamics of the partially molten upper mantle: deformation in the diffusion creep regime”. In: *Journal of Geophysical Research* 100.B2, pp. 1981–2001.

— (1996). “Water in the oceanic upper mantle: Implications for rheology, melt extraction and the evolution of the lithosphere”. In: *Earth and Planetary Science Letters* 144.1-2, pp. 93–108.

Holtzman, B. K., N. J. Groebner, M. E. Zimmerman, S. B. Ginsberg, and D. L. Kohlstedt (2003). “Stress-driven melt segregation in partially molten rocks”. In: *Geochemistry, Geophysics, Geosystems* 4.5.

Holtzman, B. K. and J. Kendall (2010). “Organized melt, seismic anisotropy, and plate boundary lubrication”. In: *Geochemistry, Geophysics, Geosystems* 11.12.

Holtzman, B. K. and D. L. Kohlstedt (2007). “Stress-driven Melt Segregation and Strain Partitioning in Partially Molten Rocks: Effects of Stress and Strain”. In: *Journal of Petrology* 48.12, pp. 2379–2406.

Holtzman, B. K., D. L. Kohlstedt, M. E. Zimmerman, F. Heidelbach, T. Hiraga, and J. Hustoft (2003). “Melt segregation and strain partitioning: Implications for seismic anisotropy and mantle flow”. In: *Science* 301.5637, pp. 1227–1230.

Holzheid, A., P. Sylvester, H. S. C. O’Neill, D. C. Rubie, and H. Palme (2000). “Evidence for a late chondritic veneer in the Earth’s mantle from high-pressure partitioning of palladium and platinum”. In: *Nature* 406.6794, pp. 396–399.

Hong, X., G. Shen, V. B. Prakapenka, M. L. Rivers, and S. R. Sutton (2007). “Density measurements of noncrystalline materials at high pressure with diamond anvil cell”. In: *Review of Scientific Instruments* 78.10.

Hunt, P. K., P. Engler, and C. Bajsarowicz (1988). “Computed Tomography as a Core Analysis Tool: Applications Instrument Evaluation and Image Improvement Techniques”. In: *Journal of petroleum technology* 40.09, pp. 1–203.

Hustoft, J. W. and D. L. Kohlstedt (2006). “Metal-silicate segregation in deforming dunitic rocks”. In: *Geochemistry Geophysics Geosystems* 7.

Ikeda, S., T. Nakano, A. Tsuchiyama, K. Uesugi, Y. Suzuki, K. Nakamura, Y. Nakashima, and H. Yoshida (2004). “Nondestructive three-dimensional element-concentration mapping of a Cs-doped partially molten granite by X-ray computed tomography using synchrotron radiation”. In: *American Mineralogist* 89.8-9, pp. 1304–1313.

Ismail, W. B. and D. Mainprice (1998). “An olivine fabric database: an overview of upper mantle fabrics and seismic anisotropy”. In: *Tectonophysics* 296.1, pp. 145–157.

Jackson, I. (2007). “Properties of rocks and minerals: Physical origins of anelasticity and attenuation in rock”. In: *Treatise on geophysics*, pp. 493–525.

Jacobsen, S. B. (2004). *The Hf-W Isotopic System and the Origin of the Earth and Moon*.

Jamieson, J. C., J. N. Fritz, and M. H. Manghnani (1982). “Pressure measurement at high temperature in X-ray diffraction studies: gold as a primary standard”. In: *High-pressure research in Geophysics* 12, pp. 27–48.

Jin, Z.-M., H. W. Green, and Y. Zhou (1994). “Melt topology in partially molten mantle peridotite during ductile deformation”. In: *Nature* 372.6502, pp. 164–167.

Johns, R. A., J. S. Steude, L. M. Castanier, and P. V. Roberts (1993). “Nondestructive measurements of fracture aperture in crystalline rock cores using X ray computed tomography”. In: *Journal of Geophysical Research: Solid Earth* 98.B2, pp. 1889–1900.

Jones, J. H. and M. J. Drake (1986). “Geochemical constraints on core formation in the Earth”. In: *Nature* 322.6076, pp. 221–228.

Jung, H. and S. Karato (2001). “Water-induced fabric transitions in olivine”. In: *Science* 293.5534, pp. 1460–1463.

Jurewicz, S. R. and A. J. G. Jurewicz (1986). “Distribution of apparent angles on random sections with emphasis on dihedral angle measurements”. In: *Journal of Geophysical Research: Solid Earth* 91.B9, pp. 9277–9282.

Karato, S. (1998). “Some remarks on the origin of seismic anisotropy in the D layer”. In: *Earth, planets and space* 50.11-12, pp. 1019–1028.

— (2008). *Deformation of Earth Materials*. Cambridge University Press, p. 454.

— (2012). “On the origin of the asthenosphere”. In: *Earth and Planetary Science Letters* 321, pp. 95–103.

— (2014). “Does partial melting explain geophysical anomalies?” In: *Physics of the Earth and Planetary Interiors* 228, pp. 300–306.

Katz, R. F., M. Spiegelman, and B. Holtzman (2006). “The dynamics of melt and shear localization in partially molten aggregates”. In: *Nature* 442.7103, pp. 676–679.

Kelemen, P. B. and H. J. B. Dick (1995). “Focused melt flow and localized deformation in the upper mantle: juxtaposition of replacive dunite and ductile shear zones in the Josephine peridotite, SW Oregon”. In: *Journal of Geophysical Research: Solid Earth* 100.B1, pp. 423–438.

Kelemen, P. B., G. Hirth, N. Shimizu, M. Spiegelman, and H. J. B. Dick (1997). "A review of melt migration processes in the adiabatically upwelling mantle beneath oceanic spreading ridges". In: *Philosophical Transactions of the Royal Society a-Mathematical Physical and Engineering Sciences* 355.1723, pp. 283–318.

Kelemen, P. B., N. Shimizu, and V. J. M. Salters (1995). "Extraction of mid-ocean-ridge basalt from the upwelling mantle by focused flow of melt in dunite channels". In: *Nature* 375.6534, pp. 747–753.

Ketcham, R. A. (2005a). "Computational methods for quantitative analysis of three-dimensional features in geological specimens". In: *Geosphere* 1.1, pp. 32–41.

— (2005b). "Three-dimensional grain fabric measurements using high-resolution X-ray computed tomography". In: *Journal of Structural Geology* 27.7, pp. 1217–1228.

Ketcham, R. A. and W. D. Carlson (2001). "Acquisition, optimization and interpretation of X-ray computed tomographic imagery: applications to the geosciences". In: *Computers & Geosciences* 27.4, pp. 381–400.

King, D. S. H., M. E. Zimmerman, and D. L. Kohlstedt (2010). "Stress-driven Melt Segregation in Partially Molten Olivine-rich Rocks Deformed in Torsion". In: *Journal of Petrology* 51.1-2, pp. 21–42.

Kleine, T., K. Mezger, H. Palme, and C. Munker (2004). "The W isotope evolution of the bulk silicate Earth: constraints on the timing and mechanisms of core formation and accretion". In: *Earth and Planetary Science Letters* 228.1-2, pp. 109–123.

Kleine, T., C. Munker, K. Mezger, and H. Palme (2002). "Rapid accretion and early core formation on asteroids and the terrestrial planets from Hf-W chronometry". In: *Nature* 418.6901, pp. 952–955.

Kleine, T., M. Touboul, B. Bourdon, F. Nimmo, K. Mezger, H. Palme, S. B. Jacobsen, Q. Z. Yin, and A. N. Halliday (2009). "Hf-W chronology of the accretion and early evolution of asteroids and terrestrial planets". In: *Geochimica Et Cosmochimica Acta* 73.17, pp. 5150–5188.

Koeberl, C. (2006). *Impact Processes on the Early Earth: A review of the first 2.5 billion years*.

Kohlstedt, D. L. (1992). "Role of water and melts on upper mantle viscosity and strength". In: *Mantle Flow and Melt Generation at Mid-Ocean Ridges. Am. Geophys. Union, Washington DC*, pp. 103–121.

— (1993). "Structure, rheology and permeability of partially molten rocks at low melt fractions". In: *Mantle flow and melt generation at mid-ocean ridges*, pp. 103–121.

Kohlstedt, D. L. and B. K. Holtzman (2009). “Shearing melt out of the Earth: An experimentalists perspective on the influence of deformation on melt extraction”. In: *Annual Review of Earth and Planetary Sciences* 37, pp. 561–593.

Koplik, J., C. Lin, and M. Vermette (1984). “Conductivity and permeability from microgeometry”. In: *Journal of Applied Physics* 56.11, pp. 3127–3131.

Langmuir, C. H. and D. W. Forsyth (2007). “Mantle melting beneath mid-ocean ridges”. In: *Oceanography* 20.1, pp. 78–89.

Langmuir, Charles H, Emily M Klein, and Terry Plank (1993). “Petrological systematics of mid-ocean ridge basalts: Constraints on melt generation beneath ocean ridges”. In: *Mantle flow and melt generation at mid-ocean ridges*, pp. 183–280.

Lesher, CE and D Walker (1988). “Cumulate maturation and melt migration in a temperature gradient”. In: *Journal of Geophysical Research: Solid Earth 1978-2012* 93.B9, pp. 10295–10311.

Lev, Einat and Bradford H Hager (2008). “Prediction of anisotropy from flow models: A comparison of three methods”. In: *Geochemistry, Geophysics, Geosystems* 9.7.

Lindquist, W. B., S.-M. Lee, D. A. Coker, K. W. Jones, and P. Spanne (1996). “Medial axis analysis of void structure in three-dimensional tomographic images of porous media”. In: *Journal of Geophysical Research: Solid Earth (1978–2012)* 101.B4, pp. 8297–8310.

Lister, J. R. and R. C. Kerr (1991). “Fluid-mechanical models of crack propagation and their application to magma transport in dykes”. In: *Journal of Geophysical Research: Solid Earth* 96.B6, pp. 10049–10077.

Lundstrom, C. C. (2003). “Uranium-series disequilibria in mid-ocean ridge basalts: Observations and models of basalt genesis”. In: *Uranium-Series Geochemistry* 52, pp. 175–214.

Maire, E. and P. J. Withers (2014). “Quantitative X-ray tomography”. In: *International materials reviews* 59.1, pp. 1–43.

McCoy, T. J., D. W. Mittlefehldt, and L. Wilson (2006). “Asteroid Differentiation”. In: *Meteorites and the Early Solar System II*, pp. 733–745.

McKenzie, D. (1984). “The generation and compaction of partially molten rock”. In: *Journal of Petrology* 25.3, pp. 713–765.

— (1989). “Some remarks on the movement of small melt fractions in the mantle”. In: *Earth and Planetary Science Letters* 95.1-2, pp. 53–72.

Mezouar, M., P. Faure, W. Crichton, N. Rambert, B. Sitaud, S. Bauchau, and G. Blattmann (2002). “Multichannel collimator for structural investigation of liquids

and amorphous materials at high pressures and temperatures". In: *Review of Scientific Instruments* 73.10, pp. 3570–3574.

Mezouar, M., T. Le Bihan, H. Libotte, Y. Le Godec, and D. Haeusermann (1999). "Paris-Edinburgh large-volume cell coupled with a fast imaging-plate system for structural investigation at high pressure and high temperature". In: *Journal of Synchrotron Radiation* 6.6, pp. 1115–1119.

Miller, K. J., W. Zhu, L. G.J. Montesi, and G. A. Gaetani (2014). "Experimental quantification of permeability of partially molten mantle rock". In: *Earth and Planetary Science Letters* 388, pp. 273–282.

Minarik, W. G., F. J. Ryerson, and E. B. Watson (1996). "Textural entrapment of core-forming melts". In: *Science* 272.5261, pp. 530–533.

Mittlefehldt, D. W., T. J. McCoy, C. A. Goodrich, and A. Kracher (1998). "Non-chondritic meteorites from asteroidal bodies". In: *Reviews in Mineralogy and Geochemistry* 36.1, pp. 4–1.

Miyazaki, T., K. Sueyoshi, and T. Hiraga (2013). "Olivine crystals align during diffusion creep of Earth's upper mantle". In: *Nature* 502.7471, pp. 321–326.

Montagner, J.-P. and T. Tanimoto (1991). "Global upper mantle tomography of seismic velocities and anisotropies". In: *Journal of Geophysical Research: Solid Earth* 96.B12, pp. 20337–20351.

Morgan, J. P. (1987). "Melt migration beneath mid-ocean spreading centers". In: *Geophysical Research Letters* 14.12, pp. 1238–1241.

Mori, S., E. Ohtani, and A. Suzuki (2000). "Viscosity of the albite melt to 7 GPa at 2000 K". In: *Earth and Planetary Science Letters* 175.1, pp. 87–92.

Nabarro, F.R.N. (1948). "Deformation of crystals by the motion of single ions". In: *Report of conference on Strength of Solids, Physical Society, London*.

Neumann, W, D Breuer, and T Spohn (2012). "Differentiation and core formation in accreting planetesimals". In: *Astronomy & Astrophysics* 543, A141.

Nichols, F. A. (1976). "Spheroidization of rod-shaped particles of finite length". In: *Journal of Materials Science* 11.6, pp. 1077–1082.

Ofte, D. (1967). "The viscosities of liquid uranium, gold and lead". In: *Journal of nuclear materials* 22.1, pp. 28–32.

Ozerov, A., I. Ispolatov, and J. Lees (2003). "Modeling strombolian eruptions of Karymsky volcano Kamchatka Russia". In: *Journal of Volcanology and Geothermal Research* 122.3, pp. 265–280.

Pak, T., I. B. Butler, S. Geiger, M. I. J. van Dijke, and K. S. Sorbie (2015). "Droplet fragmentation: 3D imaging of a previously unidentified pore-scale process during

multiphase flow in porous media". In: *Proceedings of the National Academy of Sciences* 112.7, pp. 1947–1952.

Paradisa, P. F., T. Ishikawaa, and N. Koikeb (2008). "Density of liquid gold measured by a non-contact technique". In: *Gold Bulletin* 41.3, pp. 242–245.

Parfitt, L. and L. Wilson (2009). *Fundamentals of physical volcanology*. John Wiley and Sons.

Pavlinsky, G.V. (2008). *Fundamentals of X-ray Physics*. Cambridge International Science Publishing.

Peate, D. W. and C. J. Hawkesworth (2005). "U series disequilibria: Insights into mantle melting and the timescales of magma differentiation". In: *Reviews of Geophysics* 43.1, RG1003.

Pereiro-Lopez, E., W. Ludwig, and D. Bellet (2004). "Discontinuous penetration of liquid Ga into grain boundaries of Al polycrystals". In: *Acta Materialia* 52.2, pp. 321–332.

Perona, P. and J. Malik (1990). "Scale-space and edge detection using anisotropic diffusion". In: *Pattern Analysis and Machine Intelligence, IEEE Transactions on* 12.7, pp. 629–639.

Phipps Morgan, J., W J. Morgan, and E. Price (1995). "Hotspot melting generates both hotspot volcanism and a hotspot swell?" In: *Journal of Geophysical Research: Solid Earth* 100.B5, pp. 8045–8062.

Piermarini, G. J., R. A. Forman, and S. Block (1978). "Viscosity measurements in the diamond anvil pressure cell". In: *Review of Scientific Instruments* 49.8, pp. 1061–1066.

Plank, T. and C. H. Langmuir (1992). "Effects of the melting regime on the composition of the oceanic crust". In: *Journal of Geophysical Research: Solid Earth (1978–2012)* 97.B13, pp. 19749–19770.

Poirier, J. P. (1994). "Light-elements in the Earth's outer core - A critical review". In: *Physics of the Earth and Planetary Interiors* 85.3-4, pp. 319–337.

Raleigh, C. B. (1968). "Mechanisms of plastic deformation of olivine". In: *Journal of Geophysical Research* 73.16, pp. 5391–5406.

Renner, J., B. Evans, and G. Hirth (2000). "On the rheologically critical melt fraction". In: *Earth and Planetary Science Letters* 181.4, pp. 585–594.

Renner, J., K. Viskupic, G. Hirth, and B. Evans (2003). "Melt extraction from partially molten peridotites". In: *Geochemistry Geophysics Geosystems* 4.

Ricci, E. and R. Novakovic (2001). "Wetting and surface tension measurements on gold alloys". In: *Gold Bulletin* 34.2, pp. 41–49.

Rietmeijer, F. J. M., T. Nakamura, A. Tsuchiyama, K. Uesugi, T. Nakano, and H. Leroux (2008). “Origin and formation of iron silicide phases in the aerogel of the Stardust mission”. In: *Meteoritics & Planetary Science* 43.1-2, pp. 121–134.

Righter, K. and M. J. Drake (1996). “Core formation in Earth’s Moon, Mars, and Vesta”. In: *Icarus* 124.2, pp. 513–529.

Riley, G. N. and D. L. Kohlstedt (1991). “Kinetics of melt migration in upper mantle-type rocks”. In: *Earth and Planetary Science Letters* 105.4, pp. 500–521.

Ringwood, A. E. (1977). *Composition of the core and implications for the origin of the Earth*. Research School of Earth Sciences, Australian National University.

— (1979). *Origin of the Earth and Moon*. Vol. 1. Springer-Verlag.

Roberts, J. J., J. H. Kinney, J. Siebert, and F. J. Ryerson (2007). “Fe-Ni-S melt permeability in olivine: Implications for planetary core formation”. In: *Geophysical Research Letters* 34.14.

Rubie, D. C. and S. A. Jacobson (2015). “Mechanisms and Geochemical Models of Core Formation”. In: *arXiv preprint arXiv:1504.05417*.

Rudge, J. F., T. Kleine, and B. Bourdon (2010). “Broad bounds on Earth’s accretion and core formation constrained by geochemical models”. In: *Nature Geoscience* 3.6, pp. 439–443.

Rushmer, T., N. A. Dixon, and S. M. Clark (2015). “High pressure, down under: the first Australian high-pressure synchrotron facility for geoscience research”. In: *Australian Journal of Earth Sciences* 62.2, pp. 181–188.

Rushmer, T., N. Petford, M. Humayun, and A. J. Campbell (2005). “Fe-liquid segregation in deforming planetesimals: Coupling Core-Forming compositions with transport phenomena”. In: *Earth and Planetary Science Letters* 239.3-4, pp. 185–202.

Russell, C. T., C. A. Raymond, A. Coradini, H. Y. McSween, M. T. Zuber, A. Nathues, M. C. De Sanctis, R. Jaumann, A. S. Konopliv, and F. Preusker (2012). “Dawn at Vesta: Testing the protoplanetary paradigm”. In: *Science* 336.6082, pp. 684–686.

Rutqvist, J., Y.-S. Wu, C.-F. Tsang, and G. Bodvarsson (2002). “A modeling approach for analysis of coupled multiphase fluid flow, heat transfer, and deformation in fractured porous rock”. In: *International Journal of Rock Mechanics and Mining Sciences* 39.4, pp. 429–442.

Ruzicka, A., G. A. Snyder, and L. A. Taylor (1997). “Vesta as the howardite, eucrite and diogenite parent body: Implications for the size of a core and for large-scale differentiation”. In: *Meteoritics & Planetary Science* 32.6, pp. 825–840.

Sahijpal, S., P. Soni, and G. Gupta (2007). “Numerical simulations of the differentiation of accreting planetesimals with 26Al and 60Fe as the heat sources”. In: *Meteoritics & Planetary Science* 42.9, pp. 1529–1548.

Savage, M. K. (1999). “Seismic anisotropy and mantle deformation: what have we learned from shear wave splitting?” In: *Reviews of Geophysics* 37.1, pp. 65–106.

Scott, T. and D. L. Kohlstedt (2006). “The effect of large melt fraction on the deformation behavior of peridotite”. In: *Earth and Planetary Science Letters* 246.3, pp. 177–187.

Shanker, J., B. P. Singh, and S. K. Srivastava (2004). “Volume-temperature relationship for iron at 330 GPa and the Earth’s core density deficit”. In: *Physics of the Earth and Planetary Interiors* 147.4, pp. 333–341.

Shankland, T. J., R. J. OConnell, and H. S. Waff (1981). “Geophysical constraints on partial melt in the upper mantle”. In: *Reviews of Geophysics* 19.3, pp. 394–406.

Shankland, T. J. and H. S. Waff (1977). “Partial melting and electrical conductivity anomalies in the upper mantle”. In: *Journal of Geophysical Research* 82.33, pp. 5409–5417.

Shannon, M. C. and C. B. Agee (1996). “High pressure constraints on percolative core formation”. In: *Geophysical Research Letters* 23.20, pp. 2717–2720.

— (1998). “Percolation of core melts at lower mantle conditions”. In: *Science* 280.5366, pp. 1059–1061.

Shaw, H. R. (1963). “Obsidian-H2O viscosities at 1000 and 2000 bars in the temperature range 700 to 900C”. In: *Journal of Geophysical Research* 68.23, pp. 6337–6343.

Shearing, P. R., J. Gelb, and N. P. Brandon (2010). “X-ray nano computerised tomography of SOFC electrodes using a focused ion beam sample-preparation technique”. In: *Journal of the European Ceramic Society* 30.8, pp. 1809–1814.

Shi, C. Y., L. Zhang, W. Yang, Y. Liu, J. Wang, Y. Meng, J. C. Andrews, and W. L. Mao (2013). “Formation of an interconnected network of iron melt at Earths lower mantle conditions”. In: *Nature Geoscience* 6.11, pp. 971–975.

Sijbers, J. and A. Postnov (2004). “Reduction of ring artefacts in high resolution micro-CT reconstructions”. In: *Physics in Medicine and Biology* 49.14, N247.

Spetzler, H. and D. L. Anderson (1968). “The effect of temperature and partial melting on velocity and attenuation in a simple binary system”. In: *Journal of Geophysical Research* 73.18, pp. 6051–6060.

Spiegelman, M. and T. Elliott (1993). “Consequences of melt transport for uranium series disequilibrium in young lavas”. In: *Earth and Planetary Science Letters* 118.1-4, pp. 1–20.

Spiegelman, M. and D. McKenzie (1987). “Simple 2-D models for melt extraction at midocean ridges and island arcs”. In: *Earth and Planetary Science Letters* 83.1-4, pp. 137–152.

Sramek, O., L. Milelli, Y. Ricard, and S. Labrosse (2012). “Thermal evolution and differentiation of planetesimals and planetary embryos”. In: *Icarus* 217.1, pp. 339–354.

Steeb, S. and R. Bek (1976). “Structure and compressibility of Au-Co melts”. In: *Zeitschrift f r Naturforschung* 31.11, pp. 1348–1353.

Stevenson, D. J. (1981). “Models of the Earths core”. In: *Science* 214.4521, pp. 611–619.

Sundberg, M. and R. F. Cooper (2008). “Crystallographic preferred orientation produced by diffusional creep of harzburgite: Effects of chemical interactions among phases during plastic flow”. In: *Journal of Geophysical Research: Solid Earth* 113.B12.

Takafuji, N., K. Hirose, S. Ono, F. F. Xu, M. Mitome, and Y. Bando (2004). “Segregation of core melts by permeable flow in the lower mantle”. In: *Earth and Planetary Science Letters* 224.3-4, pp. 249–257.

Takei, Y. and B. K. Holtzman (2009). “Viscous constitutive relations of solid-liquid composites in terms of grain boundary contiguity: 2. Compositional model for small melt fractions”. In: *Journal of Geophysical Research: Solid Earth* 114.B6.

Tang, X. and J. Dong (2010). “Lattice thermal conductivity of MgO at conditions of Earths interior”. In: *Proceedings of the National Academy of Sciences* 107.10, pp. 4539–4543.

Taylor, G. J., K. Keil, T. Mccoy, H. Haack, and E. R. D. Scott (1993). “Asteroid Differentiation - Pyroclastic Volcanism to Magma Oceans”. In: *Meteoritics & Planetary Science* 28.1, pp. 34–52.

Terasaki, H., D. J. Frost, D. C. Rubie, and F. Langenhorst (2005). “The effect of oxygen and sulphur on the dihedral angle between Fe-O-S melt and silicate minerals at high pressure: Implications for Martian core formation”. In: *Earth and Planetary Science Letters* 232.3-4, pp. 379–392.

— (2007). “Interconnectivity of Fe-O-S liquid in polycrystalline silicate perovskite at lower mantle conditions”. In: *Physics of the Earth and Planetary Interiors* 161.3-4, pp. 170–176.

Terasaki, H., D. J. Frost, D. C. Rubie, and F. Langenhorst (2008). “Percolative core formation in planetesimals”. In: *Earth and Planetary Science Letters* 273.1-2, pp. 132–137.

Terasaki, H., T. Kato, S. Urakawa, K. Funakoshi, A. Suzuki, T. Okada, M. Maeda, J. Sato, T. Kubo, and S. Kasai (2001). “The effect of temperature, pressure, and sulfur content on viscosity of the Fe-FeS melt”. In: *Earth and Planetary Science Letters* 190.1-2, pp. 93–101.

Tkalcec, B. J., G. J. Golabek, and F. E. Brenker (2013). “Solid-state plastic deformation in the dynamic interior of a differentiated asteroid”. In: *Nature Geoscience* 6.2, pp. 93–97.

Tommasi, Andrea, David Mainprice, Gilles Canova, and Yvan Chastel (2000). “Viscoplastic self-consistent and equilibrium-based modeling of olivine lattice preferred orientations: Implications for the upper mantle seismic anisotropy”. In: *Journal of Geophysical Research: Solid Earth* 105.B4, pp. 7893–7908.

Tonks, W. B. and H. J. Melosh (1993). “Magma Ocean Formation due to Giant Impacts”. In: *Journal of Geophysical Research-Planets* 98.E3, pp. 5319–5333.

Tsuno, K., H. Terasaki, E. Ohtani, A. Suzuki, Y. Asahara, K. Nishida, T. Sakamaki, K. Funakoshi, and T. Kikegawa (2007). “In situ observation and determination of liquid immiscibility in the Fe-O-S melt at 3 GPa using a synchrotron X-ray radiographic technique”. In: *Geophysical Research Letters* 34.17.

Turcotte, D. L. and G. Schubert (2002). *Geodynamics*. 2nd Edition. New York: Cambridge University Press, 456 pp.

Uchic, M. D., M. A. Groeber, D. M. Dimiduk, and J. P. Simmons (2006). “3D microstructural characterization of nickel superalloys via serial-sectioning using a dual beam FIB-SEM”. In: *Scripta Materialia* 55.1, pp. 23–28.

Urakawa, S., H. Terasaki, K. Funakoshi, T. Kato, and A. Suzuki (2001). “Radiographic study on the viscosity of the Fe-FeS melts at the pressure of 5 to 7 GPa”. In: *American Mineralogist* 86.4, pp. 578–582.

Usselman, T. M. (1975). “Experimental Approach to State of Core .1. Liquidius Relations of Fe-rich portion of Fe-Ni-S System from 30 to 100 kb”. In: *American Journal of Science* 275.3, pp. 278–290.

Vernon, R. H. (2000). “Review of microstructural evidence of magmatic and solid-state flow”. In: *Visual Geosciences* 5.2, pp. 1–23.

VonBargen, N. and H. S. Waff (1986). “Permeabilities, Interfacial-areas and Curvatures of Partially Molten Systems - Results of Numerical Computation of

Equilibrium Microstructures". In: *Journal of Geophysical Research-Solid Earth and Planets* 91.B9, pp. 9261–9276.

Wade, J. and B. J. Wood (2005). "Core formation and the oxidation state of the Earth". In: *Earth and Planetary Science Letters* 236.1-2, pp. 78–95.

Walte, N. P., D. C. Rubie, P. D. Bons, and D. J. Frost (2011). "Deformation of a crystalline aggregate with a small percentage of high-dihedral-angle liquid: Implications for core and mantle differentiation during planetary formation". In: *Earth and Planetary Science Letters* 305.12, pp. 124–134.

Walter, M. J. and R. G. Tronnes (2004). "Early Earth differentiation". In: *Earth and Planetary Science Letters* 225.3-4, pp. 253–269.

Wang, Y., C. Lesher, G. Fiquet, M. L. Rivers, N. Nishiyama, J. Siebert, J. Roberts, G. Morard, S. Gaudio, and A. Clark (2011). "In situ high-pressure and high-temperature X-ray microtomographic imaging during large deformation: A new technique for studying mechanical behavior of multiphase composites". In: *Geosphere* 7.1, pp. 40–53.

Wang, Y., T. Uchida, F. Westferro, M. L. Rivers, N. Nishiyama, J. Gebhardt, C. E. Lesher, and S. R. Sutton (2005). "High-pressure x-ray tomography microscope: Synchrotron computed microtomography at high pressure and temperature". In: *Review of Scientific Instruments* 76.7.

Wark, D. A., C. A. Williams, E. B. Watson, and J. D. Price (2003). "Reassessment of pore shapes in microstructurally equilibrated rocks, with implications for permeability of the upper mantle". In: *Journal of Geophysical Research* 108.B1, p. 2050.

Warren, J. M. and G. Hirth (2006). "Grain size sensitive deformation mechanisms in naturally deformed peridotites". In: *Earth and Planetary Science Letters* 248.1, pp. 438–450.

Watson, H. C. and J. J. Roberts (2011). "Connectivity of core forming melts: Experimental constraints from electrical conductivity and X-ray tomography". In: *Physics of the Earth and Planetary Interiors* 186.3, pp. 172–182.

Wetherill, G. W. (1994). "Provenance of the Terrestrial Planets". In: *Geochimica Et Cosmochimica Acta* 58.20, pp. 4513–4520.

White, R. S., S. A. T. Redfern, and S. Chien (2012). "Episodicity of seismicity accompanying melt intrusion into the crust". In: *Geophysical Research Letters* 39.8.

Wilson, L. and K. Keil (2012). "Volcanic activity on differentiated asteroids: A review and analysis". In: *Chemie der Erde-Geochemistry* 72.4, pp. 289–321.

Wimert, J. and S. Hier-Majumder (2012). “A three-dimensional microgeodynamic model of melt geometry in the Earth’s deep interior”. In: *Journal of Geophysical Research-Solid Earth* 117.

Winter, J.D. (2001). *An Introduction to Igneous and Metamorphic Petrology*. Prentice Hall, p. 694.

Wood, B. J., M. J. Walter, and J. Wade (2006). “Accretion of the Earth and segregation of its core”. In: *Nature* 441.7095, pp. 825–833.

Yoshino, T., M. Laumonier, E. McIsaac, and T. Katsura (2010). “Electrical conductivity of basaltic and carbonatite melt-bearing peridotites at high pressures: Implications for melt distribution and melt fraction in the upper mantle”. In: *Earth and Planetary Science Letters* 295.3, pp. 593–602.

Yoshino, T., Y. Nishihara, and S. Karato (2007). “Complete wetting of olivine grain boundaries by a hydrous melt near the mantle transition zone”. In: *Earth and Planetary Science Letters* 256.3-4, pp. 466–472.

Yoshino, T., M. J. Walter, and T. Katsura (2003). “Core formation in planetesimals triggered by permeable flow”. In: *Nature* 422.6928, pp. 154–157.

— (2004). “Connectivity of molten Fe alloy in peridotite based on in situ electrical conductivity measurements: implications for core formation in terrestrial planets”. In: *Earth and Planetary Science Letters* 222.2, pp. 625–643.

Young, D. A (2003). *Mind over magma: the story of igneous petrology*. Princeton University Press.

Zhu, W., G. A. Gaetani, F. Fusseis, L. G. J. Montesi, and F. De Carlo (2011). “Microtomography of Partially Molten Rocks: Three-Dimensional Melt Distribution in Mantle Peridotite”. In: *Science* 332.6025, pp. 88–91.

Zimmerman, M. E., S. Zhang, D. L. Kohlstedt, and S. Karato (1999). “Melt distribution in mantle rocks deformed in shear”. In: *Geophysical Research Letters* 26.10, pp. 1505–1508.

Appendices

APPENDIX A

Appendix A: Additional Information

A.1 Appendix A1: Materials relating to Introduction and Methods chapters

A.1.1 EBSD Noise reduction and processing

The majority of EBSD maps created will suffer from a certain level of noise created by e.g. misindexing of diffraction bands. Although qualitative interpretation of the map data is not necessarily hindered by this noise, the use of the data for grain identification can be significantly affected, as is the interpretation of overall orientation from pole figures, as misindexed orientations can reduce the strength of a CPO within a map, by 'diluting' it with false orientations. Noise reduction on Channel5 software is carried out by either removing 'wild spikes' – single pixels of highly contrasting orientation to its surrounding neighbours, or by an extrapolation method where a pixel is replaced by the value of its neighbours when surrounded by 'n' (1-8) or more pixels of the same value. This can be carried out in one step, or by an iterative process. If used to liberally, this extrapolation technique can lead to the creation of unrealistic grain boundary textures and the growth of grains, leading to unrealistic results. The following noise reduction steps were carried out on each EBSD map created for this PhD project. The process has been developed by Dr E. Mariani, Liverpool University, and allows significant noise reduction while limiting issues of grain growth or loss of textural information from extrapolation. The process takes advantage of the band contrast map, which gives data on signal quality. Generally grain edges will be areas of poor signal quality, so by using a masking technique it is possible to stop extrapolation to pixels of low band contrast levels, limiting noise reduction to grain interiors. Maps were of varying quality, step-size and grain size, therefore the exact processing required for each map was altered accordingly. However the overall processing steps and order remains the same. Processing steps were carried out as follows, using Tango software of Channel5:

1. Band contrast data is examined using 'Current Record' function, which gives a greyscale value for individual pixels. By examining greyscale values, the boundary between dark pixels reflecting lack of data (between grains) and bright areas in crystal interiors, can be defined.

2. Using the data legend, it is possible to rescale the map to remove data below a certain band contrast value (somewhere between 60 and 100 greyscale value). This should clip areas between grains, leaving grain interiors visible. The exact value may need to be

adjusted to optimise the mask. In some experimental samples, top greyscale values (i.e. best quality) were also clipped as these represented regions of MgO that occasionally falsely indexed as olivine.

3. This clipped data range is saved as a new data subset by choosing the 'range to subset' option.

4. In the Noise Reduction menu, the new data subset can be chosen to carry out noise reduction. Extrapolation functions can be carried out more readily on the new dataset without leading to extensive grain growth:

    a. A 6- or 5- neighbourhood extrapolation (with iteration) is now carried out.

    b. Wild spikes extrapolation is carried out after the initial extrapolation to remove anomalous single pixel values.

    c. This processing step is then applied to the whole dataset.

5. If an appropriate step size is chosen in relation to grain size, 'grains' 2 pixels or less in diameter are also likely to be noise. These grains can be removed by using the 'Detect Grains' function in Tango. Grains will be listed with their diameter / area.

    a. The grain detection function operates by assuming a grain boundary has a critical mis-orientation, which can be changed by the user. We have used 10°as a misorientation value for these maps.

    b. Grains less than 2 pixels in diameter are selected and saved to a new subset.

    c. This subset can be nullified to remove data. As an example, this method will reduce a 'grain' dataset from ~17000 grains, to a more realistic ~1000 grains within a full map.

6. Removed data will lead to gaps in the dataset, which can be removed by further noise reduction, repeating step 4 with the new dataset (still using the mask).

7. A final noise reduction is carried out on the full dataset (without masking) but with a weaker extrapolation e.g. 7 neighbourhood value with iteration.

8. A final check is carried out by comparing the original dataset to the processed. The processed euler values can be overlayed in transparency onto the band contrast map and grain edges can be compared for major errors.

A.1.2 Resolution calculations of *in-house* CT scans

Chapter	Scan set	Description	s-x (a)	s-d (a+b)	x-d (b)	M	E, kV	I (mA)	spot size	rs	rd*	rtotal
Chapter 3												
	Cam3FeOl1-2	2012	18	308	290	17	100	28	1.5	24	48	**3.1**
	Cam3FeOl3	2012	14	309	295	22	100	28	1.5	32	48	**2.6**
	FeOlPC8	2013	9	287	278	32	70	26	1.5	46	48	**2.1**
	Cam3FeOl2	2013	11	287	276	26	120	46	2.4	60	48	**3.0**
	starting material	2013	5	311	306	62	60	70	2	122	48	**2.1**
	FeOlPC8	2014 (new cam)	6	399	393	67	120	43	2.5	164	200	**3.9**
	Cam3FeOl2	2014 (new cam)	5	396	391	79	120	43	2.5	196	200	**3.5**
Chapter 4												
	Pdef 1-9	full gasket	40	311	271	8	100	33	1.7	12	48	**6.3**
	Pdef1	high res	10	311	301	31	120	43	2.5	75	48	**2.9**
	Pdef2,3	high res	12	311	299	26	120	43	2.5	62	48	**3.0**
	VS3, VS4	high res	4.5	396	391.5	88	100	36	1.8	157	200	**2.9**
	VS1, TS1, TS3	high res	4	396	392	99	80	29	1.4	137	200	**2.4**
Chapter 5												
	ESRF OlBa2	full gasket	40	311	271	8	100	33	1.7	12	48	**6.3**
	ESRF OlBa2		17	311	294	18	120	43	2.5	43	48	**3.5**
	ESRF OlBa2	highest res	10	311	301	31	120	43	2.5	75	48	**2.9**
	DLS5	summer 2013	13	287	274	22	80	35	1.5	32	48	**2.6**
	DLS6		13	287	274	22	80	35	1.5	32	48	**2.6**

Table A.1: Resolution calculated for *in-house* CT scans using calculations described in section 2.3.

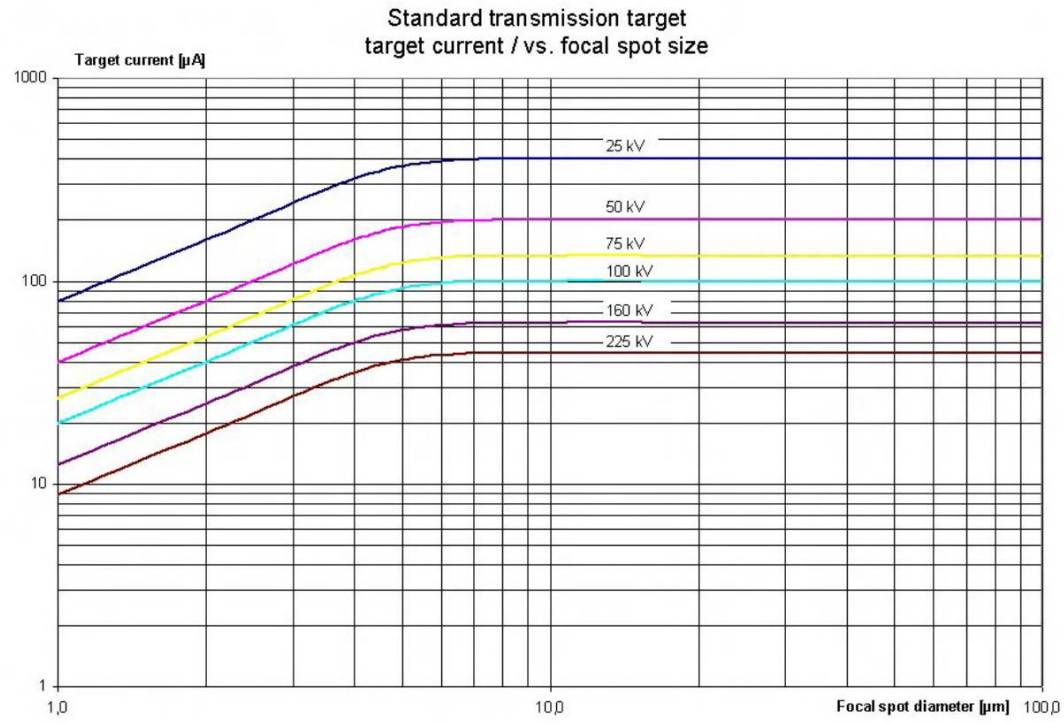

Figure A.1: Graph used to estimate spot size from energy and current of X-ray beam for the X-ray source of the University of Edinburgh in-house CT system (see previous table).

A.2 Appendix A2: Materials relating to Chapter 3

A.2.1 FeS

Olivine deformation experiments on roPEC: Experimental Logs

The following tables document experiments carried out in Cambridge using the rotational Paris-Edinburgh cell, on synthetic mixtures of olivine + FeS. Information includes time, current, voltage and power of experiment, oil pressure on the line (not equivalent to pressure on sample), and comments indicating specific notes of interest occurring during the experiment.

A.2.2 FeS

Olivine deformation experiments on roPEC: Experimental Logs

Calculation of EPMA errors (δ), as shown in table 3.2, combined errors associated with each individual point analysis (instrumental error), with the overall variation across point analyses

Date	Time / clock	A	V	Power / W	OiL P/bars	Comments
27/07/2011	17:00	10	0.49	5	100	
	17:07	41	1.58	65		
	17:09	50	1.76	88		
	17:13	58	1.9	110		
						left at P overnight but not high T, but found at 0 bars next day
28/07/2011	09:30:00				0	Found at 0 bars.
	09:38	/	/		150	
	10:39	/	/			
	10:40	20	0.88	18		Preliminary heat
		50	1.72	86		
	10:50	92	2.31	213		
	10:57	110	2.53	278		
	11:00	100	2.38	238		Heated too high - up to 350W
	12:26	117	2.6	304	150	
						Added fan to cool fown the front of ropec to cool upper anvil
	12:48					QUENCH
	13:40					START - reheat
	13:41	18	0.87	16		
		36	1.34	48		
	13:49	112	2.58	289		
	13:51	118	2.64	312		
	13:54					START ROTATION at 5rpm
	14:40	119	2.59	308		anvil rotating ok
	17:30	119	2.58	307	154	TOTAL ROTATION SO FAR = 3.5hrs = 7.7 deg
						Low temp. Over night
29/07/2011	09:30				130	
	09:31	30	0.96	29	150	
		70	1.91	134		
		100	2.37	237		
		110	2.5	275		
		120	2.62	314		

Table A.2: Deformation sample FeOl1: Experimental log

Date	Time / clock	A	V	Power / W	OiL P/bars	Comments
	09:38	125	2.67	334	168	
	09:39					Start rotation at 5rpm
	12:03	125	2.64	330		slight drop in P - extrusion?
	13:58	125	2.7	338	75	P down to 75 bars! Extrusion or movement of cell?
	14:45	125	2.66	333	150	
	17:25	125	2.66	333		P appears rel. Stable
	18:25	0	0	0		QUENCH overnight
30/07/2011	11:44				120	pump back to pressure
	11:47	30	0.97	29	150	
	11:49	50	1.48	74		
	11:51	89	2.22	198		
	11:54	120	2.63	316		
	11:55	124	2.67	331		
						Top anvil - 55 deg.
	11:59	124	2.65	329		START ROTATION, 5rpm
	14:43	124	2.64	327	170	
	17:45	125	2.64	330		QUENCH Overnight
31/07/2011	11:19				140	140 bars overnight
		31	1	31	150	
		52	1.52	79		
	11:23	124	2.66	330		
	11:38	123	2.64	325	162	
	17:16	100	2.67	267	0	Blow out! - Pumped back up to P,
	17:19	123	2.75	338	140	5rpm
	17:30					QUENCH - leave overnight
01/08/2011	09:23				120	pump back to P
		28	1	28	150	
		75	2.11	158		
		116	2.66	309		
	09:37	124	2.75	341		START ROTATION, 5rpm
	11:10	124	2.7	335		QUENCH

Table A.3: Experimental log: Sample FeOl1 continued

Cam3FeOl2						
Date	**Time**	**A**	**V**	**P / W**	**Oil P/bars**	**Comments**
01/08/2011	12:38:00	18	1.17	21	150	
		34	1.91	65		
		41	2.08	85		
	12:47	55	2.33	128		P fell slightly here as T was held
	12:49	70	2.57	180		
	12:55	90	2.81	253		
	13:00	90	2.76	248		
	13:03	101	2.93	296		
	13:05	106	2.99	317		
		112	3.05	342		~1450°: leave for 2 hours
	13:08	112	3.02	338		
	14:14	114	3.01	343		
	14:38	114	2.98	340		
	15:19	114	2.97	339		START ROTATION 50rpm
	15:43	118	2.91	343		
	15:46	123	2.96	364		
	16:39	123	2.93	360		
	18:19	123	2.92	359		3hours = 66°
						quench overnight
02/08/2011	09:47				125	Pumped back to 150
	09:55	51	1.7	87	150	
		65	2.03	132		
	09:58	87	2.43	211		
	10:01	95	2.54	241		
	10:04	114	2.8	319		
	10:11			0		Start Rotation
		114	2.79	318		
	11:19	120	2.88	346	40-150	P drop to 40 bars, tried repumping
	11:31					Quench
						P still dropping even after rotation stopped and Power off

Table A.4: Sample FeOl2: Experimental log

Date	Time / clock	A	V	Power / W	Oil Pressure/bars	Comments
02/08/2011	11:04					loaded, pressurised, rotated to make electric contact
		42	1.79	75.18		P-loss very fast
	11:11	82	2.49	204.18		T having no effect on Pressure stability
	11:31				150	P suddenly stabilised - pump to 150bars
	11:36					start heating
	11:37	25	1.1	27.5		
	11:39	50	1.89	94.5		
	11:42	61	2.16	131.76		
	11:45	81	2.55	206.55		
	11:47	91	2.68	243.88		
	11:51	107	2.89	309.23		
	11:53	121	3.03	366.63		bit too high t
	11:55	121	2.98	360.58		P still not stabilised
		115	2.91	334.65		T too high
	12:00	115	2.91	334.65		anneal for 2 hours
	13:35	115	2.88	331.2		START ROTATION at 30rpm
	13:44	115	2.84	326.6		slight P drop due to gasket flow
	14:39	115	2.82	324.3		pumped up P
	15:49	115	2.81	323.15		
	17:49					QUENCH
03-Aug	09:26				130	
	09:35	116	2.8	324.8	150	
	09:40	116	2.78	322.48		START ROTATION at 30rpm
	10:20					v slight cracking noise
	13:15	121	2.76	333.96		
	14:12	121	2.76	333.96		motor stopped!
						QUENCH

Table A.5: Experimental log: FeOl3

Date	Time / clock	A	V	Power / W	Oil Pressure/bars	Comments
04-Aug	09:00					load and repressurise
	09:39				150	p relatively stable
	09:43	34	1.75	59.5		
	09:44	57	2.3	131.1		
	09:49	64	2.37	151.68		
	09:58	81	2.62	212.22		
	10:09	90	2.65	238.5		
	10:11	101	2.84	286.84		P still not fully stable
	10:20	106	2.89	306.34		
	10:21	112	2.96	331.52		
	10:30	112	2.91	325.92		leave for 2 hours
	10:33	113	2.92	329.96		
	11:32	113	2.89	326.57		
	11:50	113	2.89	326.57		START ROT 20rpm (1.5hr anneal)
	12:25	115	2.86	328.9		
	12:52	115	2.84	326.6		
	21:25	121	2.79	337.59		QUENCH
05-Aug	09:22				120	pump back to p and reheat
	09:26	65	1.94	126.1	150	
		76	2.15	163.4		
	09:30	90	2.18	196.2		
	09:34	111	2.68	297.48		
	09:38	119	2.76	328.44		START ROTATION
	09:50	119	2.75	327.25		
	10:07					QUENCH

Table A.6: Experimental log: sample FeOl4

in the datasets. This was carried out by following error propagation methods as follows (see table A.7 for an example of how this was done for olivine (central) values.):

1. Calculate mean and standard deviation (δ_s) of dataset
2. Use instrumental errors given from EPMA raw data to calculate average instrumental error using the formula $\delta_i = \sqrt{\delta_1^2 + \delta_2^2 + ...\delta_n^2}/n$
3. Combine two errors using formula $\delta_t = \sqrt{\delta_m^2 + \delta_i^2}$

   This was carried out for each material in question.

Analysis no.	Sample	material	Wt %									
			Na	**Mg**	**Ca**	**Ti**	**Mn**	**Fe**	**Ni**	**Si**	**O**	**Total**
1	FeOl2	Ol (central)	0.0053	31.1615	0.2369	0.0003	0.0688	5.4411	0.0709	19.4921	44.4171	**100.894**
2	FeOl2	Ol (central)	-0.0046	30.9411	0.2941	0.0027	0.0686	5.6143	0.1914	19.554	44.446	**101.108**
3	FeOl2	Ol (central)	0.0009	31.2078	0.0091	0.0021	0.0862	5.4585	0.3061	19.4652	44.4	**100.936**
4	FeOl4	Ol (central)	0.0066	31.2462	0.0067	0.0019	0.0748	5.5081	0.2966	19.5838	44.5695	**101.294**
5	FeOl4	Ol (central)	-0.0002	31.32	0.0059	0.0046	0.0739	5.4848	0.295	19.5409	44.5609	**101.286**
6	FeOl4	Ol (central)	0.0016	31.2511	0.0028	-0.0004	0.0768	5.4549	0.2972	19.4949	44.4521	**101.031**
7	FeOl4	Ol (central)	-0.0018	30.4272	0.0051	0.0035	0.0701	7.0981	0.2756	19.3777	44.2414	**101.497**
8	FeOl4	Ol (central)	0.003	31.3259	0.0037	0.0027	0.073	5.4398	0.2933	19.5794	44.594	**101.315**
9	FeOl4	Ol (central)	0.009	31.2748	0.0048	0.0021	0.0594	5.6196	0.3067	19.637	44.6793	**101.593**
10	FeOl1	Ol (central)	0.0049	31.1939	0.0132	-0.0009	0.0837	5.3812	0.2882	19.4676	44.3667	**100.798**
11	FeOl1	Ol (central)	0.0073	31.3407	0.0191	0.0022	0.0772	5.5517	0.3125	19.6263	44.7031	**101.64**
12	FeOl1	Ol (central)	-0.0009	31.2054	0.0203	0.0003	0.0765	5.3289	0.295	19.5122	44.4116	**100.849**
13	FeOl1	Ol (central)	0.0007	30.7953	0.0104	0.0045	0.0605	6.2392	0.2875	19.1934	44.0318	**100.623**
14	FeOl1	Ol (central)	-0.0015	31.2364	0.007	0.0078	0.0646	5.55	0.2904	19.444	44.4123	**101.011**
15	FeOl1	Ol (central)	-0.0033	30.9743	0.0294	0.0077	0.0728	6.0135	0.0885	19.2811	44.1426	**100.607**
			Instr. error, δ									
1			0.0168	0.2139	0.0084	0.0061	0.0245	0.2296	0.0222	0.241		
2			0.0172	0.2132	0.0091	0.0061	0.0251	0.2327	0.0252	0.2414		
3			0.0174	0.2142	0.0052	0.0061	0.0245	0.2305	0.0272	0.2409		
4			0.0167	0.2141	0.0051	0.0061	0.0248	0.2309	0.0272	0.2413		
5			0.0166	0.2143	0.0051	0.0061	0.0245	0.2297	0.0272	0.241		
6			0.0167	0.2141	0.0052	0.0061	0.0248	0.2281	0.0271	0.241		
7			0.0167	0.2117	0.0051	0.0061	0.0249	0.2602	0.0271	0.2396		
8			0.0167	0.2144	0.0051	0.0061	0.0244	0.2289	0.0272	0.2414		
9			0.0173	0.2145	0.0051	0.006	0.0257	0.2335	0.0273	0.2419		
10			0.0161	0.2141	0.0053	0.0062	0.0247	0.2277	0.0272	0.2409		
11			0.0165	0.2148	0.0055	0.0062	0.0246	0.2321	0.0274	0.242		
12			0.0161	0.2144	0.0054	0.0061	0.0245	0.2272	0.0266	0.2414		
13			0.0162	0.213	0.0053	0.0061	0.0249	0.2443	0.0272	0.2391		
14			0.0163	0.2144	0.0052	0.0062	0.025	0.2324	0.0271	0.2409		
15			0.0165	0.2137	0.0055	0.0062	0.0251	0.2402	0.0232	0.24		
Average (FeOl1)			0.0012	31.1243	0.01657	0.0036	0.07255	5.67742	0.26035	19.4208	44.3447	**100.921**
sample sd / δ_s			0.00408	0.20078	0.00807	0.0037	0.0086	0.36601	0.0847	0.15782	0.23526	0.38283
measurement sd / δ_m			0.00665	0.08739	0.00219	0.00252	0.01012	0.09556	0.01081	0.09827	na	
Combined / δ_t			**0.0078**	**0.219**	**0.00837**	**0.00447**	**0.0133**	**0.378**	**0.0854**	**0.186**	**0.235**	**0.383**

Table A.7: Example of the method for calculating overall error of analyses combining instrumental error and the overall variation within the dataset. The table shows the processing of results for central olivine values (further than 100μm from edge of capsule). See text for descriptions and definition of terms.

A.3 Appendix A3: Materials relating to Chapter 4

A.3.1 Paris-Basalt Deformation Samples (Pdef Series): Experimental Logs

The following tables document laboratory experiments carried out at UPMC in Paris, France, using the rotational tomography Paris-Edinburgh cell (rotoPEC). Only those samples used for detailed analysis are described below, i.e. Pdef 1-3. In each case, the power, voltage and current of the experiment is given during pressurisation, heating and deformation. During deformation, the total degrees rotated are noted, later converted to strain and strain-rate (see chapter 4). A summary of each sample is given at the top of each table.

Sample	Pdef1						**Composition**	30% Hf-doped bas + Ol
Anneal Time	16hr	**Deformation**	10rpm	**Total Rotation**	41.91			
Date	**Time**	**Min def**	**V**	**I**	**Power**	**Pressure**	**Degrees rot**	**Comments**
25/02/2014	16:30:00							started P increase
	17:12							started heating
	17:50		3.43	119	400	120	0	START ANNEAL
26/02/2014	10:25:00	0	3.43	120	411.6	120	0	START ROTATION
	10:40:00		3.43	119	408.17	119.89	1.78	
	11:06						4.6	
	11:17						5.25	
	11:56		3.43	119	408.17	119.89	8.96	
	12:10						10.2	
	12:41		3.43	118	404.74	119.89	13.1	
	13:54		3.35	120	402	119	19.95	
	15:04		3.43	120	411	119.89	26.5	
	17:05		3.43	120	411	119	37.88	
	17:56	451	3.3	120	396		41.91	MOTOR STOPPED
	18:00		0	0	0			QUENCH

Table A.8: Experimental log: Sample Pdef1

Sample	Pdef2						**Composition**	1.5% Hf-doped bas + Ol
Tann	120	**Deformation**		10rpm				
Tdef	**min**		618		**Total rot**	**min**	55.425	
	max		1320			**max**	123.33	
Date	**Time**	**Minutes**	**V**	**I**	**Power**	**Pressure**	**Deg rot. (min)**	**Comments**
27/02/2014	12:34:00	0	3.42	118	404	119		Start annealing
	13:41	0	3.39	120	407	119		annealing
	14:32	0	3.43	117	401	124		START ROTATION
	14:45		3.43	115	394	124		current fluctuating a little
	15:17		3.43	118	405	117	4.47	falling P? And burning smell
	15:27		3.42	120	410	116		Pump recharged all ok
	15:47				0		7.03	
	16:46		3.43	118	405	123	12.584	
	17:19		3.43	119	408	122	15.62	
	17:52		3.36	120	403		18.73	
	18:11		3.39	120	407		20.53	
	18:50		3.33	120	400		24.14	
	19:28		3.34	120	401		27.72	
	20:14	342	3.42	120	410		32.1	
28/02/2014	07:40		3.21	122	392		??	Unknown total rotation overnight
	08:08		3.43	122	418			(max est. 67 °)
	10:17		3.26	122	398			START ROTATION
	11:04				400	120	36.21	
	12:25				400	120	43.8	
	13:52				400	120	50.04	Had stopped rotating earlier
	13:56				400	120		START ROTATION
	14:30				400	120	53.35	
	14:53	276			400	120	55.425	QUENCH + REMOVE

Table A.9: Experimental log: Sample Pdef2

Sample	Pdef3						**Composition**	15% Hf-doped bas + Ol
Tann	120	**Deformation**	10rpm		**min rotation**		107	
Tdef	1441				**max rotation**		136	
Date	**Time**	**Minutes def**	**V**	**I**	**Power, W**	**P, bar**	**Rot / °**	**Comments**
28/02/2014	15:00		0	0	0	123	0	Pressurising
	15:54		0	0	0		0	
	16:16		3.5	115	402.5	123	0	START ANNEALING
	16:50		3.5	113	395.5		0	
	18:16		3.47	115	399.05	123	0	
	18:23						0	START ROTATION
	18:31						0.013	
	19:22		3.44	115	395.6		0.013	No change, moved up to 10rpm
	19:44		3.46	115	397.9		2.23	
	20:20		3.46	115	397.9		5.64	
	20:43						7.74	
	21:17		3.5	104	364	105		P has dropped to 105 bars
	21:44		3.5	102	357	102	13.48	manual drop in T due to P drop
	21:52	209	0	0	0		14.29	Quench overnight
						96		P dropped to 80 overnight
01/03/2014	11:33		0	0	0	120		back up to P
	11:46		3.78	106	400.68	124		10 min anneal
	12:02		3.78	106	400.68	124	14.17	START ROTATION
	12:14		3.8	106	402.8	124	15.77	
	14:17	123.00						back to 0, started rotation again
	14:22						17.27	juddery motor?
	17:38							
	17:46		3.8	106	402.8	124		Motor not working
	18:01							Quench as motor stopped working
03/03/2014	07:35		0	0	0	124		Reheat and turn on air / motors etc
	07:51		3.85	104	400.4	124		

Table A.10: Experimental log: Sample Pdef3

Sample	Pdef3	(cont.)						
Date	**Time**	**Minutes def**	**V**	**I**	**Power, W**	**P, bar**	**Rot.**	**Comments**
	07:55		3.9	102	397.8	124		START ROTATION
	09:50		3.9	101	393.9	124	26.48	
	10:25	150	3.9	102	397.8	124	29.78	top motor stopped
	10:41		3.89	102	396.78	124		started bottom motor in opposite direction
	10:55		3.94	102	401.88	124	31.03	
	11:01	170.00					31.57	motor overheating? high mA
	11:04							START ROTATION
	11:14		3.91	102	398.82		32.59	
	11:36		3.87	102	394.74	124	34.23	
	13:52		3.87	102	394.74	124	47.42	
	14:28		3.9	102	397.8	124	50.67	
	14:57						53.44	
	15:34		3.88	102	396.78	124	56.97	
	16:19		3.9	102	396.78		61.13	
	17:22		3.9	102	397.8	124	66.66	
	18:20		3.93	102	397.8	124	72.47	
	19:03		3.97	102	405.94	124	76.55	
	19:35		3.97	102	405.96		79.5	
	20:04						81.57	
	20:34						84.69	
	20:51		4	102	404	124	86.3	
							88.54	
	22:10		4	98	392	124	93.78	
	22:25	670	4	98	392	124	95.1	quenched overnight
04/03/2014	07:48		0	0	0	124		reheated
	08:00		4.04	99	399.96	124		START ROTATION
	09:45		4.1	97	397.7	124	105.31	
	09:53	119					106.04	QUENCH

Table A.11: Experimental log: Sample Pdef3 - continued

A.4 Appendix A4: Materials relating to Chapter 5

A.4.1 In-situ experiments: Experimental Logs

The following tables detail experiments of interest carried out at ESRF for phase I and phase II of beamtime conducted there (Samples OlBa2, and AuBN1, as analysed in detail in chapter 5). The details of scans and experiments carried out at DIAMOND are already described in chapter 5 methods, therefore the detailed tables of these experiments are not shown.

		XP		Diffraction	CT	
Date	**Time**	**Power /W**	**Pump Pressure / bars**	**Diffraction Scan**	**Tomo Scan**	**Comments**
28/10/2013	8:15:00 PM	0	0	OlBa2_01		
	8:48:00 PM	0	120	OlBa2_05		P increase over 20 minutes
	9:48:00 PM	0	120		OlBa2_scan1	
	11:00:00 PM	200	120	OlBa2_06		sample seems to have shifted away from centre
	11:45:00 PM	250	120	OlBa2_07		
2:58:00 AM	11:50:00 PM	300	120	OlBa2_08		
29/10/2013	12:46:00 AM	350	120	OlBa2_09		Power at transformers 500W!
	12:50:00 AM	400	120		OlBa2_scan2	MOVEMENT IN SAMPLE!!!
	1:05:00 AM	400	120	OlBa2_10		
	2:30:00 AM	400	120		OlBa2_scan3	
	3:30:00 AM	400	120		OlBa2_scan4	
	4:40:00 AM	400	120	OlBa2_11		Lots of evidence for melting and recrystallisation
3:54:00 AM	4:44:00 AM	0	120			QUENCH
	4:54:00 AM	0	120	OlBa2_12		
	4:59:00 AM	0	120		OlBa2_scan5	FAILED SCAN - top motor stopped rotating after ~45min

Table A.12: Experimental log: Sample OlBa2

Date	Time	Power, W	Diffraction		CT	exp:	10ms	Comment
			Name	theta (200)	Name	lamda	no. proj.	
25/01/2015	22:30		AuBN1_0001					Pressurised to 100bar
	22:45	0	AuBN1_0014					Heated without diffraction patterns due to misalignment
	23:00	0			AuBN1_1	45		
26/01/2015	00:28	0						Start heating to 100, 5W/min
	00:49	100						
		200						change in shape of Au?
	01:18	200			AuBN1_2	45		gold leaves FOV
	02:10	220			AuBN1_3	45		tried rescan but not enough memory
	03:45	250						
	04:00	280						
	04:20	300						
	04:29	320						
	04:36	330						sample moving, solid creep?
	04:52	340						
	05:00	360						assembly appears stable
	05:36	300			Au BN1_4	45	1800	gold moved out of FOV so cannot reconstruct
	09:00	0						P dropped to 0 overnight, repressurised
	10:15	0	AuBN1_0015	10.41921				Diffraction w new alignment makes gold visible
		0	AuBN1_0016		AuBN1_5	55	930	m-slits widened to incr. field of view
		100						heated to 200W at5 W/min
	12:22	200						
		200	AuBN1_0018	10.42852				best scan at this T
	12:45	200			AuBN1_6	55	930	
	13:55	200	AuBN1_0020	10.42646				
	14:20	250	AuBN1_0023	10.42402				
		270	24-26	10.39624				beam optimisation

Table A.13: Experimental log: Sample AuBN1

Date	Time	Power, W	Diffraction		CT			Comment
			Name	theta (200)	Name	lamda	no. proj.	
	14:37	300	AuBN1_0027	10.39656				
		330	AuBN1_0028	10.37808				heated to 330
	15:07	360	AuBN1_0029	no peak				EVIDENCE FOR MELTING IN DIFFRACTION PATTERN
	15:14	360			movie1			
	15:19	370			movie2			incr. temp further to ensure fully molten
	15:26	370			movie3			Previous tomo scans only to 160°
	15:50	370			AuBN1_7	55	930	NB changed motor step from 214 to 240 to ensure rot to 180
	17:00	370						dropped T to 320 at 5W/min
	17:30	320	AuBN1_0030	10.43076				peaks show gold recrystallised
	18:10	320			AuBN1_8	55	930	
	19:08	320						reheating to 360 at 5W/min
	19:10	360			movie4			movie @ 1 frame every 10s for 40 min
	20:01	400			movie5			movie @ 1 frame every 20s, taken during heating
	21:01	320						reduced T for tomography
	21:19	320			AuBN1_9	55	930	avils closed during scan, cannot reconstruct
	22:07	320			movie6			movie during reheat to 400at5W/min, 300 frames
		400						
		400						
	23:23	400	AuBN1_0032	10.39079				
		400	AuBN1_0033	10.39068				Gold peaks despite high power. Furnace resistance changed?
	23:30	300						lowered T at 5W/min
	23:37	100						lowered T at 10 W/min
26/01/2015	00:14	0	AuBN1_0035					room T high P scan
								depressurising
	00:30	0	AuBN1_0036	10.72789				

Table A.14: Experimental log: AuBN1

APPENDIX B

Appendix B: Digital Appendix

This Appendix describes digital data available on the CD copy of this thesis, provided to accompany sections of this thesis where data is not fully represented using 2D figures alone. This written section gives a brief description of these additional datasets.

B.1 B1 - Movie data to accompany chapter 5

In-situ radiography was collected of sample AuBN1 during data collection at ESRF (phase II), as described in section 5.3.3. As figures cannot represent the full dataset, I have supplied the full movies associated with figures as referenced below. Movies are in the form of 3D tiffs, which can be viewed using windows photo viewer, or more effectively using ImageJ.

B.1.1 Movie2

Movie associated with figure 5.28. Time interval between frames is 1s.

normalised

Normalised using flat-field and dark current images using Octopus 3.8 using the same initial processing steps as used for tomographic projections. A selection of frames from this movie is used in figure 5.28, left-hand column.

subtractframe1

The same movie, once processed to highlight differences between frames, in the process described in section 5.3.3. The movie has been cropped to frames 1-400, representing the timeframe of interest. A selection of frames from this movie is used in figure 5.28, right-hand column.

B.1.2 Movie5

Movie associated with movements M1-M3, figures 5.30 and 5.31, and used for estimating melt velocity in section . Time interval between frames is 20s.

normalised

Normalised using flat-field and dark current images using Octopus 3.8 using the same initial processing steps as used for tomographic projections. A selection of frames from this movie is used in figures 5.30 and 5.31, left-hand column.

p1to130-p0

Movie processed to highlight changes from frame 1, as described in section 5.3.3. A selection of frames from this movie is used in figure 5.30, right-hand column.

p20to130-p20

Movie processed to highlight changes from frame 20, as described in section 5.3.3. A selection of frames from this movie is used in figure 5.31, right-hand column.